Current Applied Physics 16 (2016) 57–62

Contents lists available at ScienceDirect

Current Applied Physics

journal homepage: www.elsevier.com/locate/cap

Application of tot'hema eosin sensitized gelatin as a potential eye protection filter against direct laser radiation

Branka D. Muric*, Dejan V. Pantelic, Darko M. Vasiljevic, Svetlana N. Savic-Sevic, Branislav M. Jelenkovic

Institute of Physics, University of Belgrade, Pregrevica 118, 11080 Zemun, Serbia

ARTICLE INFO

Article history:
Received 7 July 2015
Received in revised form
11 September 2015
Accepted 25 September 2015
Available online 9 October 2015

Keywords:
Microstructure fabrication
Laser safety
Eye protection
Polymers
Optical properties
Filter
Damage

ABSTRACT

The optical limiting properties of tot'hema and eosin sensitized gelatin layer (short TESG) under continuous second harmonic Nd:YAG laser light were investigated. In contrast to classical eye protection filters the microlens formation and carbonization in TESG are the main mechanisms for eye protection from direct laser radiation. Results have shown that safety goggles made on TESG can protect the eye from up to 10 W of incident laser power. Filters for other wavelengths can be manufactured by varying the sensitizer.

© 2015 Published by Elsevier B.V.

1. Introduction

The growing number of laser applications requires development of materials which protect against laser radiation. Special attention is dedicated to eye protection, due to focussing power of the eye lens. It is well known the eye lens produces high intensities at the retina surface [1–7] potentially leading to permanent vision impairment. Different parts of the eye can be damaged, depending on the laser wavelength and intensity. UV light (<400 nm) and part of IR light (>1400 nm) damage the cornea and the eye lens, while light at wavelengths between 400 nm and 1400 nm endanger the retina, which is the most sensitive part of eye [1–7].

The usual method of eye protection is based on different types of filters, (absorption, reflection, interference, or polarization) inside goggles or protective windows [8–11]. The majority of safety filters are plastic materials which protect human eye from scattered or otherwise diffusely reflected laser light. Some manufacturers offer glass-based filters, either as absorption or thin-film interference devices. A good quality laser eye protection goggles are characterized by a very small transmission for particular laser wavelength, and high transmission of visible light. According to European laser eye protection standards EN 207 [12] and EN 208 [13] a laser goggle must be able to protect the user for a minimum of 5 s (CW laser) or 50 pulses (pulsed laser) of direct laser radiation. The maximum permissible exposure (MPE), measured at the cornea of the human eye, is the highest laser power density or energy density that is considered safe for a given wavelength and exposure time [14]. In all cases, the protection level is limited by the laser energy absorbed within the material. Above certain threshold, the material absorbs enough energy to be melted and punctured, letting the full laser power to pass-through.

Here we report on the material exhibiting three different protective mechanisms. At low powers, absorption reduces the intensity of transmitted radiation below the MPE. In the intermediate range, microlens is produced which diverges the radiation, again reducing the eye irradiance below the MPE. Finally, at high powers the material carbonizes rather than melting, thus making the irradiated zone opaque.

This paper investigates the optical limiting behaviour of tot'hema and eosin Y sensitized gelatin layer (short TESG) as well as possible application as an eye protection filter against high-power direct laser beams. The tot'hema is a mixture of Fe(II)-, Mn(II)-

* Corresponding author.
E-mail address: muric@ipb.ac.rs (B.D. Muric).

http://dx.doi.org/10.1016/j.cap.2015.09.014
1567-1739/© 2015 Published by Elsevier B.V.

and Cu(II) gluconates used in medicine for curing iron deficiencies. Eosin is an organic dye with absorption maximum about 532 nm, used in medicine, too. Previously, we have shown that TESG is an excellent optical material [15,16]. The microlens formation and dye bleaching occur simultaneously during laser exposure. Although the TESG layer is initially coloured due to presence of eosin and tot'hema, after irradiation with a 532 nm laser the dye bleaches leaving an irradiated layer with completely transparent microlenses. The process of microlenses formation is thermal as we have verified using a thermal camera [17]. The protection mechanism of the TESG layer is based on microlenses formation during the laser irradiation. The layer carbonization at higher laser power additionally protects an eye. As a result of all mentioned processes the TESG layer was able to reduce 10 W (CW operation at 532 nm) direct laser beam to the safe level.

The TESG layer is chemically stable (under the normal laboratory conditions), elastic [18] and not very sensitive to scratches and tearing. However, it is slightly sticky and dust and fingerprints may collect on the surface. In practice, the laser goggles require sandwiching of TESG between two transparent plastic plates (such as thin polycarbonate). This enables mechanical protection of the filter and goggle cleaning. Additional advantages of TESG such as easy manufacturability, low cost, non-toxicity and stability, make this layer very interesting for eye protection applications.

2. Material and methods

The layers were prepared as described in our previous papers [15,16]. The 5 g of gelatin powder (Gelatin from bovine skin gel strength ~225 g Bloom, Type B, Sigma) was swelled in 100 ml deionised water for 60 min. The gelatin is heated for 10 min in a water bath (Vela™, Cole Parmer) at 50 °C, with stirring. In order to prevent crystallization of the layer and keep elasticity, 1 g of sodium chloride (puriss. p.a. were purchased from Sigma–Aldrich) was added together with the 20 ml of tot'hema oral solution (Laboratorie Innotech International, France). At the end 0.3 ml of 1% water solution of eosin Y (5 wt.% in H_2O, Sigma–Aldrich) is supplemented. Eosin Y enhances absorption of TESG layer at 532 nm. The TESG solution is than centrifuged (Cole Parmer at 3400 rpm/min) for 30 min in order to remove impurities. In the next step the 10 ml of TESG solution is poured onto a precisely levelled and well-cleaned 2 mm thick polycarbonate (lexan) plate. The layer is dried in the dark, in relatively stable laboratory conditions. After drying, TESG layer thickness of 1 mm was obtained. The thickness of each deposited layer is an average of measurements at eight different points with a digital micrometre. The resulting layer is very elastic and sticky, and can be easily peeled and transferred to another substrate.

Protection filter prepared by adhering 1 mm thick layers of TESG on both sides of 2 mm thick transparent lexan plate was positioned 20 mm in front of a 5 mm diameter aperture, as shown in Fig. 1. The aperture is simulating the human pupil which normally opens about 2 mm in daylight, and 7 mm in the dark [19]. This configuration is analogous to laser protective goggles placed in front of eyes.

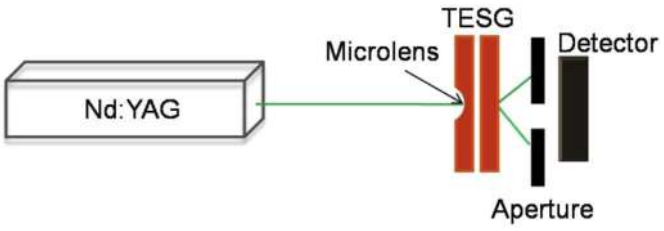

Fig. 1. Experimental setup: The transmitted power of CW laser light operating at 532 nm after passing an optical filter (made of a lexan plate sandwiched between two TESG layers) and aperture were measured by a power meter.

A 10 W, 532 nm Nd:YAG laser was used (Verdi V-10 manufactured by Coherent Inc.) to test the protective properties of TESG. The beam diameter was 2.3 mm. Transmitted laser power was measured by OPHIR power meter (NOVA II) with a photometric head placed close to the aperture (see Fig. 1). The laser power used to test TESG filter was varied between 100 mW and 10 W. Transmission spectra of TESG were analysed by a fibre-type spectrometer (Ocean Optics) with a tungsten-halogen light as illumination source. The morphology of the TESG layer and a plastic protective layer were investigated using a high resolution scanning electron microscope equipped with a high brightness Schottky field emission gun (FEGSEM).

3. Results and discussions

3.1. Power limiting and protective properties of TESG

At the beginning, we would like to emphasize the difference between TESG layer and classical plastic absorptive filters. TESG layer and one plastic filter were exposed with direct Nd:YAG laser beam at 532 nm wavelength, and power of 100 mW. After less than a second the plastic layer was perforated, as shown in Fig. 2a. In the case of TESG layer, after 10 s exposure, the microlens is formed (see Fig. 2b). The scanning electron microscopy images of a perforated hole and TESG microlens are shown in Fig. 2c and d, respectively. Important characteristic of the TESG layer is its property to bleach under the laser beam action. The bleaching (photochemical transition of eosin dye from pink to colourless state) and microlens formation occurs simultaneously during laser irradiation. The increased transmission due to bleaching is compensated by expansion of the laser beam by a microlens. As a result the irradiation level behind the microlens is constant. This is very important since bleaching prevents the layer overheating (within certain power levels) and perforating. The pink colour of TESG layer is due to eosin, but otherwise the visibility through the 1 mm thick layer is good.

3.1.1. A generic eye model and protection mechanism

To illustrate the eye protection principle, a generic model of the human eye is constructed (Fig. 3) and ray tracing is used to calculate the beam propagation through the eye [20,21]. In the case when the laser beam enters an unprotected eye (see Fig. 3a) the radiation is focused on the retina (0.17 mm spot diameter). The power density is high and retinal damage is possible.

If a protective filter, with the microlens (created under the influence of the beam) is placed in front of the eye the situation is changed. A microlens is an additional optical component between the laser beam and the human eye. It expands the beam, and only a small fraction of the radiation goes through the pupil of an eye. Even more, the radiation is not tightly focused (Fig. 3b) as in the previous situation (Fig. 3a). According to ray tracing calculation, the resulting spot on retina has 2.01 mm diameter, which is about 12 times larger compared to the direct laser beam spot size. As can be seen in Fig. 3b there are two effects– one is reduction of the amount of light transmitted through the eye pupil and another is increased size of the focused spot. The overall reduction of power density is approximately six orders of magnitude.

As we can see in Fig. 4 the protection mechanism is determined by the laser power and exposure time.

According to Fig. 4, the absorption of laser light dominates up to the laser power of 50 mW, and it doesn't affect the protective layer.

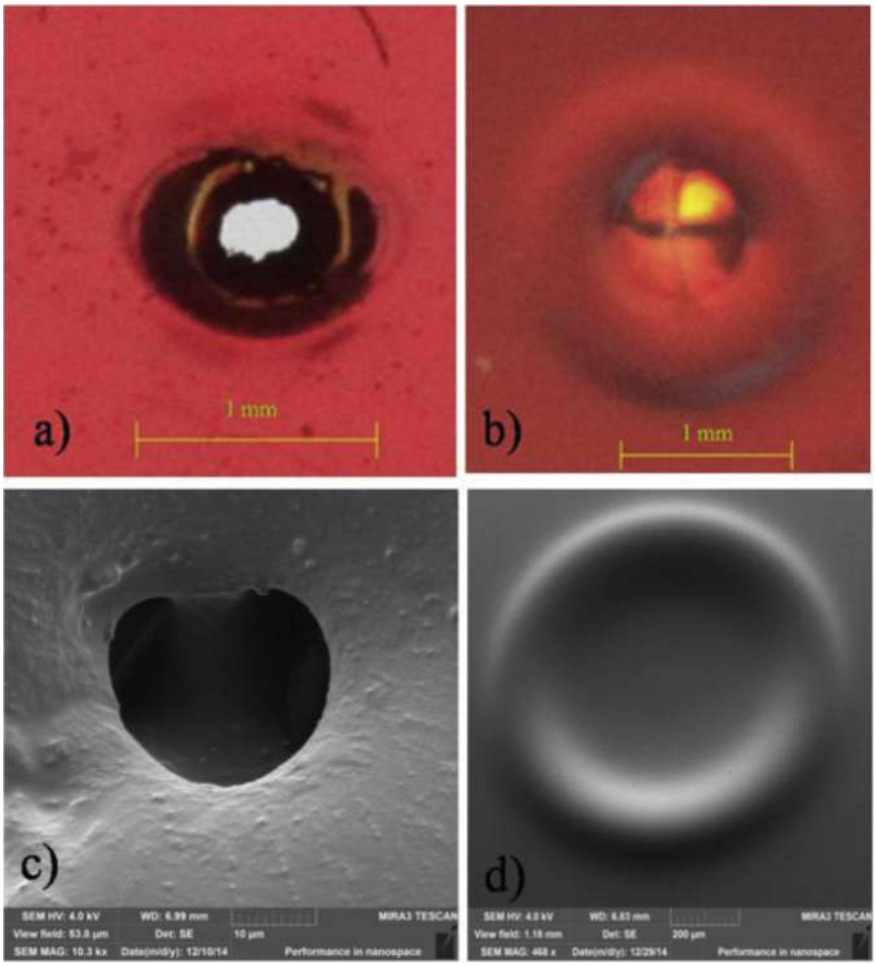

Fig. 2. Effects of the laser radiation on the layers of plastic protective material (a, c) and TESG (b, d). Images a) and b) are recorded using an optical microscope, and c) and d) are recorded using a field-emission gun scanning electron microscope.

Within this power range TESG is linear absorber for both CW and pulsed radiation, since the mechanism of laser material interaction is of thermal nature [17]. The microlens formation starts above 50 mW after certain irradiation period (see middle section in Fig. 4).

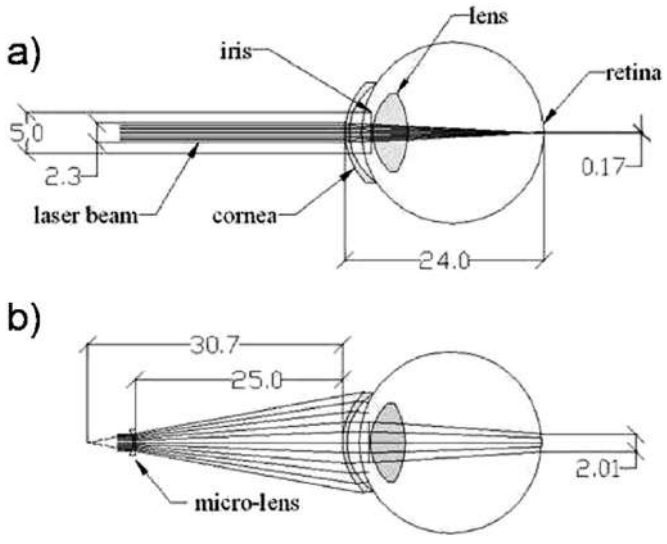

Fig. 3. The laser beam focussing by: (a) the unprotected eye (b) the eye protected with microlens forming filter. All dimensions are in millimeteres.

The laser beam diverges through the microlens. The significantly reduced energy density then reaches the second layer deposited on other side of a lexan plate, which absorbs the attenuated laser beam. Above 600 mW of laser power the protection layer starts to carbonize (right section in Fig. 4). The layer carbonization produces a localized opaque black area which further blocks the laser beam.

In order to investigate if the TESG layer can be used as an eye protection filter, the laser power behind the TESG filter was measured for different laser powers using the experimental setup from Fig. 1. The output power density after the filter (E) was calculated according to expression: $E = P/A$, where P is the measured laser power after the filter. The aperture area (A = 19.6 mm^2) corresponds to 5 mm diameter, used in our experiments.

It has to be emphasized that for laser powers above 50 mW, TESG layer goes through a sequence which starts with the absorption, continues with the microlens formation and ends with the carbonization (see Fig. 4). The duration of each part of a sequence depends on the laser power, but the transmitted power density trough the filter is always well below MPE (see Fig. 5). Since the basic mechanism is thermal, overall effect depends only on the average laser power, no matter whether the beam is pulsed or continuous. For the first 150 ms, the intensity of transmitted radiation is constant, even at the maximum measured input laser power of 9.6 W (see Fig. 5). Additionally, for shorter times MPE is higher (for 1 ms MPE is 0.01 W/cm^2, while for 1 μs, MPE is 0.8 W/cm^2). After the first 150 ms, the power density oscillates, but always

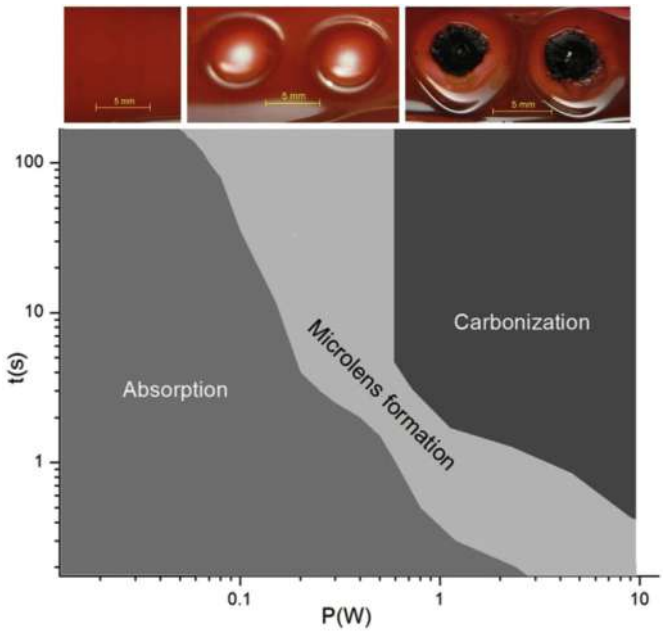

Fig. 4. The influence of the laser power (for the second harmonic Nd:YAG laser) and irradiation time on the protection mechanism of TESG filter. Note the logarithmic scale on both axes. Three photographs above the graph depict appearance of the TESG layer at different laser powers.

stays significantly below MPE (as a consequence of stochastic nature of carbonization). The reduction of output power density (0.017 mW/cm^2–0.34 mW/cm^2) is approximately six orders of magnitude compared to the input laser power density (1.5 W/cm^2–49 W/cm^2). We emphasize that output power density is always far below MPE during 7 s of exposure – although standards require period of 5 s.

3.1.2. TESG laser goggles

To demonstrate TESG filter capabilities, we made laser protective eyewear by modifying welder's goggles (see Fig. 6). The protection level can be controlled by flipping the front set of TESG filters. When the front filter set is up, the goggles offer lower protection level but allow one to see the beam and adjust the laser. If both layers are used, goggles efficiently protect from direct laser beam exposure.

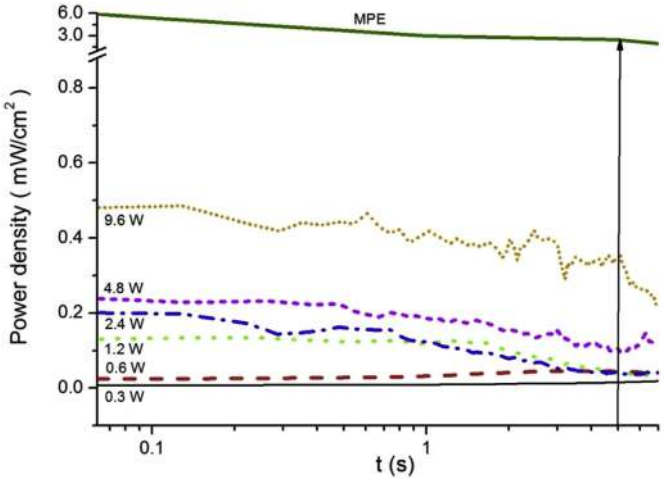

Fig. 5. Power density measured after the TESG filter vs. exposure time for different Nd:YAG laser input powers. Five measurements were made for each input laser power and the average values are shown. Note the break on the ordinate and logarithmic scale on abscissa. Numbers inside the diagram indicate input laser power.

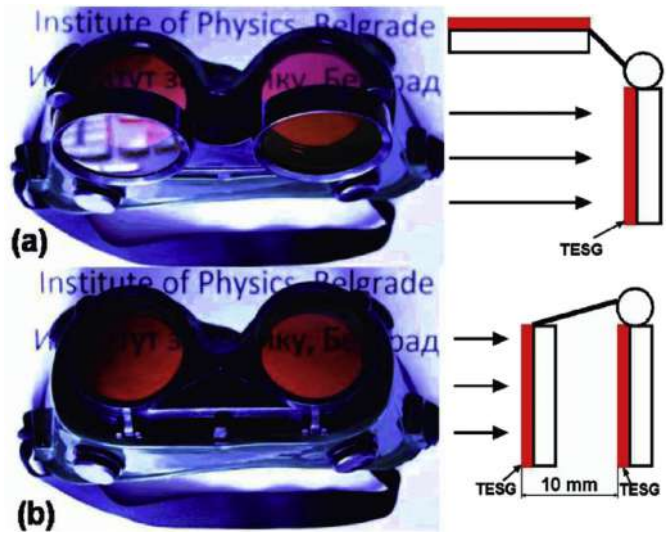

Fig. 6. Photograph of eye-protection goggles with TESG layers on both movable and stationary pair of filters of the commercial welder goggles: (a) when the first set of filters is lifted – goggles are suitable for adjustment of laser beam and (b) with both filters protecting from direct light exposure. Insets on the right schematically show the filter arrangement.

The transmitted laser power density (after 5 s) vs. input laser power density was recorded (Fig. 7). One curve is for a TESG filter and another one for laser goggles. In both cases output power density is well below MPE. Compared to TESG filter, goggles offer better protection (by about two orders of magnitude) due to 10 mm distance between two TESG layers (see Fig. 6).

Additionally, the transmission of the visible light (using white LED lamp as a light source) through TESG and commercial THORLABS LG10 glasses was also measured. Fig. 8 shows that transparency of TESG goggles is comparable with commercial THORLABS LG10.

In Fig. 9 we present a transparency of TESG goggles as a function of wavelength for one and two TESG layers. As can be seen, the 532 nm Nd:YAG laser beam transmission is very small.

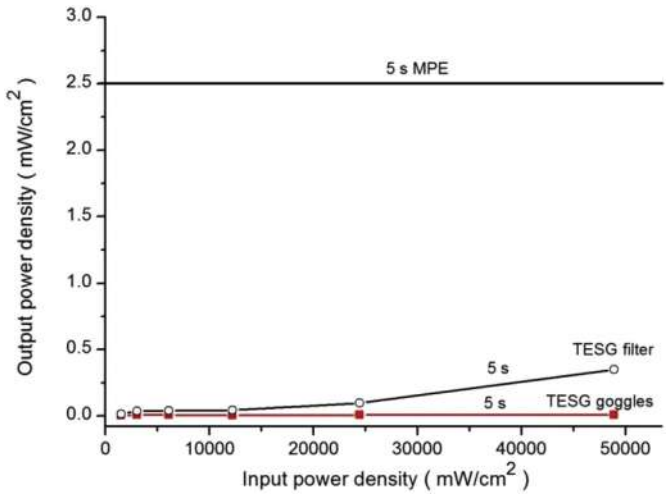

Fig. 7. Output laser power density (after 5 s) vs. input power density for TESG filter and goggles.

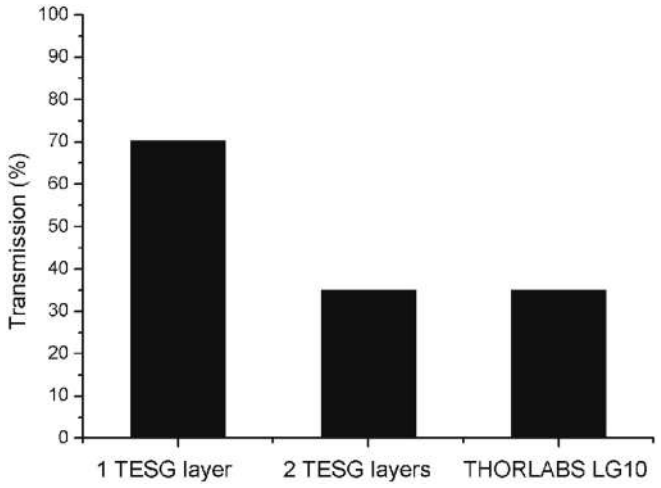

Fig. 8. Visible light transmission for TESG goggles (one or two layers) and THORLABS LG10 goggles. The transmission is almost the same for two layers and THORLABS LG10, while it is doubled for a single TESG layer.

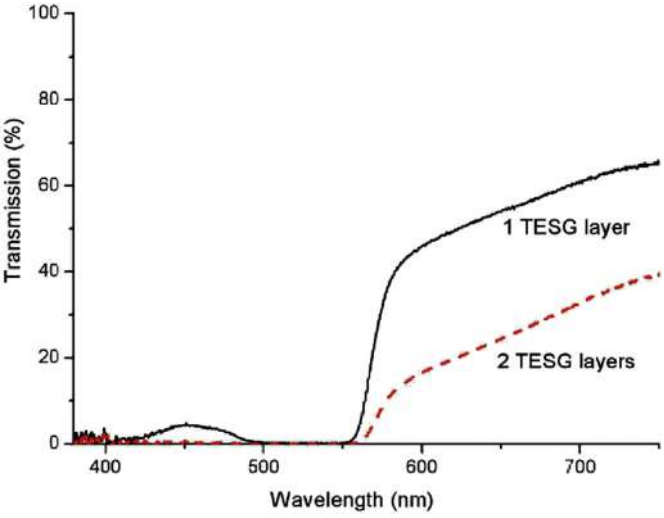

Fig. 9. Transmission spectra of TESG goggles (for one or two sets of TESG filters). The increase of transmission around 450 nm for single TESG layer is related to transmission properties of TESG. The amount of light transmitted around 450 nm decreases with increasing the layer thickness [15].

Spectral transparency depends on the TESG layer thickness, concentrations of eosin and tot'hema, and number of layers. Increasing the number of layers increases the total thickness of the filter, and thus reduces its transmission (see Fig. 9). However, even single layer thickness can't be increased more due to decreasing of visible light transmission.

As we already mentioned TESG layer is very easy to produce from cheap and environmentally friendly materials making it very interesting for production of laser goggles and large-area filters. Additionally, if TESG layer is damaged, it can easily be replaced. To demonstrate the effectiveness of TESG goggles we show the sequence of images during the 30 s irradiation time (Fig. 10).

Supplementary video related to this article can be found at http://dx.doi.org/10.1016/j.cap.2015.09.014.

Laser-induced microlenses and carbonization are universally applicable for protection against the laser radiation. Our

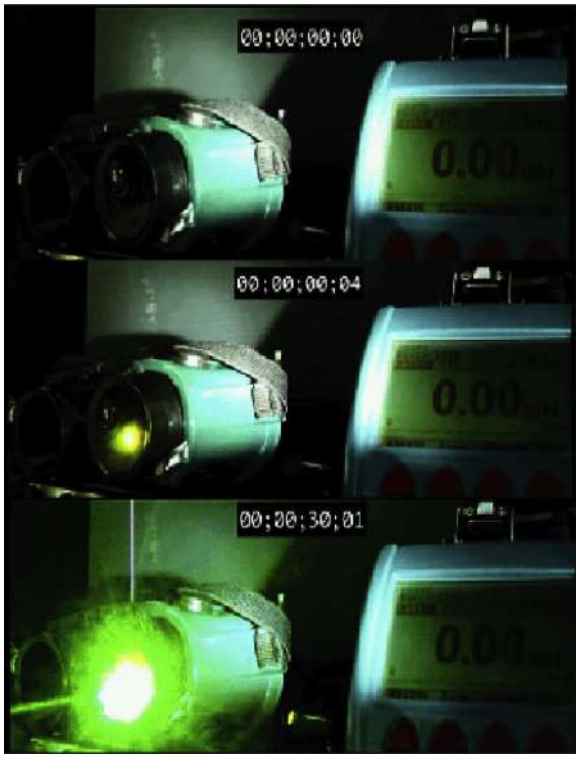

Fig. 10. Laser goggles irradiated with 10 W 532 nm Nd:YAG laser: Sequence of images corresponding to moment just before the laser was turned on (0 s), 4 s and 30 s (see the Supplementary Information).

preliminary results show that the protection wavelength can be tailored by using various sensitizing dyes. As a test, we replaced eosin Y with naphthol green B, and obtained an 800 nm protective layer, capable of withstanding 2 W of femto-second radiation.

4. Conclusions

Optical limiting properties of tot'hema eosin sensitized gelatin (TESG) were investigated. It was demonstrated that TESG can be used as a protection filter against the second harmonic Nd:YAG laser beam. The laser protection mechanism is based on microlens formation and layer carbonization. A simple, cheap and effective protection goggles are tested and used in laboratory environment. The results are demonstrating that protective goggles based on two single layer filters made of TESG can be used for the eye protection from 10 W of direct laser beam power.

According to our preliminary results the transmission spectral range of the TESG can be easily tuned to any part of the spectrum, by choosing the appropriate organic dye as sensitizer. Because the interaction of the TESG with laser radiation is based on a purely thermal mechanism the filter use can be extended to any laser type.

Optical and protective properties of TESG layer depend on its thickness and chemical composition (tot'hema and eosin concentrations). These were found experimentally as a compromise between the visible light transmission and protective properties against the highest power laser at our disposal (10 W at 532 nm). For protection against even higher power lasers, systematic research will be needed to establish the relation between the layer thickness, chemical composition and its protective properties.

Nevertheless, it has to be emphasized that approving TESG filters for universal eye protection requires additional measurements related to exposure to lasers of ultrashort pulse duration and of different wavelengths.

Acknowledgements

This paper was written as a part of research supported by the Ministry of Education, Science and Technological Development of the Republic of Serbia under grants ON 171038 and III 45016.

References

[1] A. Schirmacher, Med. Laser Appl. 25 (2010) 93–98.
[2] M. Chen, C. Li, Xu Mai, W. Wang, S. Ma, Y. Xia, Opt. Laser Technol. 39 (2007) 214–218.
[3] M.J. Grout, Opt. Mater. 14 (2000) 155–160.
[4] Y. Liu, J. Zhou, X. Zhang, Z. Liu, X. Wan, J. Tian, T. Wang, Y. Chen, Carbon 47 (2009) 3113–3121.
[5] E. Sutter, A. Schirmacher, Opt. Laser Technol. 33 (2001) 255–258.
[6] E. Buckley, J. SID 18 (2010) 944–951.
[7] D.H. Sliney, R.W. Wajnant, M.N. Ediger (Eds.), Electro-optics Handbook, McGraw-Hill, New York, 1993 (chap. 23).
[8] M. Lenner, C. Spielmann, Appl. Opt. 44 (2005) 3532–3539.
[9] M. Lenner, C. Spielmann, Appl. Phys. B 78 (2004) 689–692.
[10] J. Krüger, M. Lenzner, S. Martin, M. Lenner, C. Spielmann, A. Fiedler, W. Kautek, Appl. Surf. Sci. 208–209 (2003) 233–237.
[11] C.H. Lee, B. Bihari, R. Filler, B.K. Manda, Opt. Mater. 32 (2009) 147–153.
[12] EN 207: 2009 Personal eye-protection equipment—Filters and eye-protectors against laser radiation (laser eye-protectors).
[13] EN 208: 2009 Personal eye-protection—Eye-protectors for adjustment work on lasers and laser systems (laser adjustment eye-protectors).
[14] American National Standards Institute, “Safe Use of Lasers,” Standard Z-136.1, ANSI, New York, 1986.
[15] B. Murić, D. Pantelić, D. Vasiljević, B. Panić, Opt. Mater. 30 (2008) 1217–1220.
[16] B.D. Murić, D.V. Pantelić, D.M. Vasiljević, B.M. Panić, Appl. Opt. 46 (2007) 8527–8532.
[17] B. Murić, D. Pantelić, D. Vasiljević, B. Panić, B. Jelenković, Appl. Opt. 48 (2009) 3854–3859.
[18] B. Murić, D. Pantelić, D. Vasiljević, B. Zarkov, B. Jelenković, S. Pantović, M. Rosić, Phys. Scr. T157 (2013) 014018 (4pp).
[19] D.A. Atchison, C.C. Girgenti, G.M. Campbell, J.P. Dodds, T.M. Byrnes, A.J. Zele, Clin. Exp. Optom. 94 (2011) 545–548.
[20] A.V. Goncharov, M. Nowakowski, M.T. Sheehan, C. Dainty, Opt. Express 16 (2008) 1692–1703.
[21] D.A. Atchinson, G. Smith, Optics of the Human Eye, Butterworth-Heinemann, Oxford, 2000.

Applied Microbiology and Biotechnology
https://doi.org/10.1007/s00253-020-10498-y

APPLIED MICROBIAL AND CELL PHYSIOLOGY

Bat guano-dwelling microbes and antimicrobial properties of the pygidial gland secretion of a troglophilic ground beetle against them

Ivica Dimkić[1] · Slaviša Stanković[1] · Jovana Kabić[1] · Miloš Stupar[1] · Marija Nenadić[1] · Milica Ljaljević-Grbić[1] · Vladimir Žikić[2] · Ljubodrag Vujisić[3] · Vele Tešević[3] · Nikola Vesović[1] · Dejan Pantelić[4] · Svetlana Savić-Šević[4] · Jelena Vukojević[1] · Srećko Ćurčić[1]

Received: 7 November 2019 / Revised: 26 January 2020 / Accepted: 23 February 2020
© Springer-Verlag GmbH Germany, part of Springer Nature 2020

Abstract

Bat guano is an important source of microbial diversity in caves and can be a source of potential pathogens. *Laemostenus* (*Pristonychus*) *punctatus* is a guanophilic ground beetle species, which pygidial gland secretion exhibits action against pathogenic and other microbes. The distribution and diversity of microbes in bat guano from a karstic cave were determined in this study. Additionally, antimicrobial activity of the pygidial gland secretion of *L*. (*P.*) *punctatus* against guano-dwelling microbes was tested; minimal inhibitory concentration (MIC) and chemical composition of the secretion were analyzed. In total, 63 different bacterial species and 16 fungal morphotypes were isolated from guano samples by the cultivation method and confirmed using and phenotypic characterization and molecular identification. There was a difference in the composition of certain microorganisms between the sampling points (cave locations) and between the guano layers. The largest number of bacterial isolates belongs to the genera *Lysinibacillus* and *Paenibacillus*, while *Pseudomonas* species were highly abundant at the innermost sampling point. For the guanophilic fungi, the majority are ascomycetes, with *Penicillium* and *Aspergillus* as the most dominant genera. *Meyerozyma guilliermondii* was the only yeast species found in the guano samples. The most sensitive isolates were *Enterococcus eurekensis* (MIC 0.007 mg/mL) and *Escherichia fergusonii* (MIC 0.028 mg/mL). The most sensitive fungal isolates were *M. guilliermondii*, *Penicillium expansum*, and *Trichoderma harzianum* (MIC 0.15 mg/mL). This study opens a new possibility for better understanding of ecological relations between microorganisms and troglophilic ground beetles and for detailed investigations of morpho-anatomical aspects of pygidial glands.

Keywords Microbial diversity · Bat guano · Karstic cave · *Laemostenus* (*Pristonychus*) *punctatus* · Pygidial glands

Introduction

Caves represent nutritionally deficient environments, where energy sources and nutrients generally enter in the form of atmospheric gases, as aromatic and polyaromatic compounds from the ground or through water sources. Bat guano is the most important energy source in caves in temperate climates (Poulson and Lavoie 2000). The main sources of microorganisms, although widespread in caves, are usually guano, excrements from other animals and carcasses of animals (Barton 2006; Mulec 2008). In addition to fur-borne bat microorganisms, guano is an important source of microorganisms in caves. Bacterial species identified in guano samples mainly belong to the family *Enterobacteriaceae*, although species from the families

Electronic supplementary material The online version of this article (https://doi.org/10.1007/s00253-020-10498-y) contains supplementary material, which is available to authorized users.

✉ Ivica Dimkić
ivicad@bio.bg.ac.rs

[1] University of Belgrade - Faculty of Biology, Studentski Trg 16, Belgrade 11000, Serbia

[2] Department of Biology and Ecology, University of Niš - Faculty of Science and Mathematics, Višegradska 33, Niš 18000, Serbia

[3] University of Belgrade - Faculty of Chemistry, Studentski Trg 12-16, Belgrade 11000, Serbia

[4] University of Belgrade - Institute of Physics, Pregrevica 118, Belgrade 11080, Serbia

Published online: 05 March 2020

Pseudomonadaceae and *Enterococcaceae* have been identified as well (Di Bella et al. 2003). Jurado et al. (2010) reported the presence of a large number of pathogenic and opportunistic bacteria in caves. Bat guano can serve as a vector for the transmission of diseases between humans and animals (Borda et al. 2014; Vandžurová et al. 2013). Micromycetes (the mycobiota), together with other microorganisms, primarily bacteria, cyanobacteria, and algae, form an integral part of the cave microbiota. Guanophilic fungi are an ecological group of fungi which inhabit guano. They are very common in caves (Barton 2006). Since bat guano can represent a source of potential human and animal pathogens, such as *Pseudogymnoascus destructans* and *Histoplasma capsulatum*, guanophilic fungi were extensively studied in recent years (Medellin et al. 2017; Rocha-Silva et al. 2014). Guano is an important source of microbial aerosolization in caves and thus a threat to human and bat health (Julg et al. 2008). Research of microbial diversity in caves could be of particular importance for determining potential biohazards, especially because interest in cave tourism is increasing nowadays.

Laemostenus (*Pristonychus*) *punctatus* (Dejean, 1828) (*Coleoptera*: *Carabidae*) is an epigean and sub-lapidicolous ground beetle species, very often troglophilic and guanophilic, found in caves, burrows of mammals, and artificial hypogean habitats in the southern part of its range (Casale 1988). In the older literature, it was considered a subspecies of the closely related *Laemostenus* (*Pristonychus*) *terricola* (Herbst, 1784) (Casale 1988). The range of *L.* (*P.*) *punctatus* includes mainly the Balkan Peninsula, but also extends northwards to Slovakia (Casale 1988). It has been reported from caves in eastern, southeastern, and southwestern Serbia (Ćurčić et al. 2007). This predatory beetle mostly feeds in caves on small invertebrates living in guano (Nešić et al. 2008). Troglophilic populations of the species are more abundant compared to epigean ones (Nenadić et al. 2017), most likely due to the almost constant environmental conditions in caves throughout the year. *L.* (*P.*) *punctatus* is adapted to environmental conditions via production of a secretion mixture by paired pygidial exocrine glands composed of two sets of secretory lobe aggregations, collecting canals, reservoirs, and efferent ducts, which probably serve to protect the beetle from predators (Blum 1981; Nenadić et al. 2016, 2017). Besides the defensive role against predators, the secretion of *L.* (*P.*) *punctatus* has also shown an antimicrobial potential (Nenadić et al. 2016, 2017). Recently, chemical composition of the beetle's secretion has been identified using dichloromethane as the extraction chemical (Vesović et al. 2015). The antibacterial and antifungal action of the beetle's secretion against human microbial pathogens (Nenadić et al. 2016) and its antifungal effect against cave-dwelling micromycetes (Nenadić et al. 2017) were recently determined. During biospeleological research conducted in a karstic cave near the city of Niš in southeastern Serbia (Ogorelička Pećina Cave), it has been observed that the abundance of *L.* (*P.*) *punctatus* is surprisingly high compared to any other invertebrate species inhabiting the same cave or any other cave in Serbia. This suggests that one of the reasons for its high abundance could be that the beetle has certain mechanisms which protect it from pathogenic microbes inhabiting guano situated on the cave floor.

Although morphology of the pygidial glands of *L.* (*P.*) *punctatus* has been recently elucidated (Nenadić et al. 2016), nothing is known about their detailed anatomy and ultrastructure. There is therefore a need to obtain better insight into internal structures of the glands using available novel microscopic techniques. A combination of several modern microscopic techniques (scanning electron microscopy (SEM), focused ion beam (FIB) microscopy, and fluorescence microscopy) was used to investigate the pygidial gland system in some ground beetles of the subfamily *Brachininae* (*Brachinus* spp., *Pheropsophus* spp., and *Aptinus* spp.), which possess a similar, but evolutionarily more developed and more complex pygidial glands than the one occurring in *Platyninae*, to which *L.* (*P.*) *punctatus* belongs (Di Giulio et al. 2015). Use of fluorescence microscopy without labeling is possible in carabidology due to the autofluorescence of resilin in the cuticular structures of individuals. This phenomenon is very important in morphological and optical analyses of various cuticular structures in ground beetles (e.g., genitalia) (Rabasović et al. 2015). Within the family *Carabidae*, the two-photon excitation fluorescence (TPEF) modality of nonlinear microscopy (NLM) was applied in order to examine and determine *Pheggomisetes*, a specific trechine genus, primarily on the basis of anatomy (Vrbica et al. 2018). Cuticle and certain types of tissues, such as connective tissue (due to the presence of collagen) (Jiang et al. 2011) and muscle tissue (due to the presence of myosin) (Ibrahim et al. 2015; Wallace et al. 2008), the most dominant components of the pygidial gland structures of ground beetles, have a possibility of autofluorescence. Thus, the TPEF modality of NLM can be applied to investigate the morphology of these structures, especially different anatomical aspects of them, both in ground beetles and other insects.

The aims of the current study were (i) to give for the first time an inventory of microbial communities associated with bat guano in a karstic cave from southeastern Serbia (Ogorelička Pećina Cave); (ii) to evaluate culturable communities and explore the potential of the pygidial gland secretion of *L.* (*P.*) *punctatus* against selected bacteria and micromycetes from the same microenvironment using the traditional cultivation approach; (iii) to conduct chemical analysis of the secretion using methanol extraction; and (iv) to report the first detailed data on morpho-anatomy of the pygidial glands of *L.* (*P.*) *punctatus* using SEM and the TPEF modality of NLM.

Material and methods

Microbial diversity of the Ogorelička Pećina Cave

Guano samples (each of approximately 8–20 g) were collected in the Ogorelička Pećina Cave from five different sampling points and two layers (top and bottom layers) followed the protocol described by Ogórek et al. (2016) and Newman et al. (2018). Collection of guano samples was allowed by the Ministry of Agriculture and Environmental Protection of the Republic of Serbia (Permission No. 353-01-2588/2016-17). One sampling point was in the middle part of each cave section. The average thickness of the guano layers was approx. around 6 cm. Samples of guano layers were collected at top and bottom depths of 0.5 and 4 cm, respectively. Names of isolates were given after the cave sampling points and layers of guano where samples were isolated (Supplementary Table S1). Bat guano taken from each sampling site and layer (1 g) was suspended in sterile saline solution (9 mL) and then shaken three times vigorously for 20 min in an Erlenmeyer flask (250 mL), with a 5-min interval of resting between shakings. For differential bacterial growth, R2 minimal medium (bioMérieux, Marcy-I'Étoile, France), and Gibco Luria-Bertani medium (LB) (Thermo Fisher Scientific, Waltham, USA) were used for growing at 25 °C for 48 h. Also, samples were thermally inactivated at 80 °C for 10 min and further grown on LB at room temperature for 48 h. For isolation of fungi, samples from the same batch were plated using serial dilution on potato dextrose agar (PDA) (LAB M Ltd., Heywood, UK), malt extract agar (MEA) (LAB M Ltd., Heywood, UK) and dichloran (18%) glycerol agar (DG18) (LAB M Ltd., Heywood, UK) and incubated at 25 °C. After a 7-day incubation period, the number of colony-forming units (CFUs) per 1 g of guano was calculated as the average from replicates of all used nutrient media.

Preliminary identification of bacterial isolates was performed using phenotypic characterization (morphological observations, Gram staining, and catalase assay). The obtained guanophilic fungal isolates were identified based on macroscopic cultural characteristics of 7-day-old colonies and morphological characteristics of reproductive structures, respectively. Reproductive structures were observed by light microscopy using a Zeiss Axio Imager M.1 microscope equipped with the AxioVision Release 4.6 software (Carl Zeiss AG, Oberkochen, Germany). Preliminary identification of micromycetes was performed using the following identification keys: Raper and Fennel (1965), Pitt (1979), Watanabe (2002), and Samson et al. (2010). To verify identifications based on morphology, molecular identification was applied for selected isolates. The total DNA of bacterial strains was extracted from an overnight bacterial culture incubated at 30 °C in LB with shaking at 180 rpm. Single-spore fungal isolates were grown on MEA for 7 days at 25 °C. After incubation, mycelium (approx. 100 mg) was harvested and suspended in 200 μL of sterile distilled water. Total genomic DNA extraction for all fungal isolates was performed using the ZR Fungal/Bacterial DNA MiniPrep KIT, according to the protocol of the manufacturer (Zymo Research, Irvine, USA).

Primers used to amplify the regions of specific genes, as well as their corresponding PCR profiles (Jovčić et al. 2009; Kim et al. 2003; O'Donnell and Cigelnik 1997; Roe et al. 2011; White et al. 1990), are listed in Supplementary Table S2. The amplification of all the regions was performed in final volumes of 25 μL, as described by Dimkić et al. (2013) and Savković et al. (2016). The PCR conditions for amplification of bacterial DNA were as follows: an initial denaturation step at 94 °C for 5 min; 30 cycles consisting of a denaturation step of 30 s at 94 °C, primer annealing at 50 °C for 1 min and extension at 72 °C for 30 s; and one last cycle of extension at 72 °C for 7 min. The PCR conditions for amplification of fungal DNA were as follows: one cycle of denaturation at 94 °C for 4 min; 30 cycles of denaturation at 94 °C for 30 s, annealing at 55 °C for 50 s, and extension at 72 °C for 50 s; and one final cycle of extension at 72 °C for 10 min. All PCR products were purified using the QIAquick PCR Purification KIT/250 (QIAGEN GmbH, Hilden, Germany) according to the manufacturer's protocol. Purified PCR products were sequenced commercially using Sanger dideoxy sequencing or chain-termination method with universal primers (Macrogen Inc., Amsterdam, the Netherlands). The obtained sequences were analyzed for homology with gene sequences deposited in the GenBank database through the National Center for Biotechnology Information (NCBI) via the Basic Local Alignment Search Tool (BLAST) search for nucleotides (cutoff value for BLAST hits was 99% of similarity). All sequences were aligned using the ClustalW multiple sequence alignment in the BioEdit program (ver. 7.1.3.0) (Hall 1999). In loci with duplications or transversions, corrections were made according to the reference strain sequences. Phylogenetic trees were constructed in MEGA 7 (Kumar et al. 2016) using the neighbor-joining method with Kimura's two-parameter nucleotide substitution model (Kimura 1980) for bacterial sequences and the maximum likelihood method based on Tamura's three-parameter model (Tamura et al. 2013) for fungal sequences. The trees are drawn to scale, with branch lengths measured in the relative number of substitutions per site. All positions containing gaps and missing data were eliminated. Additionally, the obtained bacterial sequences were grouped based on the layer of guano samples and the cave section. Within each group, the sequences were clustered into bacterial classes based on similarity of the BLAST results and the Ribosomal Database Project (RDP) classifier (cutoff value for BLAST and RDP classifier results was each 99% of similarity).

Bacterial and fungal sequences were submitted to the NCBI database under the GenBank submission numbers

SUB6039655 and SUB6046415, respectively. GenBank accession numbers were received for bacterial strains (MN197930-MN198090), as well as for fungal species based on the ITS region (MN206946-MN206972) and the β-tubulin gene (under BankIt number 2248777) (MN233612-MN233631) (Supplementary Tables S3 and S4).

Collection and handling of ground beetle specimens

Adult individuals (41 specimens of both genders) of *L.* (*P.*) *punctatus* were collected manually during November of 2017 from the guano situated on the floor of the Ogorelička Pećina Cave, village of Sićevo, near Niš, Svrljiške Planine Mts., southeastern part of Serbia. Collection of the ground beetle was allowed by the Ministry of Agriculture and Environmental Protection of the Republic of Serbia (Permission No. 353-01-2588/2016-17). Beetles were gathered at five sampling points, which correspond to sampling points of guano. Insects were collected from a defined surface with a high amount of guano at each sampling point. Collection time was not limited and lasted approximately 2 h (in average 25 min per sampling point). Detected environmental conditions within the cave sections and the number of collected adult beetles are shown in Supplementary Table S5. Live ground beetles were transported and kept in cool portable plastic boxes for a few days before taking samples of the pygidial gland's content. We maintained constant temperature of 10 °C, total darkness, and moist soil conditions using soil from the collecting site. The beetles were fed on earthworms and springtails collected from the Ogorelička Pećina Cave. After analyses, dry pinned beetle specimens were deposited in the collection of the Institute of Zoology, University of Belgrade - Faculty of Biology, Belgrade, Serbia (Supplementary Fig. S1).

Chemical extraction and analyses

Preparation of samples for gas chromatography-mass spectrometry (GC-MS) was performed in the laboratory at room temperature. Specimens of *L.* (*P.*) *punctatus* were milked into a 12-mL glass vial with absolute methanol (0.5 mL) for 5 min. The beetles were stimulated to discharge pygidial gland secretions by squeezing the abdomens against the wall of a vial containing extraction solvent. To eliminate the effects of composition-altering oxidation and degradation of compounds, GC-MS was performed immediately after sampling. The amount of discharged pygidial gland secretion was measured on a Sartorius Model 2405 analytical balance with 0.001 mg resolution (Sartorius Group, Göttingen, Germany). Weight of the vial was measured on the analytical balance prior to (empty vial) and after discharging the pygidial gland secretion (with the secretion inside). The difference in weight represented the total amount of secretion released by the analyzed beetle species.

The GC and GC-MS analyses were performed in the splitless mode. A 7890A GC system (Agilent Technologies, Santa Clara, USA) equipped with a 5975C inert XL EI/CI mass selective detector (MSD) and a flame ionization detector (FID) (Agilent Technologies, Santa Clara, USA) connected by capillary flow technology through a two-way splitter were used for analyses. The injection volume was 1 μL, the injector temperature was 240 °C and the transfer line temperature was 280 °C. The carrier gas (He) flow rate was 2.0 mL/min at 40 °C (constant pressure mode). Temperature of the HP-INNOWax column (30 m length, 0.32 mm i.d., 0.25 μm film thickness) (Agilent Technologies, Santa Clara, USA) was programmed linearly in a range of 40–240 °C at a rate of 10 °C/min, with a final 10-min hold. The FID temperature was 300 °C. The EI mass spectra (70 eV) were acquired in a range of 40–550 *m/z*, and the ion source temperature was 230 °C for all analyses. Library search and mass spectral deconvolution and extraction were performed at the Faculty of Chemistry, University of Belgrade database containing 4951 spectra and commercially available NIST11 and Wiley07 libraries containing approximately 500,000 spectra using the NIST Automated Mass Spectral Deconvolution and Identification System (AMDIS) software (ver. 2.70) (Kind 2003). Relative percentages of identified compounds were computed from corresponding peak areas from a GC-FID chromatogram.

Antimicrobial assays

Preparation of samples for antimicrobial analyses was performed in the laboratory at room temperature. To eliminate the effects of composition-altering oxidation and degradation of compounds, antimicrobial analyses were performed immediately after sampling. The broth microdilution method of Ristivojević et al. (2016) was used in the antibacterial assay to determine the minimum inhibitory concentration (MIC) and minimum bactericidal concentration (MBC) for the secretion obtained from the pygidial glands of *L.* (*P.*) *punctatus* specimens. A modified microdilution technique (Daouk et al. 1995; Hänel and Raether 1988) was used in the antifungal assay. Final tested concentration of the secretion was in a range of 0.007–0.225 mg/mL for 12 selected bacterial species and in a range of 0.1–1 mg/mL for the five most common isolated fungal species. Concentration of the solvent (methanol) was 10%. Two-fold serial dilutions of the secretion were made with Luria-Bertani (LB) broth and Malt Extract Broth (MEB) in 96-well microtiter plates. In addition to a negative control (bacterial and fungal growth control) and a sterility control, the antibiotic streptomycin (in concentration range of 0.0063–0.2 mg/mL)

and the commercial fungicide nystatin (in a concentration range of 0.1–1 mg/mL) were used as positive controls. Each well, except in the case of the sterility control, was inoculated with 20 μL of bacterial culture (1×10^6 CFU/mL, suspensions were adjusted to McFarland 0.5 standard turbidity), reaching a final volume of 200 μL. Conidia and yeast cells in the case of *Meyerozyma guilliermondii* were washed from the surface of agar slants with sterile saline (0.85%) containing 0.1% Tween 20 (*v*/*v*). In order to prepare inocula, conidia/cell suspensions were adjusted with sterile saline (0.85%) to a concentration of approximately 1.0×10^5 in a final volume of 100 μL per well in 96-well microtiter plates. The plates were incubated at 30 °C for 24 h and at 25 °C for 72 h for bacterial and fungal growth, respectively. Spectrophotometric bacterial growth readings were performed using a microplate reader (Multiskan FC Microplate Photometer, OD 570 nm, Thermo Fisher Scientific, Waltham, USA), after which 22 μL of resazurin (resazurin sodium salt ($C_{12}H_6NNaO_4$)) (TCI, Zwijndrecht, Belgium), at a final concentration of 0.675 mg/mL, was added to each well and the microtiter plates were incubated at 30 °C for two additional hours. Following incubation, the resazurin color change reaction was observed. The MIC values were determined as indicated by no change in color, while MBCs were obtained by sub-culturing the test dilutions from each well without color change on agar plates and incubating them for 24 h. The lowest concentration showing no bacterial growth was defined as the MBC value. In the case of the tested fungal species, MIC values of the secretion were determined as the lowest used concentration without visible growth detected with a binocular microscope. Further, minimum fungicidal concentrations (MFCs) were determined by serial sub-cultivation (2 μL) into microtiter plates each containing 100 μL of MEB. The lowest concentration with no detected visible fungal growth was defined as the MFC, indicating 99.5% killing of the original inoculum. The results were expressed in mg/mL.

SEM and TPEF modality of NLM analyses

Preparation of tissues

Pygidial glands of *L.* (*P.*) *punctatus* were first isolated and tissue of the glands was then dehydrated through a series of ethanol solutions of increasing concentrations (30, 50, 70, 90, and 100%). The structures were stored in 100% ethanol at 4 °C before SEM recording. In order to obtain a detailed insight into morphology of the pygidial glands of *L.* (*P.*) *punctatus*, the TPEF modality of NLM was used for visualization. After isolation, the pygidial glands were stored in concentrated glycerol.

Experimental setup and procedure

Scanning electron microscope images were obtained with a field emission gun scanning electron microscope (MIRA3 FEGSEM, Tescan, Brno, Czech Republic) in the high-vacuum mode at an acceleration voltage of 15 kV. The electron beam current was between 750.18 pA and 1.40 nA, depending on imaging conditions, while pressure in the column was around 127.19e−3 Pa. The samples were coated with gold/palladium to make them conductive for SEM analyses.

Two-femtosecond lasers were used for the TPEF modality of NLM of all samples: a Ti-sapphire laser (76-MHz repetition rate, within the tuning range of 700–1000 nm) (Mira 900-F, Coherent, Santa Clara, USA) pumped by a 10-W laser (Verdi V10, Coherent, Santa Clara, USA) at 532 nm, and (as a secondary source of excitation) a 1040-nm Yb KGW femtosecond laser (GLX-Yb) (Time-Bandwidth Products AG, Schlieren, Switzerland). A Plan Apochromat microscope objective (20 × 0.8, 500 μm field of view) (Carl Zeiss, Jena, Germany) was used for sample imaging. Galvanometric scanning mirrors (Cambridge Technology 6215H, Cambridge, USA) were used for raster-scanning. Recordings were performed at different power settings (80–150 mW), depending on the sample. An EOS 50D digital camera (Canon, Tokyo, Japan) was used for adjustment and classical transmission microscopy. VolView 3.4 open-source software (Kitware, Inc., Clifton Park, USA) was used for 3D visualization of a set of slices.

Results

Microbial diversity of the studied cave

Bacterial diversity

In total, 220 bacterial isolates were originally obtained from the guano samples, but 161 isolates were selected for further identification based on their biochemical and morphological characteristics. We preliminarily identified 117 isolates as Gram-positive bacteria, nine isolates as Gram-negative bacteria, while 35 isolates exhibited a variable Gram reaction. A positive catalase reaction was shown by 119 isolates, while 42 isolates showed a negative reaction. The obtained and purified isolates were divided into three groups, depending on the different isolation method and media applied. Isolates that showed growth after incubation at 80 °C were placed in the group of thermal inactivation (designated T); the oligotrophic group (designated O) contains isolates that grew on depleted substrates; and the third group was the LB growth group of isolates (without a prefix).

Further identification of the selected isolates involved amplification and sequencing of the 16S rRNA gene. The

conducted BLAST analysis of 161 isolates yielded 135 Gram-positive and 26 Gram-negative members of the phyla *Actinobacteria*, *Firmicutes*, and *Proteobacteria*. Dendrograms with phylogenetic relationships of isolates and reference strains were divided into two groups, depending on the Gram reaction (Figs. 1 and 2). Only one of each representative bacterial species among all identified isolates was placed on the dendrograms for a better and easier presentation.

Within the Gram-positive bacteria group (Fig. 1), we identified 26 strains of *Viridibacillus arvi*; 13 strains of *Bacillus mycoides*; 10 strains of *Lysinibacillus parviboronicapiens*; nine strains of *Bacillus simplex*; seven strains of *Paenibacillus odorifer*; six strains of *Bacillus thuringiensis*; five strains of *Enterococcus faecalis*, *Staphylococcus epidermidis*, and *Paenibacillus polymyxa*; four strains of *Bacillus toyonensis*; three strains of *Brevibacterium frigoritolerans* and *Psychrobacillus psychrodurans*; two strains of *Paenibacillus wynnii*, *Paenibacillus taichungensis*, *Paenibacillus anaericanus*, *Sporosarcina globispora*, *Sporosarcina aquimarina*, *Bacillus amyloliquefaciens*, and *Bacillus mojavensis*; and one strain of *Lysinibacillus macrolides*, *Lysinibacillus contaminans*, *Lysinibacillus sphaericus*, *Lysinibacillus mangiferihumi*, *Rhodococcus jialingiae*, *Rhodococcus cerastii*, *Staphylococcus aureus*, *Staphylococcus caprae*, *Staphylococcus arlettae*, *Paenibacillus peoriae*, *Paenibacillus ginsengisoli*, *Paenibacillus amylolyticus*, *Micrococcus yunnanensis*, *Microbacterium hydrocarbonoxydans*, *Bacillus subtilis*, *Bacillus cereus*, *Bacillus weihenstephanensis*, *Bacillus pumilus*, *Bacillus clausii*, *Bacillus eiseniae*, *Bacillus bataviensis*, *Bacillus oceanisediminis*, *Bacillus soli*, *Bacillus endoradicis*, and *Enterococcus eurekensis*.

Within the group of Gram-negative bacteria (Fig. 2), we identified three strains of *Pseudomonas brenneri* and *Serratia proteamaculans*; two strains of *Pseudomonas putida*, *Comamonas jiangduensis*, and *Citrobacter freundii*; and one strain of *Serratia quinivorans*, *Buttiauxella noackiae*, *Citrobacter gillenii*, *Escherichia fergusonii*, *Kluyvera intermedia*, *Brevundimonas bullata*, *Pseudomonas oryzihabitans*, *Pseudomonas miguelae*, *Pseudomonas fragi*, *Pseudomonas psychrophila*, *Pseudomonas mucidolens*, *Pseudomonas donghuensis*, *Pseudomonas monteilii*, and *Pseudomonas helmanticensis*.

By the selected methods of cultivation and identification, a total of 63 different bacterial species were isolated from the guano samples. Thirty-three different bacterial species were isolated within the thermal inactivation group, 28 within the LB group, and 23 within the oligotrophic group. The isolated bacterial species partly overlapped using different cultivation methods. When the thermal inactivation method was used, most of the isolated bacteria belonged to *Paenibacillus* and *Sporosarcina* sporulating bacteria, while some nonsporulating species of the genera *Pseudomonas*, *Micrococcus*, and *Microbacterium* were also obtained by this method of cultivation. Within the LB group, most of the isolated bacteria belonged to the genera *Bacillus* and *Lysinibacillus*, and representatives of *L. contaminans*, *L. mangiferihumi*, *L. macroides*, *B. subtilis*, *B. eiseniae*, *B. pumilus*, *B. clausii*, and *B. bataviensis* were isolated only within this group. Within the group of oligotrophic bacteria, representatives of the species *B. bullata*, *C. freundii*, *C. gillenii*, *K. intermedia*, *L. sphaericus*, and *E. fergusonii* were characteristic. All of the analyzed sequences were identified as members of five bacterial classes: *α-Proteobacteria*, *β-Proteobacteria*, *γ-Proteobacteria*, *Actinobacteria*, and *Bacilli*. The results showed that bacteria of the *Bacilli* class have the highest diversity and prevalence according to identified number of species, regardless of their count, in the cultured microbial community, in both of the examined guano layers and in different parts of the cave's premises. The number of species collected per each bacterial class in the two guano layers is shown in Fig. 3a. In the upper guano layer, *Bacilli* were represented by less species (75%) than in the lower layer (88.6%), while more cultured species from *γ-Proteobacteria* and *Actinobacteria* were present in the upper layer. Members of *α-Proteobacteria* and *β-Proteobacteria* had comparable number of identified species. *Bacilli* were also prevalent at all sampling points, as shown in Fig. 3b. The highest bacterial richness was observed at the second (24 bacterial species) and last (26 bacterial species) sampling points. At the first and third sampling points, somewhat fewer species were recorded (20 and 19 species, respectively), while the fourth point had the lowest bacterial richness (13 species) (Supplementary Table S3).

Fungal diversity

In total, 67 fungal isolates were obtained at all sampling points. After identification of macro- and micromorphological features, 29 at first glance different morphotypes were sent for ITS and β-tubulin gene sequencing. Fungi were identified on the basis of homology of the obtained sequences with reference strains from the GenBank database, thereby confirming the identification based on morphological features (Fig. 4). A total of 16 fungal morphotypes were isolated from the tested guano samples (Supplementary Table S4). The majority of fungi were ascomycetes (87.5%). *Mucor racemosus*, *Peniophora lycii*, and *M. guilliermondii* were the only *Mucoromycotina*, basidiomycete, and ascomycetous yeast species in the analyzed samples, respectively. The largest group of guanophilic fungi in the Ogorelička Pećina Cave consisted of members of the genera *Penicillium* and *Aspergillus* (25%), both represented with four identified species (*P. citrinum*, *P. sanguifluum*, *P. expansum* and *P. purpurogenum* (teleomorph *Talaromyces*

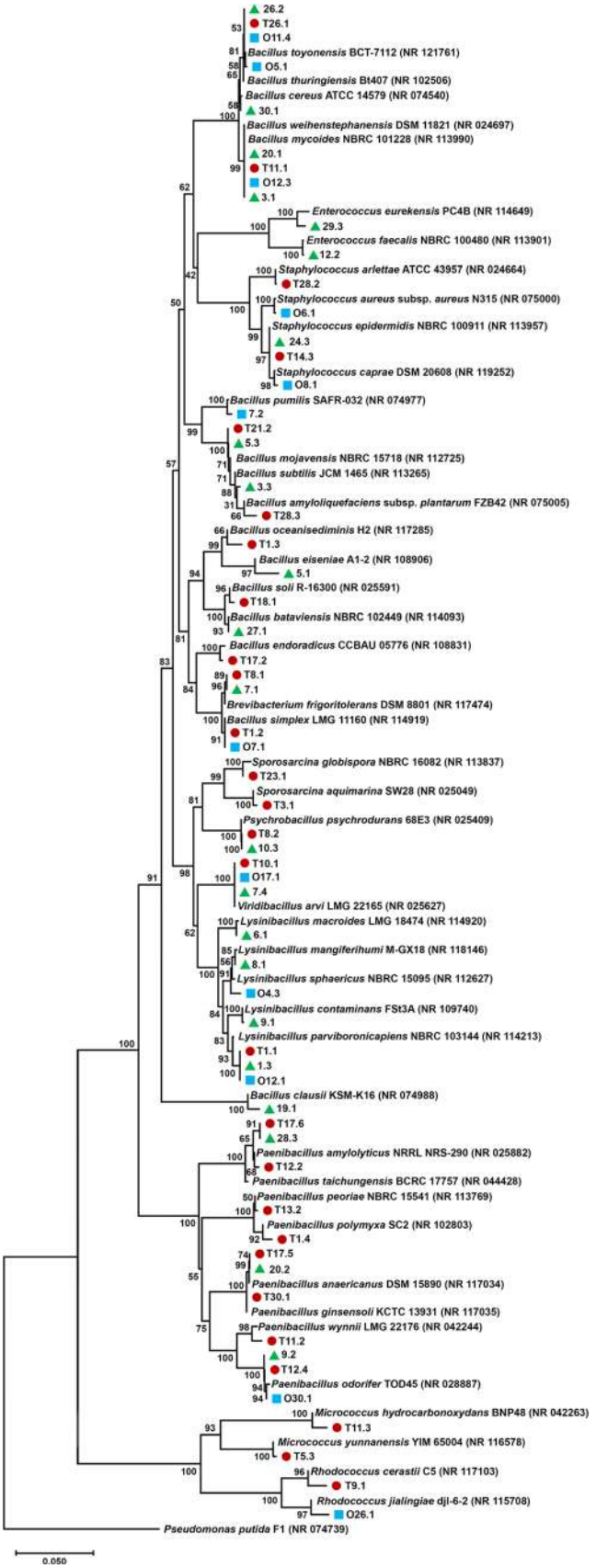

Fig. 1 Neighbor-joining phylogenetic tree based on 16S rRNA sequences (1500 bp) showing relationship of the representative Gram-positive isolates from the bat guano. Distances were calculated using Kimura's two-parameter model. *P. putida* was used as an outgroup. Red circles represent strains from the thermal inactivation group; blue squares, strains from the oligotrophic group; and green triangles, strains from the LB group

purpurogenus); and *A. flavus*, *A. aureolatus*, *A. pallidofulvus* and *A. creber*). *A. creber* and *Cosmospora viridescens* were isolated only from the upper guano layer (Supplementary Table S1), and both were documented only at the innermost sampling point (Supplementary Table S4). *Humicola grisea* was also isolated at the same sampling point. Apart from that, no other significant differences of fungal distribution were observed between the examined guano layers. The highest fungal diversity (75% of all identified species) was documented at the innermost sampling point, followed by the fourth sampling point (68.8%). The highest isolation frequency (100%) was recorded for *M. guilliermondii*, *P. citrinum*, and *Trichoderma harzianum*. These species were documented in both guano layers at all sampling points in the Ogorelička Pećina Cave. Among all *Penicillium* species, *P. citrinum* was the most common isolated fungal species. Apart from lower diversity in general, the highest concentrations of fungal propagules detected at the fourth (on MEA growth medium) and second (on DG18 growth medium) sampling points were 7146.2 and 6384.61 CFU/g, respectively. The lowest fungal concentration was recorded in the lower layer at the first sampling point on DG18 (286.73 CFU/g). In all examined parts of the cave's premises and on all media used for fungal isolation, a significantly higher fungal concentration was recorded in the upper guano layer than in the lower one (Fig. 5).

Occurrence and abundance of *L.* (*P.*) *punctatus* in the investigated cave

The largest number of adult specimens of *L.* (*P.*) *punctatus* was collected in the Ogorelička Pećina Cave in total darkness, at sampling points 2 (relative atmospheric humidity 86%, air temperature 15 °C) and 3 (relative atmospheric humidity 90%, air temperature 13.8 °C) (12 and 11 individuals, respectively) (Supplementary Table S5).

Total amount of discharged pygidial gland secretion of *L.* (*P.*) *punctatus* and its chemical composition

The total amount of the discharged pygidial gland secretion from 41 specimens of the tested ground beetle species was 0.189 ± 0.001 mg. The amount of discharged secretion per one beetle specimen was 0.005 ± 0.001 mg.

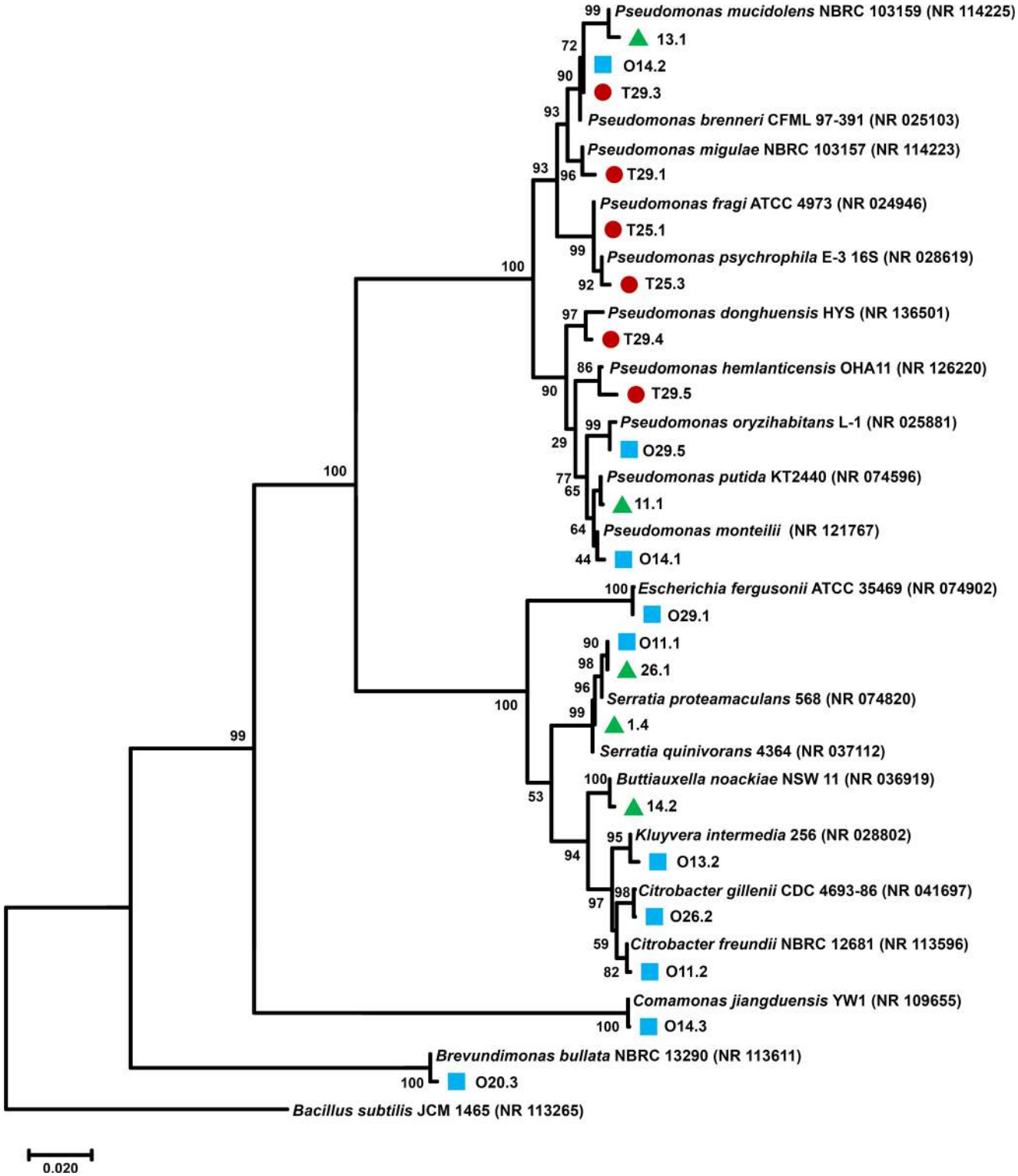

Fig. 2 Neighbor-joining phylogenetic tree based on 16S rRNA sequences (1500 bp) showing relationship of the representative Gram-negative isolates from the bat guano. Distances were calculated using Kimura's two-parameter model. *B. subtilis* was used as an outgroup. Red circles represent strains from the thermal inactivation group; blue squares, strains from the oligotrophic group; and green triangles, strains from the LB group

Concentration of the secretion dissolved in absolute methanol was 0.063 mg/ml. The experiment was repeated three times during a short period of time in order to confirm validity of the results.

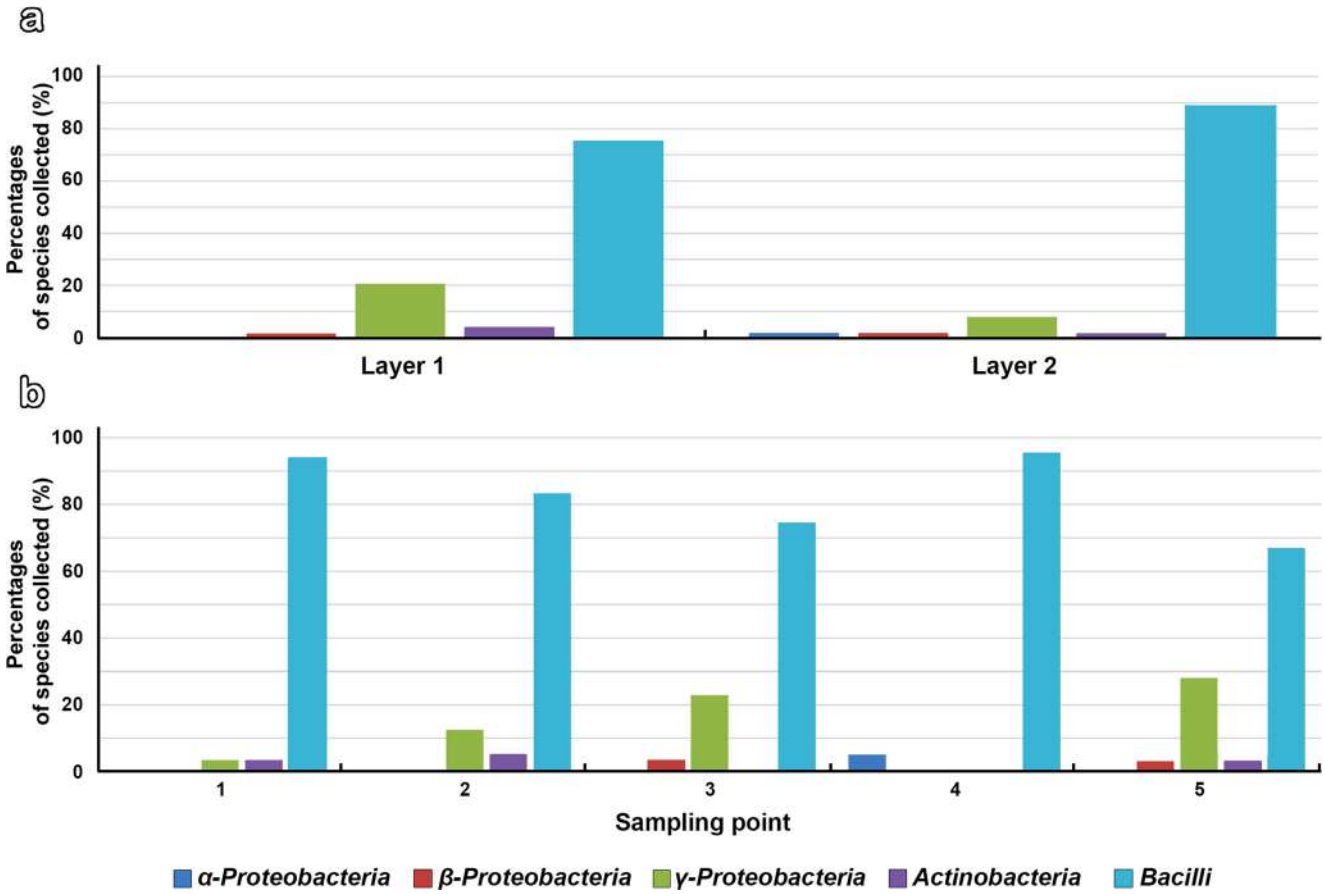

Fig. 3 Percentages of species collected per bacterial class depending on guano layers (**a**) and sampling points (**b**). Relative distribution was obtained by statistical and phylogenetic analysis of their 16S rRNA sequence. Layer 1, upper guano layer; layer 2, lower guano layer

Chemical analysis yielded a total of four detected and identified compounds from the methanol extract of the pygidial gland secretion of *L.* (*P.*) *punctatus*: one alkane, two low molecular weight carboxylic acids, and one ester. Major components of the secretion are undecane (58.9%) and dodecyl acetate (36.7%), followed by acetic (2.5%) and formic (1.9%) acids (Supplementary Fig. S2; Table 1).

Antimicrobial effect of the pygidial gland secretion of *L.* (*P.*) *punctatus* against guano-dwelling microbes

In the initial testing, 12 of the most common Gram-positive isolates (*E. faecalis* 3.2; *E. eurekensis* 29.3; *R. jialingiae* O26.1; *M. yunnanensis* T5.3; *B. thuringiensis* 26.2; *B. cereus* 30.1; *L. sphaericus* O4.3; *P. polymyxa* T21. 1; *V. arvi* T26.2; *B. frigoritolerans* 7.1; *S. aureus* O6.1; and *S. epidermidis* 24.3) and five Gram-negative isolates (*E. fergusonii* O29.1; *P. putida* 11.1; *C. freundii* O11.3; *S. proteamaculans* O11.1; and *K. intermedia* O13.2) were chosen from all of the cave's sampling points. On the basis of initial testing using the well diffusion method (data not shown), 12 of the most sensitive bacterial strains were selected for further testing using the MIC assay technique. Isolates *E. faecalis*, *B. frigoritolerans*, *S. aureus*, *S. epidermidis*, and *K. intermedia* were the most resistant in the initial testing of antibacterial activity of the secretion, so they were excluded from further analyses. The results obtained in testing antibacterial activity of the secretion, spectrophotometrically measured at OD 570 nm, are shown in Supplementary Fig. S3. As the final confirmation of spectrophotometric readings, we used the resazurin reaction of MIC and MBC values (Table 2). The most sensitive bacterial isolate was *E. eurekensis* (with the lowest MIC value, namely, 0.007 mg/mL), and at the same time, it possessed antibiotic resistance to streptomycin at the highest tested concentration. Other Gram-positive isolates generally also showed higher susceptibility, between 0.056 and 0.113 mg/mL for the majority of them (the most resistant were *B. cereus* and *P. polymyxa*), compared to Gram-negative ones. Interestingly, among all the tested Gram-negative isolates, *E. fergusonii* showed a marked sensitivity to the secretion (0.028 mg/mL), almost twice as high as sensitivity to the tested antibiotic. On the other hand, the pygidial gland secretion of *L.* (*P.*) *punctatus* had a weaker effect on the tested fungal strains than on the bacterial strains. Lower MIC and MFC values were achieved against *M. guilliermondii*, *P. expansum*, and *T. harzianum*, with fungistatic and

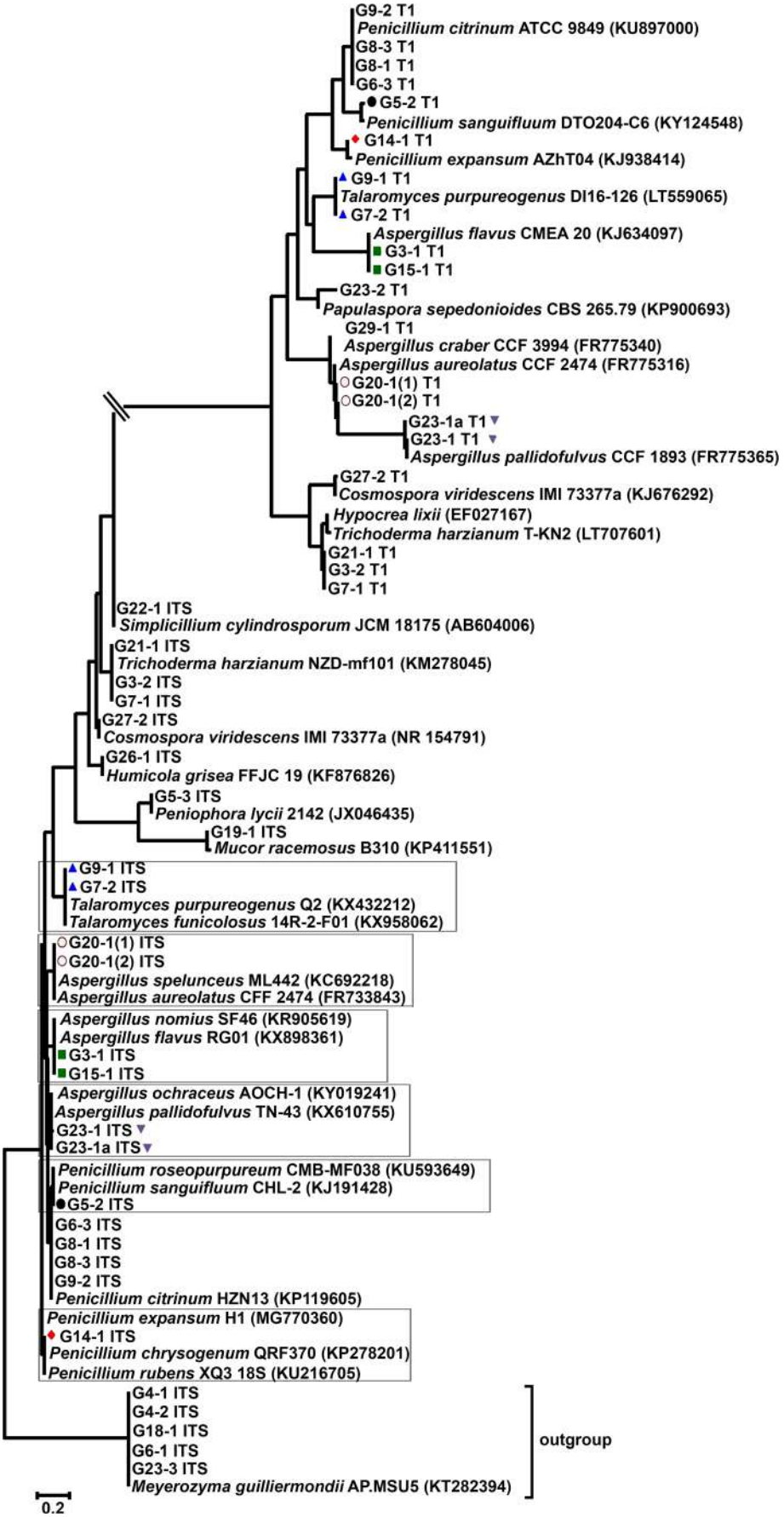
G9-2 T1
Penicillium citrinum ATCC 9849 (KU897000)
G8-3 T1
G8-1 T1
G6-3 T1
G5-2 T1
Penicillium sanguifluum DTO204-C6 (KY124548)
G14-1 T1
Penicillium expansum AZhT04 (KJ938414)
G9-1 T1
Talaromyces purpureogenus DI16-126 (LT559065)
G7-2 T1
Aspergillus flavus CMEA 20 (KJ634097)
G3-1 T1
G15-1 T1
G23-2 T1
Papulaspora sepedonioides CBS 265.79 (KP900693)
G29-1 T1
Aspergillus craber CCF 3994 (FR775340)
Aspergillus aureolatus CCF 2474 (FR775316)
G20-1(1) T1
G20-1(2) T1
G23-1a T1
G23-1 T1
Aspergillus pallidofulvus CCF 1893 (FR775365)
G27-2 T1
Cosmospora viridescens IMI 73377a (KJ676292)
Hypocrea lixii (EF027167)
Trichoderma harzianum T-KN2 (LT707601)
G21-1 T1
G3-2 T1
G7-1 T1
G22-1 ITS
Simplicillium cylindrosporum JCM 18175 (AB604006)
G21-1 ITS
Trichoderma harzianum NZD-mf101 (KM278045)
G3-2 ITS
G7-1 ITS
G27-2 ITS
Cosmospora viridescens IMI 73377a (NR 154791)
G26-1 ITS
Humicola grisea FFJC 19 (KF876826)
G5-3 ITS
Peniophora lycii 2142 (JX046435)
G19-1 ITS
Mucor racemosus B310 (KP411551)
G9-1 ITS
G7-2 ITS
Talaromyces purpureogenus Q2 (KX432212)
Talaromyces funicolosus 14R-2-F01 (KX958062)
G20-1(1) ITS
G20-1(2) ITS
Aspergillus spelunceus ML442 (KC692218)
Aspergillus aureolatus CFF 2474 (FR733843)
Aspergillus nomius SF46 (KR905619)
Aspergillus flavus RG01 (KX898361)
G3-1 ITS
G15-1 ITS
Aspergillus ochraceus AOCH-1 (KY019241)
Aspergillus pallidofulvus TN-43 (KX610755)
G23-1 ITS
G23-1a ITS
Penicillium roseopurpureum CMB-MF038 (KU593649)
Penicillium sanguifluum CHL-2 (KJ191428)
G5-2 ITS
G6-3 ITS
G8-1 ITS
G8-3 ITS
G9-2 ITS
Penicillium citrinum HZN13 (KP119605)
Penicillium expansum H1 (MG770360)
G14-1 ITS
Penicillium chrysogenum QRF370 (KP278201)
Penicillium rubens XQ3 18S (KU216705)
G4-1 ITS
G4-2 ITS
G18-1 ITS
G6-1 ITS
G23-3 ITS
Meyerozyma guilliermondii AP.MSU5 (KT282394)
outgroup
0.2

◀ **Fig. 4** Maximum likelihood phylogenetic tree based on the ITS region and β-tubulin gene (T1) as ultimate confirmation of species status. Distances were calculated using Tamura's three-parameter model. A group of strains belonging to *M. guilliermondii* was used as an outgroup. Framed squares show all unidentified species at the ITS level, in contrast to confirmation by sequencing the β-tubulin gene

fungicidal action in the concentration range of from 0.15 to 0.30 mg/mL. The highest MIC and MFC values were scored for *P. citrinum* (0.3 and 0.6 mg/mL, respectively). This isolate also proved to be the most resistant in nystatin treatment.

Morphology and anatomy of the pygidial glands of *L.* (*P.*) *punctatus*

Spherical secretory lobes of variable diameter (average value of 200 μm) are present in a large number (approximately 50–60 per gland) (Figs. 6, 7a, b, and 8a; Supplementary Files S1 and S2). In the TPEF modality of NLM images, these are of circular form in cross section (Fig. 8b). Diameter of a randomly selected single radial collecting canal (Fig. 7c) is approximately 16.19 μm. Tracheoles are in close connection with the pygidial gland system, especially with radial collecting canals (Figs. 7b and 8a). The main collecting canal (Figs. 6, 7f, and 8c) connects secretory lobes with a reservoir in the reservoir's concave zone called the hilum, positioned in its middle part (Fig. 6; Supplementary Files S3 and S4). The length of the main collecting canal is 10–15 mm, while its diameter is about 120 μm (Fig. 8d). The muscle-coated reniform reservoir is about 1.1 mm in diameter (Fig. 7d) and shows a fine regular parallel arrangement of muscle fibers (Fig. 7e). The thickness of its muscle wall is about 130 μm (Fig. 8e). The secretion of the pygidial glands is transported from the reservoir to an efferent duct (Fig. 7d), through which it is discharged to the outside via an opening (Fig. 6). No morphological or anatomical differences of glandular structure were observed between the sexes.

Table 1 Chemical composition of methanol extract of the pygidial gland secretion of *L.* (*P.*) *punctatus* analyzed by GC-FID and GC-MS

Peak	t_R (min)[a]	Compound	Relative percentage (%)[b]
1	3.91	Undecane	58.9
2	8.80	Acetic acid	2.5
3	9.54	Formic acid	1.9
4	14.22	Dodecyl acetate	36.7

t_R retention time

[a] Obtained from GC-MS data on HP-INNOWax capillary column

[b] Percentages calculated from GC-FID peak areas

Discussion

Microbial distribution and diversity of cave guano samples

Of the 63 different bacterial species detected using three methods of cultivation, only some of them overlapped using

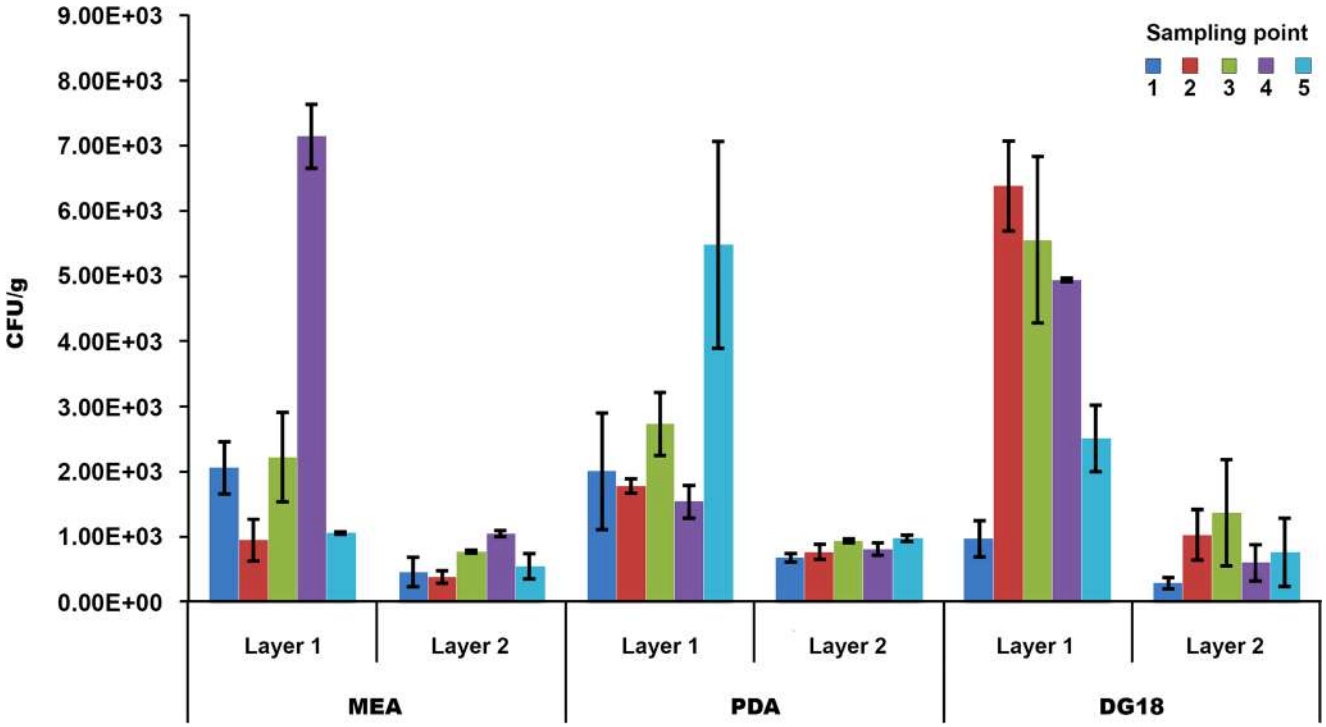

Fig. 5 Fungal density (CFU/g) documented on media used (MEA, PDA, DG18) at all sampling points in both guano layers. Layer 1, upper guano layer; layer 2, lower guano layer

Table 2 Minimum inhibitory concentration (MIC), minimum bactericidal concentration (MBC) and minimum fungicidal concentration (MFC) (mg/mL) of the pygidial gland secretion of *L* (*P.*) *punctatus* compared to a positive control (streptomycin/nystatin)

No.	Strain name	*L.* (*P.*) *punctatus* pygidial gland secretion		Streptomycin/nystatin	
		MIC	MBC/MFC	MIC	MBC/MFC
1	*Enterococcus eurekensis* 29.3	0.007	0.113	–	–
2	*Rhodococcus jialingiae* O26.1	0.056	0.113	0.050	0.200
3	*Micrococcus yunnanensis* T5.3	0.113	0.225	0.200	–
4	*Bacillus thuringiensis* 26.2	0.056	0.225	–	–
5	*Bacillus cereus* 30.1	0.225	–	0.025	0.200
6	*Lysinibacillus sphaericus* O4.3	0.056	0.113	–	–
7	*Paenibacillus polymyxa* T21.1	0.225	–	0.013	0.025
8	*Viridibacillus arvi* T26.2	0.113	0.225	0.006	0.013
9	*Escherichia fergusonii* O29.1	0.028	0.225	0.050	0.200
10	*Pseudomonas putida* 11.1	0.225	–	0.200	–
11	*Citrobacter freundii* O11.3	0.225	–	–	–
12	*Serratia proteamaculans* O11.1	0.225	–	0.200	–
13	*Meyerozyma guilliermondii* G13-4	0.15	0.30	0.05	0.05
14	*Aspergillus flavus* G3-1	0.22	0.30	0.05	0.25
15	*Penicillium citrinum* G5-1	0.30	0.60	0.50	1.00
16	*Penicillium expansum* G14-1	0.15	0.30	0.50	0.75
17	*Trichoderma harzianum* G3-2	0.15	0.30	0.25	0.75

– not determined at the maximum concentration tested

different methods of cultivation, indicating that these methods proved to be adequate for testing the diversity of sporulating and oligotrophic bacteria. The oligotrophic method of selection made it possible to isolate bacterial species (slow growers and less abundant) which in plating on a rich nutrient medium would be suppressed by other, more dominant heterotrophic bacterial species. Although the thermal inactivation method made isolation of sporulating bacteria possible, some nonsporulating species from the genera *Pseudomonas* and *Micrococcus* were also obtained. Suzina et al. (2004) indicated that certain nonsporulating bacteria, ones such as *Pseudomonas* spp. and *Micrococcus* spp., under unfavorable environmental conditions can form specialized structurally complex resting cells, which are important for the state of constitutive dormancy. In the same research, it was shown that these resting cells included cyst-like cells, which were characterized by a thickened or a multiprofiled cell wall (CW), typically made up of a layer of preexisting CW and one to three de novo synthesized murein layers, and by the presence of large intramembrane particles. Additionally, there was a difference in the composition of certain species between the sampling points. At the first two sampling points, a greater number of bacteria from the genera *Lysinibacillus* and *Paenibacillus* occurred, while there were fewer members of these genera at the last three sampling points. Bacteria from the phylum *Actinobacteria* were detected only at the first two sampling points and at the last, innermost sampling point. At the last sampling point, the highest percentage of members of the class *γ-Proteobacteria* was observed, among which the highest diversity was of *Pseudomonas* species. Bacteria of the genus *Pseudomonas* can prevail in certain guano microenvironments, probably due to their tolerance to different physical conditions and metabolic diversity (Mulec et al. 2002). The great diversity of bacterial species in the cave's guano can also be explained by structure of the Ogorelička Pećina Cave, proximity to its entrance in the case of the first two sampling points, or high humidity in the cave's inner part in the case of the last sampling point. The identified bacteria coincide with the previously described composition of bacterial communities in caves. Examination of a cave in Dunhuang (Gansu Province, China) revealed the presence of bacteria from different genera, among which the most prominent members were from the genera *Bacillus* and *Paenibacillus* (Ma et al. 2015). Analysis of microbial diversity in the Fairy Cave (Colorado, USA) showed species of the phylum *Actinobacteria* to be predominant, followed by bacteria of the phylum *Firmicutes*, and classes of *α-Proteobacteria*, *β-Proteobacteria*, and *γ-Proteobacteria* (Barton 2006). In the present case, however, the composition of certain bacterial species deviates from the results obtained in earlier examinations of guano samples (De Mandal et al. 2015; Di Bella et al. 2003). In the light of those results (De Mandal et al. 2015; Di Bella et al. 2003), a higher abundance of *Chloroflexi*, *Actinobacteria*, and *Proteobacteria* was

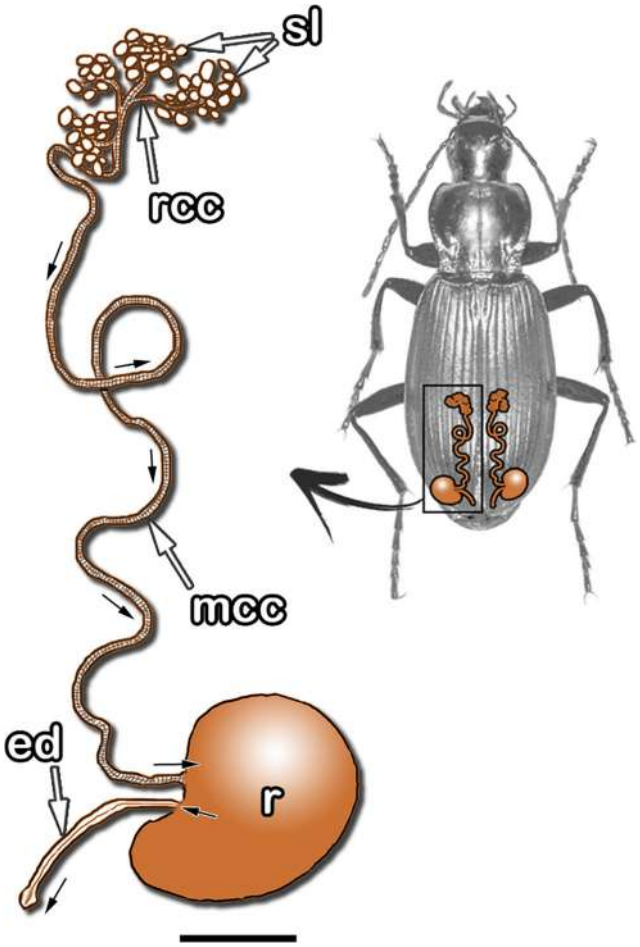

Fig. 6 Schematic depiction of location (right) and general morphology (left) of the pygidial glands of *L.* (*P.*) *punctatus*. sl cluster of secretory lobes with radial collecting canals (rcc); mcc main collecting canal, r reservoir, ed efferent duct. Small black arrows show direction of secretion flow. Scale 1 mm

expected to be present. The reason for this deviation probably lies in the chosen method of cultivation of bacterial isolates, which does not provide a realistic picture of the environment's diversity (Hugenholtz et al. 1998) as metagenomic analysis does. A large number of bacteria observed in natural habitats have not yet been successfully cultivated in laboratory conditions. Our methods were selected for the isolation of potential antagonists and their further testing. The resulting differences in bacterial populations between guano layers were expected due to different conditions between the layers. In the upper guano layer, a higher percentage of aerobic, heterotrophic bacterial species (*Pseudomonas* spp., *Bacillus* spp.) and a higher percentage of enterobacteria (*Citrobacter* spp., *Kluyvera* spp., and *Escherichia* spp.) were observed. In the lower guano layer, facultative anaerobic and oligotrophic bacterial species (*Paenibacillus* spp., *Lysinibacillus* spp., and *Staphylococcus* spp.) were mainly present. In a study of the microbial diversity of guano samples from Romanian caves, smaller number of bacteria and lower bacterial diversity (without the presence of coliform bacteria) were detected in deeper layers of guano than in the guano surface (Borda et al. 2014).

Concerning fungal distribution, the total of 16 identified species indicates that moderate fungal diversity occurs in guano samples from the Ogorelička Pećina Cave. Published data on the diversity of guanophilic fungi in other European caves are rather scarce. A moderate diversity of guanophilic fungi was reported in other European caves, especially in caves of Slovakia: in the Ardovská and Domica Caves (Nováková et al. 2005), as well as in the Harmanecká and Driny Caves (Ogórek et al. 2016). By way of contrast, high diversity of guanophilic fungi was reported by Nieves-Rivera et al. (2009) for three caves in southwestern Puerto Rico, where the presence of 50 different species was recorded. Differences in fungal diversity reported in various investigations of guano samples are due to use of different isolation and cultivation methods, different numbers of samples examined, and different environmental factors in the caves. The obtained results concerning the density of fungal spore concentration either correspond with the data presented by Ogórek et al. (2016) for the Harmanecká (3498.3 CFU/g) and Driny (4720.1 CFU/g) Caves in Slovakia, or else the density in the current study is higher. It should be emphasized that the highest fungal concentration was documented on the DG18 medium (6384.61 CFU/g, sampling point 2, upper guano layer). To our knowledge, this medium has not so far been used for isolation of guanophilic fungi, and the results obtained with it suggest xerophilic preferences of some isolates. Nevertheless, the highest fungal diversity was documented at the last, innermost sampling point (75% of all identified species), using the non-selective PDA medium (5447.78 CFU/g), which could point to the existence of optimal conditions for the majority of guanophilic fungi detected in the present study. The results of our qualitative analyses of fungi correspond with previously published data on the guanophilic mycobiota in other cave systems worldwide. The fungal isolates recorded in our research to have the highest isolation frequency, namely, isolates of *M. guilliermondii*, *P. citrinum*, and *T. harzianum*, were also found in guano samples from other caves previously investigated. Nováková et al. (2005) reported the presence of *T. harzianum* and *P. citrinum* in guano samples from the Domica Cave in Slovakia. *T. harzianum* was also documented in stone samples from the Niedźwiedzia Cave in Poland (Ogórek et al. 2013). Ulloa et al. (2006) found *M. guilliermondii* in guano samples collected in the Juxtlahuaca Cave (Guerrero, Mexico). However, fungi with lower isolation frequency were also recorded in studies dealing with cave guano microbiology. Porca et al. (2011) isolated *M. racemosus* from the Castañar Cave in Spain, while Vanderwolf et al. (2016) reported the

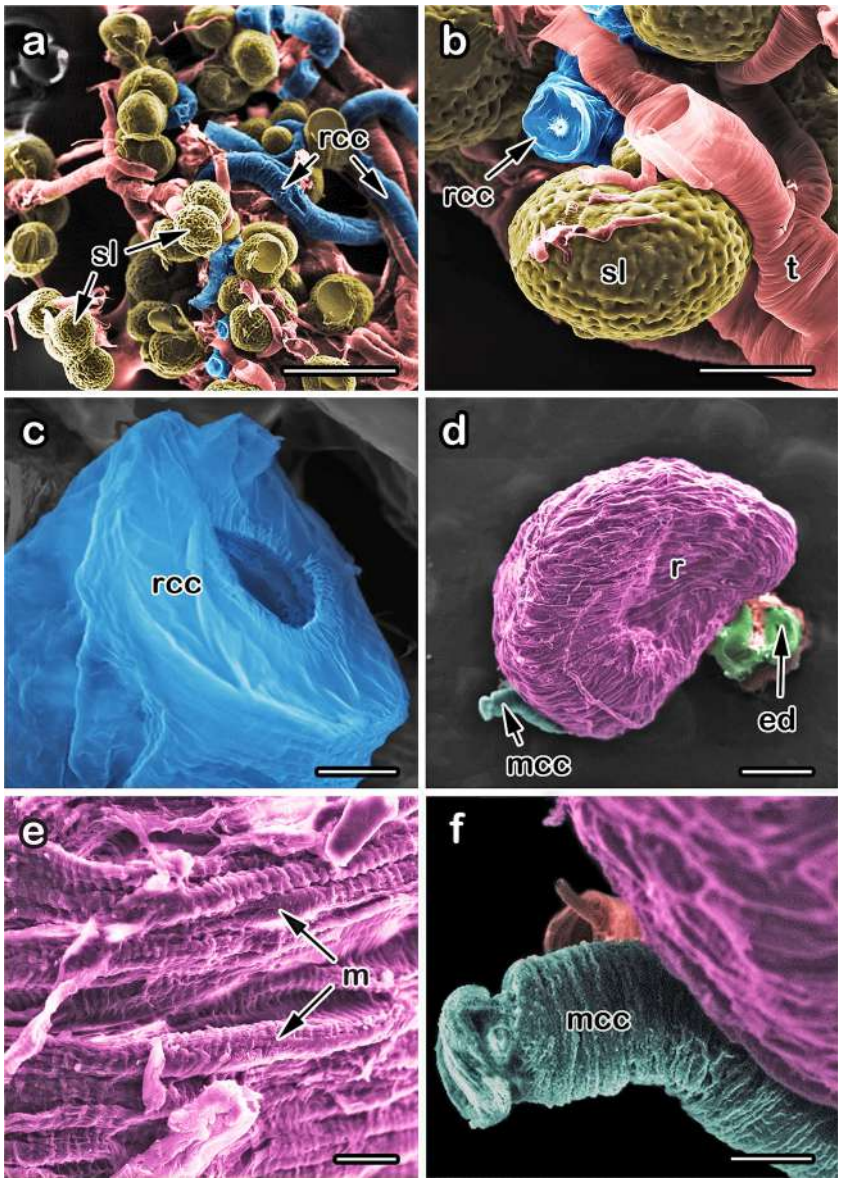

Fig. 7 SEM images of the pygidial glands of *L.* (*P.*) *punctatus*. **a** Cluster of grouped secretory lobes (sl) and radial collecting canals (rcc). **b** Single secretory lobe (sl) and radial collecting canal (rcc) intertwined with tracheoles (t). **c** Cross section of radial collecting canal (rcc). **d** Reservoir (r) with main collecting canal (mcc) and efferent duct (ed). **e** Fine structure of reservoir muscle fibers (m). **f** Part of main collecting canal (mcc). Scales: 200 μm (**a** and **d**), 50 μm (**b** and **f**), 20 μm (**e**), and 10 μm (**c**)

presence of *C. viridescens* in two caves in Canada: Grotte de la Baie de la Tour and Grotte du lac Maloin. *A. flavus* was documented in guano samples from the Domica Cave in Slovakia (Nováková 2009) and several caves in Puerto Rico (Nieves-Rivera et al. 2009).

Occurrence and abundance of *L.* (*P.*) *punctatus* in the cave

Environmental factors favorable for the occurrence and abundance of *L.* (*P.*) *punctatus* in the investigated cave included the presence of total darkness, relative atmospheric humidity between 86 and 90%, and air temperature between 13.8 and 15 °C. Lower air temperatures (below 13.8 °C) and higher relative atmospheric humidity (greater than 90%) seem to be unfavorable for the beetle's existence in the cave. Moreover, its abundance was lowest in the innermost part of the cave (last cave section) and highest in its middle part (second and third cave sections) (50–70 m from the entrance).

Chemical characterization of the pygidial gland secretion of *L.* (*P.*) *punctatus*

The pygidial gland secretion of *L.* (*P.*) *punctatus* was previously analyzed using dichloromethane as an extraction chemical (Vesović et al. 2015). There are numerous differences between the results of previous research (Vesović et al. 2015) and those of the current study. Firstly, the number of identified components in the secretion is not the same: 13 compounds were reported in previous research (Vesović et al. 2015), while only four compounds are recorded in the present study. The most dominant compound in both the

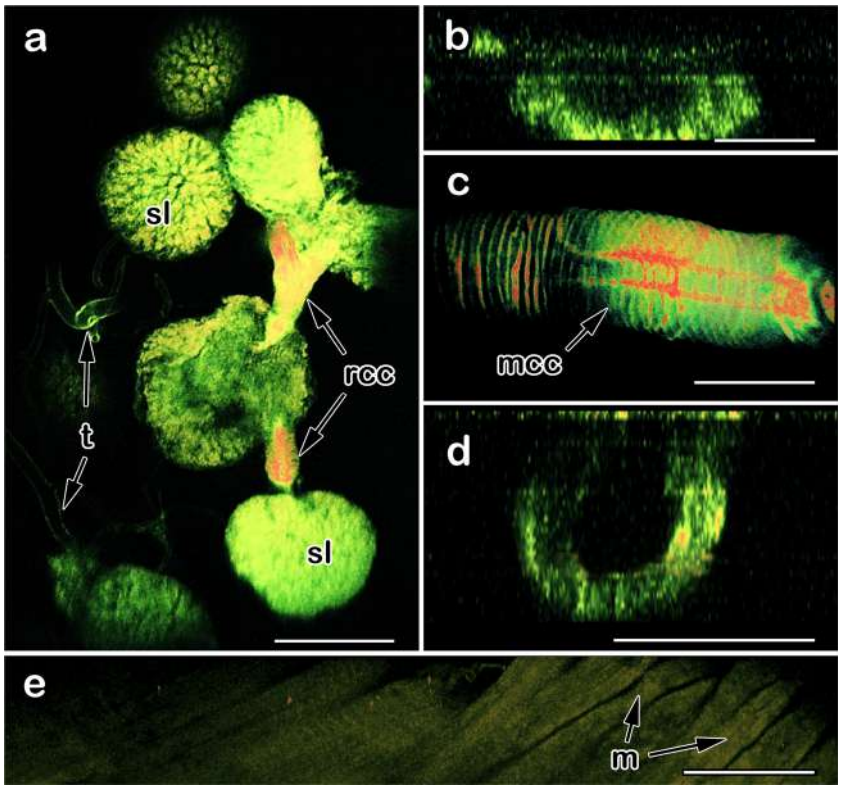

Fig. 8 TPEF modality of NLM images of the pygidial glands of *L.* (*P.*) *punctatus*. **a** Part of a cluster of grouped secretory lobes (sl) and radial collecting canals (rcc) intertwined with tracheoles (t). **b** Cross section of secretory lobe. **c** Part of main collecting canal (mcc). **d** Cross section of main collecting canal. **e** Cross section of part of reservoir's muscle wall with visible muscle fibers (m). Scales: 200 μm (**a**), 130 μm (**d**), 120 μm (**c**), and 100 μm (**b** and **e**)

previous study and the present research was undecane (40.4% vs. 58.9%, respectively), followed by dodecyl acetate (34.2% vs. 36.7%, respectively). Using different extraction method, Vesović et al. (2015) reported that the content of formic acid in the secretion was 19.4%, compared to only 1.9% in the present study. Conversely, the share of acetic acid in the secretion was 0.6% in the previous study (Vesović et al. 2015), while was 2.5% in the current research. Vesović et al. (2015) identified an additional nine compounds (oleic, palmitic, stearic and caproic acids, decyl acetate, undecyl acetate, 1-dodecanol, 9-methyltetracosane, and 7-hexyldocosane) but were not detected using a methanol extract of the secretion. Four out of five of the secretion's most abundant components extracted by dichloromethane (undecane, dodecyl acetate, formic, and acetic acids) were also identified by extraction using absolute methanol. The only compound expected to be found in the secretion but not identified in the current study was 9-methyltetracosane. In the study of Vesović et al. (2015), the concentration of this compound in the secretion was 2.6% (even greater than that of acetic acid). The reason for such qualitative differences between the two studies is most likely connected with the type of extracting solvent. To be specific, dichloromethane as a standard chemical for extracting chemical components from various secretions of arthropods seems to be better than absolute methanol for this purpose because most of the minor components of the secretion (below 1%) are not detected using the latter solvent. Methanol was used as the extraction solvent in the present study because it is the solvent best suited for testing the antimicrobial potential of arthropod secretions (Ilić et al. 2018; Stanković et al. 2016). It is also frequently used as a solvent in analyzing the chemical composition of such secretions (Clark 2009), especially for species having polar short-chain organic acids in their secretions. Additionally, it is recommended that the same solvent be used in all analyses.

Antimicrobial action of the pygidial gland secretion of *L.* (*P.*) *punctatus* against guano-dwelling microbes

The in vitro antibacterial assay demonstrated that the pygidial gland secretion of the ground beetle species *L.* (*P.*) *punctatus* possesses a significant level of antibacterial activity, mostly against Gram-positive isolates. Results of a previous study on the antibacterial potential of the pygidial gland secretion of *L.* (*P.*) *punctatus* (Nenadić et al. 2016) indicated that this secretion has moderate antibacterial activity against human pathogens. *Listeria monocytogenes*, *Enterobacter cloacae*, *Pseudomonas aeruginosa*, *S. aureus*, and *Salmonella typhimurium* showed moderate resistance to the secretion of *L.* (*P.*) *punctatus* at (MIC value of 2.2 mg/mL) (Nenadić et al. 2016). The same research also confirmed high MIC values for *B. cereus* (2.2 mg/mL), which were much higher than the MIC values obtained in our study (0.225 mg/mL). On the other hand, *E. fergusonii* in this study showed significant sensitivity to the secretion (MIC value of 0.028 mg/mL), while in the study of Nenadić et al. (2016), *E. coli* was inhibited with an

MIC value of 3.7 mg/mL. Additionally, *Micrococcus flavus* was a highly resistant strain (MIC value of 4.3 mg/mL), as shown by Nenadić et al. (2016), in comparison with our guanophilic *M. yunnanensis* isolate, which showed greater susceptibility (0.113 mg/mL).

In vitro antifungal testing indicated a fungistatic and fungicidal potential of the pygidial gland secretion of *L.* (*P.*) *punctatus* against selected guano-dwelling isolates. Fungal isolates already cited as components of the cave-dwelling mycobiota with mass sporulation and small conidia or cells (as in the case of *M. guilliermondii*) were chosen to investigate the antifungal potential of the pygidial gland secretion of the ground beetle *L.* (*P.*) *punctatus* against fungi from the cave's guano. In the case of *P. citrinum* and *T. harzianum*, the lower obtained MIC and MFC values suggested that the secretion has a stronger antifungal potential than the commercial fungicide nystatin. Antifungal activity of the pygidial gland secretion of *L.* (*P.*) *punctatus*, not only against cave-dwelling *Penicillium* and *Trichoderma* species but also against clinical isolates and laboratory strains, has already been proven by Nenadić et al. (2016, 2017), but in significantly higher concentrations than in the present study. It should be emphasized that investigations on the antimicrobial potential of ground beetle secretions are scarce.

Analysis of chemical composition of the secretion indicates the existence of variable organic components (some of them belonging to the group of fatty acids) such as formic, acetic, palmitic, and oleic acids, in a low percentage (Lečić et al. 2014; Vesović et al. 2015). It can be assumed that the presence of such compounds can be responsible for the secretion's antimicrobial potential (Nenadić et al. 2016). This assertion is apparently confirmed by the low level of cytotoxicity of the secretion (Nenadić et al. 2018).

Concerning ecological conditions, which are stable and suitable in the Ogorelička Pećina Cave throughout the year in terms of temperature and humidity, and due to significant deposits of the bat guano, the cave's population of troglophilic *L.* (*P.*) *punctatus* is particularly abundant. As reported by Casale (1988), the beetle is not strictly hypogean (troglophilic and guanophilic) and can be located in habitats above the soil surface too. We also report a great richness of microorganisms in this cave. However, the exact understanding of ecological relationship between *L.* (*P.*) *punctatus* and microorganisms living in the bat guano cannot be established at this point with certainty due to the fact that we estimated only a small portion of microbial composition of the bat guano. Due to limitation of the used conventional methods, we cannot give an estimate of the actual microbial taxa richness in the bat guano analyzed. Currently, we can only assume that chemical products of the pygidial glands of *L.* (*P.*) *punctatus* might additionally contribute to general allomonic role, by possessing a considerable antimicrobial activity against some of the microorganisms in microbiota of their natural environment. That potential secondary (i.e., antimicrobial) role of the pygidial gland secretion might be particularly significant in the stationary (pupal) stage of post-embryonic development of ground beetles (Giglio et al. 2009). However, we still cannot confirm with certainty that the pygidial gland secretion is being used for this purpose in the habitat.

In the future, studies such as ours will open possibilities of further research on ecological relationships between the analyzed and other troglophilous and guanophilous ground beetle species and microbes from the same habitat.

Morphological characterization of the pygidial glands of *L.* (*P.*) *punctatus*

Previous investigations of morphology and anatomy of the pygidial glands of *L.* (*P.*) *punctatus* (Forsyth 1972; Nenadić et al. 2016), studies in which conventional light microscopy (LM) was applied proved to be insufficient for detailed observations of these structures. A more complete investigation of the ultrastructure and anatomy of these organs was conducted in the present study using SEM and the TPEF modality of NLM.

Compared to SEM and the TPEF modality of NLM, LM is less satisfactory because it provides insight only into simple external morphology and allows conducting measurements of certain exterior structures (Forsyth 1972; Nenadić et al. 2016). The undeniable fact is that SEM is the most suitable microscopic method for observing external morphology of the pygidial glands of *L.* (*P.*) *punctatus*, since it provides detailed insight into form of the reservoir and yields the most information about the external appearance of other glandular structures (e.g., diameter, thickness and detailed structure of radial collecting canals of the secretory lobes and efferent ducts). On the other hand, the TPEF modality of NLM proved to be the most appropriate method in examining internal structure of the glands (e.g., shape, diameter and dimensions of internal structures of reservoirs, secretory lobes, collecting canals and efferent ducts; arrangement of muscle fibers) without prior preparation of the tissues, thereby providing additional three-dimensional information about the analyzed structures. Acquiring three-dimensional cross sections without preparation and cutting of tissues, their staining and labeling, as well as obtaining diameters and other dimensions of inner microstructures of the observed pygidial gland system are significant advantages of the TPEF modality of NLM over SEM and conventional LM. On the basis of all the advantages/disadvantages of the three microscopy techniques applied so far in analyzing structure of the pygidial glands in *L.* (*P.*) *punctatus*, it can be asserted that the combination of SEM and the TPEF modality of NLM provide the most detailed information about the morphology and anatomy of these biological structures.

Acknowledgments We are grateful to Dr. Saša Stanković (University of Niš - Faculty of Science and Mathematics, Niš, Serbia), who helped us in

field research. The assistance of Marina Todosijević, B.Sc., in secretion measuring is acknowledged.

Author contributions All authors contributed to the study conception and design. Material preparation, data collection, and analysis were performed by Ivica Dimkić, Jovana Kabić, Marija Nenadić, Miloš Stupar, Ljubodrag Vujisić, Svetlana Savić-Šević, Vladimir Žikić, and Nikola Vesović. The first draft of the manuscript was written by Ivica Dimkić, Jovana Kabić, Miloš Stupar, Marija Nenadić, Milica Ljaljević Grbić, and Srećko Ćurčić, and all authors commented on previous versions of the manuscript. Funding acquisition: Slaviša Stanković, Jelena Vukojević, Dejan Pantelić, Vele Tešević, Srećko Ćurčić. Supervision: Ivica Dimkić, Slaviša Stanković, Milica Ljaljević Grbić, and Srećko Ćurčić. All authors read and approved the final manuscript.

Funding information The work was financially supported by the Serbian Ministry of Education, Science and Technological Development (Grants Nos. ON173026, ON173032, ON173038, III43001, ON172053, III45016, and ON171038). This study was additionally funded jointly by the Serbian Ministry of Education, Science and Technological Development and the Ministry of Science and Technology of the People's Republic of China (Grant "Mimetics of Insects for Sensing and Security," I-2).

Compliance with ethical standards

Conflict of interest The authors declare that they have no conflict of interest.

Ethical approval All applicable international, national, and/or institutional guidelines for the care and use of animals were followed.

References

Barton HA (2006) Introduction to cave microbiology: a review for the non-specialists. J Cave Karst Stud 68(2):43–54

Blum MS (1981) Chemical defenses of arthropods. Academic Press, New York

Borda DR, Năstase-Bucur RM, Spînu M, Uricariu R, Mulec J (2014) Aerosolized microbes from organic rich materials: case study of bat guano from caves in Romania. J Cave Karst Stud 76(2):114–126

Casale A (1988) Revisione degli *Sphodrina* (*Coleoptera*, *Carabidae*, *Sphodrini*). Monografie V. Regional Museum of Natural Science, Turin

Clark VC (2009) Collecting arthropod and amphibian secretions for chemical analyses. In: Zhang W, Liu H (eds) Behavioral and chemical ecology. Nova Science Publishers, Hauppauge, pp 1–46

Ćurčić SB, Brajković MM, Ćurčić BPM (2007) The carabids of Serbia. Monographs, volume 11. Institute of Zoology, Faculty of Biology, University of Belgrade, Committee for Karst and Speleology, Serbian Academy of Sciences and Arts, Department of Conservation Biology, Vegetation- and Landscape Ecology, Faculty of Life Sciences, University of Vienna & UNESCO MAB Committee of Serbia, Belgrade-Vienna, Serbia-Austria

Daouk KD, Dagher MS, Sattout JE (1995) Antifungal activity of the essential oil of *Origanum syriacum* L. J Food Prot 58:1147–1149

De Mandal S, Zothansanga AKP, Bisht SS, Senthil KN (2015) First report of bacterial community from a bat guano using Illumina next-generation sequencing. Genom Data 4:99–101

Di Bella C, Piraino C, Caracappa S, Fornasari L, Violani C, Zava B (2003) Enteric microflora in Italian *Chiroptera*. J Mt Ecol 7:221–224

Di Giulio A, Muzzi M, Romani R (2015) Functional anatomy of the explosive defensive system of bombardier beetles (*Coleoptera*, *Carabidae*, *Brachininae*). Arthropod Struct Dev 44:468–490

Dimkić I, Živković S, Berić T, Ivanović Ž, Gavrilović V, Stanković S, Fira Đ (2013) Characterization and evaluation of two *Bacillus* strains, SS-12.6 and SS-13.1, as potential agents for the control of phytopathogenic bacteria and fungi. Biol Control 65(3):312–321

Forsyth DJ (1972) The structure of the pygidial defence glands of *Carabidae* (*Coleoptera*). Trans Zool Soc Lond 32:249–309

Giglio A, Brandmayr P, Dalpozzo R, Sindona G, Tagarelli A, Talarico F, Brandmayr TZ, Ferrero EA (2009) The defensive secretion of *Carabus lefebvrei* Dejean 1826 pupa (*Coleoptera*, *Carabidae*): gland ultrastructure and chemical identification. Microsc Res Tech 72(5):351–361

Hall TA (1999) BioEdit: a user-friendly biological sequence alignment editor and analysis program for Windows 95/98/NT. Nucleic Acids Symp Ser 41:95–98

Hänel H, Raether W (1988) A more sophisticated method of determining the fungicidal effect of water-insoluble preparations with a cell harvester, using miconazole as an example. Mycoses 31(3):148–154

Hugenholtz P, Goebel BM, Pace NR (1998) Impact of culture-independent studies on the emerging phylogenetic view of bacterial diversity. J Bacteriol 180(18):4765–4774

Ibrahim A, Hage CH, Souissi A, Leray A, Héliot L, Souissi S, Vandenbunder B (2015) Label-free microscopy and stress responses reveal the functional organization of *Pseudodiaptomus marinus* copepod myofibrils. J Struct Biol 191:224–235

Ilić B, Dimkić I, Unković N, Ljaljević-Grbić M, Vukojević J, Vujisić L, Tešević V, Stanković S, Makarov S, Lučić L (2018) Millipedes vs. pathogens: defensive secretions of some julids (*Diplopoda*: *Julida*) as potential antimicrobial agents. J Appl Entomol 142:775–791

Jiang X, Zhong J, Liu Y, Yu H, Zhuo S, Chen J (2011) Two-photon fluorescence and second-harmonic generation imaging of collagen in human tissue based on multiphoton microscopy. Scanning 33:53–56

Jovčić B, Begović J, Lozo J, Topisirović L, Kojić M (2009) Dynamics of sodium dodecyl sulfate utilization and antibiotic susceptibility of strain *Pseudomonas* sp. ATCC19151. Arch Biol Sci 61:159–165

Julg B, Elias J, Zahn A, Koppen S, Becker-Gaab C, Bogner J (2008) Bat-associated histoplasmosis can be transmitted at entrances of bat caves and not only inside the caves. J Travel Med 15:133–136

Jurado V, Laiz L, Rodriguez-Nava V, Boiron P, Hermosin B, Sanchez-Moral S, Saiz-Jimenez C (2010) Pathogenic and opportunistic microorganisms in caves. Int J Speleol 39:15–24

Kim JJ, Kim SH, Lee S, Breuil C (2003) Distinguishing *Ophiostoma ips* and *Ophiostoma montium*, two bark beetle-associated sapstain fungi. FEMS Microbiol Lett 222:187–192

Kimura M (1980) A simple method for estimating evolutionary rates of base substitutions through comparative studies of nucleotide sequences. J Mol Evol 16:111–120

Kind T (2003) Automated mass spectral deconvolution and identification system (AMDIS). www.amdis.net. Accessed 27 December 2019

Kumar S, Stecher G, Tamura K (2016) MEGA7: molecular evolutionary genetics analysis version 7.0 for bigger datasets. Mol Biol Evol 33(7):1870–1874

Lečić S, Ćurčić S, Vujisić L, Ćurčić B, Ćurčić N, Nikolić Z, Anđelković B, Milosavljević S, Tešević V, Makarov S (2014) Defensive secretions in three ground-beetle species (*Insecta*: *Coleoptera*: *Carabidae*). Ann Zool Fenn 51:285–300

Ma Y, Zhang H, Du Y, Tian T, Xiang T, Liu X, Feng H (2015) The community distribution of bacteria and fungi on ancient wall paintings of the Mogao Grottoes. Sci Rep 5:7752

Medellin RA, Wiederholt R, Lopez-Hoffman L (2017) Conservation relevance of bat caves for biodiversity and ecosystem services. Biol Conserv 211:45–50

Mulec J (2008) Microorganisms in hypogeon: examples from Slovenian karst caves. Acta Carsol 7(1):153–160

Mulec J, Zalar P, Hajna NZ, Rupnik M (2002) Screening for culturable microorganisms from cave environments (Slovenia). Acta Carsol 31(2):177–187

Nenadić M, Soković M, Glamočlija J, Ćirić A, Perić-Mataruga V, Tešević V, Vujisić L, Todosijević M, Vesović N, Ćurčić S (2016) Antimicrobial activity of the pygidial gland secretion of the troglophilic ground beetle *Laemostenus* (*Pristonychus*) *punctatus* (Dejean, 1828) (*Insecta*: *Coleoptera*: *Carabidae*). Bull Entomol Res 106:474–480

Nenadić M, Ljaljević-Grbić M, Stupar M, Vukojević J, Ćirić A, Tešević V, Vujisić L, Todosijević M, Vesović N, Živković N, Ćurčić S (2017) Antifungal activity of the pygidial gland secretion of *Laemostenus punctatus* (*Coleoptera*: *Carabidae*) against cave-dwelling micromycetes. Sci Nat 104:52

Nenadić M, Soković M, Calhelha RC, Ferreira ICFR, Ćirić A, Vesović N, Ćurčić S (2018) Inhibition of tumour and non-tumour cell proliferation by pygidial gland secretions of four ground beetle species (*Coleoptera*: *Carabidae*). Biologia 73(8):787–792

Nešić D, Pavićević D, Zatezalo A, Mijatović M, Grubač B (2008) Rezultati kompleksnih istraživanja Ogoreličke pećine. Zaštita Prirode 59:51–66

Newman MM, Kloepper LN, Duncan M, McInroy JA, Kloepper JW (2018) Variation in bat guano bacterial community composition with depth. Front Microbiol 9:914

Nieves-Rivera ÁM, Santos-Flores CJ, Dugan FM, Miller TE (2009) Guanophilic fungi in three caves of southwestern Puerto Rico. Int J Speleol 38(1):61–70

Nováková A (2009) Microscopic fungi isolated from Domica cave system (Slovak karst National Park, Slovakia). A review. Int J Speleol 38(1):71–82

Nováková A, Elhottová D, Krištůfek V, Lukešová A, Hill P, Kováč L, Mock A, Luptačik P (2005) Feeding sources of invertebrates in the Ardovská Cave and Domica Cave systems – preliminary results. In: Tajovský K, Schlaghamerský J, Pižl V (eds) Contributions to soil zoology in Central Europe. Institute of Soil Biology of the Czech Academy of Sciences, České Budějovice, pp 107–112

O'Donnell K, Cigelnik E (1997) Two divergent intragenomic rDNA ITS2 types within a monophyletic lineage of the fungus *Fusarium* are nonorthologous. Mol Phylogenet Evol 7:103–116

Ogórek R, Lejman A, Matkowski K (2013) Fungi isolated from Niedźwiedzia cave in Kletno (lower Silesia, Poland). Int J Speleol 42(2):161–166

Ogórek R, Dyląg M, Kozak B, Višnovska Z, Tančinová D, Lejman A (2016) Fungi isolated and quantified from bat guano and air in Harmanecká and Driny Caves (Slovakia). J Cave Karst Stud 78(1):41–49

Pitt JI (1979) The genus *Penicillium* and its teleomorphic state *Eupenicillium* and *Talaromyces*. Academic Press, London

Porca M, Jurado V, Martin-Sanchez MP, Hermonis B, Bastian F, Alabouvette C, Saiz-Jimenez C (2011) Aerobiology: an ecological indicator for early detection and control of fungal outbreaks in caves. Ecol Indic 11:1594–1598

Poulson TL, Lavoie KH (2000) The trophic basis of subsurface ecosystems. In: Wilkens H, Culver DC, Humphreys WF (eds) Ecosystems of the world, Subterranean ecosystems, vol 30. Elsevier, Amsterdam, pp 231–249

Rabasović MD, Pantelić DV, Jelenković BM, Ćurčić SB, Rabasović MS, Vrbica MD, Lazović VM, Ćurčić BPM, Krmpot AJ (2015) Nonlinear microscopy of chitin and chitinous structures: a case study of two cave-dwelling insects. J Biomed Opt 20:016010

Raper BK, Fennel DI (1965) The genus *Aspergillus*. The Williams and Wilkins company, Baltimore

Ristivojević P, Dimkić I, Trifković J, Berić T, Vovk I, Milojković-Opsenica D, Stanković S (2016) Antimicrobial activity of Serbian propolis evaluated by means of MIC, HPTLC, bioautography and chemometrics. PLoS One 11:e0157097

Rocha-Silva F, Figueiredo SM, Silveira TT, Assunção CB, Campolina SS, Pena-Barbosa JP, Rotondo A, Caligiorne RB (2014) Histoplasmosis outbreak in Tamboril cave—Minas Gerais state, Brazil. Med Mycol Case Rep 4:1–4

Roe AD, Rice AV, Coltman DW, Cooke JE, Sperling FA (2011) Comparative phylogeography, genetic differentiation and contrasting reproductive modes in three fungal symbionts of a multipartite bark beetle symbiosis. Mol Ecol 20:584–600

Samson RA, Houbraken J, Thrane U, Frisvad JC, Andersen B (2010) Food and indoor fungi. CBS-KNAW Fungal Biodiversity Centre, Utrecht

Savković Ž, Unković N, Stupar M, Franković M, Jovanović M, Erić S, Šarić K, Stanković S, Dimkić I, Vukojević J, Grbić ML (2016) Diversity and biodeteriorative potential of fungal dwellers on ancient stone stela. Int Biodeterior Biodegradation 115:212–223

Stanković S, Dimkić I, Vujisić L, Pavković-Lučić S, Jovanović Z, Stević T, Sofrenić I, Mitić B, Tomić V (2016) Chemical defence in a millipede: evaluation and characterization of antimicrobial activity of the defensive secretion from *Pachyiulus hungaricus* (Karsch, 1881) (*Diplopoda*, *Julida*, *Julidae*). PLoS One 11:e0167249

Suzina NE, Mulyukin AL, Kozlova AN, Shorokhova AP, Dmitriev VV, Barinova ES, Mokhova ON, Duda VI (2004) Ultrastructure of resting cells of some non-spore-forming bacteria. Microbiology 73(4): 435–447

Tamura K, Stecher G, Peterson D, Filipski A, Kumar S (2013) MEGA6: molecular evolutionary genetics analysis version 6.0. J Mol Evol 30: 2725–2729

Ulloa M, Lappe P, Aguilar S, Park H, Pérez-Mejía A, Toriello C, Taylor LM (2006) Contribution to the study of the mycobiota present in the natural habitats of *Histoplasma capsulatum*: an integrative study in Guerrero, Mexico. Rev Mex Biodivers 77:153–168

Vanderwolf KJ, Malloch D, Ivanova VN, McAlpine FD (2016) Lack of cave-associated mammals influences the fungal assemblages of insular solution caves in eastern Canada. J Cave Karst Stud 78(3): 198–207

Vandžurová A, Bačkor P, Javorský P, Pristaš P (2013) *Staphylococcus nepalensis* in the guano of bats (*Mammalia*). Vet Microbiol 164: 116–121

Vesović N, Ćurčić S, Vujisić L, Nenadić M, Krstić G, Perić-Mataruga V, Milosavljević S, Antić D, Mandić B, Petković M, Vučković I, Marković Đ, Vrbica M, Ćurčić B, Makarov S (2015) Molecular diversity of compounds from pygidial gland secretions of cave-dwelling ground beetles (*Insecta*: *Coleoptera*: *Carabidae*): the first evidence. J Chem Ecol 41:533–539

Vrbica M, Petrović A, Pantelić D, Krmpot A, Rabasović M, Pavlović D, Jovanić S, Guéorguiev B, Goranov S, Vesović N, Antić D, Marković Đ, Petković M, Stanisavljević L, Ćurčić S (2018) The genus *Pheggomisetes* Knirsch, 1923 (*Coleoptera*: *Carabidae*: *Trechinae*) in Serbia: taxonomy, morphology and molecular phylogeny. Zool J Linnean Soc 183:347–371

Wallace SJ, Morrison JL, Botting KJ, Kee TW (2008) Second-harmonic generation and two-photon-excited autofluorescence microscopy of cardiomyocytes: quantification of cell volume and myosin filaments. J Biomed Opt 13:064018

Watanabe T (2002) Soil and seed fungi. Morphologies of cultured fungi and key to species. CRC Press, London

White TJ, Bruns T, Lee S, Taylor J (1990) Amplification and direct sequencing of fungal ribosomal RNA genes for phylogenetics. In: Innis MA, Gelfand DH, Sninsky JJ, White TJ (eds) PCR protocols: a guide to methods and applications. Academic Press, New York, pp 315–322

Publisher's note Springer Nature remains neutral with regard to jurisdictional claims in published maps and institutional affiliations.

IOPscience iopscience.iop.org

Home Search Collections Journals About Contact us My IOPscience

Biomechanical model produced from light-activated dental composite resins: a holographic analysis

This content has been downloaded from IOPscience. Please scroll down to see the full text.

2013 Phys. Scr. 2013 014021

(http://iopscience.iop.org/1402-4896/2013/T157/014021)

View the table of contents for this issue, or go to the journal homepage for more

Download details:

IP Address: 147.91.1.41
This content was downloaded on 14/04/2014 at 13:45

Please note that terms and conditions apply.

Phys. Scr. **T157** (2013) 014021 (5pp) doi:10.1088/0031-8949/2013/T157/014021

Biomechanical model produced from light-activated dental composite resins: a holographic analysis

Dejan Pantelić[1], Darko Vasiljević[1], Larisa Blažić[2], Svetlana Savić-Šević[1], Branka Murić[1] and Marko Nikolić[3]

[1] Photonics Center, Institute of Physics, University of Belgrade, Belgrade, Serbia
[2] Vojvodina Clinic of Dentistry, Faculty of Medicine, University of Novi Sad, Novi Sad, Serbia
[3] Laboratory for Radiation Chemistry and Physics, Vinca Institute of Nuclear Sciences, University of Belgrade, Belgrade, Serbia

E-mail: darko@ipb.ac.rs

Received 25 August 2012
Accepted for publication 18 December 2012
Published 15 November 2013
Online at stacks.iop.org/PhysScr/T157/014021

Abstract
Light-activated dental composites, commonly applied in dentistry, can be used as excellent material for producing biomechanical models. They can be cast in almost any shape in an appropriate silicone mold and quickly solidified by irradiation with light in the blue part of the spectrum. In that way, it is possible to obtain any number of nearly identical casts. The models can be used to study the behavior of arbitrary structure under mechanical loads. To test the technique, a simple mechanical model of the tooth with a mesio–occluso–distal cavity was manufactured. Composite resin restoration was placed inside the cavity and light cured. Real-time holographic interferometry was used to analyze the contraction of the composite resin and its effect on the surrounding material. The results obtained in the holographic experiment were in good agreement with those obtained using the finite element method.

PACS numbers: 42.40.Kw, 42.40.My, 87.85.G−, 87.85.J−

(Some figures may appear in color only in the online journal)

1. Introduction

Bio-mechanical structures are frequently modeled in order to study their functionality and properties when loaded. Models can be either mechanical (in hardware) or digital (in software). Even though contemporary computers are capable of modeling complicated structures, mechanical models are still closer to reality—especially if biological (anatomical) structures are analyzed.

Bio-mechanical models can be directly produced from computer-aided design (CAD) drawings or computer aided tomography (CAT) and magnetic resonance imaging (MRI) images [1, 2] using rapid prototyping [3, 4]. Models are usually made from plastic materials (e.g. acrylonitrile butadiene styrene) [5] or composites (glass fiber epoxy) [6]. In order to analyze internal stresses, photo-elastic techniques are used. Replicas of various biological structures are made from epoxy resin and polycarbonate- [7] or methacrylate- [8] based substances.

Mechanical models can be fabricated using alternative materials provided they are readily available, have useful mechanical properties and can be easily molded. In that respect, light-curing dental composite resins seem to be good candidates [9]. These are paste-like substances composed of three essential components: a resin-based polymer matrix, a photo-initiator (usually camphorquinone) and a filler (hard material particles). After irradiation with blue light (with the spectrum centered at 474 nm), a polymerization reaction is initiated, transforming composite resin to a solid state [10]. When cured, dental composite resin is a hard material, imitating dentin and enamel, with regard to modulus of elasticity, hardness, color and translucency [11, 12].

Once produced, models are mechanically loaded in order to study their deformation. Deformation can be measured in

 © 2013 The Royal Swedish Academy of Sciences Printed in the UK

various ways: using transducers [13], photo-elasticity [7, 8], and speckle or holographic interferometry [14], just to name a few techniques.

Holographic interferometry seems to be well suited to analysis in biomechanics, due to its ability to observe arbitrary, irregular objects in three dimensions. It is very sensitive—capable of measuring micron and submicron deformations.

The goal of our research was to use holography to analyze the behavior of a mechanical model made of dental composite resin. To test the model, we decided to analyze the problem of polymerization shrinkage that accompanies the polymerization reaction during setting of composite resin restoration. Light-induced polymerization, which follows composite resin insertion, leads to material contraction and transfer of mechanical stress to cavity walls, which may result in coronal deformation, post-operative sensitivity, microfractures and microleakage due to failure of tooth-restoration adhesive interfaces [15].

2. Mechanical model manufacturing using composite resins

The tooth model with simplified geometry representing a class II mesio–occluso–distal (MOD) cavity was produced. Such geometry enabled reliable comparison of the experimental results with finite element method (FEM) calculations. Thus, predictions of finite element analysis could be verified and internal stress distribution calculated.

Firstly, a template was made of aluminum and impressed into Elite HD (Zhermack, Italy) addition-type silicone impression material (which guaranteed accuracy of the order of 1.5 μm [16]). The composite resin (Gradia direct anterior A2—manufactured by GC Dental Products Corp., Japan) was inserted in increments of 2 mm into the mold and cured (Smartlite PS, Dentsply, USA). Insertion of an equal amount of composite resin was obtained by weighing the material portions before placement. After finishing a light-curing procedure, the composite resin was extracted and the same silicone mold was used over and over for further production of the models.

The MOD cavity models were placed in the aluminum holders and rigidly attached using the dental plaster (Marmorock 20; Dr Böhme & Schöps, GmbH, EN 26873/ ISO 6873, class IV-green). In this way, they could be inserted into the experimental setup, with the stability required in holography. Models had to be silver painted in order to record high-contrast interference fringes (PX-20(L), Mitsubishi Pencil Co. Ltd). Otherwise, the light would penetrate deep into the model with back-scatter from inside the material. The correlation between the wavefront reflected from the mechanical loaded model and its holographic image (in an unloaded state) would then be lost. As a result, the contrast of the resulting interference pattern would become extremely low. It should be noted that the paint layer was so thin that it could not influence the mechanical properties of the model as a whole.

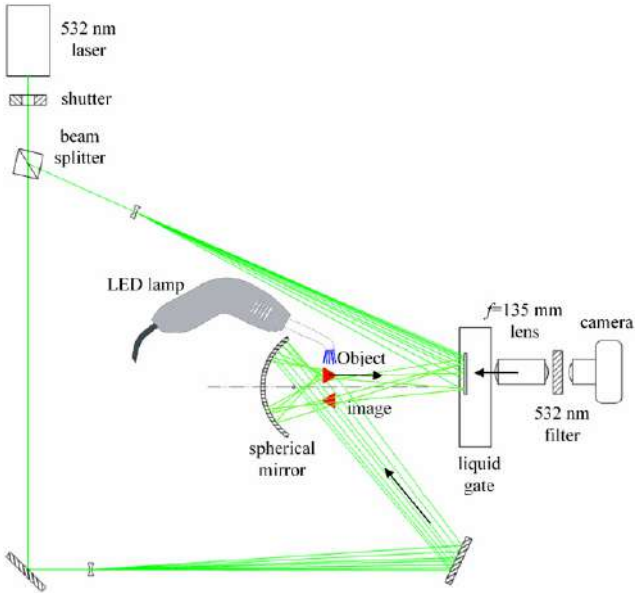

Figure 1. Real-time holography setup. Red triangles in the figure represent the object and its inverted mirror image.

3. Real-time holography measurements

Real-time-holographic interferometry has previously been used in biomechanical research [17, 18]. The hologram of an object in its initial, unperturbed state was recorded. After hologram reconstruction, electromagnetic waves emanated from the three-dimensional holographic image and reflected from the object interfered. If an object were mechanically loaded, interference fringes would appear, indicating an amount of deformation.

The real-time, split-beam holographic setup was used (figure 1). The laser beam (532 nm wavelength, 80 mW power) was divided into an object and a reference component. The object beam illuminated the tooth model, while the reference beam illuminated the photosensitive (holographic) plate. The photosensitive material was placed in a container with glass walls (so-called liquid gate) and used to perform wet chemical processing without disturbing the hologram (*in situ*).

A spherical mirror was used to produce an image of the back of the model. In this manner we could simultaneously observe both the sides, giving us a complete picture of the deformation field. This is particularly important when investigating asymmetrical objects or asymmetrical loads. The interference pattern was recorded using a CCD camera, by observing through the liquid gate. In order to enlarge the image, the lens (135 mm focal length) was placed between the liquid gate and the camera. An interference filter was used to block polymerization light (470 nm) and transmit the laser light (532 nm) used in the holographic experiment.

The measurements were performed as follows. The MOD cavity of the tooth model was bulk filled with the composite resin and placed inside the holographic setup. For each cavity, the material was weighed in order to ensure placement of an equal amount. The holographic plate (green-sensitive VRP-M type, manufactured by Slavich, Russia) was loaded in the

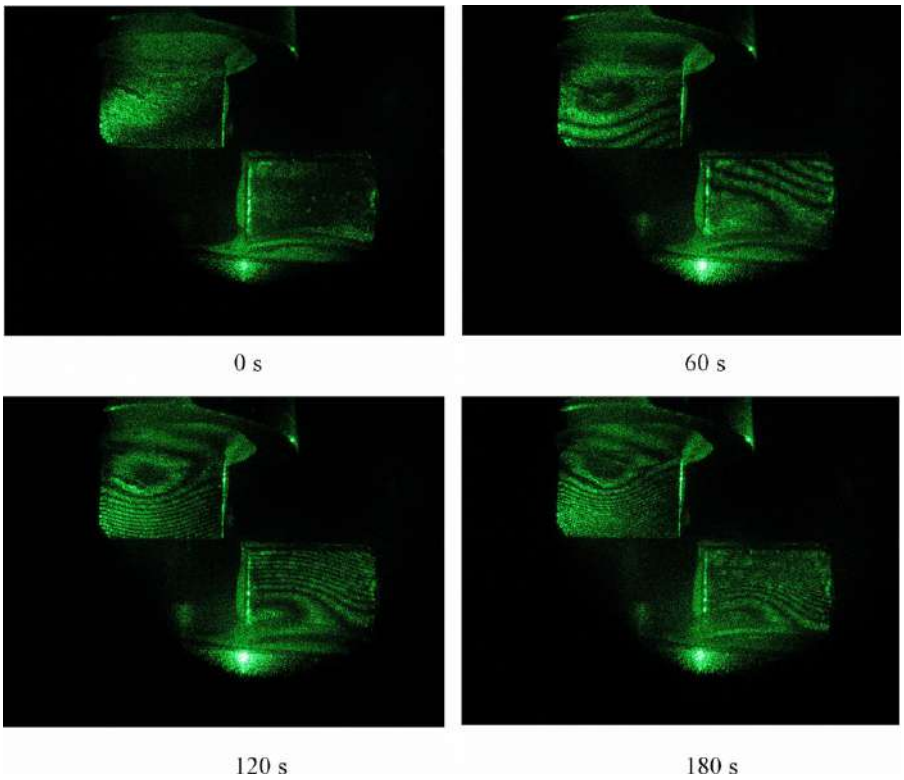

Figure 2. Sequence of holographic interferograms, recorded at 60 s intervals. The model itself is on the right, while its image in a spherical mirror is on the left, turned upside down.

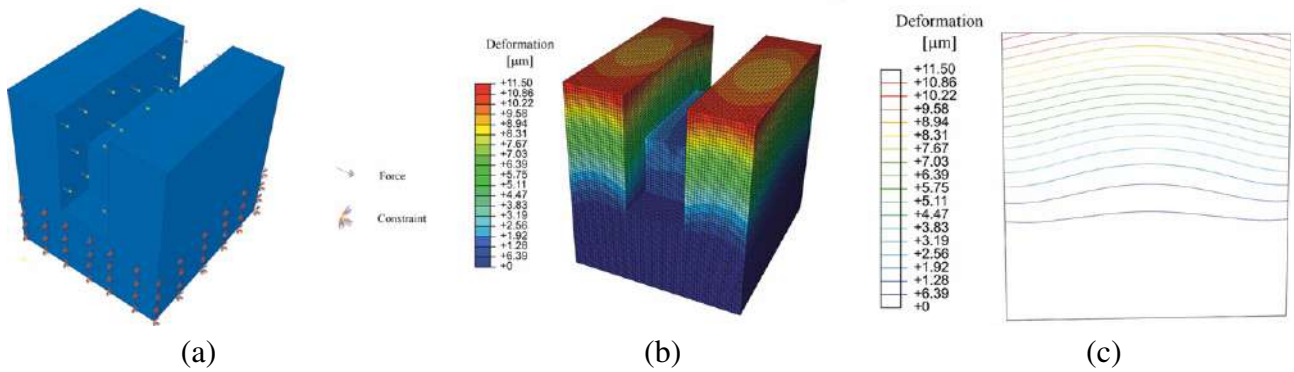

Figure 3. (a) FEM model with constraints (marks at the bottom of the model) and forces (arrows), (b) three-dimensional deformation field calculated using FEM and (c) lines of equal deformation on the external wall of the model—compare them to experimentally recorded interference patterns in previous figures.

liquid gate filled with distilled water. The photosensitive material was left in the gate for several minutes, in order to swell the gelatin layer. Exposure was made by opening the laser beam shutter for 1 s. The liquid gate was emptied, and the developer (Ilford ID-11) was poured in. After 30 s of development, the developer was poured out. Several distilled water baths followed, in order to thoroughly wash the film. This completed the hologram process recording. The final water bath was left inside the liquid gate, and the hologram was observed through the water.

The light polymerization of the composite resin restoration was initiated by the LED light source positioned directly above the model. The resulting contraction of the composite resin induced the deformation of the model and the reflected wavefront was distorted. The interference between the reflected and the holographically 'frozen' wavefronts produced dark and bright fringes.

At the beginning of the polymerization, fringes appeared at the top of the external cavity wall. During polymerization, fringes floated downwards to the bottom of the model and their number increased. After 3 min the interference pattern stabilized, indicating that the polymer was cured. The sequence of images was recorded (using a CCD camera at 1 frame s^{-1}) corresponding to the temporal variation of the interference pattern (four out of 140 images are shown in figure 2). The number of interference maxima gave information on the total deformation at any particular object point.

In order to test the reproducibility of the model making and the analysis, the holographic procedure was repeated on five identical tooth models. They were produced using the same type of composite resin and utilizing the same silicone mold. The holographic experiment was repeated for each model. Every time practically the same interference pattern was seen on the model surface.

4. Finite element analysis of the model

It is important to point out that the deformation measurement was just the starting point for the calculation of internal stress using the finite element method. The digital geometric model of the object under investigation was constructed. The model was meshed, directions of forces and pressures were defined and boundary conditions were given in accordance with the experiment (see figure 5(a)).

The mechanical structure under investigation was simple, and the construction of the digital model was straightforward. It had 242 576 nodes in 228 520 brick (linear hexahedral) elements and was constrained at its base (see figure 3(a)). Uniform pressure was applied to all free surfaces of the MOD cavity. The elasticity modulus of the dental composite used in this research (Gradia direct anterior) was 5.2 GPa and its Poisson's ratio was 0.22, according to [19].

The pressure reproducing the measured deformation was determined (see figures 3(b) and (c)). It could be seen that the numerical results matched the experimentally recorded interference pattern (figure 2).

5. Discussion and conclusion

In this work, we detected an effect of the composite resin restoration polymerization contraction on the surrounding structure. From a dental practitioner's point of view, the whole method was a good approximation to the real therapeutic procedure. Performing the testing procedure was easy, since the inserted restoration of an uncured composite resin adhered well to the model (made of cured composite resin). The molds and the restorations were made from the same composite resin in order to obtain a totally maintained interface between the tooth model and the composite restoration during light-induced polymerization. Such an interface represented the same pattern used while restoring a cavity preparation in an everyday dental practice; composite resin material is inserted in a portion, while every increment adheres to a previous one.

When a composite restoration is cured inside the model of a MOD cavity, accompanying contraction is transferred to the cavity walls expressed as a deformation. In a clinical surrounding, where a gap might develop between a tooth and restorative material, the free surface of a composite resin plays an important role in stress relief, decreasing its impact on the surrounding structure. The flow capacity of restoration with debonding is increased and the resulting deformation of cavity walls cannot be detected completely. That is why it is expected that the method presented would give more accurate insight into the stresses transferred to the bounded tooth structure while performing the restorative procedure.

We showed that dental composite resins could be effectively used for the manufacture of mechanical models. A great number of dental composite resins are available on the market, with a range of mechanical properties, which can be matched to a particular application. Using the silicone mold, an almost arbitrary number of identical casts could be manufactured. This can be particularly important in biomechanics, where collecting of biological samples is time consuming and raises ethical questions. In addition, there is great variability between biological specimens, making it difficult to perform the same measurement under the same conditions. Coupled with holographic interferometry, reproducible and reliable results were obtained regarding deformation and stress measurement. Anyway, small structures (teeth, small bones) could be effectively produced, at quite reasonable cost.

The method described in this paper is particularly suited to studying various dental procedures, such as composite resin polymerization techniques and strategies, loading of teeth and dental implants. The findings obtained could help dental practitioners choose therapeutic procedures that are most favorable for patients.

Acknowledgment

This research was funded by the Serbian Ministry of Education and Science under contract numbers III 45016 and OI 171038.

References

[1] Undt G, Wild K, Reuther G and Ewers R 2000 MRI-based stereolithographic models of the temporomandibular joint: technical innovation *J. Cranio-Maxillofacial Surg.* **28** 258–63
[2] Kantardžić I, Vasiljević D, Blažič L and Tasić M 2012 Computed-tomography scan based finite element analysis of stress distribution in premolars restored with composite resin *Phys. Scr.* **T149** 014075
[3] Ready J F and Farson D F 2001 *Handbook of Laser Materials Processing* (Orlando, FL: Laser Institute of America) pp 541–81
[4] Steen W M 2003 *Laser Material Processing* (London: Springer) pp 279–99
[5] Sanghera B, Naique S, Papaharilaou Y and Amis A 2001 Preliminary study of rapid prototype medical models *Rapid Prototyping J.* **7** 275–84
[6] Katz D M, Blatcher S and Shelton J C 1998 Quantification of holographic fringe data: comparison of intact and implanted femurs *Med. Eng. Phys.* **20** 114–23
[7] Shuster M, Sherman D, Siegmann A, Narkis M, Jennewein C M and Eyerer P 1996 Stress distribution in and around a spherically ended fiber embedded in a polymer matrix *Polym. Compos.* **17** 568–77
[8] Cehreli M, Duyck J, De Cooman M, Puers R and Naert I 2004 Implant design and interface force transfer: a photoelastic and strain-gauge analysis *Clin. Oral Implant. Res.* **15** 249–57
[9] Moszner N and Salz U 2006 Composites for dental restoratives *Polymers for Dental and Orthopedic Applications* ed S W Shalaby and U Salz (Baton Range, FL: CRC Press/Taylor and Francis) pp 13–69
[10] Cook W D 1982 Spectral distribution of dental photopolymerization sources *J. Dent. Res.* **61** 1436–8
[11] Delfino C S, Pfeifer C S C, Braga R R, Youssef M N and Turbino M L 2009 Shrinkage stress and mechanical properties of photoactivated composite resin using the argon ion laser *Appl. Phys.* B **96** 79–84
[12] Lee Y K and Powers J M 2007 Color changes of resin composites in the reflectance and transmittance modes *Dent. Mater.* **23** 259–64
[13] Jantarat J, Panitvisai P, Palamara J E A and Messer H H 2001 Comparison of methods for measuring cuspal deformation *J. Dent.* **29** 75–82
[14] Shahar R and Weiner S 2007 Insights into whole bone and tooth function using optical metrology *J. Mater. Sci.* **42** 8919–33

[15] Blažić L, Pantelić D, Savić-Šević S, Murić B, Belić I and Panić B 2011 Modulated photoactivation of composite restoration—measurement of cuspal movement using holographic interferometry *Lasers Med. Sci.* **26** 179–86

[16] Verran J, Rowe D L and Boyd R D 2003 Visualization and measurement of nanometer dimension surface features using dental impression materials and atomic force microsscopy *Int. Biodeterioration Biodegradation* **51** 221–8

[17] Ko K, Erickson R, Schmidt T and Webster J 2005 Holographic interferometry of cerebral pulsations *Surg. Neurol.* **63** 118–22

[18] Gesualdi M R R, Mori M, Muramatsu M, Liberti E A and Munin E 2007 Phase-shifting real-time holographic interferometry applied to load transmission evaluation in dried human skull *Appl. Opt.* **46** 5419–29

[19] Sorrentino R, Aversa R, Ferro V, Auriemma T, Zarone F, Ferrari M and Apicella A 2007 Three-dimensional finite element analysis of strain and stress distributions in endodontically treated maxillary central incisors restored with diferent post, core and crown materials *Dent. Mater.* **23** 983–93

Optical Materials xxx (2013) xxx–xxx

Contents lists available at SciVerse ScienceDirect

Optical Materials

journal homepage: www.elsevier.com/locate/optmat

Butterfly scales as bionic templates for complex ordered nanophotonic materials: A pathway to biomimetic plasmonics

Zoran Jakšić [a,*], Dejan Pantelić [b], Milija Sarajlić [a], Svetlana Savić-Šević [b], Jovan Matović [c], Branislav Jelenković [b], Dana Vasiljević-Radović [a], Srećko Ćurčić [d], Slobodan Vuković [a], Vladimir Pavlović [e], Jelena Buha [f], Vesna Lačković [g], Milica Labudović-Borović [g], Božidar Ćurčić [d]

[a] Centre of Microelectronic Technologies and Single Crystals, Institute of Chemistry, Technology and Metallurgy, University of Belgrade, Njegoševa 12, 11000 Belgrade, Serbia
[b] Institute of Physics, University of Belgrade, Pregrevica 118, 11080 Zemun, Serbia
[c] Institute of Sensors and Actuator Systems, Vienna University of Technology, Floragasse 7/E366 A, 1040 Vienna, Austria
[d] University of Belgrade, Faculty of Biology, Institute of Zoology, Studentski Trg 16, 11000 Belgrade, Serbia
[e] University of Belgrade, Faculty of Agriculture, Dept. Agricultural Engineering, Nemanjina 6, 11080 Zemun, Belgrade, Serbia
[f] EMPA, Swiss Federal Laboratories for Materials Science and Technology, Überlandstrasse 129, 8600 Dübendorf, Switzerland
[g] University of Belgrade, Faculty of Medicine, Institute of Histology and Embryology, Višegradska 26, 11000 Belgrade, Serbia

ARTICLE INFO

Article history:
Available online xxxx

Keywords:
Nanophotonics
Plasmonics
Biomimetics
Nanocomposites
Butterfly scales

ABSTRACT

In this paper we propose a possible use of butterfly scales as templates for ordered 2D or 3D nanophotonic materials, with complexity not easily reproducible by conventional micro/nanofabrication methods. Functionalization through laminar nanocompositing is utilized to impart novel properties to the biological scaffold. An extremely wide variability of butterfly scale forms, shapes, sizes and fine structures is observed in nature, many of them already possessing peculiar optical properties. Their nanophotonic functionalization ensures a large choice of forms and functions, including enhanced light localization, light and plasmon waveguiding and general metamaterial behavior, to mention a few. We show that one is able to achieve a combination of plasmonics and bionics, resulting in functionalities seldom if ever met in nature. As an illustration we have analyzed the photonic properties of the nanostructured scales on the wings of Purple Emperor butterflies *Apatura ilia*, *Apatura iris* and *Sasakia charonda*. Their intricate nanometer-sized structures produce remarkable ultraviolet-blue iridescence, spectrally and directionally narrow. We present our analysis of their plasmonic/nanophotonic functionalization including preliminary calculations and initial experimental results. As a simple example, we used radiofrequent sputtering to produce nanoaperture-based plasmonic structures at a fraction of the cost and necessary engineering efforts compared to the conventional top-down methods. We conclude that the described pathway to biomimetic plasmonics offers potentials for significant expansion of the nanophotonic and nanoplasmonic material toolbox.

© 2013 Elsevier B.V. All rights reserved.

1. Introduction

Plasmonics is playing an ever increasing role in contemporary photonics, nanophotonics, nanosciences and physical sciences generally. Propagation of surface plasmons polaritons (SPPs) has been proposed as the operating principle of a new generation of ultrafast and ultra-compact electronics, merging the density of contemporary integrated circuits with extreme speeds of all-optical photonic devices [1]. Plasmonics also represents the basis of modern adsorption-based ultrasensitive, label-free chemical and biological sensors. Last but not least, plasmonics opens a pathway toward optical metamaterials with electromagnetic properties surpassing those of ordinary materials, thus opening a door to novel phenomena and novel principles of operation, even opening the new field of transformation optics [2].

Basically plasmonics is based on artificial 1D, 2D or 3D ordered metal-dielectric superlattices with subwavelength dimensions (subwavelength plasmonic crystals) – or, more generally, nanostructures containing parts with both positive and negative values of relative dielectric permittivity ε. The frequency dispersion of the negative ε parts is most often described by Drude or Lorentz model. Plasmonic structures support the formation of SPP electromagnetic waves that are evanescent in the directions perpendicular to the surface. Due to the highly nonlinear spectral dispersion of plasmonic materials SPP waves may have extremely large values of wavevector, i.e. their wavelengths are often much smaller than in vacuum at the identical frequency, reaching down to tens of nanometers at optical frequencies [3]. A wealth of different modes may

* Corresponding author. Tel.: +381 11 2628 587, mobile: +381 64 3257 897; fax: +381 11 2182 995.
E-mail address: jaksa@nanosys.ihtm.bg.ac.rs (Z. Jakšić).

0925-3467/$ - see front matter © 2013 Elsevier B.V. All rights reserved.
http://dx.doi.org/10.1016/j.optmat.2013.04.004

appear in such structures, including those with superluminal group velocities, slow light and negative group velocities. These modes may be tailored by the design of plasmonic nanostructures.

One of the large obstacles toward a more widespread use of nanoplasmonic structures and devices is the complexity of their fabrication. Typically the dimensions of their building blocks should be much smaller than the operating wavelengths, and, as mentioned above, the wavelengths themselves in plasmonic structures are much shorter than those of visible light in vacuum. This leaves one with a need to fabricate ordered nanostructures in the range of tens of nanometers and smaller. While such a task is relatively straightforward for 1D structures, the ultrathin film deposition technologies being mature and well developed, this is not the case with 2D and even less with 3D structures.

A source of the most complex forms man has ever encountered is biology, living organisms being a wealth of intricate structures with an infinity of variations. Ordered structures with characteristic dimensions in the micrometer and nanometer range and with a plethora of different properties are readily found in living organisms. However such structures nevertheless cannot be harvested and straightforwardly utilized in plasmonics, and indeed, as far as the authors of this text know, until now man has not encountered biological plasmonic structures. However, one can always adopt bionic approach, where one of the possibilities is to use a biological pattern as a template for the fabrication of artificial nanostructures [4]. Thus it obviously occurs that one could utilize the intricacy of the structural traits of biological forms to obtain biomimetic/bionic structures for plasmonics.

In optics, a wealth of different shapes and forms with a plethora of optical functionalities is met in zoological structures, and especially within the insect world [5]. A large diversity of optical nanostructures is met among butterflies (order Lepidoptera), where an extremely wide variability of butterfly scale forms, shapes, sizes and fine structures is observed [6]. This leads to various optical effects that can be observed. A bionic use of iridescent butterfly scales as a biological platform for sensing was reported in [7], where *Morpho* butterfly scales were used as low-thermal-mass resonator for infrared detection. Another example is the use of butterfly scales for sensing with highly selective vapour response [8]. Metallization of butterfly scales was utilized to obtain naturally inspired substrates for biochemical analysis utilizing surface enhanced Raman spectroscopy [9].

In this work we propose the use of butterfly scales for bionic structures for nanoplasmonics. To this purpose we analyze the applicability of nanostructured scales of *Apatura ilia* (Denis and Schiffermüller, 1775), *Apatura iris* (Linnaeus, 1758) and *Sasakia charonda* (Hewitson, 1863) butterflies [10–12]. We theoretically and experimentally consider the possibility to functionalize the scales utilizing the deposition of plasmonic materials, thus obtaining a biological–nonbiological hybrid with plasmonic functionality.

2. Material and method

We consider a specific case of the Purple Emperor (*A. iris*), Lesser Purple Emperor (*A. ilia*), and Great Purple Emperor (*S. charonda*). Their wings show a variety of optical effects, one of which is angle-dependent iridescence, i.e. high angular and spectral selectivity [10]. A similar situation is naturally occurring in many other Lepidoptera species [6], where the observed color strongly depends on the mutual position of the light source, the butterfly wing and the observer. In Fig. 1 orange or brown[1] color of the dorsal side of the wings of male *A. ilia* butterfly can be seen from all angles, while

Fig. 1. Example of directional iridescence in *A. ilia* butterfly. (The overall appearance and pattern of iridescence of *A. iris* and *Sasakia Charonda* is similar to *A. ilia*).

purple iridescence is seen only from some specific and rather well defined positions. The position of the butterfly when making the photograph shown in Fig. 1 was so adjusted to show angular iridescence on the right fore and hind wings only. Thus the left fore and hind wings appear orange-brownish, while the right fore and hind ones are with purple hue, although the color of both pairs of wings is actually identical.

Let us consider first the microstructure of the wings of the Purple Emperor (*A. iris*) butterflies we analyzed. When observed by scanning electron microscope (SEM) they show scale-like structures that completely cover their surface. Each scale is a small plate-like structure and they are arranged on the wings like tiles on the roof (Fig. 2). Two types of scales on the dorsal side of both the fore and hind wings exist – cover and ground scales. Iridescence is observed only in the former ones.

Finer examination (Fig. 3) shows that the cover scales in the case of *A. ilia*, *A. iris* and *S. charonda* butterflies [10,11,13] possess a series of parallel ridges which behave like a surface-relief diffraction grating. The ridges have a very intricate structure resembling a stack of slanted lamellas. Each pair of ridges is connected by cross ribs, thus forming a network of submicrometer holes.

The cross section of an *A. ilia* scale as seen under transmission electron microscope (Fig. 4) shows dimensional relations between the characteristic features. Ridges are separated by a distance of 1 μm, 50 nm-thick lamellas are separated by a distance of 100 nm, the ventral surface of the scale is separated from the ridges of the dorsal side of the scale by a distance of 2 μm, while the characteristic dimensions of the bottom holes (width–length) are 400–600 nm.

Our approach can be described as follows. We observed that there is a structural and geometrical similarity between the structure of the *Apatura* and *Sasakia* butterfly cover scales and the extraordinary optical transmission (EOT) aperture arrays [14], as well as the designer (spoof) plasmon structures [15]. All of these exhibit 2D ordered subwavelength hole arrays. As an illustration, Fig. 5 shows a comparison of an SEM image of an *A. ilia* cover scale (Fig. 5a) with a 2D array plasmonic crystal with EOT functionality (Fig. 5b). The similarity of the fine structures is apparent. However, it is only geometrical and does not extend to materials and compositions. The essential difference is that the scales are all-dielectric, while EOT and spoof plasmon structures are metal-dielectric.

Our idea was to deposit an ultrathin layer of plasmonic metal onto the scales of *A. ilia*, thus imparting plasmonic functionality to them and effectively turning them into a 2D subwavelength plasmonic crystal. In this manner EOT/spoof plasmon structure is obtained in a straightforward way without a need to fabricate

[1] For interpretation of color in Fig. 1, the reader is referred to the web version of this article.

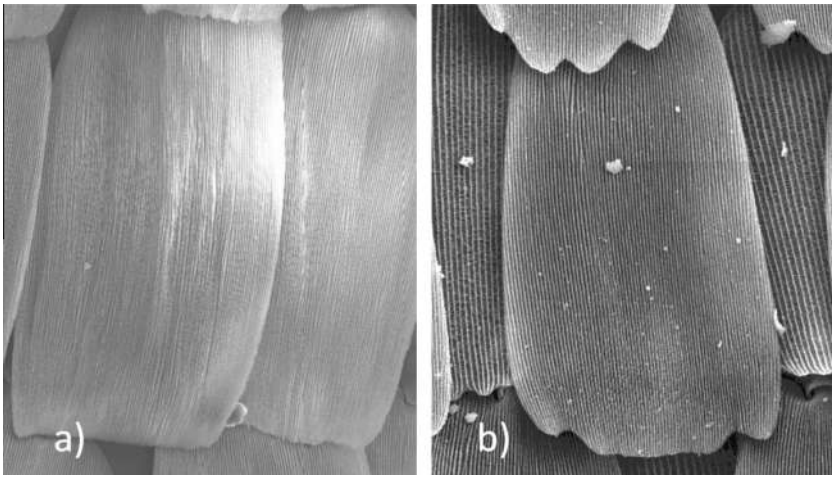

Fig. 2. Scales of (a) *S. charonda* and (b) *A. iris* as seen under SEM.

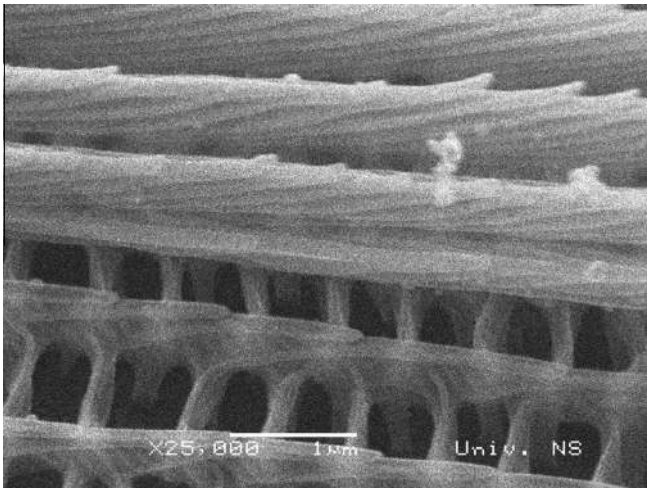

Fig. 3. Higher magnification SEM image of an *A. ilia* scale.

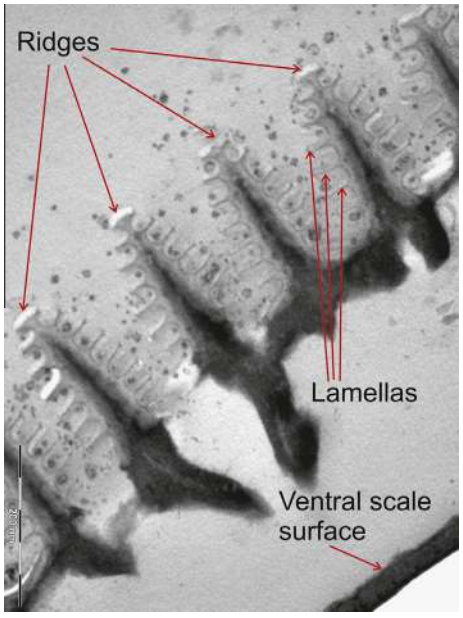

Fig. 4. Transmission electron microscope image of the cross section of *A. ilia* butterfly scale.

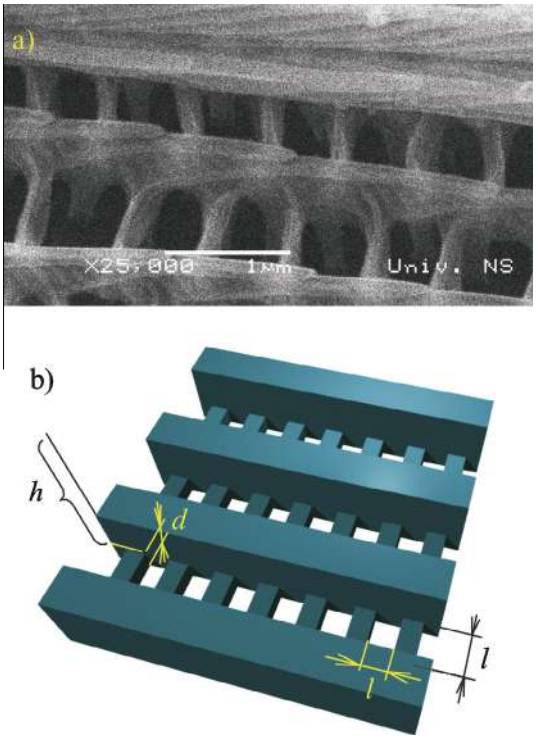

Fig. 5. (a) SEM image of a detail of *A. ilia* cover scale; (b) simplified rendering of a 2D EOT structure; l is the characteristic dimension of an aperture (equal to side length for square openings and hole diameter for circular openings), d is the metal layer thickness, and h is the distance from the observation point to the surface.

ordered arrays of subwavelength holes, replacing the expensive submicrometer photolithography process by simple and relatively inexpensive thin film deposition.

3. Calculation

We performed a rule-of-thumb calculation of the achievable performance for a natural structure (schematically shown in Fig. 5b), covered by a metal film about 40 nm thick. It is well known that metal layer permittivity may be described by the Drude model

$$\varepsilon_1 = 1 - \frac{\omega_p^2}{\omega^2} \quad (1)$$

where ω_p is the plasma frequency and omega is the angular frequency of the incident radiation. The peak wavelength can be assessed by considering the EOT array as a 2D diffractive grating enabling coupling of propagating photons, thus the in-plane wave vector of surface plasmons is

$$k_x = \frac{\omega}{c}\sin\theta \pm 2m\pi/a \tag{2}$$

where a is the lattice constant (the distance between the neighboring holes), θ is the incident angle, and m is an integer. Since the transmission peak wavelength is $\lambda_{peak} = 2\pi/k_x$

$$\lambda_{peak} = \frac{a}{m}\sqrt{\frac{\varepsilon_1(\lambda_{peak})\varepsilon_2}{\varepsilon_1(\lambda_{peak})+\varepsilon_2}} \tag{3}$$

and thus λpeak is straightforwardly determined from the implicit Eq. (3). Here ε1 and ε2 denote the real and the imaginary part of the complex permittivity, respectively.

The transmission coefficient may be approximately calculated using the generalized Ohm's law approach. This method is presented in [16] and may be shortly described as an approximation for optical parameters of nonhomogeneous thin films in the case when the quasistatic approximation is not applicable, but the inhomogeneity length scale is much smaller than the wavelength, albeit not smaller than the skin depth. In that case the transmission coefficient can be calculated as

$$T = \frac{16p^2|u_m^2(1+u_h v_h)|^2}{|C_1C_2|^2} \tag{4}$$

$$\begin{aligned} C_1 &= u_h - pu_h + (1+p)(1-iu_h)u_m - i(1-p)u_m^2 \\ C_2 &= (i+u_m)(u_m v_h - 1) + p(i-u_m)(u_m v_h + 1) \end{aligned} \tag{5}$$

where u and v are effective Ohmic parameters, the subscript m denotes their value in metal, the subscript h denotes the value in the holes, while p is the ratio of hole surface to the whole sample surface (the filling factor of the quasi-two-dimensional nanocomposite).

The effective Ohmic parameters are given as

$$u_h = \frac{k\,tg(2hk) - \gamma\sqrt{\xi^2-k^2}}{k + \gamma\sqrt{\xi^2-k^2}tg(2hk)} \tag{6}$$

$$v_h = \frac{\sqrt{\xi^2-k^2}tg(2hk) + k\gamma}{\sqrt{\xi^2-k^2} - k\gamma tg(2hk)} \tag{7}$$

$$u_m = -ctg(hk) \tag{8}$$

$$\gamma = \tanh\left[\left(\frac{d}{2}-h\right)\sqrt{\xi^2-k^2}\right] \tag{9}$$

where $\xi = 3.68/l$ is the eigenvalue for the basic mode for a cylindrical waveguide, k is the wavevector, h is the distance from the surface, l is the hole characteristic dimension (diameter for round holes and side length for square holes) and d is the metal layer thickness that must be larger than the skin depth in metal.

Finally, the resonant transmission coefficient of a subwavelength EOT structure can be calculated as

$$T = 4|u_m|/|1+u_m^2| \tag{10}$$

Fig. 6 shows the functional dependence between the characteristic dimension a and the approximate position of the peak wavelength for gold, as calculated according to (3). The spectral dependence of the real and the imaginary part of the relative dielectric permittivity of gold has been taken from [17].

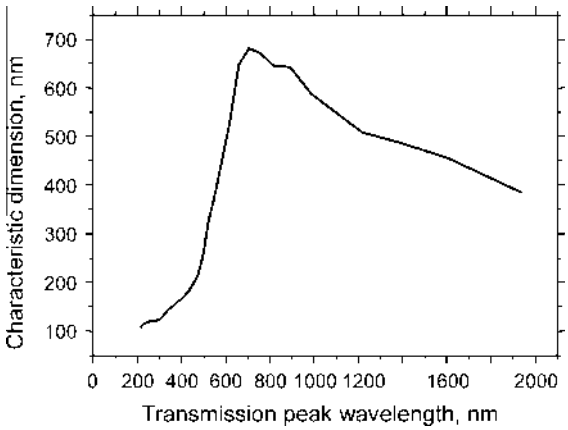

Fig. 6. Characteristic dimension a of a nanoaperture array in gold slab versus peak wavelength.

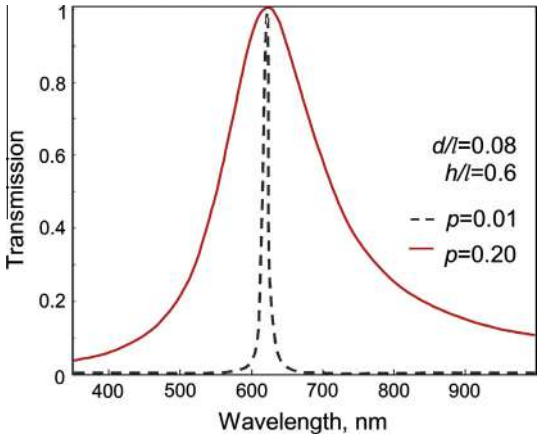

Fig. 7. Calculated spectral transmission peak of an EOT array with square matrix of nanoapertures with a characteristic dimension of $l = 0.5$ μm.

Fig. 7 shows the extraordinary transmission peak calculated approximately according to the above analytical approach. The calculation was done for a lattice constant $a = 1$ μm, the ratios $d/l = 0.08$, $h/l = 0.6$. It can be seen that the transmission peak is narrower for smaller number of nanoholes on the surface.

4. Experimental

We considered plasmonic functionalization of butterfly scales using radiofrequent sputtering. Regarding materials, it is possible to sputter different plasmonic materials including common plasmonic metals like gold, silver, chromium, etc., or alternative plasmonic materials like transparent conductive oxides. For our experiments we chose gold.

The first step was immobilization of scales to a substrate surface. For the substrate we used single-side polished single-crystalline silicon wafers, 10 cm diameter, thickness 525 μm, n-type. Epoxy resin was used to fix the samples to the surface. We considered two different approaches to scale preparation. One was to retain a sample cut from the desired area of a butterfly wing and to glue it by epoxy to the silicon surface. The other approach was to first place the wing sample on an auxiliary surface to serve as an intermediary substrate (e.g. microscopic glass slide) and to transfer scales from the wing to this auxiliary surface using a weak adhesive or an electrostatic force. Thus prepared intermediary

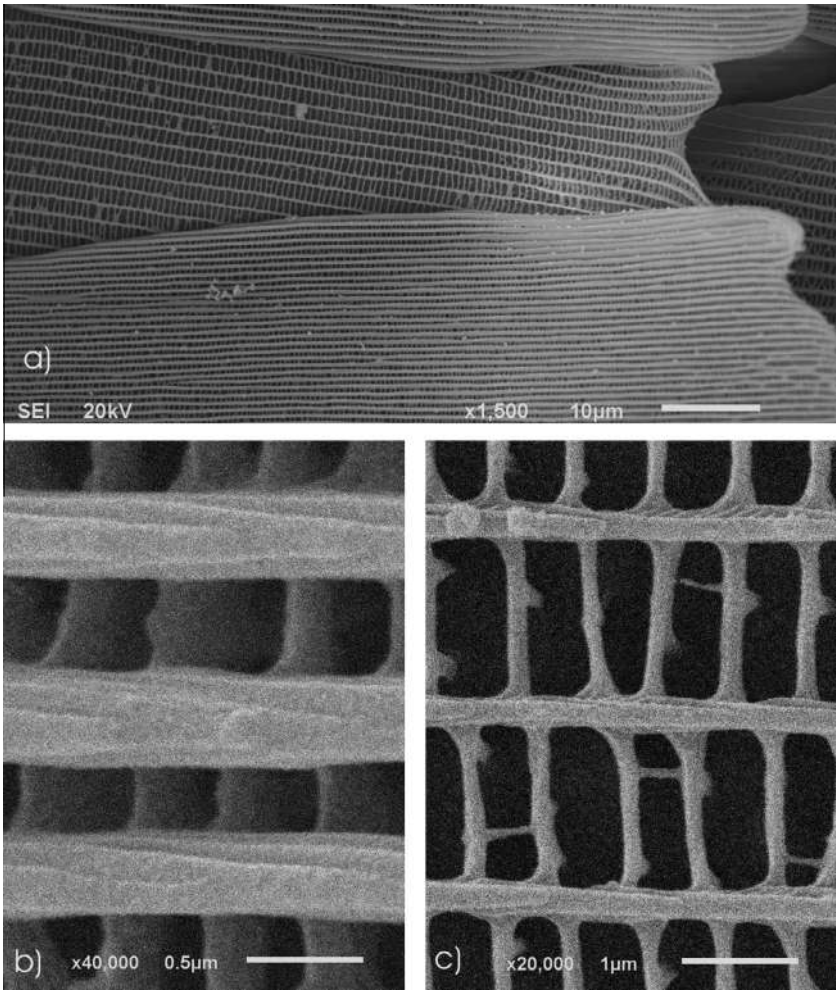

Fig. 8. SEM micrographs of *A. ilia* wing scales after 32 nm of gold has been deposited over them. (a) overall pattern of the scales; (b) details of a covering scale; (c) details of an underlying scale.

surface is brought into contact with the final substrate covered with epoxy resin. Due to adhesive effect the scales stick to the final surface and remain on it. In both cases the cover scales are turned in the same direction as was their original position on the wing and they even retain their tiled arrangement. However, since complete scales are used, together with their base plates and even with the underlying wing structure, the prepared samples are convenient for observation in reflected spectrum only.

Sputtering was done at a base pressure of $p_0 = 2.6 \times 10^{-5}$ Pa, with argon sputtering pressure $p_{sp} = 0.67$ Pa. The applied radiofrequent power was $P = 0.5$ kW at a frequency of 13.56 MHz, non-magnetronic. The target voltage was 2200 V, and the distance

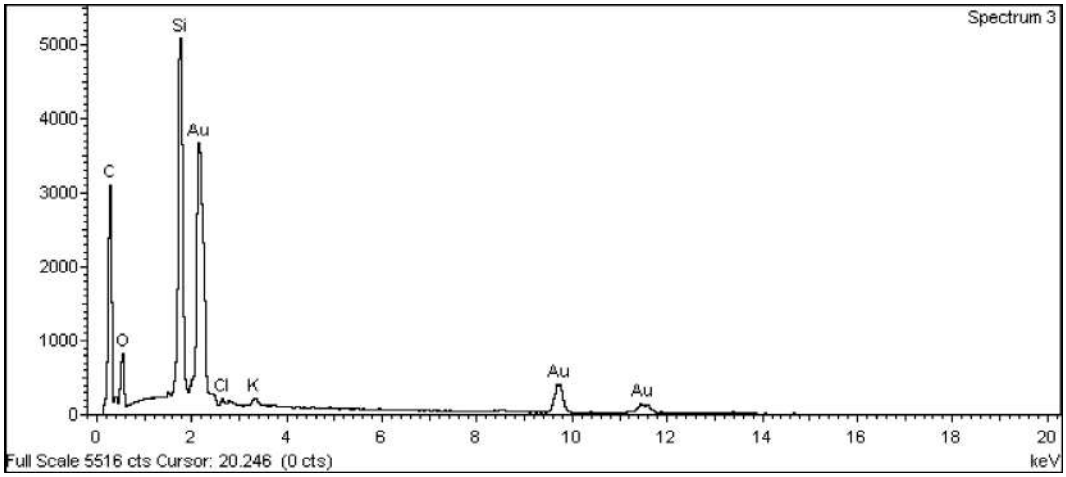

Fig. 9. Energy-dispersive X-ray spectrum of an *A. ilia* sample with 32 nm thick sputtered layer.

Please cite this article in press as: Z. Jakšić et al., Opt. Mater. (2013), http://dx.doi.org/10.1016/j.optmat.2013.04.004

target-substrate was $d = 6.35$ cm. Sputtering was performed at room temperature. Several different thicknesses of gold layers was deposited onto different butterfly scale samples. Gold layers of about 11 nm were sputtered after 20 s, 22 nm after 40 s, and 32 nm after 2×30 s, with a pause of 10 min to avoid overheating and damaging the biological samples.

We performed SEM analysis of the sputtered samples in order to check if their morphology and structure has been damaged or modified, since this would effectively render our approach useless for bio-templating. As an example, Fig. 8a shows the overall pattern of the scales on an *A. ilia* wing with 32 nm gold, where the cover scales with pronounced ridges are interleaved with the underlying scales characterized by much thinner structure. Fig. 8b shows a detail of one of the cover scales, and Fig. 8c represents the structure of an underlying ground scale. It is readily observed that the complexity and precision of starting butterfly tissue is fully retained and that no damages whatsoever occurred during the gold deposition process.

Further we performed energy-dispersive X-ray spectroscopy (EDS) analysis of the bio-templated samples. Fig. 9 shows an EDS diagram of our sample with 32 nm thick sputtered layer showing that its main constituent after sputtering is indeed gold. Other constituents, expectedly, include organic carbon and oxygen as constituents of the organic template, as well as silicon stemming from the substrate.

Visual observation of *A. ilia* wings before and after processing shows that the deposited gold layer decreases their reflection, the more so the thicker the layer is. At first sight this may appear paradoxical, since the deposition of highly reflective metal actually decreases reflection, but if we observe our approximate calculation results shown in Fig. 7 (the curve for $p = 0.20$), we see that a reflection dip (corresponding to the transmission peak in Fig. 7) is indeed expected.

Fig. 10 shows measured UV–vis reflection spectra of our bio-templated samples. The measurement was performed under an angle of 45° to the wing surface, from the direction normal to the larger ridges in the covering scales. It is seen that a wide dip in the measured reflection appears. Counter-intuitively at a first glance, the measured reflectance decreases proportionally to the thickness of the deposited gold. Actually this is a natural consequence of increasingly plasmonic behavior of the whole structure. If we consider the dependence in Fig. 7, we observe that a dip in reflectance should correspond to the presented peak in transmittance. The wavelength position of the measured reflectance dip is approximately between 420 nm and 520 nm.

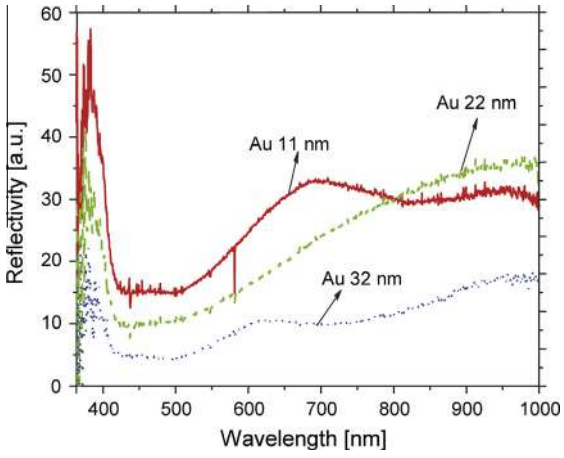

Fig. 10. Measured UV–vis reflection spectra of *A. ilia* scales with plasmonic functionalization using gold layers of different thickness.

Qualitatively this behavior corresponds to the one predicted by our rule-of-thumb calculations, where a reflection dip also appears, exactly corresponding to the transmission peak. The calculated reflection dip is positioned at approximately 600 nm and is narrower than the measured one (the calculated width being dependent on the filling factor of the nanocomposite p). Such behavior is expected, since the generalized Ohm's law approach itself is only approximate to begin with, while at the same time neither the shape of the apertures in the simplified model (squares) corresponds to the real ones (elongated rectangles), nor does the incident angle (45° instead of 90°). Finally, the measurements are actually performed with two types of interleaved scales, the cover and the ground scales, each of which has different geometry.

If we observe carefully the cover and ground scale structure in Fig. 8b and c, we see that the characteristic dimensions of some apertures are smaller than 500 nm and consequently their corresponding transmission peak/reflection dip wavelengths move to the left in Fig. 6. Actually the geometry shows significant variations both within a single scale and among different ones, as one could expect from the living tissue. A real reflectance spectrum will be a superposition of these slightly different geometries, resulting in the spectrum widening. The increased wavelength width of the dips of the spectra of experimental structures thus represents a logical consequence of the real geometry of the scales. This variety actually represents an advantage, since one can choose among a wide range of different structures and parameters.

5. Conclusion

The functionalization of butterfly scales as bio-templates by metal/plasmonic material ensures a relatively straightforward fabrication of complex plasmonic structures that are difficult or impossible to produce by conventional top-down methods and opens a pathway toward biomimetic plasmonics. We considered a possibility to fabricate 2D plasmonic crystals with nanoaperture arrays using butterfly scales and functionalization by lamellar nanocompositing. To this purpose we first did a simplified calculation to assess the obtainable photonic properties of the biological–nonbiological hybrid and then performed experiments using radio-frequent sputtering of gold layers with different thicknesses to prove the concept. Our SEM analysis has shown that the original geometry of the biological tissue of *A. ilia* is remarkably well preserved after plasmonic functionalization by sputtering of gold, thus proving the concept of bio-templating for plasmonic/metamaterial purposes. Depending on the particular wing area where they have been harvested and on the species of Lepidoptera used, the basic biological nanostructures show different dimensions and properties. Obviously a large range of different plasmonic structures can be obtained, their electromagnetic behavior may be very rich and the method itself leaves room for different optimizations and can be thus used for different purposes. We conclude that bionic approach offers potentials for vast expansion of the nanophotonic and nanoplasmonic material toolbox.

Acknowledgments

This work was supported by the Serbian Ministry of Education, Science and Technological Development through the Projects TR32008, III45016, OI171038, OI173038 and III41002.

References

[1] E. Ozbay, Plasmonics: merging photonics and electronics at nanoscale dimensions, Science 311 (2006) 189.
[2] H. Chen, C.T. Chan, P. Sheng, Transformation optics and metamaterials, Nat. Mater. 9 (2010) 387.

[3] S.A. Maier, Plasmonics: Fundamentals and Applications, NY: Springer Science+Business Media, New York, 2007.
[4] J. Matović, Z. Jakšić, Bionic (Nano)Membranes Biomimetics – Materials, Structures and Processes. Examples, Ideas and Case Studies, in: P. Gruber, D. Bruckner, C. Hellmich, H-B. Schmiedmayer, H. Stachelberger, I.C. Gebeshuber (Eds.), Springer, Berlin, 2011, pp. 9–24.
[5] P. Vukusic, J.R. Sambles, Photonic structures in biology, Nature 424 (2003) 852.
[6] AL. Ingram, AR. Parker, A review of the diversity and evolution of photonic structures in butterflies incorporating the work of John Huxley (The Natural History Museum, London from 1961 to 1990), Phil. Trans. Royal Soc. B: Biol. Sci. 363 (2008) 2465.
[7] AD. Pris, Y. Utturkar, C. Surman, WG. Morris, A Vert, S. Zalyubovskiy, T. Deng, HT. Ghiradella, RA. Potyrailo, Towards high-speed imaging of infrared photons with bio-inspired nanoarchitectures, Nat. Photonics 6 (2012) 195.
[8] RA. Potyrailo, H. Ghiradella, A. Vertiatchikh, K. Dovidenko, JR. Cournoyer, E. Olson, *Morpho* butterfly wing scales demonstrate highly selective vapour response, Nat. Photonics 1 (2007) 123.
[9] NL. Garrett, P. Vukusic, F. Ogrin, E. Sirotkin, CP. Winlove, J. Moger, Spectroscopy on the wing: naturally inspired SERS substrates for biochemical analysis, J. Biophotonics 2 (2009) 157.
[10] D. Pantelić, S. Ćurčić, S. Savić-Šević, A. Korać, A. Kovačević, B. Ćurčić, B. Bokić, High angular and spectral selectivity of purple emperor (Lepidoptera: *Apatura iris* and *Apatura ilia*) butterfly wings, Opt. Express 19 (2011) 5817.
[11] S.B. Ćurčić, D.V. Pantelić, B.P. Ćurčić, S.N. Savić-Šević, S.E. Makarov, V.B. Lačković, M.M. Labudović-Borović, N.B. Ćurčić, D.V. Stojanović, Micro- and nanostructures of iridescent wing scales in purple emperor butterflies (Lepidoptera: *Apatura ilia* and *Apatura iris*), Microsc. Res. Tech. 75 (2012) 976.
[12] A. Masui, GC. Bozano, A. Floriani, Guide to the butterflies of the palearctic region: nymphalidae Part 4: Subfamily Apaturinae, Omnes Artes (2011).
[13] J. Matejková-Plšková, S. Shiojiri, M. Shiojiri, Fine structures of wing scales in *Sasakia charonda* butterflies as photonic crystals, J. Microsc. 236 (2009) 88–93.
[14] T.W. Ebbesen, H.J. Lezec, H.F. Ghaemi, T. Thio, P.A. Wolff, Extraordinary optical transmission through sub-wavelength hole arrays, Nature 391 (1998) 667.
[15] JB. Pendry, L. MartÃ-n-Moreno, FJ. Garcia-Vidal, Mimicking surface plasmons with structured surfaces, Science 305 (2004) 847.
[16] A.K. Sarychev, V.A. Podolskiy, A.M. Dykhne, V.M. Shalaev, Resonance transmittance through a metal film with subwavelength holes, IEEE J. Quant. Electr. 38 (2002) 956.
[17] PB. Johnson, RW. Christy, Optical constants of the noble metals, Phys. Rev. B 6 (1972) 4370.

Please cite this article in press as: Z. Jakšić et al., Opt. Mater. (2013), http://dx.doi.org/10.1016/j.optmat.2013.04.004

Materials Research Bulletin 88 (2017) 121–126

Contents lists available at ScienceDirect

Materials Research Bulletin

journal homepage: www.elsevier.com/locate/matresbu

Characterization and luminescence kinetics of Eu^{3+} doped YVO_4 nanopowders

D. Sevic[a,*], M.S. Rabasovic[a], J. Krizan[b], S. Savic-Sevic[a], M. Mitric[c], M. Gilic[a], B. Hadzic[a], N. Romcevic[a]

[a] Institute of Physics, University of Belgrade, Serbia
[b] Ami DOO, Ptuj, Slovenia
[c] Vinča Intitute of Nuclear Science, University of Belgrade, P.O. Box 522, 11001 Belgrade, Serbia

ARTICLE INFO

Article history:
Received 7 November 2016
Received in revised form 28 November 2016
Accepted 19 December 2016
Available online 21 December 2016

Keywords:
Phosphors
Optical properties
Luminescence
Time – resolved optical spectroscopy

ABSTRACT

In this paper we describe the synthesis and characterization of the $YVO_4:Eu^{3+}$ nanopowder. The material was prepared using simple solution combustion synthesis. X-ray powder diffraction (XRD), scanning electron microscope (SEM), Raman and photoluminescence (PL) techniques were used to confirm and characterize the prepared material. The time resolved analysis of emission spectra was achieved by using the streak camera system. Beside luminescence lifetime of slow decayed transitions we also measured their rise time and lifetime of fast decayed transitions. We also determined the excitation spectra of this nano material. Results of our analysis prove that $YVO_4:Eu^{3+}$ nanopowder is appropriate material for various optoelectronic devices.

© 2016 Elsevier Ltd. All rights reserved.

1. Introduction

Yttrium Vanadate (YVO_4) phosphors doped with europium ions (Eu^{3+}), $YVO_4:Eu^{3+}$ are vastly investigated and have found many applications, see [1–10] and references therein. Various methods of synthesis and studies of structural and luminescent characteristics of nano phosphors based on $YVO_4:Eu^{3+}$ are reported in [1,2,10–20].

In this study, nanopowders $YVO_4:Eu^{3+}$ were efficiently prepared using a Solution Combustion Synthesis (SCS) method [21,22]. The main characteristics of this process are simplicity and low cost. Moreover, it is possible to tune the size and morphology of particles. The structure of prepared materials has been confirmed and characterized using X-ray powder diffraction (XRD), scanning electron microscope (SEM), Raman and photoluminescence (PL) techniques. The excitation and emission spectra and luminescence lifetimes and rise time of synthesized nanopowders were analyzed by using the streak camera system. PL spectra were obtained at different excitation wavelengths using Optical Parametric Oscillator and 532 nm laser line. Transitions from the $^5D_0$ state, from which most of europium luminescence comes, are slow decayed. Lifetimes of slow decayed lines of europium doped YVO_4 are measured and reported in many publications. However, there are not so many publications where results regarding lifetimes of fast decayed transitions or rise times of slow decayed transitions [23–26] of europium are provided. In this study, beside luminescence lifetime of slow decayed transitions from the $^5D_0$ state, we also measured their rise time and lifetime of fast decayed transitions from the $^5D_1$ state. The luminescence rise time measurements can be used for high temperature remote thermometry [24,25].

This paper is continuation of our previously published works regarding europium atom, where some other hosts were also used [21,27].

2. Experimental procedures

2.1. The preparation of samples

Europium doped YVO4 nanopowders were prepared, as described in [21,22]. Stoichiometric quantities of starting chemicals $Y(NO_3)_3{*}6H_2O$, NH_4VO_3, NH_4NO_3, $Eu(NO_3)_3{*}6H_2O$ with the purity of 99.99% were chosen to obtain the Eu^{3+} concentration in YVO_4 of 2 mol%. The listed chemicals were purchased from ABCR and urea, $(NH_2)_2CO$, from Sigma-Aldrich. The dry mixture of 15.32 g (40 mmol) of $Y(NO_3)_3{*}6H_2O$, 4.676 g (40 mmol) of NH_4VO_3 and 0.357 g (0.8 mmol) of $Eu(NO_3)_3{*}6H_2O$ was combined with the mixture of 4.8 g (60 mmol) of ammonium nitrate and 3.003 g (50 mmol) of urea which were used as organic fuels. The prepared

* Corresponding author.
E-mail address: sevic@ipb.ac.rs (D. Sevic).

http://dx.doi.org/10.1016/j.materresbull.2016.12.021
0025-5408/© 2016 Elsevier Ltd. All rights reserved.

starting reagents were combusted with the flame burner at approximately 500 °C, yielding the voluminous foamy pink powder in intensive exotermic reaction. After the solution combustion synthesis, the nanopowder was annealed for 2 h in air atmosphere at 1200 °C. The annealing of material is needed to achieve optimal optical characteristics of synthesized material.

2.2. Experimental details

X-ray diffraction measurements were done at room temperature over the 2θ range of 10–90° with a scanning step width of 0.05° and a counting time of 8 s per step. We used a Philips PW 1050 instrument, with Ni filtered Cu $K_{\alpha 1,2}$ radiation (λ = 0.15405 nm). The nanopowders were also observed by scanning electron microscopy (SEM).

The Raman spectra in a spectral range from 100 to 900 cm^{-1}, in back scattering geometry, were obtained by the micro-Raman Jobin Yvon T64000 spectrometer, equipped with a nitrogen cooled charge-coupled device detector. Our Raman setup uses the continuous laser excitation at 532 nm.

As an excitation source for photoluminescence measurements we used the output of the Optical Parametric Oscillator (Vibrant OPO), continuously tunable over a spectral range from 320 nm to 475 nm. To better discern the Raman lines from the luminescent ones in obtained spectra we also measured the luminescence response of synthesized $YVO_4:Eu^{3+}$ using the second harmonic of our OPO pumping Nd:YAG laser at 532 nm.

Time-resolved streak images of the luminescence response of $YVO_4:Eu^{3+}$ excited by our OPO system were acquired by Hamamatsu streak camera. The camera is equipped with the spectrograph. The details of our acquisition system can be found in [21]. We also used Ocean Optics 2000 spectrometer. Measurements presented here are obtained at room temperature.

3. Results and discussion

3.1. Structure

XRD pattern of our sample of $YVO_4:Eu^{3+}$ nanopowder is shown in Fig. 1. Observed peaks are in good agreement with the published results [11,16] and JCPDS card 17-0341. The diffractogram shown in Fig. 1. proves that monophased sample is crystallized, and that its nature is tetragonal. The fact that doping of Eu^{3+} into YVO_4 material does not change the crystalline structure is proved by the lack of any additional peaks. The average grain size, D, was estimated by the Scherer equation, $D = K\lambda/\beta cos\theta$, where K is a constant related to the shape of the crystallite and is approximately equal to unity, we used K=0.89, the same as in [11], λ is the X-ray wavelength (0.15405 nm), θ and β are the diffraction angle and Full Width at Half Maximum (FWHM, in radians) of the corresponding peak. Using θ and β of two most intense diffraction peaks for calculation, we obtained the average grain size of about 51 nm.

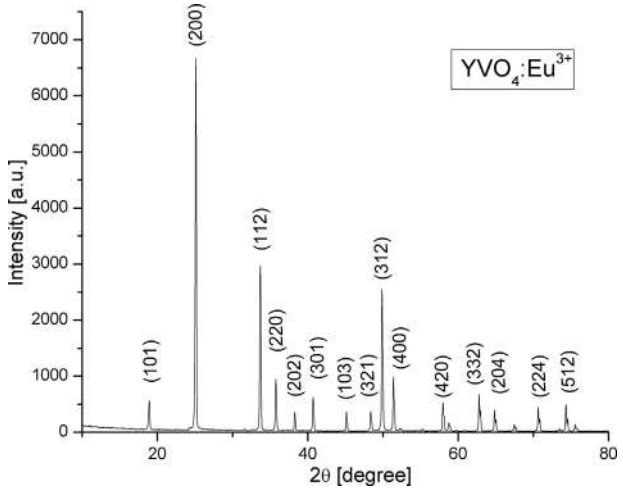

Fig. 1. XRD profile of $YVO_4:Eu^{3+}$ nano phosphor prepared by solution combustion method, with respective Miller indices.

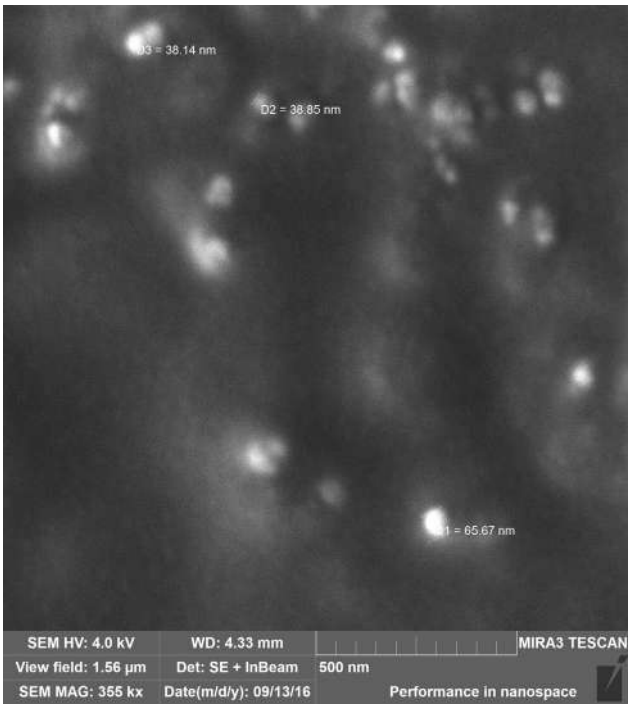

Fig. 2. SEM image of $YVO_4:Eu^{3+}$ nano phosphor prepared by solution combustion method.

The representative SEM image of our sample of $YVO_4:Eu^{3+}$ material is presented in Fig. 2. The SEM micrograph confirms the previously calculated average size of the prepared YVO_4 material doped with Eu^{3+}. The SEM image of the material shows the irregular crystallite size distribution. The agglomerated grains could be also noticed. The particles with dimensions from 37 nm to over 70 nm could be observed in Fig. 2. Effects of particle size on the luminescence of YVO_4:Eu nanocrystals are studied in detail in [7]. The size of particles, just after the synthesis, is about 6 nm. It was observed, that, with increasing the annealing temperature, the grain sizes increase. The annealing temperature of 1200 °C was chosen to obtain optimal luminescence response of synthesized material.

3.2. Raman spectroscopy

The Raman spectrum of $YVO_4:Eu^{3+}$ nanopowder phosphor is presented in Fig. 3. The peaks corresponding to Raman spectrum of YVO_4 material are marked on graph, by their shift in cm^{-1}. However, there are some other peaks on diagram. Our analysis of excitation spectra of $YVO_4:Eu^{3+}$ (Section 3.3.1) shows that our sample, if excited at 532 nm with average laser power comparable with power of excitation laser used in our Raman measurements, provides luminescence response similar in intensity with Raman spectrum of the sample. The existence of luminescence response of europium ions hosted in YVO_4 excited at 532 nm was also reported in [7,12]. Time resolved analysis, using streak camera and pulsed OPO laser excitation (of 5 ns duration), shows that these peaks are

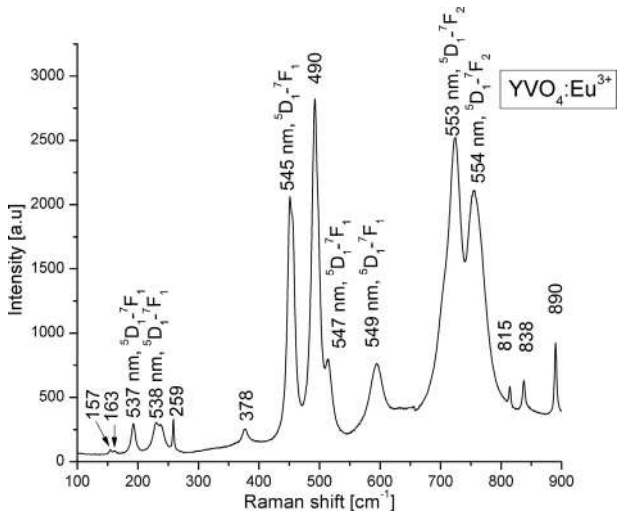

Fig. 3. Raman spectrum of $YVO_4:Eu^{3+}$ nano phosphor prepared by solution combustion synthesis. Peaks which are due to luminescence response of the sample are also denoted.

undoubtedly luminescent in nature, because their duration is in microsecond domain (Section 3.3.2, see Fig. 7). Peaks which are due to luminescence response of the sample are also denoted in Fig. 3, by their wavelength in nm. These relatively small, fast decayed luminescence responses of the sample could be observed in our Figs. 6 and 7 and in [17,23,27,28].

We have detected the external modes of Raman spectra at low vibrational frequencies, $B_{1g}(1)$ at 157 cm^{-1} and $E_{g2}(2)$ 163 cm^{-1}. Internal modes are also observed, B_{2g} at 259 cm^{-1}, $A_{1g}(1)$ at 378 cm^{-1}, $B_{1g}(3)$ at 490 cm^{-1}, $B_{1g}(4)$ at 815 cm^{-1}, $E_g(5)$ 838 cm^{-1} and $A_{1g}(2)$ at 890 cm^{-1}.

The positions of Raman peaks observed by us are in a good agreement with published results [9–11,29–33]. These peaks, detected in our measurements, imply strong interactions between the atoms, arising mainly from the stretching and bending of the shorter metal-oxygen bonds within the anionic groups [10,11,34]. The similarity of our spectrum with published spectra of undoped samples proves that crystal structure was not disturbed by doping material with europium.

3.3. Optical properties

3.3.1. Luminescence excitation and emission spectra

The excitation spectrum of $YVO_4:Eu^{3+}$ nano phosphor, corresponding to 619 nm emission, is shown in Fig. 4. As excitation source we used our OPO (320–475 nm) and the emission spectra were recorded using a step of 2 nm. The broad band up to 350 nm corresponds to strong absorption of light by YVO_4 host and charge transfer from host to Eu dopant [2,12,18]. The narrow lines observed in the 350–475 nm range refer to direct excitation of Eu (intra −4f transitions) [12]. Our aim, when recording the excitation spectra, was to include the wavelengths of direct excitation of Eu. The similar excitation spectra are presented in [8,16,19,20,32]. The small peak at about 350 nm, visible in Fig. 4, could be seen only in one of the excitation spectra presented in [20].

To complete the analysis of $YVO_4:Eu^{3+}$ nano phosphor excitation, we also recorded, using additionally Ocean Optics 2000 spectrometer, the emission spectrum when 532 nm laser line is used for excitation, see Fig. 5. Because both our spectrographs (used for luminescence measurements) have not enough stray light rejection for 532 nm excitation, the part of the spectrum near 532 nm was omitted from the diagram. We have investigated the existence of luminescence response of europium ions hosted in YVO_4 excited at 532 nm because of encountered problems in our analysis of Raman spectra. Compared to the main luminescence emission this emission is of relatively small intensity. The emission, making problems in our Raman spectroscopy, is due to transitions from $^5D_1$ state. Because we did not measure the emission for excitation wavelengths between 475 nm and 532, this peak, even smaller then peak on 466 nm, is not included on diagram in Fig. 4. This weak emission is due to $^7F_0$–$^6D_1$ transition [12].

The streak image of time resolved photoluminescence spectrum of $YVO_4:Eu^{3+}$ material using the 320 nm excitation is presented in Fig. 6. As usual, the streak image is presented in pseudocolor. The Eu transitions are denoted in Fig. 6 according to [23,35]. The slow decayed transitions observable in Fig. 6, originating from $^5D_0$ level, are well explained in literature and their detailed description can be found in our previous work [21].

Let us add that the emission spectrum shown in Fig. 6. is similar to spectra presented in [11,17,19,20,28,32]. The fast decayed lines (538 nm and 587 nm) shown in Fig. 6. are detected in [14,15,17,32]. The transitions between $^5D_1$–$^7F_2$ states are barely discernible in

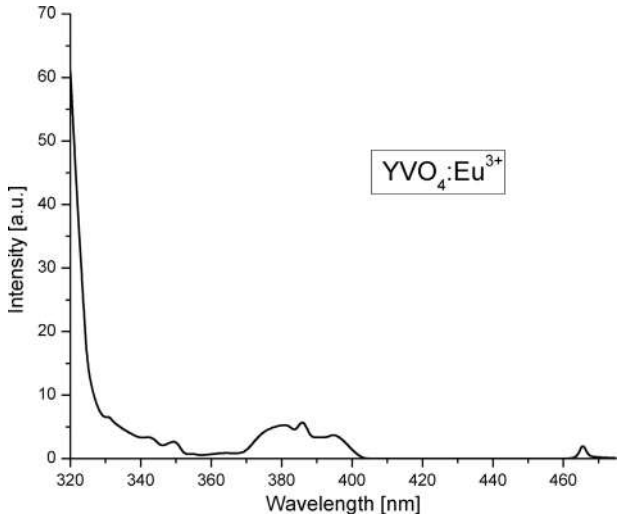

Fig. 4. Excitation spectrum of $YVO_4:Eu^{3+}$ nano phosphor, corresponding to 619 nm emission.

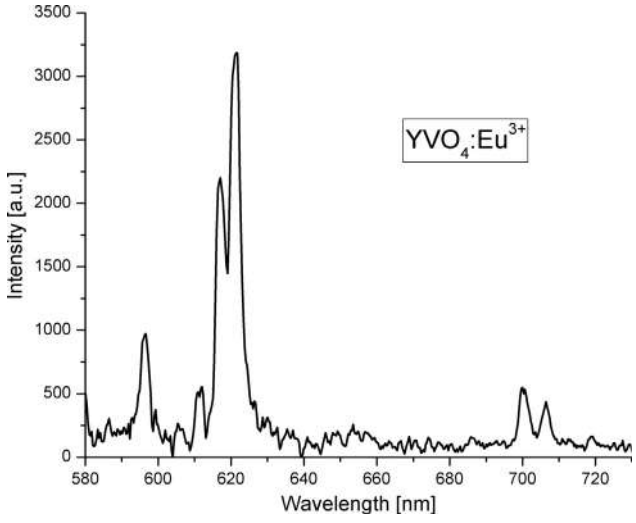

Fig. 5. Emission spectrum of $YVO_4:Eu^{3+}$ nano phosphor excited at 532 nm. The horizontal and vertical scales are adapted for better visualization of luminescence emission.

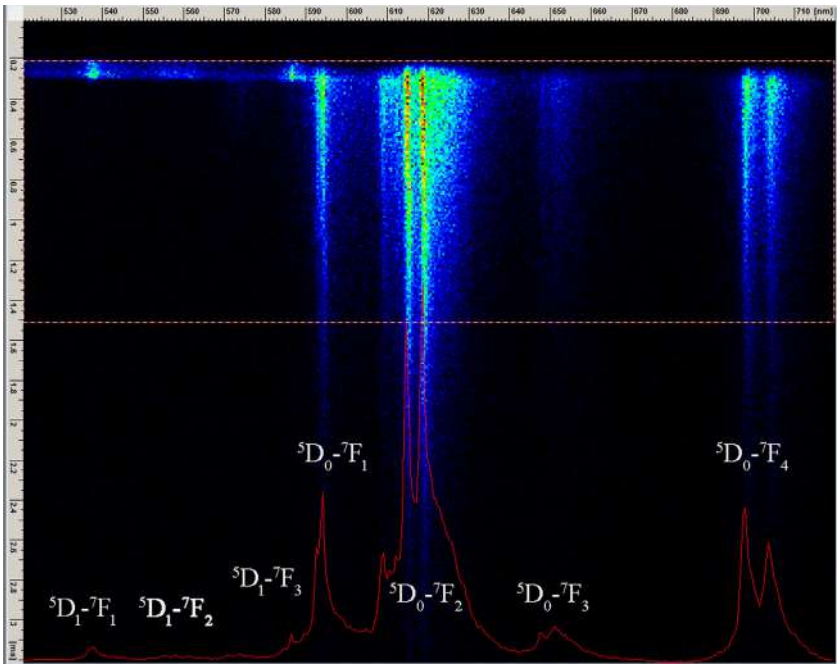

Fig. 6. Streak image of photoluminescence spectrum of YVO_4:Eu^{3+} nano phosphor. OPO excitation is at 320 nm.

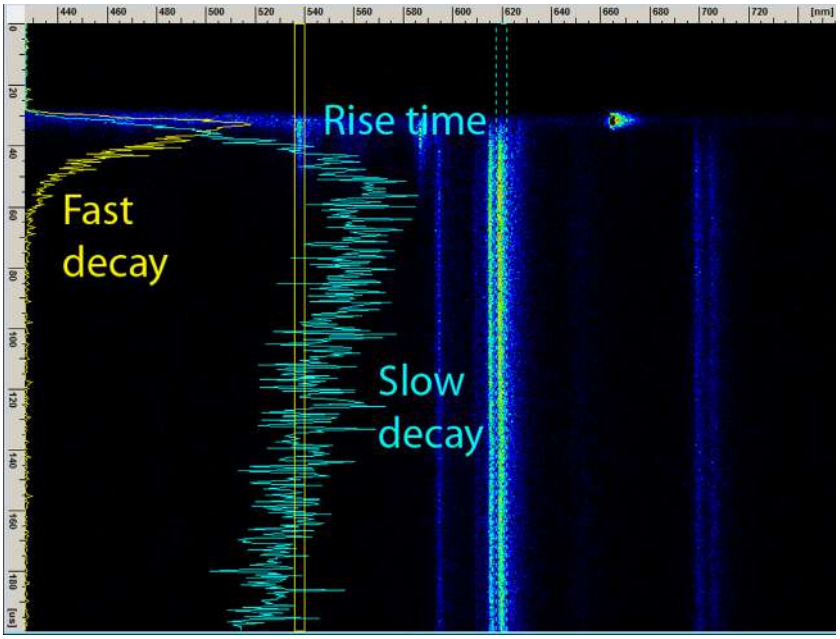

Fig. 7. Streak image of photoluminescence spectrum of YVO_4:Eu^{3+} nano phosphor with the time range of 200 μs tuned for analysis of rise time of slow decayed transitions and lifetime of fast decayed transitions. OPO excitation is at 330 nm (its second harmonic generated by diffraction grating is visible on 660 nm).

Fig. 6. They are slightly better visible in Fig. 7. These transitions are clearly observed in [15].

The transitions from $^5D_1$ visible in region below 550 nm are relatively smaller and we didn't detect these lines in our previous experiments regarding $Gd_2Zr_2O_7$:Eu^{3+} [21,27]. However, in our present measurements of YVO_4:Eu^{3+} nano phosphor we have clearly detected the line at 538 nm, see Fig. 6.

3.3.2. Lifetime and rise time analysis

We conducted the time resolved analysis for transitions which are identified in Fig. 6. The transitions are characterized by emission peaks at 538 nm and 587 nm (fast decayed, from the level $^5D_1$), 594 nm, 609 nm, 615 nm, 619 nm 699 nm and 704 nm wavelengths (slow decayed, from the level $^5D_0$). The streak image of photoluminescence spectrum of YVO_4:Eu^{3+} nano phosphor with the time range of 200 μs tuned for analysis of rise time of slow decayed transitions and lifetime of fast decayed transitions is shown in Fig. 7.

We obtained that the lifetimes of transitions from the level $^5D_1$ are about 8.7 μs and from the level $^5D_0$ the lifetimes are about 0.93 ms. For the fast decay it is similar as reported in [23], where transition from $^5D_1$ level has a fast decay with the lifetime of about 10.2 μs, while the decays of peaks which belong to $^5D_0$ have the lifetime of about 1.5 ms. Other references provide the values of fast

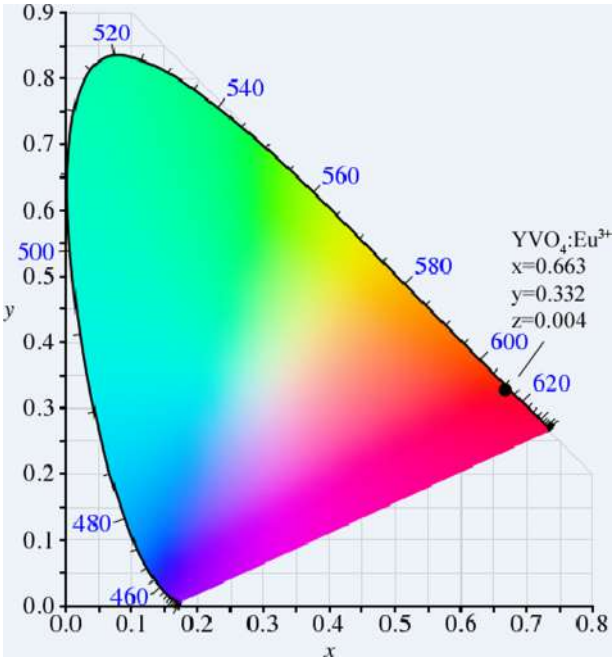

Fig. 8. The CIE chromaticity diagram of emission spectra of Eu doped YVO4 nanopowder.

[28] and slow [12,15,19,20,38] decay time more or less similar to our result. Decay curve of the most intensive $^5D_0$–$^7F_2$ transition is usually used for europium luminescence lifetime measurements [23,36].

We calculated the rise time according to Ranson equation [24,39]. We obtained that the rise time of luminescence of our sample of YVO_4:Eu^{3+} for the $^5D_0$–$^7F_2$ line is about 8.1 μs. The phenomenon that the rise time of slow decayed luminescence is similar to the lifetime of fast decayed transition was observed long ago [26] (interestingly enough, there are only a few references regarding the europium rise time since then). It could be concluded that these time periods are related to energy transfer from host to Eu dopant. Schematic diagram of the energy transfer between the host YVO_4 and Eu^{3+} ions and explanation is provided in [2], however, without measuring the rise time. The nice explanation and diagram of decay pathways in Eu^{3+}, (although for different host, $Ca_2Gd_8Si_6O_{26}$), including the measured rise time, is presented in [23].

Rise time of luminescence of many phosphors, including Eu, is temperature dependent, so it is possible to use this phenomenon for remote high temperature sensing [24].

3.3.3. CIE chromaticity coordinates

The chromaticity coordinate values, CIE 1931, were calculated for our sample of YVO4:Eu^{3+} and presented in Fig. 8. By using the CIE diagram, it is easy to see that our sample of YVO_4:Eu^{3+} red phosphor, combined with appropriate green and blue phosphors, maximizes the area of the color gamut compared to red phosphors based on other hosts described in [27,40–44]. The nano phosphor studied in our paper has similar chromaticity coordinates as materials analyzed in [10,17,45].

4. Conclusions

In this paper we described the synthesis and characterization of the YVO_4:Eu^{3+} nanopowder. Solution combustion synthesis method was used to prepare the analyzed material. The structure of prepared material has been verified and characterized using X-ray powder diffraction (XRD), scanning electron microscope (SEM), Raman and photoluminescence (PL) techniques. The excitation and emission spectra and luminescence kinetics of synthesized nanopowders were analyzed by using the streak camera system. PL spectra were obtained at different excitation wavelengths. Beside luminescence kinetics of slow decayed transitions we also measured their rise time and lifetime of fast decayed transitions. To the best of our knowledge, the detailed luminescence time resolved analyses of both slow decayed (including their rise time) and fast decayed transitions of the YVO_4:Eu^{3+} nano powder, provided by using the streak camera system, are first presented here. Measured values of rise time of luminescence emission of lines originating from transitions from $^5D_0$ level could be used for remote temperature sensing. YVO_4:Eu^{3+} nanopowder maximizes the area of the color gamut in CIE diagram. So, results of our analysis prove that YVO_4:Eu^{3+} nanopowder prepared by a simple and low cost process is appropriate material for various optoelectronic devices.

Acknowledgement

This work was financially supported within the Projects Ministry of Education, Science and Technological Development of the Republic of Serbia under Projects III45003 and OI171020.

References

[1] L. Shirmane, C. Feldmann, V. Pankratov, to appear in: Physica B: Physics of Condensed Matter, 10.1016/j.physb.2016.10.007.
[2] R.S. Ningthoujam, L.R. Singh, V. Sudarsan, S.D. Singh, J. Alloys Compd. 484 (2009) 782–789.
[3] A. Huignard, T. Gacoin, J.-P. Boilot, Chem. Mater 12 (2000) 1090–1094.
[4] A. Huignard, V. Buissette, G. Laurent, T. Gacoin, J.-P. Boilot, Chem. Mater 14 (2002) 2264–2269.
[5] K. Riwotzki, M. Haase, J. Phys. Chem. B 102 (1998) 10129–10135.
[6] V.B. Bhatkar, Int. J. Eng. Sci. Inn. Tech. 2 (2013) 426–432.
[7] S. Georgescu, E. Cotoi, A.M. Voiculescu, O. Toma, Rom. Rep. Phys. 60 (2008) 947–955.
[8] W.J. Park, M.K. Jung, T. Masaki, S.J. Im, D.H. Yoon, Mater. Sci. Eng. 146 (2008) 95–98.
[9] A. Sanson, M. Giarola, B. Rossi, G. Mariotto, E. Cazzanelli, A. Speghini, Phys. Rev. B 86 (2012) 214305.
[10] S. Thakur, A.K. Gathania, J. Electronic Materials 44 (10) (2015) 3444–3449.
[11] B.K. Grandhe, V.R. Bandi, K. Jang, S. Ramaprabhu, S.-S. Yi, J.-H. Jeong, Electron. Mater. Lett. 7 (2) (2011) 161–165.
[12] Y.-S. Chang, F.-M. Huang, Y.-Y. Tsai, L.-G. Teoh, J. Lumin. 129 (2009) 1181–1185.
[13] R. Han, R. Hu, K. Chen, Opt. Mater. 32 (2009) 329–333.
[14] Q. Yan-bo, L. Xiao-feng, Z. Qiang, C. Dan-ping, W. Ye-wen, M. Wen-bo, Mater. Lett. 64 (2010) 1306–1308.
[15] M. Yu, J. Lin, Z. Wang, J. Fu, S. Wang, H.J. Zhang, Y.C. Han, Chem. Mater 14 (2002) 2224–2231.
[16] M.G. Matos, E.H. de Faria, L.A. Rocha, P.S. Calefi, K.J. Ciuffi, E.J. Nassar, V. Hugo, V. Sarmento, J. Lumin. 147 (2014) 190–195.
[17] P. Kumari, P.K. Baitha, J. Manam, Indian J. Phys. 89 (2015) 1297–1306.
[18] N. Shanta Singh, R.S. Ningthoujam, M. Niraj Luwang, S. Dorendrajit Singh, R.K. Vatsa, Chem. Phys. Lett. 480 (2009) 237–242.
[19] M. Saltarelli, M.G. Matos, E.H. de Faria, K.J. Ciuffi, L.A. Rocha, E.J. Nassar, J Sol-Gel Sci. Technol. 73 (2015) 83–292.
[20] M. Saltarelli, P.P. Luz, M.G. Matos, E.H. de Faria, K.J. Ciuffi, P.S. Calefi, L.A. Rocha, E.J. Nassar, J. Fluoresc. 22 (2012) 899–906.
[21] M.S. Rabasovic, D. Sevic, J. Krizan, M. Terzic, J. Mozina, B.P. Marinkovic, S. Savic Sevic, M. Mitric, M.D. Rabasovic, N. Romcevic, J. Alloys Compd. 622 (2015) 292–295.
[22] J. Krizan, M. Mazaj, V. Kaucic, I. Bajsic, J. Mozina, Acta Chim. Slov. 61 (2014) 608–614.
[23] M.D. Chambers, P.A. Rousseve, D.R. Clarke, J. Lumin. 129 (2009) 263–269.
[24] S.W. Allison, S.M. Goedeke, M.R. Cates, W.A. Hollerman, J.I. Eldridge, T.J. Bencic, Oak Ridge National Laboratory Report No 123055, (2005) (Published through SciTech Connect, 03/24/2005).
[25] X. Li, X. Wei, Y. Qin, Y. Chen, C. Duan, M. Yin, J. Alloys Compd. 657 (2016) 353–357.
[26] J.R. Darwent, C.D. Flint, P.J. O'Grady, Chem. Phys. Lett. 127 (1986) 547–550.
[27] M.S. Rabasovic, J. Krizan, P. Gregorcic, M.D. Rabasovic, N. Romcevic, D. Sevic, Opt. Quantum Electron. 48 (2016) 163.
[28] D.-K. Kim, W. Kang, Korean Chem. Soc. 25 (2004) 1859–1862.
[29] Yu.K. Voron'ko, A.A. Sobol', V.E. Shukshin, A.I. Zagumennyi, Yu. D. Zavartsev, S. A. Kutovoi, Phys. Solid State 51 (2009) 1886–1893.

[30] B.M. Jin, S. Erdei, A.S. Bhalla, F.W. Ainger, Material Research Bulletin 30 (1995) 1293–1300.
[31] S.A. Miller, H.H. Caspers, H.E. Rast, Phys. Rev. 168 (1968) 964–969.
[32] B. Shao, Q. Zhao, N. Guo, Y. Jia, W. Lv, M. Jiao, W. Lu, H. You, CrystEngComm 15 (2013) 5776–5783.
[33] A. Jayaraman, G.A. Kourouklis, G.P. Espinosa, A.S. Cooper, L.G. Van Uitert, J. Phys. Chem. Solids 48 (1987) 755–759.
[34] Z.C. Ling, H.R. Xia, W.L. Liu, H. Hand, X.Q. Wang, S.Q. Sun, D.G. Ran, L.L. Yu, Mater. Sci. Eng. B 128 (2006) 156–160.
[35] K. Binnemans, Coord. Chem. Rev. 295 (2015) 1–45.
[36] Y.-S. Chang, H.-J. Lin, Y.-L. Chai, Y.-C. Li, J. Alloy Compd. 460 (2008) 421–425.
[38] N. Shanta Singh, R.S. Ningthoujam, M. Niraj Luwang, S. Dorendrajit Singh, R.K. Vatsa, Chem. Phys. Lett. 480 (2009) 237–242.
[39] R.M. Ranson, E. Evangelou, C.B. Thomas, Appl. Phys. Lett. 72 (1998) 2663–2664.
[40] C.A. Rao, P.R.V. Nannapaneni, K.V.R. Murthy, J. Sci. Res. 5 (2013) 1–11.
[41] C.A. Rao, P.R.V. Nannapaneni, K.V.R. Murthy, Adv. Mater. Lett. 4 (2013) 207–212.
[42] I.P. Sahu, D.P. Bisen, N. Brahme, R.K. Tamrakar, J. Radiat. Res. Appl. Sci. 8 (2015) 104–109.
[43] I.P. Sahu, D.P. Bisen, N. Brahme, J. Radiat. Res. Appl. Sci. 8 (2015) 381–388.
[44] W. Lu, Y. Jia, W. Lv, Q. Zhao, H. You, J. Lumin. 147 (2014) 159–162.
[45] P.C. de Sousa Filho, T. Gacoin, J.-P. Boilot, R.I. Walton, O.A. Serra, J. Phys. Chem. C 119 (2015) 24062–24074.

Journal of Alloys and Compounds 622 (2015) 292–295

Contents lists available at ScienceDirect

Journal of Alloys and Compounds

journal homepage: www.elsevier.com/locate/jalcom

Characterization and luminescent properties of Eu^{3+} doped $Gd_2Zr_2O_7$ nanopowders

M.S. Rabasovic [a,*], D. Sevic [a], J. Krizan [b], M. Terzic [c], J. Mozina [b], B.P. Marinkovic [a], S. Savic-Sevic [a], M. Mitric [d], M.D. Rabasovic [a], N. Romcevic [a]

[a] Institute of Physics, University of Belgrade, Serbia
[b] Faculty for Mechanical Engineering, University of Ljubljana, Slovenia
[c] Faculty of Science, University of Novi Sad, Serbia
[d] Vinča Institute of Nuclear Science, University of Belgrade, P.O. Box 522, 11001 Belgrade, Serbia

ARTICLE INFO

Article history:
Received 11 September 2014
Received in revised form 7 October 2014
Accepted 13 October 2014
Available online 22 October 2014

Keywords:
Phosphors
Optical properties
Luminescence
Time – resolved optical spectroscopies

ABSTRACT

Nanopowders based on gadolinium zirconium oxide ($Gd_2Zr_2O_7$) doped by europium ions (Eu^{3+}) were successfully prepared using a flame combustion method. This material is suitable for various optical devices. The structure of prepared materials has been confirmed and characterized using X-ray powder diffraction (XRD), scanning electron microscope (SEM) and photoluminescence (PL) techniques. The luminescence properties of synthesized nanopowders were characterized by emission spectra and luminescence lifetimes by using the streak camera system. PL spectra were obtained at three different excitation wavelengths (Optical Parametric Oscilator (OPO) at 360 nm, laser diode at 365 nm and Ar laser line at 514.5 nm). The strong emission lines at 611 nm and 630 nm corresponding to the $^5D_0 \rightarrow {}^7F_2$ long lived transition could be used as a new red light source in optical devices.

© 2014 Elsevier B.V. All rights reserved.

1. Introduction

Rare earth zirconates ($Re_2Zr_20_7$) have been identified as the attractive candidates for TBC (thermal barrier coatings) applications, high temperature heating devices and host materials for luminescence applications [1]. Their crystal structure is stable in high temperature, oxidizing environments and because they emit intense, visible emission. There are two kinds of different crystal structures for $Re_2Zr_20_7$, as the pyrochlore structure, and the fluorite structure [2]. Among them, gadolinium zirconate ($Gd_2Zr_2O_7$) stand out as a material with a distinctively low thermal conductivity and high phase stability [3]. The strong fluorescent properties of the $Gd_2Zr_2O_7$ may make it excellent candidate for potential photoactive materials [4].

Rare earth ions have been extensively employed as activators for various phosphors and other organic and inorganic luminescent materials [5]. Europium as a solid-solution chromophore dopant is explored for measuring temperature in pyrochlore zirconates [6]. Also Eu^{3+} ions within the configuration [Xe] $4f^6$ doped compound in different host lattice are found to give a rise to the strong luminescence emitting bright red light. That material shows typical f–f transitions of only europium ions. It is known that luminescence is relatively independent to the host crystal field in trivalent rare earth ions because the optically active 4f electrons of the ions are shielded from the rest of ions by the outer 5s and 5p shells [7]. According to the selection rules of lanthanide ions, magnetic dipole (MD) transitions are allowed and electric dipole (ED) transitions are forbidden. However, ED transitions are possible. They are very sensitive to the environments of crystal fields and could be completely absent or very intense [8]. In the case of Eu^{3+} ions, most or all of the luminescence usually comes from the $^5D_0$ state, which is a single level and this avoids the convolution of overlapping emission peaks from different levels [9]. An example of a hypersensitive transition is the $^5D_0$–$^7F_2$ of Eu^{3+} ions.

In this work, we provide the optical structure characterization of europium ions doped gadolinium zirconate particles. The Gd^{3+} ions do not have the capacity to give out visible light. Due to the similar ionic radius and valence state of Gd and Eu ions, europium could easily replace the Gd^{3+} without lattice distortion. We also investigate photoluminescence spectra as well as lifetime analysis by using a streak camera.

2. Experimental procedures

2.1. The preparation of samples

The combustion method has been used for the synthesis of Eu^{3+} doped $Gd_2Zr_2O_7$ nanopowders. Starting chemicals $Gd(NO_3)_3 * 6H_2O$, $Zr(NO_3)_2 * H_2O$,

* Corresponding author. Tel.: +381 113713131.
E-mail address: majap@ipb.ac.rs (M.S. Rabasovic).

http://dx.doi.org/10.1016/j.jallcom.2014.10.072
0925-8388/© 2014 Elsevier B.V. All rights reserved.

$Eu(NO_3)_3 * 6H_2O$ with the purity of 99.99% were purchased from ABCR, Gd_2O_2 (99.9%) from the NOAH Technologies and urea $(NH_2)_2CO$ from Sigma–Aldrich.

Europium doped cubic $Gd_2Zr_2O_7$ nanopowders were prepared by Solution Combustion Synthesis (SCS) method. The flame combustion process is the most frequently used due to the simplicity and low cost of the synthesis procedures and also due to the possibility of tailoring the size and morphology of particles. After the synthesis, the nanopowder was annealed in air atmosphere at 1200 °C for 2 h. The morphology analysis of the synthesized materials indicates the irregular crystallite size distribution and existence of agglomerated grains which are in the submicron size. The annealing of material is needed in order to achieve the full crystallinity. The Eu^{3+} concentration in $Gd_2Zr_2O_7$ was 2 mol%.

2.2. Experimental details

X-ray diffraction measurements were obtained on a Philips PW 1050 instrument, using Ni filtered Cu $K_{\alpha 1,\ 2}$ radiation. Measurements were done at room temperature over the 2θ range of 10–90° with a scanning step width of 0.05° and a counting time of 8 s per step. The morphology of nanopowders and the size of crystallites synthesized by SCS method were examined by scanning electron microscopy (SEM).

Photoluminescence (PL) studies reported in this work were performed at room temperature using three different excitation sources: Argon laser at 514.5 nm, laser diode at 365 nm, and Optical Parametric Oscilator (OPO) at 360 nm. The output of the OPO can be continuously tuned over a spectral range from 320 nm to 475 nm. PL spectrum excited by Ar laser line at 514.5 nm was measured using a Jobin–Yvon model U-1000 monochromator with a conventional photocounting system. The spectrum obtained by the laser diode excitation at 365 nm was recorded on an Ocean Optics USB4000 spectrometer.

Time-resolved streak images of the fluorescence spectrum excited by OPO system were acquired by Hamamatsu streak camera system (model C4334-01) and the HPD-TA (High Performance Digital Temporal Analyzer) streak camera control software. The software provides advanced analysis of streak images. Fluorescence lifetime fitting analysis was carried out using the TA-Fit program.

3. Results and discussion

3.1. Structure

Structures of synthesized $Gd_2Zr_2O_7$ doped by europium ions powders were identified by XRD pattern as is shown in Fig. 1. The diffractogram confirms that monophased sample that is crystallized in fluorite type structure (space group Fm3m) was obtained and all of the observed diffraction peaks are indexed according to this space group (Fig. 1). There is no evidence of the presence of pyrochlore phase (crystallizes in space group Fd3m), which is characterized by the occurrence of "superlattice" and additional peaks at 2θ angle of about 29°, 37° and 44,7°. The Eu^{3+} ions could replace the Gd^{3+} site in lattice due to the same valence state and similar ionic radii between Eu^{3+} and Gd^{3+} that, for the coordination number 8, have values of 0.1066 nm and 0.1053 nm, respectively. Absence of any additional peaks (see Fig. 1) that could belong to Eu_2O_3, ZrO_2 or Gd_2O_3 phases is the first evidence that doping of Eu^{3+} into $Gd_2Zr_2O_7$ material does not change the crystalline structure.

Microstructure characterization of $Gd_2Zr_2O_7$:Eu material was carried out by SEM and selected images are presented in Fig. 2 (a and b). The size of cubic $Gd_2Zr_2O_7$ material doped with Eu^{3+} given by Hu et al. [4] was of about 200 nm. The morphology of the nanopowder in Fig. 2(a and b) demonstrates the structure particles with dimensions from 50 nm (Fig. 2(a)) to over 100 nm (Fig. 2(b)), so, the agglomerated particles were melted together by sintering process.

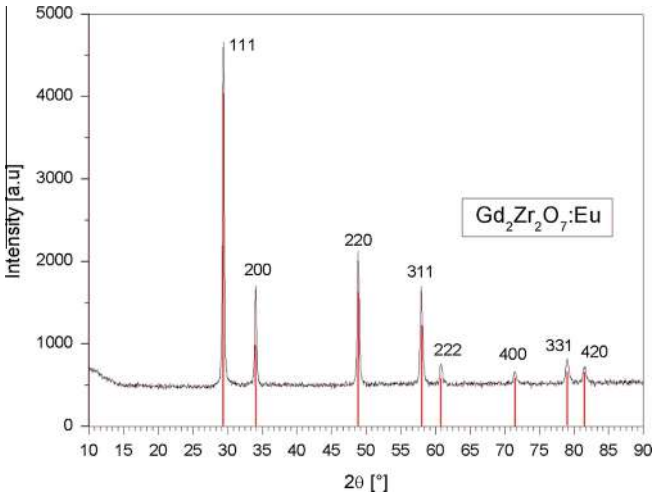

Fig. 1. XRD pattern recorded on $Gd_2Zr_2O_7$:Eu material.

3.2. Optical properties

3.2.1. Fluorescence emission spectra

The photoluminescence emission spectra of $Gd_2Zr_2O_7$ doped by europium ions obtained at room temperature under the excitations at 365 nm and 514.5 nm are presented in Fig. 3. A several recognizable fluorescence bands can be seen in emission spectra (Fig. 3) over the visible region from 580 nm to 720 nm wavelength range.

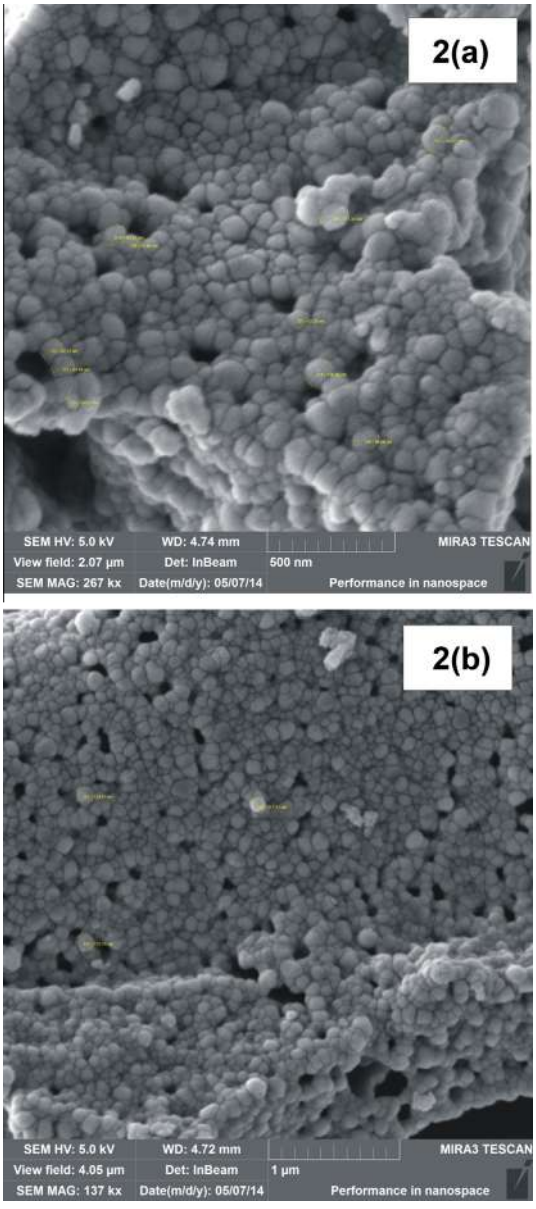

Fig. 2. SEM micrographs of $Gd_2Zr_2O_7$:Eu material.

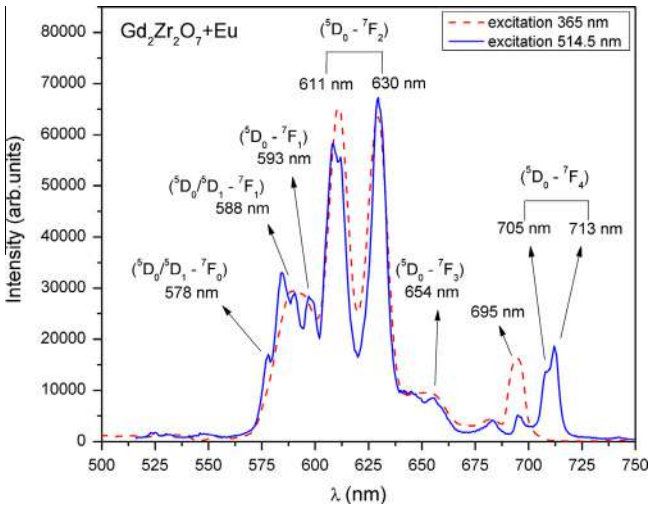

Fig. 3. Luminescence emission spectra of $Gd_2Zr_2O_7$ doped by Eu ions immediately after synthesis. The excitation wavelengths are 365 nm and 514.5 nm.

A pronounced peak at about 611 nm on the spectrum is in accordance with expectation based on the existence of f–f transitions that are responsible for luminescence in trivalent rare earth ions (Eu^{3+}) [7]. The most intense peaks are resolved between 610 and 635 nm, which are caused by forced electronic dipole transitions between $^5D_0$–$^7F_2$ states. Its intensity is hypersensitive to the variation of the local structure environment of the Eu^{3+}. The emissions between 580 nm and 610 nm are due to magnetic dipole allowed $^5D_0$-$^7F_1$ transition and its intensity hardly changes with the local structure symmetry of the Eu^{3+} ions. That transition does not depend on the site symmetry at which europium is situated. The ratio between the electric dipole and the magnetic dipole is a measure of the site symmetry in which europium is situated [10].

Transition from $^5D_1$ level has a fast decay with the lifetime of about 10.2 μs, while the decays of peaks which belong to $^5D_0$ have the lifetime of about 1.5 ms [9]. The transitions from $^5D_1$ situated in region below 550 nm are very fast and we cannot detect these lines in our emission spectrum in Fig. 3. The peaks at wavelengths of 578 nm and 585 nm in Fig. 3 are formed by overlapping the upper levels $^5D_0$ and $^5D_1$ showing double – exponential decay. It should be noted that spectrograph used for measuring the 514.5 nm excitation has much better wavelength resolution than spectrograph used in the case of 365 nm excitation, so some of the differences of spectra presented in Fig. 3 are caused by different spectral resolutions of used acquisition systems.

3.2.2. Time resolved measurements

In the time resolved fluorescence measurements reported here, the luminescence emission was collected in the reflective mode. The fluorescence emission is collected using a Spectrograph (SpectraPro 2300i) and Hamamatsu streak camera (C4334-01). Streak camera is designed to measure ultra-fast light events with a resolution up to 15 ps. The fundamental advantage of the streak scope is its two dimensional nature, enabling the acquiring of the temporal evolution of laser induced phenomena [11,12].

The streak image of the fluorescence emission spectrum of Eu doped in $Gd_2Zr_2O_7$ is presented in Fig. 4. The grayscale image is presented in pseudocolor, where different intensities are coded as different colors. For image shown in Fig. 4, the spectrograph diffraction grating of 50 lines/mm was selected, covering a 330 nm spectral range (horizontal axis) with the resolution of about 0.5 nm. The streak camera has the overall spectral range from 200 nm to 850 nm. The streak image is acquired in photon counting mode of operation with 1000 expositions and saved in .img format which contains all relevant information of the image. Further processing is accomplished by HPD-TA (High Performance Digital Temporal Analyzer) software installed on computer.

To take the streak image in the time frame of interest, it is required to set the proper delay time on digital delay generator (*Stanford* DG 535) that triggers the streak camera. The vertical axis in Fig. 4 corresponds to the plasma development in time domain of 5 ms. These results provide a good insight into the development of

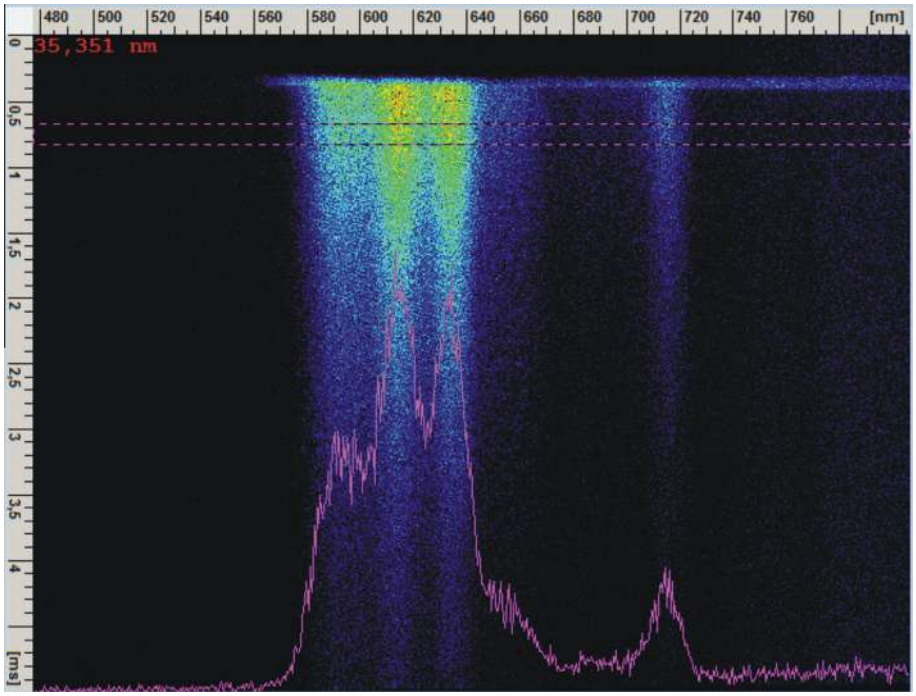

Fig. 4. Streak image of Eu doped in $Gd_2Zr_2O_7$ fluorescence spectra. OPO excitation is at 360 nm. The wavelength range (horizontal axis) is 330 nm. The time range (vertical axis) is 5 ms.

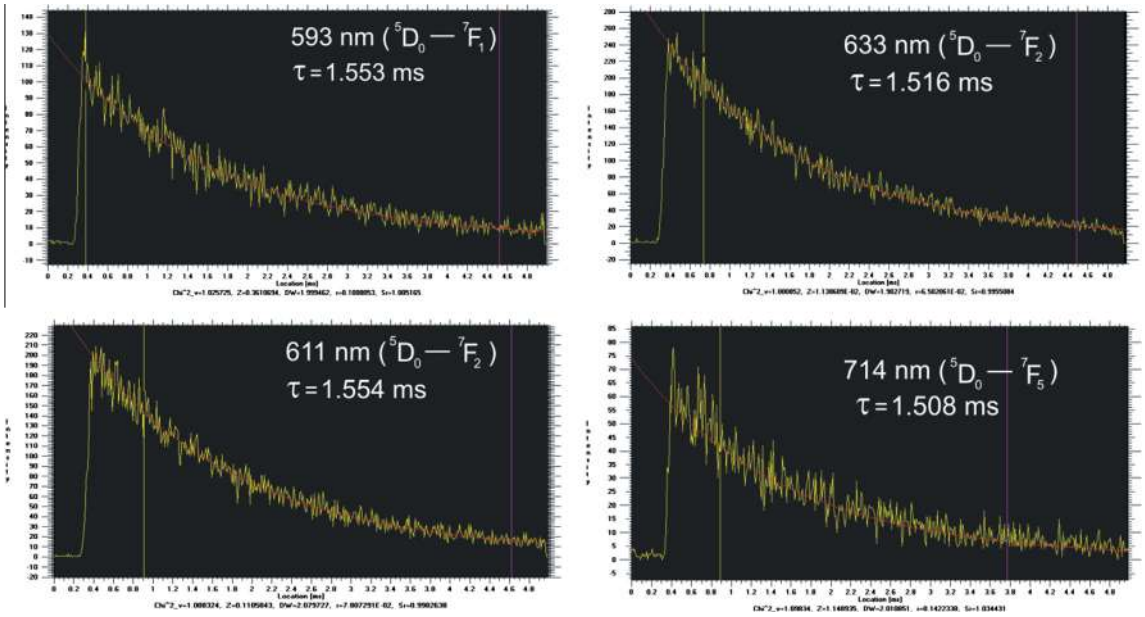

Fig. 5. Luminescence decay curves for four transitions fitted by single exponential decay.

fluorescence emission in time. Our time resolved measurements can be accomplished in the time range from 1 ns to 10 ms. The start of the fluorescence emission which can be seen in Fig. 4 is delayed for 0.3 ms regarding the beginning of the vertical (time) axis.

3.2.3. Decay curve and decay time

We conducted the fluorescence lifetime analysis for four transitions which are identified in Fig. 4. These are emission peaks at 593 nm, 611 nm, 633 nm and 714 nm wavelengths. The line at 613 nm ($^5D_0$–$^7F_2$) is the most prominent in emission spectrum with a high intensity and narrow full-width at half maximum (FWHM). That is the only one electric dipole allowed transition of the observed transitions. Namely, f–f transitions arising from forced electric dipole are parity forbidden and become partially allowed when the ion is situated at the low symmetry site. Therefore, europium trivalent ions occupy such lattices for nonsymmetric center causing very intensive $^5D_0$–$^7F_2$ transition. Because of that, the lifetime of f–f transitions lasts long, in millisecond range, so we tuned the time scale of streak camera accordingly.

Fluorescence decay and fitted curve of 593 nm ($^5D_0$–$^7F_1$), 611 nm ($^5D_0$–$^7F_2$), 633 nm ($^5D_0$–$^7F_2$) and 713 nm ($^5D_0$–$^7F_4$) transitions under the excitation at 360 nm are shown together in Fig. 5. All curves demonstrate almost perfect single – exponential decay. Fluorescence line profiles are selected from time resolved streak image shown in Fig. 5 using the integration process for radiative transitions in regions: (590,6–593,2 nm) at 593 nm, (608–612 nm) for line at 611 nm, (631,4–635,5 nm) at 633 nm and (713,38–716,99 nm) at 714 nm.

The obtained lifetimes are 1.553 ms, 1.554 ms, 1.516 ms and 1.508 ms for lines 593 nm, 611 nm, 630 nm and 713 nm, respectively (Fig. 5). Decay curve of the most prominent $^5D_0$–$^7F_2$ transition of the doped Eu^{3+} ions in different host materials has been chosen for lifetime measurements by many authors [7,9]. That is because the presence of the Eu^{3+} environment is unique in accordance with the crystal structure and decay mechanism for that transition is a single decay component between Eu^{3+} ions only. Our lifetime results are very similar with the Chambers et al. [9]. The lifetime τ is related to the radiative and nonradiative transition rates. Decrease of the lifetime could be caused by the increasing of the nonradiative transitions or by formation of the second phase [7].

4. Conclusions

In this paper we describe the synthesis and characterization of the $Gd_2Zr_2O_7$:Eu nano powder, material suitable for various optical devices. Results of our analysis show that $Gd_2Zr_2O_7$:Eu nano powder is appropriate for TBC (thermal barrier coatings) applications, high temperature heating devices and as a host material for luminescence applications. To the best of our knowledge, the detailed fluorescence lifetime analysis of the $Gd_2Zr_2O_7$:Eu nano powder, provided by using the streak camera system, is first presented here. Our lifetime analysis of europium trivalent ion doped in the $Gd_2Zr_2O_7$ confirms that this red light material is suitable for many optical applications and fabrication of various optical devices.

Acknowledgements

This work was financially supported within the Projects Ministry of Education, Science and Technological Development of the Republic of Serbia OI 171020 and Bilateral Project Serbia – Slovenia #651-03-1251/2012-09/03.

References

[1] J. Wu, X. Wei, N.P. Padture, P.G. Klemens, M. Gell, E. Garcıa, P. Miranzo, M.I. Osendi, J. Am. Ceram. Soc. 85 (12) (2002) 3031–3035.
[2] Y.H. Lee, H.S. Sheu, J.P. Deng, H.-C.I. Kao, J. Alloys Comp. 487 (2009) 595–598.
[3] L. Wang, J.I. Eldridge, S.M. Guo, Scripta Mater. 69 (2013) 674–677.
[4] K.-J. Hu, Z.-G. Liu, J.-Y. Wang, T. Wang, J.-H. Ouyang, Mater. Lett. 89 (2012) 276–278.
[5] I.E. Kolesnikov, D.V. Tolstikova, A.V. Kurochkin, A.A. Manshina, M.D. Mikhailov, Opt. Mater. (2014) (in press).
[6] M.M. Gentleman, D.R. Clarke, Surf. Coat. Technol. 200 (2005) 1264–1269.
[7] Y.-S. Chang, H.-J. Lin, Y.-L. Chai, Y.-C. Li, J. Alloys Comp. 460 (2008) 421–425.
[8] M.H.V. Werts, Sci. Prog. 88 (2) (2005) 101–131.
[9] M.D. Chamber, P.A. Rousseve, D.R. Clarke, J. Luminesc. 129 (2009) 263–269.
[10] A. Patra, E. Sominska, S. Ramesh, Yu. Koltypin, Z. Zhong, H. Minti, R. Reisfeld, A. Gedanken, J. Phys. Chem. B 103 (1999) 3361–3365.
[11] D. Sevic, M.S. Rabasovic, B.P. Marinkovic, IEEE Trans. Plasma Sci. 39 (11) (2011) 2782.
[12] M.S. Rabasovic, D. Sevic, M. Terzic, B.P. Marinkovic, Nucl. Instrum. Meth. B 279 (2012) 16–19.

polymers

MDPI

Article

Characterization and Optimization of Real-Time Photoresponsive Gelatin for Direct Laser Writing

Branka D. Murić [1,*], Dejan V. Pantelić [1], Mihajlo D. Radmilović [1], Svetlana N. Savić-Šević [1] and Vesna O. Vasović [2]

[1] Institute of Physics, University of Belgrade, Pregrevica 118, 11080 Belgrade, Serbia; pantelic@ipb.ac.rs (D.V.P.); mihajlor@ipb.ac.rs (M.D.R.); savic@ipb.ac.rs (S.N.S.-Š.)
[2] Western Serbia Academy of Applied Studies, Užice Department, Trg Svetog Save 34, 31000 Užice, Serbia; bolex65@yahoo.com
* Correspondence: muric@ipb.ac.rs

Abstract: There is an abundance of plastic materials used in the widest range of applications, such as packaging, machine parts, biomedical devices and components, etc. However, most materials used today are non-decomposable in the environment, producing a huge burden on ecosystems. The search for better, safer alternatives is still on. Here we present a detailed analysis of a simple, cheap, non-toxic, even edible, eco-friendly material, which can be easily manufactured, laser patterned and used for the fabrication of complex structures. The base substance is gelatin which is made photoresponsive by adding plasticizers and sensitizers. The resulting films were analyzed with respect to their optical, thermal and mechanical properties, which can be modified by a slight variation of chemical composition. The material is optimized for rapid laser-manufacturing of elastic microstructures (lenses, gratings, cantilevers, etc.) without any waste or residues. Overall, the material properties were tailored to increase photothermal responsivity, improve the surface quality and achieve material homogeneity, transparency and long-term stability (as verified using electron microscopy, infrared spectroscopy and differential scanning calorimetry).

Keywords: gelatin; bio-eco-polymers; physicochemical properties; optical elastomers; rapid laser printing; microstructures

check for updates

Citation: Murić, B.D.; Pantelić, D.V.; Radmilović, M.D.; Savić-Šević, S.N.; Vasović, V.O. Characterization and Optimization of Real-Time Photoresponsive Gelatin for Direct Laser Writing. *Polymers* **2022**, *14*, 2350. https://doi.org/10.3390/polym14122350

Academic Editor: Oh Seok Kwon

Received: 29 April 2022
Accepted: 5 June 2022
Published: 9 June 2022

Publisher's Note: MDPI stays neutral with regard to jurisdictional claims in published maps and institutional affiliations.

Copyright: © 2022 by the authors. Licensee MDPI, Basel, Switzerland. This article is an open access article distributed under the terms and conditions of the Creative Commons Attribution (CC BY) license (https://creativecommons.org/licenses/by/4.0/).

1. Introduction

The mechanical strength, low production cost and manufacturability of petroleum-based plastics established them as the most popular packaging materials [1]. Unfortunately, their non-biodegradability makes them an important source of pollution [2]. The ecological impact of petroleum-based plastics has accelerated the worldwide interest in biodegradable polymers from renewable resources. Despite the great potential of biodegradable polymers to solve the problem of plastic waste, they are rarely used, considering that their production is relatively expensive and they do not possess all the other properties (e.g., mechanical, optical, and electrical) required by various end-applications [3]. Additionally, such materials may have quite variable properties. For example, tensile strength, strain at break and elasticity (Young's modulus) depend on the raw material source, additives, molecular structures, etc. [4,5].

A good example of a natural biodegradable polymer from renewable resources is starch which is inexpensive, readily available and biodegradable. However, its mechanical strength is strongly modulated by its moisture sensitivity while being difficult for thermal processing (it thermally decomposes before being melted). To modify these characteristics, starch is blended with other polymers [6–8]. Unfortunately, these blends can affect biodegradability. Furthermore, there is a direct relationship between the starch-based bioplastic properties and different starch botanical sources. Namely, the amylose and amylopectin proportion, which depends on starch biosynthesis enzymes, soil type, and

climatic conditions during plant growth, strongly influences the bioplastic gelation temperature and mechanical and rheological properties [9]. Nevertheless, significant research and technological work invested in the development of starch-based polymers in the packaging sectors of food, cosmetics, pharmaceuticals, etc. [10–12].

Gelatin, yet another biocompatible and biodegradable polymer, is widely used in photography, food, pharmaceutical, biomedical and many others applications [13–17]. It has poor mechanical properties that limit its potential applications. A variety of chemical agents (formaldehyde, epoxy, glutaraldehyde and some others) are capable of crosslinking gelatin, consequently overcoming the brittleness of gelatin films, improving its flexibility, reducing the degree of swelling and enhancing its thermal stability. Glutaraldehyde [18] is usually used but is being replaced with genipin because of its lower cytotoxicity [19,20].

Besides gelatin, many other natural polymers (such as albumen, alginate, cellulose, chitosan, pullulan, etc.) can be used too [21,22]. We emphasize that the photoresponsiveness and photosensitivity of most materials stem from harmful and poisonous chemicals (such as dichromate compounds).

Also, gelatin is often mixed with other substances, e.g., chitosan, poly(vinyl alcohol), alginate and carbon nanotubes. These hybrid materials are specifically of interest in biomedicine for drug delivery, wound healing, cell culture and tissue engineering [23–25].

Gelatin hydrogels are photosensitized by various dyes, making them suitable for laser writing of microstructures (such as microfluidic channels, microlenses, micro-optoelectromechanical systems (MOEMS), lab on a chip, etc.) intended for a wide variety of applications [26–28]. Gelatin was widely used previously in optics, primarily as a photosensitive material for holography. Photo-crosslinking was achieved by adding ammonium dichromate or potassium dichromate, which resulted in holograms of excellent quality. It is known that gelatin doped with ammonium dichromate (dichromated gelatin—DCG) represents an almost ideal high-resolution holographic photosensitive material [29]. Additionally, DCG can be used as a material for the production of micro-optical components [30,31]. Most of them are toxic, difficult to manufacture and require complex chemical postprocessing. Various silicate-based materials (silicones, silica glass, etc.) were used for the fabrication of micro-optical components [32,33]. Compared to gelatin, they have higher thermal and chemical stability, but the fabrication processes are manly complex, multistep, time-consuming and costly, frequently including the use of poisonous chemicals.

Emerging applications in biomedicine, micro-mechanics, micro-optics, energy storage, and sensors require new materials, simultaneously possessing advanced optical, electrochemical, mechanical and biological properties [34–36]. Previously, we have described photosensitive tot'hema-gelatin as a good candidate material for applications requiring real-time manufacturing of micro-optical and micro-mechanical components [37–40]. Gelatin was modified with a complex aqueous mixture of various salts, plasticizers, humectants and preservatives (commercially sold under the trade name tot'hema, which is used to treat iron anemia). The material is simple to prepare, low-cost, non-toxic, biodegradable and can be patterned by direct laser writing (DLW—widely used non-contact high-precision processing technique [41,42]). Here, a variety of micro-optical and microfluidic structures were fabricated using DLW, and threshold laser energy was established. This kind of microprocessing is neither additive nor subtractive as the material is only redistributed without any waste.

Therefore, in order to fully explore and optimize the capabilities of tot'hema-gelatin films for real industrial applications, the physicochemical characteristics of the film were studied in more detail and disclosed in this paper. We correlated the applied concentration of tot'hema with the film properties, such as color, thickness, light transmission, mechanical (tensile strength, elongation at break and Young's modulus), thermal properties, moisture content, swelling, the functional group on the film surface as well as surface morphology. These properties are essential for establishing optimal conditions of material used as an elastomer for adaptive, rapid prototyping of micro-optics and micro-mechanics.

2. Materials and Methods

2.1. Materials

All chemical components were analytical grade, well known, easily available, cheap and non-toxic. Commercial gelatin from bovine skin (gel strength ~225 g Bloom, Type B) and NaCl (puriss, p.a.) were purchased from Sigma Aldrich. Tot'hema, an oral solution for the treatment of human anemia, was manufactured by Laboratoire Innotech International, France. According to the manufacturer's data [43], this is a complex water solution of gluconate (iron, manganese and copper) and excipients (glycerol, glucose liquid, saccharine, citric acid, polysorbate 80, etc.). Saline solution was purchased from Hemofarm (Serbia).

2.2. Film Preparation

A 5% water solution of gelatin with added NaCl (20% by weight of dry gelatin) was prepared as described in previous papers [37,38]. The tot'hema (ranging from 0% to 30% v/v) was mixed with gelatin solution by a magnetic stirrer. The series of five solutions (denoted as TG_X, where the letter X indicates the tot'hema percentage in solution) were prepared and centrifuged in order to remove all remaining impurities.

TG_X films were prepared by the gravity settling method [39]. Namely, the accurately measured volume of TG_X solution was pipetted onto a very clean, horizontally leveled microscope glass slide and dried in a stable environmental condition over the night.

2.3. Mechanical Properties

A film thickness was determined using a digital micrometer (an accuracy of 0.01 mm) at eight randomly selected points in the center and edges of the films. Measurements were averaged and taken as the film thickness.

The surface morphologies of the tot'hema-gelatin films were analyzed using a high-resolution scanning electron microscope equipped with a high brightness Schottky field emission gun (FEGSEM) and using non–contact profilometry (3D optical surface profiler—Zygo New View 7100).

The mechanical properties of the films were determined using a tensile testing machine, at a strain rate of 20 mm/min, as previously described for photosensitive tot'hema-gelatin, with minor modifications [44]. The dried film was cut by a brass mold, designed according to the ASTM standard [45], into a dog-bone-shaped specimen (see Figure 1). Three measurements were made for each film, and the average value was calculated. The tensile strength, elongation at break and Young's modulus were determined.

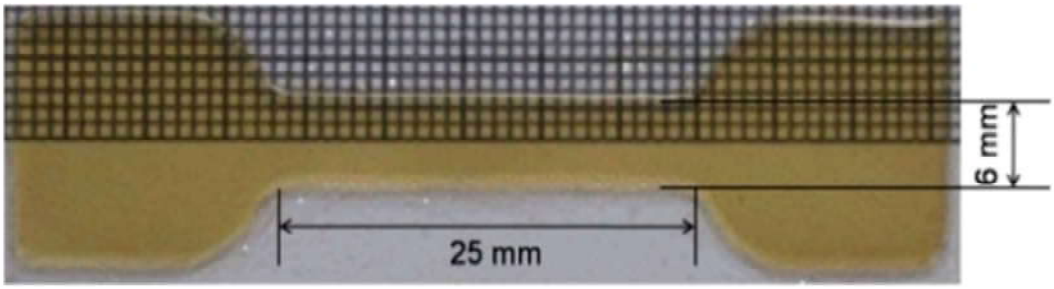

Figure 1. Optically transparent TG_20 film is used for tensile testing with dimensions according to the ASTM standards (gauge length 25 mm, width 6 mm).

2.4. Optical Properties

The transmittance of the TG_X films was analyzed using a fiber-type spectrometer (Ocean Optics) with a tungsten-halogen light as an illumination source in the wavelength range from 200 nm to 800 nm at room temperature.

A home-made direct laser writing system was used to fabricate microfluidic, micro-mechanic and micro-optical components on tot'hema modified gelatin film. A laser beam (488 nm wavelength, up to 100 mW power–iBEAM SMART, manufactured by Toptica)

was focused through the long-working-distance microscope objective. The samples were mounted on an xyz-coordinate stage to enable precise movement of the material along with the arbitrary pattern. The system was computer-controlled using G-code (standard programming language for CNC machines). More details about the system are given in a previous publication [46].

2.5. Physicochemical Properties

To determine how the number of water changes during the drying–dehydration of the film, the water content (WC) was measured. The TG_X films were weighted (w_1), then dried for 24 h at normal laboratory conditions, and weighted again (w_2). The WC for each film was determined as an average value of three measurements by the equation: $WC(\%) = [(w_1 - w_2)/w_1] \cdot 100$ [47].

In order to determine the influence of tot'hema concentration on the film swelling, TG_X films were immersed in saline solution for different intervals at laboratory conditions. Wet, swollen samples, after wiping with filter paper to remove excess liquid, were weighted again (w_w). The swelling factor (SF) of the films was calculated as the average value of three measurements by the equation: $SF(\%) = [(w_w - w_d)/w_d] \cdot 100$ where (w_d) corresponds to the weight of TG_X films before immersion [48].

Functional groups on the films were inspected by Fourier transformed infrared (FTIR) spectroscopy. The spectra were recorded on a Nicolet iS10 FTIR Spectrometer (Thermo Scientific Instruments) equipped with an attenuated total reflectance (ATR) accessory. ATR/FTIR measurements were done in the wavenumber interval from 500 to 4000 cm^{-1} with a resolution of 4 cm^{-1}.

The thermal stability of the films was analyzed by differential scanning calorimetry (DSC). An amount of about 2.5 mg of each film sample was packed in an aluminum pan (30 µL). The pan was sealed and analyzed using a DSC 131 EVO (SETARAM Instrumentation) differential scanning calorimeter previously calibrated with indium. An empty sealed pan was used as a reference. Both pans were placed in a chamber under the nitrogen flow of 20 mL/min, kept at 20 °C for 5 min and subsequently heated from 20 to 250 °C with a heating rate of 10 °C/min. To construct a baseline, two empty pans were placed in the chamber and measured under the same experimental conditions. The baseline subtraction was performed using the CALISTO Processing software (SETARAM Instrumentation).

3. Results

The pure gelatin film (TG_0) has a uniform, relatively smooth and flat surface, which indicates that the gelatin has a good film-forming ability. We have found that there is no noticeable difference in the gelatin film surface after tot'hema adding. Films still keep a rather smooth, uniform and homogeneous surface (without pores or cracks), indicating that there is good compatibility between tot'hema and gelatin molecules. Smoothness remains high after laser processing, as verified by SEM analysis of hexagonal concave microlenses array fabricated on photoresponsive tot'hema-gelatin film (Figure 2a). The lens-shaped dip is very symmetric (verified by the concentric shape of the corresponding interferogram in Figure 2b), and its roughness is of the order of several tens of nanometers (see Figure 2c). This makes photoresponsive tot'hema-gelatin an excellent material for the fabrication of micro-optical components.

To study mechanical properties, equal volumes of solution were used to prepare all TG_X films. An increase in tot'hema concentration resulted in the film thickening from 25 µm (pure gelatin) to 200 µm (30% of tot'hema) as a result of the plasticizer's interaction with the polymer chains. Tot'hema added to gelatin increases the distance between protein chains, increasing the film thickness. It can be noticed that the highest tot'hema concentration (30%) results in the thickest film due to the fact that most tot'hema ingredients are hydrophilic molecules that retain water and further increase the film thickness. Moreover, increased tot'hema content in gelatin film decreases the stress at break (reaching a minimum of 0.72 MPa at 30% of tot'hema) and increases the strain at break (turning tot'hema-gelatin

into an elastomer—maximum elasticity of about 220% was obtained). Mechanical properties of TG_X films, as a function of the concentration of tot'hema, are summarized in Table 1. The tot'hema addition (which is a mixture of different plasticizers and humectants) to the gelatin matrix improves the film flexibility and, consequently, makes it less rigid. Namely, glycerol is well known as a plasticizer. As a hydrophilic molecule with low molecular weight, glycerol can easily fit into protein chains creating hydrogen bonds [49]. Furthermore, tot'hema provides additional mobility of protein chains by increasing their distance, influencing a significant decrease of Young's modulus of elasticity, from 1933 MPa for pure gelatin (TG_0) to 948 MPa for the 5% tot'hema concentration (TG_5). As the tot'hema content increases further, Young's modulus value decreases even more (see Table 1). As demonstrated, the TG_30 film has Young's modulus of 0.32 MPa (which is very close to 0.35 MPa for PDMS), making it suitable for contact copying. Elastic properties of TG_X films are very important for the production of adaptive micro-optical components.

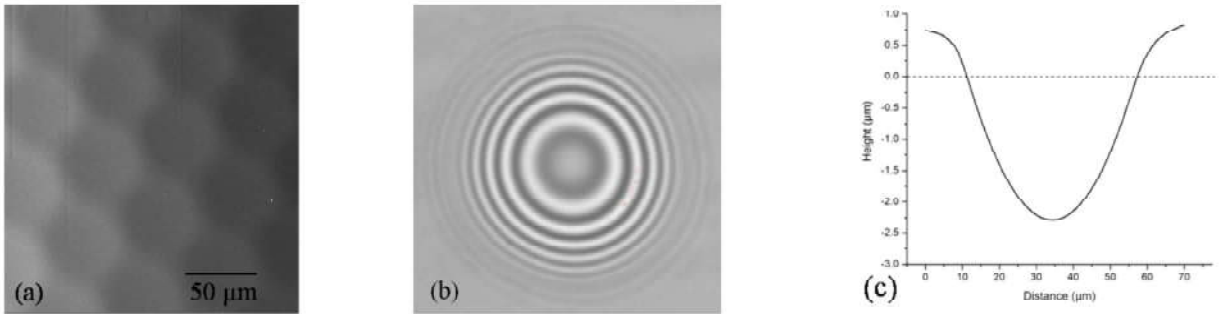

Figure 2. (**a**) SEM image of hexagonal microlenses array; (**b**) Interference fringe pattern of a microlens; and (**c**) 2D surface profile of a microlens.

Table 1. The film thickness, stress at break, strain at break and Young's modulus.

Film	Tot'hema (%)	Thickness (µm)	Stress at Break (MPa)	Strain at Break (%)	Young's Modulus (MPa)
TG_0	0	25 ± 10	58 ± 1	2 ± 0.1	1933 ± 40
TG_5	5	35 ± 10	37.92 ± 0.76	4 ± 0.2	948 ± 10
TG_10	10	50 ± 10	4.89 ± 0.10	40 ± 2	12.23 ± 0.06
TG_20	20	100 ± 10	1.71 ± 0.03	140 ± 6	1.22 ± 0.02
TG_30	30	200 ± 10	0.72 ± 0.01	224 ± 10	0.32 ± 0.01

Results are expressed as mean value ± standard deviation.

The change of color and transparency of the films varied from transparent (pure gelatin) and slightly yellow to yellow with increasing tot'hema content (see Figure 3).

Figure 3. Colors of TG_X films − (gelatin with 0%, 5%, 10%, 20%, and 30% of tot'hema).

The corresponding spectral light transmittance of the TG_X films as a function of wavelength is presented in Figure 4. Light transmission (in the visible range of 350–800 nm) of the pure gelatin (TG_0) film was above 80%, and the transmission increased with increasing wavelength (see Figure 4). By adding tot'hema, a layer is transformed into a spectral filter whose characteristics strongly depend on the concentration. In all cases, UV

radiation is strongly suppressed, making tot'hema-gelatin films an excellent filter for UV-sensitive applications. As we see, pure gelatin film transmits light very well at wavelengths from 350 nm to about 800 nm, but this can be changed at will using appropriate colorants.

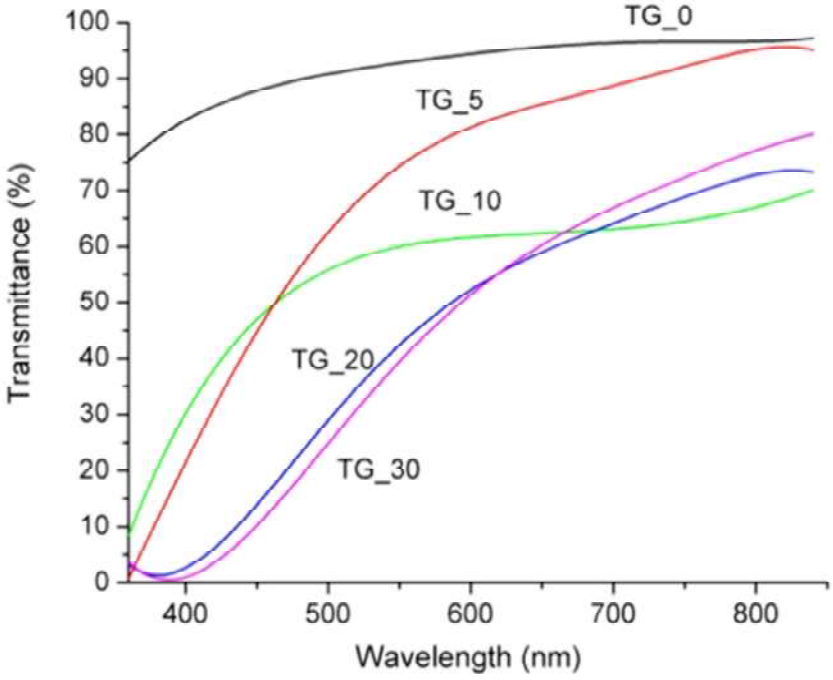

Figure 4. Spectral transmittance of the TG_X films (X− 0, 5, 10, 20, and 30% of tot'hema).

It was noticed that, after the initial rapid decrease of water content for all TG_X films during the drying process (see Figure 5a), the water content remains constant after 24 h of drying. After that, all the other properties remain stable, and the film is ready for further use (e.g., direct laser writing). Pure gelatin film had the lowest water content that exponentially increased with tot'hema content (see Figure 5b). This behavior is consistent irrespective of film thickness. The increase in water content in the presence of a tot'hema can be attributed to the additional hydrogen bonds formed between water molecules and gelatin chains. Water content can influence the physical properties of films (low-humidity films are generally stiff, while films with increased humidity are flexible and malleable). However, relatively high water content does not necessarily mean better physical properties in films [50] but makes the material suitable for a range of applications in biomedicine.

The influence of tot'hema concentration on the swelling of TG_X films during 1 h, 4 h and 24 h are shown in Figure 6. The longer the film is immersed in the saline solution, the higher swelling (without deterioration) was observed (after 24 h, the film is fully saturated). Water content and swelling factor of the films were correlated. Opposite to the water content, the film swelling (see Figure 6) decreases with increasing concentration of tot'hema: pure gelatin film has the highest swelling factors (around 220%), while the tot'hema addition reduces the film swelling. This might be due to the limited spaces in film (gelatin network) for absorbing water as already occupied by tot'hema (plasticizer) molecules. The lowest swelling factor for TG_30 is correlated with the largest water amount in the film. Namely, in contact with the film, water diffuses into it, which results in the movement of polymer chains, incorporating between them and the dissolving of added ingredients. In this way, swelling enhances the release effect of some ingredients added to the film, which later diffuse into the system, manifesting different roles (for example, protective) [51].

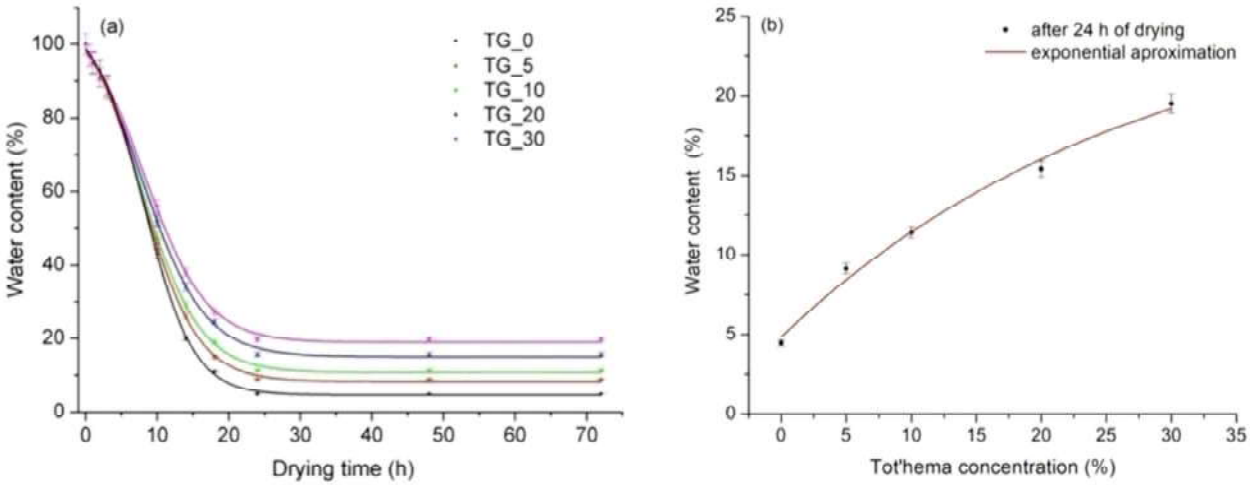

Figure 5. (**a**) Influence of drying time on the water content of TG_X films (X − 0, 5, 10, 20, and 30% of tot'hema); (**b**) The equilibrium water content as a function of tot'hema concentration.

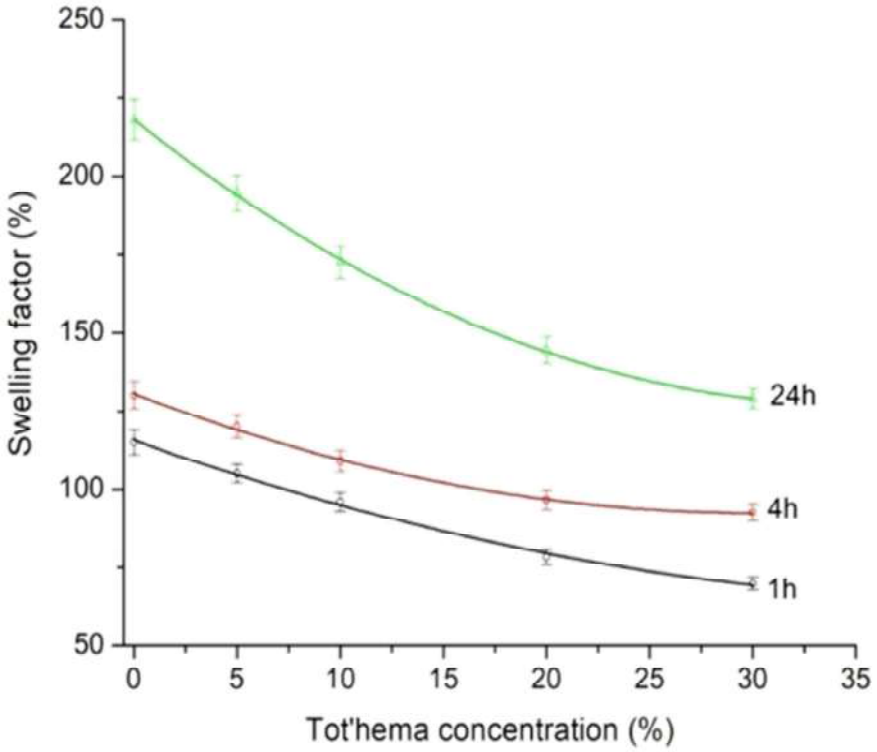

Figure 6. TG_X film (X− 0, 5, 10, 20, and 30% of tot'hema) swelling (during 1, 4 and 24 h) as a function of tot'hema concentration.

FTIR analysis was performed to study the interactions between tot'hema and gelatin matrix, i.e., to illustrate possible conformational changes in the gelatin films containing tot'hema. FTIR spectra of TG_X films are presented in Figure 7. A wide band in the range of 3500–3000 cm^{-1} can be attributed to O–H stretching and N–H bending, which are able to form a hydrogen bond with the carbonyl group of the peptide bond in the gelatin, as suggested by a literature review [52,53].

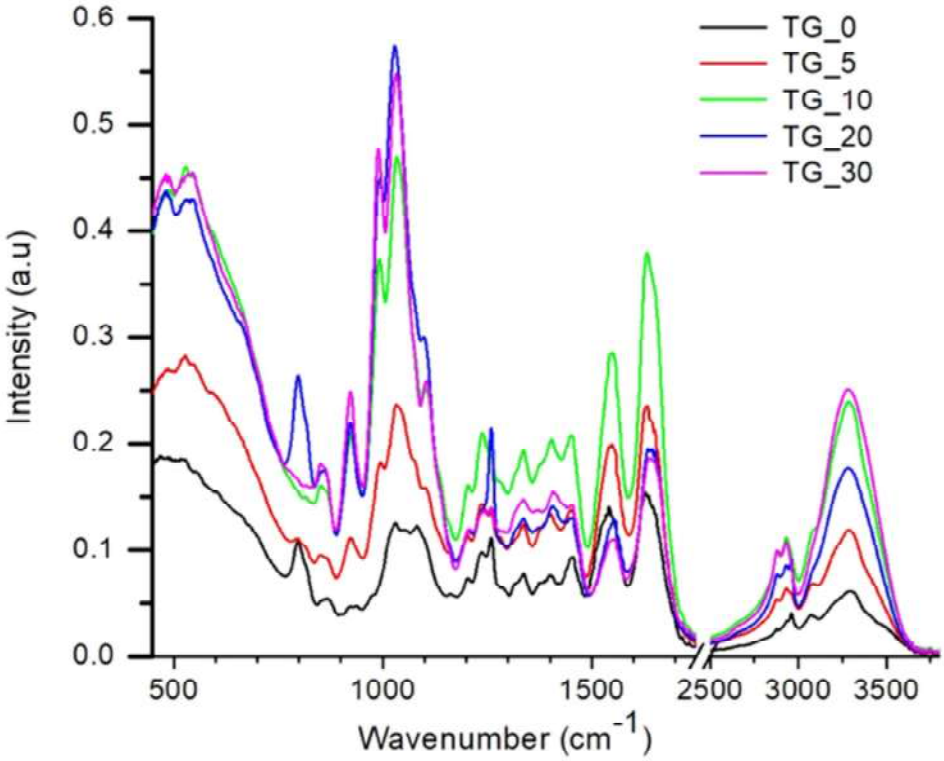

Figure 7. FTIR spectra of TG_X films (X− 0, 5, 10, 20, and 30% of tot'hema).

The FTIR spectrum of the pure gelatin film contains characteristic peaks at 3297 cm^{-1} and 2963 cm^{-1}, which can be attributed to –OH and –CH vibration stretching peaks. Further, it showed the characteristic amide I, amide II and amide III bands [54]. It is observed that the main absorption of the gelatin film such as C=O stretching at 1629 cm^{-1} (Amide I), N–H bending at 1542 cm^{-1} (Amide II), C–H deformation at 1403 cm^{-1}, and C–N stretching (Amide III) at 1237 cm^{-1} remains present in all films.

Compared to pure gelatin film, it was noticed that there are no new peaks in the spectrum of TG_X films. At the same time, the addition of tot'hema caused noticeable changes in the intensity of the Amide I, Amide II, and Amide III band. The peaks characteristic of C–H stretching of CH_2 and CH_3 at 2963 cm^{-1} and 2876 cm^{-1} in TG_X films vary significantly in intensity relative to the TG_0. Further, there is a slight shift in the peak's position, which can be explained by the formation of hydrogen bonds. The shift of these bands to a lower wavelength can be explained by the crosslinking between the components of TG_X films. These data indicate that the polar groups of tot'hema solution interact with the amino acids of the protein chains via inter-and intra-molecular hydrogen bonding and hydrophobic interaction. Therefore, tot'hema adding does not change the chemical composition of gelatin, but it changes the structure of gelatin due to intermolecular hydrogen bonding.

DSC is used to establish thermal stability due to changes in the physical and chemical properties of a material as a function of temperature or time [55]. It is well known that heat can cause structural transitions in protein networks that break chemical bonds [56]. The thermal properties of the film are closely related to their applications. The DSC thermograms of the TG_X films up to a temperature of 250 °C are shown in Figure 8.

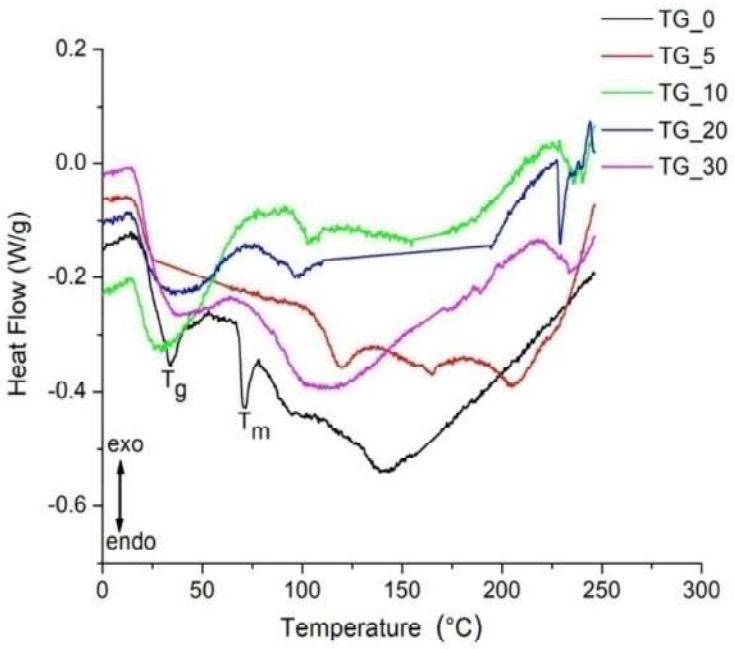

Figure 8. DSC curves of the TG_X films (X− 0, 5, 10, 20, and 30% of tot'hema). Tg and Tm − Endothermic peaks (denoted for pure gelatin film −TG_0) represent glass transition and melting temperature, respectively.

The first endothermic peak of pure gelatin film (TG_0) is recorded at a temperature of about 40 °C (see Figure 8). This endothermic peak represents glass transition (T_g) and is attributed to the transition from the glassy state to rubber. The endothermic peak that follows T_g, at a temperature around $T_m \approx 70$ °C is attributed to the melting and dissociation of arranged polymer parts. Some authors attribute this peak to the overlap of various processes such as the water evaporation, melting and recrystallization of small and/or imperfect gelatin crystals [57,58].

It was found that the peak temperatures and the enthalpies of these endothermic processes depend on the film preparation and drying conditions [57]. The endothermic peak at about 160 °C represents the gelatin decomposition temperature. It was observed that by adding and increasing the tot'hema content, the endothermic peaks become significantly wider and larger than that of the pure gelatin film. In addition, DSC analysis demonstrated that tot'hema addition, depending on its content, improves gelatin thermal stability. The melting temperature (T_m) increased when compared to pure gelatin film for all concentrations of tot'hema. T_m is typically associated with thermal stability: a high value of T_m corresponds to high thermal stability. It is already established that the thermal stability of polymers is related to crosslinking density [59]. In Figure 8, it is noticed that pure gelatin film (TG_0) has the lowest melting temperature (T_m). This temperature increases after crosslinking gelatin by tot'hema. The highest value of T_m was obtained for TG_5 film, while the T_m for films prepared with 10–30% of tot'hema show lower values. This behavior is attributed to the hydrophobicity of the gelatin molecular structure resulting from the addition of a large quantity of tot'hema. The improved thermal stability of TG_X films indicates that the temperature range of the use has been extended to about 100 °C, which is very important for practical applications.

To summarize—tot'hema is added to gelatin in order to increase the light absorption, modify its melting temperature and make it permanently elastomeric. Tot'hema concentration was optimized in order to make a compromise between gelatin thermal (e.g., melting temperature), mechanical (flatness) and optical (transparency) properties.

4. Discussion

The gelatin-based material described above has a number of useful optical, thermal and mechanical properties, which can be modulated by slight variations of its chemical composition. In this way, it becomes suitable for a range of applications, primarily dealing with micro-mechanics, microfluidics and micro-optics.

The most important property is photoresponsiveness. The photoresponsive gelatin studied here belongs to the class of waste and natural biopolymers (such as alginates and eggshells already reported for the electronics industry [35,36]), which is very important for developing non-toxic, eco-friendly materials. In contrast to the classical photosensitive materials (for example, silver-halide films, photoresists, dichromated gelatin), the response of tot'hema modified material is a consequence of physical, rather than chemical, processes. Here, absorbed light locally heats the material above the melting point, and surface tension pushes the fluidized layer, thus producing a dip (concave, lens-shaped recess), as can be seen in Figure 2. After the light is turned off, rapid cooling "freezes" the surface shape. Due to the low melting point of the gel (approximately 50 °C), the effect is easily achieved by a few milliwatt laser beams and millisecond irradiation times. Depending on the focal point size, micron-sized structures are easily formed. It is important to note that there is no material ablation because the melting point is much higher, and the material is simply displaced [60].

This makes the material extremely useful for rapid fabrication of micron-sized features using direct laser writing (DLW)—see Video S1 in a Supplementary Material of this paper demonstrating manufacturing of a complex array of microlenses. By controllably guiding the laser beam across the surface, virtually any shape can be formed (see Figure 9), where a rather complex microchannel structure (with three Tesla valves) is shown [61,62]. The whole pattern was fabricated in less than a minute using a 488 nm laser with 10 mW power (focused by 0.4 NA microscope objective).

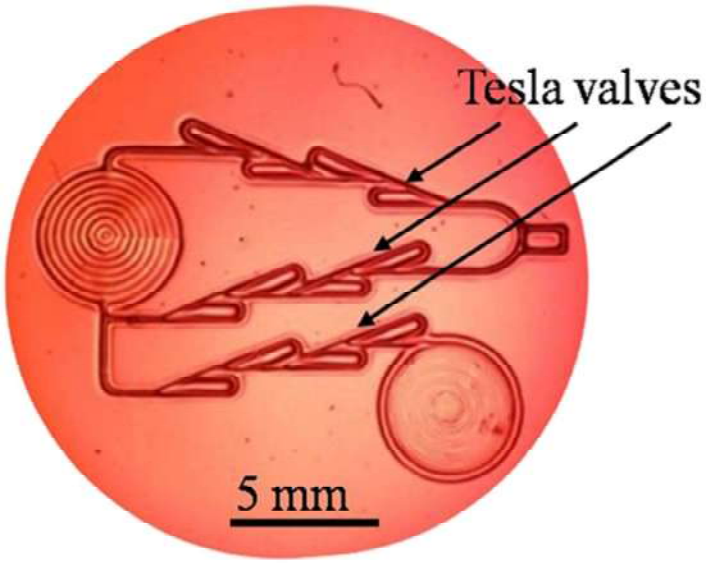

Figure 9. Complex microfluidic channels, with three Tesla valves formed on a tot'hema-gelatin.

Physicochemical processes during interaction with light depend strongly on the laser beam power and focus. The sensitivity threshold is reached at approximately 7.5 nJ/μm^2 of laser energy, which is easily achieved by focusing the laser beam through the long-working–distance microscope objective (Mitutoyo 20×, 0.4 NA). By appropriately controlling the laser beam size and power, irradiation time and writing speed, features can be fabricated with characteristic widths between 10 μm and 1000 μm and depths up to several hundred micrometers. By using high-power lasers, fabrication time can be significantly reduced

to milliseconds for the fabrication of individual microlenses or seconds for more complex structures like the one in Figure 9. Of course, the scanning speed of the laser beam must be increased to prevent material destruction. In most cases, there is no postprocessing, so the optical structures are usable immediately after fabrication.

We have mostly studied optical applications of the material [37,38], which simultaneously offers several key features—optical homogeneity, transparency, surface quality, easy fabrication and environmental friendliness. We have found that tot'hema ingredients mostly determine the material properties. As shown above, spectral absorption and melting point enable tailoring of the material to efficiently absorb the DLW beam.

The concept of microfabrication using meltable gels can be easily extended by replacing tot'hema with a suitable combination of plasticizers, humectants, preservatives and sensitizing dyes (e.g., betanin, eosin, anthocyanin, etc.) to achieve improved characteristics (faster melting, improved sensitivity, optical transparency after laser processing), which we described elsewhere [37]. In this way, we were able to fabricate a range of optical components, such as diffraction gratings and arrays of positive and negative microlenses.

Gelatin-based materials are biocompatible, and additional chemicals used in this research are non-toxic (even food grade), giving the advantage of quick and natural biodegradability. We have covered a piece of the material with a few centimeters of soil and found that it was completely absorbed, without a trace, within a few days. For some applications, this might be a problem as we observed fungi growing on the material after some time (several days). To prevent that, we added table salt (NaCl), which made it durable and usable over a long period of exposure time to normal room conditions. Normal laboratory conditions (humidity, temperature) do not affect the material properties, and laboratory illumination does not diminish the material sensitivity (i.e., the material does not have to be kept in darkness). Dust is the major problem because of the stickiness of the film, and the material surface must be protected by an additional cover glass.

Softness is yet another possible disadvantage. Surfaces should not be scratched or punched with hard objects as this will certainly damage the structure. On the positive side, films can be easily cut, peeled from the substrate, stacked together and transferred. Mechanical hardness can be further significantly increased by removing the plasticizer (by submerging the films in cold water and letting the plasticizer diffuse out) or by hardening (tanning) with, e.g., alum [63]. In addition, we have been able to use tot'hema-gelatin as a template for contact copying into harder materials (epoxies, photopolymer composites).

The usable temperature range is limited by the melting point to somewhere between 50 °C and 100 °C, depending on tot'hema concentration. For the majority of applications, this is quite satisfactory and makes the material usable in the widest range of applications: lab on a chip, sensors and micro-optics. We have also found that above the critical power density of the laser beam, material locally carbonizes and can be used as a blocking filter [39] and, possibly, as an electrical conductor.

Finally, the fabrication cost is really low. Materials used here are cheap and ubiquitous. Most of them can be found in the kitchen, while the fabrication of layers is straightforward and simple. Production methods are well known in the film industry and can be used both in low- and large-scale production.

5. Conclusions

To conclude, here we disclosed an innovative combination of well-known substances producing really versatile material for safe, real-time, low-cost, rapid microfabrication. Physicochemical properties of the material have been thoroughly studied, aiming to establish operational limits and optimize properties for the desired application. Application potential is high due to the simplicity of fabrication of highly complex structures, good optical properties, and manufacturability by direct laser writing without any further post-processing, micrometers resolution, elastomeric characteristics, environmental friendliness, and non-toxic character—a rare combination of properties concentrated in a single material. Elasticity, uniform and homogeneous surface and optical transparency were achieved,

making the material suitable for the production of adaptive micro-optical components and protective filters. The temperature range of the material's applicability is extended up to 100 °C.

Supplementary Materials: The following supporting information can be downloaded at: https://www.mdpi.com/article/10.3390/polym14122350/s1, Video S1: Microoptics fabrication.

Author Contributions: B.D.M.: Conceptualization, methodology, investigation, visualization, writing original draft, reviewing, editing, resources, project administration; D.V.P.: Software, supervision, writing, editing, reviewing; M.D.R.: Software, data curation, reviewing; S.N.S.-Š.: Investigation, editing, reviewing; V.O.V.: Editing, project administration. All authors have read and agreed to the published version of the manuscript.

Funding: The authors acknowledge funding provided by the Institute of Physics University of Belgrade through the grant by the Ministry of Education, Science and Technological Development of the Republic of Serbia.

Data Availability Statement: Not applicable.

Acknowledgments: We thank Smilja B. Marković from the Institute of Technical Sciences of the Serbian Academy of Sciences and Arts, Belgrade, Serbia for help with FTIR and DSC measurements.

Conflicts of Interest: The authors declare no conflict of interest.

References

1. Chaudhary, V.; Bangar, S.P.; Thakur, N.; Trif, M. Recent advancements in smart biogenic packaging: Reshaping the future of the food packaging industry. *Polymers* **2022**, *14*, 829. [CrossRef] [PubMed]
2. Tokiwa, Y.; Calabia, B.P.; Ugwu, C.U.; Aiba, S. Biodegradability of plastics. *Int. J. Mol. Sci.* **2009**, *10*, 3722–3742. [CrossRef] [PubMed]
3. Vroman, I.; Tighzer, L. Biodegradable polymers. *Materials* **2009**, *2*, 307–344. [CrossRef]
4. Shamsuddin, I.M.; Jafar, J.A.; Shawai, A.S.A.; Yusuf, S.; Lateefah, M.; Aminu, I. Bioplastics as better alternative to petroplastics and their role in national sustainability: A review. *Adv. Biosci. Bioeng.* **2017**, *5*, 63–70. [CrossRef]
5. Rosenboom, J.G.; Langer, R.; Traverso, G. Bioplastics for a circular economy. *Nat. Rev. Mater.* **2022**, *7*, 117–137. [CrossRef] [PubMed]
6. Hassan, M.M.; Le Guen, M.J.; Tucker, N.; Parker, K. Thermo-mechanical, morphological and water absorption properties of thermoplastic starch/cellulose composite foams reinforced with PLA. *Cellulose* **2019**, *26*, 4463–4478. [CrossRef]
7. Souza, C.R.; Andrade, C.T. Processing and properties of thermoplastic starch and its blends with sodium alginate. *J. Appl. Polym. Sci.* **2001**, *81*, 412–420. [CrossRef]
8. Abe, M.M.; Martins, J.R.; Sanvezzo, P.B.; Macedo, J.V.; Branciforti, M.C.; Halley, P.; Botaro, V.R.; Brienzo, M. Advantages and disadvantages of bioplastics production from starch and lignocellulosic components. *Polymers* **2021**, *13*, 2484. [CrossRef]
9. Rivadeneira-Velasco, K.E.; Utreras-Silva, C.A.; Díaz-Barrios, A.; Sommer-Márquez, A.E.; Tafur, J.P.; Michell, R.M. Green nanocomposites based on thermoplastic starch: A review. *Polymers* **2021**, *13*, 3227. [CrossRef]
10. Onyeaka, H.; Obileke, K.; Makaka, G.; Nwokolo, N. Current research and applications of starch based biodegradable films for food packaging. *Polymers* **2022**, *14*, 1126. [CrossRef]
11. Jiang, T.; Duan, Q.; Zhu, J.; Liu, H.; Yu, L. Starch-based biodegradable materials: Challenges and opportunities. *Adv. Ind. Eng. Polym. Res.* **2020**, *3*, 8–18. [CrossRef]
12. Estrada-Monje, A.; Alonso-Romero, S.; Zitzumbo-Guzmán, R.; Estrada-Moreno, I.A.; Zaragoza-Contreras, E.A. Thermoplastic starch-based blends with improved thermal and thermomechanical properties. *Polymers* **2021**, *13*, 4263. [CrossRef] [PubMed]
13. Chauhan, S.; Bansal, M.; Khan, G.; Yadav, S.K.; Singh, A.K.; Prakash, P.; Mishra, B. Development, optimization and evaluation of curcumin loaded biodegradable crosslinked gelatin film for the effective treatment of periodontitis. *Drug Dev. Ind. Pharm.* **2018**, *44*, 1212–1221. [CrossRef] [PubMed]
14. Yang, J.; Sun, X.; Kang, Q.; Zhu, L.; Qin, G.; Chen, Q. Freezing-tolerant and robust gelatin-based supramolecular conductive hydrogels with double-network structure for wearable sensors. *Polym. Test.* **2021**, *93*, 106879. [CrossRef]
15. Liu, J.; Li, Y.; Hu, D.; Chao, X.; Zhou, Y.; Wang, J. An essential role of gelatin in the formation process of curling in long historical photos. *Polymers* **2021**, *13*, 3894. [CrossRef]
16. Lu, Y.; Luo, Q.; Chu, Y.; Tao, N.; Deng, S.; Wang, L.; Li, L. Application of gelatin in food packaging: A review. *Polymers* **2022**, *14*, 436. [CrossRef]
17. Maiti, S.; Khillar, P.S.; Mishra, D.; Nambiraj, N.A.; Jaiswal, A.K. Physical and self–crosslinking mechanism and characterization of chitosan-gelatin-oxidized guar gum hydrogel. *Polym. Test.* **2021**, *97*, 107155. [CrossRef]
18. Farris, S.; Song, J.; Huang, Q. Alternative reaction mechanism for the cross-linking of gelatin with glutaraldehyde. *J. Agric. Food Chem.* **2010**, *58*, 998–1003. [CrossRef]

19. Bigi, A.; Cojazzi, G.; Panzavolta, S.; Roveri, N.; Rubini, K. Stabilization of gelatin films by crosslinking with genipin. *Biomaterials* **2002**, *23*, 4827–4832. [CrossRef]
20. Zhao, Y.; Sun, Z. Effects of gelatin-polyphenol and gelatin–genipin cross-linking on the structure of gelatin hydrogels. *Int. J. Food Prop.* **2017**, *20*, S2822–S2832. [CrossRef]
21. Savić, S.; Pantelić, D.; Jakovijević, D. Real-time and postprocessing holographic effects in dichromated pullulan. *Appl. Opt.* **2002**, *41*, 4484–4488. [CrossRef] [PubMed]
22. Haniffa, M.A.C.M.; Ching. Y., C.; Abdullah, L.C.; Poh, S.C.; Chuah, C.H. Review of Bionanocomposite Coating Films andTheir Applications. *Polymers* **2016**, *8*, 246. [CrossRef] [PubMed]
23. Salahuddin, B.; Wang, S.; Sangian, D.; Aziz, S.; Gu, Q. Hybrid gelatin hydrogels in nanomedicine applications. *ACS Appl. Bio Mater.* **2021**, *4*, 2886–2906. [CrossRef] [PubMed]
24. Rakhshaei, R.; Namazi, H.; Hamishehkar, H.; Kafil, H.S.; Salehi, R. In situ synthesized chitosan−gelatin/ZnO nanocomposite scaffold with drug delivery properties: Higher antibacterial and lower cytotoxicity effects. *J. Appl. Polym. Sci.* **2019**, *136*, 47590. [CrossRef]
25. Afnas, V.M.; Unnikrishnan, G.; Budhe, S.; Manaf, O.; Ameen, J. PVA/gelatin/chitin ternary blend as a humidity sensing material. *J. Mater. Sci. Mater. Electron.* **2022**, *33*, 2031–2043. [CrossRef]
26. Nawroth, J.C.; Scudder, L.L.; Halvorson, R.T.; Tresback, J.; Ferrier, J.P.; Sheehy, S.P.; Cho, A.; Kannan, S.; Sunyovszki, I.; Goss, J.A.; et al. Automated fabrication of photopatterned gelatin hydrogels for organ-on-chips applications. *Biofabrication* **2018**, *10*, 25004. [CrossRef] [PubMed]
27. Liu, J.; Su, C.; Chen, Y.; Tian, S.; Lu, C.; Huang, W.; Lv, Q. Current understanding of the Applications of photocrosslinked hydrogels in biomedical engineering. *Gels* **2022**, *8*, 216. [CrossRef]
28. Pinto-Iguanero, B.; Olivares-Perez, A.; Mendez-Alvarado, A.W.; Fuentes-Tapia, I.; Trevino-Palacios, C.G. Non-hydroscopic vanilla doped dichromated gelatin holographic material. *Opt. Mater.* **2003**, *22*, 397–404. [CrossRef]
29. Pantelić, D.; Murić, B. Improving the holographic sensitivity of dichromated gelatin in the blue–green part of the spectrum by sensitization with xanthene dyes. *Appl. Opt.* **2001**, *40*, 2871–2875. [CrossRef]
30. Yao, J.; Cui, Z.; Gao, F.; Zhang, Y.; Guo, Y.; Du, C.; Zeng, H.; Qiu, C. Refractive micro lens array made of dichromate gelatin with gray-tone photolithography. *Microelect. Eng.* **2001**, *57–58*, 729–735. [CrossRef]
31. Calixto, S.; Scholl, M.S. Relief optical microelements fabricated with dichromated gelatin. *Appl. Opt.* **1997**, *36*, 2101–2106. [CrossRef] [PubMed]
32. Pan, A.; Gao, B.; Chen, T.; Si, J.; Li, C.; Chen, F.; Hou, X. Fabrication of concave spherical microlenses on silicon by femtosecond laser irradiation and mixed acid etching. *Opt. Express* **2014**, *22*, 15245–15250. [CrossRef] [PubMed]
33. Marcinkevičius, A.; Juodkazis, S.; Watanabe, M.; Miwa, M.; Matsuo, S.; Misawa, H.; Nishii, J. Femtosecond laser-assisted three-dimensional microfabrication in silica. *Opt. Lett.* **2001**, *26*, 277–279. [CrossRef] [PubMed]
34. Calixto, S.; Ganzherli, N.; Gulyaev, S.; Figueroa-Gerstenmaier, S. Gelatin as a photosensitive material. *Molecules* **2018**, *23*, 2064. [CrossRef]
35. Minakshi, M.; Higley, S.; Baur, C.; Mitchell, D.R.G.; Jonesd, R.T.; Fichtner, M. Calcined chicken eggshell electrode for battery and supercapacitor applications. *RSC Adv.* **2019**, *9*, 26981–26995. [CrossRef]
36. Wickramaarachchi, K.; Minakshi Sundaram, M.; Henry, D.J.; Gao, X. Alginate Biopolymer Effect on the Electrodeposition of Manganese Dioxide on Electrodes for Supercapacitors. *ACS Appl. Energy Mater.* **2021**, *4*, 7040–7051. [CrossRef]
37. Murić, B.D.; Pantelić, D.V.; Vasiljević, D.M.; Panić, B.M. Properties of microlenses produced on a layer of tot'hema and eosin sensitized gelatin. *Appl. Opt.* **2007**, *46*, 8527–8532. [CrossRef]
38. Murić, B.; Pantelić, D.; Vasiljević, D.; Panić, B. Microlens fabrication on tot'hema sensitized gelatin. *Opt. Mater.* **2008**, *30*, 1217–1220. [CrossRef]
39. Murić, B.D.; Pantelić, D.V.; Vasiljević, D.M.; Savić-Šević, S.N.; Jelenković, B.M. Application of tot'hema eosin sensitized gelatin as a potential eye protection filter against direct laser radiation. *Curr. Appl. Phys.* **2016**, *16*, 57–62. [CrossRef]
40. Murić, B.; Pantelić, D.; Vasiljević, D.; Zarkov, B.; Jelenković, B.; Pantović, S.; Rosić, M. Sensitized gelatin as a versatile biomaterial with tunable mechanical and optical properties. *Phys. Scr.* **2013**, *T157*, 14018. [CrossRef]
41. Krmpot, A.J.; Tserevelakis, G.J.; Murić, B.D.; Filippidis, G.; Pantelić, D.V. 3D imaging and characterization of microlenses and microlens arrays using nonlinear microscopy. *J. Phys. D Appl. Phys.* **2013**, *46*, 195101. [CrossRef]
42. Wu, Z.-L.; Qi, Y.-N.; Yin, X.-J.; Yang, X.; Chen, C.-M.; Yu, J.-Y.; Yu, J.-C.; Lin, Y.-M.; Hui, F.; Liu, P.-L.; et al. Polymer-Based Device Fabrication and Applications Using Direct Laser Writing Technology. *Polymers* **2019**, *11*, 553. [CrossRef] [PubMed]
43. Available online: www.vidal.fr/medicaments/tot-hema-sol-buv-en-ampoule-16626.html (accessed on 10 February 2022).
44. Keinonen, T.; Riihola, P.; Huttu, K.; Parkkonen, S. Dye films for optical demonstrations in the undergraduate laboratory. *Opt. Mater.* **1998**, *11*, 79–86. [CrossRef]
45. *ISO 527–3:2018*; Plastics—Determination of Tensile Properties—Part 3: Test Conditions for Films and Sheets. ISO: Geneva, Switzerland, 2018. Available online: https://www.iso.org/standard/70307.html (accessed on 12 March 2022).
46. Radmilović, M.D.; Murić, B.D.; Grujić, D.; Zarkov, B.; Nenadić, M.Z.; Pantelić, D.V. Rapid direct laser writing of microoptical components on a meltable biocompatible gel. *Opt. Quantum Electron.* **2022**, *54*, 361. [CrossRef]
47. Tabatabaei, S.D.; Ghiasi, F.; Gahruie, H.H.; Hosseini, S.M.H. Effect of emulsified oil droplets and glycerol content on the physicochemical properties of Persian gum-based edible films. *Polym. Test.* **2022**, *106*, 107427. [CrossRef]

48. Gahruie, H.H.; Eskandari, M.H.; Meeren, P.V.; Osseini, S.M.H. Study on hydrophobic modification of basil seed gum-based (BSG) films by octenyl succinate anhydride. *Carbohydr.Polym.* **2019**, *219*, 155–161. [CrossRef]
49. Rivero, S.; García, M.A.; Pinotti, A. Correlations between structural, barrier, thermal and mechanical properties of plasticized gelatin films. *Innov. Food Sci. Emerg. Technol.* **2010**, *11*, 369–375. [CrossRef]
50. Blanco-Pascual, N.; Fernández-Martín, F.; Montero, M.P. Effect of different protein extracts from Dosidicus gigas muscle co-products on edible films development. *Food Hydrocoll.* **2013**, *33*, 118–131. [CrossRef]
51. Siepmann, J.; Streubel, A.; Peppas, N.A. Understanding and predicting drug delivery from hydrophilic matrix tablets using the "Sequential layer" model. *Pharm. Res.* **2002**, *19*, 306–314. [CrossRef]
52. Queiroz, M.F.; Rachel, K.; Melo, T.; Sabry, D.A.; Sassaki, G.L.; Alexandre, H.; Rocha, O. Does the use of chitosan contribute to oxalate kidney stone formation. *Mar. Drugs* **2014**, *13*, 141–158. [CrossRef]
53. Farahnaky, A.; Dadfar, S.M.M.; Shahbazi, M. Physical and mechanical properties of gelatin–clay nanocomposite. *J. Food Eng.* **2014**, *122*, 78–83. [CrossRef]
54. Coates, J. Interpretation of infrared spectra, A practical approach. In *Encyclopedia of Analytical Chemistry: Applications, Theory and Instrumentation*; John Wiley & Sons, Ltd.: Hoboken, NJ, USA, 2006; pp. 1–23. [CrossRef]
55. Lin, S.-Y.; Wang, S.-L. Advances in simultaneous DSC–FTIR microspectroscopy for rapid solid-state chemicalstability studies: Some dipeptide drugs as examples. *Adv. Drug Deliv. Rev.* **2012**, *64*, 461–478. [CrossRef] [PubMed]
56. Liu, F.; Majeed, H.; Antoniou, J.; Li, Y.; Ma, Y.; Yokoyama, W.; Zhong, F. Tailoring physical properties of transglutaminase-modified gelatin films by varying drying temperature. *Food Hydrocoll.* **2016**, *58*, 20–28. [CrossRef]
57. Dai, C.A.; Chen, Y.-F.; Liu, M.-W. Thermal properties measurements of renaturated gelatin using conventional and temperature modulated differential scanning calorimetry. *Appl. Polym. Sci.* **2006**, *99*, 1795–1801. [CrossRef]
58. Mendieta-Taboada, O.; Sobral, P.J.A.; Carvalho, R.A.; Habitante, A.M.B.Q. Thermomechanical properties of biodegradable films based on blends of gelatin and poly(vinyl alcohol). *Food Hydrocoll.* **2008**, *22*, 1485–1492. [CrossRef]
59. Skopinska-Wisniewska, J.; Tuszynska, M.; Olewnik-Kruszkowska, E. Comparative Study of Gelatin Hydrogels Modified by Various Cross-Linking Agents. *Materials* **2021**, *14*, 396. [CrossRef]
60. Murić, B.; Pantelić, D.; Vasiljević, D.; Panić, B.; Jelenković, B. Thermal analysis of microlens formation on a sensitized gelatin layer. *Appl. Opt.* **2009**, *48*, 3854–3859. [CrossRef]
61. Hong, C.-C.; Choi, J.-W.; Ahn, C.H. A novel in-plane microfluidic mixer with modified Tesla structures. *Lab Chip* **2004**, *4*, 109–113. [CrossRef]
62. Tesla, N. Valvular Conduit. U.S. Patent 1329559, 3 February 1920. Available online: https://www.freepatentsonline.com/1329559.html (accessed on 12 March 2022).
63. Murić, B.D.; Panić, B.M. Microlenses with focal length controlled by chemical processes. *Phys. Scr.* **2012**, *T 149*, 14071. [CrossRef]

Journal of Luminescence 199 (2018) 285–292

Contents lists available at ScienceDirect

Journal of Luminescence

journal homepage: www.elsevier.com/locate/jlumin

Effects of temperature and pressure on luminescent properties of $Sr_2CeO_4:Eu^{3+}$ nanophosphor

A. Vlasic[a], D. Sevic[a,*], M.S. Rabasovic[a], J. Krizan[b], S. Savic-Sevic[a], M.D. Rabasovic[a], M. Mitric[c], B.P. Marinkovic[a], M.G. Nikolic[a]

[a] Institute of Physics Belgrade, University of Belgrade, P.O. Box 68, Pregrevica 118, 11080 Belgrade, Serbia
[b] AMI, d. o. o, Ptuj, Slovenia
[c] Vinca Institute of Nuclear Science, University of Belgrade, P. O. Box 522, 11001 Belgrade, Serbia

ARTICLE INFO

Keywords:
Photoluminescence
Time resolved analysis
Thermographic phosphor
High pressure sensing

ABSTRACT

In this paper we describe the synthesis and characterization of the $Sr_2CeO_4:Eu^{3+}$ nanopowder and possibilities of its application for temperature and high pressure sensing. The material was prepared using simple solution combustion synthesis. X-ray powder diffraction (XRD), scanning electron microscope (SEM) and photoluminescence (PL) techniques have been used to confirm and characterize the prepared material. Time resolved analysis of emission spectra was achieved by using the streak camera system. Measured lifetime values of luminescence emission and the intensity ratios of spectral lines were used for determining the calibration curves for remote temperature sensing. We have analyzed sensitivity improvement of the intensity ratio method by using a temporal evolution of emission lines and simulation of delayed gating of one of them. Pressure effects on optical properties of $Sr_2CeO_4:Eu^{3+}$ nanophosphor are also investigated.

1. Introduction

Thermographic phosphors are widely used in many applications [1–10]. They typically consist of a ceramic host and rare-earth dopant. These materials are structurally stable regarding various parameters, including temperature, pressure, magnetic field, electromagnetic radiation. The temperature dependency of their luminescence is used for remote temperature sensing. For obvious reasons, non contact measurements have many advantages. The luminescence lifetime is usually used for determining the temperature in a point; and the ratio of intensities of two spectral lines is often used for surface (2D) temperature measurements [3,5]. Mechanical influences on nanophosphor photoluminescence are also vastly investigated [9–13].

Strontium Cerium Oxide (Sr_2CeO_4) phosphors doped with europium ions (Eu^{3+}), $Sr_2CeO_4:Eu^{3+}$ are thoroughly investigated and several applications have been found. As pointed out in [14], emission color change in a wide range of temperatures proves a great potential of Eu3+:Sr2CeO4 nanocrystals for industrial applications, particularly in nanothermometric technology. Moreover, additional application possibilities for this material are provided by the fact that the samples with different grain sizes are characterized by various luminescence colors [14]. The possibility of application of this nanophosphor in single-color and two-color fluorescence thermometry techniques in temperature range of 303–523 K has been proposed in [15]. In [16] it was shown that the Eu^{3+} doped Sr_2CeO_4 phosphors emitting white light (by combining blue, green and red emissions) has potential applications not only in the fields of lamps and display devices under 280 nm excitation, but also in the field of LEDs under near UV (350 nm) excitation. Recently, paper considering $Sr_2CeO_4:Eu^{3+}$ as a source of anti-stokes white light generated under near infrared excitation was published [17]. Various methods of synthesis and studies of structural and luminescent characteristics of nanophosphors based on $Sr_2CeO_4:Eu^{3+}$ or nondoped Sr_2CeO_4 are reported in [14–24], and references therein.

In this study, $Sr_2CeO_4:Eu^{3+}$ nanopowders were efficiently prepared using a Solution Combustion Synthesis (SCS) method [25,26]. The main characteristics of this process are simplicity and low cost. Moreover, it is possible to tune the size and morphology of particles. The structure of prepared materials has been confirmed and characterized using X-ray powder diffraction (XRD), scanning electron microscope (SEM) and photoluminescence (PL) techniques. The excitation and emission spectra, luminescence lifetimes and rise time of synthesized nanopowders were analyzed by using the streak camera system. PL spectra were obtained at different excitation wavelengths using Optical Parametric Oscillator (OPO). Continuous excitation at 405 nm was achieved by a laser diode. The most of europium luminescence comes from slow decay transitions from the $^5D_0$ state. Lifetimes of the slow decay lines

* Corresponding author.
E-mail address: sevic@ipb.ac.rs (D. Sevic).

https://doi.org/10.1016/j.jlumin.2018.03.061
Received 20 November 2017; Received in revised form 18 March 2018; Accepted 21 March 2018
Available online 22 March 2018
0022-2313/ © 2018 Elsevier B.V. All rights reserved.

are measured and reported in many publications. However, there are not many publications providing results regarding lifetimes of fast decay transitions, or rise times of slow decay transitions [27–31] of europium. In this study, we have estimated the lifetime and the rise time of europium transitions from the $^5D_1$ and $^5D_0$ states. Beside the lifetime, the luminescence rise time measurements [32] can be used for high temperature remote thermometry [2,28,30,31] as well. However, the uncertainty of these measurements is relatively high.

In our recent publication [33] we have shown that $Sr_2CeO_4:Eu^{3+}$ made by solution combustion synthesis could be used as a red phosphor. Now we study the possibility of using the synthesized $Sr_2CeO_4:Eu^{3+}$ for temperature measurements. We analyze the temperature effects on the intensity ratio of europium lines and their photoluminescence lifetime. We estimate a possible sensitivity improvement of the intensity ratio method by using the temporal evolution of emission lines, as proposed in [3]. Pressure effects on optical properties of $Sr_2CeO_4:Eu^{3+}$ nanophosphor are also investigated and, to the best of our knowledge, firstly presented in detail here. Our research followed the approach of simultaneous analysis of temperature dependencies and mechanical influences on nanophosphor photoluminescence [9,10].

2. Experimental procedure

2.1. The preparation of samples

Europium doped Sr_2CeO_4 nanopowders were prepared by solution combustion method, similarly as described in [25,26]. Stoichiometric quantities of starting chemicals $Sr(NO_3)_2$, $5CH_4N_2O$, $Ce(NO_3)_3*6H_2O$, and $Eu(NO_3)_3*6H_2O$ with the purity of 99.99% were chosen to obtain the Eu^{3+} concentration in Sr_2CeO_4 of 2.5 at% ($Sr_{2-0.05}Eu_{0.05}CeO_4$). The used chemicals were purchased from ABCR, and urea, $(NH_2)_2CO$, from Sigma-Aldrich. The dry mixture of 10.32 g (48.75 mmol) of $Sr(NO_3)_2$, 15.015 g (250 mmol) of CH_4N_2O, 10.86 g (25 mmol) of $Ce(NO_3)_3*6H_2O$ and 0.558 g (1.25 mmol) of $Eu(NO_3)_3*6H_2O$ was combined with the mixture of 4.8 g (60 mmol) of ammonium nitrate and 3.003 g (50 mmol) of urea which were used as organic fuels. The prepared starting reagents were combusted with the flame burner at approximately 500 °C, yielding a voluminous foamy pink powder in an intensive exotermic reaction. After the solution combustion synthesis, the nanopowder was annealed for 2 h, in air atmosphere, at 900 °C. The annealing of the material is needed to achieve optimal optical characteristics of synthesized material.

2.2. Experimental details

X-ray diffraction measurements were done at room temperature using a Philips PW 1050 instrument, with Ni filtered Cu $K_{\alpha1,2}$ radiation ($\lambda = 0.15405$ nm). The structure of nanopowders was also observed by a high resolution scanning electron microscope (SEM) equipped with a high brightness Schottky Field Emission gun (FEGSEM, TESCAN) operating at 4 kV. The samples were coated with gold/palladium to make them conductive for SEM analysis.

As an excitation source for photoluminescence measurements we used the output of the Optical Parametric Oscillator (Vibrant OPO), continuously tunable over a spectral range from 320 nm to 475 nm. Laser pulse duration is about 5 ns, at a repetition rate of 10 Hz. Time-resolved streak images of the luminescence response of $Sr_2CeO_4:Eu^{3+}$ nanopowder excited by the OPO system were acquired by Hamamatsu streak camera equipped with a spectrograph.

Excitation spectrum of $Sr_2CeO_4:Eu^{3+}$ was acquired using Fluorolog SPEX. For temperature and pressure dependent measurements we also used Ocean Optics USB2000 and AVANTES AvaSpec 2048TEC USB2 spectrometers and continuous laser diode excitation at 405 nm. The experimental setup for luminescence measurement as a function of temperature is described in [34].

High pressure was achieved using Membrane Diamond Anvil Cell (MDAC) manufactured by BETSA (France), with a 300 μm culet diameter (the culet is the tiny facet at the very bottom of faceted gemstones, added to protect the fragility of the pointed tip). Principle of operation of Diamond Anvil Cell (DAC) is based on the fact that very high pressures can be obtained by reasonable mechanical forces if tips of diamond anvils have small surface area, because obtained pressure equals the ratio of mechanical force versus surface area of culet. The measured sample is placed between the tips of opposite anvils, which are tightened by mechanical force. On earlier models, the necessary mechanical force pushing the anvils to each other was obtained by tightening screw. In the case of membrane DAC used here, the force on the piston pushing the upper anvil is generated by pressurized helium, which presses a circular membrane. This solution enables fine control and adjustment of the force applied to the anvils. In order to get the uniform distribution of pressure on the sample the transmitting fluid should be used. The metal gasket is often used to prevent the leakage of this fluid. The shape of gasket is formed by pressing it between two opposed anvils of the MDAC, first without the sample. Then, the gasket with the sample, pressure transmitting fluid and a small ruby sphere is compressed by the same anvils. The diamond anvils are optically transparent, so the optical measurements of pressurized sample are possible. We used the sample in the form of powder and a 4:1 mixture of methanol and ethanol as a pressure transmitting medium. The pressure was determined from the redshift of the ruby R1 line.

3. Results and discussion

3.1. Structure

XRD pattern of our of $Sr_2CeO_4:Eu^{3+}$ nanopowder sample is shown in Fig. 1. Observed peaks are in good agreement with the published results [14–24] and ICSD card 50-0115. The XRD pattern, shown in Fig. 1, proves the good crystallinity of our sample. The lack of any significant additional peaks confirms that doping the material with Eu^{3+} did not change the crystalline structure of Sr_2CeO_4. The X-ray Line Profile Fitting Program (XFIT) with a Fundamental Parameters convolution approach to generating line profiles [35] was used for the calculation of both the crystallite size and the microstrain parameter of the synthesized powder. Three most intense peaks were included in the fitting procedure, and the obtained values for crystallite size and microstrain are 114.0 nm and 0.14%, respectively.

The representative SEM image of our sample of $Sr_2CeO_4:Eu^{3+}$ material is presented in Fig. 2. The SEM image confirms the previously calculated average size of the prepared material. The image of the

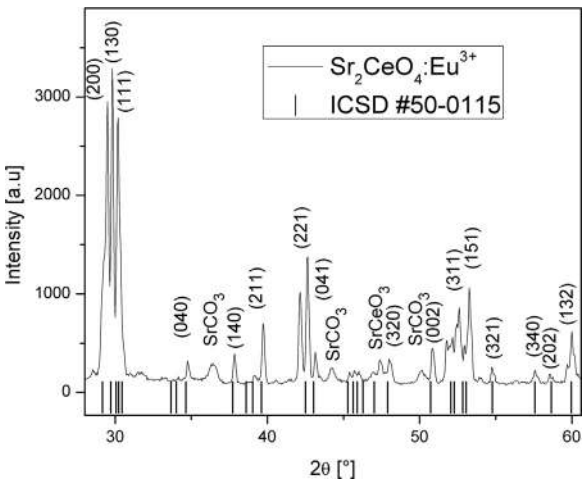

Fig. 1. XRD profile of $Sr_2CeO_4:Eu^{3+}$ nano phosphor prepared by solution combustion method, with respective Miler indices for prominent peaks.

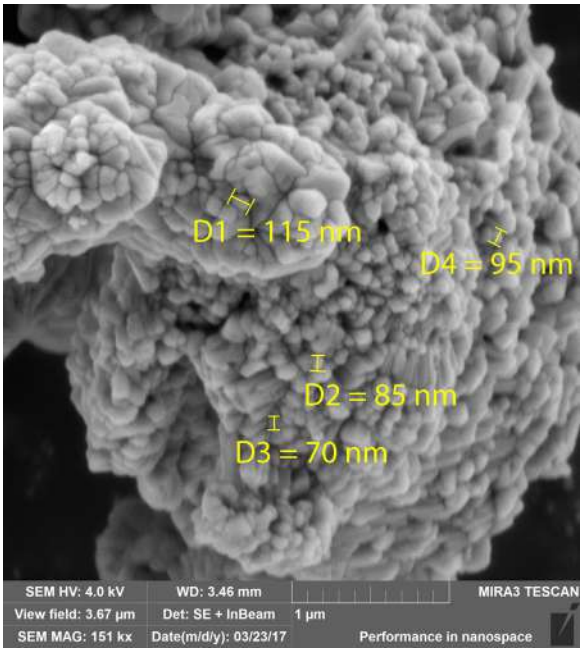

Fig. 2. SEM image of $Sr_2CeO_4:Eu^{3+}$ nano phosphor prepared by solution combustion method.

synthesized material shows the irregular crystallite size distribution. The agglomerated grains can be also noticed. The particles with dimensions from 67 nm to over 120 nm can be easily observed in Fig. 2. Effects of annealing temperatures on particle size and thus resulting overall influence on the luminescence of $Sr_2CeO_4:Eu^{3+}$ nanocrystals are studied in detail in [14,18]. It was observed that with increasing the annealing temperature the grain sizes also increase. The annealing temperature of 900 °C was chosen to obtain optimal luminescence response of synthesized material.

3.2. Optical properties

3.2.1. Luminescence excitation and emission spectra

The excitation spectrum of $Sr_2CeO_4:Eu^{3+}$ nano phosphor, corresponding to the 614 nm emission, is shown in Fig. 3. The wide band, up to about 400 nm, corresponds to a strong absorption of light by the Sr_2CeO_4 host and a charge transfer from host to Eu dopant [14–18,23]. Narrow peaks, at higher wavelengths, come from the direct excitation of europium. The peaks are denoted by corresponding europium transitions. The similar excitation spectra are presented in [14–19].

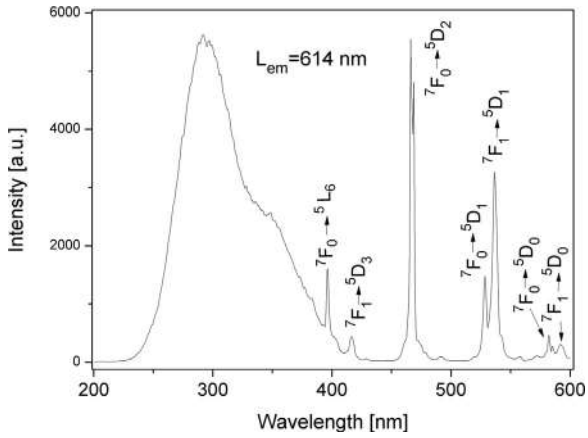

Fig. 3. Excitation spectrum of $Sr_2CeO_4:Eu^{3+}$ nano phosphor, corresponding to the 614 nm emission.

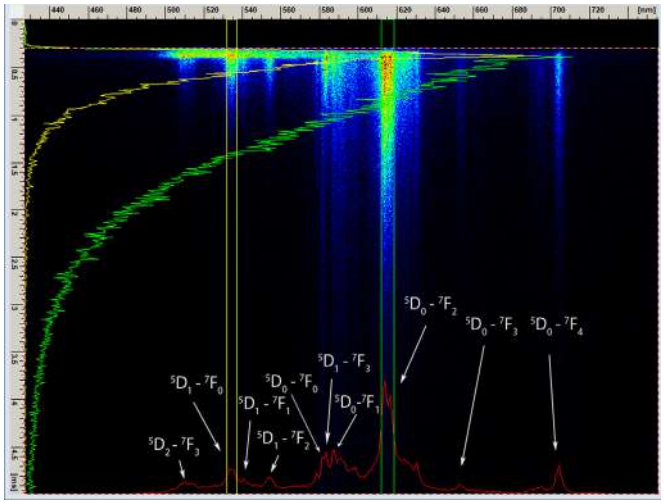

Fig. 4. Streak image of the photoluminescence spectrum of $Sr_2CeO_4:Eu^{3+}$ nanophosphor. (OPO excitation at 330 nm).

The streak image of the time resolved photoluminescence spectrum of the $Sr_2CeO_4:Eu^{3+}$ using the 330 nm excitation is presented in Fig. 4. Horizontal scale of streak image corresponds to wavelength, vertical scale shows development of spectra in time. Images are presented in pseudocolor, where different colors mean different optical intensities. The Eu transitions are denoted in Fig. 4, according to [27,36]. The slow decay transitions originating from $^5D_0$ state, are well explained in literature and their detailed description can be found in our previous work [25]. Positions of the different $^5D_0$ - ^7F_J transitions are located so that the distance between a J and the J + 1 line increases with increasing J value. Transition $^5D_0$–$^7F_1$ is very close to the $^5D_0$ - $^7F_0$ transition [36]. The weak $^5D_0$ - $^7F_0$ transition, which is forbidden by both electric-and magnetic- dipole selection rules in the case of the free ion, occurs due to a weak J mixing by the crystalline field [37]. Magnetic dipole transition like $^5D_0$–$^7F_1$ are allowed by the Laporte selection rule, but their intensities are weak and comparable to those of the induced electric dipole transitions [36]. The fast decay transitions from $^5D_2$ and $^5D_1$ are also denoted in Fig. 4. The $^5D_1$ - $^7F_3$ transition (583 nm), located closely between the $^5D_0$ - $^7F_0$ (582 nm) and the $^5D_0$ – $^7F_1$ (587 nm) transitions is easy to identify on the time resolved image. Its time integrated peak has a comparable intensity to the intensities of peaks originating from nearby $^5D_0$ levels (see the line profile denoted by a red curve in Fig. 4). The luminescence spectra presented in publications usually do not have the time resolution, so it is hard to guess which transitions are short lived. Streak image presented in Fig. 4. shows clearly that the $^5D_1$ - $^7F_3$ transition has a much higher intensity and a much shorter lifetime than nearby transitions from $^5D_0$ state.

3.2.2. Lifetime and rise time analysis

We conducted the time resolved analysis for transitions which are identified in Fig. 4. The streak image of photoluminescence spectrum of $Sr_2CeO_4:Eu^{3+}$ nanophosphor with the time range of 200 µs is shown in Fig. 5. The time range in Fig. 5. was selected to get a clear visual impression of time development of luminescence signals at their beginning and to enable a rough estimate of rise time of all transitions shown in Fig. 4. To obtain the more precise values of rise time we had to use streak camera time range of 5 µs.

We obtained that the lifetime of the level $^5D_1$ is about 0.21 ms and the level $^5D_0$ lifetime is about 0.78 ms. For the fast decay the lifetime is much longer than reported for other hosts in [27,32], where transitions from $^5D_1$ level have a fast decay with the order of lifetime of about 10 µs. Other references [14,20,33] provide the values of slow decay time of $Sr_2CeO_4:Eu^{3+}$ nanophosphor more or less similar to our result. Decay curve of the most intensive $^5D_0$ – $^7F_2$ transition is usually used for

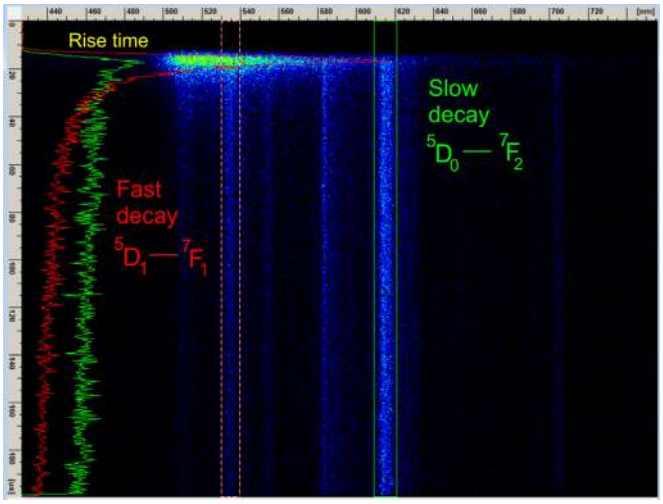

Fig. 5. Streak image of photoluminescence spectrum of $Sr_2CeO_4:Eu^{3+}$ nanophosphor with the time range of 200 μs tuned for analysis of rise time of all transitions. (OPO excitation at 330 nm.).

europium luminescence lifetime measurements [26].

In [32] we have proved that our experimental setup is capable of detecting fast rise times. We calculate the rise time according to Ranson equation [38,39]. $YVO_4:Eu^{3+}$ nanoposphor has clearly detectable rise time of slow decay transitions [32], for the $^5D_0$ – $^7F_2$ line it is about 8.1 μs. This relatively long luminescence rise time is related to energy transfer mechanism in $YVO_4:Eu^{3+}$ nanoposphor and it is useful for practical considerations. Our measurements of $Sr_2CeO_4:Eu^{3+}$ nanophosphor show that the luminescence rise time of $^5D_0$ - $^7F_2$ line of 0.39 μs is too short to be of practical use if cost effective equipment is to be used. So, it seems to us that for temperature sensing based on photoluminescence rise time measurements the other europium doped hosts, for example Yttrium orthovanadate $YVO_4:Eu^{3+}$, would be more appropriate.

3.2.3. The temperature dependency of intensity ratio of spectral lines

The luminescence of samples was measured both using pulsed (OPO) and continuous excitation. The measured luminescence spectra of Eu^{3+} doped Sr_2CeO_4 at various temperatures are presented in Fig. 6.

The spectral line intensities from the $^5D_0$ and $^5D_1$ transitions depend on two physical processes. The first process is the thermalization of the $^5D_1$ level with rising temperature, where the energy difference to populate the $^5D_1$ level from the $^5D_0$ level is fully covered by phonons. The second process is nonradiative quenching of the $^5D_0$ and $^5D_1$ levels through the charge transfer state. Configuration coordinate model,

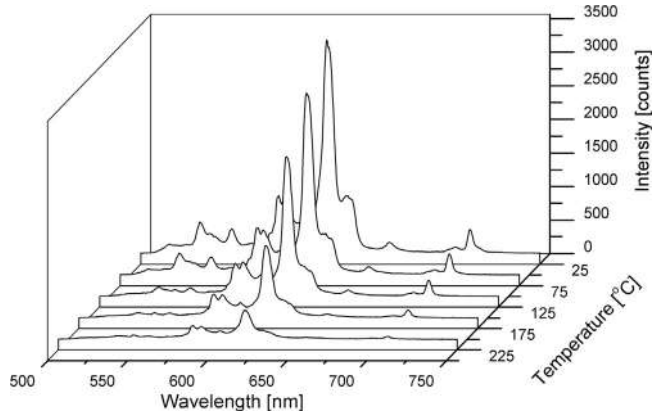

Fig. 6. Luminescence spectra of Eu^{3+} doped Sr_2CeO_4 at various temperatures. (Continuous laser diode excitation at 405 nm).

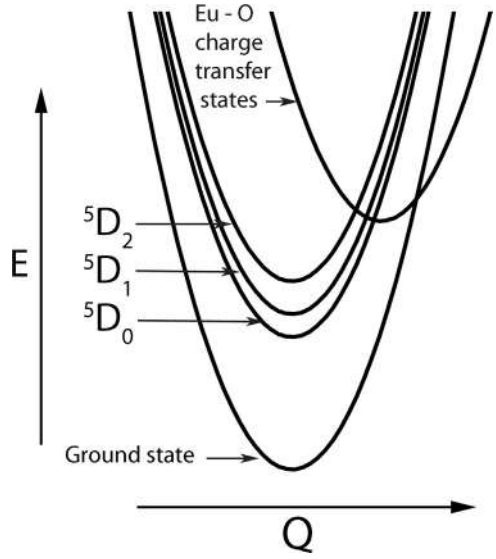

Fig. 7. Configuration coordinate model of $Sr_2CeO_4:Eu^{3+}$ nanophosphor relevant for understanding the temperature dependency of intensity ratio of spectral lines.

based on the same line of thought as presented in [15], is shown in Fig. 7. The Eu^{3+} - O_2 charge transfer state intersects not only with the europium ground state but also with three excited states, $^5D_2$, $^5D_1$ and $^5D_0$. By increasing the sample temperature the electrons in the $^5D_0$ state are thermally pushed to the crossover point and nonradiatively go to the ground state via the charge transfer state. Regarding the $^5D_1$ state, part of electrons go the same path as described for $^5D_0$ state. However, part of them go only to the $^5D_0$ level via charge transfer state. This explains why is $^5D_1$ state more rapidly quenched by temperature than $^5D_0$ state. So, the thermalization and quenching through charge transfer both have significant influence on the fluorescence intensity ratio (FIR). This means that the measured results cannot be simply fitted to the Boltzmann distribution. However, in order to apply the intensity ratio method in thermometry, it is required to calculate and fit a calibration function of analyzed potential thermophosphor. Based on considerations in [34,40], we decided to use the simple empirical equation for fitting the calculated intensity ratios of experimental data: $IR(T) = A + C \cdot e^{-T/\alpha}$, [34,40], where T is temperature in K, and empirical A, C and α are constants obtained through fitting of measured data.

The absolute thermal sensitivity Sa of the intensity ratio method is defined as the rate at which IR changes with the temperature:

$$Sa = \left| \frac{dIR}{dT} \right| \tag{1}$$

The relative thermal sensitivity of the intensity ratio method Sr is determined using formula:

$$Sr = \left| \frac{1}{IR} \frac{dIR}{dT} \right| \tag{2}$$

The temperature sensing calibration curve, shown in Fig. 8, was determined by calculating intensity ratio of photoluminescence spectral peaks at 614 nm and 537 nm. The calculation was repeated for all spectra, measured at different temperatures, first for increasing, then for decreasing temperatures. This kind of temperature sensing is useful up to 400 K, where the calculated intensity ratio values stop increasing and curve flattens beyond reasonable fitting.

3.2.4. Improved sensitivity of intensity ratio method based on temporal analysis

As proposed in [3], it is possible to improve the sensitivity of the intensity ratio method by using the temporal evolution of emission

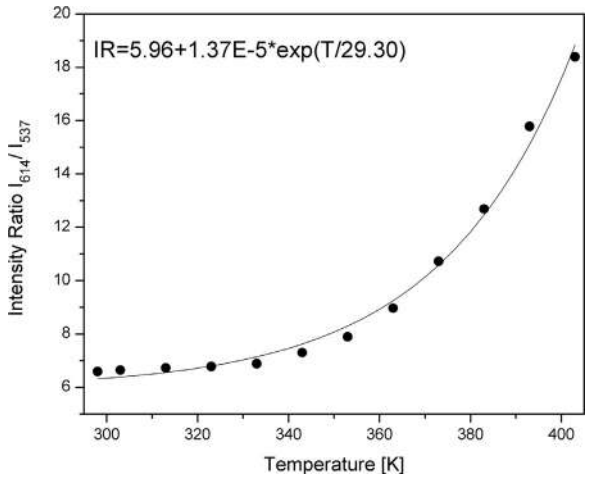

Fig. 8. Temperature sensing calibration curve of $Sr_2CeO_4:Eu^{3+}$ nanophosphor. (Continuous laser diode excitation at 405 nm).

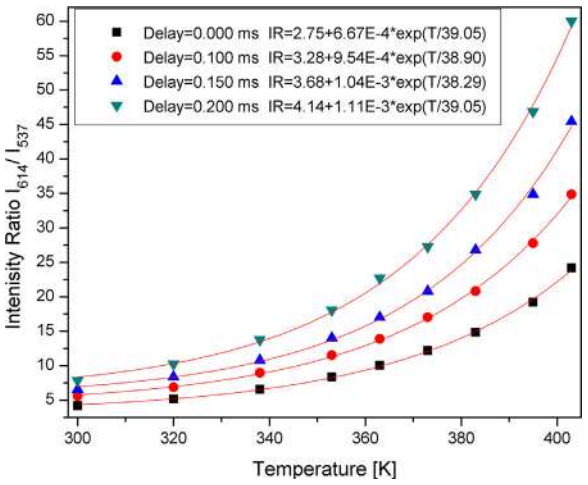

Fig. 10. Temperature sensing calibration curves of $Sr_2CeO_4:Eu^{3+}$ nanophosphor, for various delays of gating the signal at 537 nm. (Pulsed laser excitation at 330 nm).

lines. If integrated-in-time intensity of one of the signals is recorded with delayed gate, the additional temperature dependence is introduced in intensity ratio calculation. Namely, at low temperatures where emission lifetime is long the small gate delay of one of the signals will have relatively small effect on intensity ratio. However, at higher temperatures where the lifetime is short, the delayed gate will give rise to an increased signal difference. Moreover, this method of recording the signal with gated delay offers an efficient solution for minimizing or eliminating the effects of host luminescence, overlapping of emission from thermally coupled levels, and stray light originating from other intense transitions or from the laser excitation.

The method is illustrated in Fig. 9. The use of streak camera proves the concept, real application will be based on gated CCD cameras and appropriate bandwidth filters for selecting the emission lines. For calculation of intensity ratio the line at 614 nm is used integrated in time from its beginning, and line at 537 nm is integrated in time with various delays.

Temperature sensing calibration curves of $Sr_2CeO_4:Eu^{3+}$ nanophosphor for various delays of gating the signal at 537 nm are shown in Fig. 10.

It could be seen in Fig. 10 that intensity ratio between lines at 614 nm and 537 nm increases with increasing the gate delay of signal at 537 nm. However, increasing the delay decreases the integrated signal intensity, so we didn't use delays larger than 200 μs. The host luminescence and other emission not belonging to europium lines at 537 nm and 614 nm spoil the temperature sensitivity. However, they last up to 100 μs, so their influence is eliminated for delays higher than 100 μs. Absolute and relative temperature sensitivities of $Sr_2CeO_4:Eu^{3+}$ nanophosphor are shown in Fig. 11. Increased sensitivity obtained by delayed gate of 537 nm emission is obvious from Fig. 11. It should be pointed out that continuous laser excitation at 405 nm pumps mainly the europium directly, resulting with much better elimination of host emission. However, the emission is generally weaker when europium is excited directly.

We have shown that continuous laser excitation provides satisfactory results. Increased sensitivity could be obtained by much more complex measurements technique presented here.

3.2.5. *Luminescence lifetime temperature dependency*

The temperature sensing calibration curve, shown in Fig. 12, was determined by calculating lifetime of spectral line at 614 nm. When the temperature was increased higher than 200 °C the intensity of measured spectra become too low to achieve reliable calculation of luminescence lifetime. Analysis presented in [41] shows that the temperature dependence of intensity ratio and luminescence lifetime, for the ideal

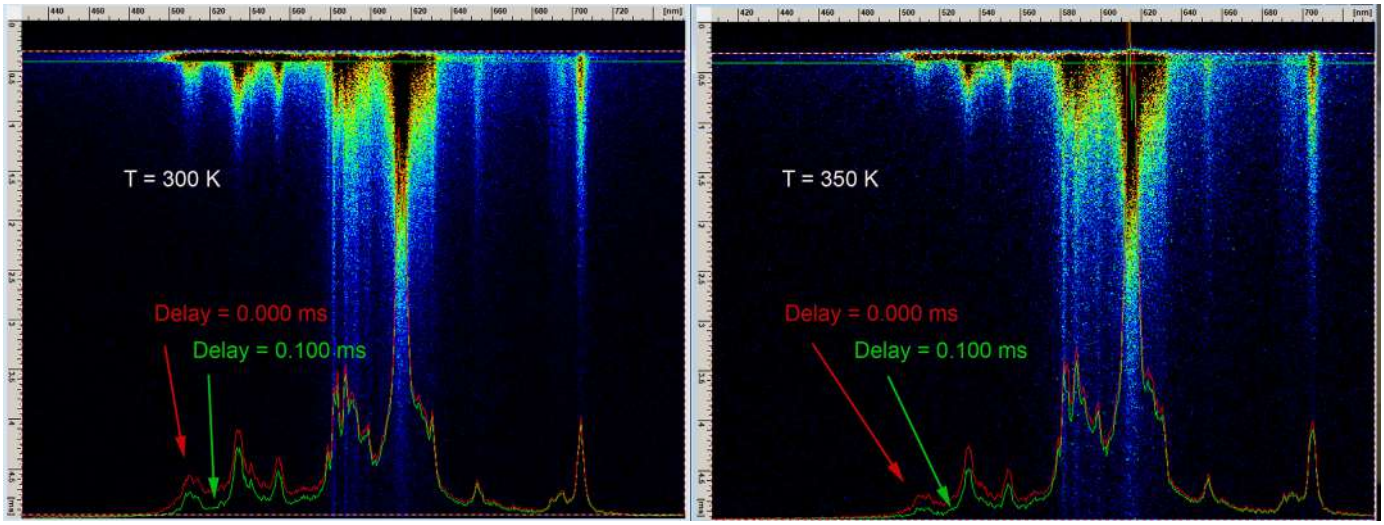

Fig. 9. Streak images of optical emission of $Sr_2CeO_4:Eu^{3+}$ at room temperature (left) and at 80 °C (right). Pulsed laser excitation is at 330 nm. The red profile corresponds to time integration of the whole signal, the green one to integration gated after 100 μs delay.

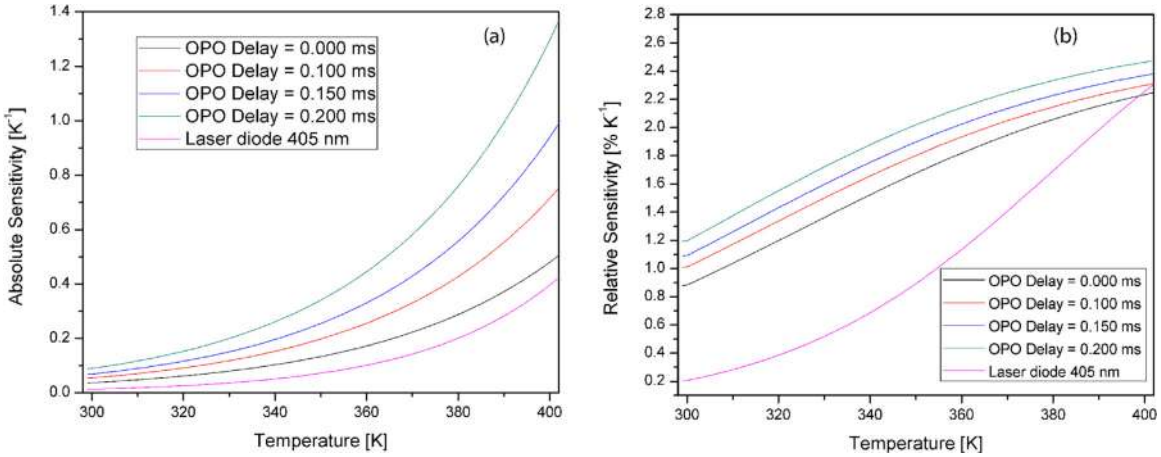

Fig. 11. (a) Absolute and (b) relative sensitivity of $Sr_2CeO_4:Eu^{3+}$ nanophosphor as a function of temperature.

case, differ only in magnitude by a certain factor. So, we will use the same form of empirical equation for fitting the lifetime experimental data as we used for fitting the intensity ratio, namely: $F(T) = A + C \cdot e^{-T/\alpha}$, [34,40], where T is temperature in K, and A, C and α empirical constants obtained through fitting of measured data.

In [42] europium hosted in PMMA matrix was used for lifetime based temperature sensing, in a range between 0 and 70 °C, with reported lifetimes between 0.28 ms and 0.4 ms. Temperature sensitive europium probes, excited at 405 nm, are described in [43], where reported lifetimes are in the range between 0.15 ms and 0.7 ms, corresponding to the same temperature sensing range as in [42], between 0 and 70 °C. In [44] the sensed temperature range is between 10 and 50 °C, measured lifetimes are between 0.12 ms and 0.35 ms. It seems that europium, hosted in another medium like PMMA, provides lesser sensing range with better sensitivity. Compared to our results of intensity ratio method, the luminescence lifetime method offers increased sensing range, because only the most intensive europium line at 614 nm is used for temperature sensing calibration curve determination. The intensity ratio calculations become unreliable when the intensity of the line at 537 nm turned out to be too small due to temperature increasing. Our measurements show that sensor based on $Sr_2CeO_4:Eu^{3+}$ nano phosphor covers not only the physiological temperature range but also the higher temperatures that are of interest when monitoring the thermal behaviour of electronic devices. Compared to other hosts doped with europium, TiO_2 [41], Gd_2O_3 [45], $YNbO_4$, [46] and Lu_2O_3 [47], including references therein, it is easy to notice that there is usual trade-off between the sensitivity and sensing range, so the optimal host could be selected based on desired sensing range.

Methods for temperature sensing based on fluorescence intensity ratio and lifetime are not sensitive, regarding errors, to fluctuations in excitation intensity and light collection efficiency [3]. Moreover, if the lifetime of the used nanophosphor (measured here between 0.2 ms and 0.78 ms) is much longer than the laser pulse (5 ns), evaluation error could be neglected [3]. So, we conclude that measurement errors mostly originate from the fitting procedures and least-square errors in extracting the temperatures from the calibration curve [3]. For all presented methods, the relative errors are smaller than 3% in the whole measuring range and bellow 1% for temperatures above 350 K.

3.2.6. *The high pressure effects on $Sr_2CeO_4:Eu^{3+}$ photoluminescence*

The spectral responses were measured at various pressures in order to analyze the high pressure effects on photoluminescence emission of $Sr_2CeO_4:Eu^{3+}$ nanophosphor. Luminescence spectra of Eu^{3+} doped Sr_2CeO_4 at various pressures are shown in Fig. 13. To check the existence of hysteresis, the spectral measurements were performed successively, first for increasing and then for decreasing pressure.

It is well known that rare earth ions are highly sensitive to local symmetry. Any change in the symmetry is observable in their luminescence spectra [48]. In the paper by Zhang et al. [49] dependencies between the phase transitions of the crystal structure induced by pressure and the changes in the luminescence spectrum of the Eu^{3+} ion are explained. It was shown in [49] that the red shift rate and relative intensity ratio of emissions vary along with increasing pressure. Namely, the red shift of emissions can be ascribed to the expansion of the f orbit of the Eu^{3+}; and the relative intensity ratio variation of emissions is attributed to the change of crystal field due to the phase

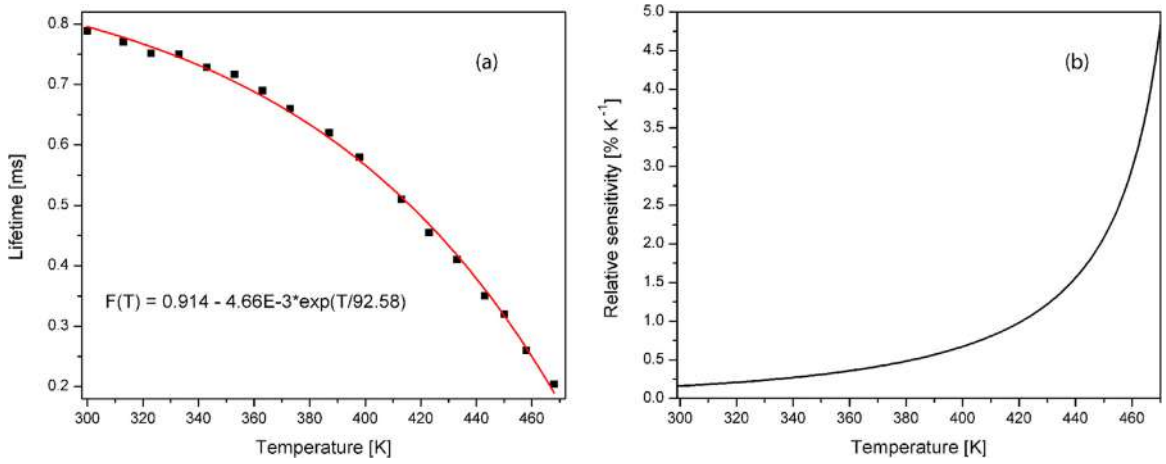

Fig. 12. Luminescence lifetime temperature dependence of $Sr_2CeO_4:Eu^{3+}$ nano phosphor and its relative sensitivity.

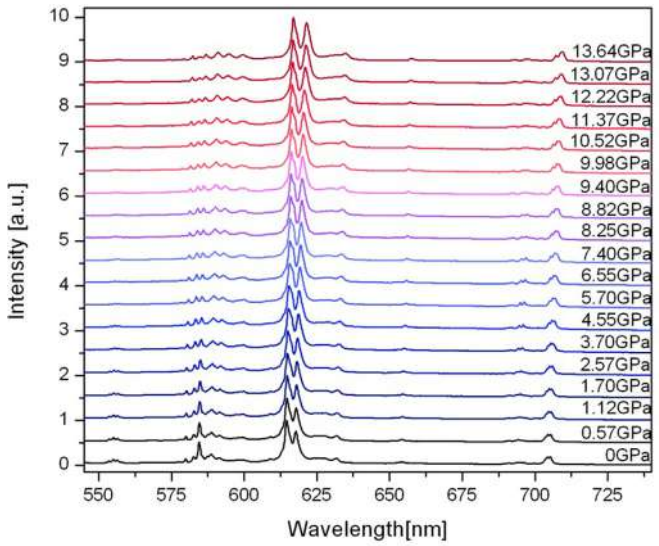

Fig. 13. Luminescence spectra of Eu^{3+} doped Sr_2CeO_4 at various pressures. (Continuous laser diode excitation at 405 nm).

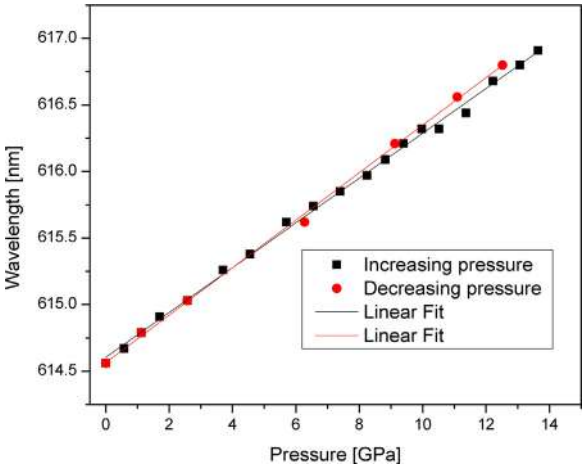

Fig. 15. Pressure induced shift in wavelength of the highest intensity peak, at 614.56 nm at atmospheric pressure.

transition.

Changes and deformations of luminescence spectrum which imply phase transitions are easily identified in Fig. 3 in [49]. Fig. 13. shows that, in presented pressure range, there are no such deformations of Sr_2CeO_4:Eu^{3+} luminescence spectrum. This means that our sample didn't undergo the phase transition.

Our measurements show that after decompression the luminescence spectrum of Sr_2CeO_4:Eu^{3+} is completely restored. Other publications show similar results for different host matrixes [13,50].

Pressure induced change in the crystal lattice parameters also disturb the position of energy levels [11–13,49–51]. The variation of

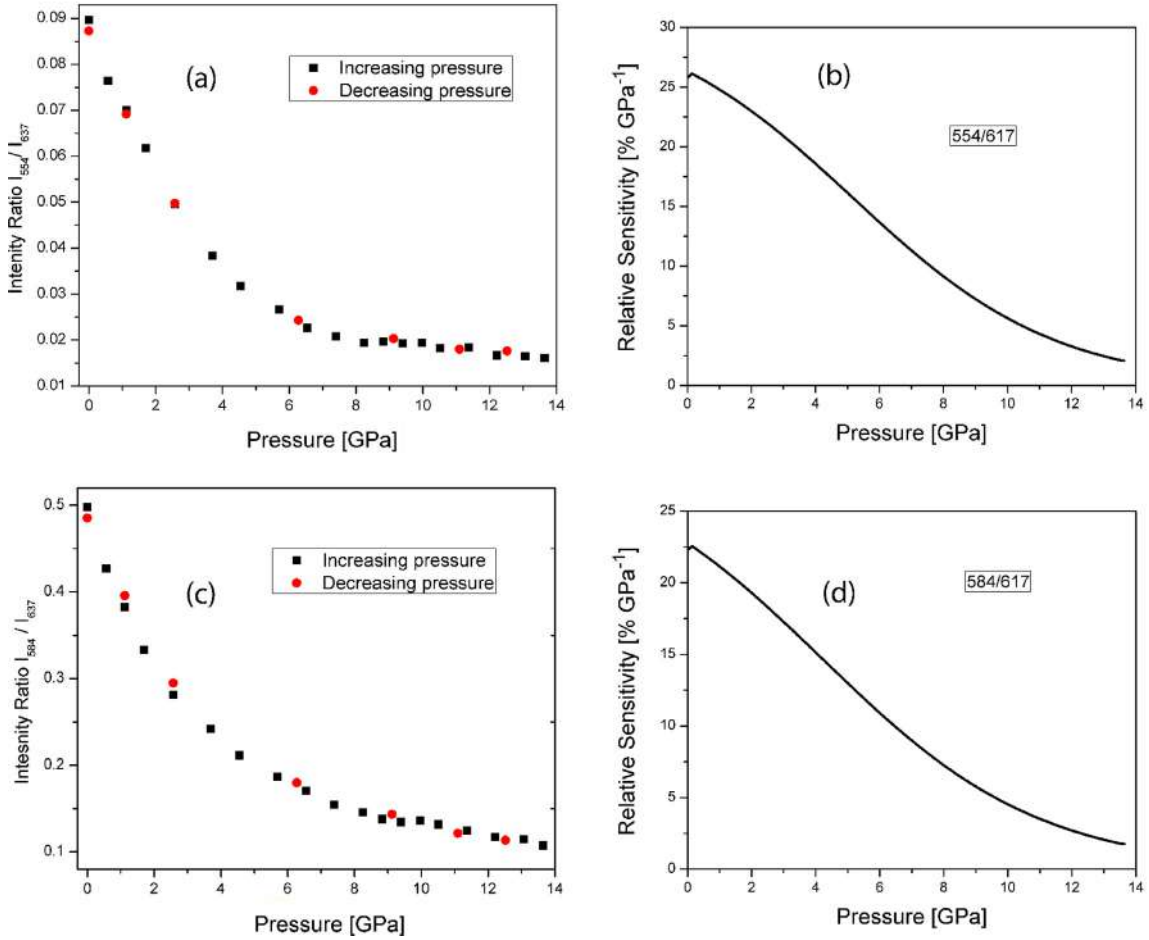

Fig. 14. High pressure sensing calibration curves of Sr_2CeO_4:Eu^{3+} nanophosphor. (a) Intensity ratio I_{554}/I_{614}. (b) Its relative sensitivity. (c) Intensity ratio I_{584}/I_{614}. (d) Its relative sensitivity. (Continuous laser diode excitation at 405 nm.).

energy of $^5D_1$ and $^5D_0$ levels and change of charge transfer region position leads to a rise in probability for non-radiative transitions. The applied pressure predominantly affects $^5D_1$ level, as can be seen in Fig. 13. A slight variation in the intensity of the most prominent $^5D_0 \rightarrow {}^7F_2$ transition lines can also be observed in Fig. 13. The intensity ratios of intensities of emission lines from $^5D_1$ and $^5D_0$ states are shown in Fig. 14. Exact positions of luminescence peaks used for calculating the intensity ratios are at 554.2 nm, 584.52 nm and 617 nm at atmospheric pressure. The observed decrease of intensity ratio with rising pressure is also due to greater dependence of non-radiative transitions from $^5D_1$ state. The values for both compression and decompression of sample are displayed in the Fig. 14. The hysteresis is negligible, which means the repeatability is good. For intensity ratio of lines at 584 nm and 637 nm, the reliable part of curve is from 0 GPa up to 10 GPa (for intensity ratio of lines at 554 nm and 637 nm the reliable part of curve is up to 8 GPa), which opens the possibility for using the material as a pressure sensor.

Another method of sensing pressure is based on measuring the pressure induced red shift in wavelength of appropriately selected, usually highest intensity peak. Pressure induced shift in wavelength of the highest intensity peak of Sr_2CeO_4:Eu^{3+} luminescence (614.56 nm at atmospheric pressure) is shown in Fig. 15. The proposed method is very usable, with almost linear curve, for high pressures up to 14 GPa. Red-shift rate was estimated to be about 0.17 nm × GPa^{-1}. The rate is the same for other emission lines from $^5D_0$ state, and for $^5D_0 \rightarrow {}^7F_1$ it is about 0.096 nm × GPa^{-1}.

To the best of our knowledge, there are no published results regarding using of Sr_2CeO_4:Eu^{3+} nanophosphor for pressure sensing. Compared to the other materials doped with the Eu^{3+} ions, Sr_2CeO_4 provides similar pressure sensing range in terms of unambiguousness as $ZrGeO_4$ [11], $LaPO_4$ [12], $GdVO_4$ [13] and TiO_2 [50]. Y_2O_3 host offers much wider unambiguous pressure sensing range [49]. Under unambiguous we mean the fact that one luminescence intensity ratio corresponds to only one pressure. So, it seems that Sr_2CeO_4 is quite promising for making devices for remote pressure sensing.

To estimate errors of pressure sensing in our study the similar line of thought holds as for temperature sensing methods. For intensity ratio method relative errors are smaller than 8% in pressure range up to 10 GPa. For method of sensing pressure based on measuring the pressure induced red shift in wavelength of highest intensity peak the relative error is below 2% for the whole measured range (up to 14 GPa).

4. Conclusion

In this paper we described the synthesis and characterization of the Sr_2CeO_4:Eu^{3+} nanopowder. Beside luminescence kinetics of slow decay transitions we also estimated their rise time and lifetime of fast decay transitions. Measured values of lifetime of luminescence emission of lines originating from transitions from $^5D_0$ level and intensity ratios of two spectral lines were used for determining the calibration curves for remote temperature sensing. We have showed that, for analyzed Sr_2CeO_4:Eu^{3+} material, the temperature sensing based on ratio of intensities of two lines is useful up to 400 K, while sensing based on lifetime of spectral line at 614 nm could be used up to 460 K. We have obtained sensitivity improvement of the intensity ratio method by simulating the delayed gating of acquiring the intensity of one of spectral lines. The using of streak camera proved the proposed concept. The real application will be based on gated cameras and appropriate bandwidth filters for selecting the emission lines. Also, we have analyzed the effects of pressure on photoluminescence response of synthesized material. To the best of our knowledge, this analysis is first presented here. Results of all our analyses prove that Sr_2CeO_4:Eu^{3+} nanopowder prepared by a simple and low cost solution combustion synthesis method is appropriate material for remote temperature and pressure sensing and for various other optoelectronic devices.

Acknowledgement

This work was financially supported within the Projects of Ministry of Education, Science and Technological Development of the Republic of Serbia OI171020, ON171038 and III45016.

References

[1] D. Jaque, F. Vetrone, Nanoscale 4 (2012) 4301–4326.
[2] C.D.S. Brites, P.P. Lima, N.J.O. Silva, A. Millan, V.S. Amaral, F. Palacio, L.D. Carlos, Nanoscale 4 (2012) 4799–4829.
[3] M. Aldén, A. Omrane, M. Richter, G. Särner, Prog. Energy Combust. Sci. 37 (2011) 422–461.
[4] S.W. Allison, G.T. Gillies, Rev. Sci. Instrum. 68 (1997) 2615–2650.
[5] L.P. Goss LP, A.A. Smith, M.E. Post ME, Rev. Sci. Instrum. 60 (1989) 3702–3706.
[6] A.L. Heyes, J. Lumin. 129 (2009) 2004–2009.
[7] M.M. Gentleman, D.R. Clarke, Surf. Coat. Technol. 188–189 (2004) 93–100.
[8] A.H. Khalid, K. Kontis, Sensors 8 (2008) 5673–5744.
[9] S.A. Wade, S.F. Collins, G.W. Baxter, J. Appl. Phys. 94 (2003) 4743–4756.
[10] S.A. Wade, D.I. Forsyth, K.T.V. Grattan, Rev. Sci. Instrum. 72 (2001) 3186–3190.
[11] R. Rao, T. Sakuntala, S.N. Achary, A.K. Tyagi, J. Appl. Phys. 106 (2009) (123517-1-5).
[12] Z. Zhi, Z. Jian, D. Zejun, J. Rare Earths 28 (2010) 254–257.
[13] C.C. Zhang, Z.M. Zhang, R.C. Dai, Z.P. Wang, J.W. Zhang, Z.J. Ding, J. Phys. Chem. C 114 (2010) 18279–18282.
[14] M. Stefanski, L. Marciniak, D. Hreniak, W. Strek, Mater. Res. Bull. 76 (2016) 133–139.
[15] L. Shi, H. Zhang, C. Li, Q. Su, RSC Adv. 1 (2011) 298–304.
[16] K. Suresh, N.V. Poornachandra Rao, K.V.R. Murthy, Bull. Mater. Sci. 37 (2014) 1191–1195.
[17] M. Stefanski, M. Lukaszewicz, D. Hreniak, W. Strek, J. Chem. Phys. 146 (2017) (104705-1-7).
[18] M. Stefanski, L. Marciniak, D. Hreniak, W. Strek, J. Chem. Phys. 142 (2015) (184701-1-7).
[19] X. Yang, Z. Shao, H. Ru, J Mater. Sci. Technol. 32 (2016) 1066–1070.
[20] T. Grzyb, A. Szczeszak, J. Rozowska, J. Legendziewicz, S. Lis, J. Phys. Chem. C 116 (2012) 3219–3226.
[21] C.A. Rao, P. Rao, V. Nannapaneni, K.V.R. Murthy, Adv. Mater. Lett. 4 (2013) 207–212.
[22] B.W.R. Kumar, K.V.R. Murthy, B.S. Rao, M. Shaik, Int. J. Sci. Innov. Discov. 1 (2011) 145–150.
[23] C.A. Rao, P.R.V. Nannapaneni, K.V.R. Murthy, J. Sci. Res. 5 (2013) 1–11.
[24] J. Gomes, A.M. Pires, O.A. Serra, Quim. Nova 27 (2004) 706–708.
[25] M.S. Rabasovic, D. Sevic, J. Krizan, M. Terzic, J. Mozina, B.P. Marinkovic, S. Savic Sevic, M. Mitric, M.D. Rabasovic, N. Romcevic, J. Alloy. Compd. 622 (2015) 292–295.
[26] J. Krizan, M. Mazaj, V. Kaucic, I. Bajsic, J. Mozina, Acta Chim. Slov. 61 (2014) 608–614.
[27] M.D. Chambers, P.A. Rousseve, D.R. Clarke, J. Lumin. 129 (2009) 263–269.
[28] S.W. Allison, S.M. Goedeke, M.R. Cates, W.A. Hollerman, J.I. Eldridge, T.J. Bencic, Oak Ridge National Laboratory Report No 123055, 2005. (Published through SciTech Connect, 03/24/2005).
[29] X. Li, X. Wei, Y. Qin, Y. Chen, C. Duan, M. Yin, J. Alloy. Compd. 657 (2016) 353–357.
[30] J.R. Darwent, C.D. Flint, P.J. O'Grady, Chem. Phys. Lett. 127 (1986) 547–550.
[31] A.H. Khalid, K. Kontis, Meas. Sci. Technol. 20 (2009) (025305-1-9).
[32] D. Sevic, M.S. Rabasovic, J. Krizan, S. Savic-Sevic, M. Mitric, M. Gilic, B. Hadzic, N. Romcevic, Mater. Res. Bull. 88 (2017) 121–126.
[33] M.S. Rabasovic, J. Krizan, P. Gregorcic, M.D. Rabasovic, N. Romcevic, D. Sevic, Opt. Quantum Electron. 48 (2016) 163.
[34] M.D. Rabasovic, B.D. Muric, V. Celebonovic, M. Mitric, B.M. Jelenkovic, M.G. Nikolic, J. Phys. D: Appl. Phys. 49 (2016) (485104-1-6).
[35] R.W. Cheary, A. Coelho, A fundamental parameters approach to X-ray line-profile fitting, J. Appl. Crystallogr. 25 (1992) 109–121.
[36] K. Binnemans, Coord. Chem. Rev. 295 (2015) 1–45.
[37] Y. Dwivedi, S.C. Zilio, Opt. Express 21 (2013) 4717–4727.
[38] S.W. Allison, S.M. Goedeke, M.R. Cates, W.A. Hollerman, J.I. Eldridge, T.J. Bencic, Oak Ridge National Laboratory Report No 123055, 2005. (Published through SciTech Connect, 03/24/2005).
[39] R.M. Ranson, E. Evangelou, C.B. Thomas, Appl. Phys. Lett. 72 (1998) 2663–2664.
[40] D. Ananias, C.D.S. Brites, L.D. Carlos, J. Rocha, Eur. J. Inorg. Chem. 2016 (2016) 1967–1971.
[41] M.G. Nikolic, Z. Antic, S. Culubrk, J.M. Nedeljkovic, M.D. Dramicanin, Sens. Actuators B 201 (2014) 46–50.
[42] J. Yu, L. Sun, H. Peng, M.I.J. Stich, J. Mater. Chem. 20 (2010) 6975–6981.
[43] S.M. Borisov, O.S. Wolfbeis, Anal. Chem. 78 (2006) 5094–5101.
[44] H.S. Peng, M.I.J. Stich, J.B. Yu, L.N. Sun, L.H. Fischer, O.S. Wolfbeis, Adv. Mater. 22 (2010) 716–719.
[45] M.G. Nikolic, A.Z. Al-Juboori, V. Đordjevic, M.D. Dramicanin, Phys. Scr. T157 (2013) (014056-1-5).
[46] Lj.R. Đačanin, M.D. Dramicanin, S.R. Lukic-Petrovic, D.M. Petrovic, M.G. Nikolic, Radiat. Meas. 56 (2013) 143–146.
[47] V. Lojpur, Z. Antic, R. Krsmanovic, M. Medic, M.G. Nikolic, M.D. Dramicanin, J. Serb. Chem. Soc. 77 (2012) 1735–1746.
[48] G. Blasse, B.C. Grabmaier, Luminescent Materials, Springer Verlag, Berlin, 1994.
[49] J. Zhang, H. Cui, P. Zhu, C. Ma, X. Wu, H. Zhu, Y. Ma, Q. Cui, J. Appl. Phys. 115 (2014) 023502.
[50] Z. Zhao, Q.G. Zeng, Z.M. Zhang, Z.J. Ding, J. Lumin. 122–123 (2007) 862–865.
[51] S. Surendra Babu, P. Babu, C.K. Jayasankar, Th Troster, W. Sievers, G. Wortmann, J. Phys.: Condens. Matter 18 (2006) 1927–1938.

AIP | Journal of Applied Physics

Femtosecond laser induced periodic surface structures on multi-layer graphene

Angela Beltaos, Aleksander G. Kovačević, Aleksandar Matković, Uroš Ralević, Svetlana Savić-Šević, Djordje Jovanović, Branislav M. Jelenković, and Radoš Gajić

Citation: Journal of Applied Physics **116**, 204306 (2014); doi: 10.1063/1.4902950
View online: http://dx.doi.org/10.1063/1.4902950
View Table of Contents: http://scitation.aip.org/content/aip/journal/jap/116/20?ver=pdfcov
Published by the AIP Publishing

Articles you may be interested in

Polarization dependent formation of femtosecond laser-induced periodic surface structures near stepped features
Appl. Phys. Lett. **104**, 231117 (2014); 10.1063/1.4882998

Surface plasmon polariton model of high-spatial frequency laser-induced periodic surface structure generation in silicon
J. Appl. Phys. **111**, 124315 (2012); 10.1063/1.4730381

On the role of surface plasmon polaritons in the formation of laser-induced periodic surface structures upon irradiation of silicon by femtosecond-laser pulses
J. Appl. Phys. **106**, 104910 (2009); 10.1063/1.3261734

Periodic ordering of random surface nanostructures induced by femtosecond laser pulses on metals
J. Appl. Phys. **101**, 034903 (2007); 10.1063/1.2432288

Formation of extraordinarily uniform periodic structures on metals induced by femtosecond laser pulses
J. Appl. Phys. **100**, 023511 (2006); 10.1063/1.2214464

[This article is copyrighted as indicated in the article. Reuse of AIP content is subject to the terms at: http://scitation.aip.org/termsconditions. Downloaded to] IP: 35.8.11.2 On: Fri, 26 Dec 2014 23:32:36

Femtosecond laser induced periodic surface structures on multi-layer graphene

Angela Beltaos,[a] Aleksander G. Kovačević, Aleksandar Matković, Uroš Ralević, Svetlana Savić-Šević, Djordje Jovanović, Branislav M. Jelenković, and Radoš Gajić
Institute of Physics, University of Belgrade, Pregrevica 118, 11080 Belgrade, Serbia

(Received 29 July 2014; accepted 18 November 2014; published online 26 November 2014)

In this work, we present an observation of laser induced periodic surface structures (LIPSS) on graphene. LIPSS on other materials have been observed for nearly 50 years, but until now, not on graphene. Our findings for LIPSS on multi-layer graphene were consistent with previous reports of LIPSS on other materials, thus classifying them as high spatial frequency LIPSS. LIPSS on multi-layer graphene were generated in an air environment by a linearly polarized femtosecond laser with excitation wavelength λ of 840 nm, pulse duration τ of ~150 fs, and a fluence F of ~4.3–4.4 mJ/cm^2. The observed LIPSS were perpendicular to the laser polarization and had dimensions of width w of ~30–40 nm and length l of ~0.5–1.5 μm, and spatial periods Λ of ~70–100 nm (~λ/8–λ/12), amongst the smallest of spatial periods reported for LIPSS on other materials. The spatial period and width of the LIPSS were shown to decrease for an increased number of laser shots. The experimental results support the leading theory behind high spatial frequency LIPSS formation, implying the involvement of surface plasmon polaritons. This work demonstrates a new way to pattern multi-layer graphene in a controllable manner, promising for a variety of emerging graphene/LIPSS applications. © *2014 AIP Publishing LLC*. [http://dx.doi.org/10.1063/1.4902950]

I. INTRODUCTION AND BACKGROUND

Graphene, a two-dimensional crystal of carbon atoms in a hexagonal lattice, has been attracting much attention in the research community since its discovery in 2004[1] as a unique new material with outstanding electronic,[2] optical,[3] and mechanical[4] properties. Being an ultra-thin, strong, transparent, flexible conductor, graphene has excellent potential for a wide variety of applications, such as solar cells.[5,6] In addition to single-layer graphene, multi-layer graphene has also been important for fundamental studies and applications, such as investigations of its electronic and magneto-optical properties,[1,7,8] second harmonic generation,[9] Q-switching and mode-locking of lasers,[10] and patterning/lithography.[11]

For many graphene applications, the ability to pattern or structure it in a controllable manner is very important, e.g., in transparent electrodes, field effect transistors, chem/biosensors, and energy devices.[12,13] So far, patterned structures have been achieved on graphene using several chemical and physical techniques mainly classified by lithography, soft lithography, and direct laser writing.[12,13] Parallel periodic structures have been produced on graphene by self-assembly onto patterned substrates,[14] multi-beam interference,[15] and strain-based techniques,[16,17] and have applications in, for example, nanoscale electronic devices.[16] In general, various patterning techniques are required to meet the needs of different graphene applications.[12]

Another patterning method, which has not yet been explored for graphene, involves laser irradiation and produces nanostructures known as "laser-induced periodic surface structures" (LIPSS). LIPSS are parallel periodic structures, also known as "surface ripples," classified by their spatial period (centre-to-centre distance between neighbouring parallel structures), and should not be confused with nanoribbons, being ultrathin strips of material.

The occurrence of LIPSS has long been known and studied (since 1965[18]) on a wide variety of other materials, including metals, semiconductors, and dielectrics[19–22] and has many applications in fields such as photonics, plasmonics, and optoelectronics.[23] For example, LIPSS applications include the modification of a material's optical, electrical, or wetting properties, structural colours, absorptance enhancement, antireflective films, biomedical applications, and optofluidics applications.

The technique of producing LIPSS offers a number of advantages useful for applications:[23] *simplicity*, *wide applicability*, *and low cost*—neither additional materials (as in lithography) nor laser scanning (as in direct writing) are required, and patterning can be done under normal ambient conditions in a quick one-step process; *high resolution*—capable of sub-wavelength nanostructuring; and *controllability*—the LIPSS orientation depends on the beam polarization direction, while the period can be varied by the laser wavelength, incidence angle, or effective refractive index of the interface between the material and surrounding medium.[23–26]

LIPSS are typically formed on a material surface by a linearly polarized pulsed laser beam at normal incidence,[23] with orientation depending on the polarization of the incident beam.[19,27,28] The resulting spatial period (Λ) is either on the order of the laser wavelength (λ) in low spatial frequency LIPSS (LSFL) or significantly smaller than λ ($\Lambda < \lambda/2$) in high spatial frequency LIPSS (HSFL).[19] For application purposes, smaller spatial periods (HSFL) are desirable, and much research is devoted to minimize the LIPSS spatial

[a]abeltaos@ualberta.ca

 © 2014 AIP Publishing LLC

[This article is copyrighted as indicated in the article. Reuse of AIP content is subject to the terms at: http://scitation.aip.org/termsconditions. Downloaded to] IP: 35.8.11.2 On: Fri, 26 Dec 2014 23:32:36

period. For example, spatial periods as little as $\Lambda \approx 70$–$90\,\text{nm}$ ($\lambda/10$) have been reported in an air environment on titanium by Bonse *et al.*[19] HSFL are fabricated using femtosecond irradiation,[19,23] and have been observed mostly on transparent materials.[27,28] The underlying process of the formation of LIPSS is not completely understood, with debate in the literature and different theories proposed. Generally, the formation is described by the interference of the incident laser beam with a surface wave, such as a laser-excited surface plasmon polariton (SPP), leading to a spatial periodic energy distribution on the material surface.[21,29–32] Second harmonic generation[33] and self-organization[34] effects have also been proposed.

Single or multi-layer graphene's high transparency and ability to be patterned or ablated with a pulsed laser in the femtosecond regime[12,35] make it a desirable material for HSFL formation. In addition, SPPs in graphene are in a new emerging field,[36] and their existence has been recently experimentally demonstrated.[37] SPPs in multi-layer graphene systems have also been investigated.[36,38] All of these properties, along with its high potential for applications, make graphene a promising candidate for the formation of LIPSS, while at the same time, the advantages of the LIPSS fabrication technique would be very useful in the applications of graphene. As an example, one potential application of graphene LIPSS could be the fabrication of graphene nanoribbons, with the advantages of mass production of nanoribbons in a quick, simple, cost-effective manner, with controllable dimensions and orientation via the laser parameters. Since LIPSS have never been observed before on graphene, the immense opportunities for new applications are apparent through the known applications of patterned graphene and the known applications of LIPSS on other materials, as mentioned above.

In this work, we present an observation of LIPSS on graphene. LIPSS on multi-layer graphene were induced by femtosecond laser irradiation. The samples and structures were analyzed using Raman spectroscopy, optical microscopy, atomic force microscopy (AFM), and scanning electron microscopy (SEM). The results were compared to previous reports on other materials.

II. EXPERIMENT

Sample preparation and characterization: Graphene samples of ~3–15 layers were prepared from kish graphite (NGS Naturgraphit GmbH) on transparent quartz substrates (Edmund Optics) by the standard micromechanical exfoliation technique,[1] and located on the substrates by optical microscopy. Characterization of the samples was performed by Raman Spectroscopy at room temperature using Micro Raman Chromex 2000 and TriVista TR557 Raman systems, each with a frequency doubled Nd^{3+}: YAG laser as an excitation source at a wavelength of $\lambda = 532\,\text{nm}$. In both systems, a 50× or a 40× microscope objective was used, and the laser power on the sample was ~1–2 mW, preventing sample degradation. Acquisition times of the micro-Raman spectra were 150–900 s with a spectral resolution of $\sim 2\,\text{cm}^{-1}$. Sample thickness was determined by a combination of Raman spectroscopy, optical microscopy in transmission mode,[39] and AFM (details described below).

Laser interaction: Femtosecond laser beam interaction with the samples was performed in an air environment using the setup shown in Figure 1. The source of the beam ($\lambda = 840\,\text{nm}$ wavelength, $\tau \approx 150$ fs pulse duration, $\nu = 76\,\text{MHz}$ repetition rate) was a Coherent Mira 900 Ti:Sapphire system. The beam power and exposure time were varied for the experiments. The beam was focused onto the samples using a focusing lens, while the position of the beam on the sample was monitored using a light microscope. The femtosecond laser experiments were performed in transmission mode, i.e., the samples were irradiated from below with the beam first passing through the transparent substrate and then irradiating the back of the sample at normal incidence. The wavelength was confirmed to be unchanged by passing through the quartz substrate and sample using an Ocean Optics HR2000CG-UV-NIR fiber-optic spectrometer.

Characterization of laser-induced structures: After the interaction, the samples were characterized by AFM and SEM. AFM measurements were done using an NTEGRA prima in the tapping mode under ambient conditions. The SEM measurements were done using a Tescan MIRA3 field emission gun SEM, with electron energies of 1–2 kV. Sample preparation for the SEM measurements was performed in two different ways, coated with ~5 nm of gold (higher resolution) and uncoated. SEM measurements were generally performed after all the other experiments, in order to avoid potential electron beam damage of the samples[40,41] and/or because of the gold coating on top, which restricted further experimentation.

III. RESULTS AND DISCUSSION

The experiment as described above was performed on selected graphene samples of 3–5 layers and ~10–15 layers. Figure 2 shows examples of a 15-layer graphene sample (Figs. 2(a) and 2(b)) and a 5-layer graphene sample (Figs. 2(c) and 2(d)) before (left) and after (right) femtosecond laser interaction. Raman spectroscopy and optical transmission microscopy, the methods used for sample characterization and thickness determination, are represented in Fig. 3(a), and Figs. 3(b) and 3(c), respectively. The occurrence of the G, G′, and 2D peaks in the Raman spectrum in Fig. 3(a) shows the presence of graphene. The shape of the 2D peak indicates the number of layers and a relatively small (or lack of) D-peak

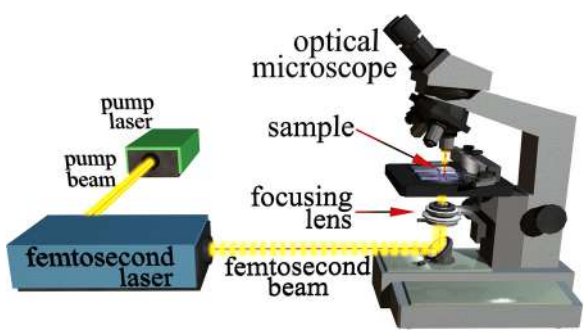

FIG. 1. Schematic of the femtosecond laser interaction set-up.

[This article is copyrighted as indicated in the article. Reuse of AIP content is subject to the terms at: http://scitation.aip.org/termsconditions. Downloaded to] IP: 35.8.11.2 On: Fri, 26 Dec 2014 23:32:36

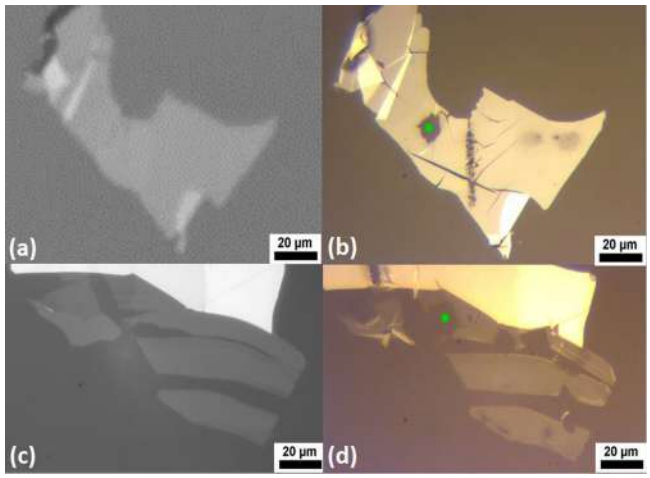

FIG. 2. Optical microscope images of (a) and (b) 15-layer graphene, and (c) and (d) 5-layer graphene samples before (left) and after (right) laser interaction. The green dots mark regions ablated for $t = 4$ min ($N \approx 1.8 \times 10^{10}$) of irradiation by a beam of $F \approx 4.3$–4.4 mJ/cm^2.

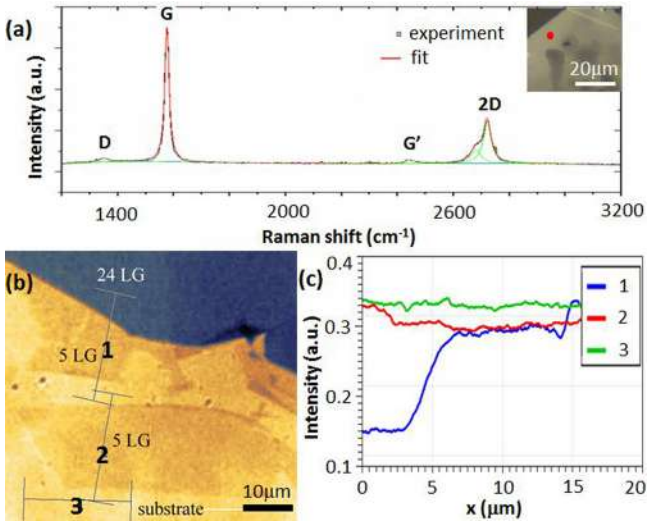

FIG. 3. (a) Micro-Raman spectrum of a 14-layer graphene sample. Inset: Optical microscope image, where the red dot indicates the position of the Raman measurement on a non-interacted area of the sample. (b) Transmission optical image of a 5-layer graphene (5 LG) sample, adjacent to a 24-layer flake (24 LG). The intensity of transmitted light for profile lines 1, 2, and 3 is shown in (c) in blue, red, and green, respectively.

indicates the presence of good quality (or defect-free) graphene.[42,43] Analysis of the optical microscope images in transmission mode (Figs. 3(b) and 3(c)) allows us to calculate the number of layers[1] based on the amount of absorption of transmitted light through the sample as compared to the substrate (each layer absorbing ~2.3% (Ref. 39)).

In the optical microscope images of the samples after laser interaction (Figs. 2(b) and 2(d)), the areas of interaction for various fluences and exposure times are seen as dark spots on the sample, which range from disordered graphene to completely ablated regions, as shown in previous work.[35]

The laser fluence (F) was varied from ~1 to 6 mJ/cm^2, while exposure time (t) was varied from 1 s to 4 min. Analysis of the various regions of interaction in SEM showed that clearly defined parallel nanostructures (LIPSS) consistently formed in the ablated regions of the 10–15 layer samples (Figs. 4(a) and 4(b)) for laser fluences slightly above the multi-layer graphene ablation threshold of 4.2 mJ/cm^2 (as found in Ref. 35 using N values similar to this work of $N = 1.5 \times 10^8$–1.8×10^{10}. Incubation effects and the dependence of N on the threshold were not investigated.) whereas structures were not found for fluences below this threshold. The obtained structures were perpendicular to the laser polarization used in the interaction (Fig. 4(c)). Our results are consistent with previous observations of LIPSS on other materials, which are generally formed at fluences slightly above the damage threshold and perpendicular to the laser polarization.[23,35] Repeated experiments showed that the most clearly defined and intact LIPSS on multi-layer graphene were produced using the parameters $F \approx 4.3$–4.4 mJ/cm^2 and $t = 4$ min (corresponding to number of laser shots (N) of $\sim 1.8 \times 10^{10}$). The green dot in Fig. 2(b) shows an ablated region using these parameters.

Using the same experimental parameters on the thinner samples of 3–5 layers (Fig. 2(d)—green dot) did not lead to the occurrence of LIPSS. Even by decreasing the fluence and exposure time to $F = 3.2$ mJ/cm^2 and $t = 2$ min ($N = 9 \times 10^9$), LIPSS were still not observed on these samples, as shown in the comparison SEM images of Figure 5.

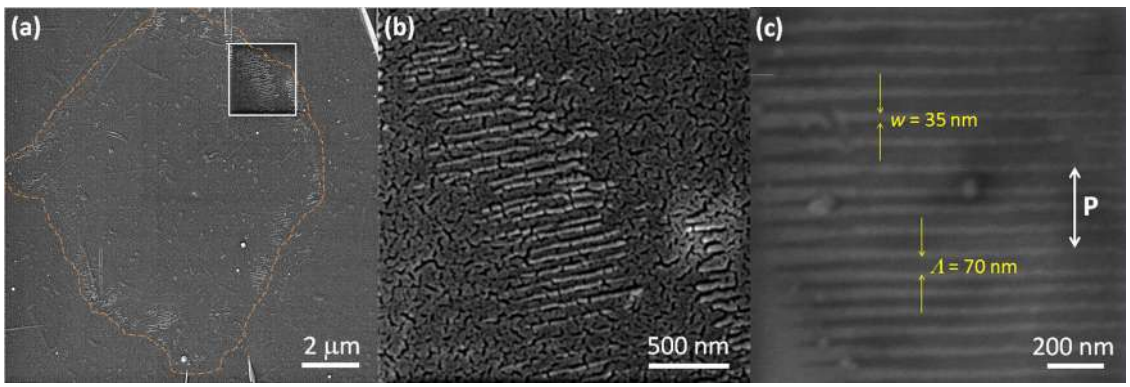

FIG. 4. SEM images of LIPSS observed on multi-layer graphene coated with a gold layer of ~5 nm: (a) ablated region due to laser interaction marked by orange dashed line. The white square shows where LIPSS were found, with a zoomed in image shown in part (b); (c) typical obtained LIPSS, showing width w and period Λ of the nanostructures and the polarization direction (**P**) of the laser used in the interaction.

[This article is copyrighted as indicated in the article. Reuse of AIP content is subject to the terms at: http://scitation.aip.org/termsconditions. Downloaded to] IP: 35.8.11.2 On: Fri, 26 Dec 2014 23:32:36

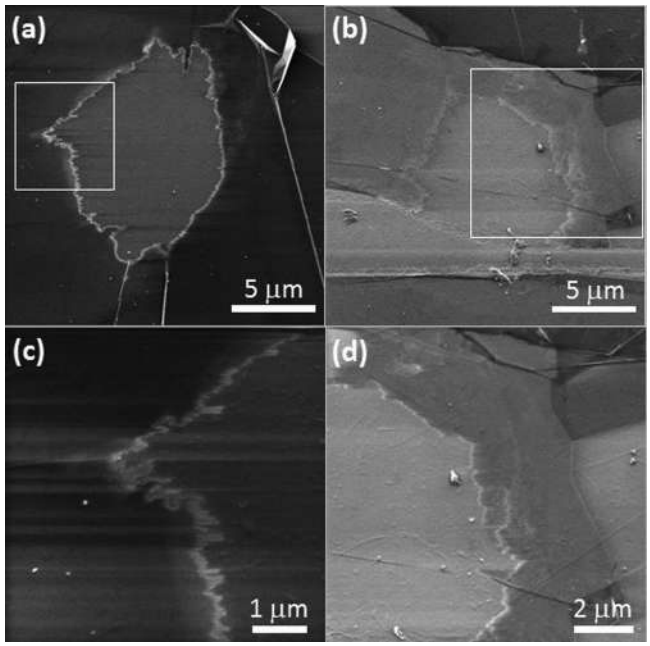

FIG. 5. Comparison SEM images of 15-layer graphene (left panel) and 5-layer graphene (right panel) samples. Ablated regions are shown in (a) and (b), where the white squares indicate the area examined in the corresponding larger image below in (c) and (d). The SEM images were taken without gold on the sample.

Parallel structures can be clearly seen at the edge of the ablated region of a 15-layer sample (Figs. 5(a) and 5(c)) but not on a 5-layer sample (Figs. 5(b) and 5(d)) for the same SEM parameters. Further studies are required to determine the ablation threshold of these thinner graphene samples and hence the laser interaction parameters for LIPSS formation.

The LIPSS on multi-layer graphene were further analyzed using AFM as shown in Figure 6. The structures were found in the ablated regions of the samples irradiated with a laser fluence of $F \approx 4.3$–4.4 mJ/cm^2 (Fig. 6(a)), usually in the peripheral area attached to the surrounding sample (Fig. 6(b)), and occasionally in the central area as well (Fig. 6(c)). A close-up phase image of the structures is shown in Fig. 6(d), in which it can be seen that the LIPSS were surrounded by dense nanostructures. Height profiles of the LIPSS (Fig. 6(e)) were obtained from which the spatial period (Λ) and width (w) of the structures were measured and found to be $\Lambda \approx 70$–100 nm and $w \approx 35 \pm 5$ nm. The height profiles (Fig. 6(e)) also showed that the LIPSS were less than or equal to the height of the surrounding sample, with some variation due to surface roughness as shown in the 3D height map of Fig. 6(f). Aside from these variations, the height of the structures was relatively constant along their length, with a sudden decrease where they were truncated, as represented in Fig. 6(f). Typical measured values of the height of the structures were ~1–2 nm less than the sample height, corresponding to ablation of 3–6 layers of graphene, which indicates why structures were not observed for the thinner samples.

The width and period of the LIPSS as measured by AFM were also confirmed by SEM measurements (as in Fig. 4(c)). In addition, from the SEM measurements, the lateral dimensions of length (l) and range (r) of the structures were obtained. The structures typically spanned a range as large as the ablated region, $r \approx 4.5$–5 μm, and the length varied from $l \approx 0.5$ to 1.5 μm (Fig. 7(a)). The variation in length of structures often displayed a wave-like behaviour (Fig. 7(b)).

To investigate the formation of LIPSS on the 10–15 layer samples, the exposure time was significantly decreased to ~16–20 s ($N \approx 1.2 \times 10^9$–$1.5 \times 10^9$), while the laser fluence was kept at $F \approx 4.4$ mJ/cm^2. The shorter exposure time led to a much smaller area of the ablated region,[35] as shown in Fig. 8(a). The existence of structures at the edges of these regions was confirmed by AFM as shown in Figures 8(a) and 8(b). The structures were much less clearly defined than those with longer exposures, and were wider ($w \approx 55$–85 nm), shorter ($l \approx 80$–200 nm), and farther apart ($\Lambda \approx 115$–120 nm) (Fig. 8(c)). As before, these structures were perpendicular to the laser polarization.

Discussion: For our incident wavelength of $\lambda = 840$ nm, the measured spatial periods of ~70–100 nm correspond to ~$\lambda/8$–$\lambda/12$, classifying the LIPSS as HSFL with periods amongst the smallest ever reported.[19] For comparison, on bulk graphite, LIPSS with periods of 110–800 nm were found.[22] The spatial period has been shown to decrease by

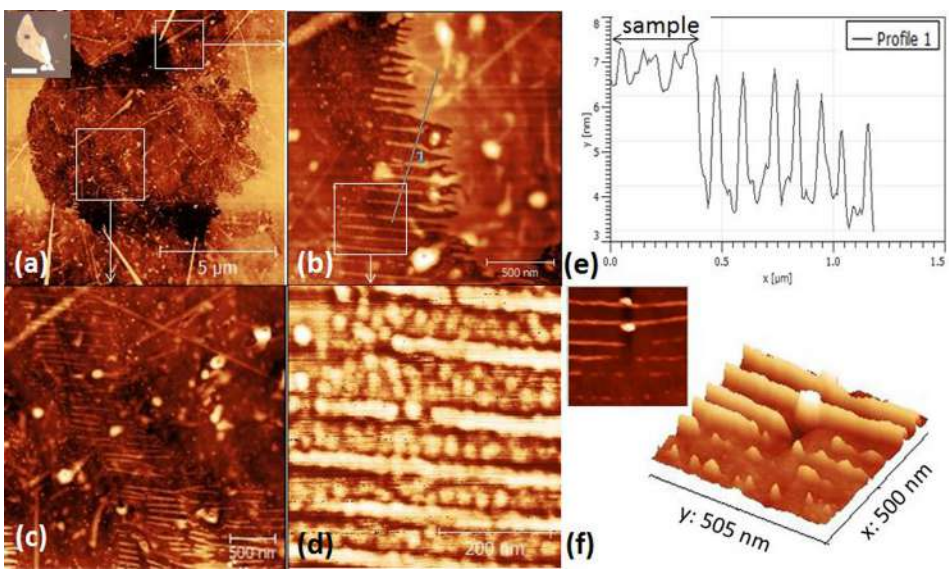

FIG. 6. AFM analysis of LIPSS on multi-layer graphene: (a) Ablated region of the sample. Inset: optical image of the sample where the ablated region can be seen as a black dot (scale bar of inset is 40 μm). White squares represent areas where structures were found, corresponding to (b) and (c), respectively; (d) phase image of the structures, zoomed in from the white square in (b); (e) height profile corresponding to the profile line "1" in (b); (f) 3D height map of structures, with inset showing corresponding 2D image.

[This article is copyrighted as indicated in the article. Reuse of AIP content is subject to the terms at: http://scitation.aip.org/termsconditions. Downloaded to] IP: 35.8.11.2 On: Fri, 26 Dec 2014 23:32:36

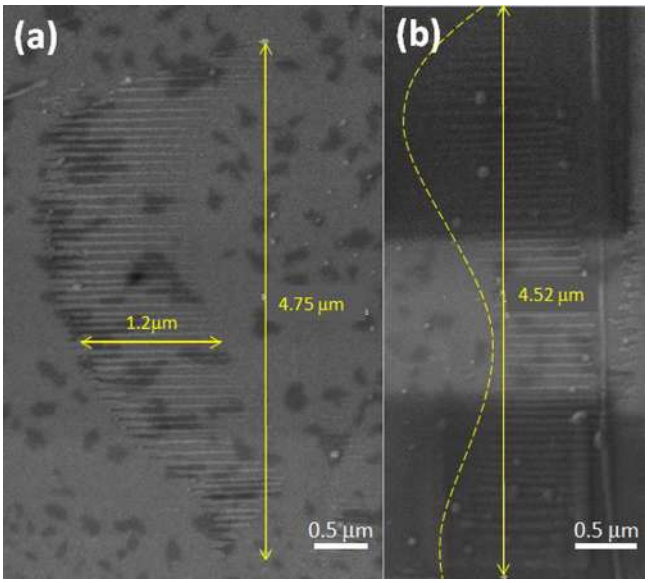

FIG. 7. SEM images showing the lateral dimensions of the LIPSS on multi-layer graphene coated with a gold layer of ~5 nm: (a) range and length; (b) variations in length, marked by the yellow dashed curve. Black squares are due to SEM charging, while black dots are due to ambient contamination.

increasing the number of laser shots N.[19,21,23,44,45] Our observations of LIPSS with larger periods for smaller N also agree with this phenomenon. Various effects of the laser fluence have been reported in the literature, with an increase in fluence resulting sometimes in an increase in period[44] and sometimes a decrease in period.[24] Here, we have observed HSFL using orders of magnitude lower values of F and higher N than typical values on other materials,[19] which is possible due to the thinness of multi-layer graphene that allows for a lower ablation threshold.[35] Therefore, our results coincide with a decrease in period for higher N and lower F values, also suggesting a reason for the smaller observed periods. In addition, reports have shown that HSFL with wavelengths significantly smaller than the laser wavelength are found, as in our case, on transparent materials, in the femtosecond regime, and around the peripheral area of ablated regions.[23,27–29] The latter effect is due to the Gaussian beam profile of the laser, and studies have even shown a transition from LSFL in the high-intensity central ablated region to HSFL around the lower-intensity edges.[34] In our case, this effect was not observed, as the central region was mainly ablated in the higher intensity area of the laser beam.

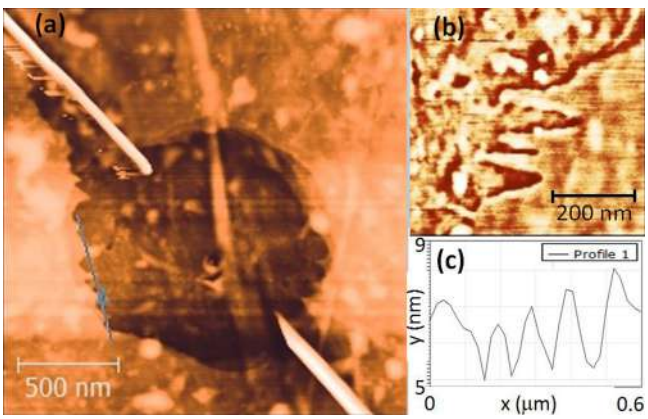

FIG. 8. AFM analysis of LIPSS on multi-layer graphene with reduced laser exposure time: (a) ablated region; structures are seen around the peripheral area; (b) phase image of structures; (c) height profile corresponding to the profile line "1" in (a).

The very small observed periods in our study as compared with other materials could be explained by following an SPP model[32] of LIPSS formation. While the origin of LSFL is typically described as the interference of the incident laser light with surface plasmons at the material-medium interface,[21,29–31] the origin of HSFL has been described as two SPPs propagating in opposite directions with interference effects leading to a reduced period equal to even fractions of the laser wavelength.[32] This is plausible for our results, since the measured spatial periods of $\Lambda \approx 70$, 80, 90, and 100 nm are within error of ~5 nm (~5%) to $\lambda/12 = 70$ nm, $\lambda/10 = 84$ nm, and $\lambda/8 = 105$ nm, and because SPPs on graphene with varying wavelengths and interference effects have also been reported.[36,38] Graphene is known to have SPPs with strong confinement and low loss, leading to wavelengths much smaller than that of the incident light,[36] and in a multi-layer system, the wavelength is predicted to be smaller as compared to single-layer graphene.[38]

Some studies have related the decrease in spatial period with increase in N to be due to the positive feedback of the SPP model;[29] a process which results in HSFL densely covered with nanostructures. A reduced period is expected by this model due to a change of effective refractive index at the air-material interface when the nanostructures develop on the surface, affecting SPP propagation. Also, a wave-like variation in height/length of the HSFL coincides with the spatial periodic energy distribution density suggested by this model. These effects are consistent with our observations, indicating further evidence for the SPP model of the formation of LIPSS on multi-layer graphene.[32]

IV. CONCLUSION

In this work, we observed laser induced periodic surface structures (LIPSS) on multi-layer graphene. Using a femtosecond laser, LIPSS perpendicular to the laser polarization with length ~0.5–1.5 μm and width ~35 ± 5 nm were induced on 10–15-layer graphene in an air environment. The measured spatial periods were ~70–100 nm (~$\lambda/8$–$\lambda/12$), amongst the smallest periods ever reported for LIPPS on other materials. The spatial period and width of the LIPSS were shown to decrease for an increased number of laser shots. The incident laser beam parameters used for the fabrication of LIPSS were $\lambda = 840$ nm, $F \approx 4.3$–4.4 mJ/cm^2, and $N \approx 1.8 \times 10^{10}$. Using the same parameters, a comparison was made with thinner graphene samples of 3–5 layers, on which LIPSS were not observed. Our results on multi-layer graphene are consistent with previous experimental findings of LIPSS on other materials. Specifically, HSFL were observed in the femtosecond regime, on a transparent material, in the peripheral of laser-ablated regions, and with the

[This article is copyrighted as indicated in the article. Reuse of AIP content is subject to the terms at: http://scitation.aip.org/termsconditions. Downloaded to] IP: 35.8.11.2 On: Fri, 26 Dec 2014 23:32:36

effect of a smaller spatial period for a higher number of laser shots. The observed HSFL are also consistent with a surface plasmon polariton model of LIPSS formation.

Through this work, we have demonstrated the patterning of graphene in a new controllable way (the width, period, and orientation are controlled using the laser parameters) by using the LIPSS technique that is well-known for other materials. The discovery of graphene LIPSS displays a fundamental property of graphene, placing it into the known field of LIPSS and giving insight into the physics of this unique material and the intriguing LIPSS formation process. Thus, our results have opened up the possibility for graphene LIPSS applications and research, laying the groundwork to build on for further studies in this direction.

ACKNOWLEDGMENTS

The authors would like to thank Miloš Bokorov (Faculty of Science, University of Novi Sad, Novi Sad, Serbia) for preliminary SEM measurements, and Dejan Pantelić (Institute of Physics, University of Belgrade, Belgrade, Serbia) for helpful discussions. This work was supported by the Ministry of Science (Republic of Serbia) under the projects OI171005, III45016, and III45018.

[1]K. S. Novoselov, A. K. Geim, S. V. Morozov, D. Jiang, Y. Zhang, S. V. Dubonos, I. V. Grigorieva, and A. A. Firsov, Science **306**, 666 (2004).
[2]N. M. R. Peres, Rev. Mod. Phys. **82**(3), 2673 (2010).
[3]K. F. Mak, L. Ju, F. Wang, and T. F. Heinz, Solid State Commun. **152**(15), 1341 (2012).
[4]C. Lee, X. Wei, J. W. Kysar, and J. Hone, Science **321**(5887), 385 (2008).
[5]K. S. Novoselov, V. I. Falko, L. Colombo, P. R. Gellert, M. G. Schwab, and K. Kim, Nature **490**, 192 (2012).
[6]F. Bonaccorso, Z. Sun, T. Hasan, and A. C. Ferrari, Nature Photon. **4**, 611 (2010).
[7]M. Koshino and T. Ando, Phys. Rev. B **77**(11), 115313 (2008).
[8]J. Hass, W. A. De Heer, and E. H. Conrad, J. Phys.: Condens. Matter **20**(32), 323202 (2008).
[9]A. Y. Bykov, T. V. Murzina, M. G. Rybin, and E. D. Obraztsova, Phys. Rev. B **85**, 121413 (2012).
[10]J. L. Xu, X. L. Li, J. L. He, X. P. Hao, Y. Z. Wu, Y. Yang, and K. J. Yang, Appl. Phys. Lett. **99**, 261107 (2011).
[11]Y. Zhou, Q. Bao, B. Varghese, L. A. L. Tang, C. K. Tan, C. Sow, and K. P. Loh, Adv. Mater. **22**, 67 (2010).
[12]J.-Y. Hong and J. Jang, J. Mater. Chem. **22**, 8179 (2012).
[13]J. Feng, W. Li, X. Qian, J. Qi, L. Qi, and J. Li, Nanoscale **4**(16), 4883 (2012).
[14]T. Kaplas and Y. Svirko, Carbon **70**, 273 (2014).
[15]Y. Li, Y. Li, W. Shi, S. Chen, G. Zhang, Z. Liu, Q. Sun, J. Tian, Y. Xu, and Y. Chen, Int. J. Nanomanuf. **8**(3), 221 (2012).
[16]W. Bao, F. Miao, Z. Chen, H. Zhang, W. Jang, C. Dames, and C. N. Lau, Nat. Nanotechnol. **4**(9), 562 (2009).
[17]A. Capasso, E. Placidi, H. F. Zhan, E. Perfetto, J. M. Bell, Y. Gu, and N. Motta, Carbon **68**, 330 (2014).
[18]M. Birnbaum, J. Appl. Phys. **36**, 3688 (1965).
[19]J. Bonse, J. Krüger, S. Höhm, and A. Rosenfeld, J. Laser Appl. **24**(4), 042006 (2012).
[20]G. Dumitru, V. Romano, H. P. Weber, M. Sentis, and W. Marine, Appl. Phys. A **74**(6), 729 (2002).
[21]M. Huang, F. Zhao, Y. Cheng, N. Xu, and Z. Xu, ACS Nano **3**(12), 4062 (2009).
[22]E. V. Golosov, A. A. Ionin, Y. R. Kolobov, S. I. Kudryashov, A. E. Ligachev, S. V. Makarov, Y. N. Novoselov, L. V. Seleznev, D. V. Sinitsyn, and A. R. Sharipov, Phys. Rev. B **83**(11), 115426 (2011).
[23]A. Y. Vorobyev and C. Guo, Laser Photon. Rev. **7**(3), 385 (2013).
[24]E. V. Golosov, A. A. Ionin, Y. R. Kolobov, S. I. Kudryashov, A. E. Ligachev, Y. N. Novoselov, L. V. Seleznev, and D. V. Sinitsyn, J. Exp. Theor. Phys. **113**(1), 14 (2011).
[25]T. Y. Hwang and C. Guo, J. Appl. Phys. **108**(7), 073523 (2010).
[26]A. Y. Vorobyev and C. Guo, J. Appl. Phys. **104**(6), 063523 (2008).
[27]M. Rohloff, S. K. Das, S. Höhm, R. Grunwald, A. Rosenfeld, J. Krüger, and J. Bonse, J. Appl. Phys. **110**(1), 014910 (2011).
[28]Q. Wu, Y. Ma, R. Fang, Y. Liao, Q. Yu, X. Chen, and K. Wang, Appl. Phys. Lett. **82**(11), 1703 (2003).
[29]A. Y. Vorobyev, V. S. Makin, and C. Guo, J. Appl. Phys. **101**(3), 034903 (2007).
[30]J. Bonse, A. Rosenfeld, and J. Krüger, J. Appl. Phys. **106**(10), 104910 (2009).
[31]J. E. Sipe, J. F. Young, J. S. Preston, and H. M. Van Driel, Phys. Rev. B **27**(2), 1141 (1983).
[32]V. S. Makin, R. S. Makin, A. Y. Vorobyev, and C. Guo, Tech. Phys. Lett. **34**(5), 387 (2008).
[33]D. Dufft, A. Rosenfeld, S. K. Das, R. Grunwald, and J. Bonse, J. Appl. Phys. **105**(3), 034908 (2009).
[34]J. Reif, *Laser-Surface Interactions for New Materials Production*, Springer Series in Materials Science Vol. 130, edited by A. Miotello and P. Ossi (Springer, Berlin, 2010), pp. 19–41.
[35]A. Beltaos, A. Kovačević, A. Matković, U. Ralević, Dj. Jovanović, and B. Jelenković, Phys. Scr. **2014**(T162), 014015 (2014).
[36]Y. V. Bludov, A. Ferreira, N. M. R. Peres, and M. I. Vasilevskiy, Int. J. Mod. Phys. B **27**(10), 1341001 (2013).
[37]J. Chen, M. Badioli, P. Alonso-González, S. Thongrattanasiri, F. Huth, J. Osmond, M. Spasenović, A. Centeno, A. Pesquera, P. Godignon, A. Z. Elorza, N. Camara, F. J. García de Abajo, R. Hillenbrand, and F. H. Koppens, Nature **487**(7405), 77 (2012).
[38]B. Wang, X. Zhang, F. J. García-Vidal, X. Yuan, and J. Teng, Phys. Rev. Lett. **109**(7), 073901 (2012).
[39]R. R. Nair, P. Blake, A. N. Grigorenko, K. S. Novoselov, T. J. Booth, T. Stauber, N. M. R. Peres, and A. K. Geim, Science **320**, 1308 (2008).
[40]D. Teweldebrhan and A. A. Balandin, Appl. Phys. Lett. **94**, 013101 (2009).
[41]I. Childres, L. A. Jauregui, M. Foxe, J. Tian, R. Jalilian, I. Jovanovic, and Y. P. Chen, Appl. Phys. Lett. **97**, 173109 (2010).
[42]A. C. Ferrari, J. C. Meyer, V. Scardaci, C. Casiraghi, M. Lazzeri, F. Mauri, S. Piscanec, D. Jiang, K. S. Novoselov, S. Roth, and A. K. Geim, Phys. Rev. Lett. **97**, 187401 (2006).
[43]D. Graf, F. Molitor, K. Ensslin, C. Stampfer, A. Jungen, C. Hierold, and L. Wirtz, Nano Lett. **7**, 238 (2007).
[44]Y. Yang, J. Yang, L. Xue, and Y. Guo, Appl. Phys. Lett. **97**(14), 141101 (2010).
[45]J. Bonse and J. Krüger, J. Appl. Phys. **108**(3), 034903 (2010).

[This article is copyrighted as indicated in the article. Reuse of AIP content is subject to the terms at: http://scitation.aip.org/termsconditions. Downloaded to] IP: 35.8.11.2 On: Fri, 26 Dec 2014 23:32:36

Soft Matter

PAPER

View Article Online
View Journal | View Issue

Check for updates

Cite this: *Soft Matter*, 2018, **14**, 5595

Golden moth-inspired structures with a synergistic effect of interference, absorption and scattering

Svetlana Savić-Šević, *[a] Dejan Pantelić,[a] Branislav Jelenković,[a] Branislav Salatić[a] and Dejan V. Stojanović[b]

Received 2nd April 2018,
Accepted 1st June 2018

DOI: 10.1039/c8sm00683k

rsc.li/soft-matter-journal

We describe a new type of photonic material inspired by a *Diachrysia chrysitis* moth, whose nano-structured wings exhibit a prominent golden color. This is a layered photonic structure with a large refractive index contrast, whose alternating layers are rough at the nanoscale level. Theoretical analysis shows that the scattering and interference interact to enhance the local field within the layers and increase the absorption of the material, particularly in the UV–blue part of the spectrum. Theory is experimentally verified using holographically manufactured Bragg gratings in the dichromated-pullulan (DCP). Alternating air-pullulan layers are produced and held in place by sparsely separated nano-pillars. Air voids are filled with 20–100 nm diameter spherical nanoparticles which act as scatterers. Such materials, with a high refractive index contrast and nano-scale scatterers, are important for achieving large reflectance and a broad spectrum, with scattering as an additional mechanism for spectral control.

Published on 04 June 2018. Downloaded by National Library of Serbia on 11/30/2018 1:47:40 PM.

Introduction

Natural nanotechnology still surpasses the technological achievements of our civilization. This is most evident, even visible by the naked eye, in the world of insects whose structural colors constantly amaze keen observers. The shiny blue colors of *Morpho* butterflies,[1] the violet tints of *Apatura iris* (Linnaeus, 1758) and *Apatura ilia* (Denis & Schiffermüller, 1775) butterflies,[2] the green colors of beetles (*Coleoptera*),[3] or the yellow-greens of certain bugs (Hemiptera),[4] are marvels of natural nanotechnology. They are produced quickly, effortlessly and in huge amounts, during the short lifecycle of insects.

Structural colors in nature mostly have a spectral distribution within a rather limited wavelength range and produce well defined colors – typically blues and greens. In spite of that, certain insects reflect light in a wide spectral range, resulting in silvery,[5] gold[5] or bronze[6] colors. Such broad spectral distributions are usually caused by chirped Bragg gratings, but color mixing[7] or local spectra averaging[8] can be found in certain insect species.

The richness of insect structures provides a constant inspiration for researchers to look for new ways of imitating natural optics and photonics structures.[9,10] There are quite a number of techniques used for biomimetics of photonic structures and a good overview is given in the paper of Butt *et al.*[11] Certain techniques are complex, slow and expensive, such as the one using focused Ga^+ ion beam chemical vapor deposition to manufacture free-standing butterfly-type structures with 80 nm resolution.[12] Other methods are simpler and use natural structures as templates for directly copying into other materials, such as TiO_2.[13] That is why industrial-scale production methods of simple biomimetic surfaces were developed, such as layer-by-layer spraying.[14]

Holography and interference methods stand out for their capability to generate complex, large-area photonic structures cheaply and efficiently.[15] Several laser beams interfere in a suitable photo-sensitive material: polymer dispersed liquid crystals,[16] photoresists,[17] dichromated gelatin[18] or silver-halide emulsions.[19] After chemical processing, nanostructures are generated, whose minimum dimension is limited by the wavelength of light. This method was used to create *Morpho*-butterfly-like structures on a photoresist.[20]

We were inspired by the Burnished brass moth, *Diachrysia chrysitis* (Linnaeus, 1758), whose wing scales and membranes represent a layered structure with rough surfaces. Here we see that several optical effects – interference, scattering and absorption[8] – cooperate to produce the golden wing color. Other insects[7,10] or their fossilized remnants[21] were found with a similar type of structure, resulting in the same, rather broad, reflection spectra.

In this paper we propose a new class of photonic materials characterized by layers with irregular, rough surfaces, residual absorption and high refractive index contrast. From the theoretical

[a] *Institute of Physics, University of Belgrade, Pregrevica 118, 11080 Zemun, Serbia. E-mail: savic@ipb.ac.rs*
[b] *Institute of Lowland Forestry and Environment, University of Novi Sad, Antona Čehova 13, 21000 Novi Sad, Serbia*

Published on 04 June 2018. Downloaded by National Library of Serbia on 11/30/2018 1:47:40 PM.

point of view, such structures exhibit a useful interplay between scattering, local field enhancement, planar waveguiding and interference. As a result, radiation is reflected in a broad spectral range. We use a transfer matrix method[22] and surface scattering theory[23] with associated intensity enhancement[24] to theoretically explain the observed optical properties.

As a proof of concept, we used holography (interference lithography) to pattern a pullulan – a linear homo-polysaccharide produced by the yeast-like fungus *Aureobasidium pullulans*. Pullulan was photo-sensitized by doping with chromium ions – we named the resulting material dichromated pullulan (DCP).[25] After exposure and simple chemical processing, the material exhibited just what we needed: a number of pullulan layers densely covered with randomly dispersed nano-spheres. The layers are separated by nano-scale pillars and the space between them is void. The resulting spectrum is wide and closely resembles the spectra of metallic gold and *D. chrysitis* moth wings.

Properties of the *Diachrysia chrysitis* moth wing and its holographically generated analogue

D. chrysitis is an attractive insect with large, golden-color patches covering its fore wings (Fig. 1a). The wings are covered with scales which are almost transparent if observed individually. However, in their natural position on the wing (Fig. 1b), wing membranes, ground and cover scales act together to produce the resulting color.[8] The spectrum is wide and visually closely corresponds to the color of gold.

From the morphological point of view, the wings have the standard structure of the vast majority of Lepidopterans (Fig. 1c), with two wing membranes (approximately 1 μm thick) covered ventrally and dorsally with two layers of scales (cover and ground). There are actually six distinct layers because each scale has two, air-spaced, laminae (air layers and laminae are 100 nm thick, each). The ventral side of the wing is not of much interest here, because wing-scales are pigmented, strongly attenuate the radiation and are incapable of reflecting a significant amount of light. All layers are structured: wing membranes have a number of hemispherical protuberances, the external surfaces of scales' upper laminae have a regular grating structure (Fig. 2a), while their internal surfaces are rough (Fig. 2b and c).

In order to imitate the optical characteristics of *D. chrysitis*, it is necessary to manufacture the layered structure having rough surfaces. We did that by holographically generating Bragg grating inside the dichromated pullulan – a homemade material produced by sensitization of pullulan with ammonium dichromate.

Diffraction gratings with spherical inclusions are fabricated by combination of the holographic method (top-down technique) and non-solvent-induced phase separation (bottom-up method).[26–28] The whole process involves several steps:

(1) preparation of a DCP film on a glass plate,
(2) film exposure using a laser,
(3) chemical development,
(4) desiccation in a non-solvent bath at room temperature, and
(5) drying in a closed vessel.

In the first step, the DCP is prepared by mixing 8% aqueous solution of pullulan (purchased from Sigma-Aldrich) and 45% of ammonium dichromate (by weight of pullulan). The solution

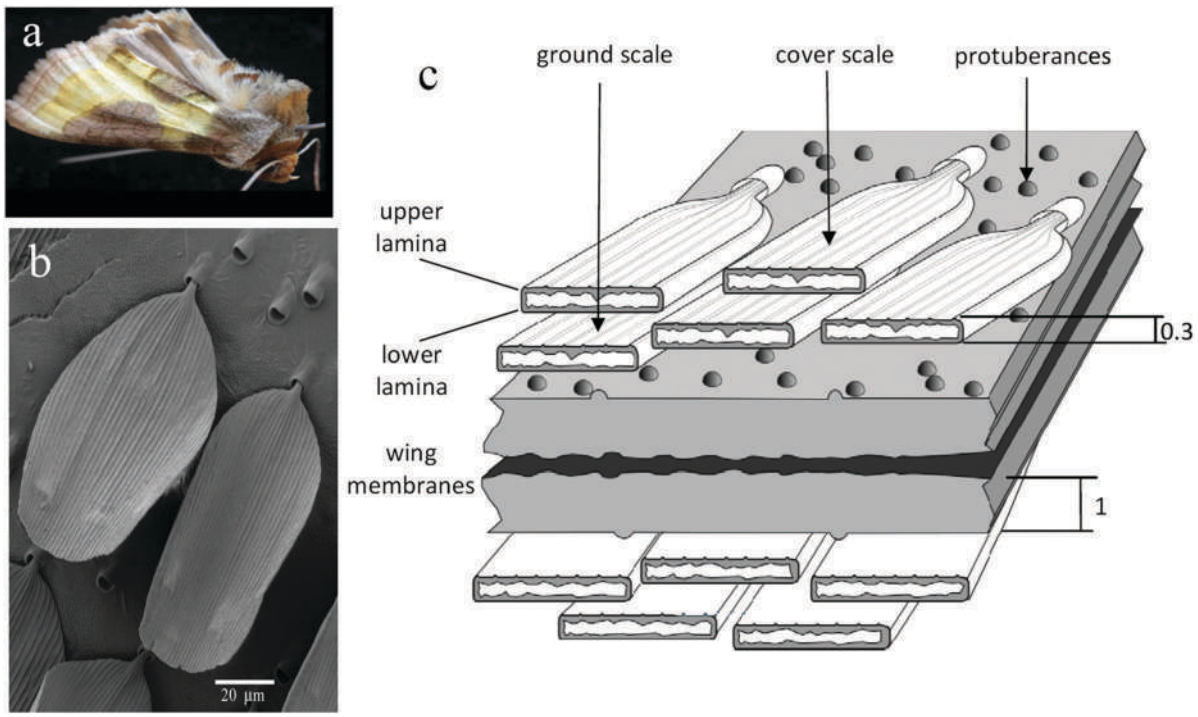

Fig. 1 (a) *Diachrysia chrysitis* moth. (b) Wing scales on the wing membrane of *D. chrysitis* moth, observed under a scanning electron microscope. (c) A scheme of the *D. chrysitis* wing's. The whole structure is cross-sectioned to display rough internal surfaces of wing scales. Dimensions are in μm.

 This journal is © The Royal Society of Chemistry 2018

Published on 04 June 2018. Downloaded by National Library of Serbia on 11/30/2018 1:47:40 PM.

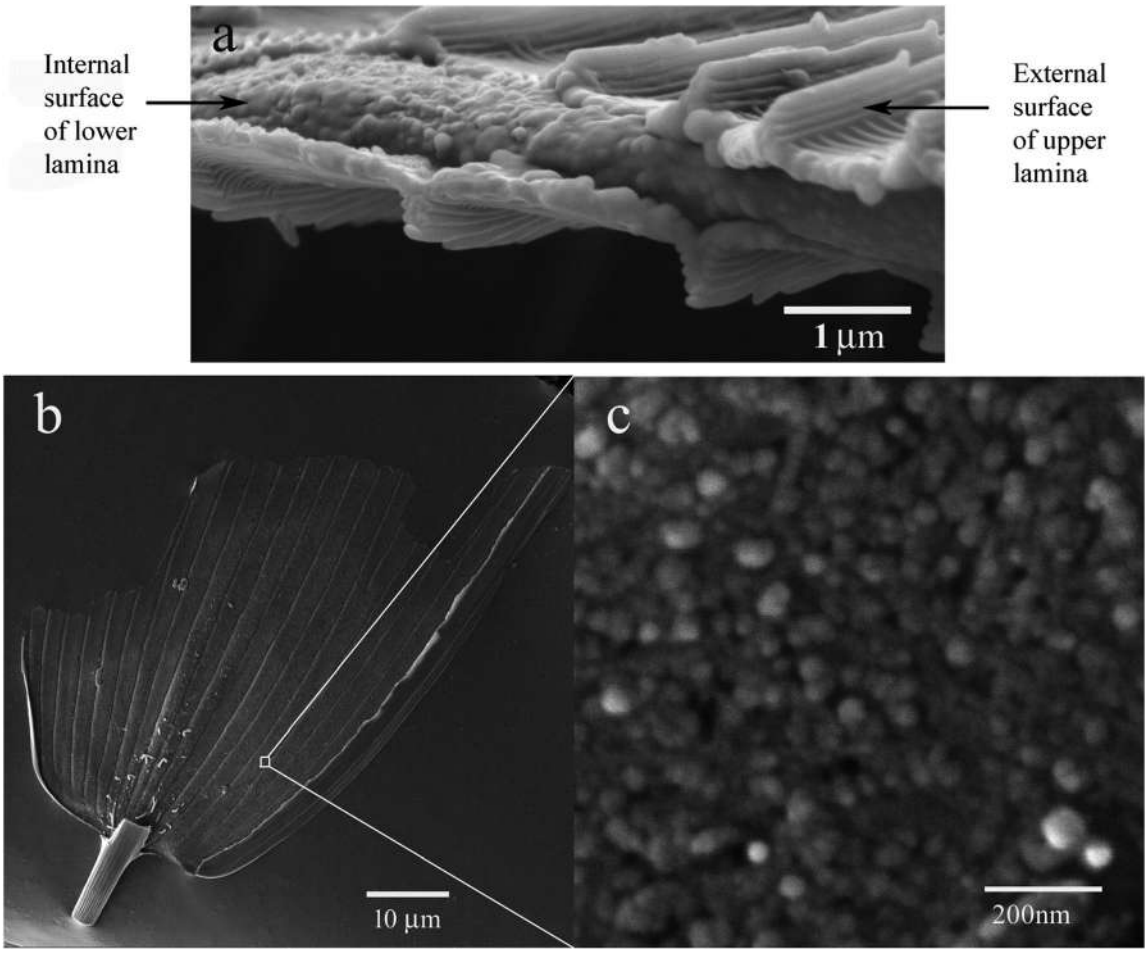

Fig. 2 (a) A broken and folded *D. chrysitis* scale revealing simultaneously the external grating-like structure and internal random structure. (b) Wing scale of *D. chrysitis* with intentionally removed lower lamina. (c) Enlarged portion of the image in (b) showing the rough internal surface in more detail.

was coated onto a clean glass slide in a horizontal position and the film was dried overnight under normal laboratory conditions. The resulting DCP film is 10 μm thick, yellowish, transparent and photosensitive.

The dried film is exposed at normal incidence using a single longitudinal mode, diode-pumped Nd-YAG laser, at 532 nm. After propagation through the film, the laser beam is back-reflected from a mirror behind the DCP plate. Two counter-propagating beams interfere to create a standing wave pattern consisting of parallel planes with spacing equal to $\lambda/2n$ (λ is the wavelength of the laser and n is the refractive index, which is 1.45 for pullulan[29]).

The DCP plate was further chemically processed using a mixture of water and isopropyl alcohol (ratio 3 : 1 respectively). Treatment lasted for two minutes, followed by pure isopropyl-alcohol dehydration. Finally, the material is fully dried in a closed vessel.

The morphology of the resulting DCP grating was investigated using a high resolution field emission gun scanning electron microscope (FEGSEM). A number of DCP layers with a spacing of about 135 nm and a similar thickness are visible. The space between them is void and they are supported and separated by tiny pillars (Fig. 3a and b). The layers are covered with nano-sized spherical particles distributed according to the Weibull distribution[30] (Fig. 3c), which exhibits maximum at 45 nm and mean at 55 nm (maximum and mean are different due to the asymmetry of the distribution).

There is a complex mechanism leading to the generation of structures in the DCP, which is based on pullulan's solubility in water and insolubility in isopropyl alcohol. During exposure, hexavalent chromium ion Cr^{6+} is photo-reduced to trivalent Cr^{3+}, which covalently cross-links with pullulan molecules in exposed areas. Cross-linking hardens the pullulan making it insoluble in water. This causes a solubility difference between exposed and unexposed regions.

After exposure, the DCP grating is chemically processed using a mixture of water and isopropyl alcohol as a developer. The unexposed regions (areas of destructive interference) are chemically unaffected and are dissolved in the developer. In contrast, areas of constructive interference are not dissolved during development, as a consequence of hardening by cross-linking. As a result, solid DCP layers are produced. At this stage,

Published on 04 June 2018. Downloaded by National Library of Serbia on 11/30/2018 1:47:40 PM.

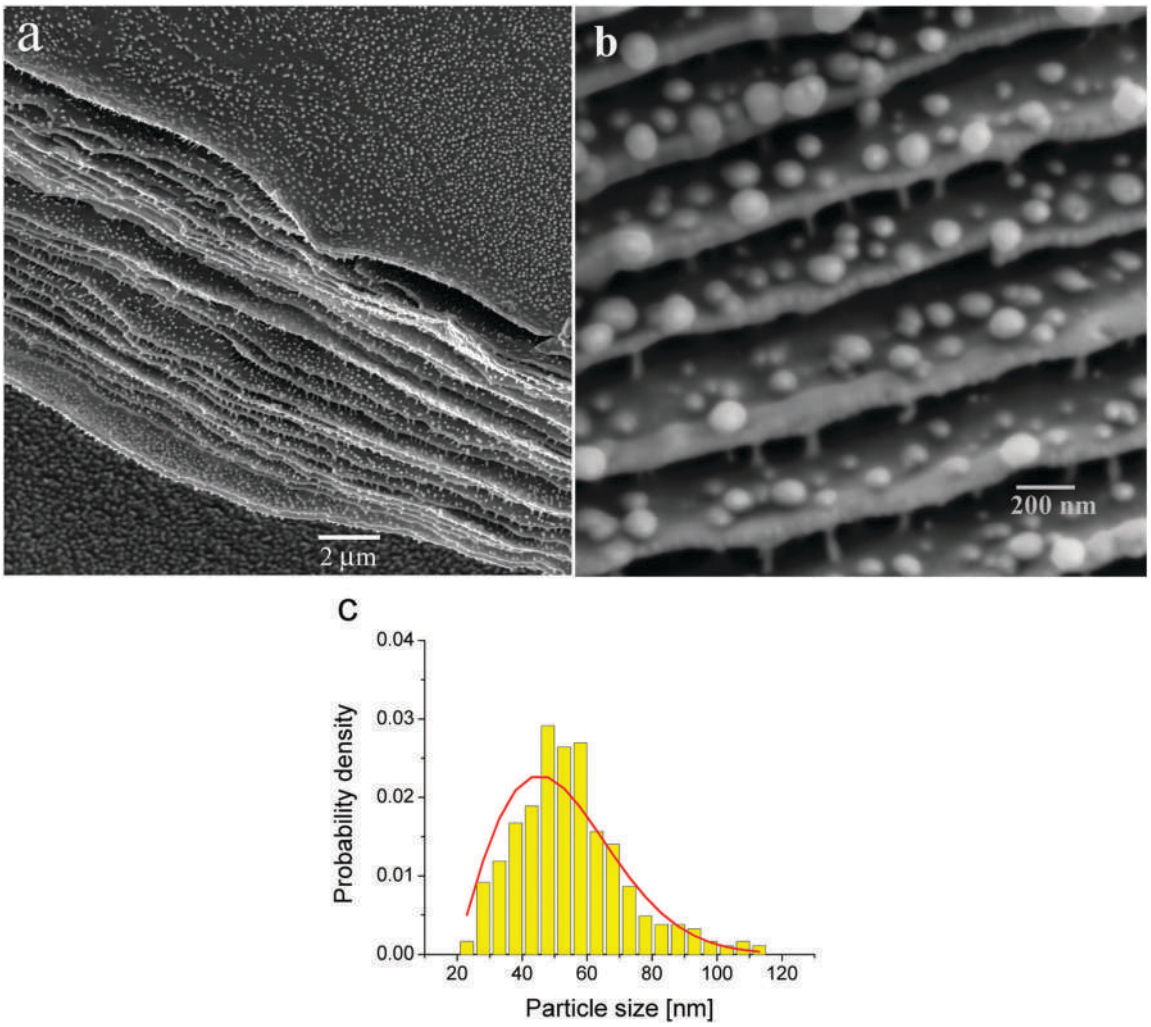

Fig. 3 (a) FEGSEM image of a cross-section of the DCP grating. Particle density is 58 ± 12 particles μm^{-2}. (b) Enlarged portion of a DCP grating with nano-spheres of average size 55 ± 17 nm. (c) Size distribution of nanospheres between DCP layers (yellow bar chart) and the corresponding Weibull distribution (red line). Distribution maximum is at 45 nm and its mean is at 55 nm.

the developer with dissolved pullulan remains trapped between solid layers. The processing is finished by immersing the DCP in pure isopropyl alcohol, which removes water and forces dissolved pullulan to aggregate into nanoparticles (as a result of non-solvent phase separation).

Fig. 4a shows the DCP sample displaying a golden color. On the microscopic level, color variation is detected (see differently colored dots in Fig. 4b), which means that the macroscopically observed color results from local spectra mixing. Transmission and reflection spectra, Fig. 4c and d, respectively, were measured using a spectrometer (Ocean Optics) attached to an optical microscope. The reflection spectrum of DCP is quite similar to that of *D. chrysitis*.[8] Both spectra are broad with a cut-off wavelength of approximately 500 nm, visually corresponding to a golden color. However, the maximum reflectance R of DCP is significantly higher ($R \approx 0.6$), compared to *D. chrysitis* ($R \approx 0.4$). This is due to the much larger number of layers in the DCP (40) *vs.* only 6 in *D. chrysitis*. In both cases, the reflectance is enhanced by the high refractive index contrast between air and material.

Theoretical analysis of the optical properties

Here we present a theoretical analysis of photonic structures characterized by regularly spaced layers with irregular surfaces and a large refractive index contrast. We treat structures as Bragg gratings, schematically shown in Fig. 5a, with scattering and internal field enhancement effects taken into account.

We first demonstrate that the scattering on the internal grating surfaces leads to significant dispersal of incident light. The wavelength of the incident visible light (inside material) is much larger than the scatterers and, widely used, scalar surface-scattering theory[23,31] is applicable to determine the amount of scattered radiation.

Under these circumstances, the incident light is split into two parts: one, regular, propagating as if the surface is perfectly flat, and the other diffusely scattered (haze), see Fig. 5b.

 This journal is © The Royal Society of Chemistry 2018

Published on 04 June 2018. Downloaded by National Library of Serbia on 11/30/2018 1:47:40 PM.

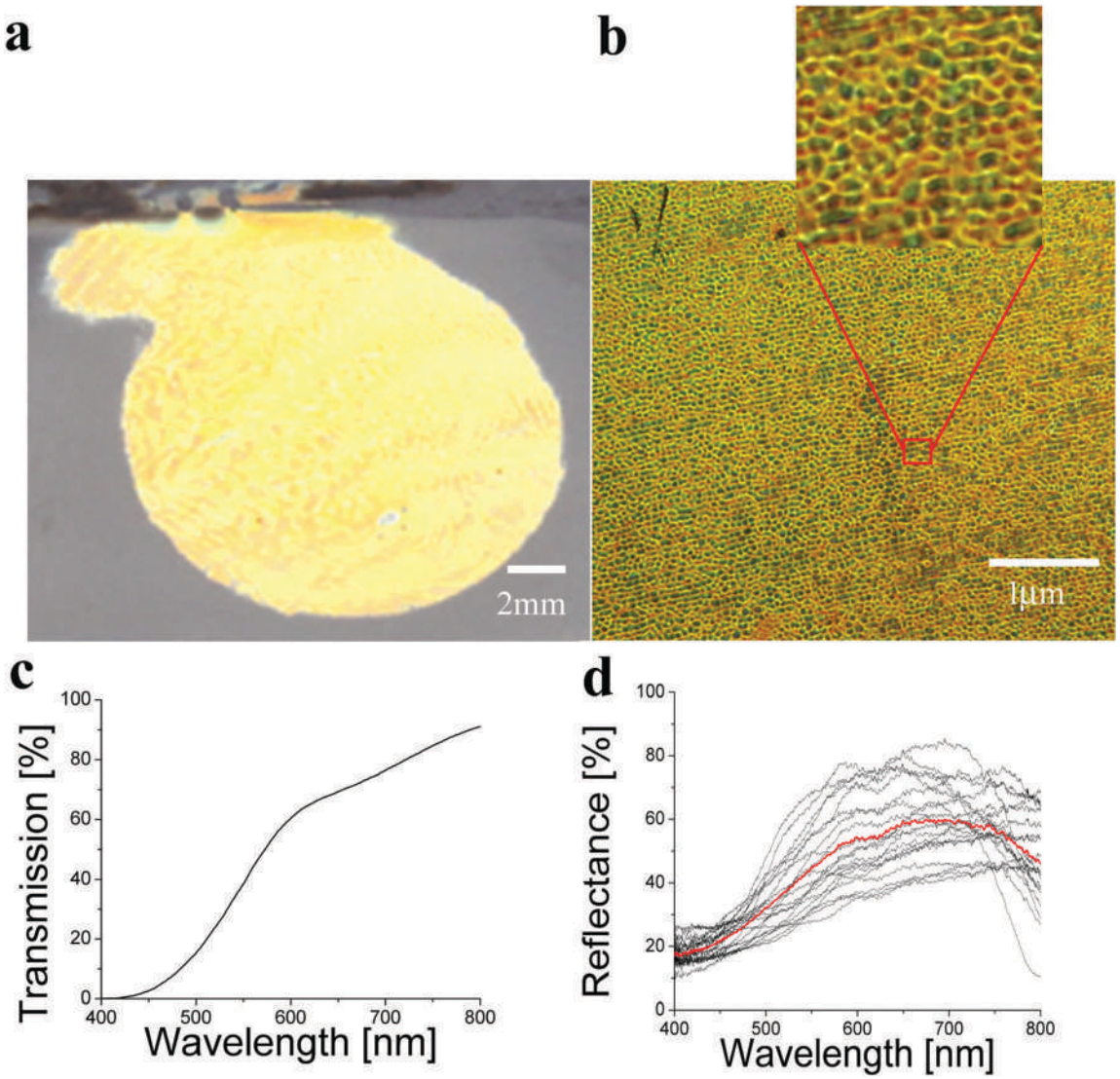

Fig. 4 (a) Golden appearance of the DCP layer. (b) Reflection from the DCP layer recorded under the reflection microscope. (c) Transmission spectrum of unexposed, chemically unprocessed dichromated pullulan, showing the strong absorption in the blue–green part of the spectrum. This spectrum is quite uniform across the sample. (d) Experimentally recorded reflection spectra of the DCP grating recorded at several positions. Individual, local, spectra (black curves) were recorded under the optical microscope and averaged (red curve).

Regularly propagating light obeys classical Fresnel reflection/transmission laws and "sees" the material as a volume Bragg grating. The haze and the regular component are described relative to transmittance T_0 and reflectance $R_0 = 1 - T_0$ of an ideally flat surface (assuming that the Fresnel equations hold). Accordingly, the haze transmittance $T_H(\lambda)$ and reflectance $R_H(\lambda)$ of a rough surface are described by:[2,3]

$$T_H(\lambda) = T_0\left[1 - \exp\left(-\left[\frac{2\pi\sigma}{\lambda}(n_i\cos\phi_i - n_t\cos\phi_t)\right]^2\right)\right] \quad (1)$$

$$R_H(\lambda) = R_0\left[1 - \exp\left(-\left[\frac{4\pi\sigma}{\lambda}n_i\cos\phi_i\right]^2\right)\right] \quad (2)$$

where T_0 and R_0 are the transmittance and the reflectance of a perfectly flat surface, respectively, λ is the wavelength of light under vacuum, ϕ_i and ϕ_t are the angles of incidence and refraction, n_i and n_t are the corresponding refractive indices, while σ is the root mean square (RMS) roughness of the surface.

We have computed the intensity of scattering for materials within the RMS range of several tens of nano-meters, and shown them in Fig. 6a and b. The intensity of transmitted haze does not depend on whether it comes from a high or low refractive index medium, Fig. 6a. In contrast, the intensity of reflected haze depends on the side from which the radiation comes, Fig. 6b. By comparing Fig. 6a and b, it is obvious that the scattering is 4–5 times stronger in transmission, compared to reflection. For both reflected and transmitted radiation, haze is much stronger at shorter wavelengths (as in Rayleigh scattering). As can be seen in Fig. 6 the intensity of scattering is much higher inside the blue–UV spectral range.

On the other hand, scattered radiation excites planar waveguide modes of Bragg layers. It was verified by the finite element

Published on 04 June 2018. Downloaded by National Library of Serbia on 11/30/2018 1:47:40 PM.

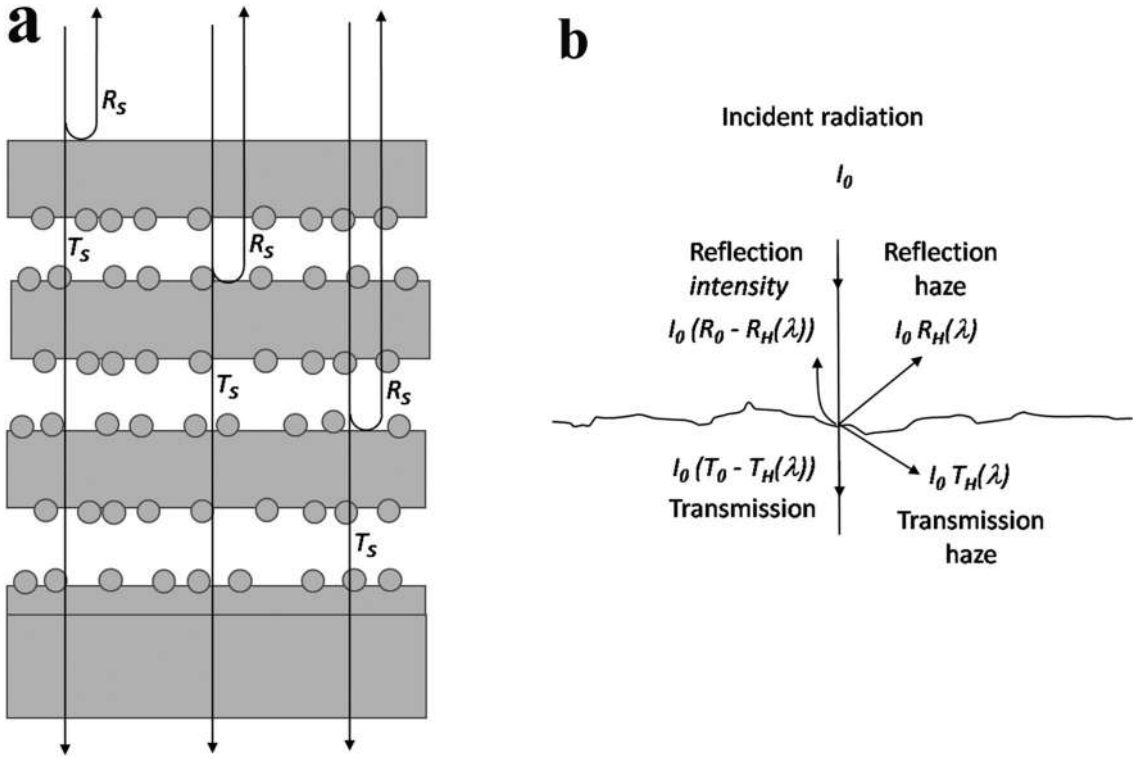

Fig. 5 (a) Scheme of a DCP diffraction grating with nano-sized particles. R_S and T_S are specular reflection and transmission coefficients, corrected for scattering effects. (b) Incident radiation is divided into specular and haze components.

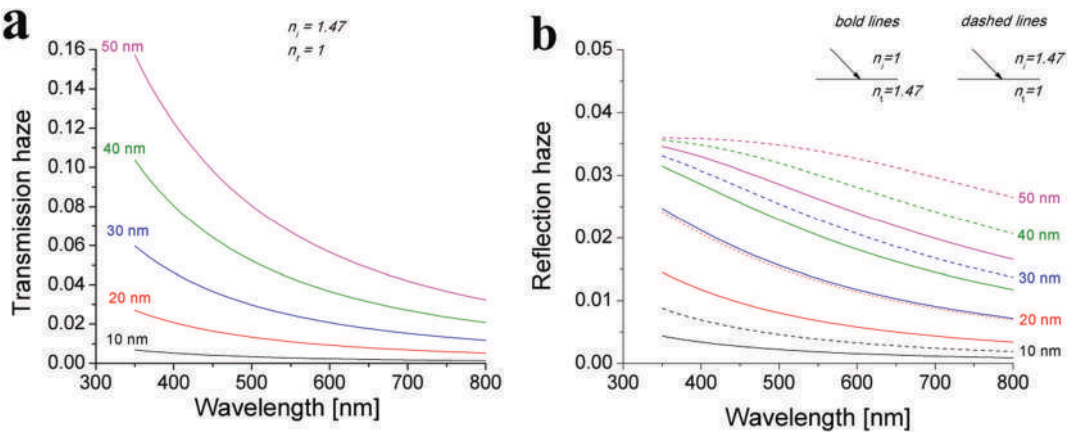

Fig. 6 Spectral dependence of haze from an interface with RMS roughness (ranging from 10 nm to 50 nm) as a parameter: (a) transmission and (b) reflection (in this case haze depends on whether light comes from the high index (dashed curves) or low index material (bold lines)). Haze was calculated for a single surface between air and pullulan.

method (FEM) applied to the DCP structure with a layer thickness of 135 nm, an air space of 130 nm and a refractive index of 1.45. The roughness was simulated using nanoparticles of 55 nm diameter (see Fig. 7a). Periodic boundary conditions were used in a simulation, and perfectly matching layers were positioned above and below the grating. Fig. 7b shows excited planar modes at the resonant wavelength, under the assumption that there is no absorption. It is interesting to note that by redistributing the spheres, the overall modal structure remains almost the same, with a possible slight shift of the wavelength of planar modes. By reducing the number of particles, the planar modes gradually disappear, as the system approaches the pure multilayer geometry (without any inclusions).

So far, all the calculations have been done assuming non-absorbing materials. In reality this cannot be neglected. Calculations show that absorption efficiently suppresses the modes (Fig. 7c) and influences the diffraction efficiency, as predicted by the model developed by Yablonovich and Cody.[24]

The FEM method cannot account for the stochastic nature of scattering surfaces. It would be possible to run many

 This journal is © The Royal Society of Chemistry 2018

Published on 04 June 2018. Downloaded by National Library of Serbia on 11/30/2018 1:47:40 PM.

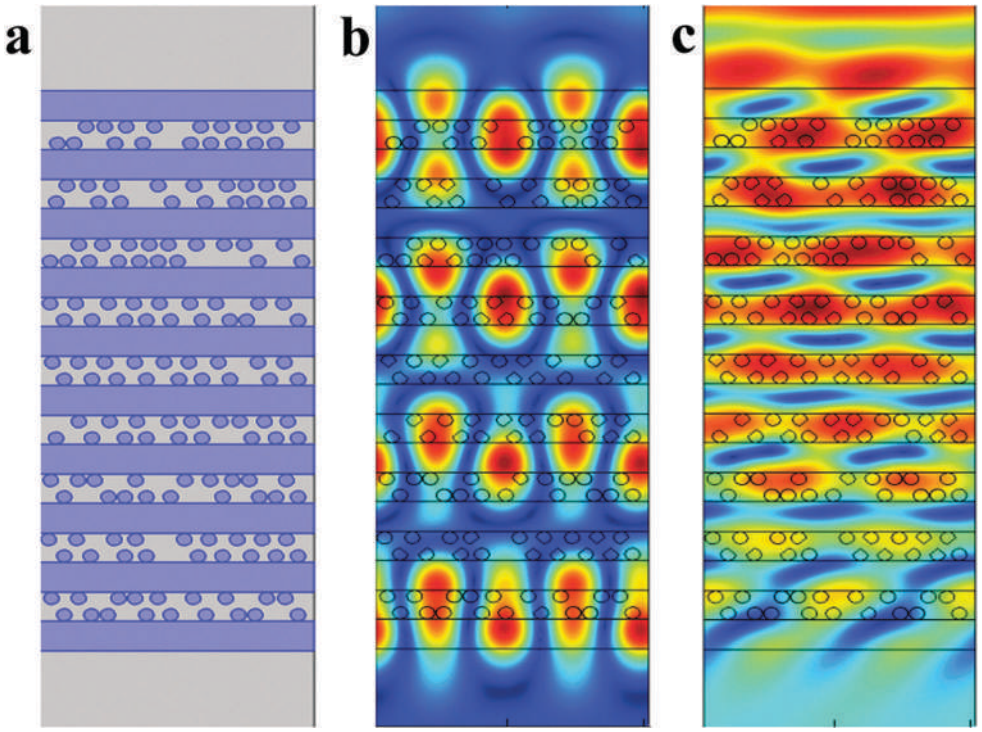

Fig. 7 (a) A geometry of the FEM model. (b) Intensity of electro-magnetic field at the resonance wavelength. Calculation were performed assuming that the angle of incidence is $\alpha = 0$, wavelength 624 nm and there is no absorption. (c) Field distribution with absorption included in the model. Parameters are the same as in (b).

variations of the same model with different surface profiles (but the same RMS) and then average the results. However, this would be very time consuming, and periodic boundary conditions would still introduce periodic repetition of spherical particle arrangements. To efficiently model this type of interaction we modified a transfer matrix method (TMM) to calculate the reflectance of the Bragg grating. This is a well known technique used to calculate the propagation of electromagnetic (EM) waves in a multilayer medium. Fresnel equations are used to establish the matrix relation between the EM field at the beginning and end of each layer.[32] The resulting EM field of the whole structure is obtained as a result of matrix multiplication of matrices corresponding to individual layers. Scattering was accounted for by simply correcting the Fresnel reflection coefficient by subtracting the intensity of scattered radiation. Absorption losses, due to scattering, were calculated using the theory of Yablonovich and Cody.[24] TMM software, developed by Junesch *et al.*[33] and made publicly available, was modified to account for scattering enhanced absorption. Further details can be found in the previous publication.[8]

We used parameters corresponding to pullulan diffraction gratings recorded in our experiments: 40 layers with 135 nm thickness and 130 nm air space, refractive index $n_i = 1.45$. The RMS roughness was calculated from the statistics of nanosphere size and their surface distribution, as determined from a series of FEGSEM images (two of them can be seen in Fig. 3). We found that the average particle size is 55 nm $\pm$ 17 nm and their density is 58 $\pm$ 12 particles μm^{-2} (corresponding to the average distance of 131 $\pm$ 14 nm). The associated RMS roughness is calculated by averaging integral of the square of the surface profile over the interval L and taking a square root of the result. The resulting RMS roughness is 34.4 $\pm$ 16.4 nm.

There is an important word of caution: in order to get a golden wing color, the dimensional and optical parameters of each individual layer should be kept within quite tight tolerances – a condition completely impossible to satisfy in the real world. It is more realistic to expect significant variability of all the parameters. We have chosen to vary the most important ones – RMS roughness and layer thickness within $\pm$30% (according to the normal distribution). The particular value of $\pm$30% was chosen in accordance with the large variability of particle size ($\pm$30%) and their surface density ($\pm$20%). The angle of incidence was also allowed to fluctuate within $\pm$10 degrees – thus imitating the finite angular range of the incident radiation.

As a result, 160 different spectra were calculated. Each individual spectral curve is irregular with multiple peaks, corresponding to irregularities in the volume grating structure. Individual spectra were averaged – corresponding to natural spectral averaging by the detecting instrument or an observer. Our calculations have shown that the best fit of the experimentally recorded spectrum is obtained assuming that the surface roughness is 45 nm. This is larger than the 34.4 nm RMS roughness, found from FEGSEM images, but still within the uncertainty interval of $\pm$16.4 nm. The resulting curve is shown in red color in Fig. 8, together with several individual

Published on 04 June 2018. Downloaded by National Library of Serbia on 11/30/2018 1:47:40 PM.

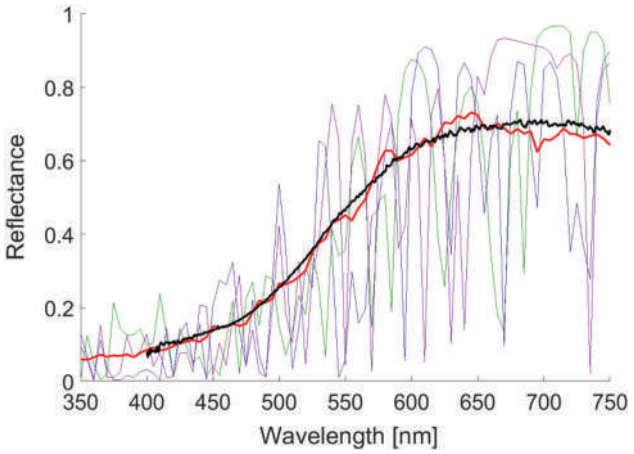

Fig. 8 Reflectance spectrum of a model in Fig. 7(a) calculated by transfer matrix method with scattering effects included (red curve). 160 individual spectra were calculated to represent natural variability of the grating (three of them can be seen in violet, green and blue color). The final reflectance spectrum (red curve) was calculated by averaging individual spectra. Experimentally recorded spectrum of DCP is shown for reference (black curve).

spectra (violet, blue and green color). The theoretical spectrum appears noisy because the finite number of individual spectral curves (used in the calculation) cannot completely make the resulting curve smooth. By comparing the averaged spectrum with the experimentally recorded one (black curve in Fig. 8), agreement appears quite good.

Discussion and conclusions

As far as we know, DCP is the only material capable of artificially introducing spherical nano-particles inside the Bragg grating, thus well imitating wing-scales of the *Diachrysia chrysitis* moth. Both pullulan (Fig. 3b) and butterfly's wing (Fig. 2c) possess a number of layers with rough internal surfaces (RMS roughness between 20 and 100 nm). The result is the same: strong suppression of radiation reflected in the UV–blue part of the spectrum. In this spectral range, light is strongly scattered by the rough surfaces and guided through the planar layers. Even a small amount of absorption is being enhanced by the increased path length.

It is interesting to discuss the mechanisms of nanoparticle formation both in *D. chrysitis* and DCP. In the case of *D. chrysitys* moth, we are not able to describe the exact mechanism of wing scale structure growth, because it was beyond this study. However, it is known that the wing scales are dead remnants of cells, whose main constituent is chitin (a natural polysaccharide). Chitin production and excretion are the result of a complicated biochemical process.[34] Additionally, according to Saranathan *et al.*[35] and Dinwiddie *et al.*,[36] wing-scale structures are produced by the complex growth of the cellular plasma membrane and intracellular smooth endoplasmic reticulum. The process is highly unpredictable as supported by the significant body of literature devoted to the, so called, cellular noise.[37] It was found that even genetically identical cells express random variation of their properties, such as size, structure or protein level. In the case of DCP, we proposed the non-solvent induced phase separation as the main process behind the pullulan nanosphere particle formation, as fully described in the main body of the paper.

In conclusion, we have created a peculiar kind of volume diffraction grating, where the nano-spherical particles are introduced between the grating layers. It was created through a combination of the holographic method (top-down technique) and non-solvent-induced phase separation (bottom-up method). The bangap is strongly influenced by the scattering and light intensity enhancement inside the grating layers. Large size gratings can be fabricated simply and quickly (in a few minutes). It was found that the DCP grating has excellent mechanical and environmental stability.

Such multilayer materials might be of interest in solar energy collection to selectively absorb the most energetic photons of UV–blue light, while reflecting unusable long wavelength radiation.[38,39]

Conflicts of interest

There are no conflicts to declare.

Acknowledgements

The authors express their gratitude to the Ministry of Education, Science and Technological Development of the Republic of Serbia for supporting this research through projects ON171038, III45016, III43002.

References

1 S. Berthier, *Photonique des Morphos*, Springer Science & Business Media, 2010.
2 D. Pantelić, S. Ćurčić, S. Savić-Šević, A. Korać, A. Kovačević, B. Ćurčić and B. Bokić, *Opt. Express*, 2011, **19**, 5817.
3 H. Arwin, T. Berlind, B. Johs and K. Järrendahl, *Opt. Express*, 2013, **21**, 22645.
4 D. Azofeifa, H. Arguedas and W. Vargas, *Opt. Mater.*, 2012, **35**, 175.
5 C. Campos-Fernández, D. Azofeifa, M. Hernández-Jiménez, A. Ruiz-Ruiz and W. Vargas, *Opt. Mater. Express*, 2011, **1**, 85.
6 M.-N. Wu, C.-Y. Chen and W. Pan, *AIP Adv.*, 2015, **5**, 127227.
7 J. P. Vigneron, M. Ouedraogo, J.-F. Colomer and M. Rassart, *Phys. Rev. E: Stat. Phys., Plasmas, Fluids, Relat. Interdiscip. Top.*, 2009, **79**, 021907.
8 D. Pantelić, S. Savić-Šević, D. Stojanović, S. Ćurčić, A. Krmpot, M. Rabasović, D. Pavlović, V. Lazović and V. Milošević, *Phys. Rev. E*, 2017, **95**, 032405.
9 O. Karthaus, *Biomimetics in photonics*, CRC Press, 2013.
10 J. P. Vigneron, M. Rassart, C. Vandenbem, V. Lousse, O. Deparis, L. Biró, D. Dedouaire, A. Cornet and P. Defrance, *Phys. Rev. E: Stat. Phys., Plasmas, Fluids, Relat. Interdiscip. Top.*, 2006, **73**, 041905.

 This journal is © The Royal Society of Chemistry 2018

Published on 04 June 2018. Downloaded by National Library of Serbia on 11/30/2018 1:47:40 PM.

11 H. Butt, A. Yetisen, D. Mistry, S. A. Khan, M. U. Hassan and S. H. Yun, *Adv. Opt. Mater.*, 2016, **4**, 497.
12 K. Watanabe, K. Kanda, Y. Haruyamaet, T. Kaito and S. Matsui, *J. Vac. Sci. Technol., B*, 2005, **23**, 570.
13 X. Liu, S. Zhu, D. Zhang and Z. Chen, *Mater. Lett.*, 2010, **64**, 2745.
14 K. Krogman, R. Cohen, P. Hammond, M. Rubner and B. Wang, *Bioinspiration Biomimetics*, 2013, **8**, 045005.
15 M. Campbell, D. Sharp, M. Harrison, R. Denning and A. Turberfield, *Nature*, 2000, **404**, 53.
16 M. Escuti, J. Qi and G. Crawford, *Opt. Lett.*, 2003, **28**, 522.
17 Y. Miklyaev, D. Meisel, A. Blanco and G. von Freymann, *Appl. Phys. Lett.*, 2003, **82**, 1284.
18 R. Ma, J. Xu and W. Tam, *Appl. Phys. Lett.*, 2006, **89**, 081116.
19 M. H. Kok, R. Ma, J. C. W. Lee, W. Y. Tam, C. T. Chan and P. Sheng, *Phys. Rev. E: Stat. Phys., Plasmas, Fluids, Relat. Interdiscip. Top.*, 2005, **72**, 047601.
20 R. H. Siddique, R. Hünig, A. Faisal, U. Lemmer and H. Hölscher, *Opt. Mater. Express*, 2015, **5**, 996.
21 M. McNamara, D. Briggs, P. Orr, S. Wedmann, H. Noh and H. Cao, *PLoS Biol.*, 2011, **9**, e1001200.
22 J. Springer, A. Porube and M. Vanacek, *J. Appl. Phys.*, 2004, **96**, 5329.
23 D. Domine, F.-J. Haug, C. Battaglia and C. Ballif, *J. Appl. Phys.*, 2010, **107**, 044504.
24 E. Yablonovich and G. Cody, *IEEE Trans. Electron Devices*, 1982, **ED-29**, 300.
25 S. Savić Šević and D. Pantelić, *Appl. Opt.*, 2007, **46**, 287.
26 N. Kasoju, N. Hawkins, O. Pop-Georgievski, D. Kubies and F. Vollrath, *Biomater. Sci.*, 2016, **4**, 460.
27 E. Piacentini, D. Shanthana Lakshmi, A. Figoli, E. Drioli and L. Giorno, *J. Membr. Sci.*, 2013, **448**, 190.
28 S. Aruna, P. Binsy, E. Richard and B. Basu, *Appl. Surf. Sci.*, 2012, **258**, 3202.
29 A. Kaya, X. Du, Z. Liu, J. Lu, J. Morris, W. Glasser, T. Heinze and A. Esker, *Biomacromolecules*, 2009, **10**, 2451.
30 Z. Fang, B. Patterson and M. Turner, *Mater. Charact.*, 1993, **31**, 177.
31 H. Davies, *Proc. IEEE*, 1954, **101**, 209.
32 B. Wolf, *Priciples of Optics*, Pergamon, 1980.
33 J. Junesch, T. Sannomiya and A. B. Dahlin, *ACS Nano*, 2012, **6**, 10405.
34 H. Merzendorfer and L. Zimoch, *J. Exp. Biol.*, 2003, **206**, 4393.
35 V. Saranathan, C. O. Osuji, S. G. J. Mochrie, H. Noh, S. Narayanan, A. Sandy, E. R. Dufresne and R. O. Prum, *PNAS*, 2010, **107**, 11676.
36 A. Dinwiddie, R. Null, M. Pizzano, L. Chuong, A. Leigh Krup, H. E. Tan and N. H. Patel, *Dev. Biol.*, 2014, **392**, 404.
37 I. Johnston, B. Gaal, R. Pires das Neves, T. Enver, F. Iborra and N. Jones, *PLoS Comput. Biol.*, 2012, **8**, e1002416.
38 J. Nagel and M. Scarpulla, *Opt. Express*, 2010, **18**, 139.
39 N. Dahan and J. Greffet, *Opt. Express*, 2012, **20**, 530.

Optical and Quantum Electronics (2022) 54:836
https://doi.org/10.1007/s11082-022-04233-2

Internal photo-activation of a dental composite using optical fibers: a holographic, thermographic and Raman study

Evgenije Novta[1] · Tijana Lainović[1] · Dušan Grujić[2] · Svetlana Savić-Šević[2] · Elvira Tóth[3] · Željka Cvejić[3] · Larisa Blažić[1,4]

Received: 15 November 2021 / Accepted: 19 September 2022 / Published online: 22 October 2022
© The Author(s), under exclusive licence to Springer Science+Business Media, LLC, part of Springer Nature 2022

Abstract

The present study aimed to introduce a novel two-step photo-activation protocol of dental resin-based composites (RBC) using optical fibers. The objective was to investigate the effect of the proposed modality on polymerization shrinkage, considered as the main disadvantage of RBCs, by measuring tooth model deformation using real-time digital holographic interferometry (DHI). Simultaneous real-time monitoring of RBC temperature rise was conducted, using infrared thermography (IRT). Degree of conversion was measured at various depths, immediately after curing and after 24 h of dark storage, using Raman spectroscopy. Standardized tooth models made of dental plaster with a class II mesial-occlusal-distal cavity were used as molds for RBC fillings. The proposed two-step curing was designed as follows: in the first step–optical fibers connected to a commercial dental LED curing unit were inserted into the dental filling to cure the RBC from within; in the second step–fibers were extracted, remaining voids were filled with the RBC, and final conventional curing was performed. The final deformation value, defined as the sum of the measured values after the first and second curing step, was significantly lower (on average 36%) compared to conventional curing, as measured by DHI. Meanwhile, no influence of the photo-activation protocol on DC was revealed. IRT was demonstrated as a simple and useful method for coupling with DHI, providing additional essential information on polymerization reaction dynamics.

Keywords Dental composite · Polymerization shrinkage · Degree of conversion · Optical fibers · Digital holography · Infrared thermography

This article is part of the Topical Collection on Photonics: Current Challenges and Emerging Applications.

Guest edited by Jelena Radovanovic, Dragan Indjin, Maja Nesic, Nikola Vukovic and Milena Milosevic.

✉ Evgenije Novta
evgenije.novta@mf.uns.ac.rs

Extended author information available on the last page of the article

1 Introduction

Light-activated dental resin-based composites (RBC) are nowadays most commonly used by dental professionals for direct restorations in clinical practice (Veloso et al. 2019). They are composed of an organic matrix based on methacrylate monomers and inorganic filler particles, bonded by a coupling agent (Schneider et al. 2010). Despite their superior esthetics and improved physical–mechanical characteristics, contemporary RBCs still demonstrate an important limitation: volumetric shrinkage created upon polymerization (typically in the range of 1.5–5%) caused by approximation of monomers (Algamaiah et al. 2021; Par et al. 2020). In addition, photo-polymerization induces temperature rise due to both an exothermic chemical reaction within the material and the radiant heat of the dental light source (Hori et al. 2019).

Clinically, in a confined environment such as a tooth cavity, shrinkage forces are transferred onto cavity walls via adhesive bonding, thereby generating polymerization shrinkage stress (PSS) (Soares et al. 2017). As a result, several negative outcomes may arise, including restoration de-bonding, tooth cusps deflection, marginal discoloration, secondary caries development, and postoperative hypersensitivity (Ferracane and Hilton 2016). However, the magnitude of PSS is not only dependent on the extent of volumetric shrinkage, but also tooth cavity configuration and RBC viscoelastic properties, particularly its flow capacity in the early stages of polymerization and elastic modulus acquisition (Leprince et al. 2013). Before reaching the so-called vitrification point, which depicts the transition from a rubbery to a glassy polymeric state preventing any further extensive reaction (Leprince et al. 2013), rearrangement of the propagating polymer chains by material flow compensates for most of the volumetric shrinkage.

Different strategies have been recommended in an attempt to reduce PSS, such as modifying the RBC chemical composition (Gorsche et al. 2014), clinical placement protocol (Politi et al. 2018), and photo-activation method (Blažić et al. 2011). The conventional photo-activation protocol considers positioning the light guide above and as close as possible to the RBC, thereby minimizing energy loss during light transmission, meanwhile emitting constant irradiance as a function of time (Palin et al. 2018). Instead, modulated curing protocols referred to as soft-start, intermittent light, exponential curing, and pulse-delay mode, modify the irradiance delivered during curing (Münchow et al. 2018).

Among these approaches, soft-start and pulse-delay photo-activation have been shown as most favorable in PSS reduction. Soft-start regards the application of an initial low irradiation intensity followed by final high irradiation (Ilie et al. 2011), whereas pulse-delay mode (similar to soft-start) implies an additional waiting period between the initial low and final high irradiance (Sousa et al. 2021; Tauböck et al. 2014). The basic idea behind these modalities is to delay the onset of the vitrification point in the reaction and allow polymer network formation at a slower rate, with more time for the viscous flow to occur and compensate for the volumetric shrinkage (Leprince et al. 2013).

A new generation of RBCs with modified chemical composition, bulk-fill RBCs, have been introduced into the market to simplify the restorative procedure since they can be placed into tooth cavities in a single increment of 4–5 mm (Veloso et al. 2019). Furthermore, it is claimed that they produce lower PSS compared to conventional composites (Boaro et al. 2019), meanwhile, other material properties, such as degree of monomer conversion (DC), can be compromised (Alshali et al. 2013; Leprince et al. 2014). DC is an important material feature, highly correlated with its mechanical performance and biocompatibility.

Besides managing light exposure and material chemistry, PSS may also be controlled by modifying the RBC placement protocol (Kwon et al. 2012; McHugh et al. 2017; Politi et al. 2018). The efficacy of a modified two-step incremental layering technique with a dental instrument embedded in the middle of the RBC was proved to be useful in decreasing PSS (Petrovic et al. 2010; Sarcev et al. 2012). By inserting an instrument into the RBC, the volume of the resin was reduced and the singular stress point in the RBC was eliminated.

On the other hand, the idea of "curing from within" was recognized as an ultimate but still unattained goal of dental researchers to overcome RBC drawbacks (Rueggeberg 2011). To the best of our knowledge, this is the first attempt to realize the concept of RBC "internal curing" by using optical fibers embedded in the dental RBC. The examined procedure presents a variation of the soft-start and pulse-delay curing and the aforementioned incremental layering, which are coupled in this study for advanced PSS control.

Based on these considerations, the present study aimed to introduce a novel two-step photo-activation protocol of dental RBCs from within using optical fibers, for reducing polymerization shrinkage. The objective was to investigate the effect of the proposed modality by measuring tooth model deformation using digital holographic interferometry (DHI), while simultaneously monitoring the RBC temperature rise using infrared thermography (IRT). The temperature change was monitored as an indicator of polymerization reaction dynamics. DC was measured at various depths, immediately after curing and after 24 h of dark storage, using Raman spectroscopy. The examined procedure was compared with the conventional photo-activation method. The null hypotheses were: (1) there is no difference in tooth model deformation between the two examined photo-activation protocols; (2) there is no difference between immediate and 24 h post-cure DC for both photo-activation protocols; (3) there is no influence of the photo-activation protocol on DC for all measurement points.

2 Materials and methods

2.1 Sample preparation

An aluminum replica of a biological class II mesial-occlusal-distal (MOD) cavity, with simplified geometry, was produced (Fig. 1). Based on a silicon impression of the replica, standardized models were made of dental plaster (Mega Unistone-M; Megadental GmbH, EN26873/ISO6873, type 4, mint-green). These specimens were further mounted in aluminum blocks using the same dental plaster, providing the mechanical stability of the system required for holography. For ensuring high-contrast interference fringes, models were painted with a silver marker covered with a thin layer of white paint, without influencing the mechanical properties of the tooth model.

Before filling the MOD cavity, a self-etch resin bonding adhesive system (Beauti-Bond®, Shofu, LOT 011,912) was applied following the manufacturer's instructions and cured for 10 s with a commercial dental LED curing unit (SmartLite® IQ™2, Dentsply). The prepared cavity was then restored by bulk filling technique, using a single increment of the selected RBC (Beautifil-Bulk Restorative®, Universal shade, Shofu, LOT 011,933) per cavity. Finally, the sample was fixed in the custom-made DHI setup. The RBC used in the study is composed of an organic matrix based on dimethacrylate monomers, and an inorganic phase based on filler particles–surface reaction type pre-reacted glass-ionomer with

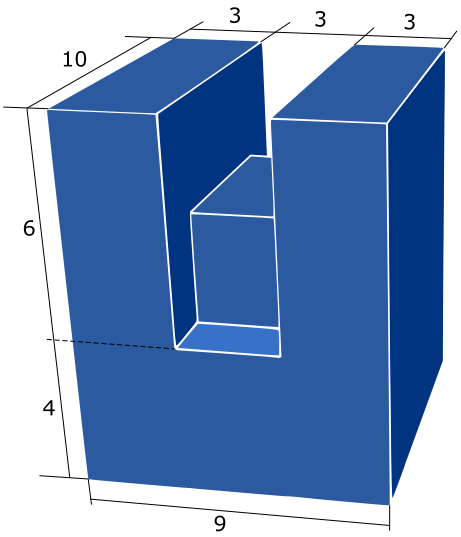

Fig. 1 Graphical representation of the MOD cavity model used. Dimensions are presented in mm

fluoro-aluminosilicate glass (87% weight and 74.5% volume filler load). A precise description of material composition can be found in the literature (Yu et al. 2017).

2.2 Experimental procedure

After fixing the specimens, the polymerization reaction was initiated by one of the two examined photo-activation protocols (Table 1), thereby forming two groups (n = 10 samples per group). In the first group (S), standard curing was performed (continuous 40 s light exposure), with the light guide of the dental LED positioned above the sample, as usually in dental clinical practice. In the second group (F), experimental two-step curing was examined: first step (F1), three optical fibers connected to the same dental LED were

Table 1 Photo-activation and measurement parameters

	Group S	Group F	
Dental LED wavelength	475 nm		
Photo-activation protocol	Standard	Experimental two-step	
		F1	F2
Light guide type	Standard	Three optical fibers	Standard
Light guide diameter	8 mm	1 mm (core)	8 mm
Light guide position	1 mm above the sample	Inside the RBC	1 mm above the sample
Irradiance	600 mW/cm^2	3 × 90 mW/cm^2	600 mW/cm^2
Light exposure	40 s	120 s	40 s
LED re-irradiation	40 s	/	40 s
DHI measurement period	300 s	300 s	300 s
IRT measurement period	180 s (+ 180 s)	180 s	180 s (+ 180 s)

inserted into the dental filling to cure the RBC from within (three consecutive 40 s light exposures); second step (F2), fibers were extracted, remaining voids were filled with the RBC, and final conventional curing (40 s) was performed. Multimode plastic optical fibers were used (1 mm core diameter), approximately 30 cm long, therefore without significant transmission loss of the optical signal at such a short distance. All photo-activation and measurement parameters are summarized in Table 1.

The output irradiance of the dental LED was measured (600 mW/cm^2) using a power meter (Ophir®, Nova II). The output irradiance of each of the three optical fibers custom-connected with the same dental LED was measured as well (90 mW/cm^2), giving 270 mW/cm^2 of integral output irradiance from all three fibers. Such loss of power is due to a much smaller diameter of the fibers (1 mm), compared to the diameter of the standard light guide (8 mm). The fibers were firmly attached to the LED light guide using a custom-built connector. It should be mentioned that two fibers were inserted in each of the proximal cavity boxes filled with the RBC, while the third fiber was embedded in the occlusal part of the RBC filling, for well-directed light distribution. The proximal fibers were inserted up to 2 mm (the occlusal fiber up to 1 mm) from the bottom surface of the cavity.

For providing mechanical stability of the setup, the fibers had to be secured above the sample using a custom-built holder (Fig. 2). Before filling the MOD cavity with the RBC, the position of the fibers inside the cavity was determined, thus enabling easy insertion afterward. Due to their insertion, some excess material leaked from both proximal sides, which was then returned to the cavity using a dental instrument.

2.2.1 Holographic measurements

Real-time non-destructive measurements of tooth model deformation due to PSS were performed in a custom-made DHI setup with a single expanded laser beam and a spherical mirror (Fig. 3). In that manner, observation and illumination of the sample from both sides were enabled, while also generating the reference beam. By generating all the necessary beams from the same input beam, excellent mechanical stability of the setup was obtained, required for the holographic experiment. Solid-state diode-pumped (DPSS), frequency-doubled Nd: Vanadate (Nd: YVO_4) laser was used, providing single-frequency green output (Coherent® Verdi V5, 532 nm, 5 W). The power

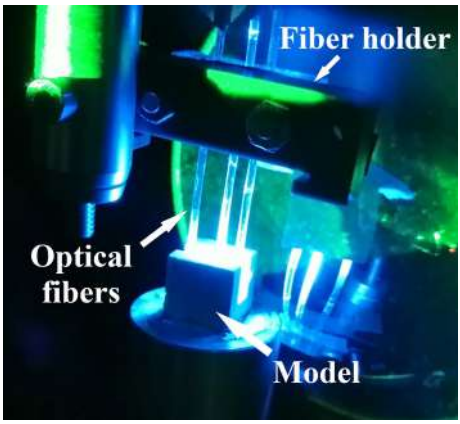

Fig. 2 The sample from group F during the F1 curing step (note that the reflection of the sample could be seen on the right, in the spherical mirror)

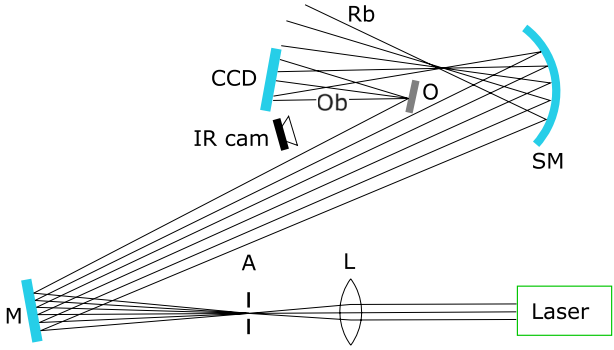

Fig. 3 DHI setup coupled with IRT (L–lens, A–aperture, M–flat mirror, SM–spherical mirror, O–object, Ob–object beam, Rb–reference beam, CCD–charge-coupled device, IR cam–infrared camera)

output of 400 mW was suitable for this experiment, while the linewidth of the laser was less than 5 MHz guaranteeing a highly coherent beam.

A digital single-lens reflex camera (Canon® EOS50d, 15.1 megapixels, 4752 × 3168 image size) recorded the holograms at 10 s intervals for 300 s from the start of every curing step. The obtained images were transferred to a computer and numerically reconstructed by parallel processing on a graphic card (NVidia® GeForce GTX 1060 6 GB) (Pantelić et al. 2014).

2.2.2 Thermographic measurements

An infrared (IR) thermal camera (FLIR®, A65) was positioned on the optical table for simultaneous real-time contactless thermal measurements of the RBC during polymerization. The camera was fixed 8 cm from the tooth model with the proximal cavity surface facing the camera lens, thereby exposing the RBC. Measurement was conducted at a room temperature of 21 ± 1 °C with 40% relative humidity. The object emissivity was established before each measurement. Thermal images were recorded from the start of every curing procedure (in group F during both F1 and F2 steps) for 180 s at a rate of 30 frames per second. The saved recordings were analyzed in the FLIR® Tools program (version 6.4.18039.1003). The temperature data were extracted from points chosen to be closest to the light source. The ambient temperature was then subtracted from the measured values to calculate the temperature rise (ΔT).

Ten minutes after curing (in group S and group F after the F2 step), when the sample reached the ambient temperature, re-irradiation was performed for determining the temperature rise due to LED irradiation (ΔT_i). Namely, during the first LED exposure (in group S and during the F2 step), it was expected that temperature rise occurred due to both heat of the exothermic reaction, and the radiant heat of the dental LED (Atai and Motevasselian 2009). However, during the subsequent exposure, most of the polymerization had already been completed (Kim et al. 2017). Accordingly, the observed temperature rise was predominantly due to irradiation by the dental LED (Hori et al. 2019). Therefore, the difference between the overall heat produced during the first LED exposure (total temperature rise—ΔT_t), and the temperature rise due to LED irradiation alone (ΔT_i), was presented as temperature rise due to the exothermic reaction ($\Delta T_e = \Delta T_t - \Delta T_i$).

2.2.3 Raman spectroscopy measurements

The same tooth models used for DHI and IRT measurements were produced for Raman spectroscopy measurements (n = 5 samples per group). Both examined photo-activation protocols were conducted in the same manner as previously described. Immediately after curing, Raman spectra were collected from three locations: bottom, middle, and top (surface). After a dark storage period of 24 h, the spectra were collected from the same points. Spectra of the uncured RBC were recorded at the start of the experiment.

All spectral acquisitions were conducted with a Raman microscope (Thermo Scientific™ DXR™3) coupled with a 10 × objective. The excitation was a DPSS laser at 780 nm wavelength, and laser power of 24 mW. The exposed sample surface was 3.1 μm, while the acquisition time for each spectrum was 50 times 10 s.

DC was calculated as the ratio of the stretching mode peaks at 1640 cm^{-1} (aliphatic) and 1610 cm^{-1} (aromatic) in the cured and uncured RBC, as previously determined in the literature (Par et al. 2015; Yu et al. 2017), using the following equation:

$$DC(\%) = \left[1 - \frac{R_{cured}}{R_{uncured}}\right] \times 100$$

R is the ratio of intensities of the 1640 cm^{-1} and 1610 cm^{-1} peaks in the spectra of the cured or uncured specimens.

2.3 Statistical analysis

Statistical analysis of the DHI results was performed in Minitab® software (19.2020.1;64-bit) using an independent samples t-test to compare tooth-model deformation between the two examined photo-activation protocols. Statistical analysis of the Raman spectroscopy results was performed in JMP® software (16.2.0). Multivariate repeated-measures analysis of variance (MANOVA) was conducted for analyzing the influence of the photo-activation protocol (method), time, and location on DC. The distribution normality of variables was verified by the Anderson–Darling and Shapiro–Wilk tests. An alpha level of 0.05 was used for all statistical tests.

3 Results

3.1 Tooth model deformation

Tooth model deformation due to PSS was presented as a series of interference lines (fringes) on the resulting DHI images (Figs. 4, 5). The fringes were easily interpreted as sample deformation by multiplying their number by 0.532 μm (wavelength of the laser light source). The deformation as a function of time is shown in Fig. 6. For a better interpretation of the results, deformation in group F was graphically presented as a continuous curve, although there was an actual time delay between the F1 and F2 steps.

In the experimental group F, an average deformation of 2.2 μm and 6.9 μm was detected at the end of the F1 and F2 curing steps, respectively. The final deformation, defined as the sum of the measured values after the F1 and F2 steps, was 9.1 μm ± 0.9 (mean value

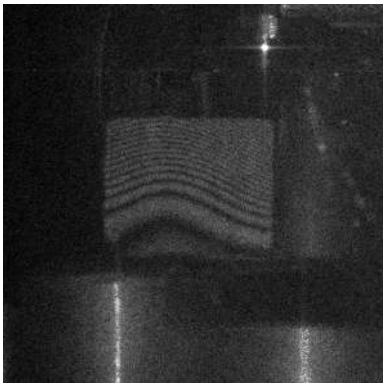

Fig. 4 The interference pattern at the end of the measurement period in the control group S. Total number of fringes = 23

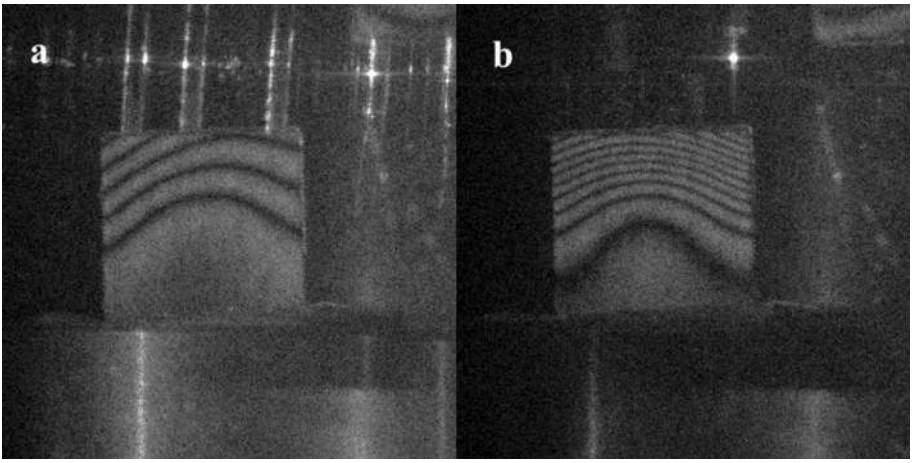

Fig. 5 The interference patterns in the experimental group F, at the end of the measurement period in: **a** F1 step, **b** F2 step. Total number of fringes (F1 + F2) = 15

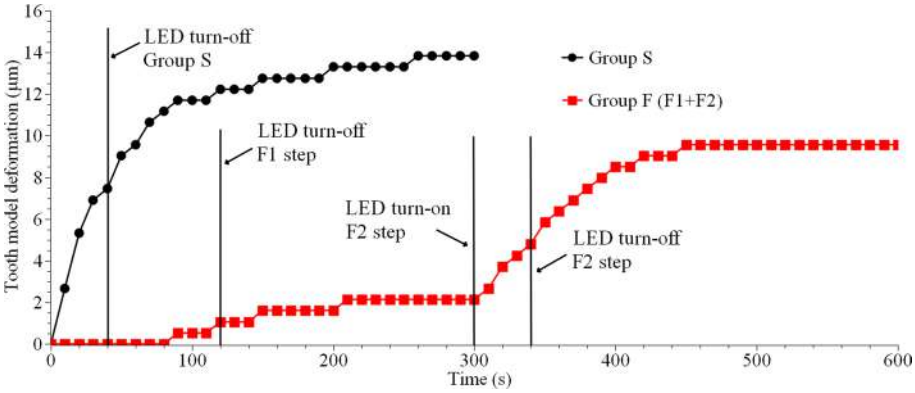

Fig. 6 Tooth model deformation (μm) as a function of time. Average deformation in the control group S (ellipse) and the experimental group F (rectangle). LED turn-on for group S and the F1 step is at the starting point of the graph

Table 2 The final deformation value–descriptive statistics (n–sample size, SD–standard deviation)

Variable	n	Mean (μm)	SD	Minimum (μm)	Median (μm)	Maximum (μm)
Group S	10	14.311	0.920	12.236	14.630	15.428
Group F	10	9.150	0.897	7.980	8.778	10.640
F1 step	10	2.181	0.811	0.532	2.128	3.192
F2 step	10	6.969	1.106	4.788	6.916	8.512

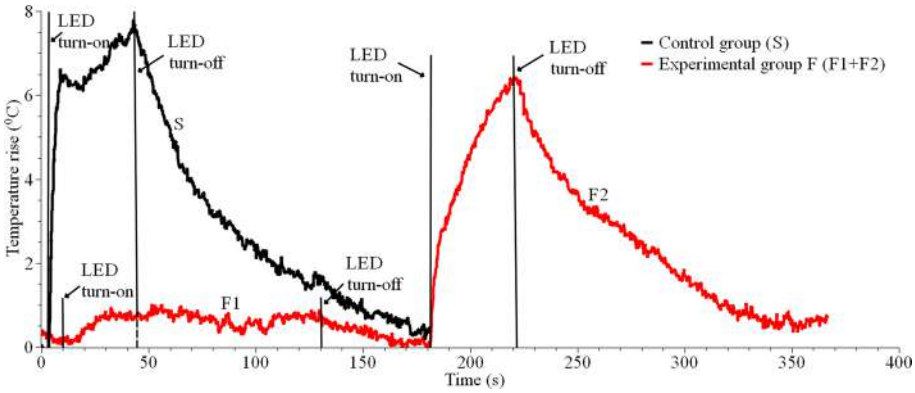

Fig. 7 Temperature rise of the RBC as a function of time. Control group S–black, experimental group F (F1 + F2 step)–red. Note that there was an actual time delay between the F1 and F2 step

(M) ± standard deviation (SD)). The results of the student's t-test presented that it was significantly lower ($t(18) = 12.7$, $p = 0.00$) compared to the control group S (M = 14.3 μm, SD = 0.9). On average, the final deformation in group F was 36% lower compared to group S. Anderson–Darling test showed that data from both group S (Anderson–Darling value (AD) = 0.6, $p = 0.07$) and group F (AD = 0.6, $p = 0.12$) followed a normal distribution. Table 2 summarizes the results of descriptive statistics.

3.2 The temperature rise of the RBC

Graphical representations of RBC temperature rise in group S and group F are shown in Fig. 7. In the control group S, the total temperature rise presented two peaks. It was assumed that the first peak was produced mostly due to the heat of the exothermic reaction, whereas the second peak was predominantly due to additional heating of LED irradiation itself. This was confirmed after calculating ΔT_e (Fig. 8). On the other hand, in the experimental group F during the F1 curing step using optical fibers, only a slight temperature increase was measured throughout the whole photo-activation period. This temperature rise was related to the start of the exothermic reaction. However, during the F2 step, it was assumed that the observed temperature rise included both an exothermic chemical reaction, and the heat of LED irradiation. It was expected that this temperature rise was mainly caused by LED heating, which was confirmed by calculating ΔT_e (Fig. 9).

ΔT_t, ΔT_i, and the calculated ΔT_e ($\Delta T_e = \Delta T_t - \Delta T_i$) in group S are shown in Fig. 8. Considering that the peak of ΔT_e coincides in time with the first peak of ΔT_t, it was

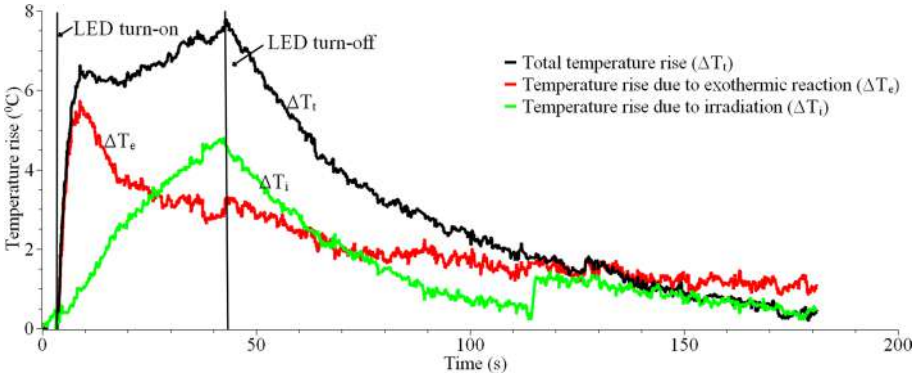

Fig. 8 Temperature rise profiles in the control group S. Total temperature rise (ΔT_t)–black, temperature rise due to irradiation (ΔT_i)–green, temperature rise due to exothermic reaction (ΔT_e)–red

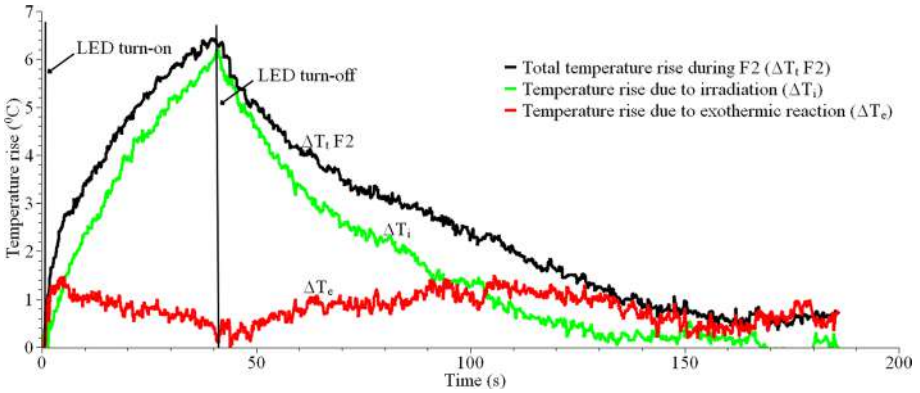

Fig. 9 Temperature rise profiles in the experimental group F. Total temperature rise during the F2 step (ΔT_t F2)–black, temperature rise due to irradiation (ΔT_i)–green, temperature rise due to exothermic reaction (ΔT_e)–red

confirmed that this peak was caused mainly due to the maximum exothermic reaction temperature rise. The time to reach the maximum ΔT_e was 5 s, which could be an approximation of the vitrification point in the reaction. The abrupt temperature increase observed during ΔT_i, was due to automatic IR camera calibration.

Total temperature rise during the F2 step (ΔT_t F2), temperature rise during re-irradiation after the F2 step (ΔT_i), and the calculated ΔT_e ($\Delta T_e = \Delta T_t$ F2 $- \Delta T_i$) are shown in Fig. 9. ΔT_e indicated temperature rise at the beginning of photo-activation caused by an exothermic reaction. In addition, it was observed that the exothermic reaction continued to progress even after finishing photo-activation. On the other hand, ΔT_i presented a constant and gradual temperature increase until the end of LED exposure, implying that no additional exothermic heat was produced. Accordingly, if the start of the F1 step was considered as the starting point of the polymerization reaction, which had continued to progress during the F2 step, the time to reach the maximum ΔT_e in group F was prolonged compared to group S.

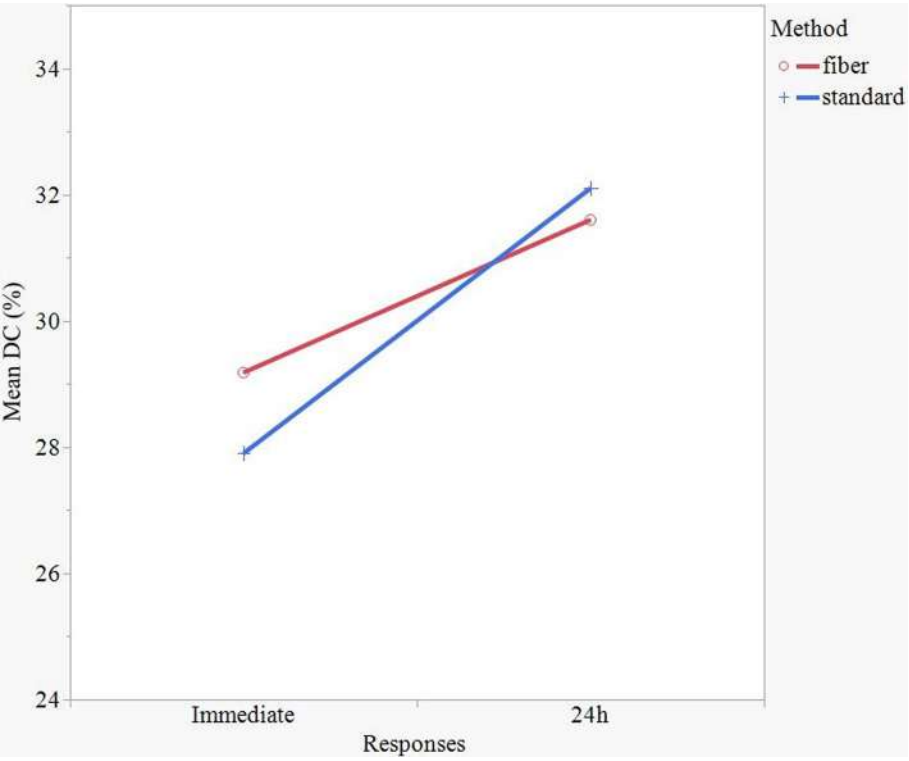

Fig. 10 Mean DC (%) for the two photo-activation protocols (methods) at two time points (immediate and 24 h post-cure). Blue–standard curing mode, red–optical fiber curing mode

Table 3 Mean immediate degree of conversion—DC (%), with the results of the post-hoc Tukey test, for the standard and the optical fiber curing mode at the three measured locations. Levels not connected by same letter are significantly different

Level				Mean immediate DC (%)
Fiber–top	A			32,44
Standard–top	A	B		31,22
Standard–middle	A	B		28,70
Fiber–middle	A	B	C	27,90
Standard–bottom		B	C	27,20
Fiber–bottom			C	23,78

3.3 Degree of conversion

Statistical analysis revealed a significant increase in DC after 24 h of dark storage for both photo-activation protocols ($F(1,24) = 5.073$, $p = 0.033$) as illustrated in Fig. 10. Further analysis revealed no significant influence of the photo-activation protocol (method) on DC for all three locations ($F(2,24) = 1.643$, $p = 0.214$). Mean immediate DC values are presented in Table 3 (with the results of the post-hoc Tukey test) and

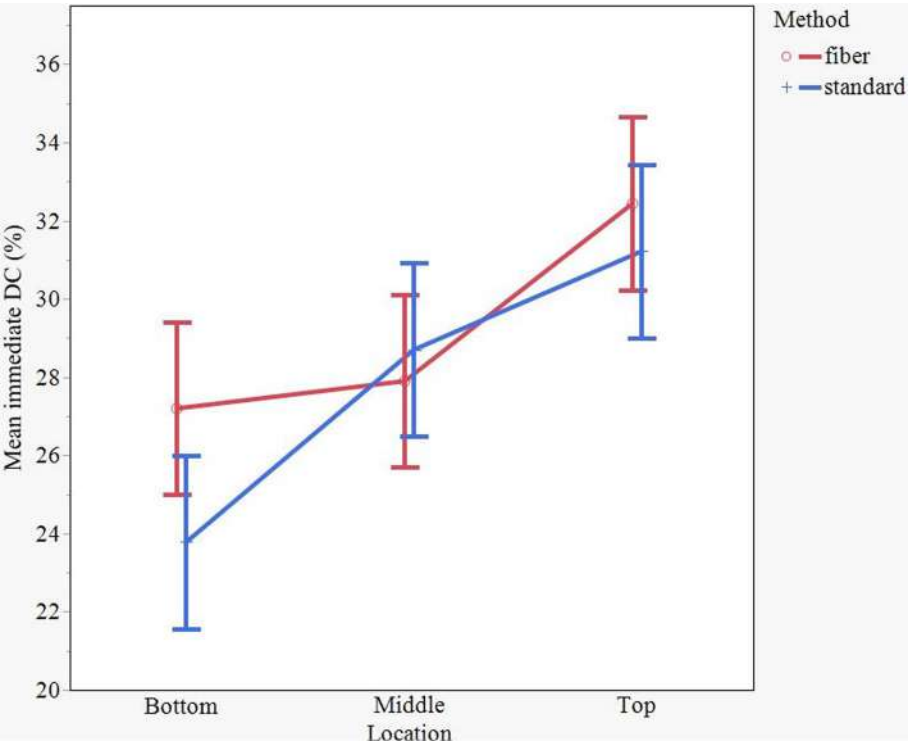

Fig. 11 Mean immediate DC (%) with standard error (95% confidence interval), at the three measured locations (bottom, middle, top). Blue–standard curing mode, red–optical fiber curing mode

Fig. 11. Mean 24 h post-cure DC values are presented in Table 4 (with the results of the post-hoc Tukey test) and Fig. 12.

4 Discussion

Various strategies, including modulated photo-activation regimes (i.e. soft-start, pulse-delay), have been developed to delay the onset of the vitrification point and thereby reduce polymerization shrinkage and the following PSS (Münchow et al. 2018). This can be

Table 4 Mean 24 h post-cure degree of conversion—DC (%) with the results of the post-hoc Tukey test, for the standard and the optical fiber curing mode at the three measured locations. Levels not connected by same letter are significantly different

Level			Mean 24 h post-cure DC (%)
Fiber–top	A		35,48
Standard–top	A		34,16
Standard–middle	A	B	33,22
Fiber–middle	A	B	30,76
Standard–bottom		B	28,92
Fiber–bottom		B	28,56

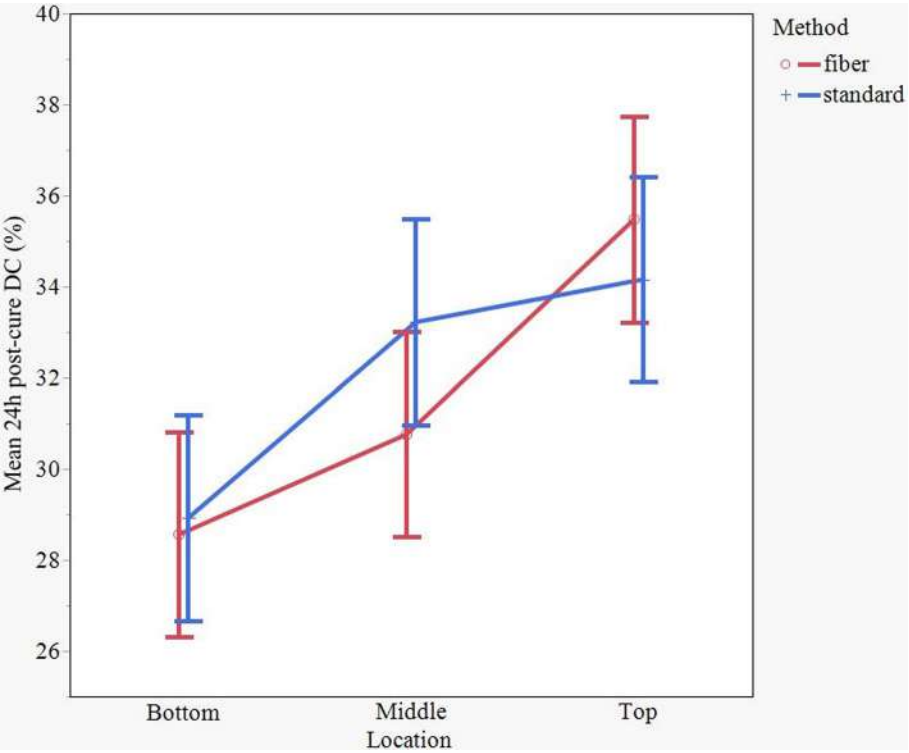

Fig. 12 Mean 24 h post-cure DC (%) with standard error (95% confidence interval), at the three measured locations (bottom, middle, top). Blue–standard curing mode, red–optical fiber curing mode

achieved by initiating the polymerization reaction at a slow rate. In this regard, a novel two-step photo-activation protocol using optical fibers was designed for our study.

The effect of the proposed modality on polymerization shrinkage was evaluated by measuring tooth model deformation using real-time DHI since it has been previously reported as an efficient method in the field (Campos et al. 2014; Novta et al. 2021; Tarle et al. 2006). Meanwhile, IRT as a real-time and non-destructive method as well, was used for simultaneous measurements of RBC temperature change and monitoring of polymerization reaction dynamics. Considering that the polymerization reaction is exothermic, ΔT_e is expected to follow the polymerization reaction pattern (Atai and Motevasselian 2009). To the best of our knowledge, this is the first application of DHI and IRT for parallel examination of polymerization shrinkage and dynamics in the field of dental biomaterials.

The comparison of the overall model deformation in the experimental group F and the control group S, showed a significant deformation decrease (on average 36%) by using the proposed two-step photo-activation method, as measured by DHI. Hence, the first null hypothesis that there is no difference in tooth model deformation between the two examined photo-activation protocols was rejected. This was related to the slow initial polymerization rate in group F, demonstrated by both real-time DHI and IRT. During the first curing step using optical fibers (F1), the DHI results presented sample deformation due to PSS and thus the start of the polymerization reaction (Figs. 5a, 6). During the second curing step (F2), an additional increase in sample deformation was observed (around 75% of overall deformation). Accordingly, this has

indicated that a larger part of the polymerization was completed at this stage, as expected in the pulse-delay curing mode with low initial pulse irradiance (Dewaele et al. 2009). However, in group S a rapid increase in deformation was measured from the beginning of curing (Fig. 6). The DHI results presented that during the photo-activation period (40 s), around 50% of final deformation had already occurred in this group.

Meanwhile, by direct insight into RBC temperature change, IRT presented a precise indication of the polymerization reaction dynamics in both groups. By calculating ΔT_e ($\Delta T_e = \Delta T_t - \Delta T_i$) in the control group S, the time to reach the maximum ΔT_e which was 5 s (Fig. 8), presented an estimation of the well-known vitrification point (Atai and Motevasselian 2009). ΔT_e confirmed that the first peak of ΔT_t was mostly caused by the maximum exothermic reaction temperature rise, while the second peak was produced due to the heat of LED irradiation since light exposure had continued up to 40 s.

On the other hand, in the experimental group F, after an initial slight temperature increase during the F1 step (Fig. 7), suggesting the start of the polymerization reaction, a rapid temperature increase was measured at the beginning of the F2 step, implying further propagation of the polymerization reaction. Indeed, ΔT_e ($\Delta T_e = \Delta T_t$ F2 $- \Delta T_i$) confirmed the occurrence of an exothermic reaction at this stage (Fig. 9). However, the time to reach the maximum ΔT_e was difficult for precise determination, since the exothermic reaction was initiated during the F1 step, and continued to slowly propagate during and upon completing the F2 step (Fig. 9). Based on these considerations, it can be concluded that the time to reach the maximum ΔT_e was prolonged compared to group S, implying modified polymerization reaction dynamics in group F. Further propagation of the exothermic reaction after finishing photo-activation was in agreement with the DHI results in our study (Fig. 6) since tooth model deformation was observed during this period. Moreover, this finding was demonstrated by the results of previous studies as well (Blažić et al. 2011; Germscheid et al. 2018; Novta et al. 2021).

Although the slow initial polymerization rate was observed using DHI as well (Fig. 6), it should be noted that DHI monitored the secondary manifestation of PSS. Therefore, it should not be considered as a precise indicator of the polymerization reaction dynamics, but rather a method for overall comparison of model deformation. Nonetheless, IRT is limited to surface temperature change measurements only, and for monitoring temperature changes within the material, it needs to be supplemented with thermocouple measurement (Kim et al. 2017).

Additionally, based on the results of Raman spectroscopy measurements, the second null hypothesis that there is no difference between immediate and 24 h post-cure DC for both photo-activation protocols was rejected. Meanwhile, the third hypothesis that there is no influence of the photo-activation protocol on DC for all measurement points was accepted. Therefore, it was presented that the PSS reduction was not due to a lower DC, as claimed in several previous studies (Dewaele et al. 2009; Feitosa et al. 2012), but rather a slow initial polymerization rate as demonstrated by the results of real-time DHI and IRT. Furthermore, the reported DC results indicate similar mechanical properties of the RBCs cured by both photo-activation protocols, since DC is considered one of the main factors in determining material mechanical properties (Alshali et al. 2013; Rosatto et al. 2015). Finally, the low DC values in our study concurred with the findings of previous works exploring the same material (Al-ahdal et al. 2015; Ilie & Fleming 2015; Yu et al. 2017), although the DC results obtained in our study were even lower (23.8–32.4%, compared to 38.9–46%). This was attributed to the longer exposure time with low irradiance employed in our experiment, leading to a higher concentration of trapped free radicals (Leprince et al. 2010). Nevertheless, the overall low DC values for Beautifil-Bulk Restorative® compared to other RBCs were associated with its specific chemical composition (surface pre-reacted glass-ionomer (S-PRG) filler) and relatively high filler content (87% weight).

Noteworthy, several studies have reported PSS reduction due to instrument insertion into the center of the RBC (Petrovic et al. 2010; Sarcev et al. 2012). Thus, a mathematical model is needed for describing stress distribution in the material and the surrounding tooth structure during the proposed photo-activation strategy in our study. Although the mechanical properties of human teeth components are well-known, it is still difficult to predict their biomechanical behavior without a complex numerical analysis (Ausiello et al. 2020). The knowledge of stress distribution in teeth restored using the proposed modality, is essential to prevent post-restorative problems.

On the other hand, it was reported that above a certain radiant exposure, the increase in material mechanical properties saturates (Leprince et al. 2013). Accordingly, there is a practical limit to the value of irradiance that can be effectively used with any RBC (Musanje & Darvell 2003). Above this limit, the photosensitizer system saturates and no further improvement in the rate of polymerization initiation is possible. Therefore, similar DC results observed for the two photo-activation protocols suggest this saturation. Additional examination with Brillouin spectroscopy could contribute to the presented research by real-time monitoring of viscoelastic changes during cross-linking of polymers of each part of the examined biomechanical system.

As a first attempt of realizing the idea referred to as "curing from within" (Rueggeberg 2011), to reduce dental RBC polymerization shrinkage, the present study was designed as a proof of the concept. Hence, tooth models made of dental plaster with simplified geometry were produced, for enabling reliable comparison between the two photo-activation protocols. Moreover, only one type of dental RBC was tested in the study, while it was previously highlighted that the effect of light-curing protocols on PSS is material-dependent as well (Tauböck et al. 2014). Further examination of various types of RBC and employing models more precisely imitating tooth tissue, will be a topic of another interesting study.

Utilizing the presented photo-activation protocol, several advantages have been achieved compared with conventional curing. First of all, in this manner light was transmitted directly into the deeper layers of the material, thereby avoiding substantial light loss (80–90%) throughout increasing depth (Palin et al. 2018). Secondly, with the low output irradiance of the fibers, a slow initial polymerization rate was provided. Finally, by inserting the optical fibers into the material, the volume of the resin was reduced, potentially influencing additional PSS decrease.

As a final remark, one might find this approach tedious and time-consuming for clinical application. However, considering that a regular dental restorative procedure takes about 30 min, additional 3 min for performing the proposed two-step photo-activation does not represent a significant increase compared to the benefit of PSS reduction obtained. Still, it should be noted that problems with pulling out the fibers may occur, which can be avoided by cleaning them with alcohol (70% ethanol) from left-over RBC (it was waited for the alcohol to dry out before the next insertion). Further adjustments to the method are necessary before any potential clinical application.

5 Conclusion

Within the limitations of this study, it can be concluded that the proposed two-step internal photo-activation of the RBC, using optical fibers, reduced tooth model deformation significantly (on average 36%) compared to conventional curing. Meanwhile, no influence of the photo-activation protocol on DC was revealed. Real-time IRT was presented as a simple

and useful method for coupling with DHI, providing additional essential information on polymerization reaction dynamics.

Acknowledgements The authors would like to thank Dejan Pantelić, PhD (Institute of Physics Belgrade) for providing valuable guidelines and advice throughout the whole experiment, as well as Ognjan Lužanin, PhD (Faculty of Technical Sciences, University of Novi Sad) for the help with the statistical analysis. The authors also want to thank Mikodental Dental depo (distributers of Shofu®—Japan dental products in Serbia) for providing the research material. The study was supported by the Ministry of Education, Science and Technological Development of the Republic of Serbia (Contract No. NIO 200114).

Author contributions All authors contributed to the study's conception and design. Material preparation, experimental work, data collection, and analysis were performed by EN, TL, DG, SSS, ET, ŽC, and LB. The first draft of the manuscript was written by EN and all authors commented on previous versions of the manuscript. All authors read and approved the final manuscript.

Funding This study was supported by the Ministry of Education, Science and Technological Development of the Republic of Serbia (contract No. NIO 200114) and Mikodental Dental depo (distributers of Shofu® (Japan) dental products in Serbia).

Data availability The datasets generated during and/or analyzed during the current study are available from the corresponding author upon reasonable request.

Code availability The software application supports the presented results and complies with the field standards.

Declarations

Conflict of interest The authors declare that they have no conflict of interest.

References

Al-ahdal, K., Ilie, N., Silikas, N., Watts, D.C.: Polymerization kinetics and impact of post polymerization on the Degree of Conversion of bulk-fill resin-composite at clinically relevant depth. Dent. Mater. **31**(10), 1207–1213 (2015). https://doi.org/10.1016/j.dental.2015.07.004

Algamaiah, H., Silikas, N., Watts, D.C.: Polymerization shrinkage and shrinkage stress development in ultra-rapid photo-polymerized bulk fill resin composites. Dent. Mater. **37**(4), 559–567 (2021). https://doi.org/10.1016/j.dental.2021.02.012

Alshali, R.Z., Silikas, N., Satterthwaite, J.D.: Degree of conversion of bulk-fill compared to conventional resin-composites at two time intervals. Dent. Mater. **29**(9), e213–e217 (2013). https://doi.org/10.1016/j.dental.2013.05.011

Atai, M., Motevasselian, F.: Temperature rise and degree of photopolymerization conversion of nanocomposites and conventional dental composites. Clin. Oral Invest. **13**(3), 309–316 (2009). https://doi.org/10.1007/s00784-008-0236-2

Ausiello, P., Ciaramella, S., De Benedictis, A., Lanzotti, A., Tribst, J.P.M., Watts, D.C.: The use of different adhesive filling material and mass combinations to restore class II cavities under loading and shrinkage effects: a 3D-FEA. Comput. Methods Biomech. Biomed. Engin. (2020). https://doi.org/10.1080/10255842.2020.1836168

Blažić, L., Pantelić, D., Savić-Šević, S., Murić, B., Belić, I., Panić, B.: Modulated photoactivation of composite restoration: Measurement of cuspal movement using holographic interferometry. Lasers Med. Sci. **26**(2), 179–186 (2011). https://doi.org/10.1007/s10103-010-0774-0

Boaro, L.C.C., Lopes, D.P., de Souza, A.S.C., Nakano, E.L., Perez, M.D.A., Pfeifer, C.S., Goncalves, F.: Clinical performance and chemical-physical properties of bulk fill composites resin–a systematic review and meta-analysis. Dent. Mater. **35**(10), e249–e264 (2019). https://doi.org/10.1016/j.dental.2019.07.007

Campos, L.M.P., Parra, D.F., Vasconcelos, M.R., Vaz, M., Monteiro, J.: DH and ESPI laser interferometry applied to the restoration shrinkage assessment. Radiat. Phys. Chem. **94**(1), 190–193 (2014). https://doi.org/10.1016/j.radphyschem.2013.05.051

Dewaele, M., Asmussen, E., Peutzfeldt, A., Munksgaard, E.C., Benetti, A.R., Finné, G., Leloup, G., Devaux, J.: Influence of curing protocol on selected properties of light-curing polymers: degree of conversion, volume contraction, elastic modulus, and glass transition temperature. Dent. Mater. **25**(12), 1576–1584 (2009). https://doi.org/10.1016/j.dental.2009.08.001

dos Sousa, G.S., Guimarães, G.F., Marcelino, E., Rodokas, J.E.P., de Júnior, A.J.O., Cesarino, I., Leão, A.L., dos Riccardi, C.S., Arjmand, M., Simões, R.P.: Shrinkage stress and temperature variation in resin composites cured via different photoactivation methods: insights for standardisation of the photopolymerisation. Polymers **13**(13), 1–14 (2021). https://doi.org/10.3390/polym13132065

Feitosa, V.P., Fugolin, A.P.P., Correr, A.B., Correr-Sobrinho, L., Consani, S., Watson, T.F., Sinhoreti, M.A.C., Sauro, S.: Effects of different photo-polymerization protocols on resin–dentine mTBS, mechanical properties and cross-link density of a nano-filled resin composite. J. Dent. **40**(10), 802–809 (2012). https://doi.org/10.1016/j.jdent.2012.05.014

Ferracane, J.L., Hilton, T.J.: Polymerization stress-Is it clinically meaningful? Dent. Mater. **32**(1), 1–10 (2016). https://doi.org/10.1016/j.dental.2015.06.020

Germscheid, W., de Gorre, L.G., Sullivan, B., O'Neill, C., Price, R.B., Labrie, D.: Post-curing in dental resin-based composites. Dent. Mater. **34**(9), 1367–1377 (2018). https://doi.org/10.1016/j.dental.2018.06.021

Gorsche, C., Griesser, M., Gescheidt, G., Moszner, N., Liska, R.: β-allyl sulfones as addition-fragmentation chain transfer reagents: a tool for adjusting thermal and mechanical properties of dimethacrylate networks. Macromolecules **47**(21), 7327–7336 (2014). https://doi.org/10.1021/ma501550b

Hori, M., Fujimoto, K., Asakura, M., Nagase, Y., Mieki, A., Kawai, T.: Measurement of exothermic heat released during polymerization of a light- curing composite resin: comparison of light irradiation modes. Dent. Mater. J. **38**(4), 646–653 (2019). https://doi.org/10.4012/dmj.2018-158

Ilie, N., Fleming, G.J.P.: In vitro comparison of polymerisation kinetics and the micro-mechanical properties of low and high viscosity giomers and RBC materials. J. Dent. **43**(7), 814–822 (2015). https://doi.org/10.1016/j.jdent.2015.04.009

Ilie, N., Jelen, E., Hickel, R.: Is the soft-start polymerisation concept still relevant for modern curing units? Clin. Oral Invest. **15**(1), 21–29 (2011). https://doi.org/10.1007/s00784-009-0354-5

Kim, M., Kim, R.J., Ferracane, J., Lee, I.: Thermographic analysis of the effect of composite type, layering method, and curing light on the temperature rise of photo-cured composites in tooth cavities. Dent. Mater. **33**(10), e373–e383 (2017). https://doi.org/10.1016/j.dental.2017.07.007

Kwon, Y., Ferracane, J., Lee, I.B.: Effect of layering methods, composite type, and flowable liner on the polymerization shrinkage stress of light cured composites. Dent. Mater. **28**(7), 801–809 (2012). https://doi.org/10.1016/j.dental.2012.04.028

Leprince, J.G., Lamblin, G., Devaux, J., Dewaele, M., Mestdagh, M., Palin, W.M., Gallez, B., Leloup, G.: Irradiation modes' impact on radical entrapment in photoactive resins. J. Dent. Res. **89**(12), 1494–1498 (2010). https://doi.org/10.1177/0022034510384624

Leprince, J.G., Palin, W.M., Hadis, M.A., Devaux, J., Leloup, G.: Progress in dimethacrylate-based dental composite technology and curing efficiency. Dent. Mater. **29**(2), 139–156 (2013). https://doi.org/10.1016/j.dental.2012.11.005

Leprince, J.G., Palin, W.M., Vanacker, J., Sabbagh, J., Devaux, J., Leloup, G.: Physico-mechanical characteristics of commercially available bulk-fill composites. J. Dent. **42**(8), 993–1000 (2014). https://doi.org/10.1016/j.jdent.2014.05.009

McHugh, L.E.J., Politi, I., Al-Fodeh, R.S., Fleming, G.J.P.: Implications of resin-based composite (RBC) restoration on cuspal deflection and microleakage score in molar teeth: placement protocol and restorative material. Dent. Mater. **33**(9), e329–e335 (2017). https://doi.org/10.1016/j.dental.2017.06.001

Münchow, E.A., Meereis, C.T.W., de Oliveira Rosa, W.L., da Silva, A.F., Piva, E.: Polymerization shrinkage stress of resin-based dental materials: a systematic review and meta-analyses of technique protocol and photo-activation strategies. J. Mech. Behav. Biomed. Mater. **82**, 77–86 (2018). https://doi.org/10.1016/j.jmbbm.2018.03.004

Musanje, L., Darvell, B.W.: Polymerization of resin composite restorative materials: exposure reciprocity. Dent. Mater. **19**(6), 531–541 (2003). https://doi.org/10.1016/S0109-5641(02)00101-X

Novta, E., Lainović, T., Grujić, D., Pantelić, D., Blažić, L.: Cuspal deflection caused by dental composite polymerization shrinkage analyzed by digital holography. Vojnosanitetski Pregled. Online Fir. (2021). https://doi.org/10.2298/VSP210603081N

Palin, W.M., Leprince, J.G., Hadis, M.A.: Shining a light on high volume photocurable materials. Dent. Mater. **34**(5), 695–710 (2018). https://doi.org/10.1016/j.dental.2018.02.009

Pantelic, D.V., Grujic, D.Ž, Vasiljevic, D.M.: Single-beam, dual-view digital holographic interferometry for biomechanical strain measurements of biological objects. J. Biomed. Opt. **19**(12), 127005 (2014). https://doi.org/10.1117/1.JBO.19.12.127005

Par, M., Gamulin, O., Marovic, D., Klaric, E., Tarle, Z.: Raman spectroscopic assessment of degree of conversion of bulk-fill resin composites-changes at 24 hours post cure. Oper. Dent. **40**(3), E92–E101 (2015). https://doi.org/10.2341/14-091-L

Par, M., Marovic, D., Attin, T., Tarle, Z., Tauböck, T.T.: Effect of rapid high-intensity light-curing on polymerization shrinkage properties of conventional and bulk-fill composites. J. Dent. **101**, 103448 (2020). https://doi.org/10.1016/j.jdent.2020.103448

Petrovic, L.M., Drobac, M.R., Stojanac, I.L., Atanackovic, T.M.: A method of improving marginal adaptation by elimination of singular stress point in composite restorations during resin photo-polymerization. Dent. Mater. **26**(5), 449–455 (2010). https://doi.org/10.1016/j.dental.2009.11.160

Politi, I., McHugh, L.E.J., Al-Fodeh, R.S., Fleming, G.J.P.: Modification of the restoration protocol for resin-based composite (RBC) restoratives (conventional and bulk fill) on cuspal movement and microleakage score in molar teeth. Dent. Mater. **34**(9), 1271–1277 (2018). https://doi.org/10.1016/j.dental.2018.05.010

Rosatto, C.M.P., Bicalho, A.A., Veríssimo, C., Bragança, G.F., Rodrigues, M.P., Tantbirojn, D., Versluis, A., Soares, C.J.: Mechanical properties, shrinkage stress, cuspal strain and fracture resistance of molars restored with bulk-fill composites and incremental filling technique. J. Dent. **43**(12), 1519–1528 (2015). https://doi.org/10.1016/j.jdent.2015.09.007

Rueggeberg, F.A.: State-of-the-art : dental photocuring–a review. Dent. Mater. **27**(1), 39–52 (2011). https://doi.org/10.1016/j.dental.2010.10.021

Sarcev, I.N., Petronijevic, B.S., Atanackovic, T.M.: A biomechanical model for a new incremental technique for tooth restoration. Acta Bioeng. Biomech. **14**(3), 85–91 (2012). https://doi.org/10.5277/abb120312

Schneider, L.F.J., Cavalcante, L.M., Silikas, N.: Shrinkage stresses generated during resin-composite applications: a review. J. Dent. Biomech. **1**(1), 1–14 (2010). https://doi.org/10.4061/2010/131630

Soares, C.J., Faria-E-Silva, A.L., de Rodrigues, M.P., FernandesVilela, A.B., Pfeifer, C.S., Tantbirojn, D., Versluis, A.: Polymerization shrinkage stress of composite resins and resin cements - What do we need to know? Braz. Oral Res. **31**, 49–63 (2017). https://doi.org/10.1590/1807-3107BOR-2017.vol31.0062

Tarle, Z., Knezevic, A., Demoli, N., Meniga, A., Sutalo, J., Unterbrink, G., Ristic, M., Pichler, G.: Comparison of composite curing parameters: effects of light source and curing mode on conversion, temperature rise and polymerization shrinkage. Oper. Dent. **31**(2), 219–226 (2006). https://doi.org/10.2341/05-15

Tauböck, T.T., Feilzer, A.J., Buchalla, W., Kleverlaan, C.J., Krejci, I., Attin, T.: Effect of modulated photoactivation on polymerization shrinkage behavior of dental restorative resin composites. Eur. J. Oral Sci. **122**(4), 293–302 (2014). https://doi.org/10.1111/eos.12139

Veloso, S.R.M., Lemos, C.A.A., de Moraes, S.L.D., do Vasconcelos, B.C.E., Pellizzer, E.P., de Monteiro, G.Q.M.: Clinical performance of bulk-fill and conventional resin composite restorations in posterior teeth: a systematic review and meta-analysis. Clin. Oral Investig. **23**, 221–233 (2019). https://doi.org/10.1007/s00784-018-2429-7

Yu, P., Yap, A.U.J., Wang, X.Y.: Degree of conversion and polymerization shrinkage of bulk-fill resin-based composites. Oper. Dent. **42**(1), 82–89 (2017). https://doi.org/10.2341/16-027-L

Publisher's Note Springer Nature remains neutral with regard to jurisdictional claims in published maps and institutional affiliations.

Springer Nature or its licensor holds exclusive rights to this article under a publishing agreement with the author(s) or other rightsholder(s); author self-archiving of the accepted manuscript version of this article is solely governed by the terms of such publishing agreement and applicable law.

Authors and Affiliations

Evgenije Novta[1] · Tijana Lainović[1] · Dušan Grujić[2] · Svetlana Savić-Šević[2] · Elvira Tóth[3] · Željka Cvejić[3] · Larisa Blažić[1,4]

[1] Faculty of Medicine, School of Dental Medicine, University of Novi Sad, Novi Sad, Serbia

[2] Institute of Physics, University of Belgrade, Belgrade, Serbia

[3] Department of Physics, Faculty of Sciences, University of Novi Sad, Novi Sad, Serbia

[4] Dental Clinic of Vojvodina, Novi Sad, Serbia

Journal of Dentistry 145 (2024) 104998

Contents lists available at ScienceDirect

Journal of Dentistry

journal homepage: www.elsevier.com/locate/jdent

Impact of optical fiber-based photo-activation on dental composite polymerization

Evgenije Novta [a,*], Dejan Pantelić [b], Larisa Blažić [a,c], Elvira Tóth [d], Željka Cvejić [d], Dušan Grujić [b], Svetlana Savić-Šević [b], Tijana Lainović [a]

[a] University of Novi Sad, Faculty of Medicine, School of Dental Medicine, Hajduk Veljkova 12, Novi Sad, Serbia
[b] University of Belgrade, Institute of Physics, Pregrevica 118, Belgrade, Serbia
[c] Dental clinic of Vojvodina, Hajduk Veljkova 12, Novi Sad, Serbia
[d] University of Novi Sad, Faculty of Sciences, Department of Physics, Trg Dositeja Obradovića 3, Novi Sad, Serbia

ARTICLE INFO

Keywords:
Bulk-fill dental composite
Optical fibers
Curing protocol
Polymerization shrinkage stress
Temperature change
Degree of conversion

ABSTRACT

Objectives: The study aimed to introduce a novel two-step optical fiber-based photo-activation of dental resin-based composites (RBCs) for reducing polymerization shrinkage stress (PSS).
Methods: Proposed protocol design – in the first step, two flexible plastic optical fibers connected to a dental light curing unit (LCU), were used as light guides inserted into the filling to initiate low-irradiance polymerization from within; in the second step, fibers were extracted and remaining voids were filled with RBC, followed by conventional high-irradiance curing to finalize polymerization. Three bulk-fill RBCs were tested (Beautifil-Bulk Restorative, Filtek Bulk-fill Posterior, Tetric PowerFill) using tooth cavity models. Three non-invasive examination techniques were employed: Digital Holographic Interferometry, Infrared Thermography, and Raman spectroscopy for monitoring model deformation, RBC temperature change, and degree of conversion (DC), respectively. A control group (for each examined RBC) underwent conventional photo-activation.
Results: The experimental protocol significantly reduced model deformation by 15 – 35 %, accompanied by an 18 – 54 % reduction in RBC temperature change, emphasizing the impact of thermal shrinkage on PSS. Real-time measurements of deformation and temperature provided indirect insights into reaction dynamics and illuminated potential mechanisms underlying PSS reduction. After a 24-hour dark-storage period, DC outcomes comparable to conventional curing were observed, affirming the clinical applicability of the method.
Conclusions: Protocol involving the use of two 1.5 mm fibers in the first step (300 mW/cm^2 x 10 s), followed by a second conventional curing step (1000 mW/cm^2 x 10 s), is recommended to achieve the desired PSS reduction, while maintaining adequate DC and ensuring efficient clinical application.
Clinical Significance: Obtained PSS reduction offers promise in potentially improving the performance of composite restorations. Additionally, leveraging the flexibility of optical fibers improves light guide approach for restorations on posterior teeth. Meanwhile, implementation in clinical practice is easily achievable by coupling the fibers with commercial dental LCUs using the provided plastic adapter.

1. Introduction

In contemporary dental clinical practice, conventional photo-activation of resin-based composite (RBC) materials involves continuous light exposure for a specified duration, dependent on light irradiance [1]. A standard protocol utilizes a rigid light guide probe of the light curing unit (LCU) strategically positioned directly above the restoration. The goal is to achieve optimal polymerization through sufficient light transmission by maintaining proximity and a perpendicular orientation to the material surface [2]. Meanwhile, modern RBCs commonly referred to as "bulk-fills" have been specifically engineered for deep cavity restoration in a single layer up to 5 mm in thickness [3]. This design capitalizes on heightened translucency [4] and an improved refractive index match between the organic and inorganic phases [5], facilitating ample light transmittance throughout increasing depth. Nevertheless, the challenge arises from the inevitable light loss (up to 80–90 % irradiance reduction) attributed to scattering and attenuation [6]. Consequently, the concept of "curing from within"

* Correspondence author.
E-mail address: evgenije.novta@mf.uns.ac.rs (E. Novta).

https://doi.org/10.1016/j.jdent.2024.104998
Received 23 February 2024; Received in revised form 4 April 2024; Accepted 16 April 2024
Available online 16 April 2024
0300-5712/© 2024 Elsevier Ltd. All rights reserved.

has been acknowledged as the ultimate, but still unattained objective for dental applications [7].

At the same time, volumetric shrinkage accompanying polymer chain formation leads to undesired polymerization shrinkage stress (PSS), which is considered detrimental to RBC performance [8]. Therefore, various strategies have been proposed to mitigate PSS, including the incremental RBC insertion technique, modified photo-activation protocols (e.g., soft-start or pulse-delay), and modern self-curing bulk-fill RBCs [9]. By placing the material in smaller increments, each up to 2 mm thickness, and decreasing the ratio of bonded to unbonded surfaces (known as C-factor), the constraint imposed on RBC shrinkage is reduced, allowing a certain amount of flow to partially dissipate the PSS [10]. Another modified insertion technique for PSS reduction involves embedding a dental instrument in the middle of the restoration during photo-activation, resulting in improved marginal adaptation by reducing the volume of the RBC that is polymerized at each step and eliminating stress singular point in the RBC [11,12].

On the other hand, alternative photo-activation techniques, collectively termed "soft-start", have been introduced as beneficial for PSS reduction due to a slow curing process activated by low light irradiance. This allows sufficient time for material viscous flow and stress relaxation without compromising polymerization efficiency, i.e., the degree of monomer-to-polymer conversion (DC) [13–16]. Among soft-start protocols, the "pulse-delay" technique has been extensively discussed for its potential ease of clinical adoption [16–19]. Specifically, this technique involves applying a first pulse of light with low irradiance, followed by a delay when the LCU is turned off, and then applying a second pulse of light with high irradiance [20]. However, conflicting claims exist regarding whether the lower PSS observed following soft-start curing techniques is due to a lower resultant DC [21–23]. Nevertheless, a recent study by Palagummi et al. [20], supported the clinical success of the pulse-delay protocol, attributing PSS reduction primarily to lower thermal shrinkage (contraction associated with cooling during post-cure).

The objective of the present study was to address the challenges of contraction stress and light loss at increasing depths during dental composite polymerization by introducing a novel two-step photo-activation protocol. The study involved the examination of three bulk-fill RBCs using tooth cavity models. The deformation of the cavity models, considered a secondary manifestation of PSS, was monitored non-invasively in real-time using Digital Holographic Interferometry (DHI). Concurrently, Infrared Thermography (IRT) was employed for the real-time measurement of RBC temperature change, serving as an indicator of the polymerization reaction dynamics. Additionally, the DC was determined based on the RBC spectra obtained through Raman spectroscopy at two distinct time points: immediately after photo-activation and after 24 h of dark storage. As a control, conventional photo-activation was performed on a separate group of samples, following the manufacturer's instructions. Four null hypotheses were proposed, assuming that the employed photo-activation protocol would have no impact on: (1) Cavity model deformation, (2) RBC temperature change, (3) Immediate DC, and (4) 24 h post-cure DC.

2. Materials and methods

2.1. Materials

Commercial, low-cost, plastic optical fibers made of polymethyl methacrylate (PMMA) were utilized in this study. Due to their advantages in terms of ease of handling, flexibility, and cost-effectiveness, various applications for such fibers have been developed and commercialized to date. These range from simple use as light transmission guides to more complex applications, such as sensors and telecommunication cables [24]. However, it is noteworthy that the authors of this article were the first (to their knowledge) to explore the potential of optical fibers as modulators in the dental RBC photo-activation protocol [25].

In essence, an optical fiber is comprised of a core (with a high refractive index) and a cladding (with a lower refractive index), surrounded by an additional protective cover, as illustrated in Fig. 1. The different refractive indices of the core and cladding, along with the core and cladding diameters, determine light propagation through the fiber core [26]. There are several types of optical fibers depending of intended application – signal transmission, energy delivery, sensing or lasing [26]. However, the fundamental principle of light propagation is based on the total internal reflection, confining light inside the fiber core and thereby promoting waveguiding [27]. In this study, multi-mode large core diameter fibers (1 mm or 1.5 mm), 30 cm in length, were employed to minimize light loss during curing.

A mesial-occlusal-distal cavity (MOD) was prepared on an intact human maxillary premolar tooth, following an established clinical protocol in the literature [28,29]. The cavity preparation employed a dental turbine with water cooling, along with a diamond flat-end fissure bur (835–014C-FG, NTI-Kahla GmbH, Germany), and a fine grit round diamond bur (801–014F-FG, NTI-Kahla GmbH, Germany) to finish and achieve rounded internal cavity angles. A schematic representation of the MOD cavity design, including precise dimensions, is provided in Fig. 2. All procedures involving human material were approved by the appropriate Ethical Board (No. 01–21/8–2021; 09.04.2021).

The study was conducted using tooth cavity models which facilitated reproducible measurements and eliminated the influence of biological variability inherent in natural human teeth. Cavity models were fabricated using a commercial dental composite and a silicon impression of the tooth crown, following methodologies established in previous studies that also utilized composite cavity models [30–32]. A fiber-reinforced bulk-fill composite was used for this purpose (ever-X-Posterior, GC, Japan), chosen for its mechanical characteristics similar to human dentin [33–36] (Table 1). To maximize the degree of conversion (DC), the composite models were irradiated twice the recommended duration and created at least 24 h before the actual experiment.

With the MOD cavity models serving as molds, three bulk-fill RBCs were tested, comprising one giomer and two nano-hybrid composites (Table 2). Prior to RBC insertion, a one-step self-etch bonding technique was employed on the MOD cavity models, utilizing a single-component light-cure adhesive from the same manufacturer as the chosen RBC. The following adhesives were applied: BeautiBond™ by Shofu, Japan (LOT 062,281); 3M™ Single Bond Universal Adhesive by 3 M ESPE, Germany (LOT 663,414); and Adhese® Universal by Ivoclar Vivadent, Liechtenstein (LOT Z000F0). All adhesives were cured using the High-power program of the employed LCU, as detailed in Table 3.

The cavities were restored using the selected RBC with a bulk-filling technique and were divided into two groups based on the employed photo-activation protocol:

(a) Control group – This group underwent one-step conventional photo-activation:

- Light guide of the commercial LCU (Bluephase PowerCure, Ivoclar Vivadent, Schaan, Liechtenstein) was positioned perpendicular to the occlusal surface of the filling at a distance of 1 mm.

Detailed information about the chosen LCU is provided in Table 3. The restored MOD composite samples in the control group were cured following manufacturer's instructions. Material Tetric PowerFill (TPF) due to its specific chemical composition, allowed photo-activation using two different light irradiances and exposure times. Output light irradiance was verified before each photo-activation using the Bluephase PowerCure base. Refer to Table 4 for detailed information on the employed light irradiances and exposure times in all material subgroups.

(b) Experimental group – This group underwent a two-step experimental photo-activation:

- 1st step: Two flexible plastic optical fibers with the same diameter (1 mm or 1.5 mm) were connected to the same commercial LCU (refer to Table 3) and inserted into the filling to initiate polymerization

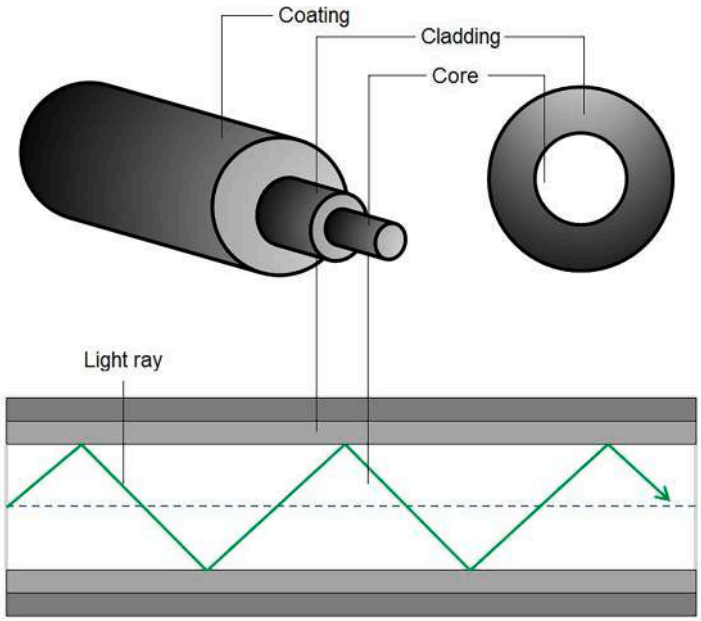

Fig. 1. Schematic representation of the optical fiber and light propagation inside the fiber core.

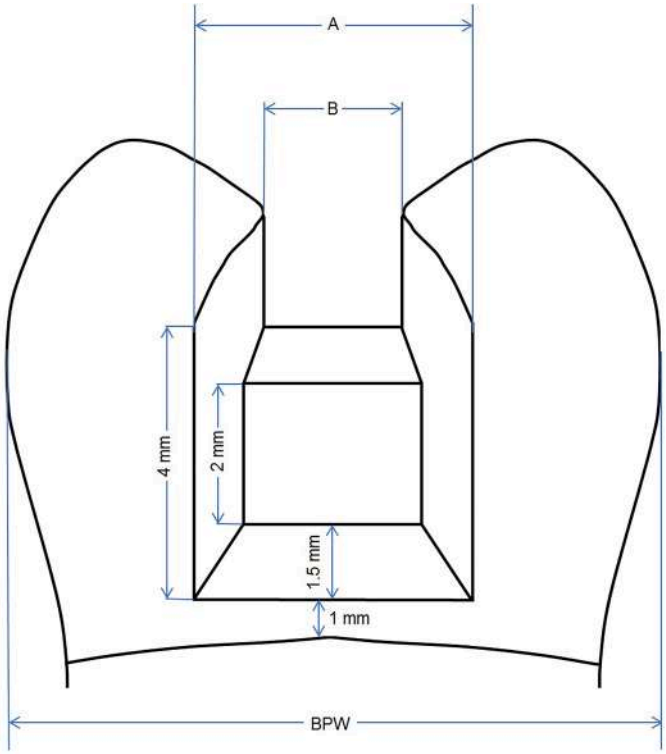

Fig. 2. Schematic representation of the MOD cavity design. Buccal-palatal width (BPW = 9 mm); Gingival floor width (*A* = 2/3 BPW); Occlusal isthmus (*B* = ½ BPW).

from within, utilizing low irradiance. A specially fabricated plastic adapter was used for secure connection between the fibers and the LCU (Fig. 3)

- 2nd step: The fibers were extracted, voids were filled with the RBC, and conventional curing (as in the control group) was performed to finalize the polymerization reaction, utilizing high irradiance. The delay time between the two curing steps was approximately 7 min (comprising the 5 min measurement period following the first curing step and the additional 2 min required for preparing the sample before the second curing step).

Two different diameter optical fibers coupled with the light guide of the commercial LCU were examined, thereby forming two experimental subgroups: b.1. *OF 1* – two optical fibers, 1 mm diameter each. b.2. *OF 1.5* – two optical fibers, 1.5 mm diameter each.

Fiber diameter was measured after removal of the protective cable sheath (i.e., coating illustrated in Fig. 1). Integral output fiber irradiance (coupled with LCU output irradiance 1000 mW/cm^2 or 3000 mW/cm^2) was measured using a power meter (Ophir, Nova II). Precise information about the measured irradiances and the employed exposure times in all material subgroups is provided in Table 4. The total amount of energy delivered during irradiation, known as radiant exposure and expressed as the product of irradiance and exposure time, is summarized in Table 5.

To ensure mechanical stability for the entire setup and facilitate manipulation of the fibers, a custom-made setup was designed (Fig. 4). This arrangement enabled precise positioning of fibers within the cavity before filling it with the composite. Each fiber was positioned in the proximal cavity box, located 2 mm above the gingival floor and aligned with the pulp floor of the occlusal cavity. After securing their positions with the stabilizer (Figs. 4, 5), the fibers were temporarily removed. Subsequently, the MOD cavity was bulk-filled with the composite, and the fibers were reinserted to the predefined level. Any excess material extruded on both proximal sides during fiber embedding was repositioned into the cavity using a plastic dental instrument.

2.2. Examination methods

2.2.1. Digital holographic interferometry (DHI)

The deformation of the MOD cavity model, as a secondary manifestation of PSS, was monitored in real-time using DHI as a non-destructive optical method. DHI relies on the interference between the object and the reference laser beam (Fig. 6), both generated from the same laser light source (Coherent Verdi V5, wavelength 532 nm, power 400 mW, 5 MHz). In order to suppress the vibrations, the experiment was placed on an optical table. In that manner excellent mechanical stability was ensured, which is a prerequisite for holography.

The interference pattern, captured by a digital single-lens reflex camera (Canon EOS50d, 15.1 megapixels, 4752 × 3168 image size),

Table 1
Material used for MOD cavity model fabrication.

Dental composite	Type	Resin matrix	Filler type/weight (wt)%, volume (vol)%	Modulus of elasticity	Manufacturer/Batch number
everX-Posterior	Fiber-reinforced bulk-fill composite	Bis-GMA, PMMA, TEGDMA	Short e-glass fiber; Barium-borosilicate glass/ 74.2 wt%, 53.6 vol%	12–16 GPa [33–35] *Dentin: 12–42 GPa [36]	GC, Tokyo, Japan/LOT 2,006,291

Bis-GMA: Bisphenol A-glycidyl methacrylate; PMMA: Polymethyl-methacrylate; TEGDMA: Triethylenglycol dimethacrylate.

Table 2
Materials examined in the study.

Dental composite/ Abbreviation	Type	Resin matrix	Filler type/ Weight (wt)%, Volume (vol)%	Photo-initiator	Shade	Manufacturer/Batch number
Beautifil-**B**ulk **R**estorative/ **BBR**	Giomer bulk-fill composite	Bis-GMA, UDMA, TEGDMA	S-PRG, Fluoro-alumino-silicate glass/ 87 wt%, 74.5 vol%	Camphorquinone	A	Shofu, Kyoto, Japan/ LOT 011,938
Filtek **B**ulk-fill **P**osterior/ **FBP**	Nano-hybrid bulk-fill composite	AUDMA, UDMA, DDMA, AFM	Ytterbium trifluoride, Silica, Zirconia/ 76.5 wt%, 58.4 vol%	Camphorquinone	A2	3 M ESPE, St. Paul, MN, USA/ LOT N968262
Tetric **P**ower**F**ill/ **TPF**	Nano-hybrid bulk-fill composite	Bis-GMA, Bis-EMA, UDMA, DCP, β-allyl sulfone	Ytterbium trifluoride, Barium-aluminum-silicate glass/ 79 wt%, 53 vol%	Camphorquinone + Ivocerin	IVA	Ivoclar Vivadent, Schaan Liechtenstein/ LOT Z019TZ

Bis-GMA: Bisphenol A-glycidyl methacrylate ; UDMA: Urethane dimethacrylate; TEGDMA: Triethylenglycol dimethacrylate ; Bis-EMA: Ethoxylated bisphenol A dimethacrylate; DCP: Tricyclodecane-dimethanol dimethacrylate ; AUDMA: Aromatic urethane dimethacrylate; DDMA: 1, 12-Dodecanediol dimethacrylate; AFM: Addition-fragmentation monomer; S-PRG: Surface reaction type pre-reacted glass-ionomer.

Table 3
Bluephase PowerCure (Ivoclar Vivadent, Liechetenstein) light curing unit.

Light source	Polywave LEDs: 3 visible (blue) light LEDs + 1 ultraviolet (UV) light LED	
Wavelength range	385–515 nm	
Spectral peaks	410 nm and 460 nm	
Employed curing programs	High power	3 s cure mode
Light irradiance	1000 mW/cm^2 ± 10 %	3000 mW/cm^2 ± 10 %
Required curing time	10 s	3 s
Light guide	Tapered (10 mm > 9 mm) rigid glass probe	

produced a hologram containing the complete phase and amplitude information of the observed object. After initiating the curing cycle, holograms were recorded every 10 s over a 5 min period (although post-curing shrinkage can develop up to 15 h after photo-activation [37], it was observed that the level of deformation after the 5 min measurement period advanced very slowly). The recorded images were then transferred to a computer and numerically reconstructed using parallel processing on a graphics card (NVidia GeForce GTX 1060, 6GB), yielding interferograms (Fig. 7). A detailed explanation of the method is provided in a previous work by the authors [38]. The resulting images depicted model deformation as a series of interference lines, or fringes. Since each fringe corresponded to a deformation of 532 nm (the wavelength of the laser beam), counting their number at the end of the observed time interval provided information about the total deformation. In the experimental groups, total deformation was represented by the sum of deformations at the end of the first and second curing step (n = 15 samples per material subgroup).

To ensure the mechanical stability required for the experiment, MOD cavity models were secured in aluminum molds using dental plaster, leaving the entire buccal surface of the model accessible for testing (Fig. 5). For enhanced contrast in the interference lines, the models were initially coated with a silver marker and then with a thin layer of white paint.

2.2.2. *Infrared thermography (IRT)*

The infrared thermal camera (FLIR, A65) was strategically positioned on the optical table (Figs. 4, 6), to enable simultaneous real-time contactless measurements of the RBC temperature change during polymerization, serving as an indicator of polymerization reaction dynamics. The camera was fixed 8 cm away from the cavity model, with the proximal RBC surface oriented towards the camera lens. Measurements were conducted at a room temperature of 21 °C with 40 % relative humidity. The object's emissivity was established before each measurement. Thermograms were captured from the start of each curing cycle over a 2 min period at a rate of 30 frames per second. Temperature data over time was extracted using the FLIR Tools program (version 6.4.18039.1003, free software) at three points on the proximal side of the RBC (top, middle, and bottom; $n = 5$ samples per material subgroup). Further analysis was performed in SciDAVis (version 1.26, free software) to subtract the ambient temperature from the measured values and calculate the temperature rise (ΔT). Since ΔT is expected due to both the heat of the exothermic reaction and the radiant heat from the LCU [39], it was regarded as total temperature rise – ΔT_t. The extracted temperature data from the three points were used to calculate sample's average ΔT_t.

Table 4
Light irradiance and exposure time in all material subgroups.

Material	Control group		Experimental group – OF 1				Experimental group – OF 1.5			
			1st step		2nd step		1st step		2nd step	
	Irradiance (mW/ cm^2)	Time (s)	Irradiance (mW/ cm^2)	Time (s)	Irradiance (mW/ cm^2)	Time (s)	Irradiance (mW/ cm^2)	Time (s)	Irradiance (mW/ cm^2)	Time (s)
BBR	1000	10	200	30	1000	10	300	10	1000	10
FBP	1000	20	200	30	1000	10	300	10	1000	10
TPF 10 s	1000	10	200	30	1000	10	300	10	1000	10
TPF 3 s	3000	3	600	6	3000	3	900	3	3000	3

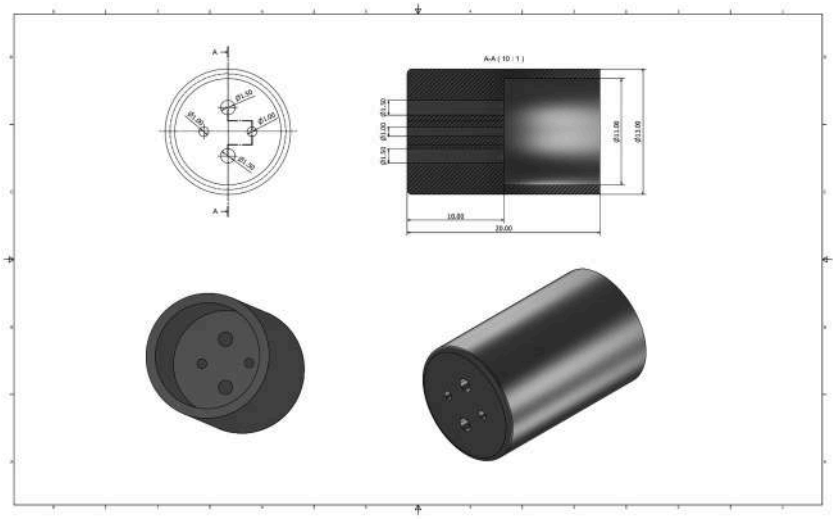

Fig. 3. Specially fabricated plastic adapter for coupling the fibers and the light curing unit. All dimensions are presented in millimeters. Note that two fibers were utilizes as light guides (either 1 mm or 1.5 mm).

Table 5
Radiant exposure (J/cm^2) employed in all material subgroups.

Material	Radiant exposure (J/cm^2)						
	Control group	OF 1 group			OF 1.5 group		
		1 st step	2nd step	Total	1 st step	2nd step	Total
BBR	10	6	10	16	3	10	13
FBP	20	6	10	16	3	10	13
TPF 10s	10	6	10	16	3	10	13
TPF 3s	9	3.6	9	12.6	2.7	9	11.7

2.2.3. Raman spectroscopy

In a separate experiment (after the holographic and thermal measurements, while following the same experimental conditions), the degree of conversion (DC) was determined using Raman spectra of the RBC samples. The spectra were acquired with a Raman spectrometer equipped with a microscope (Thermo Scientific DXR; 10x magnification objective). A Diode-Pumped Solid-State laser (780 nm, 24 mW) served as the excitation source. The recording area was 3.1 μm, and the acquisition time per spectrum was 50 × 10 s (approximately 8 min).

The same materials and curing protocols were employed in the DC calculation experiment, using Raman spectroscopy as an optical method enabling non-destructive analysis. At the start of the experiment, spectra of the unpolymerized material were recorded. Subsequently, after completion of the photo-activation protocol, a Raman spectrum was obtained non-invasively at three locations on the proximal outer layer of the RBC (bottom, middle, and top; $n = 5$ samples per material subgroup), allowing calculation of immediate DC. After a 24-hour dark storage period (21 °C, 40 % relative humidity), spectra collection was repeated on the same samples and locations, allowing 24 h post-cure DC calculation. The resulting DC (immediate or 24 h post-cure) on each of the three locations was used to calculate the sample's average DC (immediate or 24 h post-cure).

The DC was calculated as the ratio of peak intensities at 1640 cm^{-1} (aliphatic spectral band) and 1610 cm^{-1} (aromatic spectral band –

Fig. 4. The experimental configuration for simultaneous holographic and thermographic measurements. A – Light curing unit (LCU); B – Plastic custom-made connector for coupling the optical fibers and the LCU; C – Optical fibers; D – Stabilizer used for securing the fibers and defining their level within the cavity; E – Sample secured in the aluminum mold; F – Infrared camera.

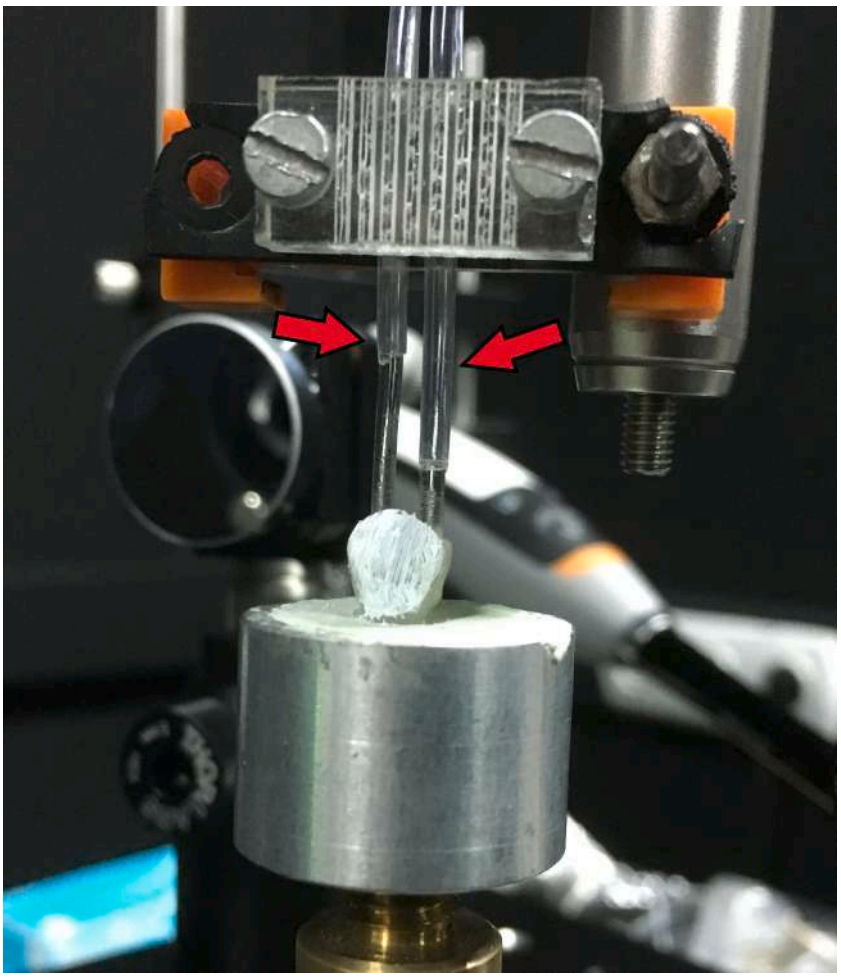

Fig. 5. Close-up view of the restored tooth cavity model, with the optical fibers (red arrows) embedded into the filling and secured by the stabilizer.

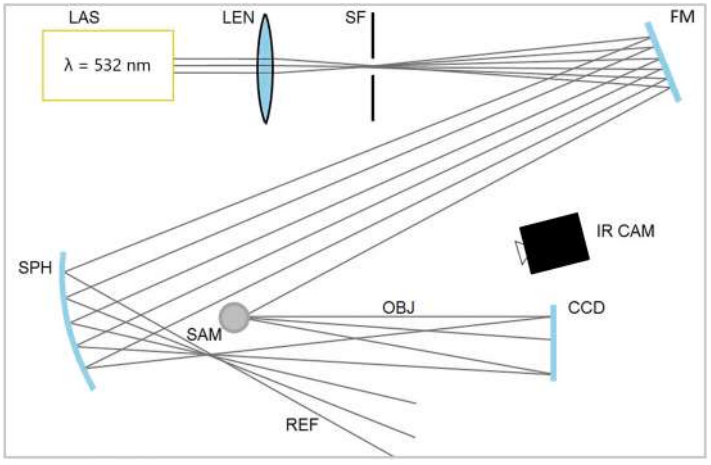

Fig. 6. Schematic representation of the experimental set-up coupling Digital Holographic Interferometry and Infrared Thermography. LAS – Laser; LEN – Lens; SF – Spatial filter; FM – Flat mirror; SPH – Spherical mirror; SAM – Sample; REF – Reference beam; OBJ – Object beam; CCD – Charge-coupled device; IR CAM – Infrared camera; λ – Wavelength of the laser light source.

reference) in the infrared spectrum, after the completion of photo-activation (R_{cured}) and before photo-activation ($R_{uncured}$), according to the following formula:

$$DC(\%) = \left[1 - \frac{R_{cured}}{R_{uncured}}\right] \times 100$$

2.2.4. Statistical analysis

The one-way Analysis of Variance (ANOVA) was employed to assess the impact of conventional curing (employed in the control group) and the two-step experimental curing (employed in the OF 1 and OF 1.5 groups) on cavity model deformation, total temperature rise (ΔT_t),

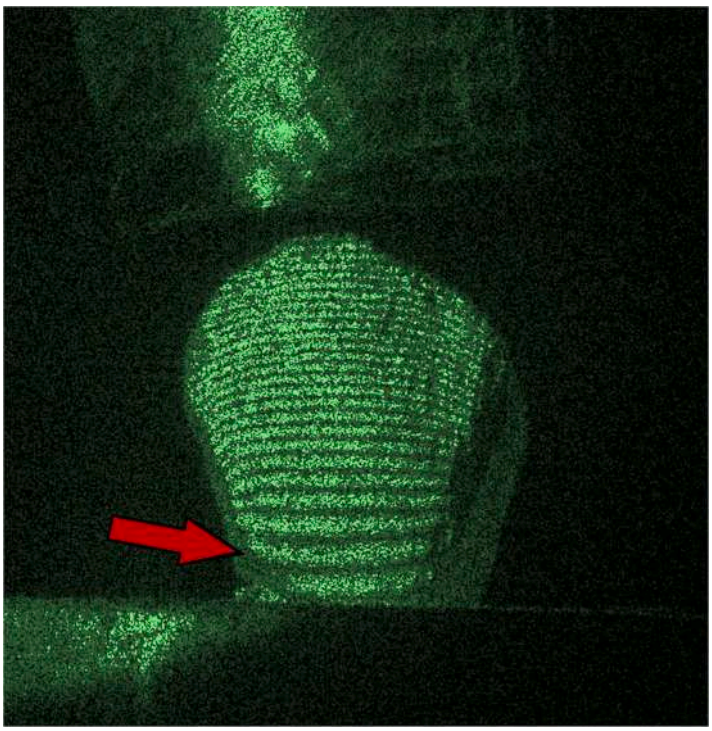

Fig. 7. The resulting interferogram at the end of the examined 5 min period. The arrow indicates an interference line (fringe). Each fringe corresponds to a deformation of 532 nm. The total number of fringes equals 26. The deformation value (in μm) is calculated as follows: 26 × 0.532 = 13.832 μm.

immediate DC, and 24 h post-cure DC. Subsequently, a post-hoc Dunnett's test was conducted in all cases, to test for the differences between the conventional curing, used as the control group, and the remaining groups. Before conducting the above-mentioned tests, normality distribution of the data was evaluated using the Shapiro-Wilk test. The alpha level of significance was set at 0.05. For all gathered data, Shapiro-Wilk test evidenced normal distribution ($p \geq 0.05$). All analyses were performed using JMP version 16.2 (Statistical Analysis System Inc., Cary, NC, USA).

3. Results

3.1. MOD cavity model deformation

In both experimental groups (OF 1 and OF 1.5), the mean total deformation values (first + second step) during RBC polymerization were significantly lower than those exhibited by their counterparts in the control group. Specifically, the registered p-values were as follows: for BBR OF1 ($p = 0.0004$); for BBR OF1.5 ($p = 0.0019$); for all other material subgroups ($p < 0.0001$); indicating a statistically significant difference. Fig. 8 illustrates the results of statistical analysis across all

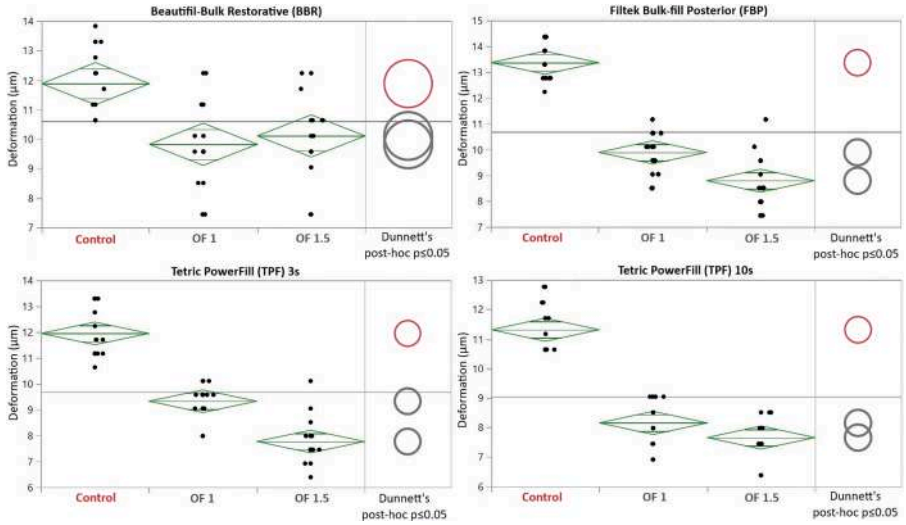

Fig. 8. Total deformation values (μm) along with the results of statistical analysis. Dunnett's post-hoc test indicated significantly lower values in both experimental groups (OF 1 and OF 1.5) compared to the control, across all examined materials ($p \leq 0.05$). Rhomboid shapes represent group means with standard deviation. The control group is presented on the left side of each material subgroup illustration. Circles, also indicating group means, are used to highlight specific differences registered in the post-hoc analysis. The control group is illustrated above the experimental groups.

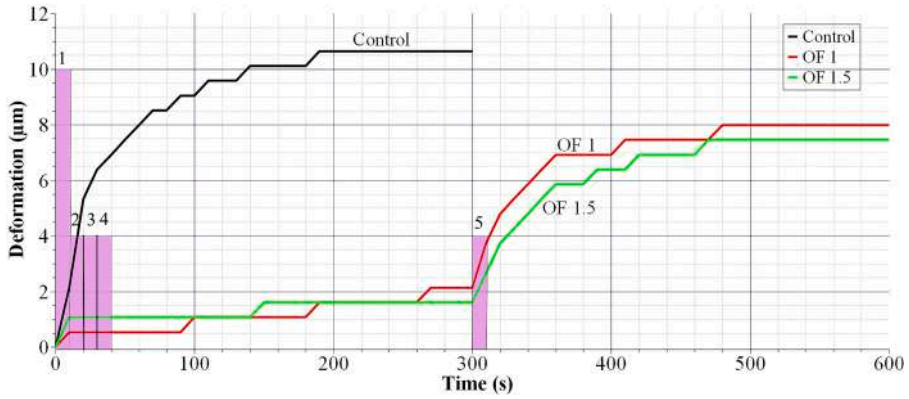

Fig. 9. Deformation development (µm) over time (s) for material TPF 10 s as a typical example. The median sample in each group is represented. For easier interpretation, deformation in the experimental groups is shown as a continuous curve, despite an actual delay between the two curing steps. Violet bars indicate LCU irradiation, each bar representing 10 s of exposure. 1: Control group – Conventional curing; 2: First curing step via optical fibers (OF 1.5 group); 2 + 3 + 4: First curing step via optical fibers (OF 1 group); 5: Second step conventional curing (both OF 1 and OF 1.5 groups).

examined materials. The effect of the experimental curing protocol on the reduction of model deformation compared to conventional curing ranged from 15 to 35 % (Table 7).

Examination of deformation development over time provided indirect insight into polymerization reaction dynamics. In Fig. 9, it is graphically represented for material TPF 10 s (comparing all three groups) as a typical example. Polymerization initiation in the first curing step via optical fibers (200 – 300 mW/cm^2) is indicated by a slow development of deformation, in contrast to the rapid increase observed during conventional curing. Following the second curing step (7 min after the initiation of the first curing cycle), polymerization dynamics intensified as expected, due to the higher light irradiance employed (1000 mW/cm^2). This is illustrated by a rapid increase in deformation, while the attained maximum values were significantly lower compared to the control group.

3.2. RBC temperature change

Fig. 10 shows the results of the statistical analysis, indicating that the mean total temperature rise (ΔT_t) during RBC polymerization in both experimental groups was significantly lower than ΔT_t exhibited by their counterpart in the control group. Specifically, the registered p-values were as follows: for BBR OF1 ($p = 0.0343$); for TPF 3 s OF1 ($p = 0.0007$); for all other material subgroups ($p < 0.0001$); indicating a statistically significant difference. Exception was BBR in the OF 1.5 group, where no significant difference was observed ($p = 0.0656$).

Ten minutes after curing, when the samples returned to ambient temperature, reirradiation was conducted (employing same light irradiance and exposure time as previously) to determine the temperature rise due to LCU irradiation only (ΔT_i). As most of the polymerization had already occurred, the observed temperature rise during the subsequent exposure was primarily attributed to irradiation by the LCU alone. Therefore, the calculated difference between ΔT_t and ΔT_i was considered as the temperature rise due to the exothermic reaction ($\Delta T_e = \Delta T_t - \Delta T_i$). ΔT_e served as an indicator of polymerization reaction dynamics, with the peak temperature approximating the vitrification point of the reaction. Due to the low irradiance employed in the first curing step of the experimental groups via optical fibers, the temperature rise in the first

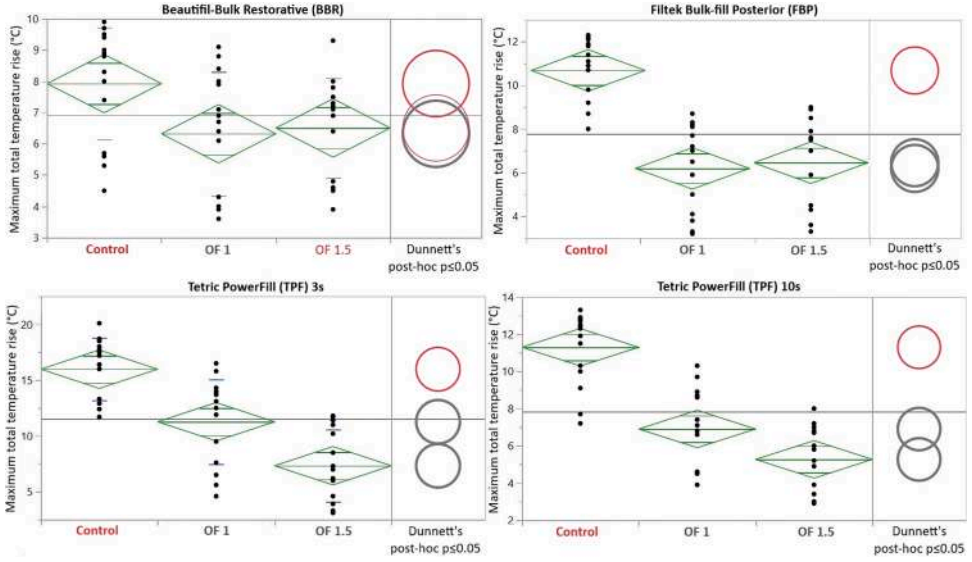

Fig. 10. Total temperature rise ΔT_t (°C) along with the results of statistical analysis. Dunnett's post-hoc test indicated significantly lower values in both experimental groups (OF 1 and OF 1.5) compared to the control, across all examined materials ($p \leq 0.05$). One exception was registered: BBR in the OF 1.5 group with no significant difference ($p = 0.0656$). Rhomboid shapes represent group means with standard deviation. The control group is presented on the left side of each material subgroup illustration. Circles, also indicating group means, are used to highlight specific differences registered in the post-hoc analysis. The control group is illustrated above the experimental groups.

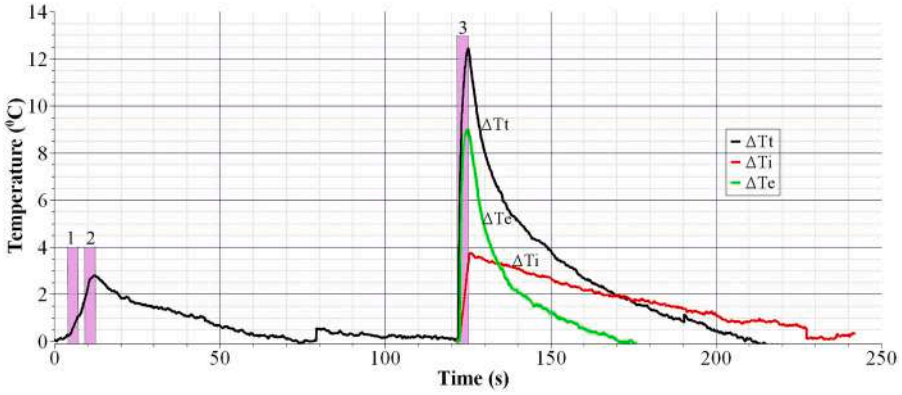

Fig. 11. Temperature change (°C) over time for material TPF 3 s in the experimental group OF 1 (location: top of the proximal RBC surface). Violet bars indicate LCU irradiation (1st step: 600 mW/cm^2, 2nd step: 3000 mW/cm^2), each bar representing 3 s of exposure. 1 + 2: First curing step via optical fibers; 3: Second step conventional curing. ΔT_t: Total temperature rise; ΔT_e: Temperature rise due to exothermic reaction; ΔT_i: Temperature rise due to LCU irradiation. Typical example for the experimental subgroups: ΔT_e maximum in the second curing step was higher than temperature rise in the first curing step via optical fibers, indicating the attainment of the vitrification point in the second step.

Table 6
Mean temperature rise (°C) with standard deviation (SD). ΔT_t: Total temperature rise; ΔT_i: Temperature rise due to LCU irradiation; ΔT_e: Temperature rise due to exothermic reaction. Bold values indicate two exceptions (TPF 3 s and TPF 10 s in the OF 1.5 group): Temperature rise in the first curing step via optical fibers exceeded ΔT_e in the second step, signifying the attainment of the vitrification point in the first step.

	Group		Mean temperature rise ± SD (°C)			
			BBR	FBP	TPF 3s	TPF 10s
ΔT_t	Control		7.9 ± 1.8	10.7 ± 1.6	16 ± 2.8	11.3 ± 2
	OF 1	1st step	0.9 ± 0.4	1.1 ± 0.2	2.7 ± 0.7	2.5 ± 0.5
		2nd step	6.3 ± 2	6.2 ± 1.9	11.3 ± 3.8	6.9 ± 2.1
	OF 1.5	1st step	1.6 ± 0.6	1.7 ± 0.3	**5.6 ± 1.8**	**4.3 ± 0.9**
		2nd step	6.5 ± 1.6	6.5 ± 2	7.3 ± 3.2	5.3 ± 1.7
ΔT_i	Control		3.3 ± 0.9	6.1 ± 1.3	4.2 ± 1.7	4.6 ± 1.5
	OF 1 (2nd step)		3.6 ± 1.1	4 ± 1.2	4.6 ± 1.8	5.1 ± 1.7
	OF 1.5 (2nd step)		3.8 ± 0.8	3.6 ± 1.2	4.3 ± 1.8	3.4 ± 1.1
ΔT_e	Control		5.3 ± 1.2	6.4 ± 1.2	12.7 ± 1.4	10.1 ± 1.6
	OF 1 (2nd step)		3.1 ± 0.9	2.3 ± 0.8	7.7 ± 2.6	2.7 ± 0.9
	OF 1.5 (2nd step)		3.2 ± 0.9	3.1 ± 1.3	**3.4 ± 1.6**	**2.4 ± 0.9**

step was considered mostly exothermal. After completion of the second curing step, ΔT_e was calculated following the aforementioned procedure. Fig. 11 illustrates temperature change over time in the OF 1 group for material TPF 3 s.

Table 6 shows mean temperature rise values in all groups, across all examined materials. The effect of the experimental curing protocol on ΔT_t reduction compared to conventional curing, ranged from 18 to 54 %. Table 7 summarizes the effect on temperature and deformation reduction for each material subgroup arranged in descending order, highlighting a consistent influence of the experimental protocol on both measured values. The results suggest that a greater impact on temperature reduction corresponded to a higher reduction in deformation.

3.3. Degree of conversion (DC)

Fig. 12 illustrates the DC results at two distinct time points: immediately after the completion of the photo-activation protocol and after 24 h of dark storage. The results of statistical analysis are presented in Tables 8 and 9 for immediate DC and 24-hour post-cure DC, respectively.

4. Discussion

The proposed curing protocol involved employing flexible optical fibers as light guides, which were inserted into the center of the restoration. Such approach integrated several strategies mentioned in Section 1. Introduction, including curing from within, a modified incremental layering technique, and pulse-delay photo-activation. The proposed two-step curing process was designed as follows: in the first step, two optical fibers connected to a commercial dental LCU were inserted into the filling to initiate polymerization from within (using low irradiance); in the second step, the fibers were extracted and the remaining voids were filled with the RBC, followed by conventional curing for completing the polymerization (using high irradiance).

The results of the holographic analysis (Fig. 8) presented a significant reduction in deformation when the RBC samples were cured using the proposed two-step method compared to conventional curing (15–35 % reduction across the examined materials). Consequently, the first null hypothesis, assuming that the employed photo-activation protocol would have no impact on cavity model deformation, was rejected.

Real-time measurements of cavity model deformation provided

Table 7
Summary of the achieved effects (%) of the experimental protocol on reduction of cavity model deformation and RBC temperature change, compared to the control level mean. The comparison is based on mean total deformation and mean maximum total temperature rise (ΔT_t). Bold value indicates the only non-significant reduction (temperature for material BBR in the OF 1.5 group).

Material	Experimental group	Reduced model deformation compared to control	Material	Experimental group	Reduced temperature change compared to control
TPF 3s	OF 1.5	−35 %	TPF 3s	OF 1.5	−54 %
FBP	OF 1.5	−34 %	TPF 10s	OF 1.5	−53 %
TPF 10s	OF 1.5	−32 %	FBP	OF 1	−42 %
TPF 10s	OF 1	−28 %	TPF 10s	OF 1	−39 %
FBP	OF 1	−26 %	FBP	OF 1.5	−39 %
TPF 3s	OF 1	−22 %	TPF 3s	OF 1	−29 %
BBR	OF 1	−17 %	BBR	OF 1	−20 %
BBR	OF 1.5	−15 %	**BBR**	**OF 1.5**	**−18 % ($p = 0.0656$)**

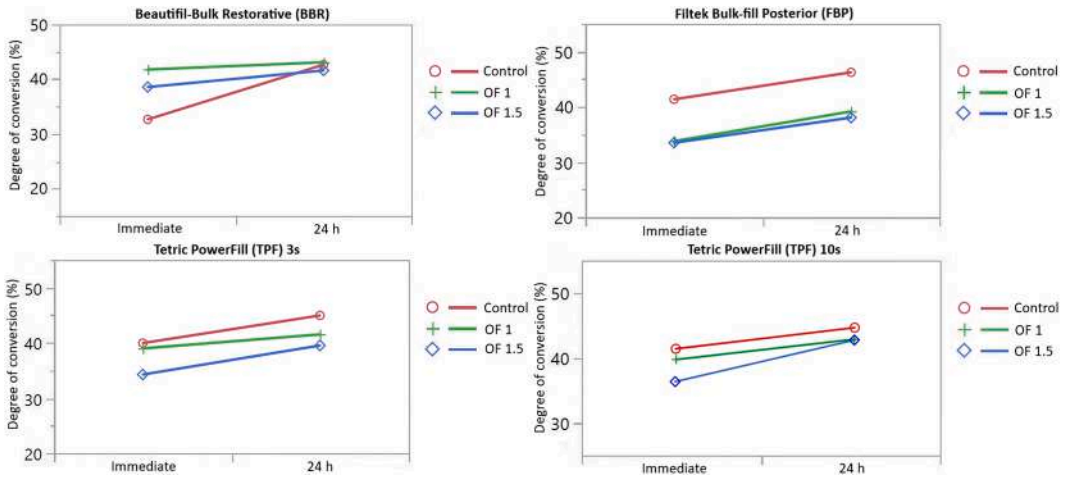

Fig. 12. Mean immediate DC and 24 h post-cure DC (%) in all groups, across all materials. At 24 h post-cure, no significant difference was registered in all experimental subgroups compared to the control, except for FBP (both experimental groups) and TPF 3 s in the OF 1.5 group. Refer to Table 8 and Table 9 for the results of statistical analysis.

Table 8
Mean immediate DC (%) with standard deviation (SD). Results of Dunnett's post-hoc multiple comparisons between conventional curing (Control) and experimental curing (OF 1 and OF 1.5) are presented by appropriate p-values ($p \leq 0.05$ was considered significantly different). Note that in the case of material BBR, DC was significantly higher than the control level mean.

	Mean immediate DC ± SD (%)							
	BBR	p-value	FBP	p-value	TPF 3s	p-value	TPF 10s	p-value
Control	32.7 ± 6.5	/	41.4 ± 6.4	/	40 ± 5.6	/	41.4 ± 6.8	/
OF 1	41.8 ± 2.8	$p = 0.000$	33.8 ± 5.5	$p = 0.003$	39 ± 5.8	$p = 0.856$	39.8 ± 3.9	$p = 0.637$
OF 1.5	38.6 ± 2.7	$p = 0.001$	33.5 ± 6.4	$p = 0.002$	34.3 ± 5.7	$p = 0.017$	36.3 ± 4.8	$p = 0.025$

Table 9
Mean 24 h post-cure DC (%) with standard deviation (SD). Results of Dunnett's post-hoc multiple comparisons between conventional curing (Control) and experimental curing (OF 1 and OF 1.5) are presented by appropriate p-values ($p \leq 0.05$ was considered significantly different).

	Mean 24 h post-cure DC ± SD (%)							
	BBR	p-value	FBP	p-value	TPF 3s	p-value	TPF 10s	p-value
Control	42.7 ± 3.3	/	46.3 ± 6.5	/	45 ± 5.4	/	44.7 ± 5.9	/
OF 1	43.1 ± 2.7	$p = 0.882$	39.2 ± 5.3	$p = 0.005$	41.6 ± 6.5	$p = 0.149$	42.8 ± 2.9	$p = 0.438$
OF 1.5	41.6 ± 2.6	$p = 0.504$	38.1 ± 6.3	$p = 0.001$	39.5 ± 3.7	$p = 0.015$	42.5 ± 4.5	$p = 0.334$

indirect insight into the polymerization reaction dynamics (Fig. 9), revealing the potential underlying mechanism of PSS reduction. This observation, indicative of slower polymer network development in the experimental groups where low light irradiance was employed during the first curing step (200 – 300 mW/cm^2), aligns with expectations as the reaction rate is proportional to the square root of the applied light irradiance [40]. Theoretically, in a polymer network developing at a slower rate, more time is available for viscous flow to occur, enabling the compensation of shrinkage forces through molecular rearrangement [41]. This could be considered one of the possible mechanisms behind the reduction in PSS obtained using the proposed two-step curing protocol.

Another indication of a slow reaction rate was observed through real-time monitoring of RBC temperature changes using Infrared Thermography, as shown in Fig. 11. The results revealed a modest temperature increase during the first curing step (0.9–2.7 °C; Table 6), suggesting a slow initiation rate. Subsequently, a rapid temperature rise occurred during the second curing step, reaching its peak exothermic temperature at this stage (for most examined RBCs, except TPF 3 s and TPF 10 s in the OF 1.5 group). These findings suggest a late-stage onset of vitrification. This could be viewed as beneficial in the context of reducing PSS, as it extends the period where the material is able to yield to contraction forces before acquiring higher elastic modulus [42].

It was previously observed that temperature rise during polymerization serves as an estimate of the reaction dynamics, with the peak temperature change approximating the onset of vitrification [39,43]. However, as the temperature rise results from both the exothermic reaction and heating due to curing light absorbance itself, it is crucial to extract the heat of the exothermic reaction (ΔT_e) from the total temperature rise (ΔT_t). In this study, the calculation of ΔT_e was performed as explained in Section 3.2, following the well-established methodology in the literature [39,43,44].

Nevertheless, it is essential to recognize the significance of thermal shrinkage (associated with cooling during the post-cure) in the overall development of PSS, as emphasized by Palagummi et al. [20]. Specifically, polymerization shrinkage results from both volumetric shrinkage and thermal shrinkage. Meanwhile, PSS is generated due to shrinkage occurring under constrained conditions (both external, through bonding to the surrounding cavity walls, and internal, linked to the evolving elastic modulus [45]), and after the RBC acquires high elastic modulus [46,47]. Hence, the importance of thermal shrinkage is underscored by Palagummi et al. [20], given that significant heat dissipation occurs near the end of the photo-activation process, where the elastic modulus of the RBC reaches its highest value.

While one might assume based on the literature [48,49], that the 7 min delay between the first and second curing step in the proposed

curing protocol impacted the overall PSS, the study by Palagummi et al. [20] provides contrasting insights. They demonstrated that although delay time can contribute to PSS reduction, significant stress relaxation does not occur during this period. Instead, notable reduction occurs at the late stage of polymerization. Furthermore, they observed that beyond a 40-second delay time, the reduction in PSS reaches a plateau.

However, it is important to note the potential influence of adhesives on PSS development, a critical consideration in clinical practice regarding interfacial gap formation [9]. The current study utilized standard composite molds to facilitate comparisons among tested protocols, thereby avoiding to replicate the hybrid layer encountered in clinical settings. This limitation could affect the accuracy of the findings concerning PSS. To mitigate this limitation, the simulated cavities were bonded prior to RBC insertion, as detailed in Section 2.1 Materials. Additionally, a fiber-reinforced RBC was employed with an elastic modulus similar to human dentin in fabricating the cavity molds (see Table 1), aiming to mimic the compliance of human tooth cavities as closely as possible.

The thermal measurement results demonstrated a significant reduction in total temperature change (ΔT_t) in both experimental groups (OF 1 and OF 1.5), when RBC samples were cured by the proposed two-step protocol, as compared to their control counterpart (Fig. 10). The only non-significant ΔT_t reduction was observed for material BBR in the OF 1.5 group. Therefore, the second null hypothesis, assuming that the employed photo-activation protocol would have no impact on RBC temperature change, was rejected.

The proposed two-step curing resulted in lower ΔT_t, leading to a diminished thermal shrinkage during the second curing step. At this stage, most RBC samples reached the maximum exothermic temperature rise (ΔT_e), signifying the achievement of vitrification (followed by a notable increase in elastic modulus). Consequently, PSS was reduced as evidenced by decreased cavity model deformation compared to samples cured conventionally. When assessing the impact of the protocol on model deformation and RBC temperature change across the examined RBCs, it became evident that a greater reduction in ΔT_t corresponded to a higher decrease in model deformation (Table 7). This observation confirms the impact of thermal shrinkage on PSS during pulse-delay curing, as suggested by Palagummi et al. [20].

However, the primary concern is to achieve PSS reduction without compromising adequate polymerization, commonly expressed through degree of conversion (DC). To address this challenge, the proposed curing protocol involved embedding the flexible fibers into the filling during the first curing step. Therefore, such two-step approach aimed to simultaneously tackle the issue of light loss at increasing depths and avoid jeopardizing the DC, while reducing PSS.

After implementing the proposed two-step curing, the immediate DC demonstrated diverse RBC behavior, including cases with non-significant differences, significantly lower values, or even significantly higher DC, compared to their respective control counterpart (refer to Fig. 12, Table 8). Hence, the third null hypothesis, which posited that the proposed photo-activation protocol would have no impact on immediate DC, was only partially accepted. Nonetheless, following a 24-hour dark storage period and the anticipated DC increase, most RBC samples cured by the experimental protocol showed no significant difference in DC compared to their control counterparts (Fig. 12, Table 9), thereby endorsing the clinical success of the proposed protocol. Consequently, the fourth null hypothesis, asserting that the proposed photo-activation protocol would have no impact on 24-hour post-cure DC, was accepted.

The significantly lower 24-hour post-cure DC was recorded only for materials FBP (in both experimental groups) and TPF 3 s (in the OF 1.5 group), and was attributed to insufficient total energy delivered to the material and a high initiation rate, respectively. The minimum energy density required for adequate polymerization varies among RBCs and is primarily determined by the viscosity of the organic phase [50]. Although it was not calculated for each of the tested materials, the manufacturer's recommendations were considered as a guideline for conventionally cured samples, as it is a common clinical practice. Accordingly, material FBP required the highest energy density (see Table 5), whereas the proposed curing protocol yielded values below this recommendation. In such cases a reduction in DC is expected [51, 52], which was confirmed by the results of our study. Meanwhile, since DC serves as an indicator of polymerization efficiency, it is reasonable to anticipate that a lower DC would result in a reduced temperature change, subsequently leading to lower contraction stress [21–23]. This hypothesis aligns with our findings for FBP, where the proposed protocol demonstrated one of the most significant impacts on reducing both ΔT_t and model deformation among the examined RBCs (Table 7).

On the other hand, it was acknowledged in the literature that a high initiation rate results in a greater loss of radical growth centers through bimolecular termination [21,53]. Consequently, DC is significantly decreased compared with using low irradiance for a longer time. The findings of the present study support this claim, since activation of the material TPF 3 s in the OF 1.5 group by irradiance of 900 mW/cm^2 yielded significantly lower DC compared to the control counterpart (Table 8, Table 9). Additionally, the results of thermal measurements for TPF 3 s presented the highest temperature increase during the first curing step among the examined RBCs (Table 6), indicating the undesired high initiation rate, which probably lead to an early-stage onset of vitrification, thereby compromising DC. As a result, the proposed protocol presented the highest impact on reduction of ΔT_t and model deformation for material TPF 3 s (Table 7).

The thermal measurement results for material TPF 10 s in the OF 1.5 group also revealed a high initiation rate. This was evident as the temperature rise during the first curing step surpassed the calculated exothermic temperature rise following the second curing step (Table 6). Despite the relatively low irradiance applied during a 10-second period in the first step (300 mW/cm^2), this observation was linked to the specific composition of the material and the use of the polywave LCU in this study. Specifically, TPF incorporates Ivocerin® as an alternative photo-initiator, thus the choice of the polywave LCU ensured an optimal absorption/emission spectrum alignment, as outlined by Wang et al. [54]. Such alignment facilitated greater light transmission and increased polymerization initiation, leading to a higher exothermic temperature rise during the first curing step. Further evidence of heightened material reactivity was observed in the thermal results for TPF 3 s in the control group (Table 6). In this case, the highest ΔT_t among the examined RBCs was achieved, with the exothermic reaction predominantly contributing to the attained temperature rise.

However, even with the substantial temperature rise observed during the first curing step for TPF 10 s in the OF 1.5 group which might suggest early-stage vitrification and compromise DC, the initiation rate was not as high as observed in the case of TPF 3 s, due to the lower irradiance applied. Thereby, the 24-hour post-cure DC results for TPF 10 s showed no significant difference when compared to the RBC control counterpart. This supports the notion that the proposed curing protocol is clinically viable, ensuring comparable DC outcomes to the conventional curing.

It is also important to discuss the significant increase in immediate DC exhibited by the material BBR when cured using the experimental protocol (Table 8). First of all, BBR demonstrated the lowest DC among the examined RBCs when cured conventionally (Tables 8, 9). This outcome was attributed to its high inorganic content (87 % by weight, Table 2), leading to a significant difference in the refractive index between the organic and inorganic phases, resulting in enhanced light scattering [5]. The increased light scattering diminishes light transmission, impacting reaction initiation and leading to a lower DC. Such observation aligns with the findings of previous studies exploring DC of giomer bulk-fill composites [55–57]. The compromised light transmission for BBR was further confirmed by thermal measurements (Table 6), since it exhibited the lowest ΔT_t and the lowest ΔT_e during conventional curing. On the contrary, the experimental protocol with a slower initiation rate and effective light guiding into deeper layers of the

filling, allowed for enhanced photon absorption, resulting in significant immediate DC improvement (Table 8).

As a final consideration, it is crucial to view the proposed protocol from a clinical perspective. In the current trend of minimizing chair time in contemporary dental practice, implementing the presented protocol may seem laborious and time-consuming. However, given that a typical restorative procedure takes at least 15 min (depending on the clinical situation), the additional time required for the proposed two-step curing (approximately 2 – 3 min) does not significantly extend the therapeutic process. Moreover, this extra time investment yields the benefit of reducing detrimental contraction stress while maintaining adequate DC. This aspect should be a compelling rationale for the adoption of the proposed protocol in comparison to clinically easier alternatives such as "soft-start", which are often followed by compromised DC [21–23]. Meanwhile, enhanced approach for restorations on posterior teeth could be obtained owing to fiber flexibility.

It is also noteworthy to address potential challenges during the application of the protocol, such as the composite adhering to the optical fiber, complicating its extraction from the filling. This issue can be preemptively mitigated by cleaning the fibers with 70 % ethanol before application. It is essential to allow the alcohol to dry out before use. However, no cases of fiber breakage were registered, thus enabling reuse of the same fibers. On the other hand, filling the small voids in the restoration after extraction of the 1 mm diameter fibers can be a tedious process that requires the use of a dental probe. Additionally, longer exposure times are necessary when using such fibers to initiate polymerization, owing to their low output irradiance. Therefore, favoring the use of 1.5 mm fibers is recommended. Further method adjustments, such as implementing even larger core diameter fibers (2 mm) or using conically shaped fibers (involving side-glow light irradiation), could lead to improvements for easier implementation in clinical practice.

5. Conclusion

Within the limitations of this study, the curing protocol demonstrated the potential to significantly reduce shrinkage stress (15–35 %) while ensuring a comparable degree of conversion (DC) to conventional curing at 24 h post-cure. To avoid compromising the DC, it is essential to deliver a total energy amount equal to or above the composite manufacturer's recommended values. Coupling 1.5 mm diameter fibers with a high-power output curing unit (3000 mW/cm^2) was found to be non-beneficial, exhibiting a high initiation rate that compromises the DC. Therefore, a comprehensive understanding of the irradiance of the LED device in use and the output irradiance after coupling the fibers with the curing unit is necessary to determine the required exposure time and ensure efficient protocol application in clinical practice. According to the presented results, the protocol involving the use of two 1.5 mm optical fibers in the first step (300 mW/cm^2 × 10 s), followed by a second conventional curing step (1000 mW/cm^2 × 10 s), is recommended. This approach not only provides a shorter exposure time, but also facilitates filling of larger voids after fiber extraction. Implementation of the proposed optical fiber-based curing protocol in clinical practice is easily achievable by coupling the fibers with any commercial LED curing unit using the provided plastic adapter.

CRediT authorship contribution statement

Evgenije Novta: Writing – original draft, Investigation, Formal analysis. **Dejan Pantelić:** Writing – review & editing, Supervision, Software, Methodology, Conceptualization. **Larisa Blažić:** Supervision, Project administration, Funding acquisition. **Elvira Tóth:** Investigation, Methodology, Writing – review & editing. **Željka Cvejić:** Project administration, Supervision. **Dušan Grujić:** Investigation, Methodology, Software, Visualization. **Svetlana Savić-Šević:** Investigation, Methodology, Supervision, Writing – review & editing. **Tijana Lainović:** Investigation, Methodology, Supervision, Writing – review & editing.

Declaration of competing interest

The authors declare that they have no known competing financial interests or personal relationships that could have appeared to influence the work reported in this paper.

Acknowledgments

This study is derived from the first author's PhD thesis (defended at the Faculty of Medicine, University of Novi Sad, Serbia), fulfilling the requirements for the PhD degree.

The work was supported by the Serbian Ministry of Science, Technological Development and Innovations (451–03–47/2023–01/200114). The authors thank professor Danimir Jevremović, (professional service manager for South-Eastern Europe, Ivoclar Vivadent AG) and Mikodental Dental depo (distributers of Shofu dental products in Serbia) for kindly donating the study material. The authors would also like to thank professor Ognjan Lužanin (Faculty of Technical Sciences, University of Novi Sad, Serbia) for the help regarding statistical analysis.

References

[1] F.A. Rueggeberg, M. Giannini, C.A. Arrais, R.B. Price, Light curing in dentistry and clinical implications : a literature review, Braz. Oral Res. 31 (2017) 64–91, https://doi.org/10.1590/1807-3107BOR-2017.vol31.0061.

[2] J.G. Leprince, W.M. Palin, M.A. Hadis, J. Devaux, G. Leloup, Progress in dimethacrylate-based dental composite technology and curing efficiency, Dent. Mater. 29 (2013) 139–156, https://doi.org/10.1016/j.dental.2012.11.005.

[3] J. Chesterman, A. Jowett, A. Gallacher, P. Nixon, Bulk-fill resin-based composite restorative materials: a review, Br. Dent. J. 222 (2017) 337–344, https://doi.org/10.1038/sj.bdj.2017.214.

[4] S. Bucuta, N. Ilie, Light transmittance and micro-mechanical properties of bulk fill vs. conventional resin based composites, Clin. Oral Investig. 18 (2014) 1991–2000, https://doi.org/10.1007/s00784-013-1177-y.

[5] B. Howard, N.D. Wilson, S.M. Newman, C.S. Pfeifer, J.W. Stansbury, Relationships between conversion, temperature and optical properties during composite photopolymerization, Acta Biomater. 6 (2010) 2053–2059, https://doi.org/10.1016/j.actbio.2009.11.006.

[6] W.M. Palin, J.G. Leprince, M.A. Hadis, Shining a light on high volume photocurable materials, Dent. Mater. 34 (2018) 695–710, https://doi.org/10.1016/j.dental.2018.02.009.

[7] F.A. Rueggeberg, State-of-the-art : dental photocuring — A review, Dent. Mater. 27 (2011) 39–52, https://doi.org/10.1016/j.dental.2010.10.021.

[8] J.L. Ferracane, Developing a more complete understanding of stresses produced in dental composites during polymerization, Dent. Mater. 21 (2005) 36–42, https://doi.org/10.1016/j.dental.2004.10.004.

[9] P.M. Pires, A. de Almeida Neves, M. Lukomska-Szymanska, P. Farrar, Á.F. Cascales, S. Sauro, Bonding performance and interfacial adaptation of modern bulk-fill restorative composites after aging in artificial saliva: an *in vitro* study, Clin. Oral Investig. 28 (2024) 1–16, https://doi.org/10.1007/s00784-024-05525-5.

[10] J. Park, J. Chang, J. Ferracane, I.B. Lee, How should composite be layered to reduce shrinkage stress: incremental or bulk filling? Dent. Mater. 24 (2008) 1501–1505, https://doi.org/10.1016/j.dental.2008.03.013.

[11] I.N. Sarcev, B.S. Petronijevic, T.M. Atanackovic, A biomechanical model for a new incremental technique for tooth restoration, Acta Bioeng. Biomech. 14 (2012) 85–91, https://doi.org/10.5277/abb120312.

[12] L.M. Petrovic, M.R. Drobac, I.L. Stojanac, T.M. Atanackovic, A method of improving marginal adaptation by elimination of singular stress point in composite restorations during resin photo-polymerization, Dent. Mater. 26 (2010) 449–455, https://doi.org/10.1016/j.dental.2009.11.160.

[13] N. Ilie, E. Jelen, R. Hickel, Is the soft-start polymerisation concept still relevant for modern curing units? Clin. Oral Investig. 15 (2011) 21–29, https://doi.org/10.1007/s00784-009-0354-5.

[14] T.T. Tauböck, A.J. Feilzer, W. Buchalla, C.J. Kleverlaan, I. Krejci, T. Attin, Effect of modulated photo-activation on polymerization shrinkage behavior of dental restorative resin composites, Eur. J. Oral Sci. 122 (2014) 293–302, https://doi.org/10.1111/eos.12139.

[15] N. Emami, K.J.M. Söderholm, Influence of light-curing procedures and photo-initiator/co-initiator composition on the degree of conversion of light-curing resins, J. Mater. Sci. Mater. Med. 16 (2005) 47–52, https://doi.org/10.1007/s10856-005-6445-1.

[16] L.G. Cunha, R.C.B. Alonso, C.S.C. Pfeifer, L. Correr-Sobrinho, J.L. Ferracane, M.A. C. Sinhoreti, Contraction stress and physical properties development of a resin-based composite irradiated using modulated curing methods at two C-factor levels, Dent. Mater. 24 (2008) 392–398, https://doi.org/10.1016/j.dental.2007.06.006.

[17] J.G. Leprince, G. Lamblin, J. Devaux, M. Dewaele, M. Mestdagh, W.M. Palin, B. Gallez, G. Leloup, Irradiation modes' impact on radical entrapment in

photoactive resins, J. Dent. Res. 89 (2010) 1494–1498, https://doi.org/10.1177/0022034510384624.
[18] G. dos S. Sousa, G.F. Guimarães, E. Marcelino, J.E.P. Rodokas, A.J. de O. Júnior, I. Cesarino, A.L. Leão, C. dos S. Riccardi, M. Arjmand, R.P. Simões, Shrinkage stress and temperature variation in resin composites cured via different photoactivation methods: insights for standardisation of the photopolymerisation, Polymers 13 (2021) 1–14, https://doi.org/10.3390/polym13132065 (Basel).
[19] E.A. Münchow, C.T.W. Meereis, W.L. de Oliveira da Rosa, A.F. da Silva, E. Piva, Polymerization shrinkage stress of resin-based dental materials: a systematic review and meta-analyses of technique protocol and photo-activation strategies, J. Mech. Behav. Biomed. Mater. 82 (2018) 77–86, https://doi.org/10.1016/j.jmbbm.2018.03.004.
[20] S.V. Palagummi, T. Hong, L. Jiang, M.Y.M. Chiang, Thermal shrinkage reveals the feasibility of pulse-delay photocuring technique, Dent. Mater. 37 (2021) 1772–1782, https://doi.org/10.1016/j.dental.2021.09.007.
[21] M. Dewaele, E. Asmussen, A. Peutzfeldt, E.C. Munksgaard, A.R. Benetti, G. Finné, G. Leloup, J. Devaux, Influence of curing protocol on selected properties of light-curing polymers: degree of conversion, volume contraction, elastic modulus, and glass transition temperature, Dent. Mater. 25 (2009) 1576–1584, https://doi.org/10.1016/j.dental.2009.08.001.
[22] V.P. Feitosa, A.P.P. Fugolin, A.B. Correr, L. Correr-Sobrinho, S. Consani, T. F. Watson, M.A.C. Sinhoreti, S. Sauro, Effects of different photo-polymerization protocols on resin–dentine mTBS, mechanical properties and cross-link density of a nano-filled resin composite, J. Dent. 40 (2012) 802–809, https://doi.org/10.1016/j.jdent.2012.05.014.
[23] H. Lu, J.W. Stansbury, C.N. Bowman, Impact of curing protocol on conversion and shrinkage stress, J. Dent. Res. 84 (2005) 822–826, https://doi.org/10.1177/154405910508400908.
[24] J. Zubia, J. Arrue, Plastic optical fibers: an introduction to their technological processes and applications, Opt. Fiber Technol. 7 (2001) 101–140, https://doi.org/10.1006/ofte.2000.0355.
[25] E. Novta, T. Lainović, D. Grujić, S. Savić-Šević, E. Toth, Ž. Cvejić, L. Blažić, Internal photo-activation of a dental composite using optical fibers: a holographic, thermographic and Raman study, Opt. Quantum Electron. 54 (2022) 1–18, https://doi.org/10.1007/s11082-022-04233-2.
[26] W.A. Gambling, The rise and rise of optical fibers, IEEE J. Sel. Top. Quantum Electron. 6 (2000) 1084–1093, https://doi.org/10.1109/2944.902157.
[27] N. Yu, P. Genevet, M.A. Kats, F. Aieta, J.P. Tetienne, F. Capasso, Z. Gaburro, Light propagation with phase discontinuities: generalized laws of reflection and refraction, Science 334 (80–) (2011) 333–337, https://doi.org/10.1126/science.1210713.
[28] L.E.J. McHugh, I. Politi, R.S. Al-Fodeh, G.J.P. Fleming, Implications of resin-based composite (RBC) restoration on cuspal deflection and microleakage score in molar teeth: placement protocol and restorative material, Dent. Mater. 33 (2017) e329–e335, https://doi.org/10.1016/j.dental.2017.06.001.
[29] I. Politi, L.E.J. McHugh, R.S. Al-Fodeh, G.J.P. Fleming, Modification of the restoration protocol for resin-based composite (RBC) restoratives (conventional and bulk fill) on cuspal movement and microleakage score in molar teeth, Dent. Mater. 34 (2018) 1271–1277, https://doi.org/10.1016/j.dental.2018.05.010.
[30] J. Hayashi, J. Tagami, D. Chan, A. Sadr, New bulk-fill composite system with high irradiance light polymerization: integrity and degree of conversion, Dent. Mater. 36 (2020) 1615–1623, https://doi.org/10.1016/j.dental.2020.10.012.
[31] D. Pantelić, D. Vasiljević, L. Blažić, S. Savić-Šević, B. Murić, M. Nikolić, Biomechanical model produced from light-activated dental composite resins: a holographic analysis, Phys. Scr. T157 (2013) 014021, https://doi.org/10.1088/0031-8949/2013/T157/014021.
[32] D. Pantelić, S. Savić-Šević, D. Vasiljević, B. Murić, L. Blažić, M. Nikolić, B. Panić, Holographic measurement of a tooth model and dental composite contraction, Mater. Manuf. Process. 24 (2009) 1142–1146, https://doi.org/10.1080/10426910902979470.
[33] D. Papadogiannis, K. Tolidis, P. Gerasimou, R. Lakes, Y. Papadogiannis, Viscoelastic properties, creep behavior and degree of conversion of bulk fill composite resins, Dent. Mater. 31 (2015) 1533–1541, https://doi.org/10.1016/j.dental.2015.09.022.
[34] L. Lassila, S. Garoushi, P.K. Vallittu, E. Säilynoja, Mechanical properties of fiber reinforced restorative composite with two distinguished fiber length distribution, J. Mech. Behav. Biomed. Mater. 60 (2016) 331–338, https://doi.org/10.1016/j.jmbbm.2016.01.036.
[35] S. Jafarnia, A. Valanezhad, S. Shahabi, S. Abe, I. Watanabe, Physical and mechanical characteristics of short fiber-reinforced resin composite in comparison with bulk-fill composites, J. Oral Sci. (2021) 1–4, https://doi.org/10.2334/josnusd.20-0436.
[36] Y.R. Zhang, W. Du, X.D. Zhou, H.Y. Yu, Review of research on the mechanical properties of the human tooth, Int. J. Oral Sci. 6 (2014) 61–69, https://doi.org/10.1038/ijos.2014.21.
[37] W. Germscheid, L.G. de Gorre, B. Sullivan, C. O'Neill, R.B. Price, D. Labrie, Post-curing in dental resin-based composites, Dent. Mater. 34 (2018) 1367–1377, https://doi.org/10.1016/j.dental.2018.06.021.
[38] D.V. Pantelić, D.Ž. Grujić, D.M. Vasiljević, Single-beam, dual-view digital holographic interferometry for biomechanical strain measurements of biological objects, J. Biomed. Opt. 19 (2014), https://doi.org/10.1117/1.jbo.19.12.127005, 127005-1–10.
[39] M. Kim, R.J. Kim, J. Ferracane, I. Lee, Thermographic analysis of the effect of composite type, layering method, and curing light on the temperature rise of photo-cured composites in tooth cavities, Dent. Mater. 33 (2017) e373–e383, https://doi.org/10.1016/j.dental.2017.07.007.
[40] R.R. Braga, J.L. Ferracane, Contraction Stress Related to Degree of Conversion and Reaction Kinetics, J. Dent. Res. 81 (2002) 114–118.
[41] C.S. Pfeifer, J.L. Ferracane, R.L. Sakaguchi, R.R. Braga, Factors affecting photopolymerization stress in dental composites, J. Dent. Res. 87 (2008) 1043–1047, https://doi.org/10.1177/154405910808701114.
[42] R.R. Braga, R.Y. Ballester, J.L. Ferracane, Factors involved in the development of polymerization shrinkage stress in resin-composites: a systematic review, Dent. Mater. 21 (2005) 962–970, https://doi.org/10.1016/j.dental.2005.04.018.
[43] M. Atai, F. Motevasselian, Temperature rise and degree of photopolymerization conversion of nanocomposites and conventional dental composites, Clin. Oral Investig. 13 (2009) 309–316, https://doi.org/10.1007/s00784-008-0236-2.
[44] Z. Wang, F.A. Landis, A.A.M. Giuseppetti, S. Lin-Gibson, M.Y.M. Chiang, Simultaneous measurement of polymerization stress and curing kinetics for photo-polymerized composites with high filler contents, Dent. Mater. 30 (2014) 1316–1324, https://doi.org/10.1016/j.dental.2014.09.006.
[45] J.W. Stansbury, Dimethacrylate network formation and polymer property evolution as determined by the selection of monomers and curing conditions, Dent. Mater. 28 (2012) 13–22, https://doi.org/10.1016/j.dental.2011.09.005.
[46] L.C.C. Boaro, F. Goncalves, T.C. Guimaraes, J.L. Ferracane, A. Versluis, R.R. Braga, Polymerization stress, shrinkage and elastic modulus of current low-shrinkage restorative composites, Dent. Mater. 26 (2010) 1144–1150, https://doi.org/10.1016/j.dental.2010.08.003.
[47] D.A. Abu-Elenain, S.H. Lewis, J.W. Stansbury, Property evolution during vitrification of dimethacrylate photopolymer networks, Dent. Mater. 29 (2013) 1173–1181, https://doi.org/10.1016/j.dental.2013.09.002.
[48] C.S.C. Pfeifer, R.R. Braga, J.L. Ferracane, Pulse-delay curing: influence of initial irradiance and delay time on shrinkage stress and microhardness of restorative composites, Oper. Dent. 31 (2006) 610–615, https://doi.org/10.2341/05-118.
[49] B.S. Lim, J.L. Ferracane, R.L. Sakaguchi, J.R. Condon, Reduction of polymerization contraction stress for dental composites by two-step light-activation, Dent. Mater. 18 (2002) 436–444, https://doi.org/10.1016/S0109-5641(01)00066-5.
[50] S.V. Palagummi, T. Hong, Z. Wang, C.K. Moon, M.Y.M. Chiang, Resin viscosity determines the condition for a valid exposure reciprocity law in dental composites, Dent. Mater. 36 (2020) 310–319, https://doi.org/10.1016/j.dental.2019.12.003.
[51] V. Miletic, P. Pongprueksa, J. De Munck, N.R. Brooks, B. Van Meerbeek, Curing characteristics of flowable and sculptable bulk-fill composites, Clin. Oral Investig. 21 (2017) 1201–1212, https://doi.org/10.1007/s00784-016-1894-0.
[52] F.C. Calheiros, Y. Kawano, J.W. Stansbury, R.R. Braga, Influence of radiant exposure on contraction stress, degree of conversion and mechanical properties of resin composites, Dent. Mater. 22 (2006) 799–803, https://doi.org/10.1016/j.dental.2005.11.008.
[53] D. Selig, T. Haenel, B. Hausnerová, B. Moeginger, D. Labrie, B. Sullivan, R.B. T. Price, Examining exposure reciprocity in a resin based composite using high irradiance levels and real-time degree of conversion values, Dent. Mater. 31 (2015) 583–593, https://doi.org/10.1016/j.dental.2015.02.010.
[54] W.J. Wang, A. Grymak, J.N. Waddell, J.J.E. Choi, The effect of light curing intensity on bulk-fill composite resins: heat generation and chemomechanical properties, Biomater. Investig. Dent. 8 (2021) 137–151, https://doi.org/10.1080/26415275.2021.1979981.
[55] P. Yu, A.U.J. Yap, X.Y. Wang, Degree of conversion and polymerization shrinkage of bulk-fill resin-based composites, Oper. Dent. 42 (2017) 82–89, https://doi.org/10.2341/16-027-L.
[56] N. Ilie, G.J.P. Fleming, *In vitro* comparison of polymerisation kinetics and the micro-mechanical properties of low and high viscosity giomers and RBC materials, J. Dent. 43 (2015) 814–822, https://doi.org/10.1016/j.jdent.2015.04.009.
[57] K. Al-ahdal, N. Ilie, N. Silikas, D.C. Watts, Polymerization kinetics and impact of post polymerization on the Degree of Conversion of bulk-fill resin-composite at clinically relevant depth, Dent. Mater. 31 (2015) 1207–1213, https://doi.org/10.1016/j.dental.2015.07.004.

Optical Properties of Volume Gratings with Nanosphere-Filled Layers – Biomimetics of Moth Structures

Svetlana Savić-Šević[1], Branislav Salatić[1], Dejan Pantelić[1], Brana Jelenković[1], Srećko Ćurčić[2], and Dejan Stojanović[3]

1 Institute of Physics, University of Belgrade, Pregrvica 118, 11080 Belgrade, Serbia

2 Institute of Zoology, University of Belgrade—Faculty of Biology, Studentski Trg 16, 11000 Belgrade, Serbia

3 Institute of Lowland Forestry and Environment, University of Novi Sad, Antona Cehova 13, 21000 Novi Sad, Serbia

Tel: (381) 62 802 6967, e-mail: savic@ipb.ac.rs

ABSTRACT

A new type of layered photonic structure, whose alternating layers are filled with randomly dispersed nano-spheres, is fabricated and its optical properties are experimentally and theoretically analysed. Structures are made on a pullulan doped with chromium ions (dichromated pullulan – DCP) using holography. We found that experimental structures are similar to those observed on wings of the *Diachrysia chrysitis* moth, having layers of overlapping scales. DCP photonic structure has alternating air-pullulan layers, held in place by sparsely separated nano-pillars, and air voids filled with 30 – 60 nm diameter nanospheres which act as scatterers. Theoretical analysis of such structures shows that the scattering and interference interact to enhance the local field within the layers and increase the residual absorption of the material. We compare optical properties of moth scales with properties of structures fabricated in DCP, and calculated from the functional model.

Keywords: holography, photonic structures, nonlinear analysis, bio-mimetics.

1. INTRODUCTION

Nano and micro structures found in insects are increasingly becoming inspiration for fabrications of similar photonic structures because of their unique optical properties [1]. In that respect, butterflies and moths (Lepidoptera) are particularly interesting, due to their intricately nano-patterned wing scales.

There are different methods to imitate natural photonic structures [1], but holography is one of the simplest. It was applied to suitable photo-sensitive materials, such as photoresists [2]. We use interference (holographic) lithography to manufacture Bragg gratings in a home-made dichromated material, based on pullulan [3] (a linear homo-polysacharide produced by a yeast-like fungus *Aureobasidium pullulans*). In that way, a number of alternating air-pullulan layers, filled with spherical nanoparticles are produced on large substrates. Nano-spheres diffuse the radiation, prevalently in the blue-green part of the spectrum.

Here we show that fabricated structures and their optical properties are similar to those found on wings of the *Diachrysia chrysitis* moth. Their wings are covered with double layer of tiny, overlapping, scales, each individual scale consists of two membranes (laminae) with rough internal surfaces, with roughness between 30 – 50 nm.

We develop theoretical model to describe optical properties of structures with ordered and disordered components, confirming a useful interplay between scattering, local field enhancement, planar waveguiding and interference. From the theoretical point of view, the incoming radiation is treated as being split into scattered and specular components, which are treated separately. Scattered radiation is analyzed by the surface scattering theory [4], supplemented by the intensity enhancement mechanism in planar layers [5]. The specular component interferes on a multilayer structure and is calculated using transfer matrix method [6].

2. FABRICATION OF DCP VOLUME HOLOGRAPHIC GRATING

Diffraction gratings with spherical inclusions are fabricated by combination of holographic method (top-down technique) and non-solvent-induced phase separation (bottom-up technique) [7]. The whole process goes in several steps: (1) preparation of DCP film on a glass plate (2) film exposure using a laser (3) development of exposed film (4) immersion in a non-solvent bath (isopropyl) at room temperature, and (5) drying in closed vessel.

In the first step, DCP was prepared by mixing 8% aqueous solution of pullulan (from Sigma-Aldrich) and 45% of the ammonium dichromate (by weight of pullulan). The solution was coated onto a clean glass slide in a horizontal position and the film was dried overnight under normal laboratory conditions. Dry DCP film is yellowish and transparent.

The film was exposed at normal incidence using a single longitudinal mode, diode pumped Nd YAG laser, at 532 nm. After propagation through the emulsion, beam was reflected back from a mirror behind the DCP plate. The two counter-propagating beams interfere to create a standing wave pattern and grating within an emulsion. The interference pattern consists of planes parallel to the substrate surface with spacing $d = \lambda/2n$,

where λ is the wavelength of the laser source and n = 1.47 is the refractive index of DCP. During exposure, hexavalent chromium ion Cr^{+6} is photo-reduced to trivalent Cr^{+3}, which covalently cross-links with pullulan molecules in the areas of constructive interference. Cross-linking hardens the pullulan, creating a solubility difference between exposed and unexposed regions.

DCP plate was chemically processed after exposure. Mixture of water and isopropyl alcohol (3:1 ratio) was used as a developer, which dissolves unexposed material. After two minutes, developer was replaced with pure isopropyl-alcohol used to dehydrate the DCP film. Finally, material is dried in closed vessel.

3. MODEL FOR SCATTERING FROM DIFRACTION GRATINGS WITH NANOPARTICLES

Here we outline a theory of volume gratings with subwavelength, nanometer sized spherical inclusions (schematically shown in Fig. 1a) – details can be found in [8]. Under these assumptions, scalar surface-scattering theory is applicable, which predicts splitting of the incident light into two components: one, regular, propagating as if the surface is perfectly flat, and the other diffusely scattered (haze) – see Fig. 1b. Scattering effectively reduces Fresnel reflection and transmission coefficients according to [4]:

$$T_H(\lambda) = T_0\left[1-\exp\left(-\left[\frac{2\pi\sigma}{\lambda}(n_i\cos\phi_i - n_t\cos\phi_t)\right]^2\right)\right] \quad (1)$$

$$R_H(\lambda) = R_0\left[1-\exp\left(-\left[\frac{4\pi\sigma}{\lambda}n_i\cos\phi_i\right]^2\right)\right] \quad (2)$$

where T_0 and R_0 are the transmittance and the reflectance of a perfectly flat surface respectively, λ is the vacuum wavelength, ϕ_i and ϕ_t are the angles of incidence and refraction, n_i and n_t are corresponding refractive indices, while σ is the surface RMS roughness. Calculation, based on Eqs. (1) and (2), shows that between 1% and 3% of incident radiation is scattered at each interface, depending on the wavelength and assuming normal angle of incidence (ϕ_i = 0), RMS roughness σ = 20 nm and the refractive index of pullulan n_i = 1.47. As expected, short wavelengths are scattered more than long. The scattered light has a tendency to be trapped inside chitin layers, in a manner similar to textured solar cells. Local field enhancement due to scattering and fraction of the incident radiation escaping the layer are calculated based on formulas in [5].

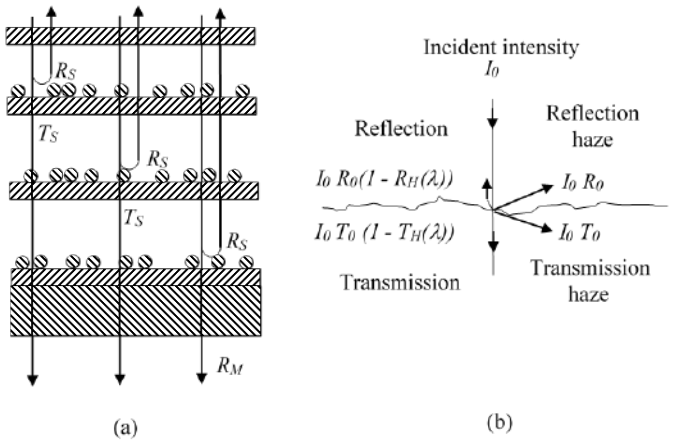

Figure. 1: (a) Schematic presentation of a diffraction grating with nano-sized particles; (b) Incident radiation is divided into specular component and haze.

4. PROPERETIES OF LAYERED SCATTERING STRUCTURES

In this section we compare morphology and optical properties of structures on moth's scales and fabricated photonic structures in DCP. And also present results of theoretical model that calculates transmission and reflection from similar structures, taking onto account interference and scattering on multiple layers and nano particles.

Morphology of the moth scales and DCP grating were investigated using high resolution field emission scanning electron microscopes (Mira FEGSEM, manufactured by Tescan). Moth wing is covered with overlapping layers of scales, which produce a volume structure. Each scale has rough internal surfaces with a number of spherical inclusions (Fig. 2a). A DCP grating has a similar structure. It is layered too, with nano-spheres filling the space between the layers (Fig. 2b).

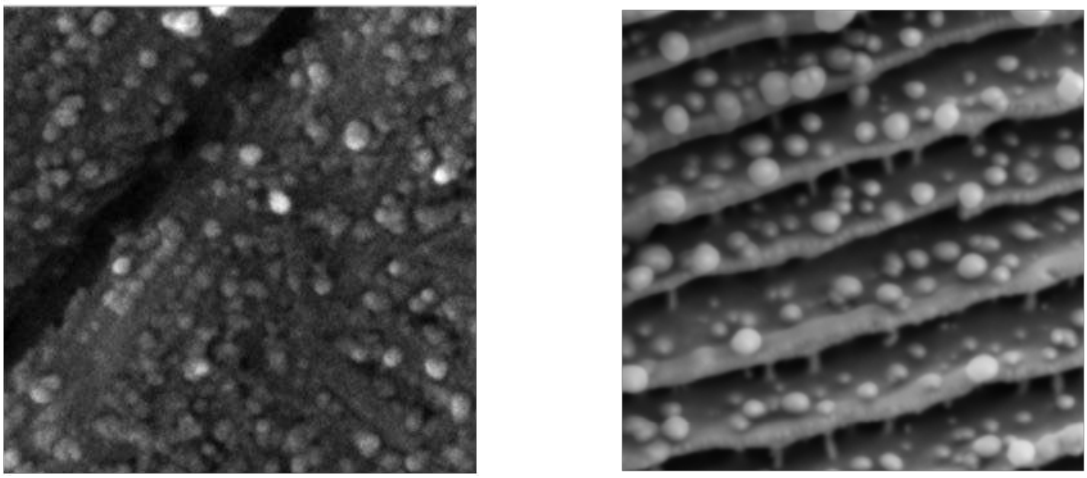

(a) (b)

Figure 2. FEGSEM image of: (a) Internal surface of the D. chrysitis wing scale; (b) Internal structure of a DCP grating.

Measured transmission and reflection spectra of the *D. chrysitis* wings and the DCP grating are presented in Figs. 3a and 3b. The maximum of reflection peaks between 500 – 550 nm. Transmission increases in the near infrared.

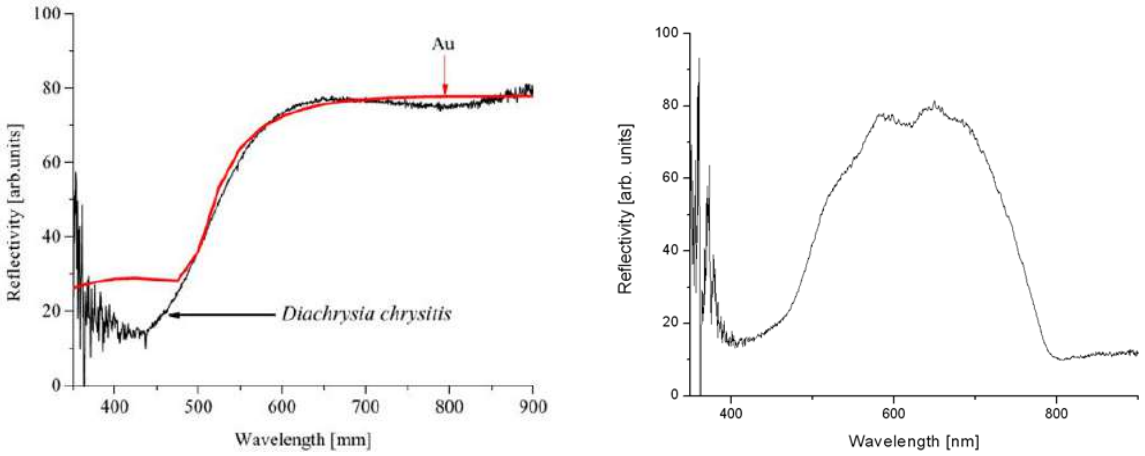

(a) (b)

Figure 3. Experimentally recorded reflection spectra of (a) the D. chrysitis wing (compared to spectrum of metallic gold) and (b) the DCP grating.

In Fig. 4 we present a reflection spectrum using transfer matrix method for several values of RMS roughness. By comparing the averaged spectrum with the experimentally recorded one agreement is qualitatively good.

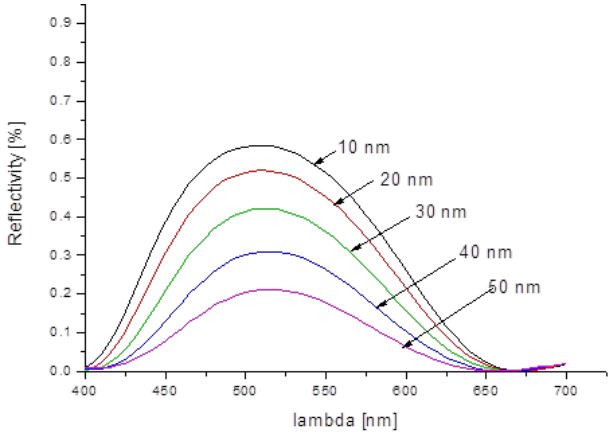

Figure. 4. Reflectance spectrum of a model calculated by transfer matrix method with scattering effects included. Family of curves presents spectra for rough surface RMS ranging from 10 – 50 nm.

5. CONCLUSIONS

We have shown that peculiar, natural photonic structure can be reproduce by using relatively simple method of holographic lithography. Fabricated photonic structures exhibit similar morphology and optical properties as structures on scales on wings of *Diachrysia chrysitis* moth. Measured optical reflection spectra and calculated by finite element method, applied to the model simulating a multi-layers with nan-sizes particles in between, have shown good agreement between the two.

ACKNOWLEDGEMENTS

Authors like to acknowledge financial support from projects ON171038 and III45016 of the Ministry of Education, Science and Technological Development of the Republic of Serbia.

REFERENCES

[1] O.Karthaus *ed*.: *Biomimetics in Photonics*, CRC Press (2013).
[2] R. H. Siddique, R. Hünig, A. Faisal, U. Lemmer, and H. Hölscher: Fabrication of hierarchical photonic nanostructures inspired by Morpho butterflies utilizing laser interference lithography, *Optical Materials Express* 5, 996-1005 (2015).
[3] S. Savić-Šević and D. Pantelić: Dichromated pullulan diffraction gratings: Influence of environmental conditions and storage time on their properties, *Applied Optics* 46 , 287-291 (2007).
[4] D. Domine, F.-J. Haug, C. Battaglia, and C. Ballif: Modeling of light scattering from micro- and nanotextured surfaces, *J. Appl. Phys* 107, 044504:1-8 (2010).
[5] E. Yablonovich and G. D. Cody: Intensity enhancement in textured optical sheets for solar cells, *IEEE Trans. Electron Devices* 29, 300 (1982).
[6] J. Springer, A. Porube, and M. Vanacek: Improved three-dimensional optical model for thin film silicon solar cells, *J. Appl. Phys*. 96, 5329 (2004).
[7] Y. Wang et al.: Phase-separation-induced micropatterned polymer surfaces and their applications, *Adv. Funct. Mater*. 15, 655-663 (2005).
[8] D. Pantelić *et al*.: Scattering-enhanced absorption and interference produce a golden wing color of the burnished brass moth, Diachrysia chrysitis, *Phys. Rev. E* 95, 032405 (2017).

Optical and Quantum Electronics (2024) 56:1674
https://doi.org/10.1007/s11082-024-07182-0

Host effects on luminescent properties of Er, Yb doped nanophosphors: visual comparison by data dimensionality reduction technique

M. S. Rabasović[1] · D. M. Pavlović[1] · J. Križan[2] · S. Savić-Šević[1] · J. Potočnik[3] · M. G. Nikolić[1] · D. Šević[1]

Received: 29 October 2023 / Accepted: 10 June 2024
© The Author(s), under exclusive licence to Springer Science+Business Media, LLC, part of Springer Nature 2024

Abstract
In this study we introduce photoluminescence analysis of nano powder $YAlO_3$ doped with Er^{3+} and Yb^{3+}. We compare this material with other hosts, Gd_2O_3, $CaGdAlO_4$ and Y_2O_2S, doped with Er^{3+} and Yb^{3+}. Beside usual ways to characterize these materials we also include visual comparison by data dimensionality reduction techniques, as a way for initial assessment of a new material. Samples were excited at 980 nm by using pulsed laser diode to analyze effects of host matrices on optical emission of erbium. For this purpose the luminescence spectra of all samples were obtained in a continuous series of measurements under the same experimental conditions. Moreover, the samples were prepared in the same way, by combustion synthesis. We compare the possibilities of using these materials for remote temperature sensing, showing that $YAlO_3$:Er^{3+}, Yb^{3+} is a good candidate for remote temperature sensing.

Keywords Photoluminescence · Thermographic phosphor · Laser spectroscopy · Machine learning

1 Introduction

Optical thermometry finds extensive application in remotely measuring temperature (Allison et al. 1997; Alden et al. 2011; Avram et Tiseanu 2018; Brites et al. 2012; Jaque and Vetrone 2012; Khalid and Kontis 2008; Zhao et al. 2019; Wang et al. 2015). Numerous established methods for temperature sensing through thermographic phosphors exist, with the luminescence intensity ratio (IR) approach being particularly favored.

✉ D. Šević
sevic@ipb.ac.rs

[1] Institute of Physics Belgrade, National Institute of the Republic of Serbia, University of Belgrade, Belgrade, Serbia

[2] AMI d.O.O, Ptuj, Slovenia

[3] Department of Atomic Physics, Vinča Institute of Nuclear Sciences, National Institute of the Republic of Serbia, University of Belgrade, Belgrade, Serbia

Often, this technique relies on examining variations in the intensity of thermally coupled transitions at various temperatures for analysis. However, IR approach can be also based on intensity ratios of thermally non coupled transitions, including intensity ratios between two dopant's transitions and intensity ratios between dopant and host matrix luminescence (Piotrowski et al. 2024; Sevic et al. 2020C).

Recent studies, which have been published, indicate that the Er^{3+} ion is predominantly employed in IR-based temperature sensing with up-conversion (UC) phosphors (Li et al. 2016a, b; Avram et al. 2018; Du et al. 2017, 2018; Dong et al. 2007; Xu et al. 2012; Liu et al. 2016; Santos et al. 1999; Wang et al. 2015; Manzani et al. 2017; Singh et al. 2009; Krizan et al. 2014).

Aim of this study is to investigate the potential of Er^{3+} and Yb^{3+} doped $YAlO_3$ for luminescence thermometry. There are many publications about $YAlO_3$, usually doped with lanthanides (Suganya et al. 2020; Shimizu et al. 2017; Sreebunpeng et al. 2020; Nemec et al. 2018) and references therein, for various applications; often for lasing. Upconversion in $YAlO_3$:Er pumped at 800 nm is described in (Weber et al. 1992). Fabrication of Er^{3+}:$YAlO_3$ fibers for upconversion luminescence applications is described in (Gan et al. 2023). In (Perisha et al. 2022) $YAlO_3$, doped with Dy is analyzed with respect to its potential applications in thermometry. The photoluminescence properties of $YAlO_3$:Er^{3+}, Yb^{3+} were analyzed in (Lü et al. 2008; Hernández-Rodriguez et al. 2018). In this study we compare this material with other hosts doped with Er^{3+} and Yb^{3+}: Gd_2O_3, $CaGdAlO_4$ and Y_2O_2S.

Only experienced researchers can visually estimate spectral data for initial assessment. Nowadays, visualization of various complex data based on machine learning becomes more and more popular. So, another goal presented in this paper is to analyze possibilities of initial assessment of photoluminescence data by using visualization techniques based on data dimensionality reduction. Number of measured points of luminescence spectra depends on spectroscope resolution and range. It is usually from several hundred to several thousands. Luminescence spectra obtained by us in this study with the aim of determining the temperature calibration curves have 640 points. If measurements are performed at 10 temperatures acquired data have 6400 dimensions. For making model we used measured spectra of (Sevic et al. 2022; Sevic et. al. 2020B, Sevic et al. 2019) as training data. For testing data we used measured spectra of synthesized $YAlO_3$ doped with Er,Yb. Data visualization is reviewed in (Runkler 2020), where role of PCA and similar methods are accentuated for visualization of high dimensional data. Our initial studies of using PCA for luminescence spectra analysis are presented in (Sevic et al. 2020B; Sevic et. al 2021).

In this paper we compare the spectral data by using data dimension reduction techniques based on machine learning (ML). Dimension reduction of data is a fundamental technique in the field of machine learning. This method involves utilizing a structured dataset to "train" a machine, allowing it to identify specific features in the input data. These discernible features are emphasized through the data dimension reduction process. Consequently, the machine becomes adept at recognizing and identifying these features in newly presented data with a similar structure and nature.

A common approach to automate this analysis is by instructing the machine on a low-dimensional representation of the data. Within this reduced-dimensional representation, each object from the original high-dimensional dataset is depicted as a point in a lower-dimensional space. This representation is designed in such a way that close points correspond to similar objects, while distant points correspond to dissimilar ones. The low-dimensional embedding is suitable for easy visualization.

In this study, we compare the methods of Principal Component Analysis (PCA), t-Distributed Stochastic Neighbor Embedding (t-SNE), and Uniform Manifold Approximation and Projection (UMAP) for analysis.

PCA has been introduced quite some time ago, as documented in (Hotelling 1933; Karhunen 1947; L´evy 1948). An efficient implementation of t-SNE was proposed by (Van der Maaten et Hinton 2008). UMAP, on the other hand, was introduced in (McInnes et al. 2020; Sainburg et al. 2020).

Like many nonlinear dimension reduction techniques, t-SNE and UMAP lack the strong interpretability of PCA. Specifically, in t-SNE and UMAP, the dimensions of the embedding space do not possess specific meanings, unlike PCA, where the dimensions represent the directions of greatest variance in the source data.

2 Experimental procedures and analysis methods

The Solution Combustion Synthesis (SCS) method, explained in detail in (Krizan et al. 2014), was used to prepare the studied nano phosphors. The samples were acquired from AMI d.o.o (Slovenia). Only one dopant ratio was available for each material. We utilized these materials to demonstrate comparisons between hosts using machine learning methods. The $YAlO_3$:Er Yb nano phosphor was prepared as follows: Stoichiometric quantities of starting chemicals $Y(NO_3)_3$ $6H_2O$, $Al(NO_3)_3$ $9H_2O$, $Er(NO_3)_3$ $5H_2O$ and $Yb(NO_3)_3$ $5H_2O$ with the high purity were chosen to obtain the Er concentration of 2.0 at% and Yb concentration of 2.5 at% in $YAlO_3$ Er,Yb; usually written as $YAlO_3$:2%Er,2.5%Yb, or $Y_{0.955}AlO_3$ $Er_{0.02}$,$Yb_{0.025}$. Starting chemicals were combined with the urea which was used as organic fuel. So prepared starting reagents were combusted with the flame burner at approximately 500 °C. Intensive exothermic reaction yielded voluminous foamy pink powder. In the second step the product was sintered at 1300 °C for 2 h.

Field emission scanning electron microscope (FESEM, FEI Scios 2, Dual Beam system) was employed for morphological examinations of $Y_{1.88}O_2S$:$Er_{0.04}$,$Yb_{0.08}$, $Y_{0.955}AlO_3$ $Er_{0.02}$,$Yb_{0.025}$,$Yb_{0.01}$ and $CaGd_{0.975}AlO_4$:$Er_{0.01}$,$Yb_{0.015}$. The structure of the $Gd_{0.95}O_3$:$Er_{0.04}$, $Yb_{0.01}$ was observed using a high-resolution scanning electron microscope (SEM) equipped with a high-brightness Schottky Field Emission gun (FEGSEM, TESCAN) operating at 4 kV.

Pulsed laser diode excitation at 980 nm was used to acquire the photoluminescence emission spectra o Er^{3+},Yb^{3+} doped nano phosphors. The optical emission of analyzed samples was detected by using the streak camera system, used and explained in (Rabasovic et al. 2023B; Sevic et al. 2022; Sevic et al. 2020B; Sevic et al. 2020C).

To perform the machine learning (ML) analysis of the data, we utilized the Solo+Mia software package (Version 9.1, Eigenvector Research Inc, USA).

To create the machine learning models, we utilized luminescence spectra from $Y_{1.88}O_2S$:$Er_{0.04}$,$Yb_{0.08}$, $Gd_{1.95}O_3$:$Er_{0.04}$,$Yb_{0.01}$ and $CaGd_{0.975}AlO_4$:$Er_{0.01}$,$Yb_{0.015}$. For testing purposes we used $Y_{0.955}AlO_3$ $Er_{0.02}$, $Yb_{0.025}$.

3 Results and discussion

Yttrium orthoaluminate, $YAlO_3$, is known to have a perovskite like crystal structure (Diehl and Brandt 1975). It is therefore usually termed YAP (Yttrium–Aluminium-Perovskite) in analogy to YAG (Yttrium–Aluminium-Garnet).

Figure 1 shows SEM images of Er^{3+},Yb^{3+} doped hosts analyzed in this study. Agglomerated grains and particles with dimensions from 30 nm to over 100 nm could be seen. Note that the images are not taken with the same magnification and they are not all from the same SEM.

The photoluminescence emission of Er^{3+}, Yb^{3+} doped hosts were measured over the temperature range 300–700 K. Streak images are shown in Fig. 2. The pseudocolored streak images are presented, with the vertical axis representing time and the horizontal axis representing the wavelength of optical emission. The emission band centered at 528 nm originates from $^2H_{11/2} \rightarrow {}^4I_{15/2}$ transition, the emission band at 555 nm originates from to $^4S_{3/2} \rightarrow {}^4I_{15/2}$ transition, and the emission bands at 675 nm originates from $^4F_{9/2} \rightarrow {}^4I_{15/2}$ transition of Er^{3+} ion. It could be seen that red emission band at 675 nm of $CaGdAlO_4$:Er,Yb is very weak.

The CIE chromaticity diagram of emission spectra of $CaGdAlO_4$:Er,Yb, $YAlO_3$:Er,Yb, Gd_2O_3:Er,Yb and Y_2O_2S:Er,Yb are shown in Fig. 3. The colors of different phosphors emissions have different nuances of green and yellow. The colors are near the boundary of CIE chromaticity diagram, in other words, they are almost saturated.

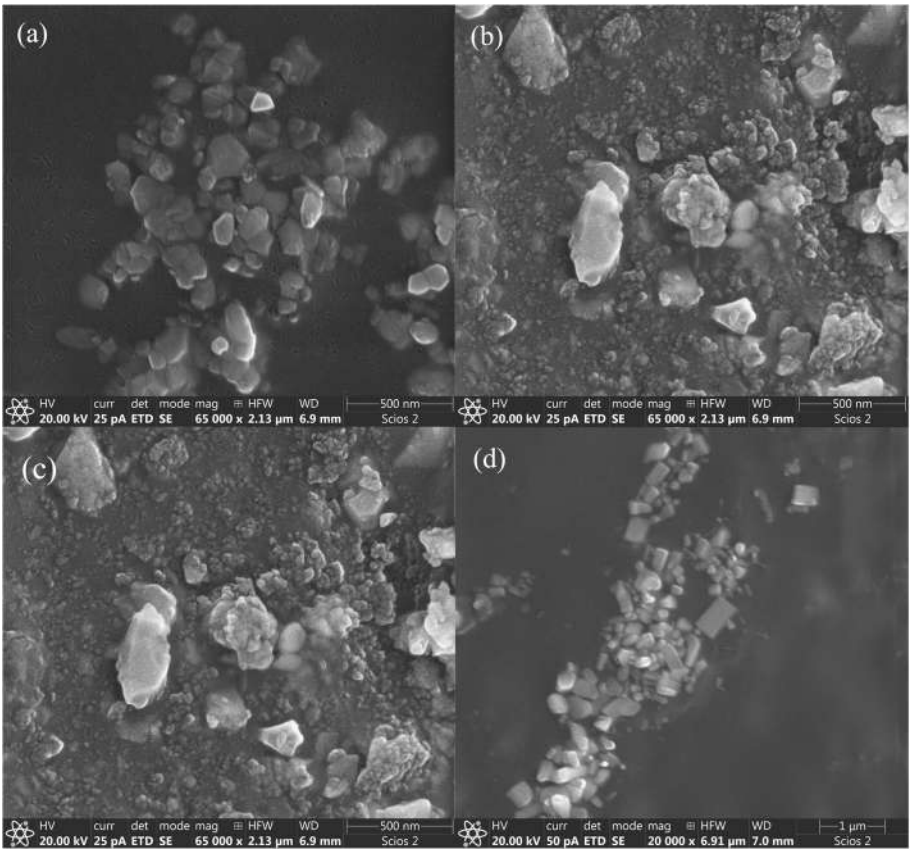

Fig. 1 SEM images of **a** $Y_{1.88}O_2S$:$Er_{0.04}$, $Yb_{0.08}$, **b** $Y_{0.955}AlO_3$ $Er_{0.02}$,$Yb_{0.025}$, **c** $Gd_{1.95}O_3$:$Er_{0.04}$,$Yb_{0.01}$ and **d** $CaGd_{0.975}AlO_4$:$Er_{0.01}$,$Yb_{0.015}$ nanophosphors

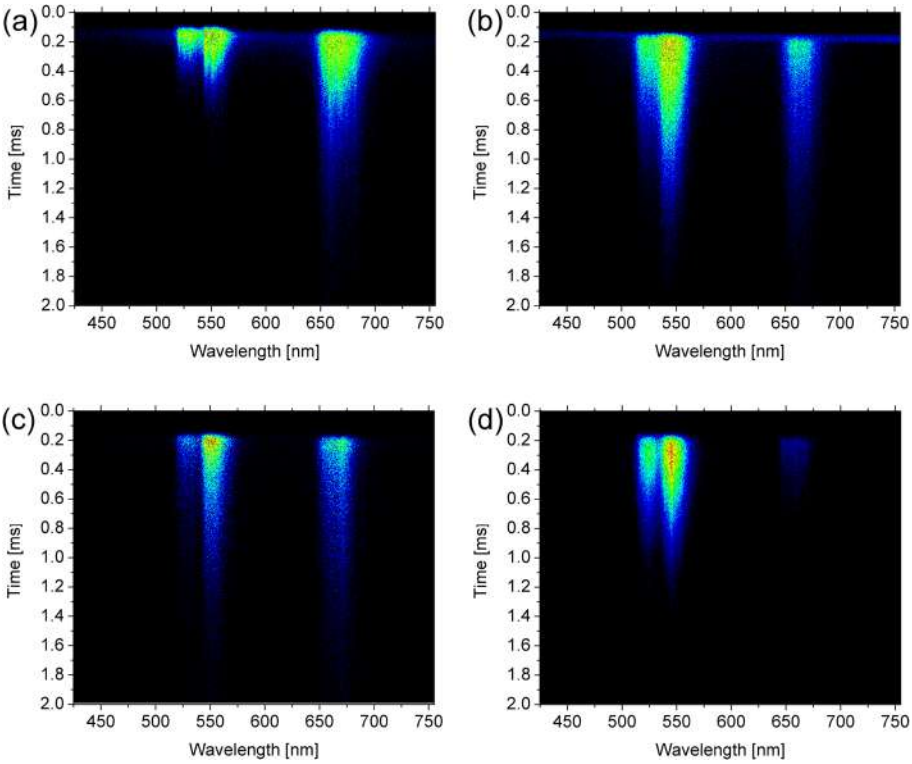

Fig. 2 Streak images of **a** $Y_{1.88}O_2S:Er_{0.04},Yb_{0.08}$, **b** $Y_{0.955}AlO_3\ Er_{0.02},Yb_{0.025}$, **c** $Gd_{1.95}O_3:Er_{0.04},Yb_{0.01}$ and **d** $CaGd_{0.975}AlO_4:Er_{0.01},Yb_{0.015}$ nanophosphors

Integrated–in-time luminescence spectra obtained from time resolved streak images of $Y_{0.955}AlO_3:Er_{0.02},Yb_{0.025}$ at several temperatures are shown in Fig. 4. Inset shows time resolved streak images at two temperatures. It could be seen that the intensities of optical emissions, their intensity ratios and the lifetimes of transitions are temperature dependent.

We will try to predict characteristics of $YAlO_3$:Er,Yb based on PCA, t-SNR and UMAP models constructed from spectral data of $CaGdAlO_4$:Er,Yb, Gd_2O_3:Er,Yb and Y_2O_2S:Er,Yb. So, we will not try to improve sensitivity of remote temperature measurements as we did in our recent publication (Rabasovic et al. 2023B), our aim here is to prove the concept of initial assessment of thermometric potentials of a newly analyzed phosphor based on its spectral characteristics and the spectral characteristics of previously measured phosphors. In (Rabasovic et al. 2023B) we have used large training sets, with 50 training spectra per each measured temperature. Here, we use only single spectrum for each measured temperature. The obvious reason for this lays in the fact that in published results of other authors, for other phosphors, usually only single spectrum is available. We are aware of the fact that the results obtained in this way are not as good as they will be if larger training sets were used.

First, the model is calibrated using spectral data of three before mentioned phosphors on all measured temperatures. Then, the corresponding spectral data of $YAlO_3$:Er,Yb are

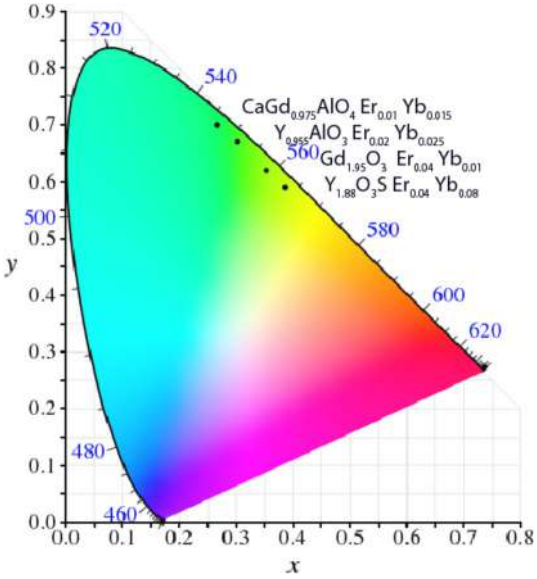

Fig. 3 The CIE chromaticity diagram of emission spectra of $CaGdAlO_4$:Er,Yb, $YAlO_3$:Er,Yb, Gd_2O_3:Er,Yb and Y_2O_2S:Er,Yb

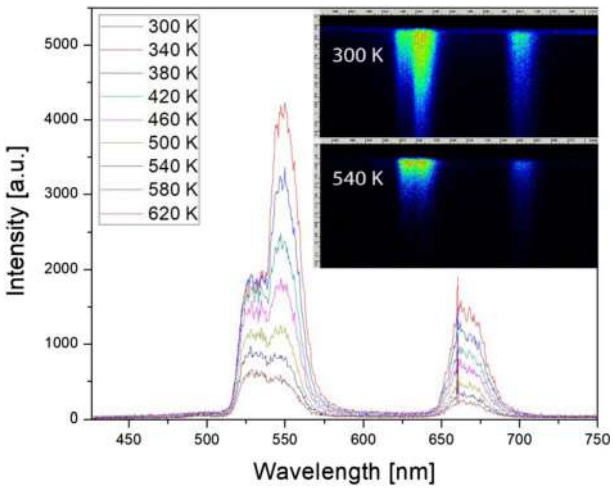

Fig. 4 Integrated-in-time luminescence spectra of $Y_{0.955}AlO_3$ $Er_{0.02}$,$Yb_{0.025}$ at several temperatures. Inset shows streak images at two temperatures. Pulsed laser diode excitation is at 980 nm

used for making prediction of position of their two components in reduced dimensional space, as shown in Figs. 5, 6 and 7.

Let us shortly remind reader about meanings of *scores* and *loadings* in principal components analysis. Each principal component is represented as multiplication of *scores* and loadings vectors. The components are ordered by the amount of variance captured. The *scores* vectors contain information on how the samples relate to each other. The loadings vectors contain information on how the variables relate to each other. So, the similarity or dissimilarity of samples is shown in PCA *scores* plot as the distance between *scores*. Here, in Fig. 5, only the first two components were used because they contain most of the information about samples (about 86% as denoted on Fig. 5). The

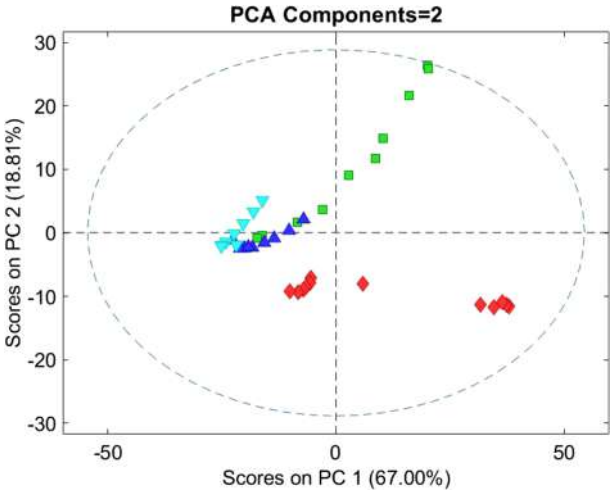

Fig. 5 First two PCA components of luminescence spectra blue triangle- $Y_{0.955}AlO_3$ $Er_{0.02}$,$Yb_{0.025}$, sky blue down triangle-$Gd_{1.95}O_3$:$Er_{0.04}$,$Yb_{0.01}$, green down square-$Y_{1.88}O_2S$:$Er_{0.04}$,$Yb_{0.08}$, red diamond-$CaGd_{0.975}AlO_4$:$Er_{0.01}$,$Yb_{0.015}$

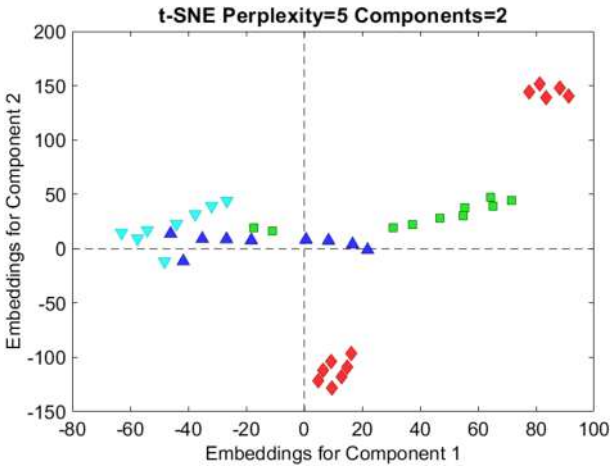

Fig. 6 First two t-SNE components of luminescence spectra blue triangle-$Y_{0.955}AlO_3$ $Er_{0.02}$,$Yb_{0.025}$, sky blue down triangle-$Gd_{1.95}O_3$:$Er_{0.04}$,$Yb_{0.01}$, green down square-$Y_{1.88}O_2S$:$Er_{0.04}$,$Yb_{0.08}$, red diamond-$CaGd_{0.975}AlO_4$:$Er_{0.01}$,$Yb_{0.015}$

clear grouping of $YAlO_3$: Er,Yb temperature dependent spectra could be seen, with small distances between them corresponding to their differences because of different temperatures.

Gd_2O_3:Er,Yb spectra have similar grouping, however on slightly different location. *Scores* of Y_2O_2S:Er,Yb are still grouped together, but occupying more space. $CaGdAlO_4$:Er,Yb *scores* take similar quantity of space as *scores* of Y_2O_2S:Er,Yb, but are not grouped so clearly; and are on clearly different position than the other phosphors. To distinguish them from PCA where *scores* have physical meaning, t-SNE and UMAP use notion of *embeddings* to characterize components. Although t-SNE and UMAP are more sophisticated visualization techniques than PCA, Figs. 6 and 7 provide similar type of spectra grouping, again with clear differences of $CaGdAlO_4$:Er,Yb. So, by using data visualization provided in Figs. 5, 6 and 7 it could be concluded that $CaGdAlO_4$:Er,Yb phosphor is very different from other phosphors. It is in accordance with Fig. 2 where only $CaGdAlO_4$:Er,Yb has very weak red emission.

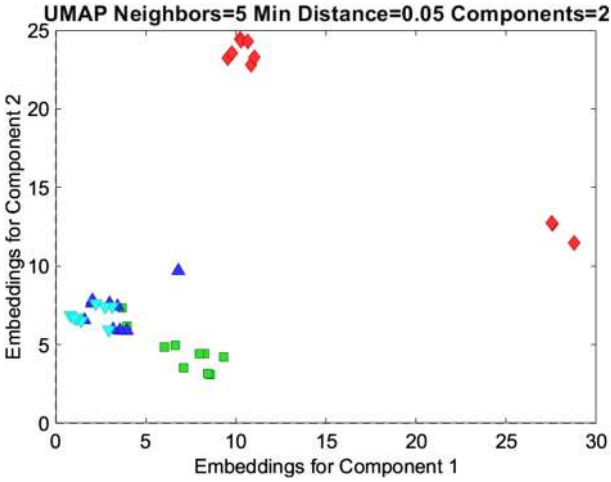

Fig. 7 First two UMAP components of luminescence spectra blue triangle-$Y_{0.955}AlO_3$ $Er_{0.02}$,$Yb_{0.025}$, sky blue down triangle-$Gd_{1.95}O_3$:$Er_{0.04}$,$Yb_{0.01}$, green down square-$Y_{1.88}O_2S$:$Er_{0.04}$,$Yb_{0.08}$, red diamond-$CaGd_{0.975}AlO_4$:$Er_{0.01}$,$Yb_{0.015}$

To check the implications and conclusions of visualizations of characteristics of analyzed phosphors the intensity ratios of luminescence peaks shown in Fig. 4 were calculated. Figure 8 shows temperature dependent luminescence intensity ratios of Er emission lines, at 528 nm, 555 nm and 675 nm. As expected from Figs. 5, 6 and 7, $CaGdAlO_4$:Er,Yb phosphor exhibits totally different nature compared to other phosphors. Samples of $YAlO_3$:Er,Yb and Gd_2O_3:Er,Yb show some similarity in behavior while it seems that Y_2O_2S:Er,Yb behaves quite differently, in a sense that all three intensity ratio curves of this sample have rising slope.

The absolute thermal sensitivity S is determined by how quickly the intensity ratio (IR) changes with temperature, Eq. (1):

$$S = \left| \frac{dIR}{dT} \right| \tag{1}$$

The absolute thermal sensitivity has limited practical utility for comparison; hence, we opt for the relative thermal sensitivity Sr, defined by, Eq. (2):

$$Sr = \left| \frac{1}{IR} \frac{dIR}{dT} \right| \tag{2}$$

Figure 9 shows the relative sensitivity curves of four Er,Yb doped hosts, calculated by Eq. (2). From the three possible intensity ratios, selected is the best result and provided in Fig. 9. Looking at the Fig. 9 we see that, for $CaGdAlO_4$:Er,Yb, $YAlO_3$:Er,Yb and Gd_2O_3:Er,Yb the relative sensitivity is highest at room temperature; however, for Y_2O_2S:Er,Yb sensitivity very slowly increases with temperature, it is almost constant. Similarity between $YAlO_3$:Er,Yb and Gd_2O_3::Er,Yb, predicted by data dimensionality techniques is greater in Fig. 8 (intensity ratios), than in Fig. 9 (relative sensitivities). However, it should be pointed out that for $YAlO_3$:Er,Yb relative sensitivity is better for 675/528 ratio, while for Gd_2O_3::Er,Yb it is better for thermally coupled transitions, 528 nm and 555 nm.

Compared to our recent publication (Rabasovic et al. 2023b) where large training sets were used for spectra discriminating and where UMAP was clearly seen as the best candidate for visualization of data, here all three methods of visualization behave similarly.

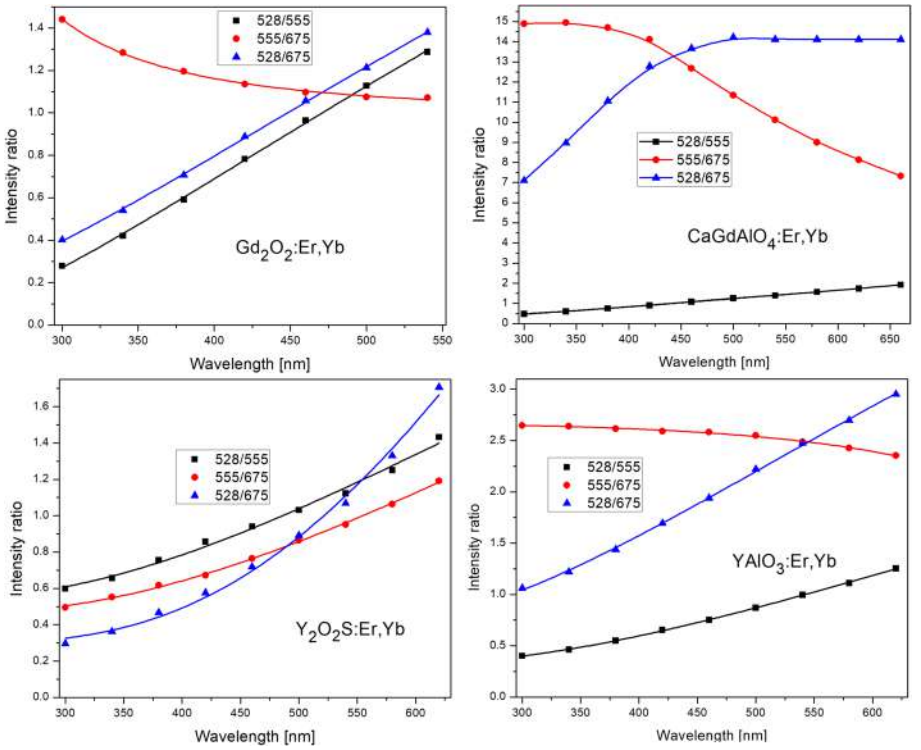

Fig. 8 Intensity ratios of luminescence spectra of Er^{3+},Yb^{3+} doped hosts at several temperatures. Pulsed laser diode excitation is at 980 nm. Experimental points are denoted by symbols and fitted temperature calibration curves are denoted by lines

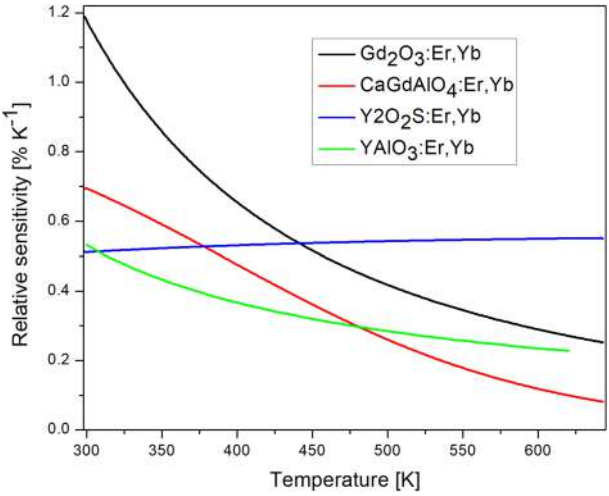

Fig. 9 Relative sensitivities of Er^{3+},Yb^{3+} doped hosts

Probable reason for this probably lies in the fact that here we have not used large training data sets.

4 Conclusion

In this study we compared $YAlO_3$:Er^{3+},Yb^{3+} material with other hosts, Gd_2O_3, $CaGdAlO_4$ and Y_2O_2S, doped with Er^{3+} and Yb^{3+}. Analyzed samples were all fabricated by simple and low-cost SCS (Solution Combustion Synthesis) method. Beside usual approach to compare samples based on intensity ratio and sensitivity calculations, we have compared luminescence characteristics of several hosts doped with Er^{3+} and Yb^{3+} using data dimensionality reduction techniques implemented by ML software. Our analysis indicates that the synthesized material $YAlO_3$:Er,Yb is suitable for temperature measurements, as predicted through machine learning techniques. These predictions are based on visualizing the spectral data of $YAlO_3$:Er,Yb after reducing its dimensionality and comparing it with other previously analyzed Er and Yb-doped host materials by our team. In our forthcoming research, we will endeavor to enhance prediction accuracy further by employing more advanced machine learning techniques.

Acknowledgements This work was financially supported by funding provided by the Institute of Physics Belgrade, through the grant by the Ministry of Science, Technological Development and Innovations of the Republic of Serbia and by the "Vinca" Institute of Nuclear science through the grant by the Ministry of Science, Technological Development and Innovations of the Republic of Serbia.

Author contribution All authors contributed equally.

Funding Institute of Physics Belgrade, through the grant by the Ministry of Science, Technological Development and Innovations of the Republic of Serbia,"Vinca" Institute of Nuclear science through the grant by the Ministry of Science, Technological Development and Innovations of the Republic of Serbia.

Declarations

Competing interests The authors declare no competing interests.

References

Alden, M., Omrane, A., Richter, M., Särner, G.: Thermographic phosphors for thermometry: a survey of combustion applications. Prog. Energy Combust. Sci. **37**, 422–461 (2011)

Allison, S.W., Gillies, G.T.: Remote thermometry with thermographic phosphors: instrumentation and applications. Rev. Sci. Instrum. **68**, 2615–2650 (1997)

Avram, D., Tiseanu, C.: Thermometry properties of Er, Yb–Gd_2O_2S microparticles: dependence on the excitation mode (cw versus pulsed excitation) and excitation wavelength (980 nm versus 1500 nm). Methods Appl. Fluoresc. **6**, 025004 (2018)

Brites, C.D.S., Lima, P.P., Silva, N.J.O., Millan, A., Amaral, V.S., Palacio, F., Carlos, L.D.: Thermometry at the nanoscale. Nanoscale **4**, 4799–4829 (2012)

Diehl, R., Brandt, G.: Crystal structure refinement of YAlO3, a promising laser material. Mater. Res. Bull. **10**, 85–90 (1975). https://doi.org/10.1016/0025-5408(75)90125-7

Dong, B., Liu, D.P., Wang, X.J., Yang, T., Miao, S.M., Li, C.R.: Optical thermometry through infrared excited green upconversion emissions in Er^{3+}–Yb^{3+} codoped Al_2O_3. Appl. Phys. Lett. **90**, 181117 (2007)

dos Santos, P.V., de Araujo, M.T., Gouveia-Neto, A.S., Medeiros Neto, J.A., Sombra, A.S.B.: Optical thermometry through infrared excited upconversion fluorescence emission in Er and Er–Yb doped chalcogenide glasses. IEEE J. Quantum Electron. **35**(395), 399 (1999)

Du, P., Yu, J.S.: Synthesis of Er(III)/Yb(III)-doped BiF_3 upconversion nanoparticles for use in optical thermometry. Microchim. Acta **185**, 237 (2018)

Du, P., Deng, A.M., Luo, L., JaeYu, J.S.: Simultaneous phase and size manipulation in $NaYF_4$:Er^{3+}/Yb^{3+} upconverting nanoparticles for a non-invasion optical thermometer. New J. Chem. **41**, 13855–13861 (2017)

Gan, X., Tian, B., Wang, Z., Xu, Y., Li, L., Wang, L., et al.: Fabrication of Er^{3+}:$YAlO_3$ fibers by electrospinning method for upconversion luminescence applications. Int. J. Appl. Ceram. Technol. **2023**, 1–9 (2023). https://doi.org/10.1111/ijac.14570

Hernández-Rodriguez, M.A., Lozano-Gorrín, A.D., Lavín, V., Rodríguez-Mendoza, U.R., Martín, I.R., Manjón, F.J.: Analysis of the upconversion emission of yttrium orthoaluminate nano-perovskite co-doped with Er3+/Yb3+ ions for thermal sensing applications. J. Lumin. **202**, 316–321 (2018). https://doi.org/10.1016/j.jlumin.2018.05.078

Hotelling, H.: Analysis of a complex of statistical variables into principal components. J. Educ. Psychol. **24**, 417 (1933). https://doi.org/10.1037/h0071325

Jaque, D., Vetrone, F.: Luminescence nanothermometry. Nanoscale **4**, 4301–4326 (2012)

Karhunen, K.: Ueber lineare Methoden in der Wahrscheinlichkeitsrechnung (1947) https://books.google.rs/books?id=Dn3gSAAACAAJ

Khalid, A.H., Kontis, K.: Thermographic phosphors for high temperature measurements: principles, current state of the art and recent applications. Sensors **8**, 5673–5774 (2008)

Krizan, J., Mazaj, M., Kaucic, V., Bajsic, I., Mozina, J.: Synthesis of Er- and Yb-doped gadolinium oxide polymorphs and influence of their structureson upconversion properties. Acta Chim. Slov. **61**, 608–614 (2014)

L´evy, P.: Processus stochastiques et mouvement brownien: suivi d'une note de M. Lo`eve (1948) https://books.google.rs/books?id=tzM7AQAAIAAJ

Li, L., Zheng, L., Xu, W., Liang, Z., Zhou, Y., Zhang, Z., Cao, W.: Optical thermometry based on the red upconversion fluorescence of Er^{3+} in $CaWO_4$:Yb^{3+}/Er^{3+} polycrystalline powder. Optics Lett. **41**, 1458–1461 (2016a)

Li, X., Song, Y., Yang, Y., Mi, C., Liu, Y., Yu, F., Liu, L., Zhang, J., Li, Z.: Structure and optical thermometry characterization of Er^{3+}/Yb^{3+} co-doped $BaGd_2CuO_5$. J. Nanosci. Nanotechnol. **16**, 3542–3546 (2016b)

Liu, L., Qin, F., Lv, T., Zhang, Z., Cao, W.: Accurate thermometry based on the red and green fluorescence intensity ratio in NaYF4: Yb Er nanocrystals for bioapplication. Optics Lett. **41**, 4664–4667 (2016)

Lü, W., Ma, X., Zhou, H., Chen, G., Li, J., Zhu, Z., You, Z., Tu, C.: White up-conversion luminescence in rare-earth-ion-doped YAlO3 nanocrystals. J. Phys. Chem. C **112**, 15071–15074 (2008)

Manzani, D., Petruci da Sileveria, J.F., Nigoghossian, K., Cardoso, A.A., Ribeiro, S.J.L.: A portable luminescent thermometer based on green upconversion emission of Er^{3+}/Yb^{3+} co-doped tellurite glass. Sci. Rep. **7**, 41596 (2017). https://doi.org/10.1038/srep41596

McInnes, L., Healy, J., & Melville, J., UMAP: Uniform manifold approximation and projection for dimension reduction. arXiv e-prints, arXiv:1802.03426v3, (2020) https://doi.org/10.48550/arXiv.1802.03426

Němec, M., Šulc, J., Švejkar, R., Jelínková, H.: Temperature influence on Er:$YAlO_3$ spectroscopy and diode-pumped laser properties. Laser Phys. **28**, 105801 (2018). https://doi.org/10.1088/1555-6611/aacfa0

Periša, J., Ćirić, A., Zeković, I., Đorđević, V., Sekulić, M., Antić, Ž, Dramićanin, M.D.: Exploiting high-energy emissions of $YAlO_3$:Dy^{3+} for sensitivity improvement of ratiometric luminescence thermometry. Sensors **22**, 7997 (2022). https://doi.org/10.3390/s22207997

Piotrowski, W.M., Szymczak, M., Rodríguez, E.M., Marin, R., Henklewska, M., Poźniak, B., Dramićanin, M., Marciniak, L.: Step by step optimization of luminescence thermometry in $MgTiO_3$:Cr^{3+}, N^{d3}+ @ Si_O2 nanoparticles towards bioapplications. Mater. Chem. Phys. **312**, 128623 (2024). https://doi.org/10.1016/j.matchemphys.2023.128623

Rabasovic, M.S., Savic-Sevic, S., Križan, J., Matovic, B., Nikolic, M., Sevic, D.: Time resolved study of temperature sensing using Gd_2O_3:Er, Yb: deep learning approach. Phys. Scr. **98**, 116003 (2023). https://doi.org/10.1088/1402-4896/ad01ed

Rabasovic, M.S., Pavlovic, D.M., Sevic, D.: Analysis of laser ablation spectral data using dimensionality reduction techniques: PCA, t-SNE and UMAP. Contrib. Astron. Observ. Skalnaté Pleso **53**, 51–57 (2023B)

Runkler, T.A.: Data Visualization. In: Data Analytics. Springer Vieweg, Wiesbaden (2020) https://doi.org/10.1007/978-3-658-29779-4_4

Sainburg, T., McInnes, L., Gentner, T. Q.: Parametric UMAP embeddings for representation and semi-supervised learning. arXiv e-prints, arXiv:2009.12981, (2020) https://doi.org/10.48550/arXiv.2009.12981

Sevic, D., Vlasic, A., Rabasovic, M.S., Savic-Sevic, S., Rabasovic, M.D., Nikolic, M.G., Muric, B.D., Marinkovic, B.P., Križan, J.: Temperature effects on luminescent properties of Sr2CeO4:Eu3+ nanophosphor: a machine learning approach. Tehnika **75**(3), 279–283 (2020). https://doi.org/10.5937/tehnika2003279S

Sevic, D., Rabasovic, M.S., Križan, J., Savic-Sevic, S., Rabasovic, M.D., Marinkovic, B.P., Nikolic, M.G.: Effects of temperature on luminescent properties of Gd2O3:Er,Yb nanophosphor. Opt. Quant. Electron. **52**, 232 (2020B). https://doi.org/10.1007/s11082-020-02348-y

Sevic, D., Rabasovic, M.S., Krizan, J., Savic-Sevic, S., Nikolic, M.G., Marinkovic, B.P., Rabasovic, M.D.: YVO_4:Eu^{3+} nanopowders: multi-mode temperature sensing technique. J. Phys. D Appl. Phys. **53**, 015106 (2020C)

Sevic, D., Krizan, J., Rabasovic, M.S., Marinkovic, B.P.: Temperature sensing using YAG:Dy single crystal phosphor. Eur. Phys. J. D **75**(2), 56 (2021). https://doi.org/10.1140/epjd/s10053-021-00068-w

Sevic, D., Rabasovic, M.S., Križan, J., Savic-Sevic, S., Marinkovic, B.P., Nikolic, M.G.: Luminescence thermometry based on Y2O2S:Er Yb nanophosphor. Opt. Quant. Electron. **54**, 523 (2022). https://doi.org/10.1007/s11082-022-03885-4

Sevic D., Rabasovic M.S., Krizan J., Savic-Sevic S., Rabasovic M.D., Marinkovic B.P., Nikolic M.G.:, Effects of temperature on luminescent properties of $CaGdAlO_4$:Er,Yb nanophosphor. Proc. PHOTONICA2019 - The Seventh International School and Conference on Photonics, Belgrade, Serbia, p.99. (2019) http://www.photonica.ac.rs/docs/PHOTONICA2019-Book_of_abstracts.pdf

Shimizu, Y., Ueda, K., Inaguma, Y.: Photoluminescence excitation spectra of lanthanide doped $YAlO_3$ in vacuum ultraviolet region. Opt. Mater. **66**, 327–331 (2017). https://doi.org/10.1016/j.optmat.2017.02.029

Singh, S.K., Kumar, K., Rai, S.B.: Er^{3+}/Yb^{3+} codoped Gd_2O_3 nano-phosphor for optical thermometry. Sens. Actuator A **149**, 16–20 (2009)

Sreebunpeng, K., Janthon, P., Chewpraditkul, W., Szczesniak, T., Nikl, M., Yoshikawa, A.: Scintillation characteristics of $YAlO_3$: Pr perovskite single crystals. Opt. Mater. **108**, 110161 (2020). https://doi.org/10.1016/j.optmat.2020.110161

Suganya, M., Ganesan, K., Vijayakumar, P., Jakathamani, S., Gill, A.S., Annalakshmi, O., Srivastava, S.K., Sarguna, R.M., Ganesamoorthy, S.: Structural and optical properties of beta irradiated $YAlO_3$ single crystals. Opt. Mater. **107**, 110095 (2020). https://doi.org/10.1016/j.optmat.2020.110095

Van der Maaten, J.P.L., Hinton, G.: Visualizing data using t-SNE. J. Mach. Learn. Res. **9**, 2579 (2008)

Wang, X., Liu, Q., Bu, Y., Liu, C.-S., Liua, T., Yan, X.: Optical temperature sensing of rare-earth ion doped phosphors. RSC Adv. **5**, 86219–86236 (2015)

Weber, T., Lüthy, W., Weber, H.P.: Upconversion in $YAlO_3$: Er pumped at 800 nm. Appl. Phys. B **55**, 144–148 (1992). https://doi.org/10.1007/BF00324065

Xu, W., Gao, X., Zheng, L., Wang, P., Zhang, Z., Cao, W.: Optical thermometry through green upconversion emissions in Er^{3+}/Yb^{3+}-codoped $CaWO_4$ phosphor. Appl. Phys. Express **5**, 072201 (2012)

Zhao, Y., Wang, X., Zhang, Y., Li, Y., Yao, X.: Optical temperature sensing of up-conversion luminescent materials: fundamentals and progress. J. Alloy. Compd. (2019). https://doi.org/10.1016/j.jallcom.2019.152691

Publisher's Note Springer Nature remains neutral with regard to jurisdictional claims in published maps and institutional affiliations.

Springer Nature or its licensor (e.g. a society or other partner) holds exclusive rights to this article under a publishing agreement with the author(s) or other rightsholder(s); author self-archiving of the accepted manuscript version of this article is solely governed by the terms of such publishing agreement and applicable law.

Pajić et al. *Microsystems & Nanoengineering* (2024)10:47
https://doi.org/10.1038/s41378-024-00664-x

Microsystems & Nanoengineering
www.nature.com/micronano

ARTICLE Open Access

In vivo femtosecond laser nanosurgery of the cell wall enabling patch-clamp measurements on filamentous fungi

Tanja Pajić[1]✉, Katarina Stevanović[1], Nataša V. Todorović[2], Aleksandar J. Krmpot[3], Miroslav Živić[1], Svetlana Savić-Šević[3], Steva M. Lević[4], Marina Stanić[5], Dejan Pantelić[3], Brana Jelenković[3] and Mihailo D. Rabasović[3]✉

Abstract

Studying the membrane physiology of filamentous fungi is key to understanding their interactions with the environment and crucial for developing new therapeutic strategies for disease-causing pathogens. However, their plasma membrane has been inaccessible for a micron-sized patch-clamp pipette for pA current recordings due to the rigid chitinous cell wall. Here, we report the first femtosecond IR laser nanosurgery of the cell wall of the filamentous fungi, which enabled patch-clamp measurements on protoplasts released from hyphae. A reproducible and highly precise (diffraction-limited, submicron resolution) method for obtaining viable released protoplasts was developed. Protoplast release from the nanosurgery-generated incisions in the cell wall was achieved from different regions of the hyphae. The plasma membrane of the obtained protoplasts formed tight and high-resistance (GΩ) contacts with the recording pipette. The entire nanosurgical procedure followed by the patch-clamp technique could be completed in less than 1 hour. Compared to previous studies using heterologously expressed channels, this technique provides the opportunity to identify new ionic currents and to study the properties of the ion channels in the protoplasts of filamentous fungi in their native environment.

Introduction

Filamentous fungi are an extremely diverse cosmopolitan group with great importance to the functioning of the biosphere. Together with bacteria, fungi represent the most important group of decomposers in almost all ecosystems, and mycorrhizal fungi form symbiotic associations with nearly 80% of land plants[1]. Moreover, the biodiversity of mycorrhizal fungi in soil has a critical impact on maintaining plant and ecosystem biodiversity[2]. In addition, some fungi are pathogenic and cause diseases in animals or plants[3], and fungi that threaten human health have enormous biomedical importance[4]. Ion channels are known or expected to play important roles in fungal physiology[5], including ion and nutrient uptake[6], signal transduction[7], and response to osmotic stress[8]. In contrast to animal and plant cells, little is known about the function of the ion channels in fungi. To date, only a handful of channels in filamentous fungi have been cloned and/or characterized by electrophysiological techniques; this has been performed mainly by heterologous expression of the channel proteins identified by screening for homologs of known yeast, animal or plant proteins[9–19]. The main reason for the near-complete lack of studies on native membranes is the rigid, chitinous cell wall that blocks access to the patch-clamp pipette. The cell wall makes it impossible to use the patch-clamp method; the gold standard for ion current measurements. For the membrane to be accessible by the glass

Correspondence: Tanja Pajić (tpajic@bio.bg.ac.rs) or
Mihailo D Rabasović (rabasovic@ipb.ac.rs)
[1]Institute of Physiology and Biochemistry "Ivan Djaja", Faculty of Biology, University of Belgrade, Studentski trg 16, 11158 Belgrade, Serbia
[2]Institute for Biological Research "Siniša Stanković", University of Belgrade, National Institute of the Republic of Serbia, Bulevar Despota Stefana 142, 11000 Belgrade, Serbia
Full list of author information is available at the end of the article

© The Author(s) 2024
Open Access This article is licensed under a Creative Commons Attribution 4.0 International License, which permits use, sharing, adaptation, distribution and reproduction in any medium or format, as long as you give appropriate credit to the original author(s) and the source, provide a link to the Creative Commons licence, and indicate if changes were made. The images or other third party material in this article are included in the article's Creative Commons licence, unless indicated otherwise in a credit line to the material. If material is not included in the article's Creative Commons licence and your intended use is not permitted by statutory regulation or exceeds the permitted use, you will need to obtain permission directly from the copyright holder. To view a copy of this licence, visit http://creativecommons.org/licenses/by/4.0/.

pipette for the patch-clamp method, all or part of the wall must be removed. The naked protoplast (cellular cytoplasm whose entire contents are enclosed by the plasma membrane) would then be released through the opening in the hyphal wall to enable access with the patch-clamp pipette. The formation of a high-resistance contact ("seal") between the tip of the glass pipette and the membrane is a prerequisite for the patch-clamp technique and is only possible if the membrane is clean[20].

There are several ways to remove the cell wall: mechanically, enzymatically and by laser cell surgery[21,22]. Mechanical dissection of tissue to release a small number of protoplasts has never been successful in filamentous fungi, while this method is used in plant tissues to avoid the deleterious effects of enzymatic treatment on the plasma membrane[23]. Enzymatic removal of the cell wall was successful in plants[24,25] but did not produce positive results in the filamentous fungi *Neurospora*[26] and *Saprolegnia*[27]. Contacts with resistances greater than 200 and 500 MΩ were not possible to attain. These results were in contrast to plant findings and occurred because the fungal cell wall is structurally and molecularly distinct from the cellulose-based plant cell wall.

However, a small localized portion of the fungal cell, such as a tiny cell wall section, is possible to remove using the laser ablation technique[28] while leaving the bulk of the wall intact. In this way, the polarity of the fungal cells is preserved, and a portion of the plasma membrane is accessible for patch-clamp measurements. Laser removal of the cell wall combined with patch-clamp recording has previously been used in some algae and plants[21,29–32] and only in two filamentous fungi[10,33]. However, these experiments were conducted more than twenty years ago with UV lasers and did not evolve into a routine protocol. The UV lasers used in these studies operated with nanosecond (ns) laser pulses, which are known to cause photothermal and photomechanical damage to samples[34–36]. Recent developments in laser technology and microscopy, especially ultrafast femtosecond (fs) lasers, enable operations with extremely high precision. The main advantage of fs lasers is that they produce negligible thermal effects compared to ns lasers because their pulses are shorter than the thermal diffusion time (picoseconds to nanoseconds)[37]. Due to the non-thermal nature of the fs laser interacting with the cellular material, the material is mainly ablated[28,34,35,38], causing minimal damage to the surrounding cellular material. In addition, the pulse energy for fs laser ablation is in the sub-nJ range, which is well below the pulse energies of UV-ns lasers. In addition, the wavelengths of fs lasers used for cell surgery are in the NIR range, which is not as harmful to the cell as UV wavelengths are; this aspect is particularly important for stray radiation during surgery.

Femtosecond lasers emit ultrashort laser pulses that allow a significant reduction in dissection size compared to ns lasers[34,35,38]. Thus, they are ideal for precise cell surgery at the nanoscale to microscale. In fs laser cell nanosurgery, a laser beam is focused down to the diffraction-limited focal spot/volume by a high numerical aperture (NA) objective lens on the cell wall or membrane[28,35,38]. In addition, the surgical process achieved with fs lasers enables the removal of very small amounts of material with high precision, creating a small incision on the cell wall/membrane or other cell structures. The high peak intensities of the fs laser pulses induce multiphoton interaction processes and provide a lower energy threshold for cell wall/membrane removal[28,35,38]. The typical peak intensity for fs laser ablation is on the order of 10^{12} W/cm^2 [39,40]. Briefly, ultrashort laser pulses with relatively low energy enable more precise submicrometer surgical incisions than ns lasers[34,35,38,41].

Laser nanosurgery has become an important tool in many biological fields because of its precision, noninvasiveness, and versatility. This technique has been used as a microdissection tool for studying the function of microtubules, mitochondria and other organelles in cultured cells, tissues, and whole organisms, as well as for optotransfection and other forms of laser-based molecular delivery[42]. Other potential applications of this technology include developmental biology studies of cell mechanics, intracellular transport, and cell signaling, as well as the development of new therapies for diseases such as cancer and genetic disorders. In the context of fungi, fs laser nanosurgery could be used to selectively remove portions of the cell wall. The combination of laser ablation and localized patch clamping allows the measurement of ionic currents through the plasma membrane while retaining information about the location of the membrane from which recordings were made. This approach enables the detection of the asymmetric distribution of the ion channels along hyphae and the exploration of the ion channel involvement in the fungal cell polarity establishment, signal integration, and hyphal tropism; all of these play key roles in establishing fungal virulence[43] and interactions with surrounding organisms or the environment[44,45]. Thus, we were motivated to develop and optimize a protocol that allows high-quality recording of currents via the patch-clamp method on the plasma membrane of fungal protoplasts released from the wall by subcellular nanosurgery using a fs titanium-sapphire (Ti:Sa) laser. Therefore, to the best of our knowledge, we present the first successful application of fs laser nanosurgery to access the plasma membrane of filamentous fungal hyphae for patch-clamp recording. We demonstrated that the released protoplasts could successfully form high-resistance contacts with a patch-clamp pipette. The incisions produced by the fs laser were smooth-edged, protoplasts were released from those incisions, and the probability of protoplast release was a

function of the incision size and was modified by the presence of a high Ca^{2+} concentration. The method could be readily used for the selective release and subsequent recording of protoplasts from different regions (tip, middle, and side branches) of the fungal hyphae. Finally, we provided the first electrophysiological snapshot obtained on filamentous fungal protoplasts after cell wall removal by fs laser nanosurgery and showed that the protoplast membrane was characterized by a number of different types of ionic currents, predominantly anionic.

Results

In vivo two-photon imaging, cell wall laser nanosurgery and patch-clamp recording

A nonlinear laser scanning microscope (NLSM) using fs laser pulses is the necessary prerequisite for the application of precision laser ablation. The NLSM system also enables in vivo imaging of single cells and cellular structures using two-photon excitation fluorescence (TPEF) before and after laser nanosurgery. We successfully created laser-generated incisions in cell wall sections of the filamentous fungus *Phycomyces blakesleeanus* using tightly focused, 160 fs, near-infrared (NIR) laser pulses (Fig. 1). To remove a small portion of the cell wall in a specific area of the hyphae, the cell wall must be visualized and distinguished from the plasma membrane and other cell structures. Since the cell wall and the plasma membrane are in close contact[46], hyphae were plasmolyzed and kept in hyperosmotic solution to retract the cytoplasm before the procedure, as shown in Fig. 1a. The plasmolyzed hyphae stained with calcofluor white (CFW) and treated with an exocytosis inhibitor and a respiratory inhibitor (sodium azide) to prevent cell wall regeneration were subjected to nanosurgery. We selected for the nanosurgery the section where the hyphal protoplast was retracted from the cell wall and placed the spot-wise pattern on the selected section (Fig. 1b). The laser-generated incision is clearly visible in the TPEF images (Fig. 1c) and in the bright-field images. The cell viability after nanosurgery was regularly verified by bright-field microscopy. The protoplast enveloped by the plasma membrane exited through the incision in the cell wall without deforming or bursting (Fig. 1d). Thus, the released round protoplasts were viable for up to several hours during the electrophysiological measurements. Representative patch-clamp current recordings obtained from the released protoplasts in the "outside-out" and "whole-cell" configurations are shown in Fig. 1f and g, respectively.

We obtained 79 fungus-released protoplasts in the patch-clamp microscopy chamber that were sufficiently large (larger than 7 μm) and spatially accessible to the patch pipette. Membrane contact with high resistance (greater than GΩ resistance) was obtained on 22 released protoplasts (28%). Eight protoplasts (10%) were very stable and allowed multiple successful pipette approaches which resulted in the formation of multiple GΩ-resistance contacts and patch excisions. A total of 36 giga-ohm seal contacts were obtained. All patch-clamp configurations were used for the recording. The current family obtained from the entire protoplast membrane in the "whole cell" configuration had a typical appearance (Fig. 1f). The single-channel currents recorded from the excised patches in the inside-out or outside-out configurations were more diverse. We used solutions with asymmetric ion concentrations to identify the general type of ion basis for selectivity (K^+, Cl^-, glutamate$^-$, or Ca^{2+}) for each recorded channel current based on the reversal potential (V_{rev}) (Fig. 1g).

Laser nanosurgery procedure—the main steps and key factors

The main steps for successful fs laser nanosurgery of the fungal cell wall to obtain viable protoplasts for patch-clamp analysis are shown in Fig. 2. The first important step was to decrease the osmolarity of the growth media to acclimate the fungi to conditions with lower osmolarity and increase their sensitivity to the plasmolysis solution. This approach ensured faster plasmolysis during the preparation phase of nanosurgery. By reducing the osmolarity of the growth medium by 30%, the plasmolysis time (in minutes) was decreased from 30 ± 10 to 5 ± 2. The introduction of two-stage plasmolysis and the increase in the Ca^{2+} concentration in the hyperosmotic solution followed, and these were considered the most important, key factors for successful surgery and the recovery of viable, patchable, released protoplasts. The Ca^{2+} concentration was increased to accelerate plasmolysis (<1 min) and stabilize the protoplasts[33]. The step before plasmolysis reduced the physiological shock that would occur if the fungi were transferred directly from the medium to a hyperosmotic solution (450 mOsm difference). This was achieved by staining the fungi with diluted dye in a standard isoosmotic solution.

To achieve precision and enable successful nanosurgery and imaging, the fungal hyphae were immobilized on the coverslip. A number of substrate-coating materials were tested (Supplementary Table 1), and a collagen coating was found to provide better immobilization of the fungal hyphae while allowing for the patch-pipette approach.

The cell wall of the filamentous fungus *Phycomyces blakesleeanus* is weakly autofluorescent and can be visualized by excitation at 730 nm, presumably as a signal from the chitin-containing (chitin and chitosan) component of the cell wall[47,48]. The removal of the cell wall by the laser nanosurgical procedure was not efficient enough on the native hyphae. After staining the cell wall with

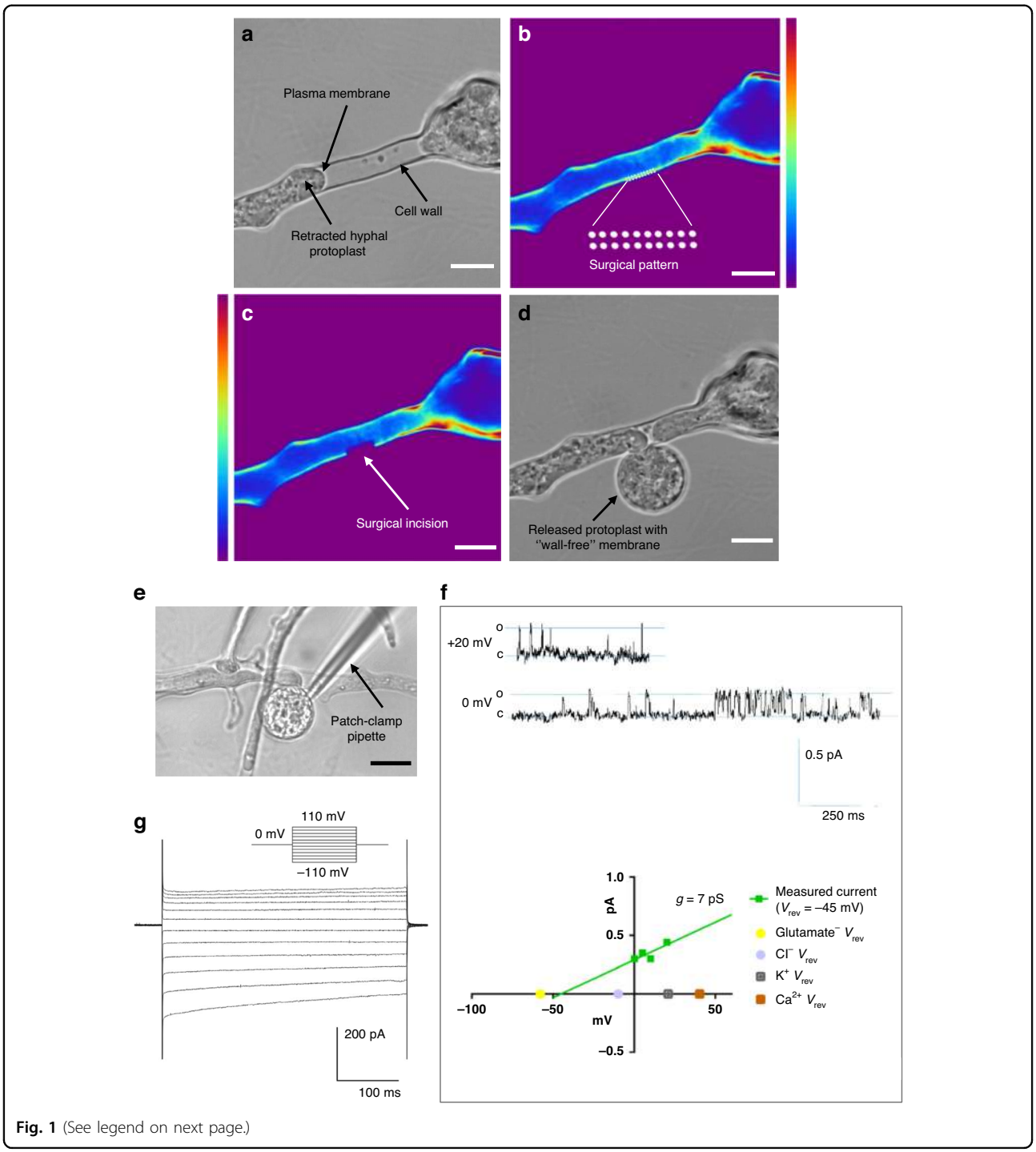

Fig. 1 (See legend on next page.)

CFW, the surgery was almost 100% successful. All nanosurgical procedures presented were performed with a cell wall stained with CFW to improve the absorption of laser energy. CFW has a high affinity for cell wall components (chitin and other polysaccharides), and the absorption maximum is at 345 nm under single-photon excitation conditions[49].

Two-photon imaging of the cell wall was performed with a very low average laser power of 0.5 mW and a pulse energy of 0.007 nJ at the sample plane. A wavelength of 730 nm was used for both multiphoton imaging and nanosurgery, bypassing the time required to change wavelengths. A diameter of hyphae (<15 μm) poses a major challenge for successfully cutting off a portion of

(see figure on previous page)

Fig. 1 In vivo laser nanosurgery of the cell wall of the filamentous fungus *Phycomyces blakesleeanus* using fs laser pulses and patch-clamp recording of the released fungal protoplast membrane current activity after the surgical procedure. a Bright-field and **b** TPEF image of the plasmolyzed and labeled hypha before surgery. A 20×2 spot-wise pattern was positioned on the cytoplasm-free section of the cell wall. The average laser power in the sample plane for imaging was 1.1 mW (dwell time 2.5 µs) at 730 nm. **c** TPEF image of the same hypha after surgery. The surgical incision is indicated by the arrow. The laser power at the sample plane for the surgery was 6.1 mW (dwell time 1 s) at 730 nm. The color intensity bars for the TPEF signal are as follows: violet/blue, lowest TPEF signal; and dark red, highest TPEF signal. The color intensity bar is linear and covers the entire range of the data. Scale bar: 10 µm. **d** Bright-field image of the same hypha with the protoplast released through the surgical incision after laser cutting. **e** Bright-field image of the patch-clamp pipette in contact with the membrane of the protoplast released through the surgical incision. Scale bar: 20 µm. All images were taken with a Zeiss 40× 1.3 oil objective. **f** Top: Representative single-channel current recordings obtained from the released protoplast at V_h of +20 mV and 0 mV. o: open channel current level; c: closed channel current level. The calibration bar is on the right side. Bottom: current-voltage (IV) dependency of the recording shown above. On the abscissa, the reversal potentials of the main ions in the bath and pipette solutions are shown, indicating that the current is carried mainly by glutamate. The obtained conductance (g) is given above the linear fit through the measured points. Recorded in SolB. **g** Representative current recorded from the entire protoplast membrane in the whole-cell configuration. The cells were recorded in SolA with a low-chloride pipette solution. The voltage stimulation protocol used to obtain the recordings is shown in the inset. The calibration bar is at the bottom

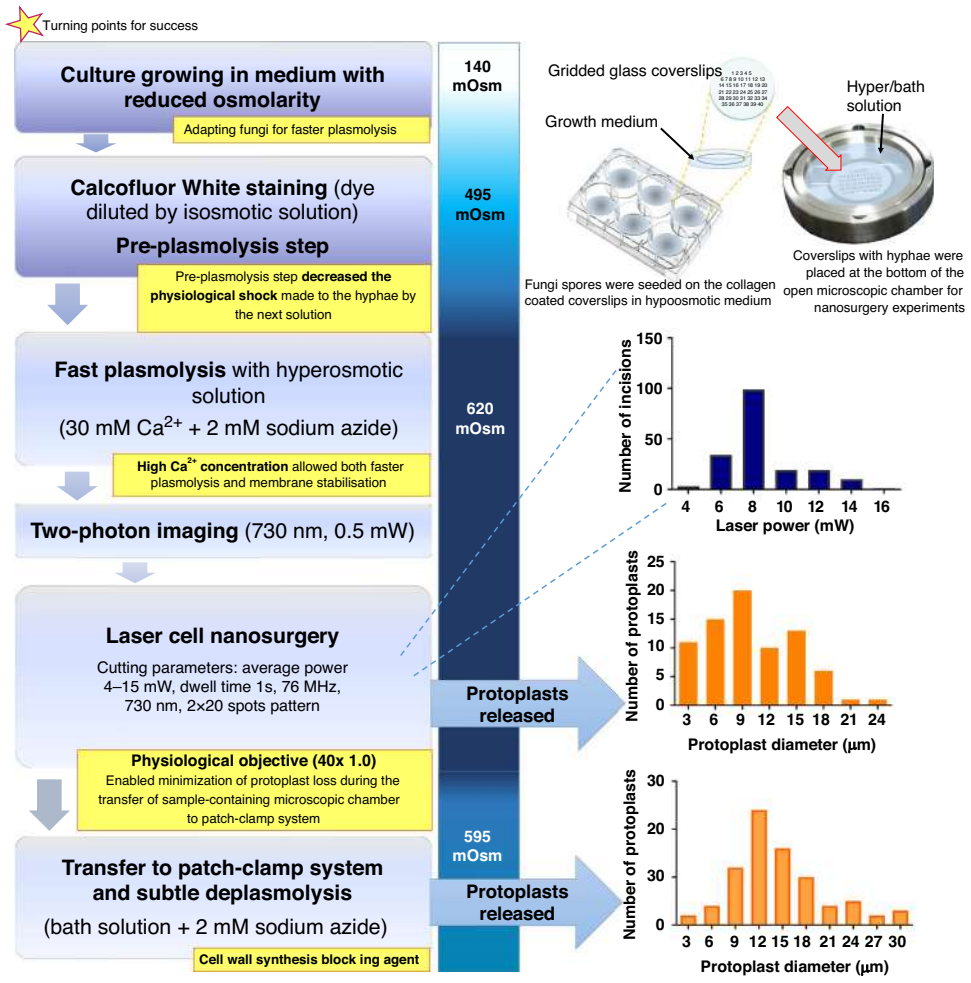

Fig. 2 Laser nanosurgery procedure main steps and turning points for successful removal of the *Phycomyces blakesleeanus* hyphae cell wall. The osmolarity of the extracellular solution at each step of the procedure is indicated on the blue gradient strip. A detailed description of the procedure can be found in the Materials and Methods section. The distribution of the average laser power used for nanosurgery of *P. blakesleeanus* cell walls is shown in the upper graph, and the distributions of the sizes of the protoplasts released in the two consecutive steps (bottom) are shown as histograms with the upper bin boundary on the abscissa

the cell wall without endangering the rest of the cell. After optimizing the surgical procedure, we selected a 2 × 20 spot-wise pattern positioned on the cytoplasm-free section of the cell wall in the TPEF image. Depending on the degree of plasmolysis, i.e., the length of the site available for cutting, the 2 × 20 dot pattern was scaled (adjusted: scale, angle, and position) for surgery to the size that would cut off as much of the wall as possible without critically approaching the plasma membrane. Based on the selected pattern length, cell wall thickness, and proximity to the protoplast, the cutting power was selected in the drawing mode of the software. We were able to control the parameters of surgery: dwell time per point, laser power and wavelength. The surgical procedure was automated, started "on click" and lasted approximately 20 s. Prior to the surgical experiments, tests were performed to determine the average laser power required to cut a small portion of the cell wall, and the damage threshold was determined. The damage threshold was approximately 3.5 mW (using a 40× 1.0 physiological objective). The overall distribution of laser powers at the sample plane used for nanosurgery is shown in the upper graph in Fig. 2; the lower power range was used in the majority of the operations. Laser powers of 6 to 12 mW were used in 90% of the cell wall operations. The dwell time of 1 s per point was maintained at the same value during the surgical procedure for all hyphae. Femtosecond pulses (160 fs) at a 76 MHz repetition rate and very low pulse energies (0.05-0.20 nJ) at the specimen plane ensured successful wall cutting with high spatial resolution of the surgical incisions.

Subsequently, subtle deplasmolysis was performed to stimulate the protoplast release without overstretching the membrane to interact with the pipette. To avoid hypoosmotic stress and maintain the integrity of the protoplast plasma membrane, the osmolarity of the solution in the microscopic chamber was reduced by only a few tens of mOsm such that slightly hyperosmotic conditions were present. The optimized concentration of sodium azide for inhibiting cell wall production was consistently present in all solutions, and its presence was an indispensable factor for success. Respiration and growth of *Phycomyces blakesleeanus* under the conditions used for nanosurgery are shown in Suppl. Fig. S1.

Because the nanosurgery (using an upright nonlinear microscope) and patch-clamp (using an inverted microscope) systems are separate, the physiological objective played a key role. Since a dip-in objective is normally used without a top coverslip, it was possible to approach the sample above and completely immerse the objective tip in the solution surrounding the sample. Consequently, there was no need for removal of the coverslip, which would otherwise lead to possible loss of the emerged protoplasts. On the other hand, the gridded coverslips on which the fungi were grown and placed at the bottom of the open microscopic chamber allowed the precise localization of the hyphae subjected to nanosurgery.

As expected, the size of the patch pipette influenced the success of giga-ohm sealing. For our purposes, the best pipettes for the fungal protoplast patch-clamp were between 10 MΩ and 15 MΩ. Smaller and larger pipettes were two times less likely to achieve good-quality contact. The protoplast size was also an important factor in the success of high membrane-pipette contact formation. When contact was successful, the released protoplasts were significantly ($p = 0.016$) larger (18 ± 6 μm) than those where contact (15 ± 5 μm) could not be achieved. Potentially, with further practice, the success rate of achieving contact with the gigaohmic seal could be significantly improved for these smaller released protoplasts. To estimate the success rate of patch-clamp contact on released protoplasts that were sufficiently large and accessible to the pipette, we divided the number of giga-ohm contacts obtained by the number of patch-pipette contacts attempted on "patchable" protoplasts. Overall, the success rate was 55%, with 23 successful contacts out of 42 pipette approaches. The entire process (cell surgery + patch clamping) was quite complex, and certain steps needed to be precisely followed for a high success rate and reproducibility. The concentration of chemicals, osmolarity of the solutions, timing and cutting parameters needed to also be kept within a specified narrow range.

Electron microscopic imaging of the surgical incision in the cell wall and released protoplast

To verify the appearance of the edges of the incisions in the plasmolyzed hyphal cell wall, we imaged the fungus subjected to nanosurgery using a scanning electron microscope (SEM).

As shown in Fig. 3, SEM images revealed crack-free precision cuts, with smooth edges of the slit in the hyphal cell wall made with the femtosecond laser ($n = 11$ incisions at 10 images). The released protoplast membrane had no large masses of remaining or deposited material ($n = 2$) (Fig. 3f). The surgical parameters used allowed localized removal of the cell wall with an average thickness of 30 nm (Fig. 3e), sometimes even at extremely short distances from the plasma membrane (0.5–3 μm), leaving the released protoplast viable. The mean length of the incisions measured from TPEF images was 6.7 ± 2.9 μm ($n = 185$), whereas mean length of the incisions measured from the SEM images was 9.3 ± 4.4 μm ($n = 6$). The width of the incisions measured from the SEM images was 2.2 ± 0.2 μm ($n = 3$).

Protoplast release parameters

After successful creation of the surgical incision in the cell wall, the release of protoplasts into the surrounding

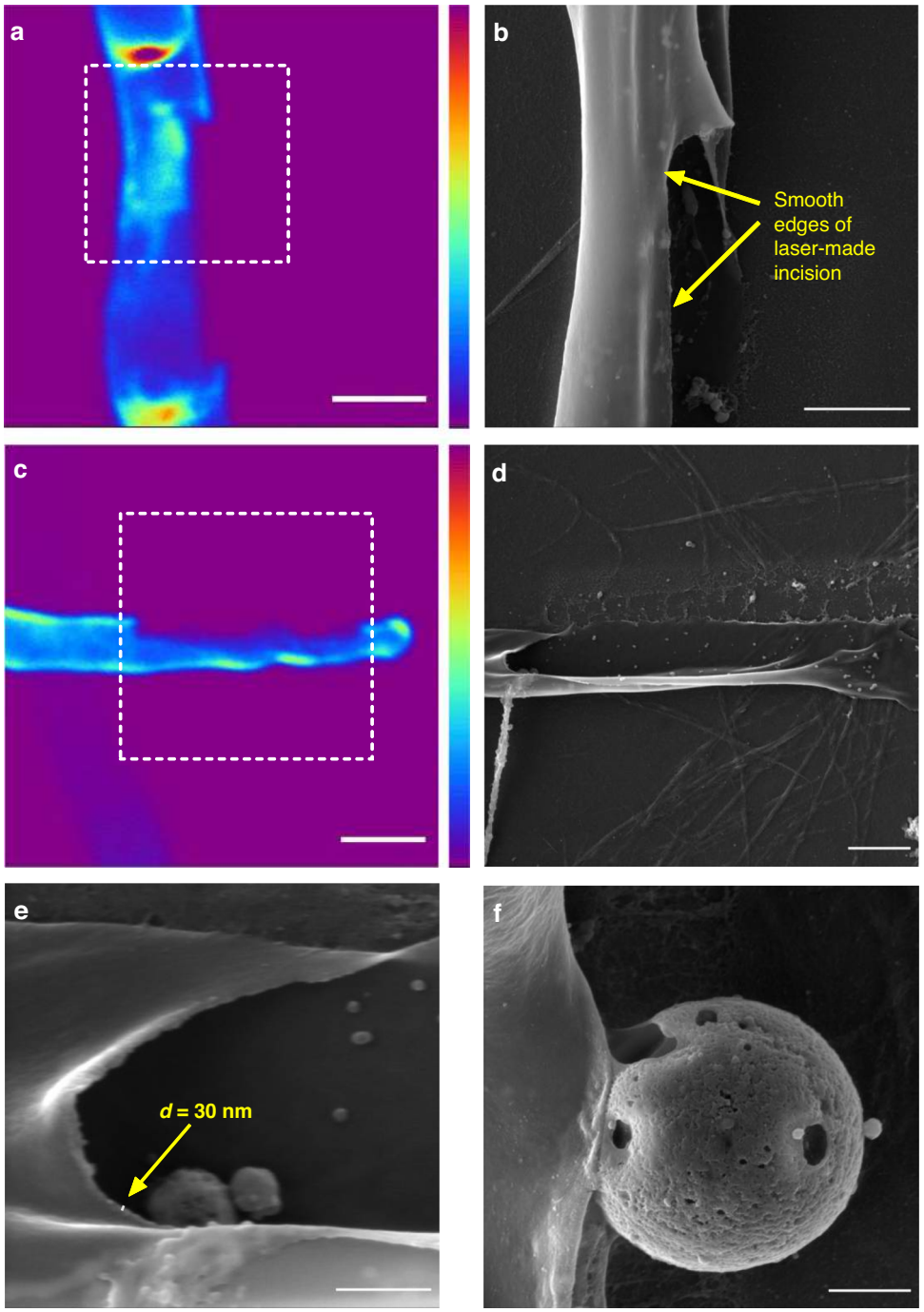

Fig. 3 SEM images of the *Phycomyces blakesleeanus* cell wall after the femtosecond laser nanosurgery. a TPEF image of the fs laser-generated incision in the hyphal cell wall. The average laser power in the sample plane was 1.0 mW for imaging (dwell time 2.5 µs) and 7.5 mW for surgery (dwell time 1 s). Scale bar: 5 µm. **b** SEM image of the same laser-generated incision shown in a. Scale bar: 2 µm. **c** TPEF image of the fs laser-made incision. The average laser power in the sample plane was 1.0 mW for imaging (dwell time 2.5 µs) and 7.6 mW for surgery (dwell time 1 s). Scale bar: 5 µm. All TPEF images were acquired with a Zeiss 40× 1.3 oil objective. The color intensity bars for the TPEF signal are as follows: violet/blue, lowest TPEF signal; and dark red, highest TPEF signal. The color intensity bar is linear and covers the entire range of the data. **d** SEM image of the entire laser-generated incision, same as that shown in c. Scale bar: 2 µm. **e** Hyphal cell wall thickness (*d*) of the incision shown in d. Scale bar: 0.5 µm. **f** Released protoplast through a laser incision made with 6.7 mW average power at 730 nm. Scale bar: 1 µm

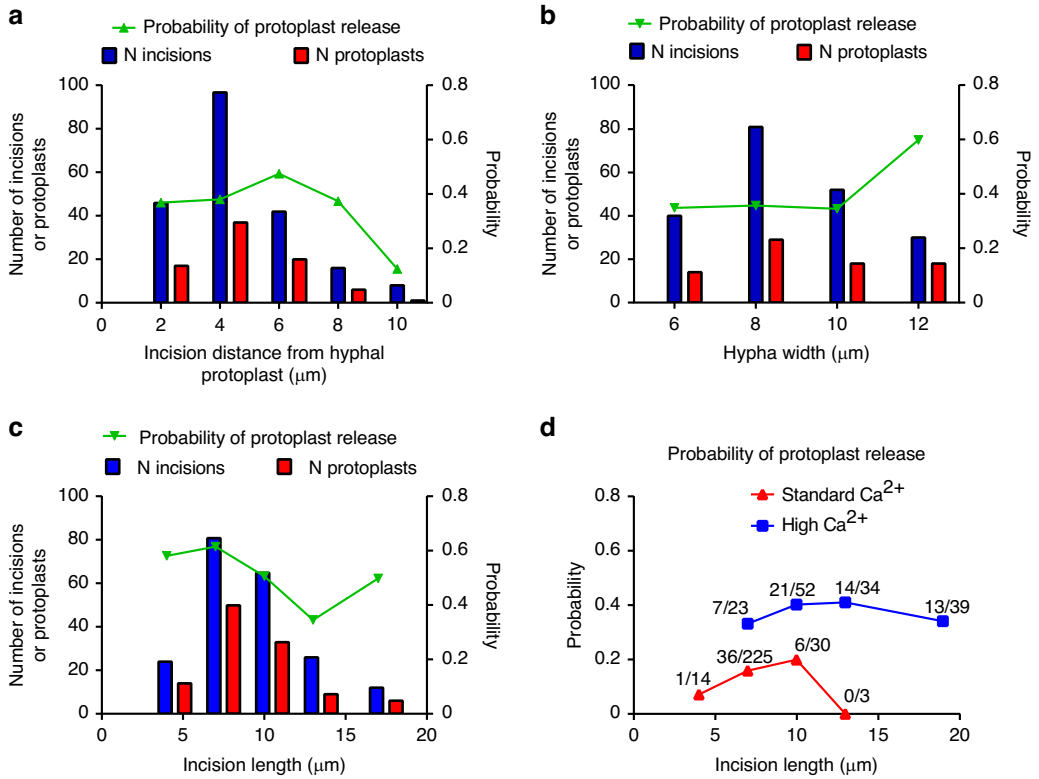

Fig. 4 Parameters affecting the probability of protoplast release. Probability of protoplast release from the nanosurgery-produced incision, superimposed on the corresponding histogram bin of parameter values. **a** Distance of the laser incision from the hyphal protoplast during nanosurgery: distribution and dependence of the probability of protoplast release. **b** Hyphal width at the site of nanosurgery: distribution and dependence of the probability of protoplast release. **c** Length of surgical incision: distribution and dependence of the probability of protoplast release. **d** In a separate series of experiments, the effect of increased calcium concentration on the probability of protoplast release was measured as a function of incision length in the nanosurgical phase of the procedure, without subsequent steps of deplasmolysis. High [Ca^{2+}]: 30 mM, as used in the surgical protocol. The hyperosmotic solution used was 600-617 mOsm throughout the protoplast release period. Standard [Ca^{2+}]: 3 mM and 1 mM (pooled data). The hyperosmotic solution used was 555-560 mOsm throughout the protoplast release time. For each 3 μm incision size bin in the histogram, the corresponding number of protoplasts obtained divided by the number of surgical sections performed is shown above the probability curve. In all graphs, the abscissa represents the upper limit of the bin. For **a**–**c**: n_{tot}(incisions) = 203 (**a**); 209 (**b**); 208 (**c**). n_{tot}(protoplast) = 71(**a**), 81(**b**), 112 (**c**). For **d**: n_{tot}(incisions) = 272 (Standard Ca^{2+}); 148 (High Ca^{2+}). n_{tot}(protoplast) = 43 (Standard Ca^{2+}); 55 (High Ca^{2+})

medium was observed. Not all incisions released protoplasts. We found that several factors influenced the probability of protoplast release (Pr = number of protoplasts/number of incisions). The distance of the laser cut from the protoplast in the hypha during the procedure influenced how many protoplasts could be recovered. As shown in Fig. 4a, when the protoplast in the hypha was more than 6 μm from the incision site, the probability of protoplast release decreased from approximately 0.4 and was lowest at the largest distances tested. This result further confirmed that the protoplasts were not damaged in our protocol, even when the site of nanosurgery was in close proximity to the retracted hyphal protoplast. The width of the hyphae (w_h), which reflected the overall size of the hyphae, did not appear to affect the possibility of obtaining released protoplasts for $w_h < 10$ μm. Wider hyphae ($w_h > 10$ μm) were more favorable for protoplast release with a Pr of 0.6, while for smaller hyphae, Pr was 0.35 (Fig. 4b). Finally, the size of the incision also affected the release probability, with smaller incisions releasing more protoplasts. As shown in Fig. 4c, the probability decreased with increasing incision length, from $Pr = 0.62$ at an incision length of 5.5 ± 1.5 μm to $Pr = 0.35$ at an incision length of 11.5 ± 1.5 μm. We are confident that all hyphae were viable after the nanosurgical procedures because they retained their characteristic cytoplasmic streaming and healthy appearance and were deplasmolyzed when transferred to less hyperosmotic conditions. Thus, the dependence of Pr on incision size was caused by the influence of underlying physiological or mechanical aspects controlling protoplast release. We also noted a slightly better protoplast yield in the plasmolyzed hyphae that exhibited a cytoplasmic bridge across the "empty" region near the incision site than in those whose hyphal

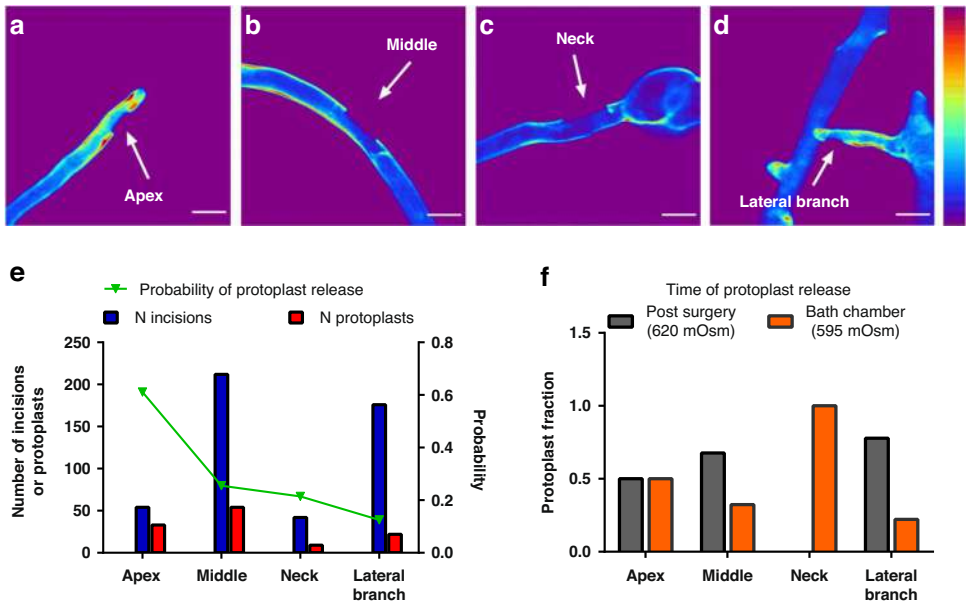

Fig. 5 Nanosurgery applied to different sites on the hyphae. TPEF images of the hyphae with a laser surgical incision at different locations: **a** apex, **b** middle, **c** "neck" and **d** lateral branch of the labeled hypha. The white arrows indicate a laser-made incision in the hyphal cell wall. All images were taken with a Zeiss 40× 1.3 oil objective. The color intensity bars for the TPEF signal are as follows: violet/blue, the lowest TPEF signal; and dark red, the highest TPEF signal. The color intensity bar is linear and covers the entire range of the data. Scale bar: 10 µm. **e** Probability of the protoplast release at each site (apex, middle, neck and lateral branch), with the corresponding number of incisions obtained. **f** Osmotic conditions during the protoplast release at the different sites are shown as fractions of the total number of protoplasts released at each site in each of the solutions used: "postsurgery"= 620 mOsm; "bath chamber" = 595 mOsm

protoplasts were completely separated ($Pr = 0.44$ and 0.36, respectively).

In a separate set of experiments on nanosurgery, we examined protoplast release immediately after nanosurgery, without a deplasmolysis step, under slightly different plasmolysis and surgical conditions, as explained in the Methods section. We investigated whether the high calcium concentration used throughout the procedure affected protoplast release (Fig. 4d). We compared protoplast release at a high Ca^{2+} concentration (30 mM) with protoplast release at a standard Ca^{2+} concentration (1 and 3 mM, merged). At standard Ca^{2+} concentrations, the probability of protoplast release was clearly dependent on the size of the incision and was quite low (< 0.2). Increasing $[Ca^{2+}]$ to 30 mM increased the probability of obtaining the protoplast for the same incision size to 0.4. The calcium dependence of the probability of protoplast release indicated that a physiological mechanism was involved in the process of expelling protoplasts from the hyphal wall through a surgically made incision.

Laser nanosurgery of the cell wall at different sites along the hyphae

Since hyphae are polarized cells, selective sampling from different hyphal regions would be highly desirable. We exploited the precision and flexibility of the nanosurgical method to perform incisions and obtain protoplasts from the localized portions of the following hyphal regions ("compartments"): 1. The tip (apex), which represents the fast-growing portion of the hyphae (Fig. 5a); 2. The middle (Fig. 5b); 3. The "neck", which represents the base of the hyphae, just below the spore (Fig. 5c); And 4. The lateral branch (Fig. 5d). The average laser power used for the cuts in the different compartments did not vary, while the distance of the incision from the hyphal protoplast at the time of nanosurgery needed to be adjusted due to the narrower space in the side branch compartment; the distance of the incision from the hyphal protoplast was shorter in the lateral branch compartment than in the middle compartment: $p = 0.0220$; compared to the tip compartment: $p = 0.0003$. Figure 5e shows the number of incisions with their *Pr* values for each site. The *Pr* was highest in the apical region (0.6) but rather low in the lateral branches (0.13). Interestingly, the protoplasts were released from the different regions under different osmotic conditions (Fig. 5f). For example, protoplasts from the neck did not appear in the hyperosmotic solution used for surgery, with 100% of protoplasts obtained from the neck were released during deplasmolysis in the bath chamber; however, protoplasts from the hyphal tip were released equally well in both

hyperosmotic and deplasmolysis solutions. The success in achieving giga-ohm contact was highest for protoplasts from lateral branches (55%), while it was 25-30% for protoplasts from other regions.

Registered currents of protoplasts obtained by nanosurgery

The excised patch currents measured from protoplasts obtained by nanosurgery were predominantly anionic. Only in one case did the measured current have a reversal potential corresponding to calcium ions. Approximately one-third (35%) of the registered currents belonged to the group mediated by nonselective anionic channels that transport both chloride ions and organic acids ("anionic unselective"), whereas 44% of the currents were mediated by channels that are highly selective for chloride ("Cl^- selective") (Fig. 6a). Some of the currents recorded (17%) were mediated by channels highly permeable to glutamate ("organic acids permeable"). These currents had a reversal potential close to the calculated V_{rev} for glutamate. Figure 6b shows the total conductance range (g) for each group, along with typical excised patch current recordings. Most frequently, Cl^- selective currents had short openings and closings at depolarized potentials ($n = 7$) (Fig. 6b bottom trace), whereas glutamate-permeating currents alternated between two modes: (I) infrequent and relatively short openings and (II) several hundred ms long openings with sub-conductance levels interspersed with very short closed states ($n = 4$). Figure 6b middle trace shows the current that started in mode I and then abruptly transitioned to mode II. Nonselective currents exhibited a wide range of conductances and likely represent a heterogeneous group. Top trace in Fig. 6b shows the most frequently recorded current activity, bursts of current accompanied by very short needle-like openings ($n = 7$).

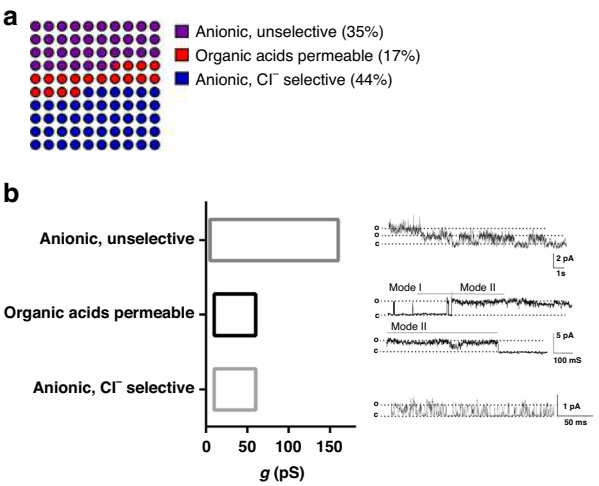

Fig. 6 Summary of the properties of the obtained currents. **a** Major types of currents present in the protoplast membrane categorized according to ion permeability. Ion permeability was determined from IV plots under asymmetric conditions, as shown in the bottom panel of Fig. 1g. **b** Conductance ranges determined for major protoplast types of ion currents, with representative current recordings shown on the right. Unselective anionic current recording, inside-out, $V_h = +80$ mV, bath solution with high glutamate content (solB), $g = 15$ pS; Organic acid-carried current, outside-out, $V_h = +30$ mV, bath solution with nitrate (solA), $g = 40$ pS, activity modes indicated above current recording. Cl^- -selective current, outside-out, $V_h = +80$ mV, solB, $g = 12$ pS. o: open channel current level; c: closed channel current level. The calibration bar for each recording is presented on the right side

Discussion

In this study, we described a highly reproducible laser-based technique for the nanodissection of the fungal cell walls to obtain released viable fungal protoplasts whose plasma membrane was suitable for patch-clamp electrophysiology. Similar approaches were reported long ago using ns-UV laser pulses but were not further developed[10,33]. Compared with ns lasers, fs lasers can target specific regions with high accuracy without damaging the out-of-focus region, resulting in better surgical outcomes. They can produce clean and precise incisions with minimal thermal or mechanical damage. The high precision of fs laser ablation enabled the cutting of a small piece of cell wall without endangering the plasma membrane of the protoplast; this cut was only a few micrometers away from the protoplast or even closer. Another advantage of fs IR lasers over ns UV lasers is the wavelength used. IR lasers have longer wavelengths than UV lasers; thus, they can penetrate deeper into tissues due to nonlinear two-photon absorption that occurs only in the focal volume[38]. UV lasers that emit shorter wavelengths have more energy, increasing the susceptibility to cellular DNA damage[50] and inducing oxidative stress and cell death[51]. Another advantage of this method is the use of the same fs IR nanosurgical laser for two-photon imaging of live hyphae to mark the desired cell wall area for surgery. Compared to previous studies in which bright-field images were used to mark and section the cell wall, in the present study, we used two-photon fluorescence of the cell wall from TPEF images. The ability to select a region on the TPEF images for cutting contributed greatly to the accuracy and precision of the overall cell surgery method[38]. We did not observe any vaporization, cavitation, or carbonization on the TPEF or BF images recorded after the surgical procedure. Imaging the specimen by either modality during the surgical action was not possible. Additionally, in the SEM images, we did not observe fragments of the removed cell wall. The processes that potentially occurred during surgery and the possible transformations of the ablated/ejected materials are described in detail in Vogel and Venugopalan 2003[52]. The nanosurgery method presented here could lead to

successful patch-clamp recording only if the conditions for each step were kept within the optimal range, as many factors influenced the biological aspects of the procedure.

Fungi exhibit a cell wall integrity response; this is a signaling pathway activated by cell wall stress or damage involving fungal-specific kinases[53] and is the basic survival mechanism. The cell wall integrity pathway is involved in the response to osmotic stress[54], fungal morphogenesis, and fungal pathogenicity. The respiratory inhibitor azide was used throughout the protocol because it is the only respiratory chain inhibitor capable of almost complete inhibition of classical respiration for prolonged periods (unlike cyanide[55]) without significant induction of alternative respiration (unlike antimycin[55]); its use resulted in a long-term reduction in total respiration to 20% while maintaining viability. Under conditions of this pronounced metabolic suppression, all intracellular signaling pathways that depended on kinase activity and therefore required ATP, including the cell wall integrity response, were assumed to be suppressed.

Prevention of new wall formation was one of the key elements in the procedure's success because when azide was omitted, the hyphal protoplasts remained in the hyphae. In rare cases, when a protoplast was released without an applied azide due to the vigorous hypoosmotic swelling immediately after producing the wall incision, the contact between the patch pipette and the protoplasts was not achieved. The high concentration of calcium used throughout the procedure could account for the complete absence of potassium permeating currents in our system. The fungal-specific tandem pore outwardly rectifying K^+ channels (TOKs) are found in the genome of filamentous fungi, and heterologous expression shows that they form functional K^+ channels that may be present in the plasma membrane of filamentous fungi[12,56]. The TOK channels are blocked by Ca^{2+} on the extracellular side of the membrane[12]. Therefore, the almost absolute dominance of anionic currents (96% of all recorded currents) could be a result of the experimental conditions. Furthermore, the hyperosmotic conditions during the procedure could influence the activation or properties of the registered ionic currents. Notably, the osmolarity of the extracellular solutions used during patch-clamp seal formation and electrophysiological recordings was approximately isosmotic (with respect to the cytoplasm) because the protoplasts were optimally "inflated"; otherwise, the membrane would not be suitable for sealing. Filamentous fungi are organisms adapted to a wide range of different environmental conditions, such as the osmolarity of the surrounding environment; therefore, the possible change in physiology caused by a shift in osmolarity is likely to be the biologically relevant physiological state[57].

Immediately after surgery, protoplast release was frequently observed, and the probability of protoplast release was higher when the wall incision was made in close proximity to the hyphal protoplast. Turgor pressure-induced release of protoplasts could not be ruled out as part of the explanation for this phenomenon since the pressure relative to the cell wall in intact hyphae is 500 kPa greater, providing turgor to the cell[58,59]. However, under hyperosmotic conditions, turgor pressure is lower[58], and an additional cellular process, likely mediated by the cytoskeleton, could be involved in the protoplast release, since an increased calcium concentration enhanced the protoplast release from the incision. The more successful formation of sealing contacts in the protoplasts released from side branches was potentially due to the favorable interaction with the young plasma membrane, as is often the case with enzymatically derived plant protoplasts[24]. Notably, the close proximity of protoplasts to the laser incisions during nanosurgery had no detrimental effect on the health of the plasma membrane; this was reflected by the ability of the protoplasts to make high-resistance contact with the patch pipette, further demonstrating that the protocol presented in this study could produce consistently healthy released protoplasts from versatile locations. Our finding that numerous anionic conductances are present on the plasma membrane of filamentous fungi is consistent with the data from a limited number of available cloned ion channels[13,15] revealing the presence of CLC-like and Bestrophin-like channels. Additionally, unidentified ion channels could be present on these membranes. The prospects for further applications of the presented method include the discovery and identification of ion currents in the native protoplast membrane that have remained undetected to date because of the low homology of the underlying channels with animal or plant counterparts. These advances would further the understanding of the physiology of filamentous fungi.

Phycomyces blakesleeanus, the filamentous fungal model system used in this work, is a member of the order Mucorales (representative of the phylum Mucoromycota); members of this order form mycorrhizal symbiotic relationships with plants[60], while other members are serious human pathogens[61] whose prevalence is increasing[62,63]. The recently published WHO recommendation[64] identifies Mucorales as a high-priority group for monitoring, researching, and developing new drug targets. Therefore, the discovery and characterization of the membrane currents of *Phycomyces blakesleeanus* involved in the physiological responses of hyphae could lead to the identification of much-needed novel drug targets to combat human pathogens[65], as well as to better protect or exploit the mycorrhyzal symbiosis with plants in ecosystems and agriculture[66]. Further modifications of the described method may be required in the future to expand its application to other filamentous fungal phyla. The

potential applications of this technique span the entire range of fungal biology applications.

Materials and methods

Culture and growth conditions

A wild-type strain of the filamentous fungus *Phycomyces blakesleeanus* (Burgeff) [NRRL 1555(-)] was used in this study. The spores were seeded at a concentration of 10^6 spores/mL in standard liquid minimal medium (SLM)[67] at pH 4–5 containing the following per liter: 2 g L-asparagine·H_2O, 5 g KH_2PO_4, 500 mg $MgSO_4·7H_2O$, and microelements (28 mg $CaCl_2$, 1 mg thiamine hydrochloride, 2 mg citric acid·H_2O, 1.8 mg $Fe(NO_3)_3·9H_2O$, 1 mg $ZnSO_4·7H_2O$, 300 µg $MnSO_4·H_2O$, 50 µg $CuSO_4·5H_2O$, and 50 µg $Na_2MoO_4·2H_2O$), with half the glucose concentration (10 g D (+)-glucose) (1/2glucSLM) to reduce the osmolarity of the growth medium. The osmolarity was additionally decreased by diluting the medium by 10% from 210 to 140 mOsm to adapt the fungus to lower osmolarity conditions and ensure faster plasmolysis during the preparatory phase of nanosurgery. Fungi were grown in illuminated stationary open 100 mm Petri dishes at 21-22 °C.

Sample preparation

For cell nanosurgery experiments, the fungi were grown on glass coverslips ($d = 15$ mm) coated with a thin layer of 50% type I collagen as an immobilizer and placed on the bottom of 6-well plates. The collagen was previously polymerized at room temperature for 24 hours. The collagen-coated coverslips were inoculated with 15 µL of spore suspension from a Petri dish culture with an additional 50 µL of diluted 1/2glucSLM medium (to prevent the sample from drying out); the sample was allowed to stand for 1 hour to allow the spores to adhere/anchor to the collagen. After 1 hour, 2 mL of diluted 1/2glucSLM medium was added to the wells. This method proved to be the best in terms of hyphal adherence and growth. The experiment was always performed with fungi from the exponential growth phase (19-30 hours old). Most of the fungal hyphae were simple, elongated cells with a "spore "head" still visible, although some hyphae had just begun to form side branches.

Previously, we performed hyphal adhesion experiments on the following substrate-coating materials and coverslip surface modifications: gelatin, silicone, laminin, poly-L-lysine, concanavalin A, collagen type I, and plasma treatment (Supplementary Table S1). The hyphae adhered to and grew best on collagen type I. The optimal collagen thickness was then determined and found to be 10 µL of working collagen solution on a 15 mm diameter coverslip. Half-millimeter numbers were engraved on the coverslips (with a diamond scribe pencil) before the collagen treatment. Mapping of the culture coverslips was necessary to accurately determine the positions of the fungal hyphae before and after surgery because the surgery itself and the electrophysiology were performed on two separate microscopes.

Before the experiments, a coverslip containing the immobilized hyphae was placed on the bottom of the microscopic chamber and filled with the appropriate amount of hyperosmotic solution.

Staining of the cell wall

Live hyphae from the exponential growth phase (19-30 h) were incubated with 1% Calcofluor White (CFW; Sigma Aldrich) dye in isosmotic solution (495 mOsm) for 10 min at 20 °C. Then, 10 µM brefeldin A was added to the isosmotic dye solution. After incubation, the hyphae were washed three times in minimal media.

Preparation of solutions

The isosmotic solution for the CFW step contained (in mM) 60 KCl, 65 K-glutamate, 2 $MgCl_2$, 1 $CaCl_2$, and 10 HEPES (pH 7) supplemented with sucrose to produce 495 mOsm.

The hyperosmotic extracellular solutions (hyperECSs) used for plasmolysis and during nanosurgery contained the following (in mM): 60 KCl, 65 K-glutamate, 2 $MgCl_2$, 30 $CaCl_2$, and 10 HEPES at pH 7 supplemented with sorbitol to achieve the desired osmolarity (620 mOsm). In some experiments, slightly more hyperosmotic conditions were used (hyperECS: 680 mOsm, bath solution: 640 mOsm). Of the 13 attempts at the pipette approach, only 2 were successful using these conditions.

In a subset of experiments, the solution was modified to match the ion content of the patch-clamp bath solution and to investigate the ion basis of the recorded currents. For experiments with nitrate-based solution, hyperECS was modified by replacing $CaCl_2$ with $Ca(NO_3)_2$. For experiments with glutamate-based solutions, the ratio of KCl to K-glutamate in hyperECS was changed to 1:4 or 1:0, while the sum of the concentration remained at 125 mM.

For the experiment on the effect of Ca^{2+} on protoplast release, solutions with the following composition were used (in mM): standard [Ca^{2+}] solution (1 mM and 3 mM; data were pooled) - 60 KCl, 65 K-glutamate, 2 $MgCl_2$, 10 HEPES, 1 or 3 $CaCl_2$, pH 7, supplemented with sorbitol to 555-560 mOsm.

The high [Ca^{2+}] solution had the same ionic composition as the standard Ca^{2+} solution; the only differences were $CaCl_2$ (30 mM) with an osmolarity of 600-617 mOsm.

Patch-clamp recording solutions

The osmolarity of the chamber bath solution was 595 ± 10 mOsm; this solution was 25 mOsm hyperosmotic

than the pipette solution (570 mOsm). During the deplasmolysis step with a solution change, appropriate solutions were used to alter the ion composition of the final solutions to the following: nitrate solution (SolA) (in mM): 82.75 Cl^-, 125 K^+, 48.75 glutamate, 23.75 Ca^{2+}, 45 NO_3^-, 2 Mg^{2+}, 10 HEPES; and high-glutamate solution (SolB) (in mM): 70.25 Cl^-, 125 K^+, 106.25 glutamate, 23.75 Ca^{2+}, 2 Mg^{2+}, and 10 HEPES. The patch pipette solutions contained the following (in mM): solution combined with SolA: 125 KCl, 5 $CaCl_2$, 2 $MgCl_2$, and 10 HEPES; low chloride solution: 50 KCl, 5 K-glutamate, 1 $CaCl_2$, 2 $MgCl_2$, and 10 HEPES. The following patch pipette solution was used in combination with SolB: 125 KCl, 5 K-glutamate 1 $CaCl_2$, 2 $MgCl_2$, and 10 HEPES. All solutions were sterile-filtered at pH 7.

Hyphal plasmolysis and deplasmolysis

Plasmolysis was performed in two steps. In the pre-plasmolysis step (10 min incubation), hyphae were transferred from hypoosmotic growth medium to an isosmotic solution (495 mOsm) containing the cell wall dye. This step prior to plasmolysis served to facilitate the transition of the hyphae into the hyperosmotic solution used during imaging and nanosurgery. The hyperosmotic solution (HoS) (620 mOsm, except for one subset in which 680 mOsm was used) contained a high concentration of calcium (30 mM) in the form of $CaCl_2$ or $Ca(NO_3)_2$. A high Ca^{2+} content enabled faster plasmolysis and stabilization of the membrane by increasing the ionic strength of the hyperosmotic solution.

The onset of plasmolysis was considered the time at which hyphal protoplast withdrawal was observed at two or more sites along the hyphae in at least 25-30% of the hyphae in the field of view. Retraction from the tip was not used as a criterion for measuring plasmolysis time. After the nanosurgical procedure, the gentle deplasmolysis step was performed. We carefully removed ¼ of the hyperosmotic solution and slowly added 520 mOsm solution in the same volume, which decreased the osmolarity of the solution in the microscopic chamber to 595 ± 10 mOsm. A difference of 25 ± 10 mOsm between hyperECS and the bath solution allowed protoplasts to exit in some cases. However, in the majority (64%) of the experiments, protoplasts exited the hyphal wall through the laser-generated incision while still in the hyperosmotic solution.

Fungi were treated with an exocytosis inhibitor (10 µM brefeldin A) added before the plasmolysis step and a respiration inhibitor (2 mM sodium azide) to prevent cell wall regeneration during the procedure. Sodium azide was continuously present in all solutions (except during CFW staining). The addition of enzymes (chitinases and chitosanase cocktail) that would breakdown cell wall residues, which we hypothesized might be present at the cut site, was tested; however, these enzymes were found to have no effect and were not used under the optimized conditions.

Measurement of the biomass yield and oxygen consumption

To measure the biomass yield, *P. blakesleeanus* mycelia were grown in Petri dishes for 16 hours in 500 (control), 760 and 860 mOsm solutions. The biomass was measured after 30 and 90 minutes for both the control and treatment groups. The yield gain was determined for each culture as the biomass at each time point reduced by the average biomass of the control at the beginning of growth. The growth inhibition percentage was calculated as follows: (yield gain/average of control) *100. Oxygen consumption by *P. blakesleeanus* mycelia was measured using a Clark-type oxygen electrode (Qubit Systems). The mycelial suspension was diluted in fresh liquid minimal medium to an appropriate concentration (oxygen consumption between 15-25 µmol/L × min) and aerated for 1 minute before measurement. Two milliliters of the suspension ($n = 3$) was transferred to a 4 mL electrode chamber and maintained at a constant temperature of 25 °C. The long-term effect of incubation in 5 mM NaN_3 was measured using a 28-hour-old culture.

Graphs can be found in the Supplemental material (Fig. S1).

Measurement of the effect of calcium on the protoplast release

The effect of Ca^{2+} on the probability of protoplast release from nanosurgical incisions was measured using images taken immediately after the incisions were made. An oil immersion objective was used for this series of experiments. Nanosurgery and imaging were performed in standard Ca^{2+} or high Ca^{2+} solutions without subsequent patch-clamp recording.

NLSM experimental setup for TPEF imaging and nanosurgery

Laser nanosurgery and TPEF imaging of live hyphae were performed via a custom-built nonlinear laser-scanning microscope (Fig. 7) based on the Jenaval upright microscope frame. Previously described in references[47] and[68]. A femtosecond tunable (700–1000 nm) mode-locked Ti:Sa laser (Mira 900, Coherent, Inc., CA, USA), which generates 160 fs, 30 nJ pulses at a 76 MHz repetition rate, was used. Power control for nanosurgery and imaging was achieved using a motorized variable neutral density filter (VNDF) and fast mechanical shutter (Sh) for blocking or transmitting the laser beam. After passing through the VNDF and shutter, the laser beam was raster scanned over the sample using two galvanometer mirrors (Cambridge Technologies, 6215H; Bedford, Massachusetts, USA). A high numerical aperture

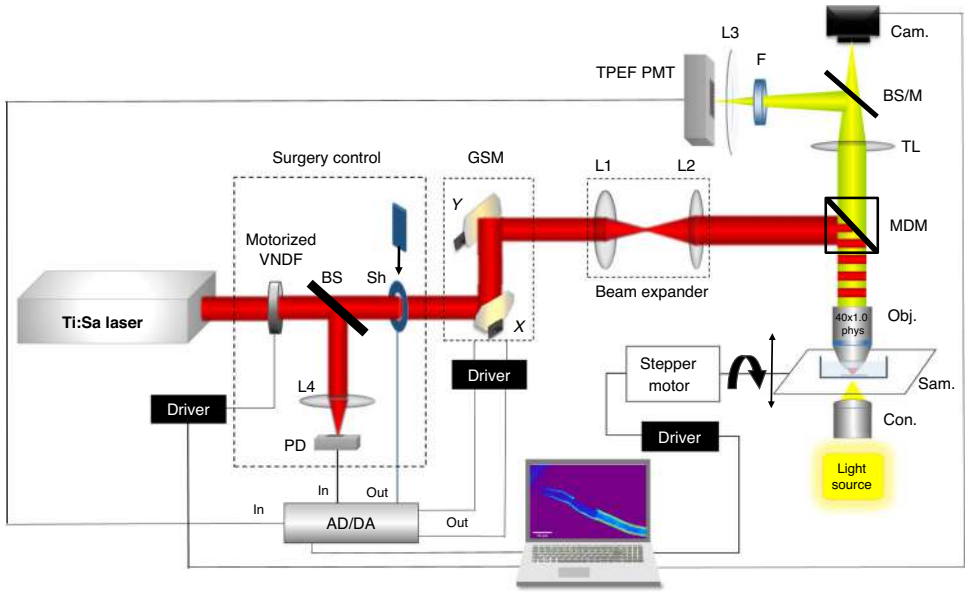

Fig. 7 Schematic drawing of the NLSM setup for nanosurgery and cell wall imaging. Ti:Sa fs laser for cell surgery and TPEF imaging, VNDF motorized variable neutral density filter, Sh shutter, GSM galvanometer-scanning mirrors, L1 and L2 - beam expander, MDM main dichroic mirror (cutoff 700 nm), Obj. microscopic objective 40 × 1.0 physiological, Sam. sample, Con. aspheric condenser lens, TL tube lens, BS/M beam splitter or mirror toggle, Cam. camera, F VIS filter 400–700 nm for CFW fluorescence, L3, L4 focusing lens, TPEF PMT photomultiplier tube for TPEF signal, PD photodiode, AD/DA acquisition card

(NA) physiological (dip-in) objective lens (Carl Zeiss W Plan-Apochromat 40X, NA = 1.0) was used for tight focusing of the laser beam into the sample. On some occasions, to obtain higher-quality images, we used an oil-immersion high-NA objective lens (Carl Zeiss, EC Plan-Neofluar 40X, NA = 1.3). In this case, the hyphal culture was placed under an additional coverslip on top to enable the use of an oil immersion objective. The physiological objective worked in the same microscopic chamber during laser surgery and patch-clamp procedures on two separate systems. The patch-clamp recordings were performed on a separate system with an inverted microscope that allows the measuring pipette to access the sample from above. A physiological objective lens was used for imaging and surgery on a nonlinear system to perform both procedures of surgery and patch-clamp on the exact same hypha in the same chamber. This process ensured faster transfer from the nonlinear system to the patch system and prevented sample perturbation and possible loss of the obtained protoplast when the upper coverslip was removed. To determine the position for surgery on the hyphal chitin cell wall, it was necessary to visualize the cell wall and ensure that there was sufficient absorption of the laser beam at the wavelength intended for surgery. The intrinsic autofluorescence of chitin enabled imaging of the cell wall. Nevertheless, the hyphae were stained to increase the absorption of the laser beam and consequently reduce the value of the laser power required for sample imaging and nanosurgery. TPEF was used to scan hyphal cell walls stained with CFW dye using the same wavelength as that used for the surgery (730 nm). The fluorescent signal was collected using back reflection by an objective lens, filtered through a visible (400–700 nm) bandpass filter and detected via a photomultiplier tube (PMT) (RCA, PF1006). The steering of the galvo mirrors, the TPEF signal acquisition and shutter were controlled by a USB-6351 National Instrument card at a sampling rate of 1.2 MHz. The power regulation and stage axial position were controlled by a microcontroller. The sample (a coverslip with immobilized hyphae at the bottom of the open microscopic chamber) was placed on the motorized translation stage. The motorized stage was powered by a stepper motor that could translate the sample along the z-axis with 0.3 µm resolution. This approach was essential for accurately targeting the middle of longitudinal sections of the cell wall.

A custom-made add-on to the imaging software was used for the surgical procedure. This approach enabled arbitrary pattern inscription onto the TPEF image, where the dwell time and the average power of the laser beam could be controlled. The surgical procedure was as follows: first, the TPEF image of the hyphae was recorded; second, the pattern (usually the BMP image) was imported and superimposed onto the TPEF image; and third, the scale, exact position and rotation angle were adjusted. Afterward, the average laser power and the dwell time

were defined. The shutter was opened at the beginning and closed at the end of the surgical procedure, and then the laser power and the software were automatically set back to the imaging mode. During surgery, the laser beam was moved from point to point for a time (<μs) much shorter than the dwell time (order of 1 s).

Bright-field images were taken by a Canon EOS 50D digital camera (Tokyo, Japan) whose CMOS sensor was placed at the image plane of the tube lens. The BS/M Toggle switch enabled the utilization of either a camera for bright-field or TPEF PMT for fluorescence imaging.

Scanning electron microscopy (SEM)

The characterization of the laser made incision and the released protoplast was performed using a high-resolution field emission gun scanning electron microscope (FEG-SEM-Mira3, TESCAN). The samples were prepared for SEM according to the standard protocol with paraformaldehyde fixation followed by drying in a critical point drying chamber (K850, Quorum Technologies, Laughton, UK) as previously described in ref. [69]. The samples were sputter-coated with 10 nm of gold/palladium using a Quorum sputter coater to make them conductive for SEM analysis.

Patch-clamp setup and method

The microscopic chamber was mounted on an inverted microscope (Zeiss Axiovert 10, Germany) with a Luis & Newman micromanipulator system. Currents were measured with an EPC8 amplifier (HEKA), digitized at 10 kHz using an Instrutec 1600 interface (HEKA); the currents were low-pass filtered at 3 kHz, recorded, and processed with Pulse software (HEKA). The pipettes used for on-cell and inside-out patch recordings had a resistance of 10-20 MΩ, while those used for whole-cell and out-out recordings were in the range of 5–10 MΩ. The pipettes were pulled from thick-walled borosilicate glass with filament on a Flaming-Brown P97 pipette puller (Sutter Instruments) and polished with a microforge (L/MCPZ 101, List Medical-Elektronic).

The contact resistance between the pipette and the membrane was monitored by continuous testing with square-wave voltage pulses. Prior to immersion in the bath, the pipette was pressurized to approximately 60 mbar to ensure that any debris between the pipette and the membrane was washed away prior to contact. After contact with the membrane, which resulted in an increase in the resistance of several MΩ, the release of positive pressure was often not sufficient for a tight seal, and a slight negative pressure was also applied to pull the membrane into the pipette; this was then released again to prevent the protoplast from being completely sucked into the pipette. Seal formation typically took a few seconds to half a minute. Giga-seal contact was reached when the contact resistance reached or exceeded 1 GΩ. Recording "on cell" was rarely used because it did not provide satisfactory voltage control. The excision of the membrane patch was achieved by moving the pipette rapidly away from the protoplast in the horizontal direction. The membrane current activity in the inside-out or outside-out configuration was recorded in the gap-free mode of the voltage clamp with the range of holding voltages (V_h) to measure the amplitude of the active channels and to generate IV plots. Alternatively, the standard voltage clamp protocol was applied when entering the whole-cell configuration: V_h of −50 mV, followed by a series of steps in 20 mV increments, from −110 mV to +110 mV. The duration of each step sequence was 500 ms, with a rest period of 0.5–1 s. Series resistances were not compensated. All experiments were performed at 20 °C.

Data analysis and statistics

Image analysis

Bright-field image analysis of the extruded protoplasts and cell wall incision lengths was performed using ImageJ (W. Rasband, National Institute of Health, Maryland, USA; http://imagej.nih.gov/ij/).

Current analysis

The current data analysis was performed using the Pulse and Clampfit software packages (Molecular Devices, USA). The reversal potentials (V_{rev}) for each ion were calculated using the calculator available at https://www.physiologyweb.com/calculators/nernst_potential_calculator.html. The conductance g (pS) was extracted as the slope of the current-voltage dependence for each detectable single-channel current recorded at three or more different V_h. The current V_{rev} was extrapolated from the linear IV plot. In rare cases where the current was rectified (nonlinear IV relationship), the nonrectified portion of the IV plot was used for extrapolation. Care was taken to design the solutions such that the V_{rev} for each of the ions was sufficiently separated from the others to allow rough typing of the currents based on the ion with the largest contribution to the V_{rev} (defined as the ion whose V_{rev} was close to the V_{rev} of the recorded single-channel current).

Statistics

Graphing and statistical comparisons were made using Graph Pad Prism software. Boxes of the box and whisker plots are enclosed by the 25th and 75th percentile ranges, respectively, with the line representing the median; whiskers extend to the minimum and maximum values, respectively. Histograms of the incision length and distance of the hyphal protoplasts from the incision were generated from all values in each group with 3 μm binning and plotted with the upper bin boundary on the x-axis.

One-way ANOVA with multiple comparisons and Holm-Sidac correction and the unpaired two-tailed *t*-test with Welch's correction for unequal variances were used to calculate statistical significance. The confidence intervals for statistical significance were 0.05 (*), 0.01 (**), 0.005 (***), and 0.0001 (****). The release probabilities were calculated from all available data. Throughout the manuscript, the data are presented as the mean ± SD.

Acknowledgements
This work was supported by the Ministry of Science, Technological Development and Innovations, Republic of Serbia [contract numbers: 451-03-47/2023-01/200178 and 451-03-47/2023-01/200007]; the Project Advanced Biophysical Methods for Soil Targeted Fungi-Based Biocontrol Agents - BioPhysFUN [Grant number 4545] from the Program DEVELOPMENT – Green program of cooperation between science and industry, Science Fund of the Republic of Serbia; the Project HEMMAGINERO [Grant number 6066079] from the Program PROMIS, Science Fund of the Republic of Serbia; and the Institute of Physics Belgrade through grants from the Ministry of Science, Technological Development and Innovations of the Republic of Serbia. We would like to thank Vladimir Lazović for his valuable technical help with some TPEF imaging and nanosurgery experiments with unlabeled hyphae. Additionally, we would like to thank Milan Minić for indispensable technical help and support.

Author details
[1]Institute of Physiology and Biochemistry "Ivan Djaja", Faculty of Biology, University of Belgrade, Studentski trg 16, 11158 Belgrade, Serbia. [2]Institute for Biological Research "Siniša Stanković", University of Belgrade, National Institute of the Republic of Serbia, Bulevar Despota Stefana 142, 11000 Belgrade, Serbia. [3]Institute of Physics Belgrade, University of Belgrade, National Institute of the Republic of Serbia, Pregrevica 118, 11080 Belgrade, Serbia. [4]University of Belgrade, Faculty of Agriculture, Nemanjina Street 6, 11080 Belgrade, Serbia. [5]Institute for Multidisciplinary Research, University of Belgrade, Kneza Višeslava 1, 11030 Belgrade, Serbia

Author contributions
M.Ž., N.V.T., B.J. and D.P. conceptualized the initial study plan. M.Ž, N.V.T., A.J.K., M.D.R., T.P. and K.S. designed the final study concept. T.P. conducted all laser nanosurgeries, performed the TPEF imaging, maintained the fungal culture and prepared the samples. K.S. conducted all patch-clamp experiments. T.P. and K.S. conducted the plasmolysis/deplasmolysis experiments. N.V.T. and K.S. designed the patch-clamp protocols. N.V.T. supervised the patch-clamp and plasmolysis/deplasmolysis experiments and performed the data analysis. The solution design for patch-clamp was performed by K.S. and N.V.T., and the design of the hyperosmotic solutions for plasmolysis by T.P. and M.Ž. A.J.K. and M.D.R. designed and developed the NLSM set up and supervised the nanosurgery and imaging experiments and TPEF image processing/analysis. M.D.R., A.J.K. and T.P. designed the laser nanosurgery protocols. M.Ž. supervised the biological part of the research. M.S. performed the oxygen consumption measurements and analysis. T.P. and M.S. performed the biomass yield measurements. S.S-Š. performed the SEM imaging. S.M.L. conducted the sample drying procedure in the critical point dryer. T.P., K.S. and N.V.T. prepared the samples for critical point drying and SEM analysis. D.P. wrote the software for TPEF imaging and nanosurgery. T.P. performed the TPEF and BF image analysis. N.V.T. performed the current analysis and statistics. T.P., N.V.T., M.D.R., A.J.K., and M.Ž. prepared the manuscript. All authors participated in the manuscript revision and approved the submitted version.

Data availability
All data needed to evaluate the conclusions in the paper are presented in the paper and/or the Supplementary Materials. Additional data related to this paper may be requested from the corresponding authors.

Conflict of interest
The authors declare no competing interests.

Supplementary information The online version contains supplementary material available at https://doi.org/10.1038/s41378-024-00664-x.

Received: 20 September 2023 Revised: 1 December 2023
Accepted: 19 December 2023
Published online: 07 April 2024

References

1. Genre, A., Lanfranco, L., Perotto, S. & Bonfante, P. Unique and common traits in mycorrhizal symbioses. *Nat Rev Microbiol* **18**, 649–660 (2020).
2. Van Der Heijden, M. G. A. et al. Mycorrhizal fungal diversity determines plant biodiversity, ecosystem variability and productivity. *Nature* **396**, 69–72 (1998).
3. Fisher, M. C. et al. Emerging fungal threats to animal, plant and ecosystem health. *Nature* **484**, 186–194 (2012).
4. Gow, N. A. R. et al. The importance of antimicrobial resistance in medical mycology. *Nat Commun* **13**, 5352 (2022).
5. Prole, D. L. & Taylor, C. W. Identification and analysis of cation channel homologues in human pathogenic fungi. *PLoS One* **7**, 42404 (2012).
6. Liu, M., Du, P., Heinrich, G., Cox, G. M. & Gelli, A. Cch1 mediates calcium entry in Cryptococcus neoformans and is essential in low-calcium environments. *Eukaryot Cell* **5**, 1788–1796 (2006).
7. Zhang, X. et al. Heat stress modulates mycelium growth, heat shock protein expression, ganoderic acid biosynthesis, and hyphal branching of ganoderma lucidum via cytosolic Ca2+. *Appl Environ Microbiol* **82**, 4112–4125 (2016).
8. Lew, R. R. & Nasserifar, S. Transient responses during hyperosmotic shock in the filamentous fungus Neurospora crassa. *Microbiology* **155**, 903–911 (2009).
9. Zhou, X. L., Stumpf, M. A., Hoch, H. C. & Kung, C. A Mechanosensitive Channel in Whole Cells and in Membrane Patches of the Fungus Uromyces. *Science* **253**, 1415–1417 (1991).
10. Roberts, S. K., Dixon, G. K., Dunbar, S. J. & Sanders, D. Laser ablation of the cell wall and localized patch clamping of the plasma membrane in the filamentous fungus Aspergillus: Characterization of an anion-selective efflux channel. *N Phytol* **137**, 579–585 (1997).
11. Silverman-Gavrila, L. B. & Lew, R. R. An IP3-activated Ca2+ channel regulates fungal tip growth. *J Cell Sci* **115**, 5013–5025 (2002).
12. Roberts, S. K. TOK homologue in Neurospora crassa: First cloning and functional characterization of an ion channel in a filamentous fungus. *Eukaryot. Cell* **2**, 181–190 (2003).
13. Oddon, D. M., Diatloff, E. & Roberts, S. K. A CLC chloride channel plays an essential role in copper homeostasis in Aspergillus nidulans at increased extracellular copper concentrations. *Biochim. Biophys. Acta - Biomembr.* **1768**, 2466–2477 (2007).
14. Živić, M., Popović, M., Todorović, N. & Vučinić, Ž. Outwardly rectifying anionic channel from the plasma membrane of the Fungus Phycomyces blakesleeanus. *Eukaryot. Cell* **8**, 1439 (2009).
15. Roberts, S. K., Milnes, J. & Caddick, M. Characterisation of AnBEST1, a functional anion channel in the plasma membrane of the filamentous fungus, Aspergillus nidulans. *Fungal Genet Biol* **48**, 928–938 (2011).
16. Malvezzi, M., Chalat, M., Janjusevic, R. et al. Ca^{2+}-dependent phospholipid scrambling by a reconstituted TMEM16 ion channel. *Nat Commun* **4**, 2367 (2013).
17. Križak, S. et al. Osmotic swelling activates a novel anionic current with VRAC-like properties in a cytoplasmic droplet membrane from Phycomyces blakesleeanus sporangiophores. *Res Microbiol* **166**, 162–173 (2015).
18. Zhao, C. & Tombola, F. Voltage-gated proton channels from fungi highlight role of peripheral regions in channel activation. *Commun Biol* **4**, 261 (2021).
19. Dionysopoulou, M., Yan, N., Wang, B., Pliotas, C. & Diallinas, G. Genetic and cellular characterization of MscS-like putative channels in the filamentous fungus Aspergillus nidulans. *Channels* **16**, 148–158 (2022).
20. Sperelakis, N. *Cell Physiology Source Book: Essentials of Membrane Biophysics*. (Elsevier, 2011). https://doi.org/10.1016/C2010-0-66479-0
21. Henriksen, G. H. & Assmann, S. M. Laser-assisted patch clamping: A methodology. *Pflug Arch Eur J Physiol* **433**, 832–841 (1997).
22. Shakoor, A., Gao, W., Zhao, L., Jiang, Z. & Sun, D. Advanced tools and methods for single-cell surgery. *Microsyst Nanoeng* **8**, 1–21 (2022).
23. Sun, S., Furtula, V. & Nothnagel, E. A. Mechanical release and lectin labeling of maize root protoplasts. *Protoplasma* **169**, (Springer-Verlag, 1992).

24. Elzenga, J. T. M., Keller, C. P. & Van Volkenburgh, E. Patch clamping protoplasts from vascular plants method for the quick isolation of protoplasts having a high success rate of gigaseal formation. *Plant Physiol* **97**, 1573–1575 (1991).
25. Fairley, K., Laver, D. & Walker, N. A. Whole-cell and single-channel currents across the plasmalemma of corn shoot suspension cells. *J Membr Biol* **121**, 11–22 (1991).
26. Levina, N. N., Lew, R. R., Hyde, G. J. & Heath, I. B. The roles of Ca2+ and plasma membrane ion channels in hyphal tip growth of Neurospora crassa. *J Cell Sci* **108**, 3405–3417 (1995).
27. Garrill, A., Jackson, S. L., Lew, R. R. & Heath, I. B. Ion channel activity and tip growth: tip-localized stretch-activated channels generate an essential Ca2+ gradient in the oomycete Saprolegnia ferax. *Eur J Cell Biol* **60**, 358–365 (1993).
28. Ronchi, P., Terjung, S. & Pepperkok, R. At the cutting edge: Applications and perspectives of laser nanosurgery in cell biology. *Biol Chem* **393**, 235–248 (2012).
29. Taylor, A. R. & Brownlee, C. Localized patch clamping of plasma membrane of a polarized plant cell: Laser Microsurgery of the Fucus spiralis rhizoid cell wall. *Plant Physiol* **99**, 1686–1688 (1992).
30. De Boer, A. H. et al. Laser microsurgery: a versatile tool in plant (electro) physiology. *Protoplasma* **178**, 1–10 (1994).
31. Henriksen, G. H., Taylor, A. R., Brownlee, C. & Assmann, S. M. Laser microsurgery of higher plant cell walls permits patch-clamp access. *Plant Physiol* **110**, 1063–1068 (1996).
32. Miedema, H., Henriksen, G. H. & Assmann, S. M. A laser microsurgical method of cell wall removal allows detection of large-conductance ion channels in the guard cell plasma membrane. *Protoplasma* **209**, 58–67 (1999).
33. Véry, A. A. & Davies, J. M. Laser microsurgery permits fungal plasma membrane single-ion-channel resolution at the hyphal tip. *Appl Environ Microbiol* **64**, 1569–1572 (1998).
34. Oraevsky, A. A. et al. Plasma mediated ablation of biological tissues with nanosecond-to-femtosecond laser pulses: Relative role of linear and nonlinear absorption. *IEEE J Sel Top. Quantum Electron* **2**, 801–809 (1996).
35. Gabel, C. V. Femtosecond lasers in biology: Nanoscale surgery with ultrafast optics. *Contemp Phys* **49**, 391–411 (2008).
36. Uchugonova, A. Nanosurgery of cells and chromosomes using near-infrared twelve-femtosecond laser pulses. *J Biomed Opt* **17**, 101502 (2012).
37. Kohli, V., Elezzabi, A. Y. & Acker, J. P. Cell nanosurgery using ultrashort (femtosecond) laser pulses: Applications to membrane surgery and cell isolation. *Lasers Surg Med* **37**, 227–230 (2005).
38. Vogel, A., Noack, J., Hüttman, G. & Paltauf, G. Mechanisms of femtosecond laser nanosurgery of cells and tissues. *Appl Phys B: Lasers Opt* **81**, 1015–1047 (2005).
39. Tserevelakis, G. J. et al. Femtosecond laser nanosurgery of sub-cellular structures in HeLa cells by employing Third Harmonic Generation imaging modality as diagnostic tool. *J Biophotonics* **5**, 200–207 (2012).
40. de Medeiros, G. et al. Cell and tissue manipulation with ultrashort infrared laser pulses in light-sheet microscopy. *Sci. Rep.* **10**, 1–12 (2020).
41. Chung, S. H. & Mazur, E. Surgical applications of femtosecond lasers. *J Biophotonics* **2**, 557–572 (2009).
42. Heinemann, D., Zabic, M., Terakawa, M. & Boch, J. Laser-based molecular delivery and its applications in plant science. *Plant Methods* **18**, 82 (2022).
43. Pérez-Martín, J., Bardetti, P., Castanheira, S., de la Torre, A. & Tenorio-Gómez, M. Virulence-specific cell cycle and morphogenesis connections in pathogenic fungi. *Semin. Cell Dev Biol* **57**, 93–99 (2016).
44. Gutjahr, C. & Parniske, M. Cell and developmental biology of arbuscular mycorrhiza symbiosis. *Annu Rev Cell Dev Biol* **29**, 593–617 (2013).
45. Bassilana, M., Puerner, C. & Arkowitz, R. A. External signal–mediated polarized growth in fungi. *Curr Opin Cell Biol* **62**, 150–158 (2020).
46. Knepper, C., Savory, E. A. & Day, B. Arabidopsis NDR1 is an integrin-like protein with a role in fluid loss and plasma membrane-cell wall adhesion. *Plant Physiol* **156**, 286–300 (2011).
47. Rabasović, M. D. et al. Nonlinear microscopy of chitin and chitinous structures: a case study of two cave-dwelling insects. *J Biomed Opt* **20**, 1 (2015).
48. Chung, L. Y. et al. Biocompatibility of potential wound management products: Fungal mycelia as a source of chitin/chitosan and their effect on the proliferation of human F1000 fibroblasts in culture. *J Biomed Mater Res* **28**, 463–469 (1994).
49. Maeda, H. & Ishida, N. Specificity of binding of hexopyranosyl polysaccharides with fluorescent brightener. *J Biochem* **62**, 276–278 (1967).
50. Niemz, M. H. *Laser-tissue Iteractions: Fundamentals and Applications*. (Springer-Verlag, 2004).
51. Tirlapur, U. K. & König, K. Femtosecond near-infrared laser pulses as a versatile non-invasive tool for intra-tissue nanoprocessing in plants without compromising viability. *Plant J* **31**, 365–374 (2002).
52. Vogel, A. & Venugopalan, V. Mechanisms of pulsed laser ablation of biological tissues. *Chem Rev* **103**, 577–644 (2003).
53. Yoshimi, A., Miyazawa, K., Kawauchi, M. & Abe, K. Cell wall integrity and its industrial applications in filamentous fungi. *J Fungi* **8**, 435 (2022).
54. Fuchs, B. B. & Mylonakis, E. Our paths might cross: the role of the fungal cell wall integrity pathway in stress response and cross talk with other stress response pathways. *Eukaryot Cell* **8**, 1616–1625 (2009).
55. Stanić, M. et al. Effect of long-term cyanide exposure on cyanide-sensitive respiration and phosphate metabolism in the fungus phycomyces blakesleeanus. *Arch Biol Sci* **66**, 847–857 (2014).
56. Ketchum, K. A., Joiner, W. J., Sellers, A. J., Kaczmarek, L. K. & Goldstein, S. A. N. A new family of outwardly rectifying potassium channel proteins with two pore domains in tandem. *Nature* **376**, 690–695 (1995).
57. Duran, R., Cary, J. W. & Calvo, A. M. Role of the osmotic stress regulatory pathway in morphogenesis and secondary metabolism in filamentous fungi. *Toxins* **2**, 367 (2010).
58. Lew, R. R. How does a hypha grow? the biophysics of pressurized growth in fungi. *Nat Rev Microbiol* **9**, 509–518 (2011).
59. Lew, R. R., Levina, N. N., Shabala, L., Anderca, M. I. & Shabala, S. N. Role of a mitogen-activated protein kinase cascade in ion flux-mediated turgor regulation in fungi. *Eukaryot Cell* **5**, 480–487 (2006).
60. Mansfield, T. M., Albornoz, F. E., Ryan, M. H., Bending, G. D. & Standish, R. J. Niche differentiation of Mucoromycotinian and Glomeromycotinian arbuscular mycorrhizal fungi along a 2-million-year soil chronosequence. *Mycorrhiza* **33**, 139–152 (2023).
61. Lax, C. et al. Genes, pathways, and mechanisms involved in the virulence of mucorales. *Genes* **11**, 317 (2020).
62. Walther, G., Wagner, L. & Kurzai, O. Outbreaks of Mucorales and the Species Involved. *Mycopathologia* **185**, 765–781 (2020).
63. Pasrija, R. & Naime, M. Resolving the equation between mucormycosis and COVID-19 disease. *Mol Biol Rep* **49**, 3349–3356 (2022).
64. World Health Organization. *WHO fungal priority pathogens list to guide research, development and public health action*. *Licence: CC BY-NC-SA 3.0 IGO* **1**, (2022).
65. Fisher, M. C. et al. Tackling the emerging threat of antifungal resistance to human health. *Nat Rev Microbiol* **20**, 557–571 (2022).
66. Mohan, J. E. et al. Mycorrhizal fungi mediation of terrestrial ecosystem responses to global change: Mini-review. *Fungal Ecol* **10**, 3–19 (2014).
67. Sutter, R. P. Mutations Affecting Sexual Development in Phycomyces blakesleeanus (car mutants/defined medium). *Proc Natl Acad Sci USA* **72**, 127–130 (1975).
68. Bukara, K. et al. Mapping of hemoglobin in erythrocytes and erythrocyte ghosts using two photon excitation fluorescence microscopy. *J Biomed Opt* **22**, 1 (2017).
69. Žižić, M. et al. Biotransformation of selenium in the mycelium of the fungus Phycomyces blakesleeanus. *Anal Bioanal Chem* **414**, 6213–6222 (2022).

polymers

MDPI

Article

Characterization and Optimization of Real-Time Photoresponsive Gelatin for Direct Laser Writing

Branka D. Murić [1,*], Dejan V. Pantelić [1], Mihajlo D. Radmilović [1], Svetlana N. Savić-Šević [1] and Vesna O. Vasović [2]

[1] Institute of Physics, University of Belgrade, Pregrevica 118, 11080 Belgrade, Serbia; pantelic@ipb.ac.rs (D.V.P.); mihajlor@ipb.ac.rs (M.D.R.); savic@ipb.ac.rs (S.N.S.-Š.)
[2] Western Serbia Academy of Applied Studies, Užice Department, Trg Svetog Save 34, 31000 Užice, Serbia; bolex65@yahoo.com
* Correspondence: muric@ipb.ac.rs

Abstract: There is an abundance of plastic materials used in the widest range of applications, such as packaging, machine parts, biomedical devices and components, etc. However, most materials used today are non-decomposable in the environment, producing a huge burden on ecosystems. The search for better, safer alternatives is still on. Here we present a detailed analysis of a simple, cheap, non-toxic, even edible, eco-friendly material, which can be easily manufactured, laser patterned and used for the fabrication of complex structures. The base substance is gelatin which is made photoresponsive by adding plasticizers and sensitizers. The resulting films were analyzed with respect to their optical, thermal and mechanical properties, which can be modified by a slight variation of chemical composition. The material is optimized for rapid laser-manufacturing of elastic microstructures (lenses, gratings, cantilevers, etc.) without any waste or residues. Overall, the material properties were tailored to increase photothermal responsivity, improve the surface quality and achieve material homogeneity, transparency and long-term stability (as verified using electron microscopy, infrared spectroscopy and differential scanning calorimetry).

Keywords: gelatin; bio-eco-polymers; physicochemical properties; optical elastomers; rapid laser printing; microstructures

check for updates

Citation: Murić, B.D.; Pantelić, D.V.; Radmilović, M.D.; Savić-Šević, S.N.; Vasović, V.O. Characterization and Optimization of Real-Time Photoresponsive Gelatin for Direct Laser Writing. *Polymers* **2022**, *14*, 2350. https://doi.org/10.3390/polym14122350

Academic Editor: Oh Seok Kwon

Received: 29 April 2022
Accepted: 5 June 2022
Published: 9 June 2022

Publisher's Note: MDPI stays neutral with regard to jurisdictional claims in published maps and institutional affiliations.

Copyright: © 2022 by the authors. Licensee MDPI, Basel, Switzerland. This article is an open access article distributed under the terms and conditions of the Creative Commons Attribution (CC BY) license (https://creativecommons.org/licenses/by/4.0/).

1. Introduction

The mechanical strength, low production cost and manufacturability of petroleum-based plastics established them as the most popular packaging materials [1]. Unfortunately, their non-biodegradability makes them an important source of pollution [2]. The ecological impact of petroleum-based plastics has accelerated the worldwide interest in biodegradable polymers from renewable resources. Despite the great potential of biodegradable polymers to solve the problem of plastic waste, they are rarely used, considering that their production is relatively expensive and they do not possess all the other properties (e.g., mechanical, optical, and electrical) required by various end-applications [3]. Additionally, such materials may have quite variable properties. For example, tensile strength, strain at break and elasticity (Young's modulus) depend on the raw material source, additives, molecular structures, etc. [4,5].

A good example of a natural biodegradable polymer from renewable resources is starch which is inexpensive, readily available and biodegradable. However, its mechanical strength is strongly modulated by its moisture sensitivity while being difficult for thermal processing (it thermally decomposes before being melted). To modify these characteristics, starch is blended with other polymers [6–8]. Unfortunately, these blends can affect biodegradability. Furthermore, there is a direct relationship between the starch-based bioplastic properties and different starch botanical sources. Namely, the amylose and amylopectin proportion, which depends on starch biosynthesis enzymes, soil type, and

climatic conditions during plant growth, strongly influences the bioplastic gelation temperature and mechanical and rheological properties [9]. Nevertheless, significant research and technological work invested in the development of starch-based polymers in the packaging sectors of food, cosmetics, pharmaceuticals, etc. [10–12].

Gelatin, yet another biocompatible and biodegradable polymer, is widely used in photography, food, pharmaceutical, biomedical and many others applications [13–17]. It has poor mechanical properties that limit its potential applications. A variety of chemical agents (formaldehyde, epoxy, glutaraldehyde and some others) are capable of crosslinking gelatin, consequently overcoming the brittleness of gelatin films, improving its flexibility, reducing the degree of swelling and enhancing its thermal stability. Glutaraldehyde [18] is usually used but is being replaced with genipin because of its lower cytotoxicity [19,20].

Besides gelatin, many other natural polymers (such as albumen, alginate, cellulose, chitosan, pullulan, etc.) can be used too [21,22]. We emphasize that the photoresponsiveness and photosensitivity of most materials stem from harmful and poisonous chemicals (such as dichromate compounds).

Also, gelatin is often mixed with other substances, e.g., chitosan, poly(vinyl alcohol), alginate and carbon nanotubes. These hybrid materials are specifically of interest in biomedicine for drug delivery, wound healing, cell culture and tissue engineering [23–25].

Gelatin hydrogels are photosensitized by various dyes, making them suitable for laser writing of microstructures (such as microfluidic channels, microlenses, micro-optoelectromechanical systems (MOEMS), lab on a chip, etc.) intended for a wide variety of applications [26–28]. Gelatin was widely used previously in optics, primarily as a photosensitive material for holography. Photo-crosslinking was achieved by adding ammonium dichromate or potassium dichromate, which resulted in holograms of excellent quality. It is known that gelatin doped with ammonium dichromate (dichromated gelatin—DCG) represents an almost ideal high-resolution holographic photosensitive material [29]. Additionally, DCG can be used as a material for the production of micro-optical components [30,31]. Most of them are toxic, difficult to manufacture and require complex chemical postprocessing. Various silicate-based materials (silicones, silica glass, etc.) were used for the fabrication of micro-optical components [32,33]. Compared to gelatin, they have higher thermal and chemical stability, but the fabrication processes are manly complex, multistep, time-consuming and costly, frequently including the use of poisonous chemicals.

Emerging applications in biomedicine, micro-mechanics, micro-optics, energy storage, and sensors require new materials, simultaneously possessing advanced optical, electrochemical, mechanical and biological properties [34–36]. Previously, we have described photosensitive tot'hema-gelatin as a good candidate material for applications requiring real-time manufacturing of micro-optical and micro-mechanical components [37–40]. Gelatin was modified with a complex aqueous mixture of various salts, plasticizers, humectants and preservatives (commercially sold under the trade name tot'hema, which is used to treat iron anemia). The material is simple to prepare, low-cost, non-toxic, biodegradable and can be patterned by direct laser writing (DLW—widely used non-contact high-precision processing technique [41,42]). Here, a variety of micro-optical and microfluidic structures were fabricated using DLW, and threshold laser energy was established. This kind of microprocessing is neither additive nor subtractive as the material is only redistributed without any waste.

Therefore, in order to fully explore and optimize the capabilities of tot'hema-gelatin films for real industrial applications, the physicochemical characteristics of the film were studied in more detail and disclosed in this paper. We correlated the applied concentration of tot'hema with the film properties, such as color, thickness, light transmission, mechanical (tensile strength, elongation at break and Young's modulus), thermal properties, moisture content, swelling, the functional group on the film surface as well as surface morphology. These properties are essential for establishing optimal conditions of material used as an elastomer for adaptive, rapid prototyping of micro-optics and micro-mechanics.

2. Materials and Methods

2.1. Materials

All chemical components were analytical grade, well known, easily available, cheap and non-toxic. Commercial gelatin from bovine skin (gel strength ~225 g Bloom, Type B) and NaCl (puriss, p.a.) were purchased from Sigma Aldrich. Tot'hema, an oral solution for the treatment of human anemia, was manufactured by Laboratoire Innotech International, France. According to the manufacturer's data [43], this is a complex water solution of gluconate (iron, manganese and copper) and excipients (glycerol, glucose liquid, saccharine, citric acid, polysorbate 80, etc.). Saline solution was purchased from Hemofarm (Serbia).

2.2. Film Preparation

A 5% water solution of gelatin with added NaCl (20% by weight of dry gelatin) was prepared as described in previous papers [37,38]. The tot'hema (ranging from 0% to 30% v/v) was mixed with gelatin solution by a magnetic stirrer. The series of five solutions (denoted as TG_X, where the letter X indicates the tot'hema percentage in solution) were prepared and centrifuged in order to remove all remaining impurities.

TG_X films were prepared by the gravity settling method [39]. Namely, the accurately measured volume of TG_X solution was pipetted onto a very clean, horizontally leveled microscope glass slide and dried in a stable environmental condition over the night.

2.3. Mechanical Properties

A film thickness was determined using a digital micrometer (an accuracy of 0.01 mm) at eight randomly selected points in the center and edges of the films. Measurements were averaged and taken as the film thickness.

The surface morphologies of the tot'hema-gelatin films were analyzed using a high-resolution scanning electron microscope equipped with a high brightness Schottky field emission gun (FEGSEM) and using non–contact profilometry (3D optical surface profiler—Zygo New View 7100).

The mechanical properties of the films were determined using a tensile testing machine, at a strain rate of 20 mm/min, as previously described for photosensitive tot'hema-gelatin, with minor modifications [44]. The dried film was cut by a brass mold, designed according to the ASTM standard [45], into a dog-bone-shaped specimen (see Figure 1). Three measurements were made for each film, and the average value was calculated. The tensile strength, elongation at break and Young's modulus were determined.

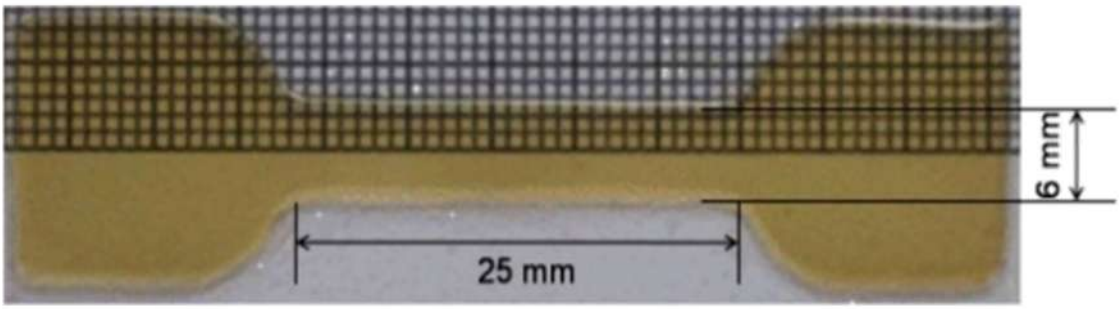

Figure 1. Optically transparent TG_20 film is used for tensile testing with dimensions according to the ASTM standards (gauge length 25 mm, width 6 mm).

2.4. Optical Properties

The transmittance of the TG_X films was analyzed using a fiber-type spectrometer (Ocean Optics) with a tungsten-halogen light as an illumination source in the wavelength range from 200 nm to 800 nm at room temperature.

A home-made direct laser writing system was used to fabricate microfluidic, micro-mechanic and micro-optical components on tot'hema modified gelatin film. A laser beam (488 nm wavelength, up to 100 mW power–iBEAM SMART, manufactured by Toptica)

was focused through the long-working-distance microscope objective. The samples were mounted on an xyz-coordinate stage to enable precise movement of the material along with the arbitrary pattern. The system was computer-controlled using G-code (standard programming language for CNC machines). More details about the system are given in a previous publication [46].

2.5. Physicochemical Properties

To determine how the number of water changes during the drying–dehydration of the film, the water content (WC) was measured. The TG_X films were weighted (w_1), then dried for 24 h at normal laboratory conditions, and weighted again (w_2). The WC for each film was determined as an average value of three measurements by the equation: $WC(\%) = [(w_1 - w_2)/w_1] \cdot 100$ [47].

In order to determine the influence of tot'hema concentration on the film swelling, TG_X films were immersed in saline solution for different intervals at laboratory conditions. Wet, swollen samples, after wiping with filter paper to remove excess liquid, were weighted again (w_w). The swelling factor (SF) of the films was calculated as the average value of three measurements by the equation: $SF(\%) = [(w_w - w_d)/w_d] \cdot 100$ where (w_d) corresponds to the weight of TG_X films before immersion [48].

Functional groups on the films were inspected by Fourier transformed infrared (FTIR) spectroscopy. The spectra were recorded on a Nicolet iS10 FTIR Spectrometer (Thermo Scientific Instruments) equipped with an attenuated total reflectance (ATR) accessory. ATR/FTIR measurements were done in the wavenumber interval from 500 to 4000 cm^{-1} with a resolution of 4 cm^{-1}.

The thermal stability of the films was analyzed by differential scanning calorimetry (DSC). An amount of about 2.5 mg of each film sample was packed in an aluminum pan (30 µL). The pan was sealed and analyzed using a DSC 131 EVO (SETARAM Instrumentation) differential scanning calorimeter previously calibrated with indium. An empty sealed pan was used as a reference. Both pans were placed in a chamber under the nitrogen flow of 20 mL/min, kept at 20 °C for 5 min and subsequently heated from 20 to 250 °C with a heating rate of 10 °C/min. To construct a baseline, two empty pans were placed in the chamber and measured under the same experimental conditions. The baseline subtraction was performed using the CALISTO Processing software (SETARAM Instrumentation).

3. Results

The pure gelatin film (TG_0) has a uniform, relatively smooth and flat surface, which indicates that the gelatin has a good film-forming ability. We have found that there is no noticeable difference in the gelatin film surface after tot'hema adding. Films still keep a rather smooth, uniform and homogeneous surface (without pores or cracks), indicating that there is good compatibility between tot'hema and gelatin molecules. Smoothness remains high after laser processing, as verified by SEM analysis of hexagonal concave microlenses array fabricated on photoresponsive tot'hema-gelatin film (Figure 2a). The lens-shaped dip is very symmetric (verified by the concentric shape of the corresponding interferogram in Figure 2b), and its roughness is of the order of several tens of nanometers (see Figure 2c). This makes photoresponsive tot'hema-gelatin an excellent material for the fabrication of micro-optical components.

To study mechanical properties, equal volumes of solution were used to prepare all TG_X films. An increase in tot'hema concentration resulted in the film thickening from 25 µm (pure gelatin) to 200 µm (30% of tot'hema) as a result of the plasticizer's interaction with the polymer chains. Tot'hema added to gelatin increases the distance between protein chains, increasing the film thickness. It can be noticed that the highest tot'hema concentration (30%) results in the thickest film due to the fact that most tot'hema ingredients are hydrophilic molecules that retain water and further increase the film thickness. Moreover, increased tot'hema content in gelatin film decreases the stress at break (reaching a minimum of 0.72 MPa at 30% of tot'hema) and increases the strain at break (turning tot'hema-gelatin

into an elastomer—maximum elasticity of about 220% was obtained). Mechanical properties of TG_X films, as a function of the concentration of tot'hema, are summarized in Table 1. The tot'hema addition (which is a mixture of different plasticizers and humectants) to the gelatin matrix improves the film flexibility and, consequently, makes it less rigid. Namely, glycerol is well known as a plasticizer. As a hydrophilic molecule with low molecular weight, glycerol can easily fit into protein chains creating hydrogen bonds [49]. Furthermore, tot'hema provides additional mobility of protein chains by increasing their distance, influencing a significant decrease of Young's modulus of elasticity, from 1933 MPa for pure gelatin (TG_0) to 948 MPa for the 5% tot'hema concentration (TG_5). As the tot'hema content increases further, Young's modulus value decreases even more (see Table 1). As demonstrated, the TG_30 film has Young's modulus of 0.32 MPa (which is very close to 0.35 MPa for PDMS), making it suitable for contact copying. Elastic properties of TG_X films are very important for the production of adaptive micro-optical components.

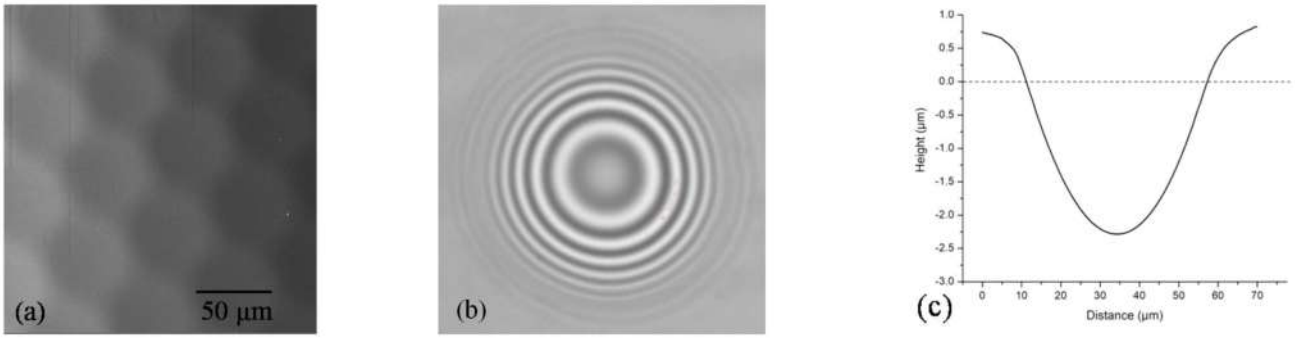

Figure 2. (**a**) SEM image of hexagonal microlenses array; (**b**) Interference fringe pattern of a microlens; and (**c**) 2D surface profile of a microlens.

Table 1. The film thickness, stress at break, strain at break and Young's modulus.

Film	Tot'hema (%)	Thickness (µm)	Stress at Break (MPa)	Strain at Break (%)	Young's Modulus (MPa)
TG_0	0	25 ± 10	58 ± 1	2 ± 0.1	1933 ± 40
TG_5	5	35 ± 10	37.92 ± 0.76	4 ± 0.2	948 ± 10
TG_10	10	50 ± 10	4.89 ± 0.10	40 ± 2	12.23 ± 0.06
TG_20	20	100 ± 10	1.71 ± 0.03	140 ± 6	1.22 ± 0.02
TG_30	30	200 ± 10	0.72 ± 0.01	224 ± 10	0.32 ± 0.01

Results are expressed as mean value ± standard deviation.

The change of color and transparency of the films varied from transparent (pure gelatin) and slightly yellow to yellow with increasing tot'hema content (see Figure 3).

Figure 3. Colors of TG_X films − (gelatin with 0%, 5%, 10%, 20%, and 30% of tot'hema).

The corresponding spectral light transmittance of the TG_X films as a function of wavelength is presented in Figure 4. Light transmission (in the visible range of 350–800 nm) of the pure gelatin (TG_0) film was above 80%, and the transmission increased with increasing wavelength (see Figure 4). By adding tot'hema, a layer is transformed into a spectral filter whose characteristics strongly depend on the concentration. In all cases, UV

radiation is strongly suppressed, making tot'hema-gelatin films an excellent filter for UV-sensitive applications. As we see, pure gelatin film transmits light very well at wavelengths from 350 nm to about 800 nm, but this can be changed at will using appropriate colorants.

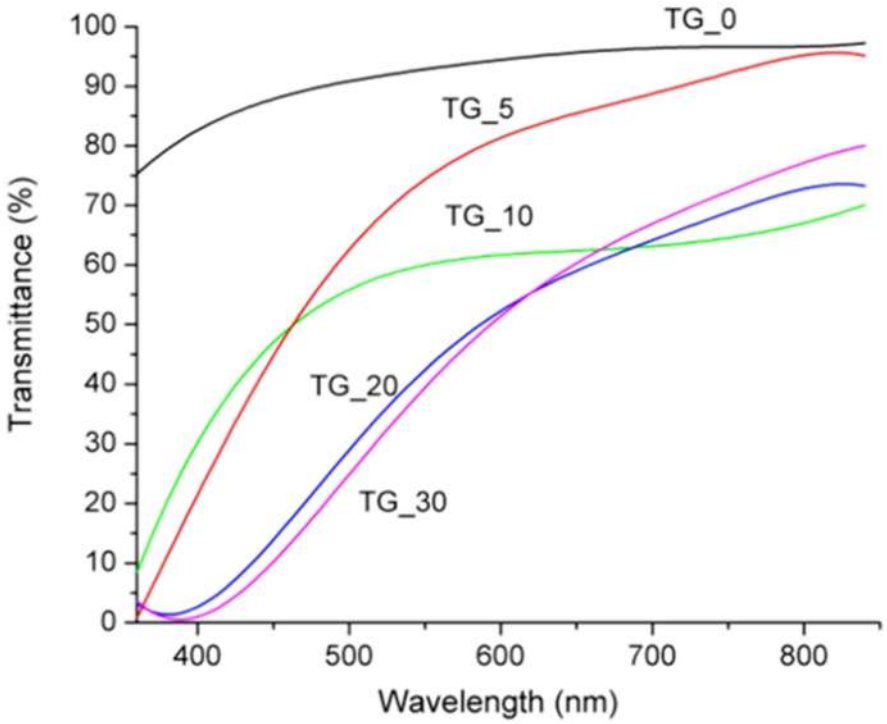

Figure 4. Spectral transmittance of the TG_X films (X− 0, 5, 10, 20, and 30% of tot'hema).

It was noticed that, after the initial rapid decrease of water content for all TG_X films during the drying process (see Figure 5a), the water content remains constant after 24 h of drying. After that, all the other properties remain stable, and the film is ready for further use (e.g., direct laser writing). Pure gelatin film had the lowest water content that exponentially increased with tot'hema content (see Figure 5b). This behavior is consistent irrespective of film thickness. The increase in water content in the presence of a tot'hema can be attributed to the additional hydrogen bonds formed between water molecules and gelatin chains. Water content can influence the physical properties of films (low-humidity films are generally stiff, while films with increased humidity are flexible and malleable). However, relatively high water content does not necessarily mean better physical properties in films [50] but makes the material suitable for a range of applications in biomedicine.

The influence of tot'hema concentration on the swelling of TG_X films during 1 h, 4 h and 24 h are shown in Figure 6. The longer the film is immersed in the saline solution, the higher swelling (without deterioration) was observed (after 24 h, the film is fully saturated). Water content and swelling factor of the films were correlated. Opposite to the water content, the film swelling (see Figure 6) decreases with increasing concentration of tot'hema: pure gelatin film has the highest swelling factors (around 220%), while the tot'hema addition reduces the film swelling. This might be due to the limited spaces in film (gelatin network) for absorbing water as already occupied by tot'hema (plasticizer) molecules. The lowest swelling factor for TG_30 is correlated with the largest water amount in the film. Namely, in contact with the film, water diffuses into it, which results in the movement of polymer chains, incorporating between them and the dissolving of added ingredients. In this way, swelling enhances the release effect of some ingredients added to the film, which later diffuse into the system, manifesting different roles (for example, protective) [51].

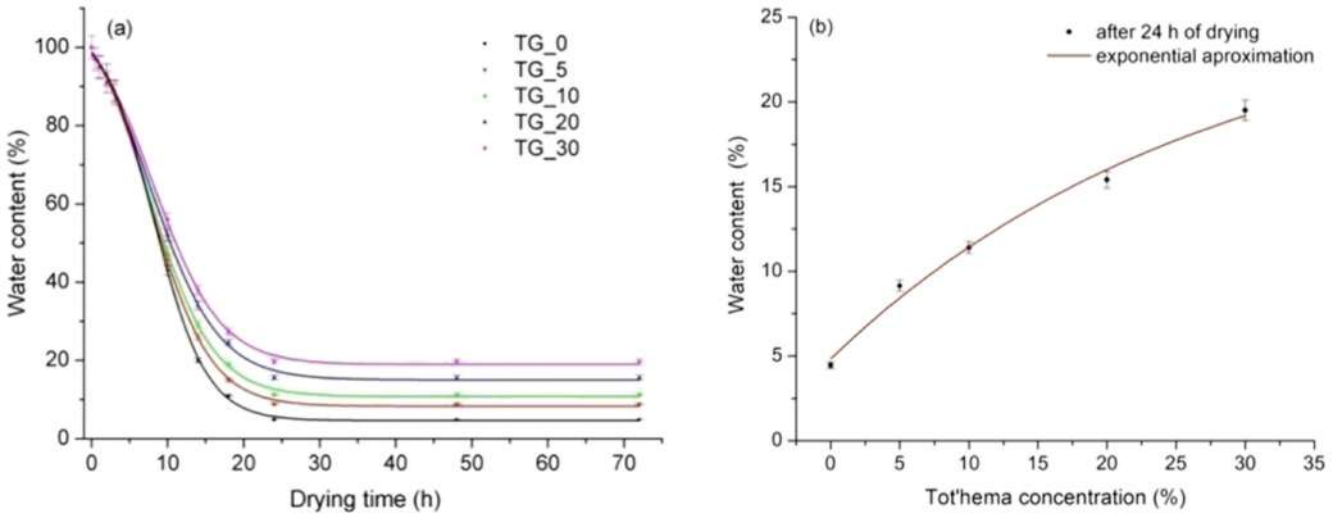

Figure 5. (**a**) Influence of drying time on the water content of TG_X films (X − 0, 5, 10, 20, and 30% of tot'hema); (**b**) The equilibrium water content as a function of tot'hema concentration.

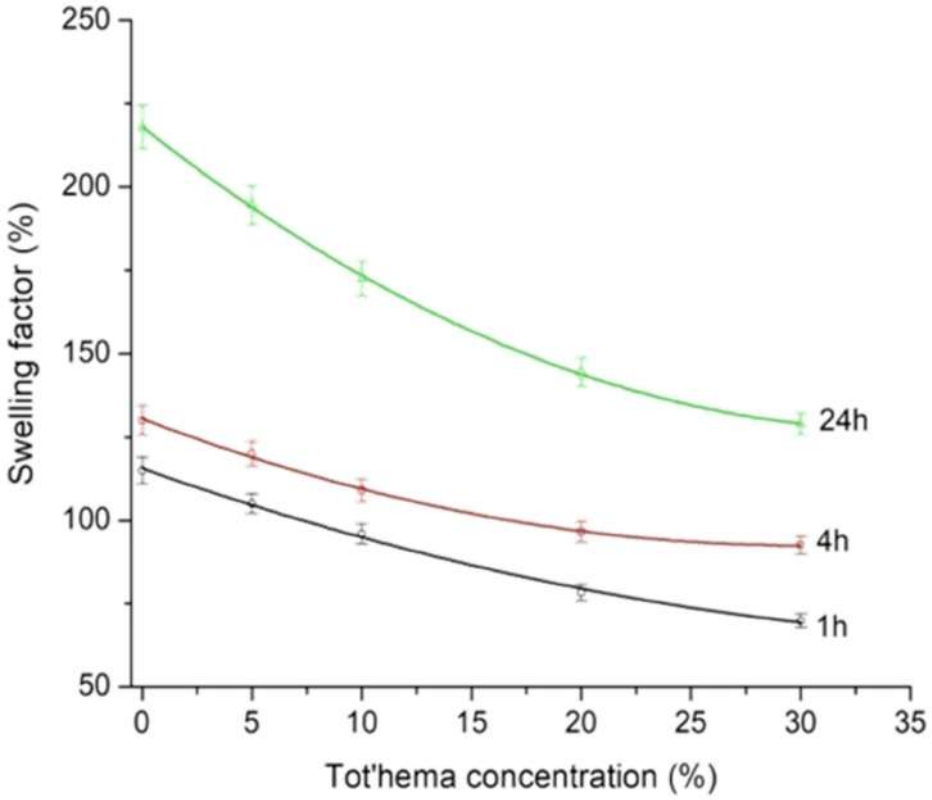

Figure 6. TG_X film (X− 0, 5, 10, 20, and 30% of tot'hema) swelling (during 1, 4 and 24 h) as a function of tot'hema concentration.

FTIR analysis was performed to study the interactions between tot'hema and gelatin matrix, i.e., to illustrate possible conformational changes in the gelatin films containing tot'hema. FTIR spectra of TG_X films are presented in Figure 7. A wide band in the range of 3500–3000 cm^{-1} can be attributed to O–H stretching and N–H bending, which are able to form a hydrogen bond with the carbonyl group of the peptide bond in the gelatin, as suggested by a literature review [52,53].

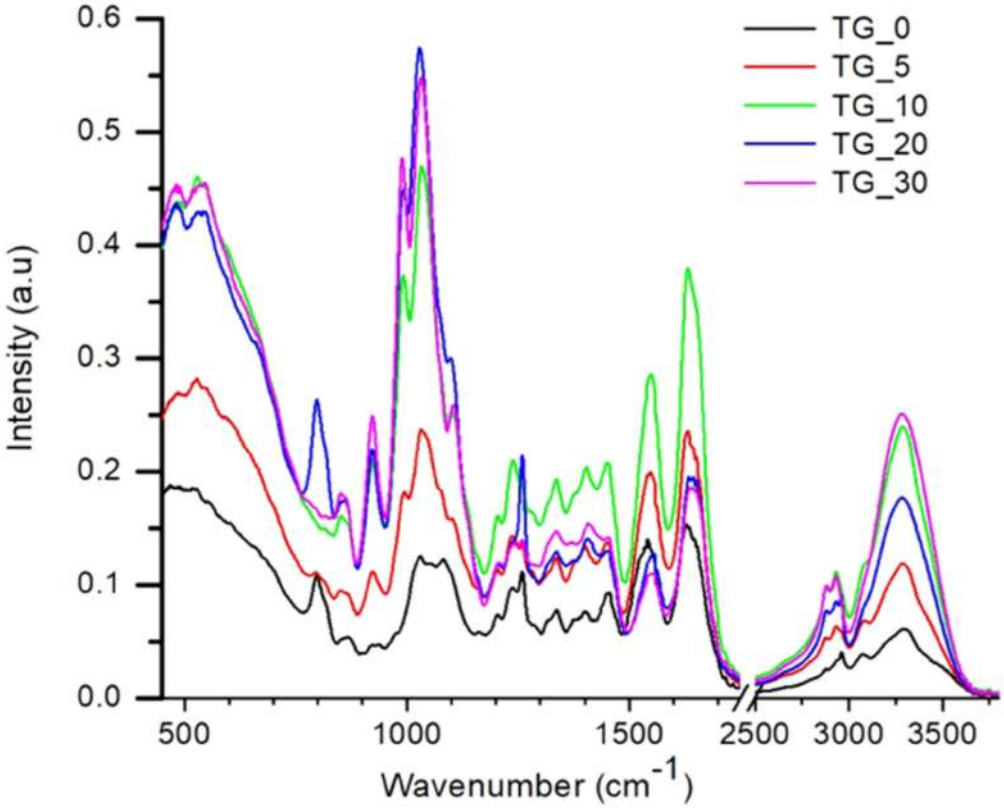

Figure 7. FTIR spectra of TG_X films (X− 0, 5, 10, 20, and 30% of tot'hema).

The FTIR spectrum of the pure gelatin film contains characteristic peaks at 3297 cm^{-1} and 2963 cm^{-1}, which can be attributed to –OH and –CH vibration stretching peaks. Further, it showed the characteristic amide I, amide II and amide III bands [54]. It is observed that the main absorption of the gelatin film such as C=O stretching at 1629 cm^{-1} (Amide I), N–H bending at 1542 cm^{-1} (Amide II), C–H deformation at 1403 cm^{-1}, and C–N stretching (Amide III) at 1237 cm^{-1} remains present in all films.

Compared to pure gelatin film, it was noticed that there are no new peaks in the spectrum of TG_X films. At the same time, the addition of tot'hema caused noticeable changes in the intensity of the Amide I, Amide II, and Amide III band. The peaks characteristic of C–H stretching of CH_2 and CH_3 at 2963 cm^{-1} and 2876 cm^{-1} in TG_X films vary significantly in intensity relative to the TG_0. Further, there is a slight shift in the peak's position, which can be explained by the formation of hydrogen bonds. The shift of these bands to a lower wavelength can be explained by the crosslinking between the components of TG_X films. These data indicate that the polar groups of tot'hema solution interact with the amino acids of the protein chains via inter-and intra-molecular hydrogen bonding and hydrophobic interaction. Therefore, tot'hema adding does not change the chemical composition of gelatin, but it changes the structure of gelatin due to intermolecular hydrogen bonding.

DSC is used to establish thermal stability due to changes in the physical and chemical properties of a material as a function of temperature or time [55]. It is well known that heat can cause structural transitions in protein networks that break chemical bonds [56]. The thermal properties of the film are closely related to their applications. The DSC thermograms of the TG_X films up to a temperature of 250 °C are shown in Figure 8.

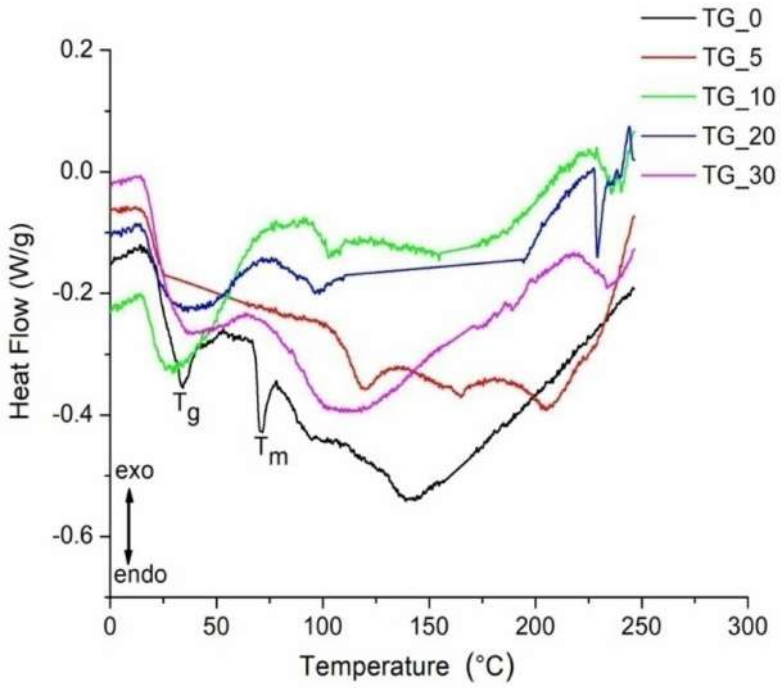

Figure 8. DSC curves of the TG_X films (X− 0, 5, 10, 20, and 30% of tot'hema). Tg and Tm − Endothermic peaks (denoted for pure gelatin film −TG_0) represent glass transition and melting temperature, respectively.

The first endothermic peak of pure gelatin film (TG_0) is recorded at a temperature of about 40 °C (see Figure 8). This endothermic peak represents glass transition (T_g) and is attributed to the transition from the glassy state to rubber. The endothermic peak that follows T_g, at a temperature around $T_m \approx 70$ °C is attributed to the melting and dissociation of arranged polymer parts. Some authors attribute this peak to the overlap of various processes such as the water evaporation, melting and recrystallization of small and/or imperfect gelatin crystals [57,58].

It was found that the peak temperatures and the enthalpies of these endothermic processes depend on the film preparation and drying conditions [57]. The endothermic peak at about 160 °C represents the gelatin decomposition temperature. It was observed that by adding and increasing the tot'hema content, the endothermic peaks become significantly wider and larger than that of the pure gelatin film. In addition, DSC analysis demonstrated that tot'hema addition, depending on its content, improves gelatin thermal stability. The melting temperature (T_m) increased when compared to pure gelatin film for all concentrations of tot'hema. T_m is typically associated with thermal stability: a high value of T_m corresponds to high thermal stability. It is already established that the thermal stability of polymers is related to crosslinking density [59]. In Figure 8, it is noticed that pure gelatin film (TG_0) has the lowest melting temperature (T_m). This temperature increases after crosslinking gelatin by tot'hema. The highest value of T_m was obtained for TG_5 film, while the T_m for films prepared with 10–30% of tot'hema show lower values. This behavior is attributed to the hydrophobicity of the gelatin molecular structure resulting from the addition of a large quantity of tot'hema. The improved thermal stability of TG_X films indicates that the temperature range of the use has been extended to about 100 °C, which is very important for practical applications.

To summarize—tot'hema is added to gelatin in order to increase the light absorption, modify its melting temperature and make it permanently elastomeric. Tot'hema concentration was optimized in order to make a compromise between gelatin thermal (e.g., melting temperature), mechanical (flatness) and optical (transparency) properties.

4. Discussion

The gelatin-based material described above has a number of useful optical, thermal and mechanical properties, which can be modulated by slight variations of its chemical composition. In this way, it becomes suitable for a range of applications, primarily dealing with micro-mechanics, microfluidics and micro-optics.

The most important property is photoresponsiveness. The photoresponsive gelatin studied here belongs to the class of waste and natural biopolymers (such as alginates and eggshells already reported for the electronics industry [35,36]), which is very important for developing non-toxic, eco-friendly materials. In contrast to the classical photosensitive materials (for example, silver-halide films, photoresists, dichromated gelatin), the response of tot'hema modified material is a consequence of physical, rather than chemical, processes. Here, absorbed light locally heats the material above the melting point, and surface tension pushes the fluidized layer, thus producing a dip (concave, lens-shaped recess), as can be seen in Figure 2. After the light is turned off, rapid cooling "freezes" the surface shape. Due to the low melting point of the gel (approximately 50 °C), the effect is easily achieved by a few milliwatt laser beams and millisecond irradiation times. Depending on the focal point size, micron-sized structures are easily formed. It is important to note that there is no material ablation because the melting point is much higher, and the material is simply displaced [60].

This makes the material extremely useful for rapid fabrication of micron-sized features using direct laser writing (DLW)—see Video S1 in a Supplementary Material of this paper demonstrating manufacturing of a complex array of microlenses. By controllably guiding the laser beam across the surface, virtually any shape can be formed (see Figure 9), where a rather complex microchannel structure (with three Tesla valves) is shown [61,62]. The whole pattern was fabricated in less than a minute using a 488 nm laser with 10 mW power (focused by 0.4 NA microscope objective).

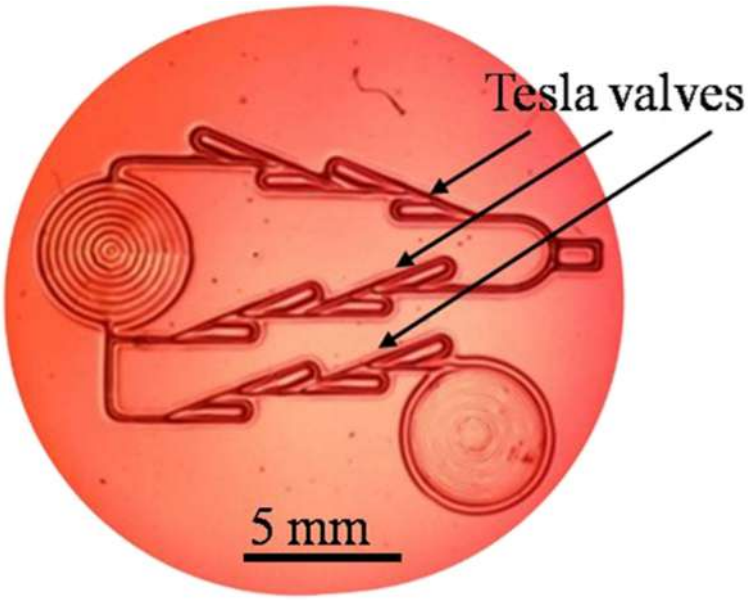

Figure 9. Complex microfluidic channels, with three Tesla valves formed on a tot'hema-gelatin.

Physicochemical processes during interaction with light depend strongly on the laser beam power and focus. The sensitivity threshold is reached at approximately 7.5 nJ/μm^2 of laser energy, which is easily achieved by focusing the laser beam through the long-working–distance microscope objective (Mitutoyo 20×, 0.4 NA). By appropriately controlling the laser beam size and power, irradiation time and writing speed, features can be fabricated with characteristic widths between 10 μm and 1000 μm and depths up to several hundred micrometers. By using high-power lasers, fabrication time can be significantly reduced

to milliseconds for the fabrication of individual microlenses or seconds for more complex structures like the one in Figure 9. Of course, the scanning speed of the laser beam must be increased to prevent material destruction. In most cases, there is no postprocessing, so the optical structures are usable immediately after fabrication.

We have mostly studied optical applications of the material [37,38], which simultaneously offers several key features—optical homogeneity, transparency, surface quality, easy fabrication and environmental friendliness. We have found that tot'hema ingredients mostly determine the material properties. As shown above, spectral absorption and melting point enable tailoring of the material to efficiently absorb the DLW beam.

The concept of microfabrication using meltable gels can be easily extended by replacing tot'hema with a suitable combination of plasticizers, humectants, preservatives and sensitizing dyes (e.g., betanin, eosin, anthocyanin, etc.) to achieve improved characteristics (faster melting, improved sensitivity, optical transparency after laser processing), which we described elsewhere [37]. In this way, we were able to fabricate a range of optical components, such as diffraction gratings and arrays of positive and negative microlenses.

Gelatin-based materials are biocompatible, and additional chemicals used in this research are non-toxic (even food grade), giving the advantage of quick and natural biodegradability. We have covered a piece of the material with a few centimeters of soil and found that it was completely absorbed, without a trace, within a few days. For some applications, this might be a problem as we observed fungi growing on the material after some time (several days). To prevent that, we added table salt (NaCl), which made it durable and usable over a long period of exposure time to normal room conditions. Normal laboratory conditions (humidity, temperature) do not affect the material properties, and laboratory illumination does not diminish the material sensitivity (i.e., the material does not have to be kept in darkness). Dust is the major problem because of the stickiness of the film, and the material surface must be protected by an additional cover glass.

Softness is yet another possible disadvantage. Surfaces should not be scratched or punched with hard objects as this will certainly damage the structure. On the positive side, films can be easily cut, peeled from the substrate, stacked together and transferred. Mechanical hardness can be further significantly increased by removing the plasticizer (by submerging the films in cold water and letting the plasticizer diffuse out) or by hardening (tanning) with, e.g., alum [63]. In addition, we have been able to use tot'hema-gelatin as a template for contact copying into harder materials (epoxies, photopolymer composites).

The usable temperature range is limited by the melting point to somewhere between 50 °C and 100 °C, depending on tot'hema concentration. For the majority of applications, this is quite satisfactory and makes the material usable in the widest range of applications: lab on a chip, sensors and micro-optics. We have also found that above the critical power density of the laser beam, material locally carbonizes and can be used as a blocking filter [39] and, possibly, as an electrical conductor.

Finally, the fabrication cost is really low. Materials used here are cheap and ubiquitous. Most of them can be found in the kitchen, while the fabrication of layers is straightforward and simple. Production methods are well known in the film industry and can be used both in low- and large-scale production.

5. Conclusions

To conclude, here we disclosed an innovative combination of well-known substances producing really versatile material for safe, real-time, low-cost, rapid microfabrication. Physicochemical properties of the material have been thoroughly studied, aiming to establish operational limits and optimize properties for the desired application. Application potential is high due to the simplicity of fabrication of highly complex structures, good optical properties, and manufacturability by direct laser writing without any further postprocessing, micrometers resolution, elastomeric characteristics, environmental friendliness, and non-toxic character—a rare combination of properties concentrated in a single material. Elasticity, uniform and homogeneous surface and optical transparency were achieved,

making the material suitable for the production of adaptive micro-optical components and protective filters. The temperature range of the material's applicability is extended up to 100 °C.

Supplementary Materials: The following supporting information can be downloaded at: https://www.mdpi.com/article/10.3390/polym14122350/s1, Video S1: Microoptics fabrication.

Author Contributions: B.D.M.: Conceptualization, methodology, investigation, visualization, writing original draft, reviewing, editing, resources, project administration; D.V.P.: Software, supervision, writing, editing, reviewing; M.D.R.: Software, data curation, reviewing; S.N.S.-Š.: Investigation, editing, reviewing; V.O.V.: Editing, project administration. All authors have read and agreed to the published version of the manuscript.

Funding: The authors acknowledge funding provided by the Institute of Physics University of Belgrade through the grant by the Ministry of Education, Science and Technological Development of the Republic of Serbia.

Data Availability Statement: Not applicable.

Acknowledgments: We thank Smilja B. Marković from the Institute of Technical Sciences of the Serbian Academy of Sciences and Arts, Belgrade, Serbia for help with FTIR and DSC measurements.

Conflicts of Interest: The authors declare no conflict of interest.

References

1. Chaudhary, V.; Bangar, S.P.; Thakur, N.; Trif, M. Recent advancements in smart biogenic packaging: Reshaping the future of the food packaging industry. *Polymers* **2022**, *14*, 829. [CrossRef] [PubMed]
2. Tokiwa, Y.; Calabia, B.P.; Ugwu, C.U.; Aiba, S. Biodegradability of plastics. *Int. J. Mol. Sci.* **2009**, *10*, 3722–3742. [CrossRef] [PubMed]
3. Vroman, I.; Tighzer, L. Biodegradable polymers. *Materials* **2009**, *2*, 307–344. [CrossRef]
4. Shamsuddin, I.M.; Jafar, J.A.; Shawai, A.S.A.; Yusuf, S.; Lateefah, M.; Aminu, I. Bioplastics as better alternative to petroplastics and their role in national sustainability: A review. *Adv. Biosci. Bioeng.* **2017**, *5*, 63–70. [CrossRef]
5. Rosenboom, J.G.; Langer, R.; Traverso, G. Bioplastics for a circular economy. *Nat. Rev. Mater.* **2022**, *7*, 117–137. [CrossRef] [PubMed]
6. Hassan, M.M.; Le Guen, M.J.; Tucker, N.; Parker, K. Thermo-mechanical, morphological and water absorption properties of thermoplastic starch/cellulose composite foams reinforced with PLA. *Cellulose* **2019**, *26*, 4463–4478. [CrossRef]
7. Souza, C.R.; Andrade, C.T. Processing and properties of thermoplastic starch and its blends with sodium alginate. *J. Appl. Polym. Sci.* **2001**, *81*, 412–420. [CrossRef]
8. Abe, M.M.; Martins, J.R.; Sanvezzo, P.B.; Macedo, J.V.; Branciforti, M.C.; Halley, P.; Botaro, V.R.; Brienzo, M. Advantages and disadvantages of bioplastics production from starch and lignocellulosic components. *Polymers* **2021**, *13*, 2484. [CrossRef]
9. Rivadeneira-Velasco, K.E.; Utreras-Silva, C.A.; Díaz-Barrios, A.; Sommer-Márquez, A.E.; Tafur, J.P.; Michell, R.M. Green nanocomposites based on thermoplastic starch: A review. *Polymers* **2021**, *13*, 3227. [CrossRef]
10. Onyeaka, H.; Obileke, K.; Makaka, G.; Nwokolo, N. Current research and applications of starch based biodegradable films for food packaging. *Polymers* **2022**, *14*, 1126. [CrossRef]
11. Jiang, T.; Duan, Q.; Zhu, J.; Liu, H.; Yu, L. Starch-based biodegradable materials: Challenges and opportunities. *Adv. Ind. Eng. Polym. Res.* **2020**, *3*, 8–18. [CrossRef]
12. Estrada-Monje, A.; Alonso-Romero, S.; Zitzumbo-Guzmán, R.; Estrada-Moreno, I.A.; Zaragoza-Contreras, E.A. Thermoplastic starch-based blends with improved thermal and thermomechanical properties. *Polymers* **2021**, *13*, 4263. [CrossRef] [PubMed]
13. Chauhan, S.; Bansal, M.; Khan, G.; Yadav, S.K.; Singh, A.K.; Prakash, P.; Mishra, B. Development, optimization and evaluation of curcumin loaded biodegradable crosslinked gelatin film for the effective treatment of periodontitis. *Drug Dev. Ind. Pharm.* **2018**, *44*, 1212–1221. [CrossRef] [PubMed]
14. Yang, J.; Sun, X.; Kang, Q.; Zhu, L.; Qin, G.; Chen, Q. Freezing-tolerant and robust gelatin-based supramolecular conductive hydrogels with double-network structure for wearable sensors. *Polym. Test.* **2021**, *93*, 106879. [CrossRef]
15. Liu, J.; Li, Y.; Hu, D.; Chao, X.; Zhou, Y.; Wang, J. An essential role of gelatin in the formation process of curling in long historical photos. *Polymers* **2021**, *13*, 3894. [CrossRef]
16. Lu, Y.; Luo, Q.; Chu, Y.; Tao, N.; Deng, S.; Wang, L.; Li, L. Application of gelatin in food packaging: A review. *Polymers* **2022**, *14*, 436. [CrossRef]
17. Maiti, S.; Khillar, P.S.; Mishra, D.; Nambiraj, N.A.; Jaiswal, A.K. Physical and self–crosslinking mechanism and characterization of chitosan-gelatin-oxidized guar gum hydrogel. *Polym. Test.* **2021**, *97*, 107155. [CrossRef]
18. Farris, S.; Song, J.; Huang, Q. Alternative reaction mechanism for the cross-linking of gelatin with glutaraldehyde. *J. Agric. Food Chem.* **2010**, *58*, 998–1003. [CrossRef]

19. Bigi, A.; Cojazzi, G.; Panzavolta, S.; Roveri, N.; Rubini, K. Stabilization of gelatin films by crosslinking with genipin. *Biomaterials* **2002**, *23*, 4827–4832. [CrossRef]
20. Zhao, Y.; Sun, Z. Effects of gelatin-polyphenol and gelatin–genipin cross-linking on the structure of gelatin hydrogels. *Int. J. Food Prop.* **2017**, *20*, S2822–S2832. [CrossRef]
21. Savić, S.; Pantelić, D.; Jakovijević, D. Real-time and postprocessing holographic effects in dichromated pullulan. *Appl. Opt.* **2002**, *41*, 4484–4488. [CrossRef] [PubMed]
22. Haniffa, M.A.C.M.; Ching. Y., C.; Abdullah, L.C.; Poh, S.C.; Chuah, C.H. Review of Bionanocomposite Coating Films andTheir Applications. *Polymers* **2016**, *8*, 246. [CrossRef] [PubMed]
23. Salahuddin, B.; Wang, S.; Sangian, D.; Aziz, S.; Gu, Q. Hybrid gelatin hydrogels in nanomedicine applications. *ACS Appl. Bio Mater.* **2021**, *4*, 2886–2906. [CrossRef] [PubMed]
24. Rakhshaei, R.; Namazi, H.; Hamishehkar, H.; Kafil, H.S.; Salehi, R. In situ synthesized chitosan−gelatin/ZnO nanocomposite scaffold with drug delivery properties: Higher antibacterial and lower cytotoxicity effects. *J. Appl. Polym. Sci.* **2019**, *136*, 47590. [CrossRef]
25. Afnas, V.M.; Unnikrishnan, G.; Budhe, S.; Manaf, O.; Ameen, J. PVA/gelatin/chitin ternary blend as a humidity sensing material. *J. Mater. Sci. Mater. Electron.* **2022**, *33*, 2031–2043. [CrossRef]
26. Nawroth, J.C.; Scudder, L.L.; Halvorson, R.T.; Tresback, J.; Ferrier, J.P.; Sheehy, S.P.; Cho, A.; Kannan, S.; Sunyovszki, I.; Goss, J.A.; et al. Automated fabrication of photopatterned gelatin hydrogels for organ-on-chips applications. *Biofabrication* **2018**, *10*, 25004. [CrossRef] [PubMed]
27. Liu, J.; Su, C.; Chen, Y.; Tian, S.; Lu, C.; Huang, W.; Lv, Q. Current understanding of the Applications of photocrosslinked hydrogels in biomedical engineering. *Gels* **2022**, *8*, 216. [CrossRef]
28. Pinto-Iguanero, B.; Olivares-Perez, A.; Mendez-Alvarado, A.W.; Fuentes-Tapia, I.; Trevino-Palacios, C.G. Non-hydroscopic vanilla doped dichromated gelatin holographic material. *Opt. Mater.* **2003**, *22*, 397–404. [CrossRef]
29. Pantelić, D.; Murić, B. Improving the holographic sensitivity of dichromated gelatin in the blue–green part of the spectrum by sensitization with xanthene dyes. *Appl. Opt.* **2001**, *40*, 2871–2875. [CrossRef]
30. Yao, J.; Cui, Z.; Gao, F.; Zhang, Y.; Guo, Y.; Du, C.; Zeng, H.; Qiu, C. Refractive micro lens array made of dichromate gelatin with gray-tone photolithography. *Microelect. Eng.* **2001**, *57–58*, 729–735. [CrossRef]
31. Calixto, S.; Scholl, M.S. Relief optical microelements fabricated with dichromated gelatin. *Appl. Opt.* **1997**, *36*, 2101–2106. [CrossRef] [PubMed]
32. Pan, A.; Gao, B.; Chen, T.; Si, J.; Li, C.; Chen, F.; Hou, X. Fabrication of concave spherical microlenses on silicon by femtosecond laser irradiation and mixed acid etching. *Opt. Express* **2014**, *22*, 15245–15250. [CrossRef] [PubMed]
33. Marcinkevičius, A.; Juodkazis, S.; Watanabe, M.; Miwa, M.; Matsuo, S.; Misawa, H.; Nishii, J. Femtosecond laser-assisted three-dimensional microfabrication in silica. *Opt. Lett.* **2001**, *26*, 277–279. [CrossRef] [PubMed]
34. Calixto, S.; Ganzherli, N.; Gulyaev, S.; Figueroa-Gerstenmaier, S. Gelatin as a photosensitive material. *Molecules* **2018**, *23*, 2064. [CrossRef]
35. Minakshi, M.; Higley, S.; Baur, C.; Mitchell, D.R.G.; Jonesd, R.T.; Fichtner, M. Calcined chicken eggshell electrode for battery and supercapacitor applications. *RSC Adv.* **2019**, *9*, 26981–26995. [CrossRef]
36. Wickramaarachchi, K.; Minakshi Sundaram, M.; Henry, D.J.; Gao, X. Alginate Biopolymer Effect on the Electrodeposition of Manganese Dioxide on Electrodes for Supercapacitors. *ACS Appl. Energy Mater.* **2021**, *4*, 7040–7051. [CrossRef]
37. Murić, B.D.; Pantelić, D.V.; Vasiljević, D.M.; Panić, B.M. Properties of microlenses produced on a layer of tot'hema and eosin sensitized gelatin. *Appl. Opt.* **2007**, *46*, 8527–8532. [CrossRef]
38. Murić, B.; Pantelić, D.; Vasiljević, D.; Panić, B. Microlens fabrication on tot'hema sensitized gelatin. *Opt. Mater.* **2008**, *30*, 1217–1220. [CrossRef]
39. Murić, B.D.; Pantelić, D.V.; Vasiljević, D.M.; Savić-Šević, S.N.; Jelenković, B.M. Application of tot'hema eosin sensitized gelatin as a potential eye protection filter against direct laser radiation. *Curr. Appl. Phys.* **2016**, *16*, 57–62. [CrossRef]
40. Murić, B.; Pantelić, D.; Vasiljević, D.; Zarkov, B.; Jelenković, B.; Pantović, S.; Rosić, M. Sensitized gelatin as a versatile biomaterial with tunable mechanical and optical properties. *Phys. Scr.* **2013**, *T157*, 14018. [CrossRef]
41. Krmpot, A.J.; Tserevelakis, G.J.; Murić, B.D.; Filippidis, G.; Pantelić, D.V. 3D imaging and characterization of microlenses and microlens arrays using nonlinear microscopy. *J. Phys. D Appl. Phys.* **2013**, *46*, 195101. [CrossRef]
42. Wu, Z.-L.; Qi, Y.-N.; Yin, X.-J.; Yang, X.; Chen, C.-M.; Yu, J.-Y.; Yu, J.-C.; Lin, Y.-M.; Hui, F.; Liu, P.-L.; et al. Polymer-Based Device Fabrication and Applications Using Direct Laser Writing Technology. *Polymers* **2019**, *11*, 553. [CrossRef] [PubMed]
43. Available online: www.vidal.fr/medicaments/tot-hema-sol-buv-en-ampoule-16626.html (accessed on 10 February 2022).
44. Keinonen, T.; Riihola, P.; Huttu, K.; Parkkonen, S. Dye films for optical demonstrations in the undergraduate laboratory. *Opt. Mater.* **1998**, *11*, 79–86. [CrossRef]
45. *ISO 527–3:2018*; Plastics—Determination of Tensile Properties—Part 3: Test Conditions for Films and Sheets. ISO: Geneva, Switzerland, 2018. Available online: https://www.iso.org/standard/70307.html (accessed on 12 March 2022).
46. Radmilović, M.D.; Murić, B.D.; Grujić, D.; Zarkov, B.; Nenadić, M.Z.; Pantelić, D.V. Rapid direct laser writing of microoptical components on a meltable biocompatible gel. *Opt. Quantum Electron.* **2022**, *54*, 361. [CrossRef]
47. Tabatabaei, S.D.; Ghiasi, F.; Gahruie, H.H.; Hosseini, S.M.H. Effect of emulsified oil droplets and glycerol content on the physicochemical properties of Persian gum-based edible films. *Polym. Test.* **2022**, *106*, 107427. [CrossRef]

48. Gahruie, H.H.; Eskandari, M.H.; Meeren, P.V.; Osseini, S.M.H. Study on hydrophobic modification of basil seed gum-based (BSG) films by octenyl succinate anhydride. *Carbohydr.Polym.* **2019**, *219*, 155–161. [CrossRef]
49. Rivero, S.; García, M.A.; Pinotti, A. Correlations between structural, barrier, thermal and mechanical properties of plasticized gelatin films. *Innov. Food Sci. Emerg. Technol.* **2010**, *11*, 369–375. [CrossRef]
50. Blanco-Pascual, N.; Fernández-Martín, F.; Montero, M.P. Effect of different protein extracts from Dosidicus gigas muscle co-products on edible films development. *Food Hydrocoll.* **2013**, *33*, 118–131. [CrossRef]
51. Siepmann, J.; Streubel, A.; Peppas, N.A. Understanding and predicting drug delivery from hydrophilic matrix tablets using the "Sequential layer" model. *Pharm. Res.* **2002**, *19*, 306–314. [CrossRef]
52. Queiroz, M.F.; Rachel, K.; Melo, T.; Sabry, D.A.; Sassaki, G.L.; Alexandre, H.; Rocha, O. Does the use of chitosan contribute to oxalate kidney stone formation. *Mar. Drugs* **2014**, *13*, 141–158. [CrossRef]
53. Farahnaky, A.; Dadfar, S.M.M.; Shahbazi, M. Physical and mechanical properties of gelatin–clay nanocomposite. *J. Food Eng.* **2014**, *122*, 78–83. [CrossRef]
54. Coates, J. Interpretation of infrared spectra, A practical approach. In *Encyclopedia of Analytical Chemistry: Applications, Theory and Instrumentation*; John Wiley & Sons, Ltd.: Hoboken, NJ, USA, 2006; pp. 1–23. [CrossRef]
55. Lin, S.-Y.; Wang, S.-L. Advances in simultaneous DSC–FTIR microspectroscopy for rapid solid-state chemicalstability studies: Some dipeptide drugs as examples. *Adv. Drug Deliv. Rev.* **2012**, *64*, 461–478. [CrossRef] [PubMed]
56. Liu, F.; Majeed, H.; Antoniou, J.; Li, Y.; Ma, Y.; Yokoyama, W.; Zhong, F. Tailoring physical properties of transglutaminase-modified gelatin films by varying drying temperature. *Food Hydrocoll.* **2016**, *58*, 20–28. [CrossRef]
57. Dai, C.A.; Chen, Y.-F.; Liu, M.-W. Thermal properties measurements of renaturated gelatin using conventional and temperature modulated differential scanning calorimetry. *Appl. Polym. Sci.* **2006**, *99*, 1795–1801. [CrossRef]
58. Mendieta-Taboada, O.; Sobral, P.J.A.; Carvalho, R.A.; Habitante, A.M.B.Q. Thermomechanical properties of biodegradable films based on blends of gelatin and poly(vinyl alcohol). *Food Hydrocoll.* **2008**, *22*, 1485–1492. [CrossRef]
59. Skopinska-Wisniewska, J.; Tuszynska, M.; Olewnik-Kruszkowska, E. Comparative Study of Gelatin Hydrogels Modified by Various Cross-Linking Agents. *Materials* **2021**, *14*, 396. [CrossRef]
60. Murić, B.; Pantelić, D.; Vasiljević, D.; Panić, B.; Jelenković, B. Thermal analysis of microlens formation on a sensitized gelatin layer. *Appl. Opt.* **2009**, *48*, 3854–3859. [CrossRef]
61. Hong, C.-C.; Choi, J.-W.; Ahn, C.H. A novel in-plane microfluidic mixer with modified Tesla structures. *Lab Chip* **2004**, *4*, 109–113. [CrossRef]
62. Tesla, N. Valvular Conduit. U.S. Patent 1329559, 3 February 1920. Available online: https://www.freepatentsonline.com/1329559.html (accessed on 12 March 2022).
63. Murić, B.D.; Panić, B.M. Microlenses with focal length controlled by chemical processes. *Phys. Scr.* **2012**, *T 149*, 14071. [CrossRef]

Physica Scripta

INCLUSIVE PUBLISHING TRUSTED SCIENCE

PURPOSE-LED PUBLISHING™

PAPER

Time resolved study of temperature sensing using Gd_2O_3:Er,Yb: deep learning approach

To cite this article: Maja S Rabasovic *et al* 2023 *Phys. Scr.* **98** 116003

View the article online for updates and enhancements.

You may also like

- Passively Q-switched Er,Yb:$GdAl_3(BO_3)_4$ laser with single-walled carbon nanotube based saturable absorber
K N Gorbachenya, V E Kisel, A S Yasukevich et al.
- Surface modification of Y_2O_3:Er,Yb upconversion nanoparticles prepared by laser ablation in water
Hikaru Kobayashi, Kunio Fujii, Takashi Nunokawa et al.
- Exploration of the crystal structures and electronic features of Y_2O_3:Er and Y_2O_3:Er,Yb crystals: a first-principles study
Meng Ju, Xiexuan Zhang, Shihao Hu et al.

This content was downloaded from IP address 147.91.1.43 on 26/11/2025 at 18:21

Physica Scripta

PAPER

Time resolved study of temperature sensing using Gd_2O_3:Er,Yb: deep learning approach

RECEIVED
4 May 2023

REVISED
12 July 2023

ACCEPTED FOR PUBLICATION
10 October 2023

PUBLISHED
19 October 2023

Maja S Rabasovic[1], Svetlana Savic-Sevic[1], Janez Križan[2], Branko Matovic[3], Marko Nikolic[1] and Dragutin Sevic[1,*]

[1] Institute of Physics Belgrade, University of Belgrade, Serbia
[2] AMI d.o.o., Ptuj, Slovenia
[3] 'Vinca' Institute of Nuclear science, University of Belgrade, Serbia
[*] Author to whom any correspondence should be addressed.

E-mail: sevic@ipb.ac.rs

Keywords: machine learning, laser induced luminescence, remote temperature measurements, thermophosphors

Abstract

This paper examines the potential applications of machine learning algorithms in the analysis of optical spectra from Gd_2O_3:Er,Yb thermophosphor. The material was synthesized using the solution combustion method. For data acquisition, we employed pulsed laser diode excitation at 980 nm and utilized a streak camera with a spectrograph to obtain time-resolved spectral data of the optical emission from Gd_2O_3:Er,Yb. To ensure data consistency and facilitate visualization, we employed principal component analysis and Uniform Manifold Approximation and Projection clustering. Our findings demonstrate that, instead of the conventional approach of identifying spectral peaks and calculating intensity ratios, it is feasible to train computer software to recognize time-resolved spectra associated with different temperatures of the thermophosphor. Through our analysis, we have successfully devised a technique for remote temperature estimation by leveraging deep learning artificial neural networks.

1. Introduction

While recent studies on remote temperature sensing primarily focus on the development of novel luminescent probes, the advancements in temperature calculation methods based on acquired spectral data have been comparatively limited. However, there is a noticeable increase in scientific interest, as evidenced by recent publications, in employing machine learning (ML) algorithms for the investigation of various scientific and social data sources [1–4], and references therein. ML techniques have demonstrated significant improvements in the analysis of luminescence, near-infrared, and other spectral data [5–15]. Furthermore, ML methods have shown promise in enhancing the analysis of laser-induced breakdown spectroscopy data [16–21]. Notably, a study [5] has demonstrated the utility of ML learning in achieving spectroscopy calibration invariance. This paper focuses on exploring the potential of ML algorithms for analyzing time-resolved optical spectra of Gd_2O_3:Er,Yb with the aim of enabling remote temperature measurements.

In [11], the authors discuss the utilization of linear (Principal Component Analysis) and non-linear (t-distributed Stochastic Neighbor Embedding) transformations on calibration datasets derived from rare-earth nanoparticles and semiconductor nanocrystals. The results showed that these transformations led to enhanced thermal resolution when compared to conventional intensity-based and ratiometric approaches.

In their work [10], the authors propose an innovative approach to luminescence thermometry through the implementation of a convolutional artificial neural network. Traditionally, luminescence thermometric methods rely on analyzing a single spectral characteristic parameter, selected based on the properties of the thermophosphor and the researcher's intuition or experience. This approach leads to a partial utilization of spectral data, limiting measurement accuracy and thermal resolution. In contrast, the authors of [10] train a deep learning artificial neural network to extract multiple temperature-dependent features for temperature

© 2023 IOP Publishing Ltd
All rights, including for text and data mining, AI training, and similar technologies, are reserved.

estimation, fully utilizing the temperature-dependent spectral data. However, the spectral data in [10] do not include temporal information. In our research, we take a step further by incorporating time-resolved spectra into ML-based temperature estimation using a deep learning artificial neural network. This approach allows us to incorporate the thermophosphor's lifetime dependence into our analysis. Recently, we proposed a multi-mode temperature sensing technique, which considered intensity ratio, thermophosphor lifetime, and rise analysis to achieve improved thermographic results [22]. However, this analysis did not involve ML techniques. It now appears to us that a multi-mode temperature sensing technique without incorporating ML methods may be considered somewhat limited in its capabilities.

Now we will provide a brief overview of conventional methods employed for remote or contactless temperature estimation through luminescence thermometry.

The luminescence intensity ratio technique is employed to determine temperature by measuring the intensities of two emission lines in the luminescence spectra of thermographic phosphors. The temperature calculation relies on the emission intensity ratio between these two lines, offering advantages such as reduced measuring errors, compensation for optical condition deviations, and alleviation of excitation power fluctuations. Typically, for temperature sensing, two closely spaced energy levels of rare earth ions, which exhibit thermal coupling, are chosen. The small energy gap between these levels facilitates the transfer of population from the lower level to the upper level through thermalization. As the temperature rises, the upper level becomes increasingly populated, resulting in a gradual increase in fluorescence from this level. The relative population between the two closely spaced levels, can be described by a Boltzmann-type population distribution [22]:

$$IR = \frac{I_1}{I_0} = C \cdot \exp\left(-\frac{\Delta E}{kT}\right) \tag{1}$$

where k is the Boltzmann constant, $k = 0.695\,034\,76(63)\ \mathrm{cm}^{-1}\,\mathrm{K}^{-1}$, C is a constant and ΔE is the energy gap between two excited levels.

Luminescence measurement instruments often encounter the detection of small signals, even in the absence of actual emissions, due to factors such as detector dark currents. Furthermore, errors in the measured signal intensity can arise from stray light in the spectrograph. To address these issues, an additional constant, denoted as A, needs to be introduced into equation (1) to consider the finite value of IR at low temperatures [22]:

$$IR = A + C \cdot \exp\left(-\frac{\Delta E}{kT}\right) \tag{2}$$

Transitions originating from the same level exhibit identical lifetimes, leading to the common practice of utilizing the luminescent line with the highest intensity for estimating the decay time [22]. Consequently, in order to establish a temperature sensing calibration curve, the most prominent spectral line of the thermophosphor is employed. Notably, the analysis discussed in [22] confirms that the same empirical equation form can be used to fit the experimental data of lifetimes, just as it is employed for fitting the intensity ratio. It is worth noting that certain thermophosphors, like YVO_4:Eu possess a noticeable rise time that can be utilized for thermometry purposes, see [22] and references therein.

The most optimal excitation for upconverting hosts doped with Erbium (Er) and Ytterbium (Yb) occurs at the 980 nm wavelength [23–27].

Upconverting phosphors, such as the one employed in this research offer numerous benefits in the field of biomedical applications, including the potential to monitor brain activity in animals that are able to move freely. [28]. The impact of Mg^{2+} and Li^{+} ion doping on the photoluminescence properties and biological applications of Gd_2O_3:Er,Yb was investigated in the study [23].

2. Experimental procedures

The Gd_2O_3:Er,Yb nano phosphor was synthesized using the Solution Combustion Synthesis (SCS) method, as detailed in [29]. To conduct our experiments on time-resolved laser-induced luminescence, we employed a specific experimental setup, which is described in [22, 30, 31]. In this study, we incorporated a pulsed laser diode emitting at 980 nm that was synchronized with a streak camera [32, 33] for measuring upconverting materials. Laser diode pulse duration used in measurements presented in paper is 50 μs. It is worth noting that the pulse duration can be adjusted as it is tunable. Longer pulse durations offer the advantage of a better signal-to-noise ratio, which contributes to the popularity of continual laser diode measurements, beside the fact that time resolved measurements are more expensive. However, it is important to consider the laser heating effects that become more significant with longer pulse durations. Additionally, since the lifetime of the Gd_2O_3:Er,Yb thermophosphor used is approximately 700 μs, using pulse durations longer than 50 μs would impede measurements of luminescence lifetime.

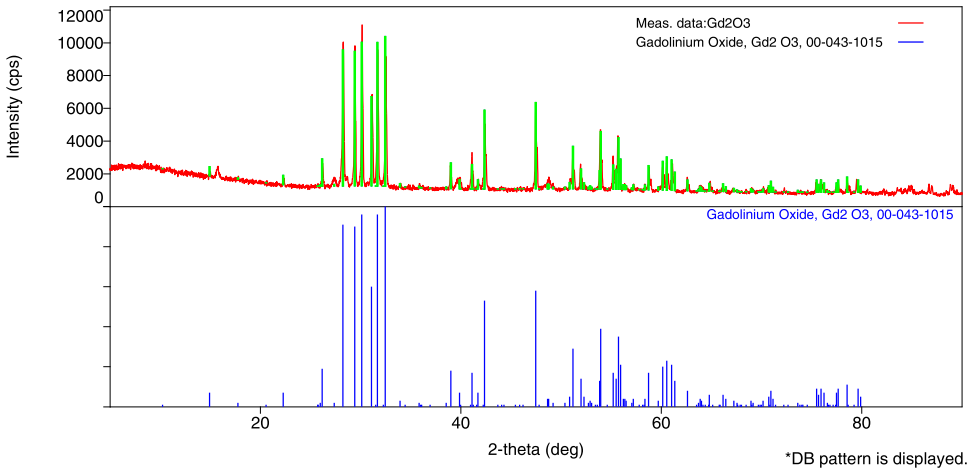

Figure 1. The x-ray diffraction (XRD) pattern of the synthesized Gd_2O_3:Er,Yb, with the measured data represented by the red pattern, The reference data for Gd_2O_3 are indicated in blue. To facilitate comparison, the reference data are superimposed on the measured data.

Time-resolved streak images of the luminescence spectra were captured using a Hamamatsu streak camera system (model C4334-01) operating in photon counting mode. The camera system's functionality relies on HPD-TA software. For the measurements presented in this study, we utilized a spectrograph (SpectraPro-2300i) with a grating of 50 lines/mm, covering a broad spectral range of 330 nm. To heat the nanoposphor sample, we employed a custom-made device based on the XMTF-808 temperature controller, as described in [34].

The Gd_2O_3:Er,Yb sample underwent characterization through the x-ray diffraction (XRD) technique using the RIGAKU Ultima IV diffractometer from Rigaku, Japan. The crystal structures of the analyzed materials were identified by subjecting them to filtered CuKα radiation (1.54178 nm) within the 2Θ range of 5° to 90°. Phase analysis was facilitated by employing the PDXL2 software v. 2.0.3.0 [35], with reference to the patterns provided by the International Centre for Diffraction Data (ICDD) v. 2012 [36]. Additionally, the structure of the nanopowders was observed using a high-resolution scanning electron microscope (SEM) equipped with a high-brightness Schottky Field Emission gun (FEGSEM, TESCAN) operating at 4 kV.

To perform the machine learning (ML) analysis of the data, we utilized the Solo+Mia software package (Version 9.1, Eigenvector Research Inc., USA). Solo provides a user-friendly environment, making it accessible to individuals without programming expertise.

The measured spectra were initially analyzed using Principal Component Analysis (PCA) and Uniform Manifold Approximation and Projection clustering (UMAP). PCA was originally introduced in [37], and for further details, we refer the reader to [38] and the referenced sources therein. UMAP, a novel clustering technique suitable for visualizing extensive datasets, was recently proposed by [39]. Ultimately, after conducting preliminary experiments, we employed a deep learning artificial neural network to estimate the temperature of the heated samples.

3. Results and discussion

Figure 1 displays the x-ray diffraction (XRD) pattern of the synthesized Gd_2O_3:Er,Yb nano material. The observed peaks indicate that the material crystallized in the monoclinic crystal system with a high degree of crystallinity and purity. By utilizing the PDXL2 software, the average grain size was estimated to be 65 nm. The structure of our Gd_2O_3:Er,Yb sample was further confirmed through high-resolution scanning electron microscopy (SEM), as depicted in figure 2. The grain sizes range from 35 nm to approximately 100 nm, and agglomerated particles are also visible in the images.

Streak images of laser-induced luminescence spectra of Gd_2O_3:Er,Yb nanopowder at two different temperatures are shown in figure 3. The pseudocolored streak images are presented, with the vertical axis representing time and the horizontal axis representing the wavelength of optical emission. The integrated-in-time spectrum (profile) is depicted by the green curve. The timing window indicating the interval for integrating the spectrum intensity is represented by two green lines.

The luminescence kinetics of the Er,Yb-doped Gd_2O_3 nanopowder sample were analyzed using the HPD-TA software, resulting in an average lifetime value of approximately 0.77 ms at room temperature. It should be noted that the lifetime decreases with increasing temperature, as shown in figure 3. However, in the case of the

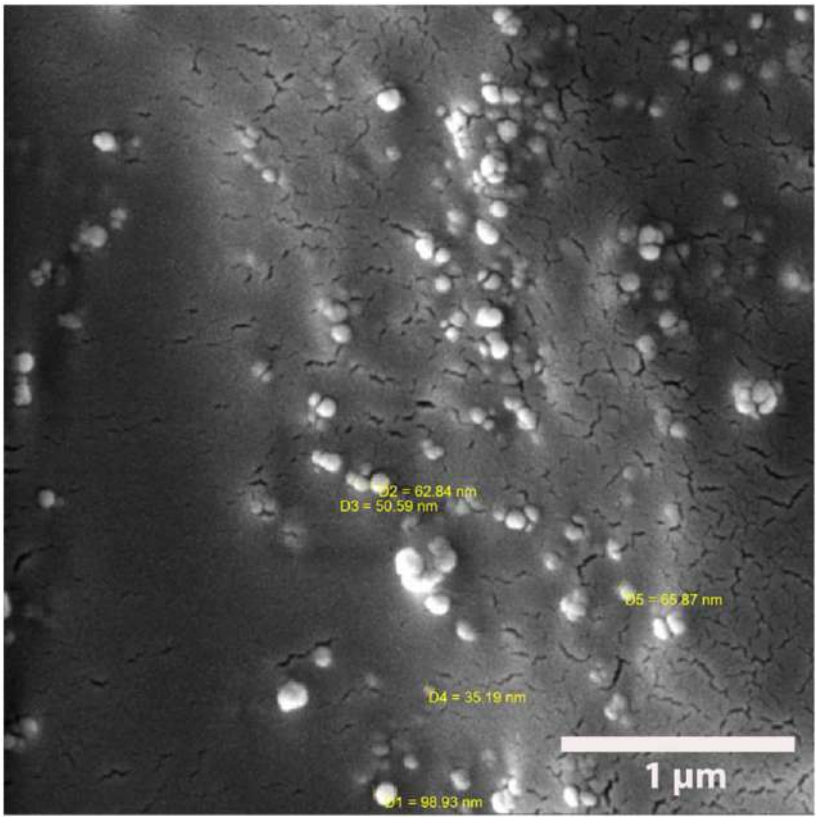

Figure 2. SEM image of Gd_2O_3:Er,Yb nanophosphor.

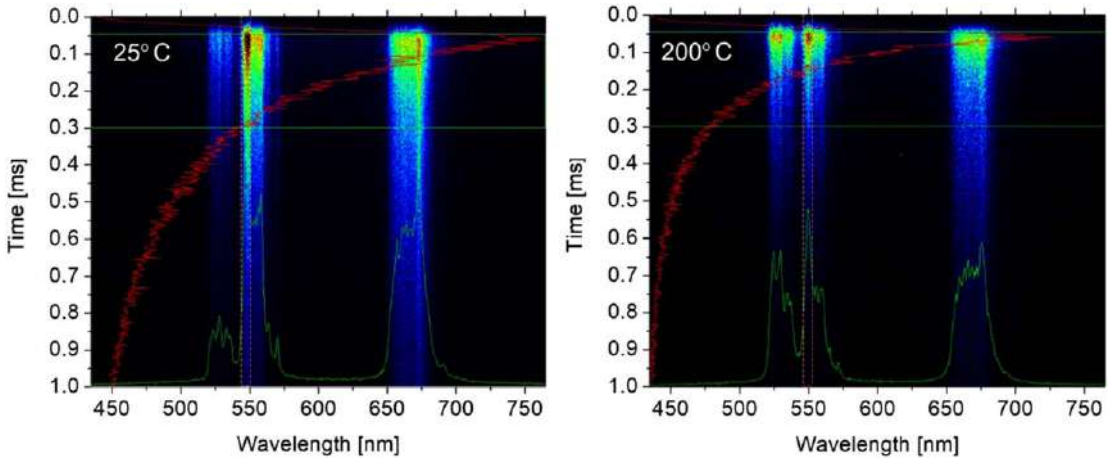

Figure 3. Streak images of luminescence spectra of Gd_2O_3:Er,Yb nanopowder at two different temperatures, with laser excitation at 980 nm. The green curve represents the spectral profile integrated over a time range of 0.05 ms to 0.3 ms, as indicated by the green lines. Additionally, the red curve illustrates the time decay of the luminescence from the spectral peak around 550 nm.

Gd_2O_3:Er,Yb thermophosphor, the rise times are relatively short and do not significantly contribute to the temperature calculations.

In this study, the spectra were measured at 640 wavelength points. To alleviate the computational burden, we selectively chose specific portions of the streak image that contained the majority of the spectral and time-resolved information. For the ML analysis, we focused on 74 spectral points corresponding to bands between 522 nm and 533 nm, 546 nm and 560 nm, and 667 nm and 680 nm. The selected time frame consisted of 80 points, equivalent to approximately 165 μs. As a result, each sample used for ML analysis comprised $74 * 80 = 5920$ data points. To generate the input vector of 5920 data points, the pixel rows of the region of interest in the image are sequentially packed row by row. To optimize computational time without sacrificing prediction

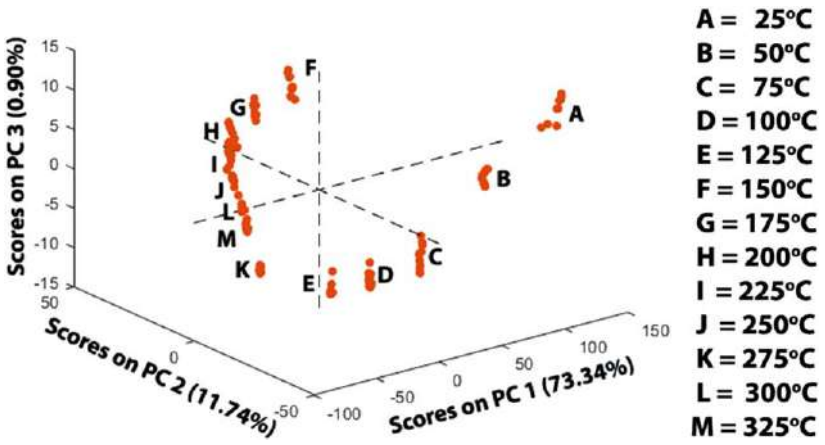

Figure 4. Scores on first three principal components of Gd_2O_3:Er,Yb spectra at different temperatures.

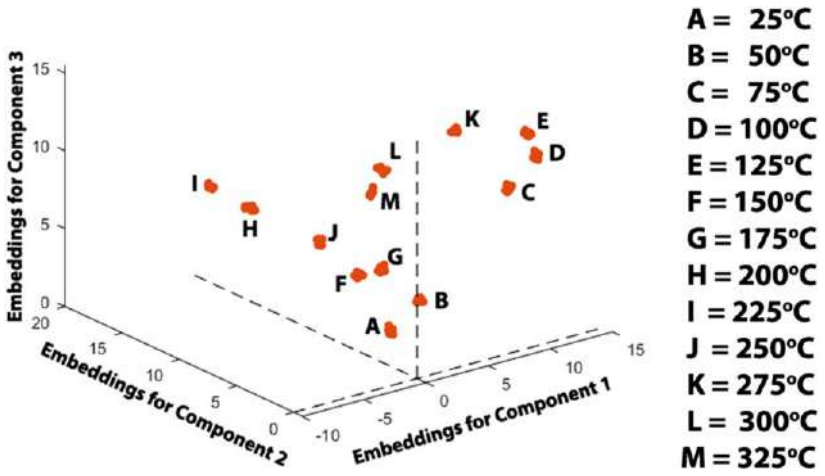

Figure 5. Uniform Manifold Approximation and Projection (UMAP) clustering of Gd_2O_3:Er,Yb spectra at different temperatures.

accuracy, we experimented with larger regions of interest (ROI) from the streak images and gradually reduced the size of the ROI.

In order to construct the training set for ML predictions, we conducted measurements on samples at regular intervals of 25 degrees Celsius, ranging from 25 °C to 325 °C. For each temperature, a set of 50 spectra was measured, resulting in a total of 650 training spectra (13 temperatures multiplied by 50 spectra per temperature).

The Principal Component Analysis (PCA) scores plots serve as a valuable tool for initial data assessment and verification. In figure 4, the scores on the first three principal components of Gd_2O_3:Er,Yb spectra at different temperatures are displayed. To represent the temperature values, we have utilized single letters to avoid overcrowding and enhance readability. It is noticeable that spectra obtained at similar temperatures tend to cluster together, although not perfectly. However, distinguishing the boundaries between classes H, I, J, L, and M proves to be challenging. Consequently, to facilitate the initial data assessment, we have incorporated Uniform Manifold Approximation and Projection (UMAP) clustering of Gd_2O_3:Er,Yb spectra at various temperatures.

The Uniform Manifold Approximation and Projection (UMAP) clustering results of Gd_2O_3:Er,Yb spectra at various temperatures are depicted in figure 5. It is evident that the classes are considerably more distinguishable compared to figure 4. The growing popularity of UMAP as a viable alternative to PCA in certain applications does not come as a surprise. If our objective was to achieve a temperature measurement resolution of 25 degrees, UMAP clustering would suffice as a suitable method. However, to attain enhanced resolution and more accurate temperature predictions between the training intervals, we opted to utilize an artificial neural network (ANN) for temperature estimation.

Initially, we experimented with a traditional ANN implemented in the SOLO software. Nevertheless, our subsequent endeavors involved employing a more sophisticated approach known as ANNDL (Deep Learning ANN), which surprisingly exhibited faster performance compared to the simple ANN. The ANNDL

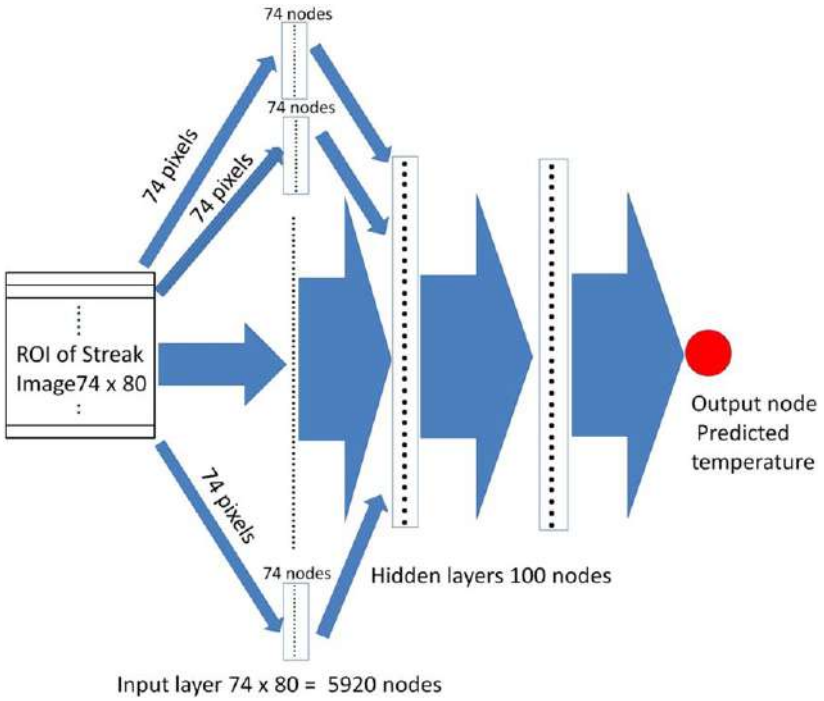

Figure 6. A schematic diagram illustrating the deep learning network used in this study. It is not possible to draw all arrows, and the shown arrows are merely symbolic. The pixel rows of the region of interest in the image are fed into the input layer as shown in the diagram.

implementation in SOLO can utilize either the SciKit or TensorFlow Python packages. In our case, we chose the TensorFlow Python package, which utilizes GPU acceleration for highly efficient computations.

The primary concept behind temperature estimation of thermophosphors using ANNDL involves training the network with sample spectra that have corresponding temperature measurements. During the training phase, the network iteratively minimizes errors between the calculated and predicted temperatures. Since the region of interest in the streak image of Gd_2O_3:Er,Yb consists of 5920 points, the input layer of the deep learning network has 5920 nodes. Considering that this network aims to approximate two types of exponential functions - one for intensity ratios and another for luminescence lifetime - we initially considered using two hidden layers. However, we experimented with different numbers and sizes of hidden layers. Ultimately, we determined that a neural network with two hidden layers, each containing 100 nodes, was the optimal solution. The output layer consists of a single node representing the predicted temperature. A schematic diagram illustrating the deep learning network used in this study is shown in figure 6.

After conducting several experiments, we determined that the *Adamax* optimizer outperformed other optimizers, including *Adam*, and the *Relu* activation function. *Adamax* utilizes a default learning rate of 0.001, but it can adaptively adjust the learning rate based on the characteristics of the data. For cross-validation, we employed the Venetian blind method with a data split of 4, meaning that in each sub-validation experiment, 75% of the data was used for training and 25% for validation. Following further experimentation, we selected a batch size of 12, which is the default batch size in SOLO. The learning curves depicting the training progress of the ANNDL model are shown in figure 7. Based on shapes of learning curves shown in figure 7, we decided to set the number of epochs to 100. Before processing data we have used normalization procedure 1-Norm (area = 1) on dataset. Then the data were smoothed using Savitzky–Golay filter. Width of filter was 5, with polynomial order of 4 and weighted tails. These preprocessing options are built-in SOLO software.

Figure 8(a) presents the plot of predicted temperatures within the training set. Visually, the plot closely resembles the plot of measured temperatures versus samples, so the latter is not shown here. The residuals, representing the differences between the calculated (used for training) and predicted temperatures obtained from the deep learning neural network model, are displayed in figure 8(b). Notably, the errors for the samples within the training set are relatively small, as depicted in figure 8(b).

Figure 9(a) displays the plot of predicted temperatures for the test points outside the training set. These 12 points were carefully selected to be positioned between the two neighboring temperatures used for training the ANNDL. The corresponding measured temperatures were recorded using a temperature controller. It is worth noting that the absolute errors for the samples outside the training set remain relatively small, with the largest

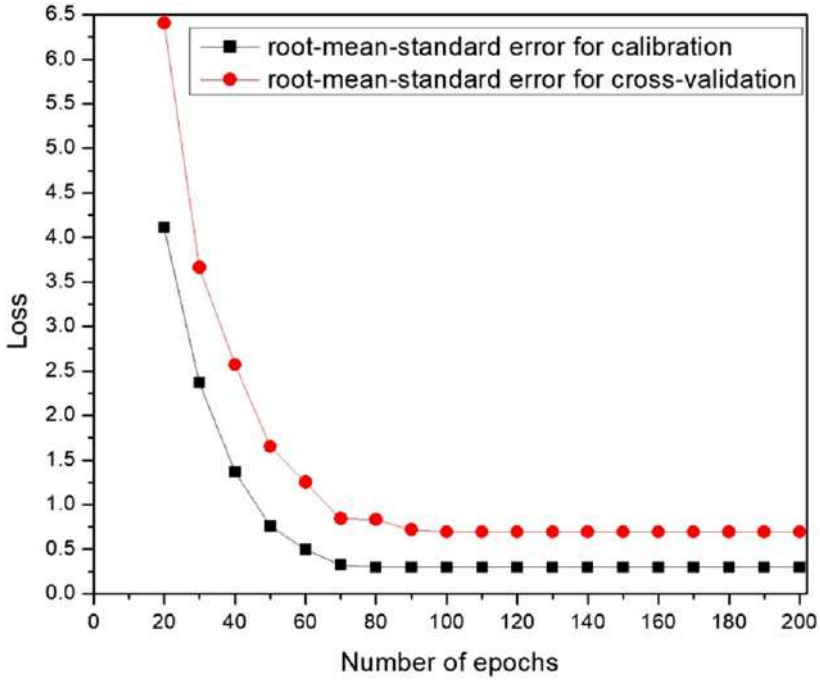

Figure 7. The learning curves depicting the training progress of the ANNDL model.

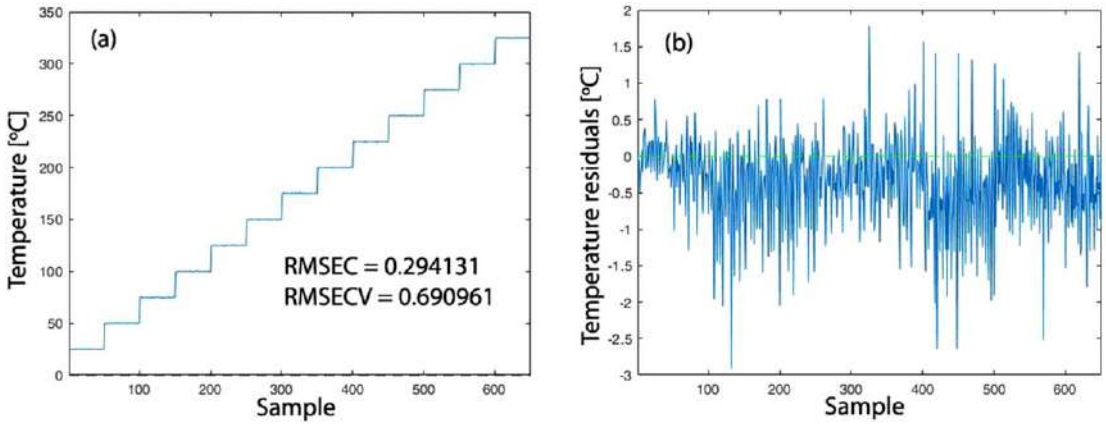

Figure 8. (a) Plot of predicted temperatures inside the training set. RMSEC refers to the root-mean-standard error of calibration; RMSECV refers to the root-mean-standard error of cross-validation. (b) Residuals plot.

error being approximately 2.5 °C, as shown in figure 9(b). The percentage error for the test samples ranges from 0.12% to 1.30%.

Despite the increasing interest in utilizing machine learning techniques to enhance studies in luminescence spectroscopy, there is a scarcity of papers available for direct comparison of our results.

In reference [11], the authors discuss the application of linear transformations (Principal Component Analysis) and non-linear transformations (t-distributed Stochastic Neighbor Embedding) on thermophosphor calibration datasets. Their findings demonstrate a clear advantage over our own results when utilizing PCA or UMAP. Nevertheless, this was precisely why we opted for employing a deep learning neural network in our approach.

When comparing the results reported in [21], our method yields slightly superior results in terms of prediction errors. Remarkably, our deep neural network model achieves optimal performance with just approximately 100 epochs, whereas the [21] study necessitates training the network for 6000 epochs.

In comparison to the results presented in [10], we observed slightly larger maximum errors. Incorporating the time development of luminescence spectra in our prediction model was expected to result in improved performance compared to the network presented in [10]. However, it should be noted that our temperature

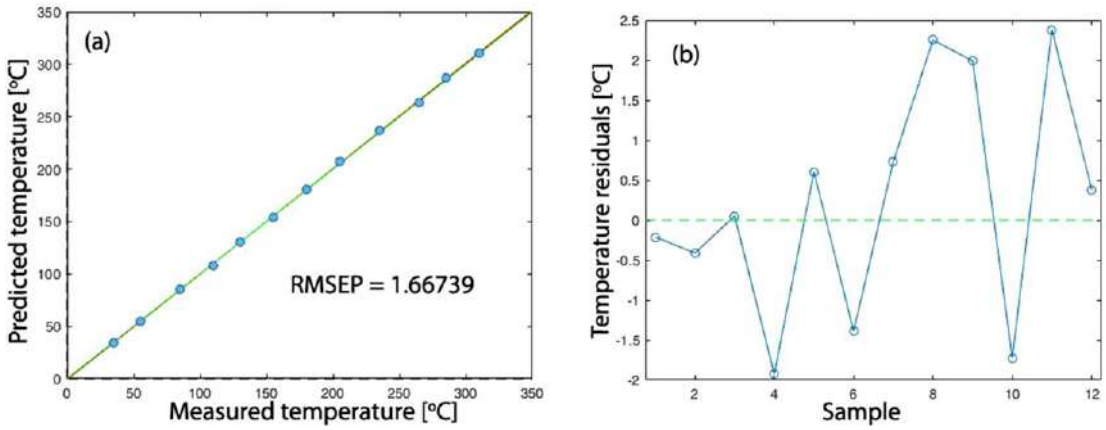

Figure 9. (a) Plot of predicted temperatures outside the training set. 'Ideal' line where the predicted and the measured points would be equal is indicated by green color. The line fit of the predicted points is indicated by the color red. RMSEP refers to root-mean-standard error of prediction. (b) Residuals plot.

controller lacks a manufacturer-specified resolution and accuracy. We estimate that its sporadic errors can reach up to 2 degrees Celsius, irrespective of the temperature value. Consequently, the relative error can be significant at lower temperatures. In contrast, the temperature controller utilized in [10] possesses a declared temperature resolution and stability of 0.01 and ±0.05 degrees Celsius, respectively. Our primary objective was to validate the concept of employing the time evolution of luminescence spectra for remote temperature estimation. The presented results serve as evidence supporting this concept.

4. Conclusion and future work

We employed machine learning techniques to analyze the optical spectra of Gd_2O_3:Er,Yb thermophosphor in order to enable remote temperature measurements. Our approach deviates from the conventional method of identifying spectral peaks and calculating their intensity ratio. Instead, we trained a computer model to recognize the time-resolved spectra associated with different temperatures of the thermophosphors. This allowed us to incorporate not only the intensity ratios of all peaks but also the luminescence lifetime as an additional parameter. Previous studies demonstrated that the Gd_2O_3:Er,Yb thermophosphor analyzed in this study does not exhibit a measurable rise time for temperature measurements. However, certain phosphors, such as YVO_4:Eu and Sr_2CeO_4:Eu, possess luminescence rise times measurable in microseconds. Hence, future research can explore these phosphors to develop more comprehensive methods for remote temperature estimation that utilize all parameters of luminescence spectra.

Acknowledgments

This work was financially supported by funding provided by the Institute of Physics Belgrade and by the 'Vinca' Institute of Nuclear science through the grant by the Ministry of Education, Science, and Technological Development of the Republic of Serbia.

Data availability statement

All data that support the findings of this study are included within the article (and any supplementary files).

ORCID iDs

Maja S Rabasovic https://orcid.org/0000-0002-4882-8080
Svetlana Savic-Sevic https://orcid.org/0000-0002-6406-0745
Janez Križan https://orcid.org/0000-0003-4195-8322
Branko Matovic https://orcid.org/0000-0001-8022-1863
Marko Nikolic https://orcid.org/0000-0001-7205-3185
Dragutin Sevic https://orcid.org/0000-0002-7206-6370

References

[1] Sangiorgio M 2022 Deep learning in multi-step forecasting of chaotic dynamics *Book chapter, Special Topics in Information Technology* (PoliMI SpringerBriefs)
[2] Scalia G 2022 Machine learning for scientific data analysis *Book chapter, Special Topics in Information Technology* (PoliMI SpringerBriefs)
[3] Sayin B, Krivosheev E, Yang J, Passerini A and Casati F 2021 A review and experimental analysis of active learning over crowdsourced data *Artif. Intell. Rev.* **54** 5283–305
[4] Yu H, Li J, Wu Z, Xu H and Zhu L 2022 Two-step learning for crowdsourcing data classification *Multimedia Tools Appl.* **81** 34401–16
[5] Chatzidakis M and Botton G A 2019 Towards calibration-invariant spectroscopy using deep learning *Sci. Rep.* **9** 2126
[6] Dramićanin T, Zeković I, Periša I , J and Dramićanin M D 2019 The parallel factor analysis of beer fluorescence *Journal of Fluorescence* **29** 1103–11
[7] Ranamukhaarachchi S A, Peiris R H and Moresoli C 2017 Fluorescence spectroscopy and principal component analysis of soy protein hydrolysate fractions and the potential to assess their antioxidant capacity characteristics *Food Chem.* **217** 469–75
[8] Sevic D, Krizan J, Rabasovic M S and Marinkovic B P 2021 Temperature sensing using YAG:Dy single-crystal phosphor *Eur. Phys. J.* D **75** 56
[9] Weng S, Yuan H, Zhang X, Li P, Zheng L, Zhao J and Huanga L 2020 Deep learning networks for the recognition and quantitation of surface-enhanced Raman spectroscopy *Analyst* **145** 4827–35
[10] Cui J, Xu W, Yao M, Zheng L, Hu C, Zhang Z and Sun Z 2023 Convolutional neural networks open up horizons for luminescence thermometry *J. Lumin.* **256** 119637
[11] Ximendes E, Marin R, Carlos L D and Jaque D 2022 Less is more: dimensionality reduction as a general strategy for more precise luminescence thermometry *Science & Applications* **11** 2047–7538
[12] Barbon Jr S, da Costa Barbon A P A, Mantovani R G and Barbin D F 2018 Machine learning applied to near-infrared spectra for chicken meat classification *Journal of Spectroscopy* **2018** 8949741
[13] Caroline Geronimo B, Mastelini S M, Carvalho R H, Barbon Júnior S, Barbin D F, Shimokomaki M and Ida E I 2019 Computer vision system and near-infrared spectroscopy for identification and classification of chicken with wooden breast, and physicochemical and technological characterization *Infrared Phys. Technol.* **96** 303–10
[14] Barbon Junior S, Mastelini S M, Barbon A P A C, Barbin D F, Calvini R, Lopes J F and Ulrici A 2020 Multi-target prediction of wheat flour quality parameters with near infrared spectroscopy *Information Processing in Agriculture* **7** 342–54
[15] Perez I M N, Badaro A T, Barbon Jr S, AC Barbon A P, Pollonio M A R and Barbin D F 2018 Classification of chicken parts using a portable near-infrared (nir) spectrophotometer and machine learning *Appl. Spectrosc.* **72** 1–7
[16] D'Andrea E, Pagnotta S, Grifoni E, Legnaioli S, Lorenzetti G, Palleschi V and Lazzerini B 2015 A hybrid calibration-free/artificial neural networks approach to the quantitative analysis of LIBS spectra *Appl. Phys.* B **118** 353–60
[17] Bellou E, Gyftokostas N, Stefas D, Gazeli O and Couris S 2020 Laser-induced breakdown spectroscopy assisted by machine learning for olive oils classification: The effect of the experimental parameters *Spectrochim. Acta, Part* B **163** 105476
[18] Yang P, Yang G, Zhang F, Jiang B and Wang M 2021 Spectral classification and particular spectra identification based on data mining *Arch. Comput. Meth. Eng.* **28** 917–35
[19] Zhang D, Zhang H, Zhao Y, Chen Y, Ke C, Xu T and He Y 2022 A brief review of new data analysis methods of laser induced breakdown spectroscopy: machine learning *Applied Spectroscopy Review* **57** 89–111
[20] Rabasovic M S, Marinkovic B P and Sevic D 2023 Time resolved study of laser triggered electric discharge spark in atmosphere: Machine learning approach *Adv. Space Res.* **71** 1331–7
[21] Lewis C, Erikson J W, Sanchez D A, McClure C E, Nordin G P, Munro T R and Colton J S 2020 Use of machine learning with temporal photoluminescence signals from cdte quantum dots for temperature measurement in microfluidic devices *ACS Appl. Nano Mater.* **3** 4045–53
[22] Sevic D, Rabasovic M S, Krizan J, Savic-Sevic S, Nikolic M G, Marinkovic B P and Rabasovic M D 2020 M.D YVO4:Eu^{3+} nanopowders: multi-mode temperature sensing technique *Phys, J.: D: Appl. Phys.* **53** 015106–015101
[23] Kamińska I *et al* 2021 Synthesis and characterization of Gd_2O_3: Er^{3+}, Yb^{3+} doped with Mg^{2+}, Li^{+} ions - effect on the photoluminescence and biological applications *Nanotechnology* **32** 245705
[24] Vukovic M, Dinic I, Jardim P, Markovic S, Veselinovic L and Nikolic M 2022 Lidija Mancic, The low-temperature sonochemical synthesis of up-converting β $NaYF_4$: Yb,Er mesocrystals *Adv. Powder Technol.* **33** 103403
[25] Stamenkovic T, Radmilovic N, Prekajski Đorđevic M, Rabasovic M, Dinic I, Tomic M, Lojpur V and Mancic L 2023 ,Quantum yield and energy transfer in up-conversion $SrGd_2O_4$:Yb, Er nanoparticles obtained via sol–gel assisted combustion *J. Lumin.* **253** 119491
[26] Vukovic M, Mancic L, Dinic I, Vulic P, Nikolic M, Tan Z and Milosevic O 2020 The gadolinium effect on crystallization behavior and luminescence of β-NaYF4:Yb,Er phase *Int. J. Appl. Ceram. Technol.* **17** 1445–52
[27] Abdelrehman M H M, Kroon R E, Yousif A, Seed Ahmed H A A and Swart H C 2022 Luminescence properties of Yb^{3+} and Er^{3+} co-doped into Gd_2O_3:Bi^{3+} phosphor powder *J. Alloys Compd.* **902** 163856
[28] Rodríguez-Sevilla P, Marin R, Ximendes E, del Rosal B, Benayas A and Jaque D 2022 Luminescence thermometry for brain activity monitoring: a perspective *Frontiers in Chemistry* **10** 941861
[29] Krizan J, Mazaj M, Kaucic V, Bajsic I and Mozina J 2014 Synthesis of Er- and Yb-doped gadolinium oxide polymorphs and influence of their structures on upconversion properties *Acta Chim. Slov.* **61** 608–14
[30] Rabasovic M S, Sevic D, Terzic M and Marinkovic B P 2012 Time resolved laser induced fluorescence measurements: considerations when using Nd:YAG based system *Nucl.Instrum. Meth.* B **279** 16–9
[31] Vlasic A, Sevic D, Rabasovic M S, Krizan J, Savic-Sevic S, Rabasovic M /D, Mitric M, Marinkovic B P and Nikolic M /G 2018 Effects of temperature and pressure on luminescent properties of Sr_2CeO_4:Eu^{3+} nanophosphor *J. Lumin.* **199** 285–92
[32] Sevic D, Rabasovic M S, Krizan J, Savic-Sevic S, Rabasovic M D, Marinkovic B P and Nikolic M G 2020 Effects of temperature on luminescent properties of Gd_2O_3:Er, Yb nanophosphor *Opt. Quantum Electron.* **52** 232
[33] Sevic D, Rabasovic M S, Križan J, Savic-Sevic S, Marinkovic B P and Nikolic M G 2022 Luminescence thermometry based on Y_2O_2S:Er,Yb nanophosphor *Opt. Quantum Electron.* **54** 523
[34] Rabasovic M D, Muric B D, Celebonovic V, Mitric M, Jelenkovic B M and Nikolic M G 2016 Luminescence thermometry via the two-dopant intensity ratio of Y_2O_3:Er^{3+}, Eu^{3+} *J. Phys. D: Appl. Phys.* **49** 485104
[35] PDXL 2011 *Version 2.0.3.0 Integrated x-ray Powder Diffraction Software.* (Rigaku Corporation) 196–8666
[36] Powder Diffraction File 2012 PDF-2 Database, announcement of new data base release *Int. Centre for Diffraction Data (ICDD)*
[37] Hotelling H 1933 Analysis of a complex of statistical variables into principal components *Journal of Educational Psychology* **24** 417–41

[38] Wise B M, Gallagher N B, Bro R, Shaver J M, Windig W and Koch R S 2006 *Chemometrics tutorial for PLS_Toolbox and Solo* (Eigenvector Research, Inc) ISBN: 0-9761184-1-6
[39] McInnes L, Healy J, Saul N and Großberger L 2018 UMAP: uniform manifold approximation and projection *Journal of Open Source Software* **3** 861

Optical and Quantum Electronics (2022) 54: 622
https://doi.org/10.1007/s11082-022-03958-4

Interaction between ordered multilayer structure and randomly distributed nanopillars in biopolymer increases the width of the photonic bandgap

Svetlana Savić-Šević[1] · **Branislav Jelenković**[1]

Received: 15 November 2021 / Accepted: 22 June 2022 / Published online: 23 August 2022
© The Author(s), under exclusive licence to Springer Science+Business Media, LLC, part of Springer Nature 2022

Abstract
Structure having both ordered and disordered components, integrated into novel photonic structure have been presented. Self-supporting photonic structure is designed, as a combination of ordered multilayer grating and randomly distributed nanopillars. It is created through a combination of holographic method and non-solvent induced phase separation in biopolymer - pullulan, a polysaccharide-based material. Interplay between Bragg regularity and random scattering results in the 35% wide photonic band-gap and high reflectivity of up to 85%.

Keywords Ordered multilayer structure · Disorder · Photonic bandgap · Holography · Biopolymer

1 Introduction

Complex nanostructures with interesting properties for photonic applications received great attention (Bae et al. 2014; Lee et al. 2014). Photonic properties of nanomaterials are considerably dependent on their structures. Initially, highly ordered photonic crystal structures have been manufactured and investigated (Busch et al. 2003; Joannopoulos et al. 2008). Interesting physical phenomena were discovered, such as: complete band gaps (Yablonovitch et al. 1987; Blanco et al. 2000; Ren et al. 2008), nonlinearities (Soljacic and Joannopoulos 2004), slow light (Baba 2008), negative refraction (Cubukcu et al. 2003). Several applications emerged and many more were envisaged: waveguides (Loncar et al. 2000), filters (Trout et al. 1998), optical switches (Tondiglia et al. 2002), lasers (Altug et al. 2006).

This article is part of the Topical Collection on Photonics: Current Challenges and Emerging Applications, Guest edited by Jelena Radovanovic, Dragan Indjin, Maja Nesic, Nikola Vukovic and Milena Milosevic.

✉ Svetlana Savić-Šević
savic@ipb.ac.rs

[1] Institute of Physics, Belgrade, Serbia

Later, it was found that strict periodicity is not the only route to photon control. It was shown that quasi-crystalline structures, which are between periodic and disordered structures, possess interesting properties, such as higher degree of symmetry than crystalline structures and a band gap (Valy Vardeny et al. 2013; Harb et al. 2010). Finally, attention was drawn to disordered materials (Wiersma 2013; García et al. 2007), random lasing (Wiersma 2008; Cerdán et al. 2013) and rediscovering effects like coherent backscattering (Van Albada and Lagendijk 1985; Wolf and Maret 1985), Anderson localization (Wiersma et al. 1997; Segev et al. 2013).

Many fabrication methods to obtain novel photonic materials were described so far: ion beam milling (Babinec et al. 2011), direct laser writing (Deubel et al. 2004), self-assembly (Galisteo-López et al. 2011), holography (Liu et al. 2012), non-solvent induced phase separation (Li and Han 2011). Holographic method has several advantages: it is simple and fast, capable of producing one-, two- and three- dimensional periodic nanostructures over a large area. We combine the holographic method with non-solvent induced phase separation to generate complex photonic structures described below.

Usually, ordered and disordered photonic structures have been generated and analyzed separately (Busch et al. 2003; García et al. 2007). However, in nature, biological photonic structures are complex and inherently disordered (Kinoshita et al. 2002). Here we present structures having both ordered and disordered components, integrated into novel photonic structure. Ordered Bragg layers are mutually separated and supported by randomly distributed nanopillars. This complex morphology is formed simultaneously by the holographic method and the nonsolvent induced phase separation. Depending on the film thickness, there can be as many as 50 Bragg layers. We show that the interplay between the Bragg regularity and random scattering increases the width of the photonic band-gap up to a 35% wide band gap, ($\Delta\lambda m/\lambda m = 35\%$).

This paper is organized as follows. First, we describe the fabrication of photonic structure and investigate its morphology. Next, we analyze optical band-gap properties of the complex multilayer structure, as a measure of the photon confinement in the layer.

2 Fabrication of complex photonic structures

Photonic structures are holographically recorded in pullulan, a linear homo-polysaccharide produced by micro-organisms - Aureobasidium pullulans (Prajapati et al. 2013), doped with ammonium dichromate - (DCP). Photosensitive layer was prepared by mixing 8% aqueous solution of pullulan (from Sigma-Aldrich) and 30% of the ammonium dichromate (by weight of pullulan). The solution was coated onto clean glass slides in a horizontal position and the film was dried overnight under normal laboratory conditions. Holographic properties of DCP material, its diffraction efficiency, surface gratings, copying and environmental stability, were previously investigated (Pantelić et al. 1998; Savić et al. 2002; Savić-Šević and Pantelić 2005, 2007). Here we use the DCP for volume (Bragg) grating generation using a simple counter- propagating beam configuration (Savić-Šević et al. 2021). We use single longitudinal mode laser, at 532 nm, as a light source. The laser beam was expanded and DCP plate was exposed at normal incidence. After propagation through the emulsion, the beam was reflected back from the mirror behind the DCP plate. The two counter-propagating beams interfere to create a standing wave pattern and grating within the pullulan layer. The

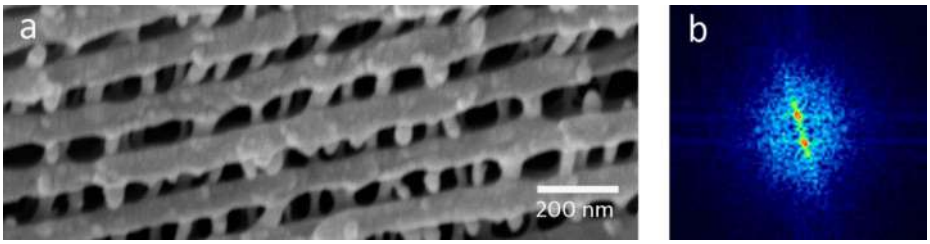

Fig. 1 (a) FEGSEM image of cross-section DCP photonic structure, (b) 2D FFT of FEGSEM image 1a

interference pattern consists of planes parallel to the substrate surface. The spacing between two adjacent planes is $\Lambda = \lambda / 2n$, where λ is the wavelength of the laser source and n is the refractive index, (1.45 for pullulan). During the exposure, hexavalent chromium ions Cr^{+6} are photo-reduced to trivalent Cr^{+3}, which then forms a covalent cross-link with pullulan molecules in the areas of constructive interference. Cross-linking hardens the pullulan, creating periodic variations of hardness (solubility) between exposed and unexposed regions. After exposure, DCP grating is chemically processed in a developer (mixture of water and isopropyl alcohol in 3:1 volume ratio) and in this way we selectively remove unexposed material, revealing the complex Bragg structure. Developer was replaced by pure isopropyl-alcohol, after two minutes and the DCP plate was dehydrated, for one minute. Finally, processed plate was dried in a closed vessel. The resulting structure has a thickness of 12 μm.

3 Morphological characterization of photonic structure

The morphology of the DCP photonic structure was investigated using a high resolution scanning electron microscope equipped with a high brightness Schottky Field Emission gun (FEGSEM) operating at 4 kV. The samples were coated with gold/palladium to make them conductive, for SEM analysis. A cross-section of the DCP sample, with a number of regularly spaced Bragg layers (217 nm periods), is shown in Fig. 1a. It could be seen that the Bragg grating is filled with nanopillars, arranged in a random way, deposited and confined between two DCP solid layers. Solid layers are formed in the area of constructive interference, which is non soluble in the developer. Nanopillars of pullulan are formed during phase separation in the area of destructive interference, which is soluble in water but non-soluble in isopropyl alcohol. Nanopillars, with diameter about 50 nm, are oriented perpendicular to the layers, enhancing their mechanical stability. The Fourier transform of the image shown in Fig. 1b. We can see two distinctive peaks, corresponding to grating periodicity, with circular area related to disordered structures.

4 Optical characterization of photonic structure

The resulting DCP sample is brightly colored when illuminated with white light as shown in Fig. 2a. The reflection and transmission spectra of photonic structures directly show their band gap, a range of wavelengths in which light cannot propagate in the crystal. Band gap in periodic structure is a consequence of the Bragg reflection. Optical spectra were measured

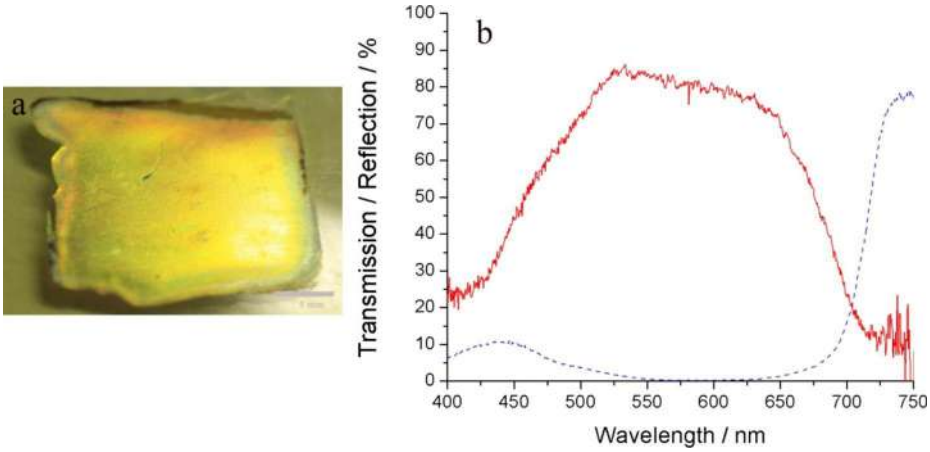

Fig. 2 **(a)** Reflection image of a DCP sample; (b) Reflection and transmission spectra of the DCP photonic structure

using the spectrometer (Ocean Optics) attached to the microscope. Figure 2b shows the spectra of the DCP grating, demonstrating high optical reflectivity, almost 85%, and a 35% wide band gap.

The experimentally obtained band gap can be compared to theoretical estimate of the band gap for a perfect multilayer photonic crystal, quater-wave stack of two materials. For a quater-wave stack with refractive indexes n_1 and n_2 and corresponding layer thicknesses d_1 and d_2, $a=d_1+d_2$, the normal-incidence gap is maximized when $d_1n_1=d_2n_2=\lambda_m/4$, where $\lambda_m=2\pi c/\omega_m$ is the vacuum wavelength that corresponds to the midgap frequency (frequency at the middle of gap) given by (Joannopoulos et al. 2008):

$$\omega_m = \frac{n_1 + n_2}{4n_1n_2} \cdot \frac{2\pi c}{a} \tag{1}$$

For $n_1=1.45$ (pullulan) and $n_2=1$ (air), and $d_1=d_2=108$ nm (obtained from FEGSEM image) we calculate $\lambda_m=514$ nm.

The gap-midgap ratio between the first two bands is (Joannopoulos et al. 2008):

$$\frac{\Delta\omega}{\omega_m} = \frac{4}{\pi}\sin^{-1}\left(\frac{|n_1 - n_2|}{n_1 + n_2}\right) \approx \frac{\Delta\lambda}{\lambda m} \tag{2}$$

Using this equation we predict the 120 nm width of band gap, which less than the experimentally obtained value, $\Delta\lambda\text{exp} \simeq 200$ nm, as obtained from Fig. 2b.

The intensity of the reflected light from the multilayer film is proportional to the index contrast between the layers and to the number of layers of equal thickness. For incident light normal to a uniform layer thickness multilayer film, the ideal reflectivity for a material composed of N layers is given by (Edrington et al. 2001):

$$R = [\frac{1 - (\frac{n_2}{n_1})^{2N}}{1 + (\frac{n_2}{n_1})^{2N}}]^2 \quad (3)$$

for $n_2 < n_1$. For 12 μm thick experimental structure there is approximately 55 Bragg layers 217 nm thick and calculated reflectivity is R > 99%. The experimentally obtained reflectivity is 85%.

We attribute increased band gap to coherent light scattering on randomly distributed nanopillars inside the Bragg layers (Savić-Šević et al. 2016). Coherent light which is incident on random media is multiply scattered causing constructive interference of waves traveling in opposite directions, this result in enhancement of the reflected intensity.

5 Conclusions

In conclusion, we created a complex, self-supporting, multilayer grating in dichromate sensitized pullulan. The grating has pullulan nanopillars arranged in a random manner, are confined between DCP Bragg layers. The photonic structure has both properties of ordered photonic crystals: band gap and high reflectivity; and disordered structures: weak localization (Savić-Šević et al. 2016). We show that combination of order and disorder widens the band gap.

We have demonstrated that the combination of holography and phase separation provides a simple, one-step method for the production of complex photonic structures. Large areas can be simply fabricated in a few minutes, with low-cost. This DCP structure could have many applications: for novel optical filters, optical document security, optical data storage media, biomimetics.

Acknowledgements This work was financially supported by funding provided by the Institute of Physics Belgrade, through the grant by the Ministry of Education, Science, and Technological Development of the Republic of Serbia.

Declarations

Conflict of interest The authors declare that they have no known competing financial interests or personal relationships that could have appeared to influence the work reported in this paper.

References

Altug, H., Englund, D., Vučković, J.: Ultrafast photonic crystal nanocavity laser.Nat. Physics. **2**, 484–488 (2006)

Baba, T.: Slow light in photonic crystals. Nat. Photon. **2**, 465–473 (2008)

Babinec, T., Choy, J., Smith, K., Khan, M., Lončar, M.: Design and focused ion beam fabrication of single crystal diamond nanobeam cavities. J. Vac Sci. Technol. B. **29**, 01060–010606 (2011)

Bae, W.-G., Kim, H., Kim, D., Park, S.-H., Jeong, H., Suh, K.-Y.: Adv. Mater. 25th Anniversary Article: Scalable Multiscale Patterned Structures Inspired by Nature: the Role of Hierarchy. **26**, 675–700 (2014)

Blanco, A., Chomski, E., Grabtchak, S., Ibisate, M., John, S., Leonard, S.W., Lopez, C.: Meseguer, F, Busch, K., Lolkes, S., Wehrspohn, R., Fol, H.: Photonic Crystals. Advance in Design, Fabrication and Characterization. Wiley-VCH, Verlag GmbH & Co. KGaA, Weinhem, Germany (2003)

Cerdán, L., Costela, A., Enciso, E., García-Moreno, I.: Random Lasing in Self-Assembled Dye-Doped Latex Nanoparticles: Packing Density Effects. Adv. Funct. Mater. **23**, 39161–33924 (2013)
Cubukcu, E., Aydin, K., Ozbay, E., Foteinopoulou, S., Soukoulis, C.M.: Negative refraction by photonic crystals. Nature. **423**, 604–605 (2003)
Deubel, M., von Freymann, G., Wegener, M., Pereira, S., Busch, K., Soukoulis, C.: Direct laser writing of three-dimensional photonic-crystal templates for telecommunications. Nat. Mater. **3**, 444–447 (2004)
Edrington, A., Urbas, A., DeRege, P., Chen, C., Swager, T., Hadjichristidis, N., Xenidou, M., Fetters, L., Joannopoulos, J., Fink, Y., Thomas, E.: Adv. Mater. **13**, 421–425 (2001)
Galisteo-López, J., Ibisate, M., Sapienza, R., Froufe-Pérez, L., Blanco, A., López, C.: Self-Assembled Photonic Structures. Adv. Mater. **23**, 30–69 (2011)
García, P., Sapienza, R., Blanco, A., López, C.: Photonic Glass: A Novel Random Material for Light. Adv. Mater. **19**, 2597 (2007)
Harb, A., Torres, F., Ohlinger, K., Lin, Y., Lozano, K., Xu, D., Chen, K.: Holographically formed three-dimensional Penrose-type photonic quasicrystal through a lab-made single diffractive optical element. Opt. Express. **18**, 20512–20517 (2010)
Joannopoulos, J., Johnson, S., Winn, J., Meade, R.: Photonic Crystals: Molding the Flow of Light, 2nd edn. Princeton University Press, Princeton, NJ (2008)
Kinoshita, S., Yoshioka, K., Kawagoe, K.: Mechanisms of structural colour in the Morpho butterfly: cooperation of regularity and irregularity in an iridescent scale. Proc. R. Soc. Lond. B **269**, 1417 – 1321 (2002)
Lee, J.-H., Koh, C., Singer, J., Jeon, S.-J., Maldovan, M., Stein, O., Thomas, E.: 25th Anniversary Article: Ordered Polymer Structures for the Engineering of Photons and Phonons. Adv. Mater. **26**, 532–569 (2014)
Li, X., Han, Y.: Tunable wavelength antireflective film by non-solvent-induced phase separation of amphiphilic block copolymer micelle solution. J. Mater. Chem. **21**, 18024–18033 (2011)
Liu, K., Xu, H., Hu, H., Gan, Q., Cartwright, A.: One-Step Fabrication of Graded Rainbow-Colored Holographic Photopolymer Reflection Gratings. Adv. Mater. **24**, 1604–1609 (2012)
Lončar, M., Nedeljković, D., Doll, T., Vučković, J., Scherer, A., Pearsall, T.: Waveguiding in planar photonic crystals. Appl. Phys. Lett. **77**, 1937–1939 (2000)
Miguez, H., Mondia, J.P., Ozin, G.A., Toader, O., van Driel, N.M.: Large-scale synthesis of a silicon photonic crystal with a complete three-dimensional bandgap near 1.5 micrometres. Nature. **405**, 437–440 (2000)
Pantelić, D., Savić, S., Jakovljević, D.: Dichromated pullulan as a novel photosensitive holographic material. Opt. Lett. **23**, 807–809 (1998)
Prajapati, V., Jani, G., Khanda, S.: Pullulan: An exopolysaccharide and its various applications. Carbohydr. Polym. **95**, 540–549 (2013)
Ren, Z., Zhai, T., Wang, Z., Zhou, J., Liu, D.: Complete Band Gaps in the Visible Range Achieved by a Low-Refractive-Index Material. Adv. Mater. **20**, 2337–2340 (2008)
Savić, S., Pantelić, D., Jakovljević, D.: Real-time and postprocessing holographic effects in dichromated pullulan. Appl. Opt. **41**, 4484–4488 (2002)
Savić-Šević, S., Pantelić, D.: Relief hologram replication using a dental composite as an embossing tool. Opt. Express. **13**, 2747–2754 (2005)
Savić-Šević, S., Pantelić, D.: Dichromated pullulan diffraction gratings: influence of environmental conditions and storage time on their properties. Appl Opt. **46**, 287–291 (2007)
Savić-Šević, S., Pantelić, D., Murić, B., Grujić, D., Vasiljević, D., Kolaric, B., Jelenković, B.: Thermo-osmotic metamaterials with large negative thermal expansion. J. Mater. Chem. C. **9**, 8163–8168 (2021)
Savić-Šević, S., Pantelić, Grujić, D., Jelenković, B.: Localization of light in a polysaccharide-based complex nanostructure. Opt. Quant. Electron. **48**–289 (2016)
Segev, M., Silberberg, Y., Christodoulides, D.: Anderson localization of light. Nat. Photon. **7**, 197–204 (2013)
Soljacic, M., Joannopoulos, J.: Enhancement of nonlinear effects using photonic crystals. Nat. mater. **3**, 211–219 (2004)
Tondiglia, V., Natarajan, L., Sutherland, R., Tomlin, D., Bunning, T.: Holographic Formation of Electro-Optical Polymer-Liquid Crystal Photonic Crystals. Adv. Mater. **14**, 187–191 (2002)
Trout, T., Schmieg, J., Gambogi, W., Weber, A.:Optical Photopolymers: Design and Applications: Adv. Mater. **10**, 1219–1224 (1998)
Valy Vardeny, Z., Nahata, A., Agrawal, A.: Optics of photonic quasicrystals. Nat. Photon. **7**, 177–187 (2013)
Van Albada, M.P., Lagendijk, A.: Observation of Weak Localization of Light in a Random Medium. Phys. Rev. Lett. **55**, 2692–2695 (1985)
Wiersma, D., Bartolini, P., Lagendijk, A., Righini, R.: Localization of light in a disordered medium. Nature. **390**, 671–673 (1997)
Wiersma, D.: The physics and applications of random lasers. Nat Phys. **4**, 359–367 (2008)
Wiersma, D.: Nat. Photon. Disordered photonics. **7**, 188–196 (2013)

Wolf, P.-E., Maret, G.: Weak Localization and Coherent Backscattering of Photons in Disordered Media. Phys. Rev. Lett. **55**, 2696–2699 (1985)
Yablonovitch, E.: Inhibited Spontaneous Emission in Solid-State Physics and Electronics. Phys. Rev. Lett. **58**, 2059–2062 (1987)

Publisher's Note Springer Nature remains neutral with regard to jurisdictional claims in published maps and institutional affiliations.

Scattering-enhanced absorption and interference produce a golden wing color of the burnished brass moth, *Diachrysia chrysitis*

Dejan Pantelić,[1,*] Svetlana Savić-Šević,[1] Dejan V. Stojanović,[2] Srećko Ćurčić,[3] Aleksandar J. Krmpot,[1] Mihailo Rabasović,[1] Danica Pavlović,[1] Vladimir Lazović,[1] and Vojislav Milošević[1]

[1]*Institute of Physics, University of Belgrade, Pregrevica 118, 11080 Zemun, Belgrade, Serbia*

[2]*Institute of Lowland Forestry and Environment, University of Novi Sad, Antona Čehova 13, 21000 Novi Sad, Serbia*

[3]*Institute of Zoology, University of Belgrade—Faculty of Biology, Studentski Trg 16, 11000 Belgrade, Serbia*

(Received 3 November 2016; published 8 March 2017)

Here we report how interference and scattering-enhanced absorption act together to produce the golden wing patches of the burnished brass moth. The key mechanism is scattering on rough internal surfaces of the wing scales, accompanied by a large increase of absorption in the UV-blue spectral range. Unscattered light interferes and efficiently reflects from the multilayer composed of the scales and the wing membranes. The resulting spectrum is remarkably similar to the spectrum of metallic gold. Subwavelength morphology and spectral and absorptive properties of the wings are described. Theories of subwavelength surface scattering and local intensity enhancement are used to quantitatively explain the observed reflectance spectrum.

DOI: 10.1103/PhysRevE.95.032405

I. INTRODUCTION

Fascinating "inventions" of evolution have been discovered in a large number of recent studies dealing with the biophysics of living creatures. In that respect, insects are an excellent research subject due to their diversity and abundance.

Biophotonics of insects is a particularly active subject which aims to explain function and imitate intricate micro- and nanostructures on their bodies. Several studies present a comprehensive overview of the current research [1–3]. Surprising results are still being published, such as the photonic system of a Saharan silver ant, enabling radiative dissipation of heat, directly through the IR atmospheric window [4]. This and a number of other studies suggest that nature has developed many technologies which can be used to solve everyday problems, if successfully imitated [5,6].

Optical photonic structures in the living world are diverse and have been classified by Land [7], based on their biological function, including tapeta (light-path doubling or image forming), camouflage, display, optical filters (e.g., corneal nipples of insect compound eyes), and anatomical accidents (features whose optical properties have no obvious biological function, e.g., mother-of-pearl in some mollusks).

More specifically, the biophotonics of Lepidoptera draws much attention, mostly due to the attractiveness of butterflies. Much less is known about moths (suborder Heterocera), which represent a group of Lepidoptera, characterized by the wings mostly having drab colors (gray or brown), and feathery or saw-edged antennae (vs club-shaped in butterflies). While moths are more numerous than butterflies, the number of structural coloration studies is significantly smaller. Only attractive and conspicuous moth species were explored, such as the Madagascan sunset moth [8]. The lack of interest is, possibly, due to the simpler wing-scale structure of moths, compared to really complex features present on the scales of day flying butterflies (e.g., Bragg gratings or photonic crystals).

Golden wing patches are prominent features of some noctuid moths. The patches might be just small marks as in *Autographa jota* (Linnaeus, 1758) and *A. bractea* (Denis & Schiffermüller, 1775), or large areas, as in *Diachrysia balluca* Geyer, 1832. The physics behind the golden moth color was previously analyzed using the diffraction theory of Stratton-Silver-Chu [9] in the case of *Thysanoplusia orichalcea* (Fabricius, 1775) (previously included in the genus *Trichoplusia* McDunnough, 1944) (Noctuidae family). However, a correspondence between theory and experimentally recorded spectra was qualitative, probably due to approximations of the mathematical formalism.

Other insects with a golden cuticle do exist, such as *Chrysina aurigans* (Rothschild & Jordan, 1894) (Coleoptera: Scarabaeidae) [10], whose broadband metallic reflection is due to a chirped Bragg mirror within the cuticle. Some species have a tunable color, which depends on atmospheric humidity [11] or stressful events [12], enabling the insects to change the color from red to golden.

Rothschild *et al.* [13] found that carotenoid pigments may also contribute to golden metallic areas of Danainae butterfly pupae. Similar results were obtained by Taylor [14] and Neville [15]. In contrast, Steinbrecht *et al.* [16] proved that golden reflections of *Euploea core* (Cramer, 1780) (Lepidoptera: Nymphalidae) pupae have an entirely physical nature. They showed that reflectance spectra of the cuticle (possessing multiple endocuticular thin alternating layers) and metallic gold are very similar, with a characteristic edge at 450–550 nm. The authors also emphasize that the carotenoids in the epidermis cannot contribute to the color effects because the cuticle practically does not transmit yellow light at all.

Scattering from an irregular surface is a secondary mechanism of structural coloration—interference and diffraction being dominant ones. For example, lycaenid butterflies (in particular, subfamily Polyommatinae) scatter light from the internal, pepper-pot-like, Bragg layers (having holes of 100 nm average diameter). The wing-scale laminae are almost hollow and permit the blue radiation to escape [17]. Pieridae can also be mentioned due to the nanobeads (pigment granules), which fill the space between the laminae [18], where the scattering

*pantelic@ipb.ac.rs

 ©2017 American Physical Society

and fluorescence extend the reflection spectrum [19,20]. Scattering in the living world is sometimes accompanied by light trapping, as in diatoms [21]. This seems to be a significant mechanism for efficient light harvesting in photosynthetic organisms.

Here we describe how several optical mechanisms interact to produce the golden wing color of the burnished brass moth, *Diachrysia chrysitis* (Linnaeus, 1758). We have studied spectral properties of the golden wing patches, as well as the internal and external ultrastructure of the wing scales and wing membranes. It was found that the scattering from irregular internal surfaces of each scale suppresses the UV-blue reflection, while interference efficiently reflects the red-infrared spectral range. A theoretical model is proposed, which combines interference and scattering from the scale laminae. The finite element method (FEM) is used to confirm the trapping and local intensity enhancement of light inside the laminae, while the modified transfer matrix method is used to calculate the reflection spectrum.

II. OPTICAL PROPERTIES AND STRUCTURE OF *D. CHRYSITIS* WING

The burnished brass moth (*D. chrysitis*; shown in Fig. 1) is a common species of the Noctuidae family (Insecta: Lepidoptera). It inhabits temperate climates in the Palearctic region [22]. *D. chrysitis* is a remarkable moth with big, golden (sometimes brassy-green) areas on each forewing. The wingspan is 28–35 mm, while the length of each forewing is 16–18 mm [23]. The burnished brass moth is usually found in marshy areas or in slightly moist forb communities. The larvae feed on plants such as *Urtica* spp., *Lamium* spp., or *Cirsium* spp. [24]. The moth flies from May to October depending on the location. It flies regularly in dusk, and was seen visiting flowers of various plants. Sometimes it can be noticed during the day, even sucking nectar. The species is widespread in Serbia [25].

It is supposed that irregular golden patches in the forewings of *D. chrysitis* are an example of disruptive coloring, as an excellent way of hiding oneself by breaking up the body contours [26]. Additionally, it was also postulated that specular reflection of the sun's rays may imitate the glittering of dew droplets. Even more, it seems that the wing color is optimized to efficiently reflect the yellowish light of the sun. As a dusk species, the moth may emit a signal in the IR spectral range from the golden patches, which might be used as a signal for intraspecific recognition. Anatomical accidents seem unlikely because metallic areas on *D. chrysitis* forewings form species-specific patterns [27].

FIG. 1. Burnished brass moth (*D. chrysitis*) with golden areas on its forewings.

From the optical point of view, the most prominent features of the studied moth are golden-color wing patches, as seen in Fig. 1. The corresponding wing spectra were recorded in reflection using a fiber optic spectrometer (manufactured by Ocean Optics, HR2000CG-UV-NIR), with a 400-μm core diameter fiber. A halogen lamp was used as a light source, and spectra were referenced to a standard white surface. The light collection angle was limited by the numerical aperture of the fiber (NA = 0.22, which is equivalent to an angular range of $\pm 12.7°$), positioned such that an approximately 40-mm^2 area is observed. This means that the spectra of individual scales are integrated both angularly and across the wing surface. This fact was accounted for in the numerical simulations.

The spectrum of *D. chrysitis* is broad, with a cutoff wavelength at approximately 500 nm. Its exact shape slightly depends on the angle between light source, wing, and detector. There is a close similarity with the spectrum of metallic gold, as shown in Fig. 2. The specular reflectance spectrum of gold is taken tabulated from Ref. [28], where it is treated as a reference standard.

Optical reflection microscopy of the *D. chrysitis* forewing reveals an almost uniform, intense golden sheen as shown in Fig. 3(a). In contrast, reflection from individual scales is yellowish, with occasional red and green bands, presented in Fig. 3(b). Overlapped scales show increased reflection and color bands, as can be observed in the same image. If observed in transmission, an individual scale in air [see Fig. 3(c)] is quite transparent, with a slight residual absorption. By immersing

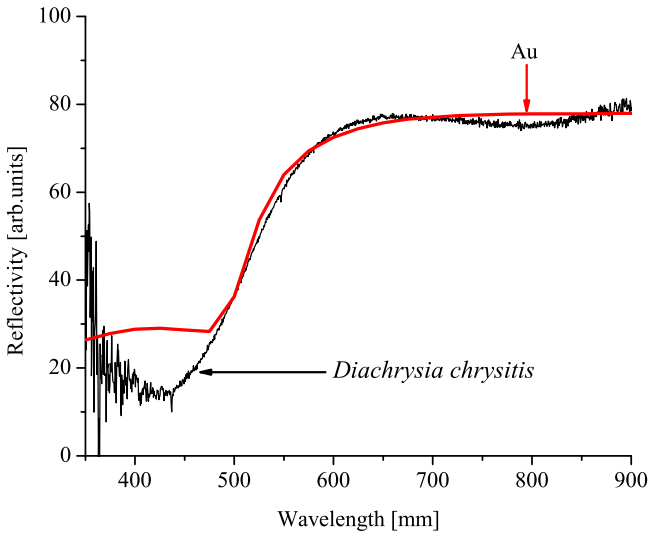

FIG. 2. Spectral reflectance of metallic gold (red curve) and golden wing patch of *D. chrysitis* forewings (black curve). Reflectance of *D. chrysitis* is scaled to emphasize the similarity with the gold.

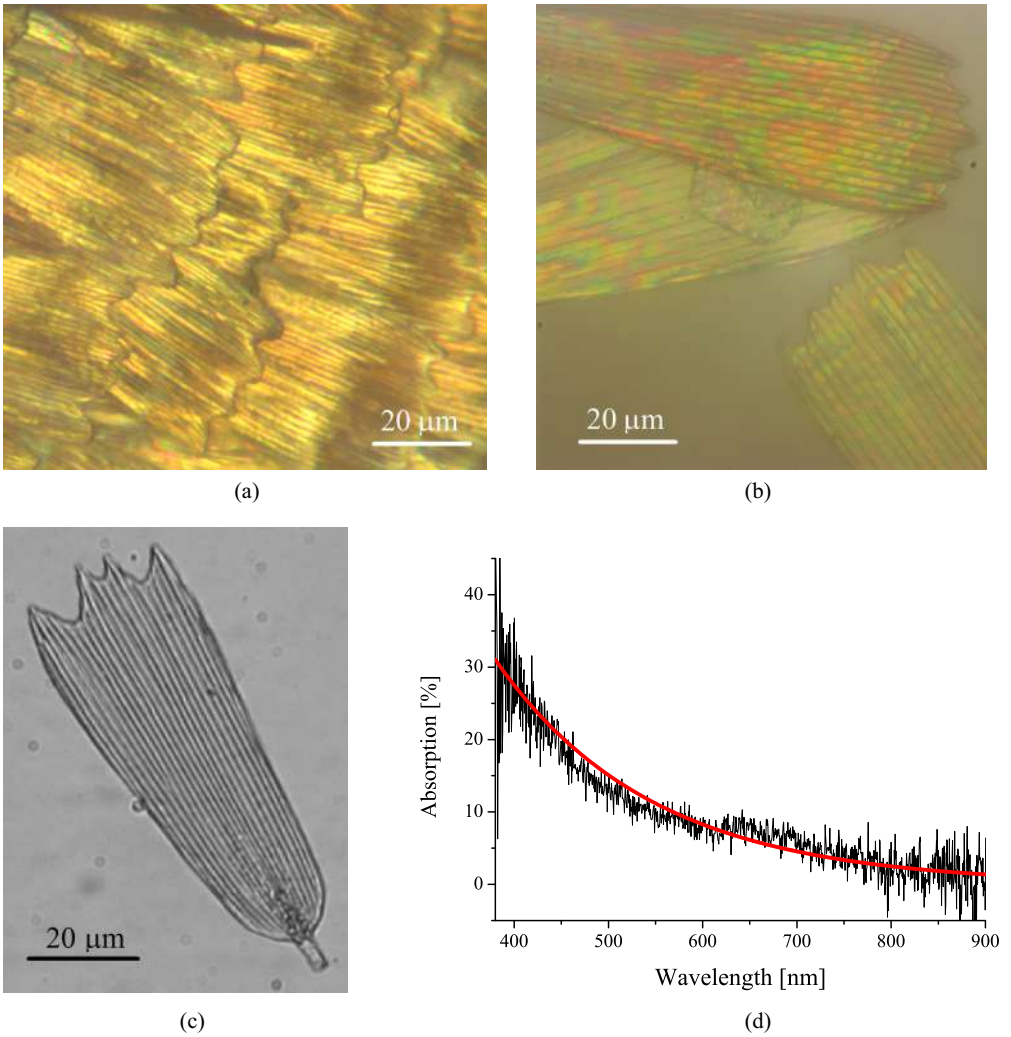

FIG. 3. Optical microscope images of *D. chrysitis*: (a) Scales on the forewing showing the uniformly golden reflection. (b) A microscope reflection image of two individual, overlapped scales. (c) A transmission image of an individual scale in air. (d) Absorption spectrum of a single scale placed in an immersion oil (black line) and the corresponding exponential fit (red line).

the scale in an index matching liquid (manufactured by Cargile, series A, with the certified refractive index 1.5700 ± 0.0002) Fresnel reflection was suppressed. We measured the absorption spectrum [Fig. 3(d)], which is very similar to that of melanin [29], showing exponential decrease from the UV to the IR part of the spectrum. We were able to estimate the value of the absorption coefficient α (or the imaginary part of the complex index of refraction $k = \alpha\lambda/4\pi$), and use it in further calculations. We have found that k ranges between 0.081 (at 380 nm) and 0.0013 (at 800 nm).

A field-emission gun scanning electron microscope (FEGSEM) was used to study the fine anatomy of the moth scales. The *D. chrysitis* forewing possesses a number of overlapping scales [as in Fig. 4(a)], but we were not able to see a difference between cover and ground scales. At higher magnification, as in Fig. 4(b), we can see that the upper lamina is ornamented with very thin lamellar ridges (separated by approximately 1.8 μm). They are connected with herringbone shaped cross ribs, which constitute a subwavelength diffraction grating with the period of roughly 150 nm. A dual wing membrane seems to be an important optical component, too. Its thickness is of the order of 500 nm and contains a number of 300-nm diameter, randomly dispersed, hemispherical protuberances [see inset in Fig. 4(a)].

Individual scales were prepared for scanning electron microscopy by the double transfer method, which was begun by detaching a scale with a low-surface-energy adhesive (adhesive layer of "Post-it" sticky note), followed by the transfer to a high-surface-energy tape (conductive carbon). By that means, the original scale orientation was preserved. Figure 5 shows one of the partially destroyed scales and its internal and external laminae structures. We see that the external side of the upper lamina (the one facing outwards) is strongly patterned, as explained above, while its internal surface is very irregular, with linear grooves directly beneath the ridges. The external side of the lower lamina (the one facing the wing membrane) is smooth, while its internal surface is completely irregular, similar to nanometer-sized "pebbles," with a diameter less than 60 nm.

We have observed a strong autofluorescence of scales, which is enough for nonlinear (NL) fluorescence microscopy. We used a nonlinear microscope for laser processing and

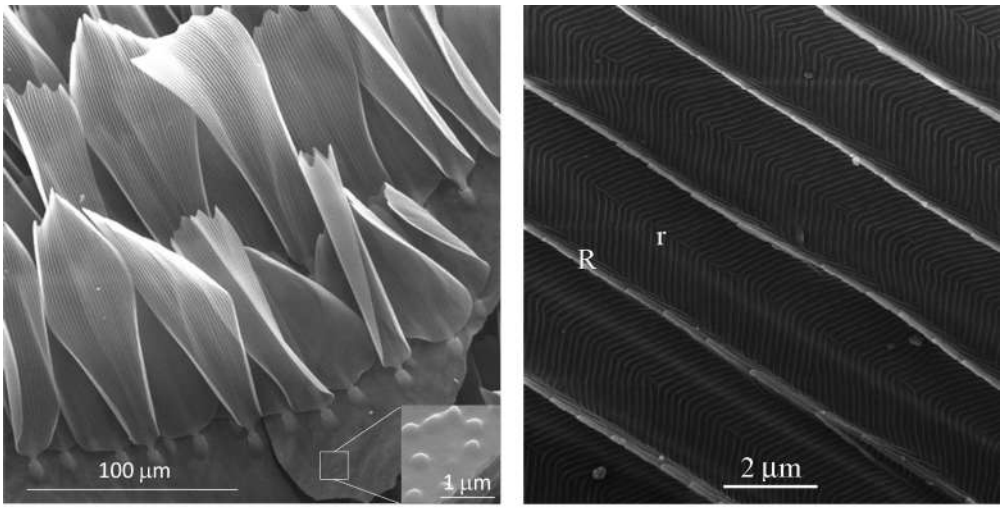

FIG. 4. (a) Scales of *D. chrysitis* in their natural position on the wing. The inset shows the enlarged part of the wing membrane with 300-nm-diameter protuberances. (b) Enlarged image of a single scale, showing lamellar ridges (R) and herringbone shaped cross ribs (r).

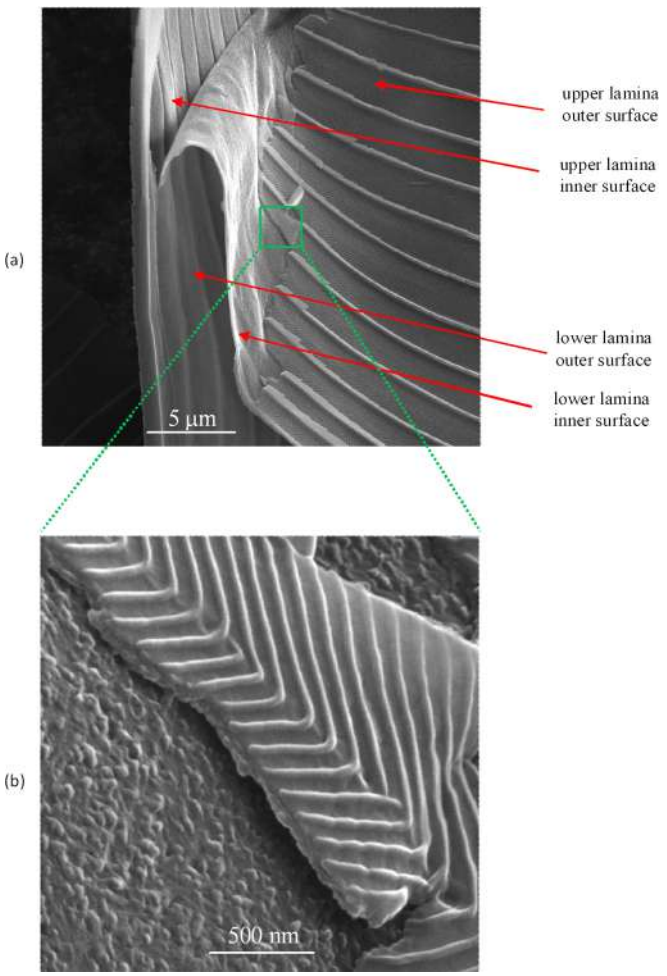

FIG. 5. FEGSEM images of a single *D. chrysitis* scale at two different magnifications. (a) This image reveals the internal and external structure of a single scale. (b) Enlarged zone of a scale showing rough internal surfaces.

cutting, too, which turned out to be a good tool for exposing otherwise hidden features. The beam power was increased above the threshold level and software was modified to enable drawing arbitrary shapes using vector images. At 840 nm and ∼100 fs pulse length we were cutting moth chitinous structures with as low as a few milliwatts of laser power. However, continuous wave (cw) radiation at the same wavelength required an order of magnitude higher power. It was interesting that the laser-cut lines were rather irregular in the case of *D. chrysitis*, in contrast to scales of other lepidopteran species, which produced clear, well defined, lines.

To further reveal the cross-sectional geometry of *D. chrysitis* moth scales, we cut them as explained above. A SEM image of a laser-cut scale is shown in Fig. 6. The internal space of the scale is not visible due to the welding of the upper and lower laminae, but we were able to estimate the thickness of the scale at 300 nm, and the height of the ridge at 400 nm. Based on the scanning electron microscope images we are able to draw a general scheme of an individual scale as presented in Fig. 7.

We emphasize that the external features of the wing scale (such as the distance between the ridges) can be measured accurately from FEGSEM images, because they are recorded at normal incidence. Other characteristics, such as laminae thickness, are more complicated to quantify due to difficulty in determining the exact relative position of the scale and the scanning electron microscope optics (see Fig. 6, where the scale is partially lifted from the substrate). In such cases, measurements were performed using external features as a reference—e.g., lamina thickness was determined at approximately 75 nm by observing that it is approximately one half of the distance between the cross ribs (150 nm). Anyway, such measurements served just as a starting point for a wing-scale model.

Variability of the moth scales is another source of uncertainty. We recorded a number of SEM images, measured relevant features at several positions, and were able to find that they vary between 15% and 20% (depending on the measured characteristics).

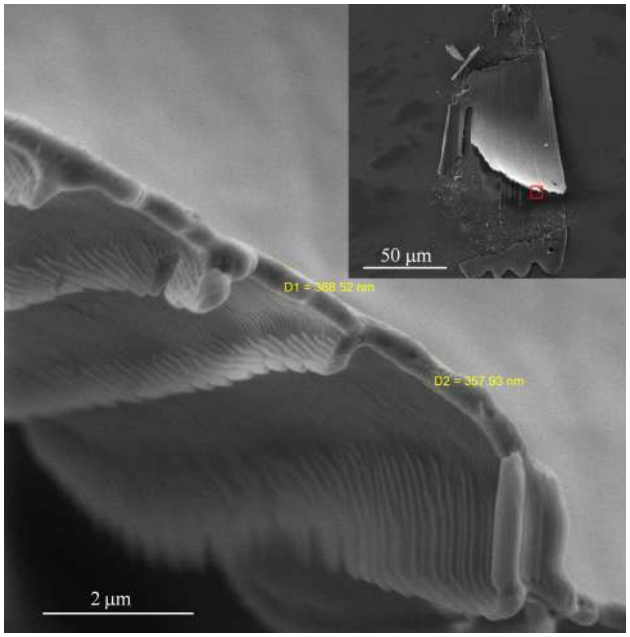

FIG. 6. A cross-sectional image of a femtosecond-laser-cut *D. chrysitis* wing scale. The image of the whole, laser-cut scale is shown in the inset.

III. OPTICAL MODELING OF THE *D. CHRYSITIS* WING SCALES

The transparency of *D. chrysitis* scales and the apparent simplicity of their internal and external structure pose a problem in explaining the golden wing color. We show that all the wing components (a double layer of scales and a wing membrane, possibly also the pigmented scales on the wing underside) work together to produce the final effect. Several features operate synergistically: slight absorbance of each scale, scattering on internal scale surfaces, interference of light within the scale, reflection of light from the wing membrane, and diffraction on the upper lamina grating.

We first demonstrate that the scattering on the internal scale surfaces leads to significant dispersal of incident light. As shown in Fig. 5, the internal scale surfaces are highly irregular, with the root mean squared (RMS) roughness estimated between 10 and 30 nm. The wavelength of the incident visible light (inside material) is much larger than the roughness and

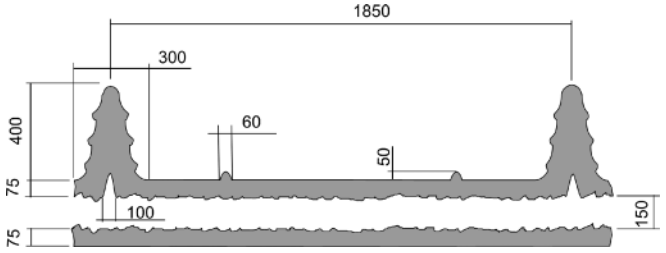

FIG. 7. A dimensional scheme of a *D. chrysitis* scale cross section. All dimensions (expressed in nanometers) are estimated from SEM images and vary across the scales. Due to the variability of features in the living world, uncertainty of all the dimensions is between 15% and 20%.

the widely used scalar surface-scattering theory [30,31] is applicable. Under these circumstances, the light is split into two parts: one, regular, propagating as if the surface is perfectly flat, and the other diffusely scattered (haze).

Quantitatively, both components are described relative to transmittance T_0 and reflectance $R_0 = 1 - T_0$ of an ideally flat surface, when Fresnel equations hold. Accordingly, the haze transmittance $T_H(\lambda)$ and reflectance $R_H(\lambda)$ of a rough surface are described by [31]

$$T_H(\lambda) = T_0\left(1 - \exp\left\{-\left[\frac{2\pi\sigma}{\lambda}(n_i\cos\phi_i - n_t\cos\phi_t)\right]^2\right\}\right), \tag{1}$$

$$R_H(\lambda) = R_0\left\{1 - \exp\left[-\left(\frac{4\pi\sigma}{\lambda}n_i\cos\phi_i\right)^2\right]\right\}, \tag{2}$$

where T_0 and R_0 are the transmittance and the reflectance of a perfectly flat surface, respectively; λ is the wavelength in vacuum; ϕ_i and ϕ_t are the angles of incidence and refraction; n_i and n_t are corresponding refractive indices; σ is the surface RMS roughness.

A simple calculation, based on Eqs. (1) and (2), shows that between 1% and 3% of incident radiation is scattered at each interface, depending on the wavelength and assuming normal angle of incidence ($\phi_I = 0$), RMS roughness $\sigma = 20$ nm, and the refractive index of chitin $n_i = 1.57$. As expected, short wavelengths are scattered more than long ones. The scattered light has a tendency to be trapped inside chitin layers, in a manner similar to textured solar cells [32]. It was shown in [33] that the local light intensity is increased by $2n^2$, and absorption by $4n^2$, where n is the refractive index. This was verified for the *D. chrysitis* moth by using the finite element method (FEM) with periodic boundary conditions, applied to the model simulating a double layer of scales, as shown in Fig. 8(a). The corresponding electromagnetic field distributions can be seen in Fig. 8(b) showing the strong electromagnetic field enhancement.

Local field enhancement due to scattering is accompanied by increased absorption as predicted by the model described in [33]. We made slight modifications to correctly describe the scales of *D. chrysitis*.

The change of the beam cross section is ignored due to the thinness of the scales. This is justified by the following arguments: Assume that the angle of divergence is $\theta = 40^\circ$ and scale laminae thickness is $D = 75$ nm; then the beam spread is defined by $2Dtg(\theta/2) = 55$ nm. This is insignificant for a beam width of approximately 7 mm, as used in our spectral measurement. The surface absorption was disregarded, too, because the residual melanin is expected to be distributed inside the laminae.

Under these assumptions, the absorption A_{int} inside the planar layer can be described by

$$A_{\text{int}} = \frac{4n^2 T_{\text{inc}}}{T_{\text{esc}} + 4n^2\alpha l}, \tag{3}$$

where α is absorption coefficient, n is the refractive index, I_{inc} is incident light intensity, l is the layer thickness, and T_{inc} is a fraction of light transmitted through the interface. T_{esc} is an

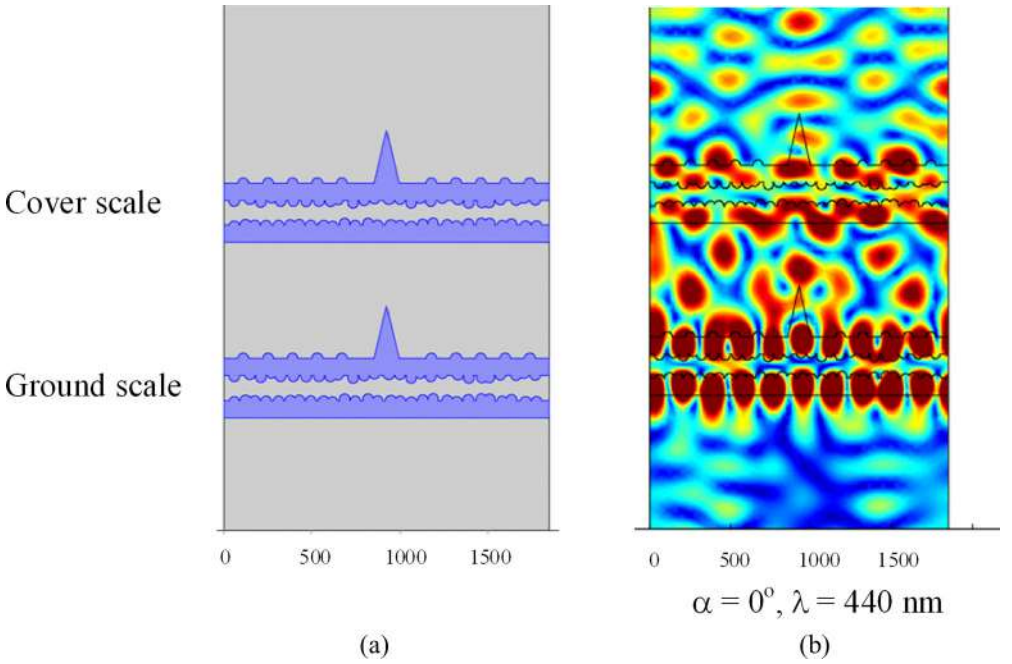

FIG. 8. (a) Geometry of the FEM model. (b) Intensity enhancement at 440 nm wavelength. The electromagnetic field is enhanced both in the ground and cover scales. Calculations were performed assuming that the angle of incidence is $\alpha = 0$ and there is no absorption.

average transmission factor of the escaping radiation, due to partial (Fresnel) transmission at the interface. According to the same model, fraction of the incident radiation escaping the layer is described by

$$F_{\text{esc}} = \frac{T_{\text{inc}} T_{\text{esc}}}{T_{\text{esc}} + 4n^2 \alpha l}. \tag{4}$$

Now we have tools to treat the problem of the golden coloration of the burnished brass moth. Its geometry includes two layers of scales and two wing membranes as shown in Fig. 9(a). It is assumed that the outside surfaces of the scales are flat, which is strictly true only for the lower lamina. The upper lamina is structured with two gratings. The coarse one will produce diffraction orders which will be treated similarly during the propagation through the scales, the only difference being the angle of incidence. The dense grating is incapable of generating any propagating modes and will not enter the calculations. The inside scale surfaces are rough with RMS roughness of 10–30 nm, and the wing membranes are treated as flat. Fresnel reflection and transmission will be taken into account at flat surfaces, while rough surfaces will also include haze in reflection and transmission as schematically shown in Fig. 9(b). In the latter case, haze $R_H(\lambda)$ and $T_H(\lambda)$ diminish Fresnel coefficients R_0 and T_0 by the amounts $R_0 R_H(\lambda)$ and $T_0 T_H(\lambda)$. The resulting transmission and reflection coefficients are described by $R_0 - R_0 R_H(\lambda)$ and $T_0 - T_0 T_H(\lambda)$.

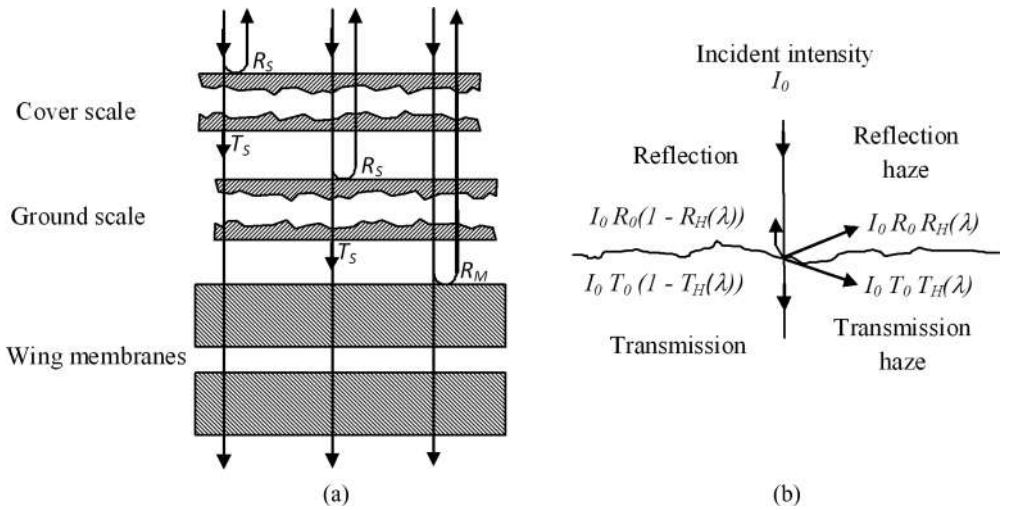

FIG. 9. (a) Geometry of the model used to simulate the wing of *D. chrysitis*. R_S and R_M are reflectance of a scale and a wing membrane, respectively. T_S is a transmittance of a single scale. (b) Reflection and transmission through the interface, as treated in a model. Incident intensity I_0 is split into four components: Fresnel reflectance (R_0), Fresnel transmittance (T_0), reflection haze (R_H), and transmission haze (T_H).

TABLE I. Numerical values of the parameters used for modeling optical reflection from *D. chrysitis* moth scales.

Parameter	Meaning	Value
N	Refractive index of chitin	1.57
α_0	Melanin absorption parameter, Eq. (5)	0.23 (1/nm)
A	Melanin absorption parameter, Eq. (5)	90 (nm)
λ_0	Melanin absorption parameter, Eq. (5)	380 (nm)
σ	RMS surface roughness	30 (nm)

The interference problem will be solved for an individual wing scale, as well as for the wing membranes, but not for the wing as a whole. This is a reasonable assumption, because the relative distances between the scales and the wing membrane are highly variable and the resulting effect is averaged across the wing surface. As a consequence, the resulting reflection spectral intensities of scales and membranes will be incoherently added.

Optical parameters of the model were estimated from the measurements performed on the scale embedded in an immersion liquid ($n = 1.57$), as described in the previous section. Therefore, the refractive index was taken to be 1.57 (consistent with the results published in [34]). According to the same study [34], the refractive index dispersion is less than 4% within the wavelength range of interest (380–900 nm) and the resulting effects were found to be insignificant. The coefficient of absorption α was modeled with an exponential function (assuming that the residual pigment is most probably melanin):

$$\alpha = \alpha_0 \exp\left(-\frac{\lambda - \lambda_0}{A}\right). \tag{5}$$

All parameters of the model are summarized in Table I.

Finding the exact solution to the multilayer interference is a problem requiring numerical tools. Here we adopt the transfer matrix method, described and used in [35] to analyze light scattering and trapping in silicon thin film solar cells. We divide incident light into two components: a scattered one, which is mostly absorbed and diffused, and an unscattered one, which interferes in wing scales and wing membranes. For the unscattered component we apply a transfer matrix method, where scattering from subwavelength rough surfaces is treated as a wavelength-dependent correction for Fresnel coefficients.

Reflection and transmission from a single scale are treated coherently using the transfer matrix method. As a result, the spectral reflectance R_S and transmittance T_S were found. Similarly, the reflection from the double wing membrane was treated coherently (with the resulting reflectance R_M). Scattering from the wing membrane was not included in calculations due to the sparsity and large dimensions of scattering inclusions (as illustrated in Fig. 4). The resulting spectrum of the wing as a whole is composed of three components: one which is reflected from the cover scales, the other reflected from the ground scales, and the final one due to the wing membranes. We combine them incoherently, because the mutual position between scales and membranes is stochastic and highly variable. The final reflected spectral distribution of the whole wing is thus

$$R = R_S + T_S R_S T_S + T_S^2 R_M T_S^2. \tag{6}$$

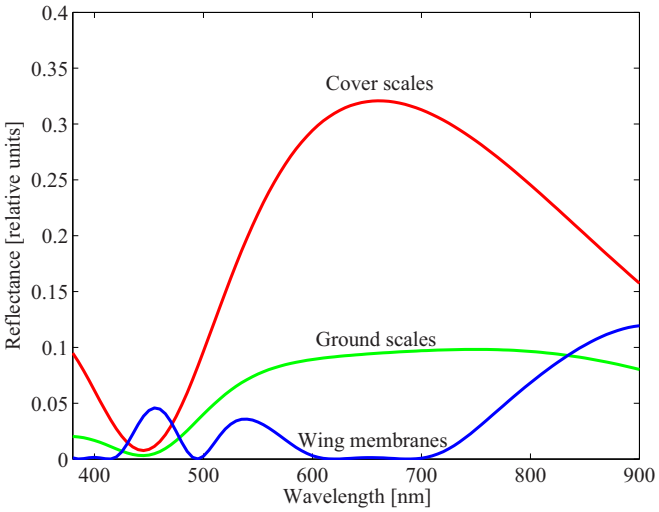

FIG. 10. Contributions of wing membranes, cover scales, and ground scales to the resulting wing spectrum. They are calculated using the transfer matrix method and normalized to the intensity of the incident light before being transmitted through the layers.

The first term corresponds to the reflection from the cover scale, the second to the transmission through the cover scale, followed by the reflection from the ground scale and return path through the cover scale. The third term describes transmission through the cover and ground scales, followed by the reflection from the wing membrane, and return path through both layers of the scales. The calculated contribution of each term to the final spectrum is shown in Fig. 10 (normalized to the intensity of light before being transmitted through the layers).

Spectral contributions of wing components significantly depend on their geometry, i.e., scale laminae and wing membrane thicknesses. For some combination of dimensional parameters, even a single scale can quite faithfully reproduce an experimentally recorded spectrum (as in Fig. 11). However, there are slight modulations within the whole spectral range, due to thin film interference effects. They disappear when spatial and angular averaging is included, as further explained. As explained above, losses are much higher inside the blue-UV spectral range, as can be seen in Fig. 11. According to Eqs. (3) and (4), most of the light energy is absorbed, and the rest of the radiation is scattered. It is interesting to note that a significant amount of radiation is transmitted through the wing membranes (green curve in Fig. 11). However, the UV component of transmitted radiation is efficiently absorbed by the dark, pigmented scales, on the wing underside.

There is an important word of caution. In order to get a consistently golden wing color, the dimensional and optical parameters of each individual scale should be kept within quite tight tolerances—a task completely impossible in the living world. It is more realistic to expect significant variability of all the parameters. Thus they were varied in our simulations (according to the normal distribution) within $\pm 15\%$ of the values producing fit in Fig. 11. The angle of incidence was also

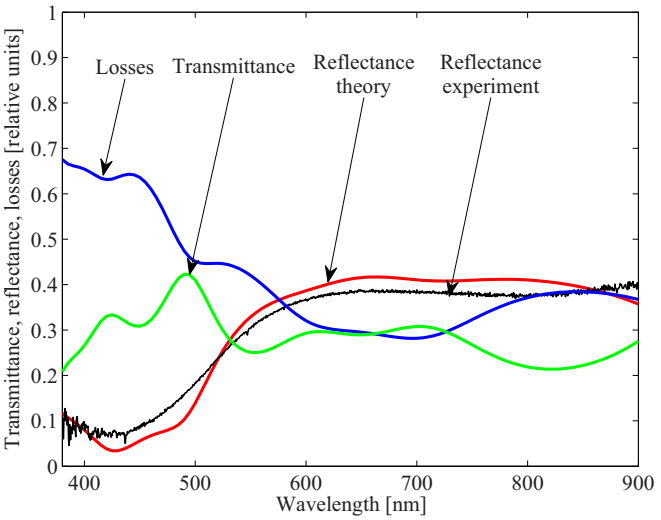

FIG. 11. A spectral reflectivity (red curve) of a *D. chrysitis* moth wing, calculated by the transfer matrix method is shown. The corresponding experimental curve (black curve) is added for reference. Losses (due to scattering and absorption, blue curve) and the wing transmittance (green curve) are displayed, too.

allowed to fluctuate within $\pm 20^\circ$, which imitates variability of scale orientations.

As a result, 100 different spectra were calculated (for clarity, only 25 of them are displayed in Fig. 12 as light blue curves). They were consequently averaged, in agreement with our experimental procedure where the light is collected from the wing area and within an angular range (the resulting curve is shown in blue). By comparing the calculated spectrum with the experimentally recorded one (red curve in the same figure), agreement appears remarkably good, except for the radiation above 800 nm.

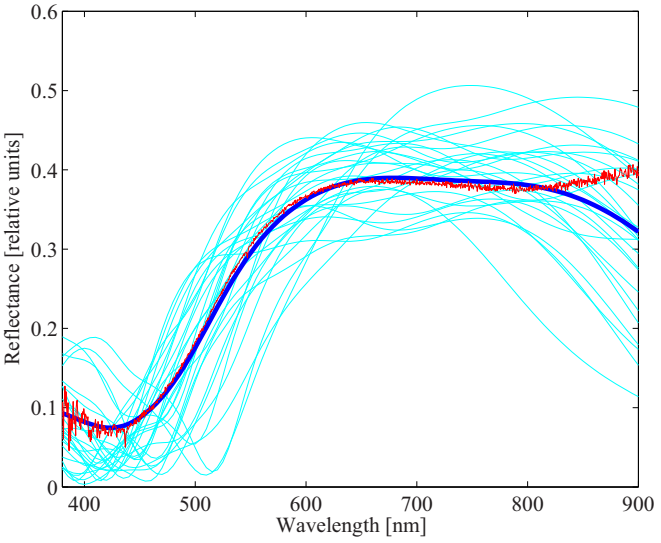

FIG. 12. Spectral averaging of light reflected from *D. chrysitis* wing, calculated by the transfer matrix method which includes scattering and local field enhancement. Light blue curves are individual spectra, blue curve is the averaged spectrum, and the red curve is the experimentally recorded spectrum.

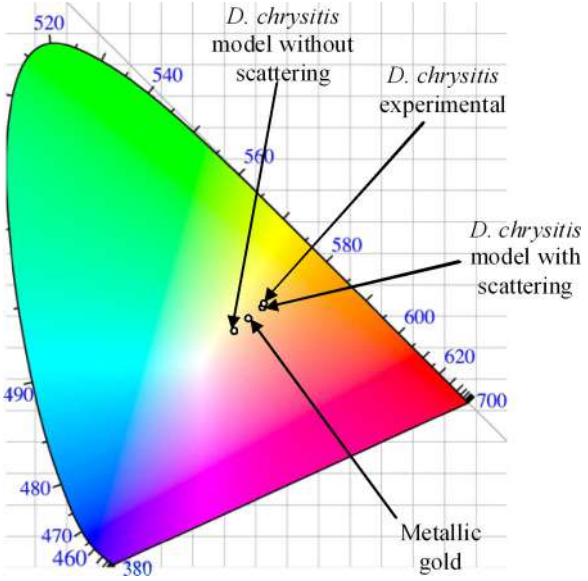

FIG. 13. CIE color coordinates of metallic gold and *D. chrysitis* forewing golden patches, with and without scattering.

The final shape of the spectrum is influenced by the layer thicknesses and the RMS surface roughness. They collectively influence the final calculated spectrum, but in general terms we have observed that increased thickness shifts the spectrum towards the red, while increased roughness depletes the blue part of the spectrum and decreases overall reflectivity.

All the computations are based on a transfer-matrix code, developed in [36] (declared free to use and made public at the URL provided therein). The program was modified by including scattering and local field enhancement effects [as defined by Eqs. (1)–(4)].

IV. DISCUSSION AND CONCLUSIONS

In contrast to most other lepidopteran species, each and every wing structure of *D. chrysitis* plays a certain role in iridescent color production. The same goes for the optical mechanisms—interference, diffraction, absorption, and surface scattering. They seem to be intricately intertwined in a synergistic manner—by omitting any of them, a significant change of the spectral profile would result. To demonstrate the fact, we calculated the resulting spectrum without taking into account scattering-enhanced absorption. As expected, reflection in the UV-blue spectral range is not attenuated. The corresponding CIE color coordinate testifies that the resulting color is whitish, as presented on a CIE 1931 diagram (Fig. 13). For reference, we have also displayed points corresponding to metallic gold, experimentally recorded spectrum, and full simulation of *D. chrysitis* wing. It is obvious that without scattering, the color coordinate would approach the achromatic center of the diagram—i.e., the wing will have only a slight coloration. It is interesting to note that the moth wing looks "yellower" than the gold.

As noted before, scattering stimulates confinement of light and increases the intensity by the $2n^2$ factor. It seems that the ground scale layer further amplifies the confinement [see Fig. 8(b)]. One possible explanation is that the cover scales

diffuse the incoming light, while the ground scales additionally disperse it and make it amenable for wave guiding within the layer.

Angular variability of *D. chrysitis* wing coloration is noticeable, and the golden color is observable within the $\pm 20°$ from the specular direction. Beyond that, the color abruptly changes from golden to brown-gray. However, within the specular range, dependence of the reflected spectrum is slight for several reasons. On one hand, it results from irregular internal surfaces of the scale laminae and irregular mutual position of scales in ground and cover layers. The other reason is that the reflectivity at air-chitin interfaces is almost constant between 0° and 30°, as predicted by Fresnel equations. Therefore, the overall shape of the spectrum is not altered, but slightly shifted with the angle of incidence. Coarse diffraction grating on the upper lamina additionally diminishes angular dependence. From whichever direction light enters the scale, at least one of the diffraction orders is being reflected. This is what gives the notable stability of the optical effect with respect to the illumination direction (within the stated angular range).

We have not observed polarization sensitivity of the described reflection spectra, even though it certainly exists at the single wing-scale level. If observed macroscopically, across the whole wing, polarization effects cancel out due to strong variability of individual scale orientations with respect to incident radiation.

It is also interesting to note that the scales from brown-gray and golden areas of the wing have very similar morphology if observed under the scanning electron microscope. The most important difference is optical: while the golden area scales are almost transparent, the others contain a significant amount of absorbing pigment which leads to suppression of the specular component in the brown wing regions. Also, the brown scales are flatter, while the golden ones are slightly curled.

Calculations, according to Eqs. (3) and (4), have shown that approximately 70% of incoming radiation at 380 nm is scattered. Forty percent of the scattered component is absorbed, while the rest is uniformly dispersed all over the full solid angle. At the other end of the spectrum (above 800 nm), only 20% of light is scattered, without being absorbed to any significant extent. As a whole, the spectrum of unabsorbed light is quite flat from UV to IR. Its contribution to the wing reflection is really small, because it is dispersed over the 4π solid angle, while the reflected light is concentrated around the specular direction.

A dual wing membrane is densely covered with nanosized spherical inclusions, conveniently situated, just beneath the scales. It seems that this could be an additional mechanism to scatter light back through the layer of scales. Transmission of the membranes is high and light further propagates to underside scales. They are gray, most probably due to melanin, which will further absorb the UV-blue part of the spectrum. In the red-infrared range, melanin absorbance is insignificant, and scales are again capable of reflecting light back through all the previous layers. This might account for the increased reflectivity in the infrared, which is not predicted by the theory described in the previous section.

Insects with golden body parts are rare and interesting from the biological point of view. The roles of the golden color may be diverse and are related mostly to possible defense mechanisms. We suppose that in *D. chrysitis* the golden forewing patches may appear to predators as warning and/or they can facilitate the conspecific recognition [15].

To summarize: All the structures—cover and ground scales, wing membranes, and underside wing scales—contribute to the golden wing color of the burnished brass moth. Interference, scattering, and absorption enhancement are optical mechanisms responsible for the effect. In short, interference on the scales produces a broad reflection spectrum with a peak in the green part of the spectrum. The blue part of the spectrum is absorbed due to scattering-enhanced absorption on a residual pigment. The red part of the spectrum is transmitted to the wing membrane, where it reflects, goes back through the scales, and combines with the reflection from the scales. The resulting spectrum is strongly attenuated below 520 nm, being almost flat up to 800 nm. The forewings of the *D. chrysitis* moth seem to be a remarkable, finely tuned, optical filter.

ACKNOWLEDGMENTS

This research was supported by Projects No. ON171038, No. III45016, and No. ON173038 funded by the Ministry of Education, Science and Technological Development of the Republic of Serbia.

[1] J. Sun, B. Bhushan, and J. Tong, Structural coloration in nature, RSC Adv. **3**, 14862 (2013).

[2] J. Zi, B. Dong, T. Zhan, and X. Liu, in *Bioinspiration: From Nano to Micro Scales*, edited by X. Y. Liu (Springer, Berlin, 2012), pp. 275–329.

[3] T. Starkey and P. Vukusic, Light manipulation principles in biological photonic systems, Nanophotonics **2**, 289 (2013).

[4] N. N. Shi, C.-C. Tsai, F. Camino, G. D. Bernard, N. Yu, and R. Wehner, Keeping cool: Enhanced optical reflection and radiative heat dissipation in Saharan silver ants, Science **349**, 298 (2015).

[5] O. Karthaus, *Biomimetics in Photonics* (CRC Press, Boca Raton, FL, 2013).

[6] Z. Gan, M. D. Turner, and M. Gu, Biomimetic gyroid nanostructures exceeding their natural origins, Sci. Adv. **2**, e1600084 (2016).

[7] M. F. Land, The physics and biology of animal reflectors, Prog. Biophys. Mol. Biol. **24**, 75 (1972).

[8] S. Yoshioka, T. Nakano, Y. Nozue, and S. Kinoshita, Coloration using higher order optical interference in the wing pattern of the Madagascan sunset moth, J. R. Soc., Interface **5**, 457 (2008).

[9] D. J. Brink, J. E. Smith, M. E. Lee, and A. Möller, Optical diffraction by the microstructure of the wing of a moth, Appl. Opt. **34**, 6049 (1995).

[10] M. Hernández-Jiménez, D. E. Azofeifa, E. Libby, C. Barboza-Aguilar, Á. Solís, L. Arce-Marenco, I. García-Aguilar, A. Hernández, and W. E. Vargas, Qualitative correlation between structural chirality through the cuticle of *Chrysina aurigans* scarabs and left-handed circular polarization of the reflected light, Opt. Mater. Express **4**, 2632 (2014).

[11] F. Liu, B. Q. Dong, X. H. Liu, Y. M. Zheng, and J. Zi, Structural color change in longhorn beetles *Tmesisternus isabellae*, Opt. Express **17**, 16183 (2009).

[12] J. P. Vigneron, J. M. Pasteels, D. M. Windsor, Z. Vértesy, M. Rassart, T. Seldrum, J. Dumont, O. Deparis, V. Lousse, L. P. Biró, D. Ertz, and V. Welch, Switchable reflector in the Panamanian tortoise beetle *Charidotella egregia* (Chrysomelidae: Cassidinae), Phys. Rev. E **76**, 031907 (2007).

[13] M. Rothschild, B. Gardiner, and R. Mummery, The role of carotenoids in the "golden glance" of danaid pupae (Insecta: Lepidoptera), J. Zool. **186**, 351 (1978).

[14] R. L. Taylor, The metallic gold spots on the pupa of the monarch butterfly, Entomol. News **75**, 253 (1964).

[15] A. C. Neville, Metallic gold and silver colours in some insect cuticles, J. Insect Physiol. **23**, 1267 (1977).

[16] R. A. Steinbrecht, W. Mohren, H. K. Pulker, and D. Schneider, Cuticular interference reflectors in the golden pupae of danaine butterflies, Proc. R. Soc. London, Ser. B **226**, 367 (1985).

[17] B. D. Wilts, H. L. Leertouwer, and D. G. Stavenga, Imaging scatterometry and microspectrophotometry of lycaenid butterfly wing scales with perforated multilayers, J. R. Soc., Interface **6**, S185 (2009).

[18] N. I. Morehouse, P. Vukusic, and R. Rutowski, Pterin pigment granules are responsible for both broadband light scattering and wavelength selective absorption in the wing scales of pierid butterflies, Proc. R. Soc. London, Ser. B **274**, 359 (2007).

[19] D. G. Stavenga, S. Stowe, K. Siebke, J. Zeil, and K. Arikawa, Butterfly wing colours: Scale beads make white pierid wings brighter, Proc. R. Soc. London, Ser. B **271**, 1577 (2004).

[20] S. M. Luke, P. Vukusic, and B. Hallam, Measuring and modelling optical scattering and the colour quality of white pierid butterfly scales, Opt. Express **17**, 14729 (2009).

[21] X. Chen, C. Wang, E. Baker, and C. Cun, Numerical and experimental investigation of light trapping effect of nanostructured diatom frustules, Sci. Rep. **5**, 11977 (2015).

[22] A. Hille, M. A. Miller, and S. Erlacher, DNA sequence variation at the mitochondrial cytochrome oxidase I subunit among pheromotypes of the sibling taxa *Diachrysia chrysitis* and *D. tutti* (Lepidoptera: Noctuidae), Zool. Scr. **34**, 49 (2005).

[23] A. Seitz, *The Macrolepidoptera of the World. A Systematic Description of the Known Macrolepidoptera. I Section. 3. Volume: The Palearctic Noctuidae. Plates* (Verlag des Seitz'schen Werkes, Stuttgart, 1914).

[24] G. S. Robinson, P. R. Ackery, I. J. Kitching, G. W. Beccalon, and L. M. Hernández, *HOSTS–a Database of the World's Lepidopteran Hostplant* (Natural History Museum, London, 2010).

[25] D. V. Stojanović and S. B. Ćurčić, The diversity of noctuid moths (Lepidoptera: Noctuidae) in Serbia, Acta Zool. Bulg. **63**, 47 (2011).

[26] M. Boardman, R. R. Askew, and L. M. Cook, Experiments on resting site selection by nocturnal moths, J. Zool. **172**, 343 (1974).

[27] I. Svensson, P. Douwes, and B. O. Stille, Are *Diachrysia chrysitis* (L.) and *D. tutti* (Kostrowicki) different species? (Lepidoptera: Noctuidae), Insect Syst. Evol. **20**, 15 (1989).

[28] A. D. Rakic, A. B. Djurisic, J. M. Elazar, and M. L. Majewski, Optical properties of metallic films for vertical-cavity optoelectronic devices, Appl. Opt. **37**, 5271 (1998).

[29] D. G. Stavenga, H. L. Leertouwer, T. Hariyama, H. A. De Raedt, and B. D. Wilts, Sexual dichromatism of the damselfly *Calopteryx japonica* caused by a melanin-chitin multilayer in the male wing veins, PLoS One **7**, e49743 (2012).

[30] H. Davies, The reflection of electromagnetic waves from rough surface, Proc. IEE-Part IV: Inst. Monogr. **101**, 209 (1954).

[31] D. Domine, F.-J. Haug, C. Battaglia, and C. Ballif, Modeling of light scattering from micro- and nanotextured surfaces, J. Appl. Phys. **107**, 044504 (2010).

[32] Y. A. Akimov, W. S. Koh, S. Y. Sian, and S. Ren, Nanoparticle-enhanced thin film solar cells: Metallic or dielectric nanoparticles? Appl. Phys. Lett. **96**, 073111 (2010).

[33] E. Yablonovich and G. D. Cody, Intensity enhancement in textured optical sheets for solar cells, IEEE Trans. Electron Devices **29**, 300 (1982).

[34] H. L. Leertouwer, B. D. Wilts, and D. G. Stavenga, Refractive index and dispersion of butterfly chitin and bird keratin measured by polarizing interference microscopy, Opt. Express **19**, 24061 (2011).

[35] J. Springer, A. Porube, and M. Vanacek, Improved three-dimensional optical model for thin film silicon solar cells, J. Appl. Phys. **96**, 5329 (2004).

[36] J. Junesch, T. Sannomiya, and A. B. Dahlin, Optical properties of nanohole arrays in metal-dielectric double films prepared by mask-on-metal colloidal lithography, ACS Nano **6**, 10405 (2012). Transfer matrix code can be found in http://adahlin.com/onewebmedia/TransferMatrix3.m.

Optical and Quantum Electronics (2022) 54:523
https://doi.org/10.1007/s11082-022-03885-4

Luminescence thermometry based on Y_2O_2S:Er,Yb nanophosphor

D. Sevic[1] · M. S. Rabasovic[1] · J. Križan[2] · S. Savic-Sevic[1] · B. P. Marinkovic[1] · M. G. Nikolic[1]

Received: 14 October 2021 / Accepted: 7 June 2022 / Published online: 13 July 2022
© The Author(s), under exclusive licence to Springer Science+Business Media, LLC, part of Springer Nature 2022

Abstract
We present possibility analysis of using Y_2O_2S:Er,Yb for temperature sensing. Material samples were obtained by solution combustion method. We have used pulsed laser diode excitation at 980 nm. Our analysis is based on time resolved luminescence spectra acquired by a streak camera. Intensity ratios of prominent luminescence peaks were used for determining the temperature sensing curves. We compare the synthesized Y_2O_2S:Er,Yb material with other thermophosphors, showing its usefulness for temperature measurements up to 620 K.

Keywords Photoluminescence · Thermographic phosphor · Laser spectroscopy · Combustion synthesis

1 Introduction

The temperature dependency of luminescence of many phosphor materials is often used for contactless temperature measurements. Basically, there are three commonly used techniques of temperature sensing using thermographic phosphors: peak intensity ratio, lifetime and rise time of luminescence. The techniques were comparatively analyzed by us using the yttrium based thermophosphor (Sevic et al. 2020 A). The luminescence intensity ratio (LIR) is the most commonly used temperature sensing method for low temperature ranges. Originally, it was based on calculating the optical emission intensity variations of thermally coupled transitions. Energy gap less than 2000 cm^{-1} is considered as the condition

This article is part of the Topical Collection on Photonics: Current Challenges and Emerging Applications, Guest edited by Jelena Radovanovic, Dragan Indjin, Maja Nesic, Nikola Vukovic and Milena Milosevic.

✉ D. Sevic
sevic@ipb.ac.rs

[1] Institute of Physics Belgrade, University of Belgrade, Beograd, Serbia

[2] AMI d.o.o, Ptuj, Slovenia

for thermal coupling of transitions. In this case, the LIR curve is usually fitted using the supposition that both the states share the electronic population according to the Boltzman distribution. However, the LIR technique has been generalized to other intensity ratios; for example, the host luminescence, or any other luminescence peak could be used as reference signal for LIR calculations. In these cases, "Boltzmann fit" would be misleading in a sense that estimated energy gap is not real. However, any (usually exponential, but often linear or any other) fit will do the job of determining the temperature sensing curve; keeping in mind that parameters of fit do not necessarily provide any insight into physical model of the system. Here, we will use both the "Boltzmann fit", for intensity ratio of luminescence peaks at 528 and 555 nm; and the exponential fit for intensity ratio of luminescence peaks at 528 and 675 nm.

The aim of this study is the analysis of potentials of using the $Y_2O_2S:Er^{3+},Yb^{3+}$ for temperature measurements. We compare it with other thermophosphors, both down- and up-converting.

The use of downconverting materials as thermophosphors has been analyzed for some time (Goss et al. 1989; Feist et al. 1999; Feist et Heyes 2000; Heyes 2009; Cates et al. 2002; Eldridge et al. 2012). There are also many review papers (Allison et al. 1997; Alden et al. 2011; Brites et al. 2012; Jaque and Vetrone 2012; Khalid and Kontis 2008).

Upconverting (UC) materials are studied, between other reasons, also because their characteristics are more appropriate for biomedical applications (Ang et al. 2011). Research of remote temperature measurements and other applications of UC materials doped with Er,Yb could be found in (Zhao et al. 2020; Gavrilovic et al. 2014; Gavrilovic et al. 2016; Lojpur et al. 2013; Li et al. 2017, Li et al. 2016; Li et al. 2016; Avram et al. 2018; Tian et al. 2015; Du et al. 2017; Du et al. 2018; Dong et al. 2007; Xu et al. 2012; Kumar et al. 2012; Liu et al. 2016; Santos et al. 1999; Manzani et al. 2017; Singh et al. 2009; Wang et al. 2014; Krizan et al. 2012, Sevic et al. 2020B). Many more references about thermophosphors are listed in Table 1, section Results and discussion. Recent comprehensive analysis of luminescence intensity ratio thermometry with Er^{3+} is provided in (Ciric et al. 2021).

To the best of our knowledge, results of the analysis of luminescence temperature dependence of the Y_2O_2S host doped with Er,Yb were not published so far.

2 Experimental procedures

The Y_2O_2S:Er,Yb nano phosphor was prepared by Solution Combustion Synthesis (SCS) method as described in (Krizan et al. 2014). Stoichiometric quantities of starting chemicals $Y(NO_3)_3*6H_2O$, CH_4N_2S, $Er(NO_3)_3*5H_2O$ and $Yb(NO_3)_3*5H_2O$ with the high purity were chosen to obtain the Er concentration of 2.0 at% and Yb concentration of 4 at% in Y_2O_2S:Er,Yb ($Y_{1.88}O_2S:Er_{0.04}$ $Yb_{0.08}$). Starting chemicals were combined with the urea which was used as organic fuel. So prepared starting reagents were combusted with the flame burner at approximately 500 °C. Intensive exothermic reaction yielded voluminous foamy pink powder. In the second step the product was sintered at 1300 °C for 2 h.

For excitation of $Y_2O_2S:Er^{3+},Yb^{3+}$ nano phosphor we have used pulsed laser excitation at 980 nm. The spectral data analyzed here were acquired using the streak camera system (Sevic et al. 2020 A; Sevic et al. 2020B; Vlasic et al. 2018).

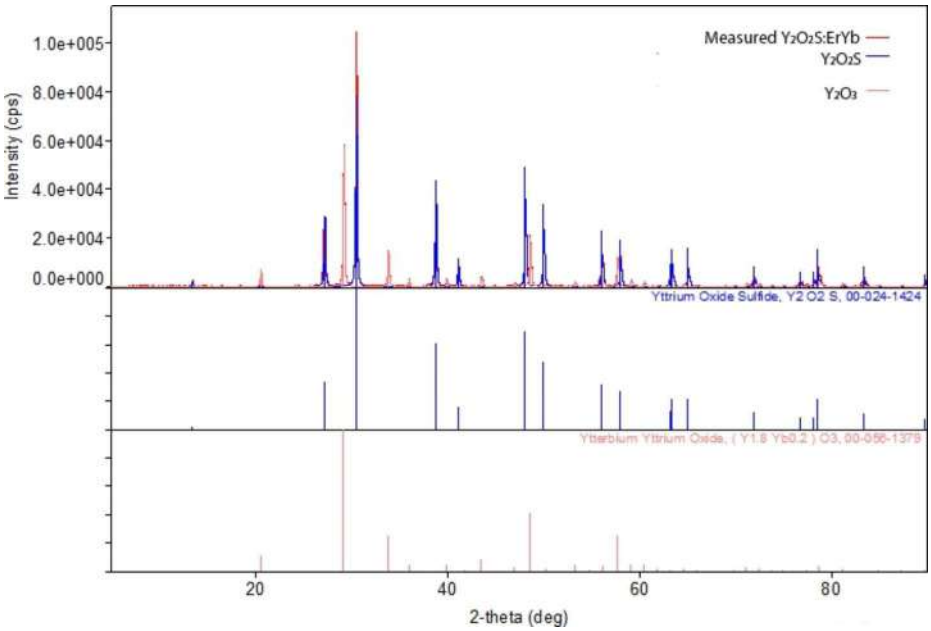

Fig. 1 XRD pattern of the synthesized $Y_2O_2S:Er^{3+},Yb^{3+}$

A high resolution scanning electron microscope (SEM) equipped with a high brightness Schottky Field Emission gun (FEGSEM, TESCAN) operating at 4 kV was used to check the structure of studied nano phosphor.

3 Results and discussion

XRD pattern of the synthesized $Y_2O_2S:Er^{3+},Yb^{3+}$ nano material is shown in Fig. 1. Observed peaks show that, beside the wanted yttrium oxide sulfide crystals, the sample contains also ytterbium yttrium oxide. The average grain size was estimated by the Williamson-Hall method, as about 37.4 nm.

The representative SEM image of the synthesized $Y_2O_2S:Er^{3+},Yb^{3+}$ nano material, see Fig. 2, shows the agglomerated grains and particles with dimensions from 30 nm to over 100 nm.

Integrated–in-time luminescence spectra of $Y_2O_2S:Er^{3+},Yb^{3+}$ at several temperatures are shown in Fig. 3. Inset shows time-resolved luminescence spectra of $Y_2O_2S:Er^{3+},Yb^{3+}$ at two temperatures. For temperatures above 620 K the measured signal gets weak and impractical for reliable analysis, so these spectra are not presented here. The emission band centered at 528 nm originates from $^2H_{11/2} \rightarrow {}^4I_{15/2}$ transition, the emission band around 555 nm originates from to $^4S_{3/2} \rightarrow {}^4I_{15/2}$ transition, and the emission bands around 675 nm originates from $^4F_{9/2} \rightarrow {}^4I_{15/2}$ transition of Er^{3+} ion. It is easily seen that intensity ratios between luminescence peaks are temperature dependent.

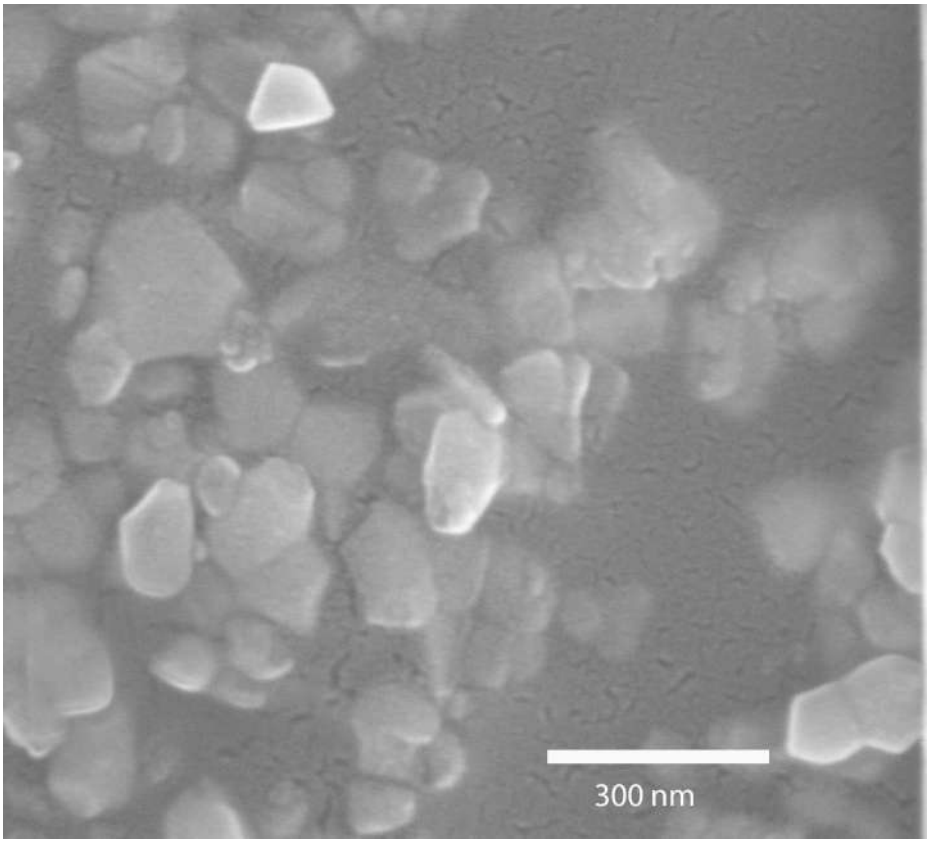

Fig. 2 SEM image of the synthesized $Y_2O_2S:Er^{3+},Yb^{3+}$ nano material

Taking into account the spectral responses and time durations of luminescence of erbium transitions shown in Fig. 3, we propose the schematic view of $Y_2O_2S:Er^{3+},Yb^{3+}$ energy transfer processes presented in Fig. 4.

The detailed explanation energy transfer for $Y_2O_2S:Er^{3+},Yb^{3+}$ material is provided in (Kumar et al. 2012). The optical emission of this material can be explained on the basis of various processes such as two photon absorption (TPA), excited state absorption (ESA) and energy transfer (ET). TPA is a nonlinear process where the visible photons are created by the simultaneous absorption of two photons and mediated through a real or virtual intermediate level. TPA occurs when excitation light sources have high enough power to create virtual intermediate levels in materials with high TPA cross section.

The $^4I_{11/2}$ level is excited by 980 nm directly (ET) through Er^{3+} or through Yb^{3+} excitation photons. Furthermore, the populated $^4I_{11/2}$ level is excited to the $^4F_{7/2}$ state by ESA of a second photon. The two photon process that populate the $^4F_{7/2}$ level is so efficient that it can give very efficient green emission transitions at 528 nm from $^2H_{11/2}$ level due to the fast multi-phonon non-radiative decay of $^4F_{7/2}$ level to $^2H_{11/2}$. Because of several closely spaced levels in between $^2H_{11/2}$ and $^4S_{3/2}$, multi-phonon relaxation results in decaying the $^2H_{11/2}$

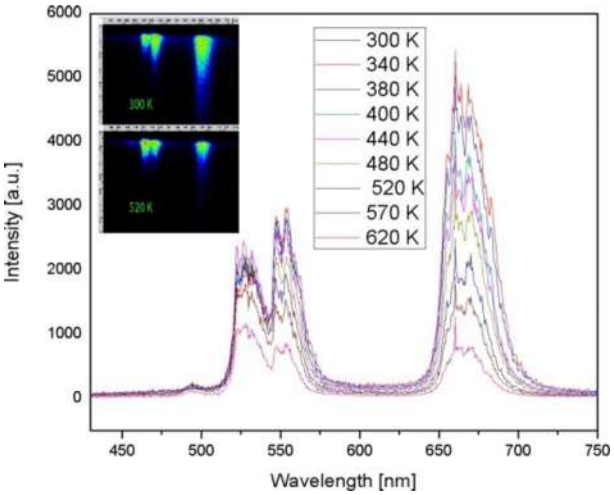

Fig. 3 Luminescence spectra of $Y_2O_2S:Er^{3+},Yb^{3+}$ at several temperatures. Pulsed laser diode excitation is at 980 nm. The time-resolved luminescence spectra at temperatures of 300 and 520 K are shown in inset

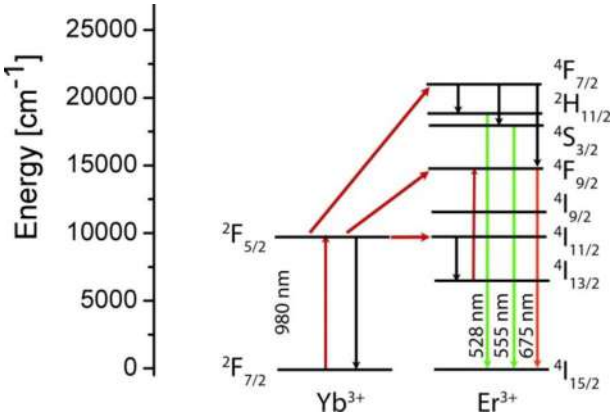

Fig. 4 Schematic view of $Y_2O_2S:Er^{3+},Yb^{3+}$ energy transfer processes

level to $^4S_{3/2}$ yielding the emission band at 555 nm. Part of the population decaying to the $^4F_{9/2}$ level can result in the red emission at 675 nm through the $^4F_{9/2}$ to $^4I_{15/2}$ transition.

To obtain temperature sensing calibration curve we fitted ratio of intensities of two peaks, at 528 and 555 nm using "Boltzmann fit", (Brites et al. 2012; Jaque and Vetrone 2012; Đačanin et al. 2014; Nikolic et al. 2018; Lojpur et al. 2016; Sevic et al. 2020B):

$$IR = \frac{I_{528}}{I_{555}} = A + C\exp\left(-\frac{\Delta E}{kT}\right) \quad (1)$$

where k is the Boltzmann constant, k=0.695 034 76(63) cm^{-1} K^{-1} and ΔE is the energy gap between two excited levels.

The temperature sensing calibration curve determined by intensity ratio of two luminescence peaks, at 528 and 555 nm and calculated relative sensitivity of Y_2O_2S:Er,Yb are shown in Fig. 5. It could be seen that the relative sensitivity is relatively small, between 0.215% K^{-1} and 0.286% K^{-1}. Estimated value of the energy gap (ΔE=943 cm^{-1}) is some-

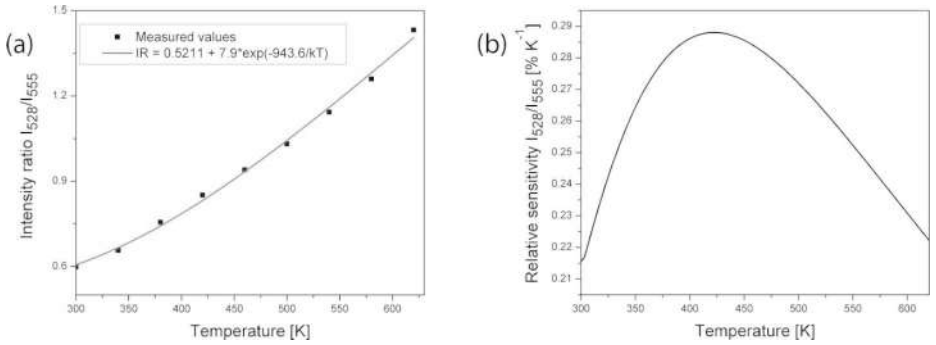

Fig. 5 (a) Temperature sensing calibration curve of Y_2O_2S:Er,Yb, using intensity ratio of two Er emission lines, at 528 and 555 nm. Experimental points are denoted by black squares and fitted temperature calibration curve is denoted by red line. (b) Relative sensitivity curve as the function of temperature of Y_2O_2S:Er,Yb

how larger than expected for this transition (Sevic et al. 2020B; Li et al. 2016; Li et al. 2016; Avram et al. 2018; Du et al. 2017; Du et al. 2018; Dong et al. 2007; Xu et al. 2012; Liu et al. 2016; Santos et al. 1999; Wang et al. 2015; Manzani et al. 2017; Singh et al. 2009). However, it roughly corresponds to calculated energy gap between 528 and 555 nm. It seemed to us that other effects, beside thermalization, could play role in temperature dependence of analyzed Y_2O_2S:Er,Yb. So, we also tried to use other peaks for calculating the intensity ratios. The best result was obtained by using peaks at 528 and 675 nm.

For calculating the ratio between peaks at 528 and 675 nm, which are not thermally coupled, we have used general exponential fit:

$$IR = \frac{I_{528}}{I_{675}} = A + C\exp\left(\frac{T}{B}\right) \tag{2}$$

Figure 6 shows the fitted intensity ratio of peaks at 528 and 675 nm and corresponding calculated relative sensitivity of Y_2O_2S:Er,Yb. It could be seen that the relative sensitivity is fairly constant, between 0.512% K^{-1} and 0.55% K^{-1}. Although this result is definitely not superior to other thermophosphors, it shows that analyzed YO_2S:Er,Yb could be used for temperature measurements. Table 1. provides comparison of YO_2S:Er,Yb with other thermophosphors, analyzed by us or used by us for comparisons in our previous papers. All data correspond to intensity ratio method.

For intensity ratio method, the relative sensitivity could be estimated theoretically, based on energy gap between transitions, by (Ciric et al. 2021):

$$Sr\,(T) = \frac{\Delta E}{kT^2} \times 100\% \tag{3}$$

Calculating this equation for 528 and 555 nm gives, for 300 K, the value of about 1.2. So, it is much higher than relative sensitivity shown in Fig. 5. However, many other Er,Yb phosphors also have relative sensitivities smaller than predicted by Eq. (3). In our case, we

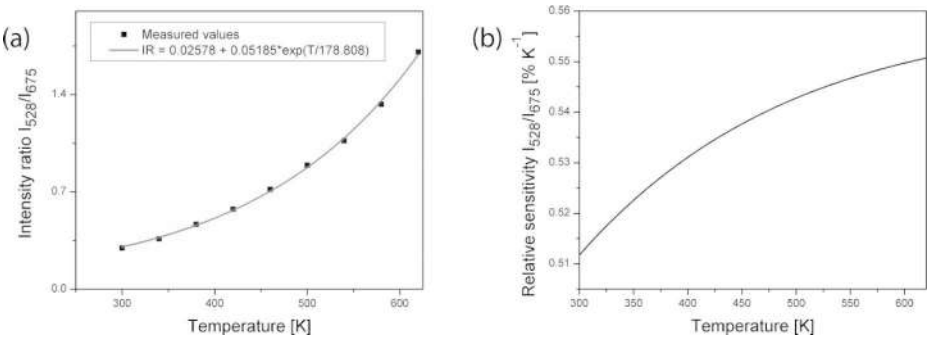

Fig. 6 (a) Temperature sensing calibration curve of Y_2O_2S:Er,Yb, using intensity ratio of two Er emission lines, at 528 and 675 nm. Experimental points are denoted by black squares and fitted temperature calibration curve is denoted by red line. (b) Relative sensitivity curve as the function of temperature of Y_2O_2S:Er,Yb

Table 1 The sensing characteristics of several thermophosphors

Thermophosphor	Sensing range [K]	Relative sensitivity [% K^{-1}]	Reference
YO_2S:Er,Yb	300–620	0.512–0.55	This work
$GdVO_4$:Er,Yb	307–473	1.11	(Gavrilovic et al. 2014)
$GdVO_4$:Er,Yb	298–374	1.2	(Ferreira et al. 2021)
$GdVO_4$:Er,Yb	297–343	0.69	(Savchuk et al. 2016 A)
$GdVO_4$@SiO2:Er,Yb	297–343	1.01	(Savchuk et al. 2016A)
$NaYF_4$:Er,Yb	298–333	0.5	(Savchuk et al. 2016B)
$SrBi_4Ti_4O_{15}$:Er,Yb	313–573	0.36	(Wei et al. 2019)
$LuVO_4$:Er,Yb	100–500	0.67	(Wu et al. 2019)
Gd_2O_3:Er,Yb	300–550	0.35–1.18	(Sevic et al. 2020B)
BaTiO3:Er	322–466	0.52	(Alencar et al. 2004)
$NaYF_4$@SiO2:Er,Yb	300–900	0.13–1.02	(Geitenbeek et al. 2017)
YAG:Dy	300–1273	0.2–0.8	(Sevic et al. 2021)
YAG:Dy	500–1000	0.2–0.7	(Hashemi et al. 2015)
YVO_4:Eu	300–650	0.33–0.63	(Sevic et al. 2020 A)
Gd_2O_3:Eu	300–800	0.25–3.25	(Nikolic et al. 2013)
$YNbO_4$:Eu	300–720	0.3–2.6	(Đacanin et al. 2013, 2014)
$Gd_2Zr_2O_7$:Eu	300–650	0.4–0.92	(Nikolic et al. 2018)
Lu_2O_3:Eu	300–800	0.3–0.33	(Lojpur et al. 2012)
$Gd_2Ti_2O_7$:Eu	300–420	0.3–0.95	(Lojpur et al. 2016 A)
TiO_2:Eu	300–530	0.12–2.3	(Nikolic et al. 2014)
$GdAlO_3$:Eu	300–750	0.3–2.9	(Lojpur et al. 2016B)
YBO_3:Eu	330–760	0.3–1.8	(Lu et al. 2017)

suppose that phenomenon could be explained by overlap of the multiple peaks at 528 and 555 nm, see Fig. 3, worsened by content of Y_2O_3:Er^{3+},Yb^{3+} material in Y_2O_2S:Er^{3+},Yb^{3+}.

4 Conclusions

Temperature dependence of $Y_2O_2S:Er^{3+},Yb^{3+}$ luminescence was analyzed in this paper. We have used luminescence intensity ratio method for temperature sensing, analyzing intensities of spectral peaks at 528 nm, 555 and 675 nm. It was shown that ratio between intensities of peaks at 528 and 555 nm provides satisfying results for determining the temperature sensing calibration curve. However, the using of peak at 675 nm instead of 555 nm provides better results in terms of relative sensitivity. We conclude that synthesized Y_2O_2S:Er,Yb thermophosphor is useful for temperature range from 300 to 620 K, with relative sensitivity of 0.512% K^{-1} at room temperature. With increasing the temperature the relative sensitivity increases up to 0.55% K^{-1} at 620 K. To the best of our knowledge, results of the analysis of luminescence temperature dependence of the Y_2O_2S host doped with Er,Yb were not published so far.

Acknowledgements This work was financially supported by funding provided by the Institute of Physics Belgrade, through the grant by the Ministry of Education, Science, and Technological Development of the Republic of Serbia.

Declarations

Conflict of interest The authors declare that they have no known competing financial interests or personal relationships that could have appeared to influence the work reported in this paper.

References

Alden, M., Omrane, A., Richter, M., Särner, G.: Thermographic phosphors for thermometry: A survey of combustion applications. Prog. Energy Combust. Sci. **37**, 422–461 (2011)

Alencar, M.A.R.C., Maciel, G.S., de Araújo, C.B.: Er^{3+}-doped $BaTiO_3$ nanocrystals for thermometry: Influence of nanoenvironment on the sensitivity of a fluorescence based temperature sensor. Appl. Phys. Lett. **84**, 4753 (2004)

Ang, L.Y., Lim, M.E., Ong, L.C., Zhang, Y.: Applications of upconversion nanoparticles in imaging, detection and therapy. Nanomedicine. **6**, 1273–1288 (2011)

Allison, S.W., Gillies, G.T.: Remote thermometry with thermographic phosphors: Instrumentation and applications. Rev. Sci. Instrum. **68**, 2615–2650 (1997)

Avram, D., Tiseanu, C.: Thermometry properties of Er, Yb–Gd_2O_2S microparticles: dependence on the excitation mode (cw versus pulsed excitation) and excitation wavelength (980 nm versus 1500 nm). Methods Appl. Fluoresc. **6**, 025004 (2018)

Brites, C.D.S., Lima, P.P., Silva, N.J.O., Millan, A., Amaral, V.S., Palacio, F., Carlos, L.D.: Thermometry at the nanoscale. Nanoscale. **4**, 4799–4829 (2012)

Cates, M.R., Allison, S.W., Jaiswal, S.L., Beshears, D.L.: YAG:Dy and YAG:Tm Fluorescence above 1400 C. Oak Ridge National Laboratory (2002). Report ORNL/TM-2002/71

Ciric, A., Gavrilovic, T., Dramicanin, M.D.: Luminescence Intensity Ratio Thermometry with Er^{3+}: Performance Overview. Crystals. **11**, 189 (2021)

Dong, B., Liu, D.P., Wang, X.J., Yang, T., Miao, S.M., Li, C.R.: Optical thermometry through infrared excited green upconversion emissions in Er^{3+}–Yb^{3+} codoped Al_2O_3. Appl. Phys. Lett. **90**, 181117 (2007)

Du, P., Deng, A.M., Luo, L., Yu, J.S.: Simultaneous phase and size manipulation in $NaYF_4$:Er^{3+}/Yb^{3+} upconverting nanoparticles for a non-invasion optical thermometer. New. J. Chem. **41**, 13855–13861 (2017)

Du, P., Yu, J.S.: Synthesis of Er(III)/Yb(III)-doped BiF_3 upconversion nanoparticles for use in optical thermometry. Microchim. Acta. **185**, 237–231 (2018)

Đačanin, L.R., Lukić-Petrović, S.R., Petrović, D.M., Nikolić, M.G., Dramićanin, M.D.: Temperature quenching of luminescence emission in Eu^{3+}- and Sm^{3+}-doped $YNbO_4$ powders. J. Lumin. **151**, 82–87 (2014)

Đačanin, L.R., Dramićanin, M.D., Lukić-Petrović, S.R., Petrović, D.M., Nikolić, M.G.: Eu^{3+} doped $YNbO_4$ phosphor properties for fluorescence Thermometry. Radiat. Meas. **56**, 143–146 (2013)

Eldridge, J.I., Jenkins, T.P., Allison, S.W., Wolfe, D.E., Jordan, E.H.: Development of YAG:Dy Thermographic Phosphor Coatings for Turbine Engine Applications, 58 h International Instrumentation Symposium San Diego, CA, June 5–8, (2012)

Feist, J.P., Heyes, A.L., Choy, K.L., Su, B.: Phosphor Thermometry for High Temperature Gas Turbine Applications. Proceedings of IEEE; **6.1** (1999)

Feist, J.P., Heyes, A.L.: The characterization of Y_2O_2S:Sm powder as a thermographic phosphor for high temperature applications. Meas. Sci. Technol. **11**, 942–947 (2000)

Ferreira, M.F., de Sousa, K.Z.R., Massarotto, W.L., Ricci, E.G., de Faria, E.H., Ciuffi, K.J., Sevic, D., Rocha, L.A., Nassar, E.J.: Er3+/Yb3+-Doped GdVO4 Obtained by the Non-Hydrolytic Sol-Gel Route and Potential Application as Up-Conversion Thermometer. J. Braz Chem. Soc. **32**, 376–384 (2021)

Gavrilovic, T.V., Jovanovic, D.J., Smits, K., Dramicanin, M.D.: Multicolor upconversion luminescence of $GdVO_4$:Ln^{3+}/Yb^{3+}(Ln^{3+} = Ho^{3+}, Er^{3+}, Tm^{3+}, Ho^{3+}/Er^{3+}/Tm^{3+}) nanorods. Dyes Pigm. **126**, 1–7 (2016)

Gavrilović, T.V., Jovanović, D.J., Lojpur, V., Dramićanin, M.D.: Multifunctional Eu^{3+}- and Er^{3+}/ Yb^{3+}-doped $GdVO_4$ nanoparticles synthesized by reverse micelle method. Sci. Rep. **4**, 4209 (2014)

Geitenbeek, R.G., Prins, P.T., Albrecht, W., van Blaaderen, A., Weckhuysen, B.M., Meijerink, A.: $NaYF_4$:Er^{3+},Yb^{3+}/SiO_2 Core/Shell Upconverting Nanocrystals for Luminescence Thermometry up to 900 K. J. Phys. Chem. C Nanomater Interfaces. **121**, 3503–3510 (2017)

Goss, L.P., Smith, A.A., Post, M.E.: Surface thermometry by laser-induced fluorescence. Rev. Sci. Instrum. **60**, 3702–3706 (1989)

Hashemi, A., Vetter, A., Jovicic, G., Batentschuk, M., Brabec, C.J.: Meas. Sci. Technol. **26**, 075202 (2015)

Heyes, A.L.: On the design of phosphors for high-temperature thermometry. J. Lumin. **129**, 2004–2009 (2009)

Jaque, D., Vetrone, F.: Luminescence nanothermometry. Nanoscale. **4**, 4301–4326 (2012)

Khalid, A.H., Kontis, K.: Thermographic Phosphors for High Temperature Measurements: Principles, Current State of the Art and Recent Applications. Sensors. **8**, 5673–5774 (2008)

Krizan, J., Mazaj, M., Kaucic, V., Bajsic, I., Mozina, J.: Synthesis of Er- and Yb-doped Gadolinium Oxide Polymorphs and Influence of Their Structureson Upconversion Properties. Acta Chim. Slov. **61**, 608–614 (2014)

Kumar, G.A., Pokhrel, M., Martinez, A., Dennis, R.C., Villegas, I.L., Sardar, D.K.: Synthesis and spectroscopy of color tunable Y_2O_2S:Yb^{3+},Er^{3+} phosphors with intense emission. J. Alloys Compd. **513**, 559–565 (2012)

Li, X., Song, Y., Yang, Y., Mi, C., Liu, Y., Yu, F., Liu, L., Zhang, J., Li, Z.: Structure and Optical Thermometry Characterization of Er^{3+}/Yb^{3+} Co-Doped $BaGd_2CuO_5$. J. Nanosci. Nanotechnol. **16**, 3542–3546 (2016)

Li, D., Qin, W., Zhang, P., Wang, L., Lan, M., Shi, P.: Efficient luminescence enhancement of Y2O2S:Ln^{3+} (Ln = Yb/Er, Eu) NCs by codoping Zn^{2+} and Li^{+} inert ions. Opt. Mater. Express. **7**, 329 (2017)

Li, L., Zheng, L., Xu, W., Liang, Z., Zhou, Y., Zhang, Z., Cao, W.: Optical thermometry based on the red upconversion fluorescence of Er^{3+} in $CaWO_4$:Yb^{3+}/Er^{3+} polycrystalline powder. Opt. Lett. **41**, 1458–1461 (2016)

Liu, L., Qin, F., Lv, T., Zhang, Z., Cao, W.: Accurate thermometry based on the red and green fluorescence intensity ratio in $NaYF_4$: Yb, Er nanocrystals for bioapplication. Opt. Lett. **41**, 4664–4667 (2016)

Lojpur, V., Ahrenkiel, P., Dramićanin, M.D.: Color-tunable up-conversion emission in Y_2O_3:Yb^{3+},Er^{3+} nanoparticles prepared by polymer complex solution method. Nanoscale Res. Lett. **8**, 131 (2013)

Lojpur, V., Antic, Z., Krsmanovic, R., Medic, M., Nikolic, M.G., Dramicanin, M.D.: Thermographic properties of Eu3+- and Sm3+-doped Lu2O3nanophosphor. J. Serb Chem. Soc. **77**, 1735–1746 (2012)

Lojpur, V., Culubrk, S., Medic, M., Dramicanin, M.D.: Luminescence thermometry with Eu^{3+} doped $GdAlO_3$. J. Lumin. **170**, 467–471 (2016B)

Lojpur, V., Culubrk, S., Dramicanin, M.D.: Ratiometric luminescence thermometry with different combinations of emissions from Eu^{3+} doped $Gd_2Ti_2O_7$ nanoparticles. J. Lumin. **169**, 534–538 (2016A)

Lu, Z., Zhongmin, C., Xiantao, W., Min, Y., Yonghu, C.: Luminescence properties of Eu3 + doped YBO_3 for temperature sensing. J. Rare Earths. **35**, 356–360 (2017)

Manzani, D., Petruci, J.F., Nigoghossian, S., Cardoso, K., Ribeiro, A.A.: S.J.L.: A portable luminescent thermometer based on green upconversion emission of Er^{3+}/Yb^{3+} co-doped tellurite glass. Scientific Reports 7:41596 (2017). DOI: https://doi.org/10.1038/srep41596

Nikolic, M.G., Rabasovic, M.S., Krizan, J., Savic-Sevic, S., Rabasovic, M.D., Marinkovic, B.P., Vlasic, A., Sevic, D.: Luminescence thermometry using $Gd_2Zr_2O_7$:Eu^{3+}. Opt. Quant. Electron. **50**, 258–251 (2018)

Nikolic, M.G., Al-Juboori, A.Z., Djordjevic, V., Dramicanin, M.D.: Temperature luminescence properties of Eu^{3+}-doped Gd_2O_3 phosphors. Phys. Scr. **T157**, 014056–014051 (2013)

Nikolic, M.G., Antic, Z., Culubrk, S., Nedeljkovic, S., Dramicanin, J.M.: Temperature sensing with Eu^{3+} doped TiO_2 nanoparticles. Sens. Actuators B. **201**, 46–50 (2014)

Santos dos, P.V., Araujo de, M.T., Gouveia-Neto, M.T., Medeiros Neto, A.S., Sombra, J.A.: Optical Thermometry Through Infrared Excited Upconversion Fluorescence Emission in Er- and ErYb -doped Chalcogenide Glasses. IEE J. Quantum Electron. **35**, 395–399 (1999)

Savchuk, O.A., Carvajal, J.J., Cascales, C., Aguilo, M., Díaz, F.: Benefits of Silica Core – Shell Structures on the Temperature Sensing Properties of Er,Yb:$GdVO_4$ Up-Conversion Nanoparticles. ACS Appl. Mater. Interfaces **8**, 7266 (2016A)

Savchuk, O.A., Carvajal, J.J., Massons, J., Cascales, C., Aguiló, M., Díaz, F.: Novel low-cost, compact and fast signal processing sensor for ratiometric luminescent nanothermometry. Sens. Actuators, A**250**, 87 (2016B)

Sevic, D., Rabasovic, M.S., Krizan, J., Savic-Sevic, S., Nikolic, M.G., Marinkovic, B.P., Rabasovic, M.D.: YVO_4:Eu^{3+} nanopowders: multi-mode temperature sensing technique Phys, J.: D: Appl. Phys. **53**, 015106–015101 (2020A)

Sevic, D., Rabasovic, M.S., Krizan, J., Savic-Sevic, S., Rabasovic, M.D., Marinkovic, B.P., Nikolic, M.G.: Effects of temperature on luminescent properties of Gd_2O_3:Er, Yb nanophosphor. Optical and Quantum Electronics **52**, 232 (2020B)

Sevic, D., Krizan, J., Rabasovic, M.S., Marinkovic, B.P.: Temperature sensing using YAG:Dy single-crystal phosphor. Eur. Phys. J. D. **75**, 56 (2021)

Singh, S.K., Kumar, K., Rai, S.B.: Er^{3+}/Yb^{3+} codoped Gd_2O_3 nano-phosphor for optical thermometry. Sens. Actuators A. **149**, 16–20 (2009)

Tian, Y., Fu, Y., Xing, M., Luo, X.: X.: Upconversion Luminescence Properties of Y_2O_3:Yb, Er and Y_2O_2S:Yb, Er Nanoparticles Prepared by Complex Precipitation. J. Nanomater., 573253 (2015)

Vlasic, A., Sevic, D., Rabasovic, M.S., Krizan, J., Savic-Sevic, S., Rabasovic, M.D., Mitric, M., Marinkovic, B.P., Nikolic, M.G.: Effects of temperature and pressure on luminescent properties of Sr_2CeO_4:Eu^{3+} nanophosphor. J. Lumin. **199**, 285–292 (2018)

Wang, X., Liu, Q., Bu, Y., Liu, C.-S., Liua, T., Yan, X.: Optical temperature sensing of rare-earth ion doped phosphors. RSC Adv. **5**, 86219–86236 (2015)

Wang, H., Xing, M., Luo, X., Zhou, X., Fu, Y., Jiang, T., Peng, Y., Ma, Y., Duan, X.: Upconversion emission colour modulation of Y_2O_2S: Yb, Er under 1.55 lm and 980 nm excitation. J. Alloys Compd. **587**, 344–348 (2014)

Wei, T., Yang, F., Jing, Q., Zhao, C., Wang, M., Du, M., Guo, Y., Zhou, Q., Li, Z.: Optical multi-functionalities of Er^{3+}- and Yb^{3+}-sensitized strontium bismuth titanate nanoparticles. J. Alloys Compd. **801**, 1–9 (2019)

Wu, J., Cheng, X., Jiang, F., Feng, X., Huang, Q., Lin, Q.: Optical temperature sensing properties of Er^{3+}/Yb^{3+} co-doped $LuVO_4$ upconversion phosphors. Phys. B. **561**, 97 (2019)

Xu, W., Gao, X., Zheng, L., Wang, P., Zhang, Z., Cao, W.: Optical Thermometry through Green Upconversion Emissions in Er^{3+}/Yb^{3+}-Codoped $CaWO_4$ Phosphor. Appl. Phys. Express. **5**, 072201 (2012)

Zhao, Y., Wang, X., Zhang, Y., Li, Y., Yao, X.: Optical temperature sensing of up-conversion luminescent materials: Fundamentals and progress. J. Alloys Compd. **817**, 152691 (2020).

Publisher's Note Springer Nature remains neutral with regard to jurisdictional claims in published maps and institutional affiliations.

Optical Materials 50 (2015) 250–255

Contents lists available at ScienceDirect

Optical Materials

journal homepage: www.elsevier.com/locate/optmat

Structural properties and luminescence kinetics of white nanophosphor YAG:Dy

M.S. Rabasovic [a,*], D. Sevic [a], J. Krizan [b], M.D. Rabasovic [a], S. Savic-Sevic [a], M. Mitric [c], M. Petrovic [a], M. Gilic [a], N. Romcevic [a]

[a] Institute of Physics, University of Belgrade, P.O. Box 68, Pregrevica 118, 11080 Belgrade, Serbia
[b] AMI, d. o. o., Ptuj, Slovenia
[c] Vinca Institute of Nuclear Science, University of Belgrade, P.O. Box 522, 11001 Belgrade, Serbia

ARTICLE INFO

Article history:
Received 23 October 2015
Received in revised form 3 November 2015
Accepted 3 November 2015
Available online 6 November 2015

Keywords:
$Y_3Al_5O_{12}$
Dy^{3+}
Nanopowders
Phosphor
Lifetime

ABSTRACT

Dysprosium (Dy^{3+} ions) doped YAG nanopowders were prepared by the solution combustion synthesis (SCS) method and undoped yttrium aluminum garnet (YAG, $Y_3Al_5O_{12}$) single crystal was grown by the Czochralski technique. The structure of the prepared materials has been confirmed and characterized using X-ray powder diffraction (XRD), scanning electron microscope (SEM), Raman and photoluminescence (PL) spectroscopy. PL spectra were acquired using Optical Parametric Oscillator (OPO) excitation tuned at 350 nm. Several emission bands in Dy^{3+} emission spectrum were observed in the blue (470–500 nm), yellow (560–600 nm), red (660–685 nm) and infra-red (750–780 nm) regions, corresponding to $^4F_{9/2}$–$^6H_{15/2}$, $^4F_{9/2}$–$^6H_{13/2}$, $^4F_{9/2}$–$^6H_{11/2}$, $^4F_{9/2}$–($^6H_{9/2}$ + $^6H_{11/2}$) transitions in the *4f* levels of Dy^{3+} ions, respectively. By using the Commission Internationale de l'Eclairage (CIE) chromaticity diagram of emission spectra it has been shown that this material can be used as a source of a white light. The result of lifetime analysis of the $^4F_{9/2}$ level in dysprosium ion has been reported, as well.

© 2015 Elsevier B.V. All rights reserved.

1. Introduction

Yttrium Aluminum Garnet (YAG) is a well-known crystalline material with many interesting optical and mechanical properties. It has a cubic garnet crystallographic structure with isotropic thermal expansion and homogeneous optical properties without birefringence effects [1,2]. Due to the structural properties of YAG, it is widely used as a host in solid state lasers, luminescence materials and scintillators [3,4].

Rare earth ions luminescence has been extensively used in applications as the active ions in phosphors for development of flat panel displays, plasma display panels (PDPs), thin film electroluminescent devices (TFEL), white light emitting diode (LED). Trivalent rare-earth ions have a partially filled 4f shell that is well shielded by $5s^2$ and $5p^6$ orbitals. The 4f–4f inner-shell transitions in trivalent rare-earth ions allow the expression of features such as high luminescence yield, narrow emission line, and long decay time constant. Because of this, most rare-earth elements are doped into many light emitting materials and laser materials [5,6].

Due to its high optical transparency (it remains transparent through the whole visible region), YAG is ideal for studying of rare earth ions in both diluted and concentrated form. As the size of lanthanide ions decreases with the increase of atomic number, $r(La) >> r(Lu)$, single rare earth garnets exist only for rare-earth ions with at least seven *4f* electrons. Others, with less than seven *4f* electrons, can replace just a certain percentage of Y^{3+} ions. The electronic structure of dysprosium is $1s^22s^22p^63s^23p^64s^23d^{10}4p^65s^24d^{10}5p^66s^24f^{10}$ – 10 of 14 possible electrons in the last *4f* shell. So, the structure $Dy_3Al_2(AlO_4)_3$ is indeed possible. If we look at the size of Y^{3+} and Dy^{3+}, the difference is only 0.69%, the radius of Dy^{3+} ion is 1.167 Å and radius of Y^{3+} ion (1.159 Å) as is depicted in Fig. 1(a).

Structural and optical properties of YAG and Nd:YAG single crystals have been analyzed previously using XRD, Raman and IR spectroscopy [7]. Nd:YAG single crystal is a well-known lasing material for more than 30 years. Now, we have extended our research to YAG:Dy phosphors. When the Dy^{3+} ions are incorporated in the host crystal field with wide band gap, the visible emission of these ions manifolds mainly in the blue and yellow spectral regions. The energy level scheme of Dy^{3+} ions in YAG phosphor is presented in Fig. 1(b). The investigations regarding the ratio of blue and yellow transition of the Dy^{3+} ions indicate that the lightly doped samples should be considered for the production of the white light emission [8,9].

The aim of this paper is to present the results of experimental investigation of Dy^{3+} doped YAG nanopowders, annealed at

* Corresponding author.
E-mail address: majap@ipb.ac.rs (M.S. Rabasovic).

http://dx.doi.org/10.1016/j.optmat.2015.11.002
0925-3467/© 2015 Elsevier B.V. All rights reserved.

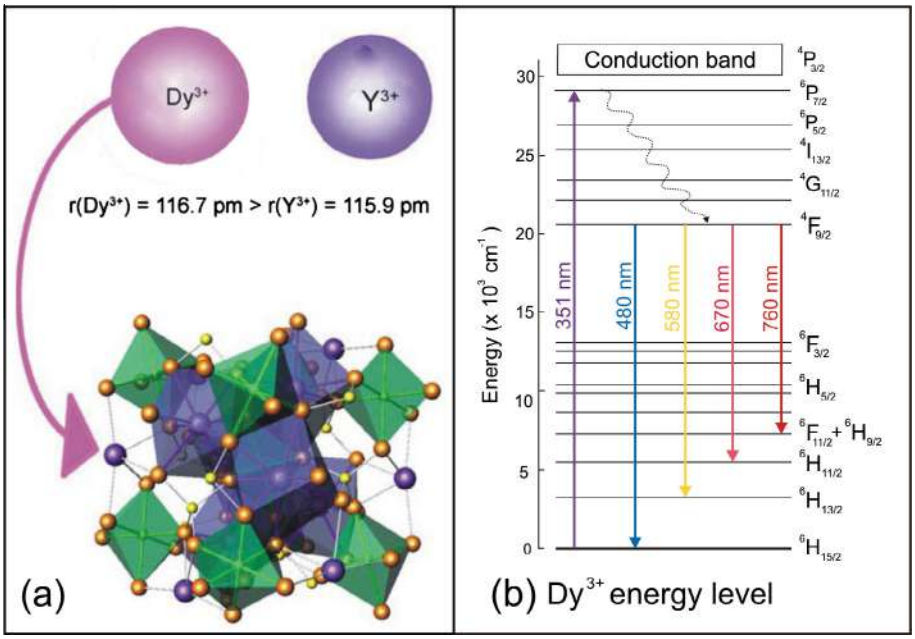

Fig. 1. (a) YAG:Dy atomic structure. Dy^{3+} is substituted in Y^{3+} sites. (b) The energy level scheme of Dy^{3+} ions.

1300 °C. YAG:Dy nanopowder was prepared by the solution combustion synthesis (SCS) method [10]. We also study time-resolved luminescence properties and differences in the visible and near IR spectral range of the YAG single crystal and dysprosium doped YAG nanopowders. The CIE chromaticity coordinates were calculated from the luminescence spectra in order to confirm the possibility of application of synthesized YAG:Dy material as the white light source.

2. Experimental procedures

2.1. The preparation of samples

Measurements were performed on samples of YAG single crystal and YAG nanopowder doped with Dysprosium ions (2 mol%). The YAG single crystal was grown by the Czochralski technique, using a MSR 2 crystal puller controlled by a Eurotherm [11]. YAG:Dy nanopowder was produced by Solution Combustion Synthesis (SCS) method. Yttrium oxide (Y_2O_3) and aluminum oxide (Al_2O_3) are used as starting materials (all 99.99%). These samples were purchased from NOAH Technologies. Synthesis was made by dissolving the oxides in HNO_3. After that a solution of carbohydrazide is added to a solution of aluminum nitrate and yttrium nitrate:

$$3Y(NO_3)_3 + 5Al(NO_3)_3 + 15CH_6N_4O \rightarrow YAG + 42N_2 + 15CO_2 + 45H_2O$$

Due to good reactivity of raw materials, no intermediate phases such as YAM ($Y_4Al_2O_9$) or YAP ($YAlO_3$) coexists in the obtained ittrium aluminum garnet (YAG or $Y_3Al_5O_{12}$) powder. After synthesis, YAG host is doped with Dy^{3+} ions at the 2 mol% concentration. In second step, in order to achieve the full crystallinity, YAG:Dy nanopowder was annealed in air atmosphere at 1300 °C.

Phase identification in the post-annealed powder samples were performed by X-ray diffraction (Philips PW 1050 instrument) using Ni filtered Cu $K_{\alpha 1,2}$ radiation ($\lambda = 0.15405$ nm). X-ray diffraction measurements were done at room temperature over the 2θ range of 10–90° with a scanning step width of 0.05° and a counting time of 8 s per step.

2.2. Experimental setup

The Raman spectra in a spectral range from 100 to 900 cm^{-1}, in back scattering geometry, were obtained by the micro-Raman Jobin Yvon T64000 spectrometer, equipped with a nitrogen cooled charge-coupled device detector. As the excitation source we used the 532 nm laser.

The morphology of the YAG:Dy nanopowders were investigated by high resolution scanning electron microscope (SEM) equipped with a high brightness Schottky Field Emission gun (FEGSEM, TESCAN) operating at 4 kV. The samples were coated with gold/palladium to make them conductive, for SEM analysis.

Photoluminescence (PL) studies reported in this work were performed at room temperature using Optical Parametric Oscillator (Vibrant OPO) tuned at 350 nm as excitation source. Time-resolved streak images of the emission spectrum excited by OPO system are collected by using a spectrograph (SpectraPro 2300i) and recorded with a Hamamatsu streak camera (model C4334). All streak camera operations are controlled by the HPD-TA (High Performance Digital Temporal Analyzer) software. The HPD-TA software also provides advanced analysis of streak images. Fluorescence lifetime fitting analysis was carried out using the TA-Fit program.

3. Results and discussion

The X ray diffraction patterns of Dy:YAG nanopowder and YAG single crystal samples are shown in Fig. 2. For both samples, the characteristic diffraction peaks corresponding to YAG phase are easy to see. The diffraction peak at 67.30° is noticed only for YAG single crystal sample. For the YAG single crystal sample all diffraction peaks are assigned to YAG phase and no other phase can be observed in the pattern. However, several diffraction peaks corresponding to other phases appear at YAG:Dy diffraction pattern. They are labeled with blue arrows ($YAlO_3$, perovskite) and green arrows (α – Al_2O_3, corundum). Existence of these impurities implies that the sample didn't turn into garnet phase completely. But the main difference between the two spectra is the fact that the YAG:Dy nanopowder diffraction peaks are slightly shifted

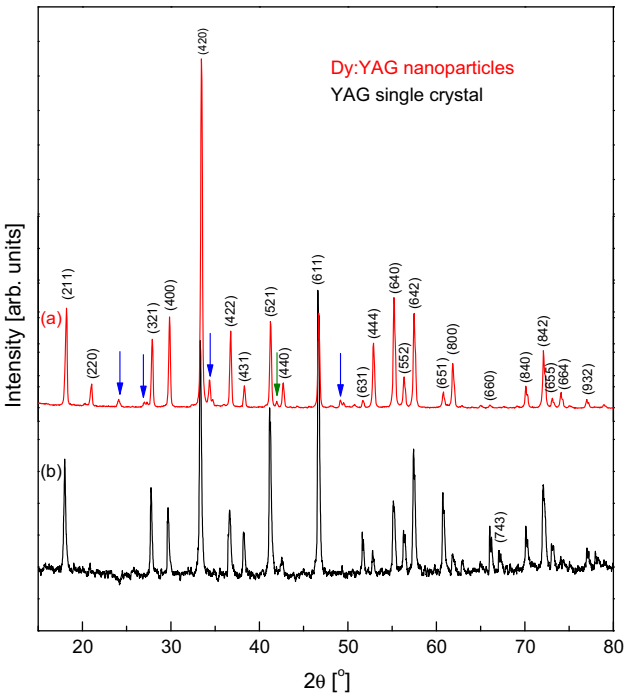

Fig. 2. X-ray diffraction patterns of YAG single crystal and YAG:Dy nanopowder.

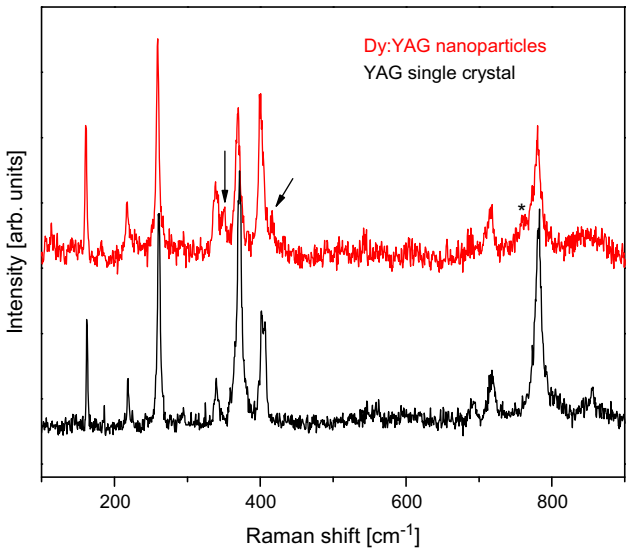

Fig. 3. Raman spectra of YAG single crystal and YAG:Dy nanopowder at room temperature.

toward higher angles in comparison with the peaks of pure YAG, which is caused by difference in lattice parameters of the two samples.

The unit cell of YAG and YAG:Dy is calculated using 15 reflections by the least square method. The calculated results revealed that the crystals have body – centered cubic Bravais lattice with space group Ia3d, with lattice parameters a = 12.00675 Å for YAG and a = 12.01068 Å for YAG:Dy. The values of these parameters are slightly lower than values presented in work [12] (12.01 Å). The radius of Dy^{3+} ion is 1.167 Å, which is slightly larger than the radius of Y^{3+} ion (1.159 Å). The difference in ionic radii results in the larger lattice parameter for YAG:Dy, which causes mentioned shift in XRD diffraction spectra.

The Raman spectra of YAG single crystal and YAG:Dy nanopowder phosphor are presented in Fig. 3. In first approximation, YAG modes can be divided into the translational modes of Y^{3+} (or Dy^{3+}), Al^{3+} and (AlO_4) group, rotational modes of (AlO_4) group and internal vibrations of (AlO_4) unit. But it was found that there is a strong coupling between the electrons of rare earth ions (or Y^{3+}) and the movements of the lattice [13]. Many authors have divided Raman spectrum of YAG into 2 groups [11,14] – low – frequency region, up to 500 cm^{-1}, and high – frequency region, above 500 cm^{-1}. The peaks below 500 cm^{-1} are attributed to the translational motion of Y^{3+} or Dy^{3+} ions together with heavy mixing of translational, rotational and ν_3 modes of (AlO_4) unit. The peaks above 500 cm^{-1} are all internal vibrations of (AlO_4) unit – ν_1, ν_2 and ν_4.

Let us now discuss these spectra in more detail. Both spectra reflect modes characteristic for YAG single crystal. The peaks of YAG:Dy nanopowder are slightly broader comparing to the peaks of YAG single crystal, probably due to phonon confinement effects [15,16]. Some of the peaks are slightly blue shifted (162 cm^{-1}, 260 cm^{-1}, 370 cm^{-1}), while the others are invariable with positions comparing to YAG single crystal.

Peaks of YAG:Dy at 145, 162 and 217 cm^{-1} exhibit hyperchromic shift comparing to those of YAG. Because of this increase in intensity, we assign these peaks to the translational movements of Y^{3+} and Dy^{3+} ions, which is in compliance with the work of Chen et al. [14]. As we pointed out before, Dy^{3+} ions are 0.69% larger than Y^{3+} ions, so substitution of Y^{3+} with Dy^{3+} leads to further distortion of the cube, and as the consequence the increase in peaks intensity.

The mode at 762 cm^{-1} which is missing in YAG single crystal spectrum becomes visible in YAG:Dy spectrum (marked with asterisks in Fig. 3). Besides that, two more peaks could be discerned in YAG:Dy spectrum, with no match in YAG spectrum. The peak at 351 cm^{-1} belongs to $YAlO_3$ – perovskite phase [17], and the peak at 414 cm^{-1} corresponds to Al_2O_3 – corundum phase [18] (marked with arrows). The presence of perovskite and corundum phase in YAG:Dy indicate that, during the synthesis, the most of but not the whole material was turned into garnet phase, as confirmed before in XRD section.

It is well established that the luminescent properties of the phosphor depend on the shape and size of its particles [19]. The SEM image of YAG: 2 mol% Dy materials annealed at 1300 °C are presented in Fig. 4. Some particles are agglomerated but there are also separated particles. Those individual particles are spherical with the size of about 30 nm. The spherical forms of particles are of great importance because of their lower scattering of light and brighter luminescence performance [20].

Time-resolved photoluminescence spectrum of Dy^{3+} doped YAG nanopowder is shown in Fig. 5. The image has been acquired in photon counting mode operation of streak camera. The grayscale image is presented in usual palette of pseudocolor, where different intensities are coded as different colors. The energy level scheme of Dy^{3+} ions in YAG phosphor is represented in Fig. 2(b).

The PL emission spectra of the YAG:Dy annealed at 1300 °C and YAG single crystal, integrated along time axis, are presented together and compared in Fig. 6. Much weaker optical response of YAG single crystal is presented magnified about forty times so the shapes of spectra could be compared. From the sharp lines in the excitation spectra reported in papers [21,22] it could be seen that the best excitation corresponds to the electronic transition at 351 nm ($^6H_{15/2} \rightarrow {}^6P_{7/2} + {}^4M_{15/2}$) in Dy^{3+} ion. Because of that, our streak images of the PL spectra (Fig. 5) are acquired under the OPO excitation wavelength at 350 nm. The two dominant emission luminescent bands in the blue (470–500 nm) and yellow (560–600 nm) regions and the weaker band in red (~660 nm) region could be clearly seen for the YAG:Dy sample. All that peaks correspond to the transitions from excited energy level $^4F_{9/2}$ of the

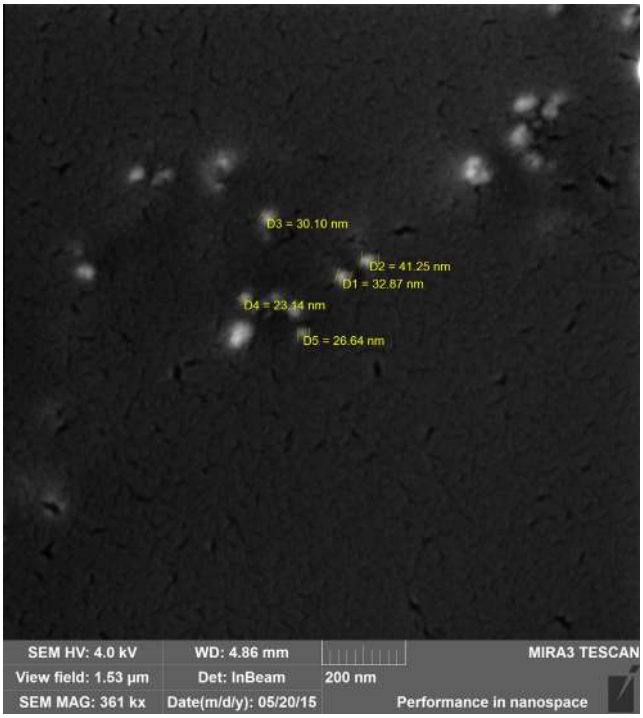

Fig. 4. SEM micrographs of material.

Dy^{3+} ion to $^6H_{15/2}$ (blue ~485 nm), $^6H_{13/2}$ (yellow ~580 nm) and $^6H_{11/2}$ (red ~680 nm) and ($^6H_{9/2}$ + $^6H_{11/2}$) (~760 nm) level, respectively. The blue and yellow regions are the prominent. The last two lines, belonging to red and IR region, are also perceptible. On magnified curve corresponding to undoped YAG single crystal, luminescence band peaks are clearly observed at ~647 and ~680 nm, see Fig. 6. It is interesting to note that the position as well as the shape of this emission band in single crystal coincides with corresponding parameters for cerium doped YAG single crystals in ref. [23].

The (blue) $^4F_{9/2}$–$^6H_{15/2}$ transition is mainly magnetic dipole (MD) transition, which hardly varies with the crystal field strength around Dy^{3+} ions, while the (yellow) $^4F_{9/2}$–$^6H_{13/2}$ transition belongs to a hypersensitive transition ($\Delta L = 2$ and $\Delta J = 2$), which is forced

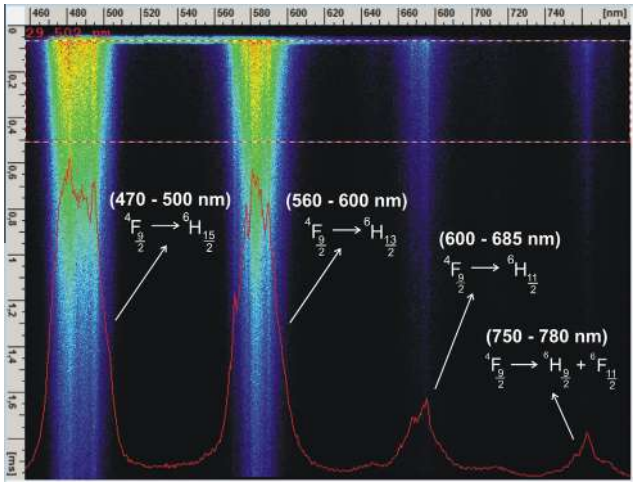

Fig. 5. Streak image of photoluminescence spectrum of Dy^{3+} doped YAG nanopowder. OPO excitation is at 350 nm. The wavelength range (horizontal axis) is 330 nm. The time range (vertical axis) is 2 ms.

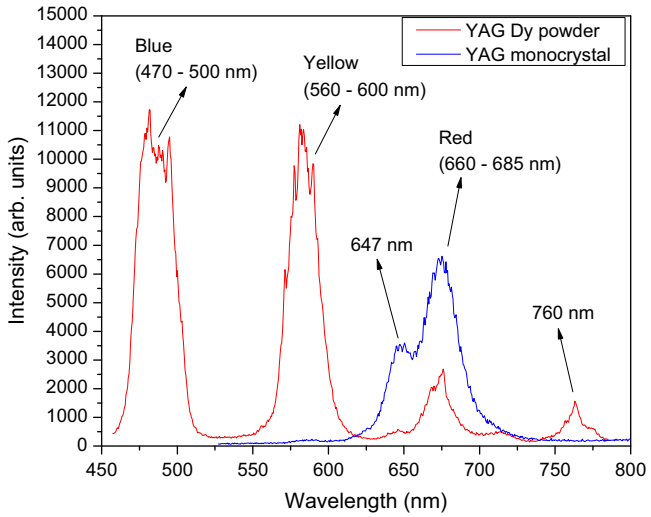

Fig. 6. The PL spectra of the YAG:Dy nanopowder annealed at 1300 °C and YAG single crystal integrated along time axis. The spectra were obtained by using the OPO excitation at 350 nm. Much weaker optical response of YAG single crystal is presented magnified about forty times so the shapes of spectra could be compared.

electric dipole (ED) transition and is strongly influenced by the chemical environment surrounding Dy^{3+} ions. As a consequence, the YAG:Dy phosphor could be good source of the white light, depending on the ratio between these two transitions [8]. Factors which influence the yellow-to-blue intensity ratio (Y/B) in Dy^{3+} ions were investigated in ref. [24]. The intensity of these two emission bands depend on the host composition, doping concentration and excitation wavelength [25]. More precisely, the intensity ratio between these two transitions is a measure of the site symmetry where Dy^{3+} ions are situated. The emission spectra of rare earth ions almost remain the same in different hosts, but the luminescent efficiency, chemical stability and durability depend on physical properties of the hosts [25].

Using the time-resolved streak images of YAG:Dy nanopowder luminescence, we have conducted the luminescence lifetime analysis for the most intensive transition $^4F_{9/2}$–$^6H_{15/2}$. For optimal concentration of 2 mol%, the vertical profile curve obtained from streak image demonstrates almost perfect single exponential decay. At the samples with low doped Dy^{3+} ions, the decay curve is a single exponential because then the effects between optically active ions are minimized. For higher concentrations the decay curve has to be bi-exponential as is explained in Raju et al. [22]. The luminescence decay and fitted curve of the $^4F_{9/2}$ level are presented in Fig. 7. The obtained lifetime of 0.870 ms agrees well with the published results corresponding to 2 mol% Dy concentration [26].

The usefulness of synthesized YAG:Dy phosphor is examined by calculating the CIE chromaticity coordinates, presented in Fig. 8. White light can be obtained by a suitable mixture of the blue[1] and yellow transitions of the Dy^{3+} ions. It is evident from Fig. 8 that the calculated color coordinates of YAG:Dy phosphors are located in the white light region of that color space. Therefore, the color coordinates for 2 mol% YAG:Dy phosphor $(x,y) = (0.353, 0.362)$ are very close to ideal white emission color $(0.313, 0.329)$ coordinate [27]. However, it should be noted that there are some weaknesses of using this material: low absorption of the excitation photons (forbidden *f–f* transitions) and slightly too high energy of the excitation transitions even when using the so-called UV-LEDs.

[1] For interpretation of color in Fig. 8, the reader is referred to the web version of this article.

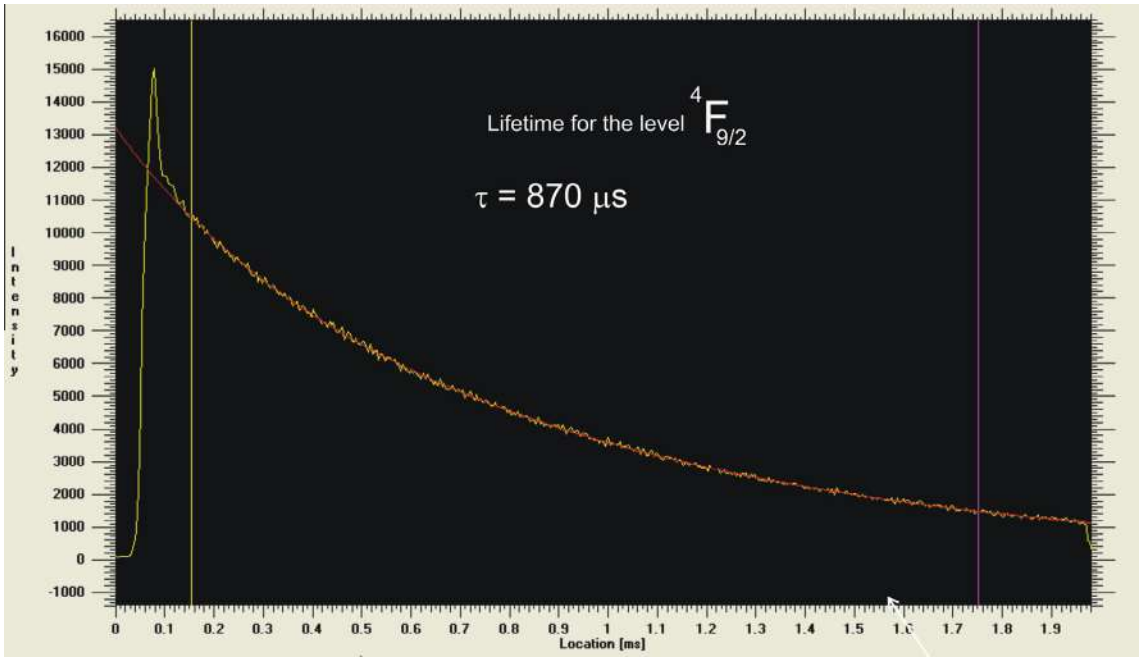

Fig. 7. Luminescence decay curve fitted by single exponential decay.

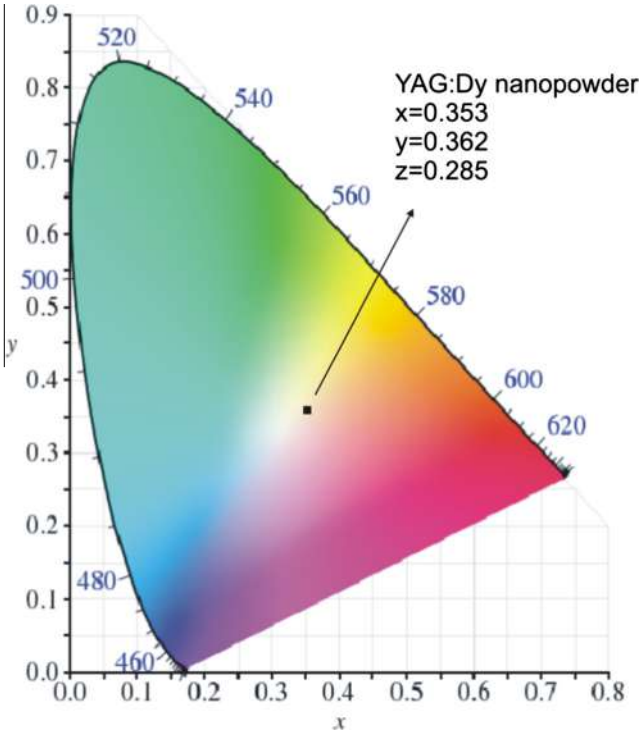

Fig. 8. The CIE chromaticity diagram of emission spectra of 2 mol% YAG:Dy.

4. Conclusion

- We have presented the new results of experimental investigation of Dy^{3+} doped YAG nanopowders, synthesized by solution combustion method and annealed at 1300 °C. Their structural and optical properties were compared with undoped yttrium aluminum garnet (YAG, $Y_3Al_5O_{12}$) single crystal grown by the Czochralski technique.
- We also study time-resolved luminescence properties and differences in the visible and near IR spectral range of the YAG single crystal and dysprosium doped YAG nanopowders.
- The structure of the prepared materials has been confirmed and characterized using X-ray powder diffraction (XRD), scanning electron microscope (SEM), Raman and photoluminescence (PL) spectroscopy.
- Several emission bands in Dy^{3+} emission spectrum were observed in the blue (470–500 nm), yellow (560–600 nm), red (660–685 nm) and infra-red (750–780 nm) regions, corresponding to $^4F_{9/2}$–$^6H_{15/2}$, $^4F_{9/2}$–$^6H_{13/2}$, $^4F_{9/2}$–$^6H_{11/2}$, $^4F_{9/2}$–($^6H_{9/2}$ + $^6H_{11/2}$) transitions in the *4f* levels of Dy^{3+} ions, respectively.
- By using the CIE chromaticity diagram of emission spectra it has been shown that this 2 mol% YAG:Dy phosphor material (x,y) = (0.353,0.362) can be used as a source of a white light.
- The decay curve and lifetime analysis of the $^4F_{9/2}$ level in dysprosium ion have also been reported.

Acknowledgements

This work was financially supported within the Projects Ministry of Education, Science and Technological Development of the Republic of Serbia III45003, OI171020 and Bilateral Project Serbia – Slovenia (2014–2015) No. 451-03-3095/2014-09/30.

References

[1] L. Wen, X. Sun, Z. Xiu, S. Chen, Chi-Tay Tsai, J. Eur. Ceram. Soc. 24 (2004) 2681–2688.
[2] J.W.G.A. Vrolijk, J.W.M.M. Willems, R. Metselaar, J. Eur. Ceram. Soc. 6 (1990) 47–51.
[3] Y. Fujimoto, T. Yanagida, H. Yagi, T. Yanagidani, V. Chani, Opt. Mater. 36 (2014) 1926–1929.
[4] C.R. Varney, D.T. Mackay, S.M. Reda, F.A. Selim, J. Phys. D Appl. Phys. 45 (2012) 015103–015106.
[5] Y-C. Li, Y.-H. Chang, Y-F. Lin, Y-S. Chang, Yi-J. Lin, J. Alloys Compd. 439 (2007) 367–375.
[6] B. Grobelna, P. Bojarski, B. Kuklinski, A.A. Kubicki, A. Synak, Opt. Mater. 34 (2011) 103–108.

[7] S. Kostić, Z. Lazarević, M. Romčević, V. Radojević, A. Milutinović, G. Stanišić, M. Gilić, Phys. Scr. T. 162 (2014) 014026.
[8] G.R. Dillip, B. Ramesh, C.M. Reddy, K. Mallikarjuna, O. Ravi, S.J. Dhoble, S.W. Joo, B. Deva Prasad Raju, J. Alloys Compd. 615 (2014) 719–727.
[9] M.R.N. Soares, M.J. Soares, A.J.S. Fernandes, L. Rino, F.M. Costa, T. Monteiro, J. Mater. Chem. 21 (2011) 15262.
[10] M.S. Rabasović, D. Šević, J. Križan, M. Terzić, J. Možina, B.P. Marinković, S. Savić Šević, M. Mitrić, M.D. Rabasović, N. Romčević, J. Alloys Compd. 622 (2015) 292–295.
[11] S. Kostic, Z.Ž. Lazarevic, V. Radojevic, A. Milutinovic, M. Romcevic, N.Ž. Romcevic, A. Valcic, Mater. Res. Bull. 63 (2015) 80–87.
[12] A. Lukowiak, R.J. Wiglusz, M. Maczka, P. Gluchowski, W. Srek, Chem. Phys. Lett. 494 (2010) 279.
[13] R.A. Buchanan, K.A. Wickersheim, J.J. Pearson, G.F. Herrman, Phys. Rew. A 159 (1967) 245.
[14] Y.F. Chen, P.K. Lim, S.J. Lim, Y.J. Yang, L.J. Hu, H.P. Chiang, W.S. Tse, J. Raman Spectrosc. 34 (2003) 882.
[15] M.C. Klein, F. Hache, D. Ricard, C. Flytzanis, Phys. Rew. B 42 (1990) 11123.
[16] G. Gouadec, Ph. Colomban, Prog. Cryst. Growth Charact. Mater. 53 (2007) 1.
[17] A. Chopelas, Phys. Chem. Miner. 38 (2011) 709.
[18] A. Misra, H.D. Bist, M.S. Navati, R.K. Thareja, J. Narayan, Mat. Sci. Eng. B79 (2001) 49.
[19] A. Potdevin, G. Chadeyron, D. Boyer, B. Caillier, R. Mahiou, J. Phys. D Appl. Phys. 38 (2005) 3251–3260.
[20] Joo-Yun Chong, Yuelan Zhang, Brent K. Wagner, Zhitao Kang, J. Alloys Compd. 581 (2013) 484–487.
[21] Z. Boruc, B. Fetlinski, M. Malinowski, S. Turczynski, D. Pawlak, Opt. Mater. 34 (2012) 2002–2007.
[22] G.S.R. Raju, H.C. Jung, J.Y. Park, J.W. Chung, B.K. Moon, J.H. Jeong, Se-Mo Son, J. H. Kim, J. Optoelectr. Adv. Mat. 12 (6) (2010) 1273–1278.
[23] C.R. Varney, S.M. Reda, D.T. Mackay, M.C. Rowe, F.A. Selim, AIP Adv. 1 (2011) 042170.
[24] Q. Su, H. Liang, C. Li, H. He, Y. Lu, J. Li, Y. Tao, J. Lumin. 122–123 (2007) 927–930.
[25] G.R. Dillip, S.J. Dhoble, B.D.P. Raju, Opt. Mater. 35 (2013) 2261–2266.
[26] Y. Zhou, J. Lin, M. Yu, S. Wang, J. Alloys Compd. 375 (2004) 93–97.
[27] https://en.wikipedia.org/wiki/Illuminant_D65.

Soft Matter

PAPER

View Article Online
View Journal | View Issue

Check for updates

Cite this: *Soft Matter*, 2021, **17**, 6477

Synergy of interference, scattering and pigmentation for structural coloration of *Jordanita globulariae* moth

Danica Pavlović, *[a] Svetlana Savić-Šević,[a] Branislav Salatić,[a] Vladimir Lazović,[a] Wang Zhang,[b] Di Zhang[b] and Dejan Pantelić[a]

Received 29th January 2021,
Accepted 25th May 2021

DOI: 10.1039/d1sm00157d

rsc.li/soft-matter-journal

Structural and pigment colorations are omnipresent in insects, producing a range of colors for camouflage, warning, mimicry and other strategies necessary for survival. Structural coloration has attracted a lot of attention due to its significance in biophotonics, biomimetics and even esthetic appeal. The coupling of structural and pigment colorations has been largely unnoticed. Herein we show how pigments, scattering and interference work together in two-dimensional waveguiding structures to produce the coloration of *Jordanita globulariae* (Huebner, 1793), a moth whose forewings sparkle with slightly iridescent green scales. We show that subwavelength structures scatter and couple light into a concave multilayered structure to enhance the absorption of pigments. A finite element method (FEM) model, adequately describing the photonic properties of *J. globulariae*, was developed based on the nanoscale architecture of the insect's wing scales. The principle of absorption enhanced by scattering and waveguiding is present in many insect species and might be imitated to tailor the spectral properties of optical devices.

Published on 27 May 2021. Downloaded by National Library of Serbia on 7/27/2021 1:26:30 PM.

1. Introduction

Animals produce colors in two fundamentally different ways: by pigments and structurally. Most animals have pigmentary coloration that is based on the selective absorption of a certain range of wavelengths. However, the most intense and brightest colors are structural. They result from the interaction of light with micro- and nanostructures comparable with visible wavelengths.[1]

Pigment coloration is prevalent, except for blue and green, which seem to be rare, but nonetheless can be found in some vertebrates,[2] the most notable being the green coloration of frogs.[3] The same is true for insects, whose blue-green colors can be produced by bile pigments such as pterobilin, phorcabilin and sarpedobilin. Some butterfly species have a bluish- or greenish-pigmented hue obtained by bile pigments (seen in two Papilionidae genera: *Papilio* and *Graphium*). Pigmented blue has not been found in other insects.[4] Structural coloration seems to be an alternative, evolutionarily developed, way to generate shiny, pronounced shades of arbitrary colors, including blues and greens.

There are many different studies and advanced techniques dealing with structural coloration.[5,6] The genesis of green coloration is particularly interesting because of its significance in camouflage. Structural green sometimes arises solely from photonic structures[7,8] or due to color mixing within concave structures (as in the wing scales of some Papilionidae species (Lepidoptera) and Cicindelidae (Coleoptera)).[9,10] It is worth noting that green may be a result of the color-mixing of structural blue and pigmentary yellow.[11,12]

Such a peculiar coloration is even more interesting if it is found on the wings of moths (Heterocera: Lepidoptera). Moths are mostly nocturnal, and therefore, generally drab in color (brown or grey). However, there are some moth species that possess attractive coloration such as the tropical Madagascan sunset moth.[13] There is also a whole group of colorful, day-flying moths of the Zygaenidae family. The majority of zygaenids are tropical, but they are nevertheless quite well represented in temperate regions. The species *Jordanita globulariae* (subfamily Procridinae) caught our attention because of the dull, slightly iridescent green coloration of its forewings.

In this study we reveal the structure and function of the scales of the *Jordanita globulariae* moth through morphological characterization, spectral measurement and numerical simulation. The synergistic operation of structure and pigments is analyzed. We also discuss the role of this particular coloration in the moth's lifestyle.

[a] *Institute of Physics Belgrade, Pregrevica 18, 11080 Zemun, Belgrade, Serbia. E-mail: danica.pavlovic@ipb.ac.rs*
[b] *State Key Lab of Metal Matrix Composite, Shanghai Jiao Tong University, 800 Dongchuan Road, Shanghai 200240, China*

This journal is © The Royal Society of Chemistry 2021

Published on 27 May 2021. Downloaded by National Library of Serbia on 7/27/2021 1:26:30 PM.

2. Materials and methods

2.1 Specimen details

Jordanita globulariae (Fig. 1) is a day-flying moth (fam. Zygaenidae, subfam. Procridinae). The species is widespread from the Iberian Peninsula in the west to the Urals in the east of Europe. The forewing's length is 10.5–17 mm in males and 7.7–10.1 mm in females. It flies during the sunny days from May to August, usually in limestone pastures.[14] Larvae are fed on species from the genera *Centaurea* L., *Cirsium* and *Globularia* L. On very hot days, the moth usually perches on flowers and other vegetation. Males occasionally fly at night.[15] Adults of this moth have green forewings, while the hind ones are grey-brown. When at rest, the hindwings are completely obscured under the green forewings, enabling the insect to hide in foliage. Several species within this family have similar morphological characteristics [*e.g. Adscita statices* (Linnaeus, 1758)]. We had three, conserved and pinned *J. globulariae* specimens at our disposal, collected during May and June of 2011 on Mt. Fruška Gora, near the city of Novi Sad, Serbia (leg. D. Stojanović).

2.2 Microscopy and spectroscopy

Field-emission gun scanning electron microscope (FEGSEM) (MiraSystem, TESCAN) was used to study the fine anatomy of the moth scales. Dried insect forewings were mounted and sputter-coated with 5–10 nm of Au/Pd in preparation for SEM. We used an Au/Pd target because it has a smaller grain size and it is the recommended metal coating for a wide range of sample types.

Individual scales were prepared for SEM by the double transfer method: a scale was detached with a low-surface-energy adhesive (''Post-it'' sticky note), followed by transfer to a high-surface-energy tape (conductive carbon). In this way, the original scale orientation was preserved. During this process some of the scales were mechanically broken, revealing the inner structure and cross section of the scales.

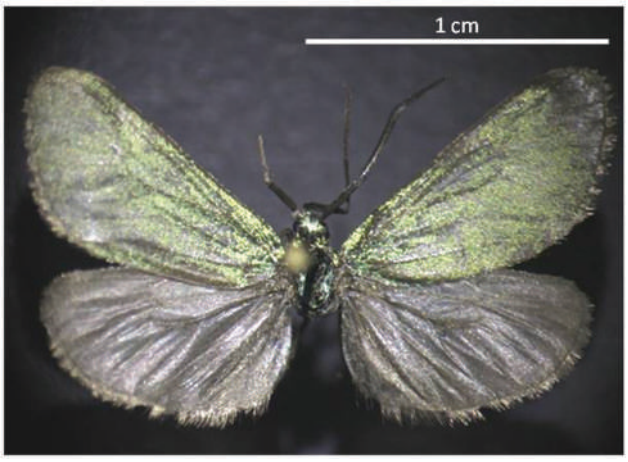

Fig. 1 *Jordanita globulariae* with structurally green dorsal sides of the forewings.

Optical characteristics of the wings and scales were analyzed on a trinocular microscope MET104 (Colo Lab Experts) with a Plan Achromatic POL Polarizing objective lens (10X/20X/40X).

To record reflectance spectra, we used a fiber optic spectrometer (Ocean Optics, HR2000CG-UV-NIR) with a 400 μm core diameter fiber. A halogen lamp was used as a light source and spectra were referenced to a standard white surface. Angular variation of the reflectance spectra was measured with a stationary sample illuminated by the light source at normal incidence. The spectrometer fiber was rotated within the angular range from 10° to 50°.

2.3 Optical modeling

A finite element method (FEM) was used to model the interaction of visible light with wing pigmented scale nanostructures. The model is two-dimensional because it saves computation time, which was approximately 20 min on our PC. It would be difficult to model the exact shape of photonic structures that are certainly not spherical, but somewhat irregular, rather oval and elongated along one axis (Fig. 2(b) and 3(a)). Thus, a 2D model (which is equivalent to a 3D infinite cylinder) is a satisfactory approximation, as the photonic structure studied here departs significantly from cylindrical only at its edges. The arrayed structure of wing scales is modeled using one unit cell with periodic boundary conditions. Perfectly matched layers (PMLs) are placed above and below the structure in order to minimize any reflected signal. In the model, the average mesh size was manually set to one-fifth

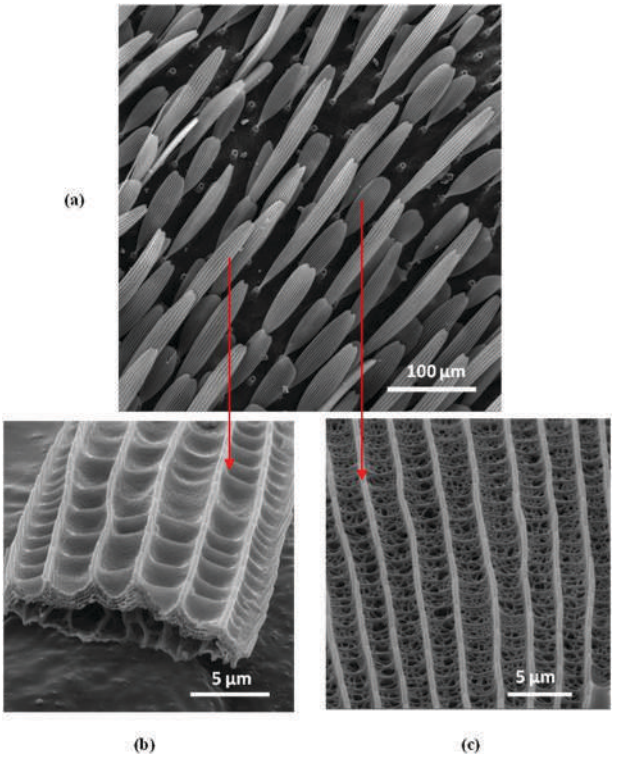

Fig. 2 (a) A SEM image of the *J. globulariae* forewing with two types of scales. Magnified SEM images of: (b) a long scale covered with several cup-shaped dips and (c) a short scale with a random, sponge-like structure.

 This journal is © The Royal Society of Chemistry 2021

Published on 27 May 2021. Downloaded by National Library of Serbia on 7/27/2021 1:26:30 PM.

of the minimum incident wavelength, which was 400 nm in our case. However, mesh density was adaptively adjusted to correctly model the tiniest structures of the model. To create a numerical simulation, it is necessary to know the complex refractive index of the biological structure. It is difficult to know the exact value, but we found that modest variation ($\Delta n \sim \pm 0.03$) of the refractive index has only a slight impact on simulations. The real part of the complex refractive index was taken from the literature: $n = 1.57$.[16,17]

The extinction coefficient was determined experimentally by measuring the transmission of light through the structure and applying Beer–Lambert's law. We assumed that the structures analyzed here had a subwavelength size and could be regarded within the effective medium approximation. Imaginary part k of the refractive index was 0.011 at 400 nm, 0.019 at 500 nm and 0.01 at 800 nm.

3. Results

3.1 Morphological and optical analysis of *J. globulariae* wing structures

The dorsal side of *J. globulariae* forewings is covered with scales that seem to be randomly distributed (Fig. 2(a)). The scales are either long with a regular internal architecture (Fig. 2(b)), or short with an irregular, sponge-like structure (Fig. 2(c)).

Long scales (with characteristic dimensions of approximately 20 μm × 150 μm) seem to be more elaborate. At higher magnification (Fig. 3(a)), we can see that their upper lamina is ornamented with thin, lamellar ridges (separated by approximately 3 μm) connected by cross ribs. Together, ridges and cross ribs produce a sequence of concave dips (cup-like structures, 0.5–3 μm deep) whose surface has a large number of tiny pores (20–50 nm). The interior of the whole scale is hollow, supported by large, 1.5 μm high, trabeculae (Fig. 3(a)) connecting the upper and lower lamina (which is irregular, single-layered and about 100 nm thick).

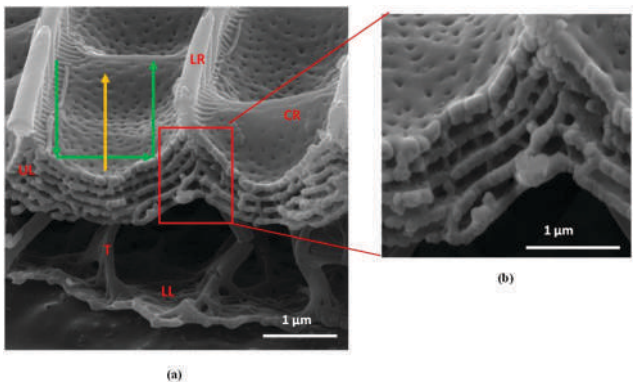

Fig. 3 SEM image of *J. globulariae* long wing-scale structure. (a) A cross section of the scale showing concave, multilayered upper lamina and single-layer lower lamina separated by trabeculae (LR – lamellar ridges; CR – cross ribs; T – trabeculae; UL – upper lamina; LL – lower lamina). Green and yellow arrows indicate different wavelengths for radiation hitting the structure at its center or its edges. (b) A concave multilayer of the upper lamina with five chitin layers.

The cross section of the scale (Fig. 3(b)) shows the concave upper lamina with five chitin layers whose thickness is approximately 110 nm. They are mutually separated by tiny, pillar-like structures, producing 90 nm-thin, air-filled, voids. This arrangement will be further considered as a curved multilayer serving as a specific, spectrally selective, filter.

On the other hand, short scales (whose approximate size is 40 μm × 80 μm) are quite different. They are almost hollow, filled with an intricate, irregular, sponge-like structure (Fig. 4(a) and (b)), but surface ridges and cross ribs can be seen as well.

From an optical point of view, the green color of the insect is diffuse, dim and slightly iridescent (Fig. 1) – *i.e.* we were able to observe a significant color shift only for large, almost grazing, angles of observation. If observed through an optical microscope, long scales reflect, while short ones absorb light (Fig. 5). If the image of a long scale is further magnified (inset in Fig. 5), a number of discrete blue-green and yellow dots can be seen.

Comparing SEM and optical images, we can see accurate matching between the morphology of long scales and the observed optical pattern. It is well known that the spectral reflection of a layered structure is influenced by the distance between the layers, the refractive index and the angle of incidence. In this case, reflection is strongly affected by the concave shape of the layers. We can see that light falling on the center of the concavity has a different angle of incidence compared to off-center zones. This is why we observe differently colored spots in the inset of Fig. 5. Macroscopically, colors are mixed to produce the insect's green color.

Apart from structural coloration, scales are slightly pigmented, as can be seen from the transmission optical image (Fig. 6(a) – scales were immersed in an index matching fluid to suppress Fresnel reflections). Interestingly, the long (structurally colored) scale has significantly higher (0.25) absorption than the short (nonstructural) one (0.16).

Absorption is much higher in the blue part of the spectrum and decreases towards the green-red part (as can be seen in Fig. 6(b)). We found that the average coefficient of absorption is between 0.35 1/μm in the blue part of the spectrum and 0.1 1/μm in the red. All the above facts signify that the effect of pigments cannot be disregarded, as we will further show.

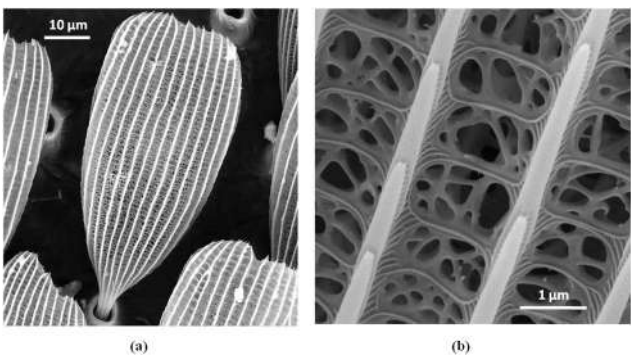

Fig. 4 SEM images of (a) a short wing scale of *J. globulariae* and (b) its hollow, sponge-like internal structure.

Published on 27 May 2021. Downloaded by National Library of Serbia on 7/27/2021 1:26:30 PM.

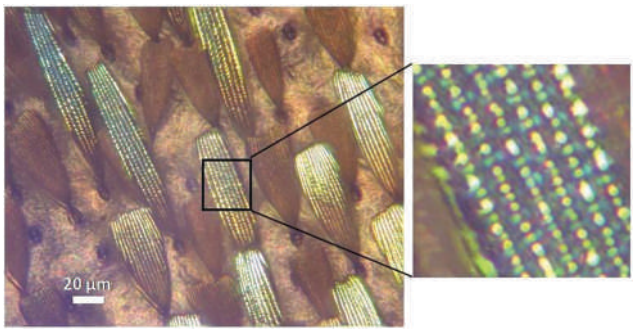

Fig. 5 Optical micrograph of *J. globulariae* wing scales. An enlarged part of a structurally colored one is shown on the right (with yellow and blue-green dots).

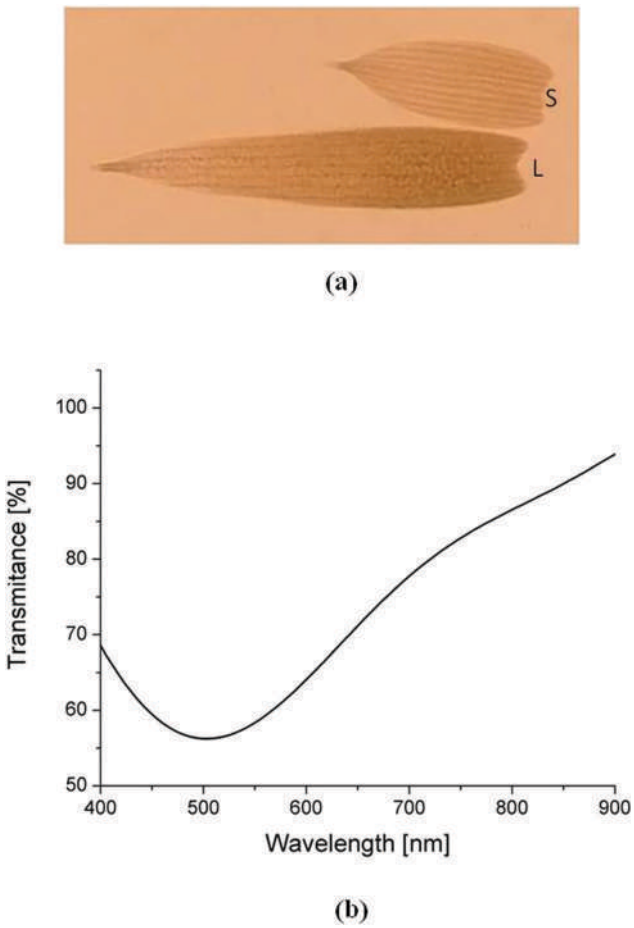

Fig. 6 *J. globulariae* moth: (a) Transmission optical image of long (L) and short (R) scales. (c) Transmittance spectrum of the long, structurally colored scale.

We measured the angular variation of the spectrum by rotating the detector (spectrometer fiber) and keeping the wing and illuminator positions fixed. Illumination was at normal incidence with respect to the wing. The reflection was recorded within the angular range of 10–50 degrees. Under these conditions we observed a slight spectral shift of 40 nm (Fig. 7(a)). This corresponds to the perception of unsaturated green color, irrespective of the angle of observation. As a final remark, we emphasize that the spectrum fits nicely into the spectrum of foliage (Fig. 7(b)), enabling the insect to hide effectively in its natural environment.

3.2 Optical modeling of *J. globulariae* wing scales

Here we present an optical model of structurally colored scales (Fig. 8(a)) designed to simulate all the characteristic features observed in SEM images (Fig. 3):

– concave dip (1.5 μm radius) with five chitin layers, 110 nm thick, and refractive index 1.57;

– layers separated by (20 nm × 90 nm) producing 90 nm air spaces;

– outer surface with a number of 10 nm-diameter holes.

On this basis, we will establish a link between the architecture and the optical response of wing scales.

In a simplified model and before going into more detail, we will approximate the structure with a collection of Bragg gratings with different orientations. According to Bragg's law:

$$\lambda = 2nd\cos\theta \quad (1)$$

where λ is the wavelength of multilayer reflectance maximum, d is the grating period, n is the effective refractive index of the grating, and θ is the angle of incidence of radiation. Observe that the incident plane wave irradiates the concave structure within the range of angles – 0 degrees in the center and 50 degrees at the edges. At the center of a concave dip (angle of incidence $\theta = 0^{\circ}$) the Bragg wavelength can be estimated at 520 nm (assuming a grating period of 200 nm and an effective refractive index of 1.3). Towards the edge, the Bragg resonance drops to 370 nm. Due to only five Bragg layers, the reflection maxima are broad (Fig. 8(b)) and the resulting spectra cover the UV-blue part of the spectrum.

We can conclude that, without an additional mechanism, *J. globulariae* wings will evenly reflect visible light, making the insect appear to be bluish. Absorption alone is not enough to modify the reflection spectrum due to the thinness of individual scales and small amount of pigment (Fig. 6). In the following we will prove that scattering amplifies absorption in accordance with the theory of Yablonovitch described in ref. 18. It was shown that rough surfaces amplify the radiation intensity within planar layers by $2n^2$ factor, where n is the refractive index of the material. This leads to increased absorption of up to $4n^2$ times compared to ideally flat layers. For chitinous structures of scales (n = 1.57), absorption may thus increase up to 9.9 times.

The Yablonovitch theory is universally applicable to layers of any thickness, as it is based on the basic laws of radiation. For subwavelength multilayer structures, as is the case here, the effects of evanescent waves certainly lead to radiation being redistributed among the layers. However, the total thickness of all layers taken together is significantly larger than the wavelength and the radiation stays entrapped and waveguided. Here we add that the theory is limited to randomly distributed (Lambertian) incoming radiation. This is usually the case for the environmental, solar, irradiation omnipresent in most natural surroundings. We have previously used the theory to

 This journal is © The Royal Society of Chemistry 2021

Published on 27 May 2021. Downloaded by National Library of Serbia on 7/27/2021 1:26:30 PM.

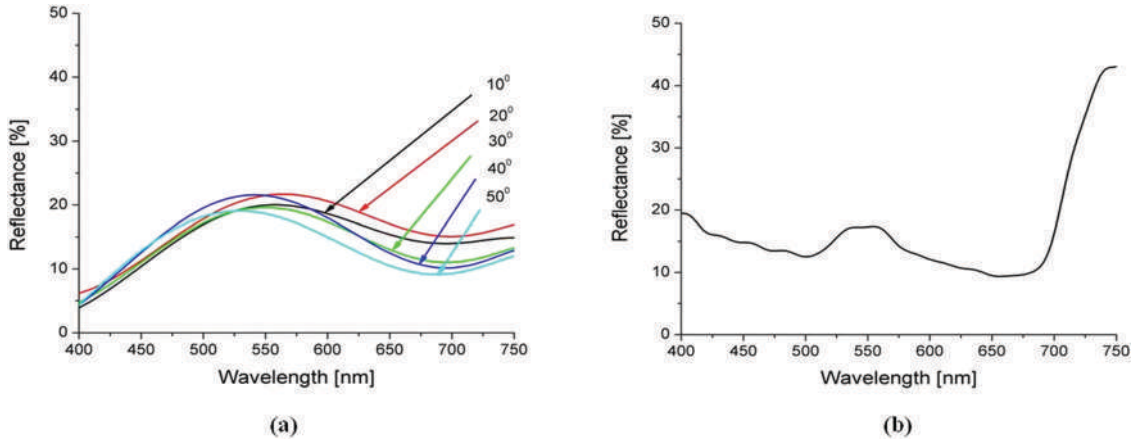

Fig. 7 (a) A slight angular variation (within a 10–50° range) of the *J. globulariae* wing reflectance spectrum. (b) A reflectance spectrum of the green leaves of Hibiscus.

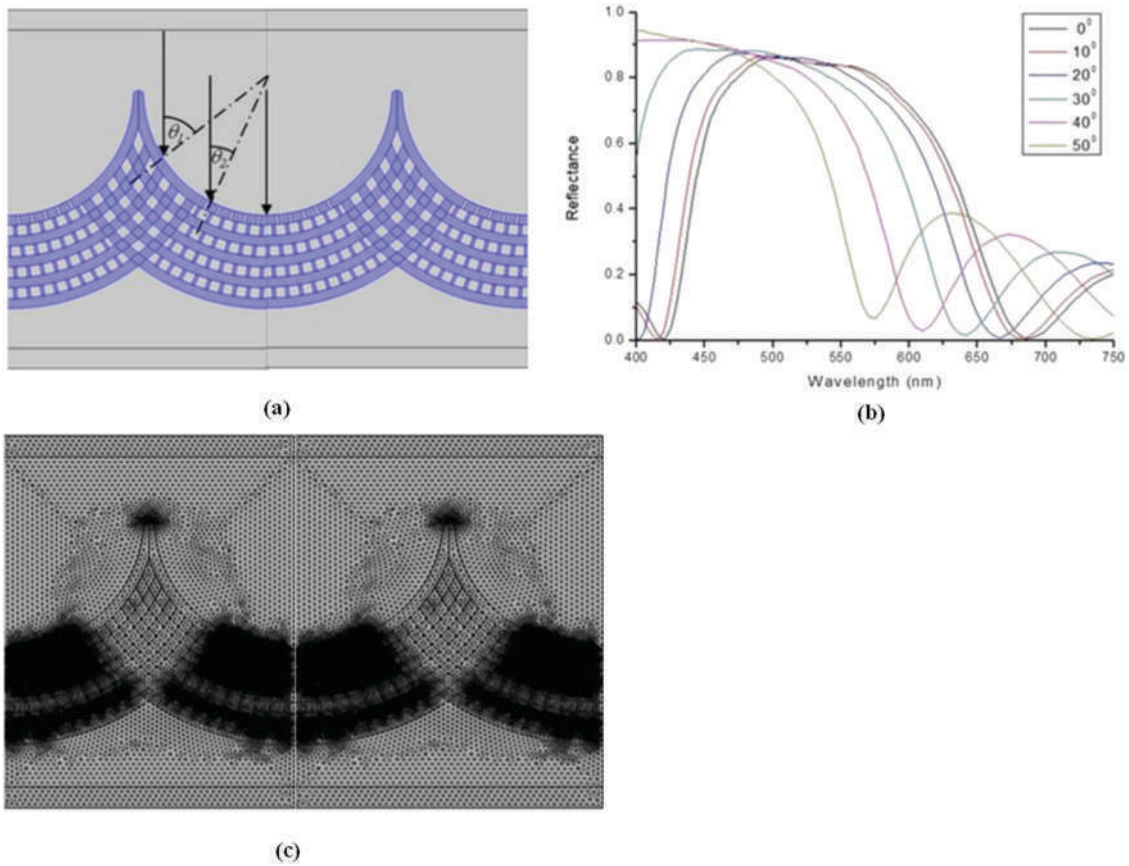

Fig. 8 (a) Geometry of a concave multilayer model used in FEM. Arrows indicate the radiation direction and θ is the angle of incidence. (b) Strong spectral shift for different angles of incidence. (c) A model, depicted in (a), is adaptively meshed for correct FEM analysis of the smallest features.

explain a golden coloration of rather simple wing scales of *Diachrysia chrysitis* moths.[19]

In the case of *J. globulariae* wing scales, scatterers are numerous and include nanometer scale pits on the surface, nanopillars between the layers and many of the other defects of otherwise regular structures. The whole problem is too complicated to be analyzed analytically because it includes the effects of scattering on subwavelength structures, spectrally dependent absorption, waveguiding and radiation localization, as well as interference effects on a very specific concave Bragg grating. This is why we had to use FEMs to calculate the reflection spectrum of the scales. A model in Fig. 8(a) was

Published on 27 May 2021. Downloaded by National Library of Serbia on 7/27/2021 1:26:30 PM.

adaptively meshed (*i.e.* finer structures were meshed more densely – Fig. 8(c)) in order to obtain the correct results.

First, we calculated the electromagnetic intensity distribution (square of the amplitude) without taking into account absorption (Fig. 9(a)). We clearly observed the localization of the field within the concave Bragg structure due to waveguided modes. They were introduced into the structure because of scattering on subwavelength structures (pillars and pits) in accordance with the Yablonovitch theory. Resulting spectra are wide and independent on the angle of incidence (Fig. 9(b)).

If absorption is introduced into the model, in accordance with the characteristics of real scales, we can clearly see that waveguided modes are strongly absorbed (Fig. 9(c)) and the resulting spectra are narrowed (Fig. 9(d)) and independent on the angle of illumination, to match those observed experimentally (Fig. 7(a)). This is in stark contrast to the completely flat Bragg grating – its reflectance is very high (up to 90%) but its angular dependence is significant (the shift is larger than 150 nm).

It seems that natural evolution has brought about a nicely balanced set of features: concave structures to induce angular insensitivity of coloration, residual pigments to absorb light and subwavelength structures to enhance scattering and waveguiding. As a result, *J. globulariae* becomes quite inconspicuous within its environment.

We can note that theoretical spectra have a number of local minima and maxima, resulting from a very complex structure with many resonances (Fig. 9(b) and (d)). In reality, the resulting spectrum is obtained by reflection from a large number of scales. They are not identical, and the resonances are averaged to produce a smooth curve as in Fig. 7(a).

To further refine the model, we sliced a spherical multilayer into 8 planar cross-sections and approximated each one as a collection of cylindrical layers (as shown in Fig. 10(a)). Due to symmetry of the structure, there were only 4 different sections (designated 1–4 in Fig. 10(a)) to which we applied an FEM technique in the manner described above. By averaging spectral distributions of all cross sections, we obtained the resulting spectrum in Fig. 10(b), which is comparable to the experimentally recorded curves in Fig. 7(a).

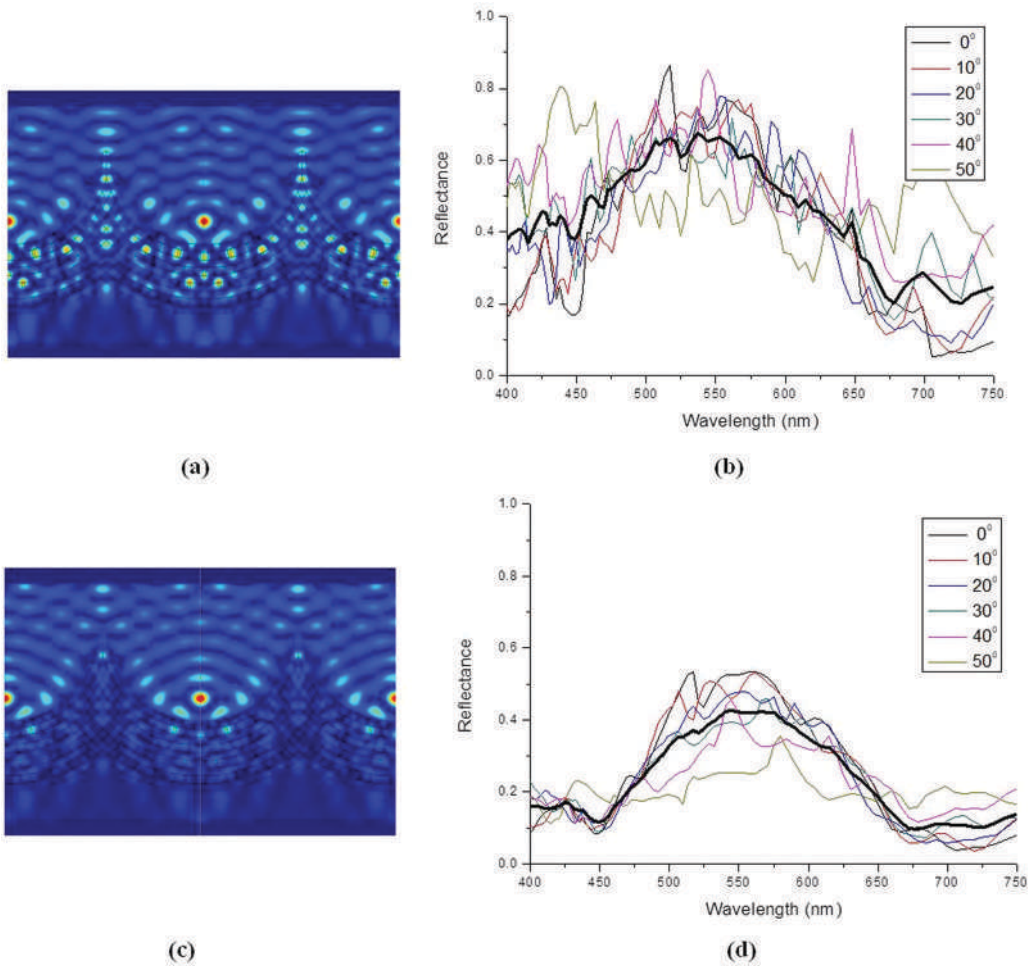

Fig. 9 (a) Strong localization of the electromagnetic field (λ = 479 nm) inside the structure (WITHOUT pigmentation taken into account), and (b) the corresponding spectra at different angles of incidence. (c) Absorption of a localized electromagnetic field (λ = 479 nm) inside the structure (WITH pigmentation taken into account), and (d) the corresponding spectra at different angles of incidence.

 This journal is © The Royal Society of Chemistry 2021

Published on 27 May 2021. Downloaded by National Library of Serbia on 7/27/2021 1:26:30 PM.

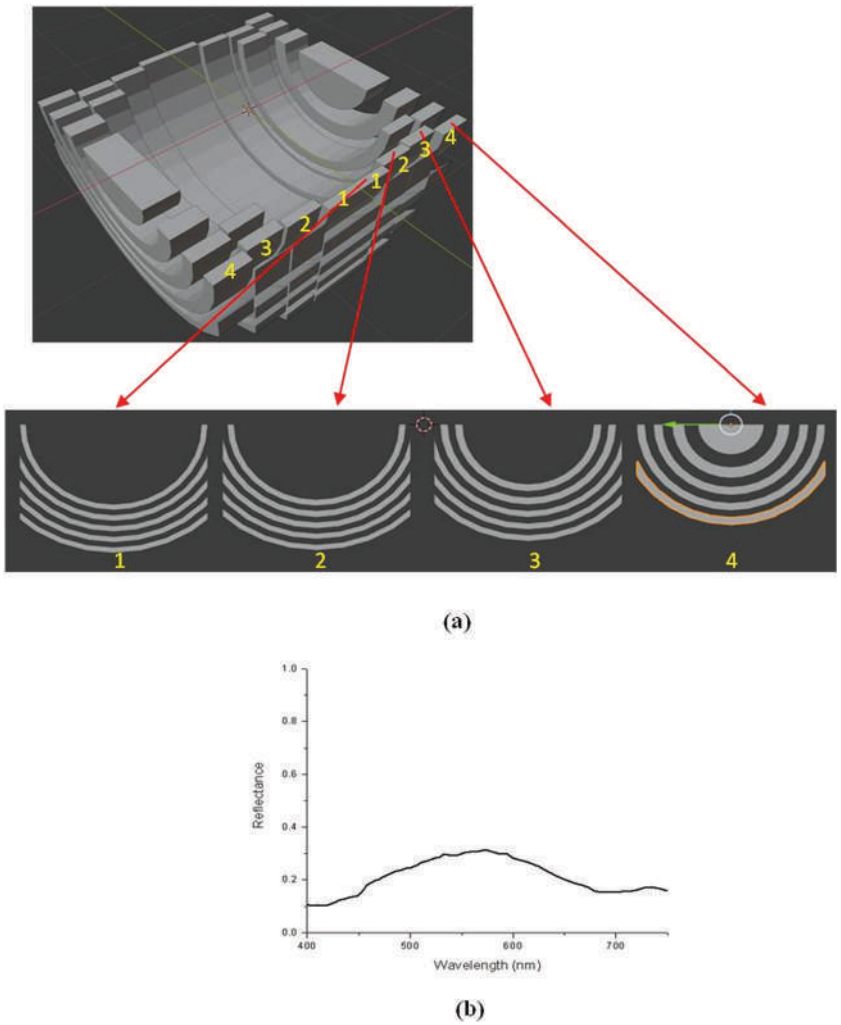

Fig. 10 (a) A characteristic multilayer dip of *J. globulariae* wing scale is modeled as a collection of cylindrical cross-sections designated by numbers 1–4. (b) The resulting spectral distribution, obtained by angular averaging spectra of cross-sections 1–4.

4. Discussion

We have shown that the wings of the *J. globulariae* moth possess a set of structural features that produce a slightly iridescent (*i.e.* observable only at grazing incidence) green structural color. This is important for a day-flying insect to remain unseen on the green background of vegetation. To do this, wings evolved with low angular variation and reflectance comparable to that of green surroundings.

Similar structural coloration was also observed in other insects. It was found that *Papilio palinurus* produces its green coloration as a result of color mixing between reflected and retroreflected light from a concave multilayer structure.[10] There, the effects of scattering and pigmentation were not analyzed, and the coloration was explained solely by the multilayer interference.

The question of adequate modeling is an important (and still open) problem for understanding the interaction of light with biophotonic structures. Three-dimensional modeling is extremely demanding, with respect to execution time and memory requirements. Massively parallel computers are used with computational time of the order of several hours (for a single 3D geometry and single wavelength) and tens (even hundreds) of gigabytes of working memory.[7]

Overall architecture of *J. globulariae* structures is variable – ranging from almost spherical to cylindrical, with several layers and a number of randomly distributed nano-pillars and holes. Such complexity is beyond the capability of most computers. Even the fastest ones are incapable of calculating irregular, stochastically distorted, nano-patterned geometries on a reasonable timescale. Here, we used 2D, cylindrical models of essentially three-dimensional structures. This is quite sufficient for oblong structures, while for those closer to spherical symmetry, a dip was sectioned in order to make the approximation more adequate. Anyway, optical microscopy (Fig. 5) shows that the overall optical effect is quite tolerant to random variation of size, shape and nanostructure. The computational results presented here confirm that slightly absorbing nanostructures restrict the radiation to the green-red part of the spectrum

Published on 27 May 2021. Downloaded by National Library of Serbia on 7/27/2021 1:26:30 PM.

(compare Fig. 9(b) and (d)) in accordance with the theory of absorption enhancement by scattering.

The role of pigments was analyzed in ref. 20. The authors described the *Eudocima materna* moth whose cover scales act as an interference mirror (not the multilayer one), while ground scales are strongly pigmented. For certain angles of observation, cover scales mirror the incoming radiation, thereby making underlying pigmented scales invisible. For other angles, radiation is redirected by the mirror scales outside the viewing direction, making the underlying pigmented scales visible. Again, interference, scattering and absorption are not interlinked and enhanced.

A somewhat different analysis of the interplay between wing coloration and visual pigments was performed in ref. 21. It was found that additional visual pigment in the photoreceptors of Lycaenidae is well tuned to the characteristic structural coloration of butterflies within this family.

A good overview of photonic structures has been given in ref. 22. The authors remark that green pigments are absent in butterfly wing scales and analyze blackness and fluorescence enhancement caused by structures.

Structures at all dimensional scales are included and work in synergy to produce the coloration of *J. globulariae*. At the molecular level, dark pigments (melanin) are needed to selectively absorb the blue part of the spectrum. However, in this particular insect there is only a small amount of pigment, which is not enough to significantly absorb the blue part of the spectrum as shown in Fig. 9(b). Therefore, nanoscales, pillars, pits and other subwavelength structures are necessary to preferentially scatter blue light and enhance its absorption. Micron-sized concave multilayers selectively filter the red part of the spectrum while making it angularly independent.

On a higher scale (in the order of hundreds of micrometers and millimeters), the wing as a whole must be accounted for. Our model shows that the reflectivity of a single structural scale is in the order of 40% (Fig. 9(d)). However, the reflectivity of the wing is much lower (20–25%, Fig. 7) as a result of sparse scale population, attenuation by nonstructural scales and the wing membrane. The resulting value corresponds well to the reflectivity of vegetation, making the insect almost invisible in its environment. We have calculated the CIE xy color coordinates of the green leaves of *Hibiscus*.[23,24] *J. globulariae* and our model show how well nature has "adjusted" the insect to the environment (Fig. 11). Here, a CIE diagram is used as a simple way to compare complex spectra, not as a measure of human color perception, which is certainly quite different compared to that of insects.

For reference, we have shown the color coordinates of a model without scattering and absorption. In this case, the insect's color would have been blue, making it highly visible.

In this paper we had no space to analyze the "nonstructural" scales, but it seems that there are structural effects too. By looking closely at Fig. 6(a), we can see that the absorption of a nonstructural scale is lower than that of the structural one, yet it is highly absorbing on the wing (Fig. 5). It seems that scattering enhances the absorption of the rather hollow structure of a "nonstructural" scale as well.

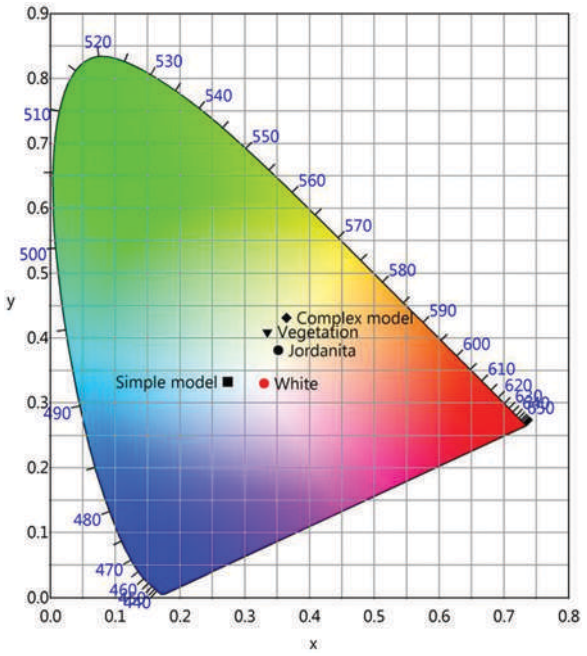

Fig. 11 A CIE diagram showing the *xy* chromatic coordinates of vegetation, *J. globulariae* and a complex model (concave layer with scattering structures and absorption). Coordinates of achromatic white and a simple, flat, layer model have been shown for reference.

From a biological point of view, the color green usually has a cryptic role in insects,[25–27] providing very effective camouflage among leaves. This greenish color, which is not highly reflective, indicates a primary defensive role in *J. globulariae*. Slight iridescence and color contrast, which are very important in communication between species, further speak in favor of the protective role of such an optical signal.[28]

On the other hand, species of this family (including *J. globulariae*) also possess a chemical defense mechanism. All Zygaenidae[15] contain hydrogen cyanide (HCN), taken from plants or synthesized from plant glucose.[29] Therefore, they are poisonous or, at least, distasteful to potential predators. Sending a warning is another reason why the species of this moth family may have such coloration. The color green becomes highly visible during feeding on flowers[14] when it acquires its second, aposematic role.[30] Other examples are also known among Lepidoptera where warning and camouflage coloration are not contradictory.[31] We can therefore assume that the role of *J. globulariae* can be cryptic, when resting, hidden in leaves, and aposematic, during nectar feeding.

In most moths, the dorsal side of the front wings is visible during rest.[32] Given that all Zygaenidae are diurnal species, evolution has ensured that they have structural coloration only on the dorsal surface of their forewings.[15]

5. Conclusion

This paper reveals the delicate combination of interference, scattering, absorption and color mixing, all working together,

 This journal is © The Royal Society of Chemistry 2021

Published on 27 May 2021. Downloaded by National Library of Serbia on 7/27/2021 1:26:30 PM.

to facilitate the survival of *J. globulariae*. The fine tuning of many structural factors, from submicron to macroscopic levels, is amazing and its imitation provides a new way to control the spectral content of light.

Conflicts of interest

There are no conflicts to declare.

Acknowledgements

The authors acknowledge funding provided by the Institute of Physics, Belgrade, through a grant from the Ministry of Education, Science and Technological Development of the Republic of Serbia and the Science and Technology Development Program – Joint Funding of Development and Research Projects of the Republic of Serbia and the People's Republic of China: Mimetics of insects for sensing and security, No. I-2. DP acknowledges support from L'Oréal-UNESCO ''For Women in Science''. We express our gratitude to Dejan Stojanović from the Institute of Lowland Forestry and Environment, Novi Sad, Serbia, who donated *J. globulariae* specimens from his insect collection.

References

1 J. Sun, B. Bhushan and J. Tong, *RSC Adv.*, 2013, **3**, 14862–14889.
2 J. T. Bagnara, P. J. Fernandez and R. Fujii, *Pigment Cell Res.*, 2007, **20**, 14–26.
3 C. Taboada, A. E. Brunetti, M. L. Lyra, R. R. Fitak, A. F. Soverna, S. R. Ron, M. G. Lagorio, C. F. B. Haddad, N. P. Lopes, S. Johnsen, J. Faivovich, L. B. Chemes and S. E. Bari, *Proc. Natl. Acad. Sci. U. S. A.*, 2020, **117**, 18574–18581.
4 P. Simonis and S. Berthier, How nature produces blue color. in *Photonic Crystals –Introduction*, ed. A. Massaro, Applications and Theory, InTech, Rijeka, 2012, pp. 3–24.
5 P. Kaspar, D. Sobola, P. Sedlák, V. Holcman and L. Grmela, *Microsc. Res. Tech.*, 2019, **82**, 2007–2013.
6 D. Sobola, S. Talu, P. Sadovsky, N. Papez and L. Grmela, *Adv. Electr. Electron. Eng*, 2017, **15**, 569–576.
7 K. Michielsen, H. De Raedt and D. G. Stavenga, *J. R. Soc., Interface*, 2010, **7**, 765–771.
8 B. D. Wilts, K. Michielsen, J. Kuipers, H. De Raedt and D. G. Stavenga, *Proc. R. Soc. B*, 2012, **279**, 2524–2530.
9 S. Berthier, *Iridescences, les couleurs physiques des insectes*, Springer Science & Business Media, 2007.
10 P. Vukusic, J. R. Sambles and C. R. Lawrence, *Nature*, 2000, **404**, 457.
11 D. L. Fox, *Animal biochromes and structural colours: physical, chemical, distributional & physiological features of coloured bodies in the animal world*, University of California Press, 1976.
12 D. G. Stavenga, M. A. Giraldo and H. L. Leertouwer, *J. Exp. Biol.*, 2010, **213**, 1731–1739.
13 S. Yoshioka, T. Nakano, Y. Nozue and S. Kinoshita, *J. R. Soc., Interface*, 2008, **5**, 457–464.
14 K. A. Efetov and G. M. Tarmann, Forester Moths: The genera Theresimima Strand, 1917, Rhagades Wallengren, 1863, Jordanita Verity, 1946, and Adscita Retzius, 1783 (Lepidoptera: Zygaenidae, Procridinae), Apollo Books, 1999.
15 C. M. Naumann, G. M. Tarmann and W. G. Tremewan, *The Western Palaearctic Zygaenidae (Lepidoptera)*, Apollo Books, 1999.
16 N. N. Shi, C. C. Tsai, F. Camino, G. D. Bernard, N. Yu and R. Wehner, *Science*, 2015, **349**, 298–301.
17 H. L. Leertouwer, B. D. Wilts and D. G. Stavenga, *Opt. Express*, 2011, **19**, 24061.
18 E. Yablonovitch and G. D. Cody, *IEEE Trans. Electron Devices*, 1982, **29**, 300–305.
19 D. Pantelić, S. Savić-Šević, D. V. Stojanović, S. Curčić, A. J. Krmpot, M. Rabasović, D. Pavlović, V. Lazović and V. Milošević, *Phys. Rev. E*, 2017, **95**, 032405.
20 J. L. Kelley, N. J. Tatarnic, G. E. Schröder-Turk, J. A. Endler and B. D. Wilts, *Curr. Biol.*, 2019, **29**, 2919–2925.
21 Z. Bálint, K. Kertész, G. Piszter, Z. Vértesy and L. P. Biró, *J. R. Soc., Interface*, 2012, **9**, 1745–1756.
22 L. P. Biró and J. P. Vigneron, *Laser Photonics Rev.*, 2011, **5**, 27–51.
23 C. Buschmann and E. Nagel, *Int. J. Remote Sens.*, 1993, **14**, 711–722.
24 C. Buschmann, S. Lenk and H. K. Lichtenthaler, *Isr. J. Plant Sci.*, 2012, **60**, 49–64.
25 F. Liu, H. Yin, B. Dong, Y. Qing, L. Zhao, S. Meyer, X. Liu, J. Zi and B. Chen, *Phys. Rev. E: Stat., Nonlinear, Soft Matter Phys.*, 2008, **77**, 1–4.
26 A. R. Parker, D. R. Mckenzie and M. C. J. Large, *J. Exp. Biol.*, 1998, **201**, 1307–1313.
27 D. G. Stavenga, Surface Colors of Insects: Wings and Eyes, in *Functional Surfaces in Biology. Little Structures with Big Effects*, ed. S. N. Gorb, Springer, The Netherlands, 2009, vol. 1, 285–306.
28 P. Vukusic, J. R. Sambles, C. R. Lawrence and R. J. Wootton, *Proc. R. Soc. B*, 1999, **266**, 1403–1411.
29 O. Niehuis, S. H. Yen, C. M. Naumann and B. Misof, *Mol. Phylogenet. Evol.*, 2006, **39**, 812–829.
30 C. Wiklund and B. Sillen-Tullberg, *Evolution*, 1985, **39**, 1155.
31 K. L. Prudic, A. K. Skemp and D. R. Papaj, *Behav. Chem. Ecol.*, 2007, **18**, 41–46.
32 N. P. Kristensen, *Handbook of Zoology, Vol. IV, Part 3.: Lepidoptera:Moths and Butterflies. Morphology, Physiology, and Development*, Walter DeGruyter Press, Berlin, 2004.

Journal of Materials Chemistry C

ROYAL SOCIETY OF CHEMISTRY

COMMUNICATION

Check for updates

Cite this: J. Mater. Chem. C, 2021, 9, 8163

Received 5th March 2021,
Accepted 6th June 2021

DOI: 10.1039/d1tc01028j

rsc.li/materials-c

Thermo-osmotic metamaterials with large negative thermal expansion

Svetlana Savić-Šević, *[a] Dejan Pantelić,[a] Branka Murić,[a] Dušan Grujić,[a] Darko Vasiljević,[a] Branko Kolaric [ab] and Branislav Jelenković[a]

Negative thermal expansion (NTE) is important for compensation of thermal dilatation effects and has significant applications in high-precision devices and instruments. Several materials with intrinsic negative expansion exist but are chemically complex, difficult to manufacture and their thermal expansion coefficients (TECs) are small, typically in the order of 10^{-5}/K–10^{-6}/K. Here we present a metamaterial with a large NTE, with TEC in the order of 10^{-3}/K, enabled by thermo-osmosis of entrapped air molecules through a multitude of nanometer-thin layers. We have generated this material by holographically patterning a biopolymer (dichromated pullulan). The presented manufacturing process is quite simple and capable of generating large-area NTE materials. The concept of achieving (NTE) through thermo-osmosis is universal and can be extended to many other polymers. Our research, for the first time, introduces a relation between NTE and thermo-osmosis.

Introduction

All materials change their dimensions with temperature due to thermally dependent interatomic distances.[1] This behavior is quantified by linear (α_l) or volumetric (α_v) thermal expansion coefficients (TEC):

$$\alpha_l = \frac{1}{l}\frac{\mathrm{d}l}{\mathrm{d}T} \quad \text{and} \quad \alpha_V = \frac{1}{V}\frac{\mathrm{d}V}{\mathrm{d}T} \tag{1}$$

where $\mathrm{d}l$ and $\mathrm{d}V$ are length l and volume V changes induced by temperature difference $\mathrm{d}T$, respectively.[2] Almost all materials expand upon heating and the thermal expansion coefficient is thus positive (PTEC). Organic materials and polymers usually have a larger coefficient of thermal expansion (PTEC greater than 10^{-4}/K) than inorganic materials (such as metals and ceramics with PTEC of about 10^{-6}/K).[3]

Materials with negative thermal expansion coefficients (NTECs) are expensive, rare (except water between 273 K–277 K) and their chemical composition is very specific.[4,5] One of the main goals of NTE research is finding materials with large NTECs to compensate PTECs. In materials associated with a magnetic, ferroelectric or charge-transfer phase transition a large NTE has been discovered and such materials are used as thermal-expansion compensators.[6]

The development of a material with a large NTEC is possible by designing special structures made of several constituents.[7,8] For example, origami structures, consisting of a bi-material's 2D or 3D lattices, enable tailoring metamaterials with novel mechanical properties, including a wide range of PTECs and NTECs.[9] Such NTE materials have important applications for the control of the thermal expansion of materials. They allow adjustment of the thermal expansion of composites and can be used in microchip devices,[10] as dental fillings,[11] in optical and electronic devices,[12] for fasteners[13] and as coating materials.[14] However, such materials have a complex geometry difficult to manufacture.

Many methods have been used to fabricate metamaterials: laser interference lithography,[15] electron-beam lithography,[16] direct laser writing,[17] and focused-ion beam (FIB),[18] to mention just a few. Metamaterials can be fabricated from different substances including photoresists,[19] semiconductors,[20] and metals.[21] Holographic methods stand out as being capable of producing one-, two- and three–dimensional periodic metamaterials. Large areas can be fabricated simply and cheaply in a matter of minutes.

Here we describe a holographic method for generation of mechanical metamaterials with simple architecture and high NTECs, much higher than those of the other materials we found in the available literature. Pullulan, a biological polysaccharide, is used as a base material, which is further sensitized and holographically patterned at the nanoscale. Structural, optical and mechanical properties of the resulting metamaterial are studied, its NTEC measured and a thermo–mechanical model, explaining NTE behavior, presented. We also disclose a new physical mechanism behind such unusual behavior.

[a] Institute of Physics, University of Belgrade, Pregrevica 118, Zemun 11080, Serbia. E-mail: savic@ipb.ac.rs
[b] MNM Group, Department of Physics, UMONS, Mons, Belgium

Holographic generation of mechanical metamaterial

Doped pullulan is a home-made holographic photosensitive material used throughout this research to manufacture layered metamaterial and analyze its thermo-mechanical behavior. Pullulan is a linear polysaccharide produced from the yeast-like fungus *Aureobasidium pullulans*. The material is composed of maltotriose units connected by α-D-1,6-glycoside linkages[22] and can be photosensitized with chromium ions to produce dichromated pullulan (DCP)[23] as a transparent, thermo-stable film. Properties of DCP films as holographic material–surface gratings, its diffraction efficiency, copying and environmental stability–were previously investigated.[24,25]

DCP film was prepared by mixing an 8% aqueous solution of pullulan and 30% ammonium dichromate, which was poured on a flat glass plate. After drying, a thin film was placed in the holographic setup to produce a volume Bragg grating.[26] To do that, the laser beam from a single-frequency, a diode pumped Nd-YAG laser, at 532 nm, was expanded to expose the pullulan film at normal incidence. A mirror was set behind the film and a volume Bragg grating was recorded inside the DCP film by interference of two counter propagating beams. The interference pattern is responsible for generation of a large number of alternating DCP and air layers, parallel to the substrate. After exposure, the pullulan film was chemically processed by washing the plate in a mixture of water and isopropanol, followed by drying in pure isopropanol. Finally, the grating is slowly and fully dried in a closed vessel.

The resulting hologram is about 10 μm thick and has a complex structure, as shown in Fig. 1. On the nanoscopic level, the structure is characterized by approximately fifty Bragg layers. They are mutually separated and supported by nano-pillars with a diameter of up to 50 nm, enabling the mechanical stability of the whole structure.

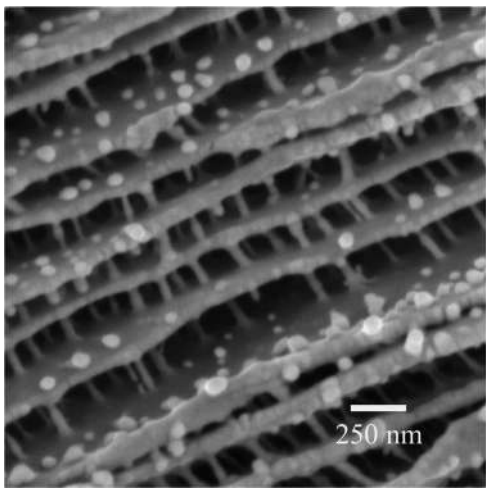

Fig. 1 A cross-section of pullulan metamaterial (recorded using a scanning electron microscope) showing pullulan layers separated by nanopillars.

The metamaterial acts as a selective reflector in the specific band of wavelengths in accordance with the Bragg's law:

$$\lambda = 2(n_a l_a + n_p l_p) \quad (2)$$

where l_a and l_p are the thicknesses of the air and pullulan layers (both about 100 nm), and refractive indices $n_a = 1$ and $n_p = 1.45$, respectively. A Bragg maximum (as defined in eqn (2)) depends on thermal variation of refractive indices and layer thicknesses. Thus, the spectral shift as a function of temperature can be found by taking the first derivative of eqn (2):

$$\frac{d\lambda}{dT} = 2\left(l_a\frac{dn_a}{dT} + n_a\frac{dl_a}{dT} + l_p\frac{dn_p}{dT} + n_p\frac{dl_p}{dT}\right) \quad (3)$$

This optical property of the DCP metamaterial was measured in a heating/cooling cycle. The sample was heated and cooled using a Peltier element (controlling temperature between 295 K and 323 K) and the reflection spectra of the white light from the halogen lamp were recorded using a fiber type spectrometer. A thermocouple was embedded within the sample to obtain accurate measurement of the temperature. As can be seen in Fig. 2a, the reflectance peaks are blue-shifted from 580 nm to 535 nm during heating, exhibiting a negative spectral shift of 45 nm for a positive temperature difference of +25 K (equivalent to 1.8 nm K^{-1}). Upon temperature decrease, a spectral maximum returns close to its initial position. Spectral shift *vs.* temperature, for the whole heating–cooling cycle, shows characteristic hysteresis, as in Fig. 2b. The hysteresis effects are inherent to many natural phenomena. In our case, we assume that hysteresis is a consequence of the nonlinear viscoelastic behaviour of the polymer,[27] *i.e.* pullulan nano-pillars, with temperature. Upon heating, air diffuses through membranes and escapes into the surrounding environment, lowering the pressure inside the multilayer. Outside pressure then compresses the layers until a new mechanical equilibrium is achieved. Due to the compression of the layers, the pullulan nano-pillars are bent. It is assumed that at higher temperatures the viscoelasticity of the pillars slightly decreases. Thanks to the capability to creep,[27] after strain due to pressure, the pillars return to their initial state, with a slightly lower temperature than the initial one.

Thermal behavior of optical systems is typically explained by thermal expansion and thermal variation of the refractive indices (as in eqn (3)). In the following, we will show that these mechanisms cannot account for the large and negative spectral shift.

First, we experimentally determined the linear TEC of a pure, unstructured DCP film. A circular, freestanding DCP membrane was produced, clamped at its perimeter, and its central zone was heated with the laser beam. The temperature of the film was measured using a thermal camera, while the resulting thermal bending was measured using digital holographic interferometry. The linear expansion coefficient was calculated from the recorded interferogram, Fig. 3, and found to be $\alpha_{DCP} = 8.8 \times 10^{-5}$/K, which is in agreement with the values obtained for other polysaccharides.[28,29]

Now we can calculate spectral shift of the Bragg maximum using eqn (3). The thermo-optic coefficient of air (dn_a/dT)[30] is

 This journal is © The Royal Society of Chemistry 2021

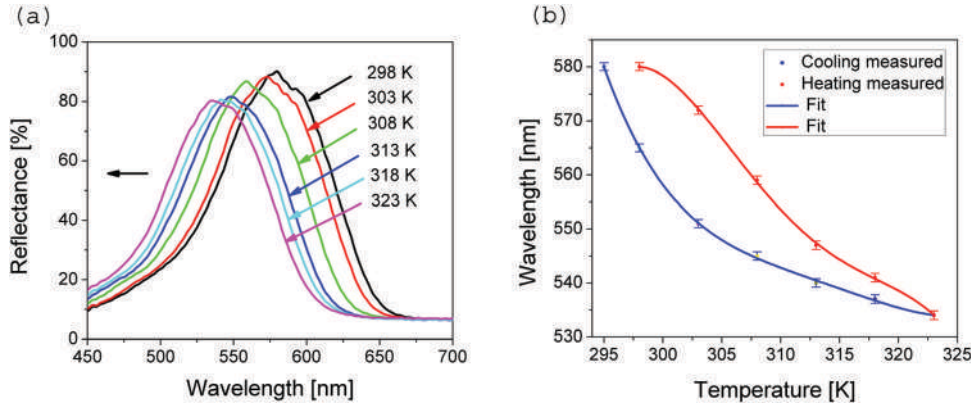

Fig. 2 (a) Reflectance spectra of DCP metamaterial during heating and (b) spectral peak shift during a heating and cooling cycle.

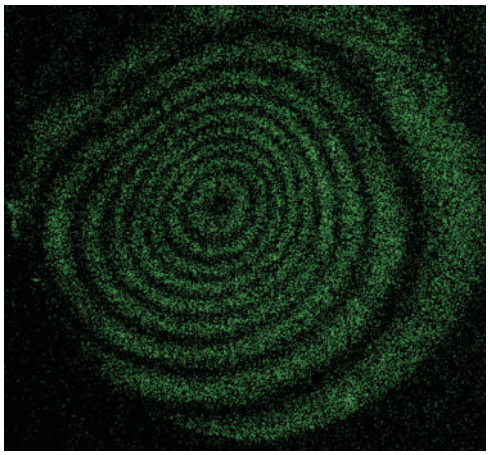

Fig. 3 Interferogram of the thermal bending of the DCP film.

very small and the first term in eqn (3) can be neglected. Additionally, thicknesses of air and pullulan layers are almost the same $l_a = l_p = l$ and eqn (3) can be simplified:

$$\frac{d\lambda}{dT} = 2\left(n_a\frac{dl}{dT} + l\frac{dn_p}{dT} + n_p\frac{dl}{dT}\right) \quad (4)$$

In a linear approximation dilatation $dl = \alpha l T$ (see eqn (1)) and finally:

$$\frac{d\lambda}{dT} = 2l\left(\frac{dn_p}{dT} + \alpha(n_p + n_a)\right) \quad (5)$$

We were not able to measure the thermo-optic coefficient of DCP, and we assumed the largest thermo-optical coefficient recorded up to now, $dn/dT = -5 \times 10^{-4}$/K.[31]

By including these values of thermal constants dn/dT and α_{DCP} into eqn (5), together with the value of the layer thickness $l = 118$ nm and refractive indices of air and pullulan, we have found that the expected temperature shift of the Bragg peak is $d\lambda/dT = -0.07$ nm K^{-1}. This value is much lower than the one recorded experimentally, $d\lambda/dT = -1.8$ nm K^{-1}, and classical thermal effects fail to explain the very large NTEC.

As shown above, while the change in the DCP film thermal expansion is small, the thickness variation of air layers must be the main contributor to the overall metamaterial contraction. From the experimentally observed spectral shift and a temperature change of +25 K, the calculated change in air layer thickness (using eqn (2)) is −22 nm. Knowing that there are fifty Bragg layers, the total thickness change is $dl = -1.1$ μm. Knowing that the initial thickness of the material is $l = 10$ μm, we estimate (using eqn (1)) that the linear thermal expansion coefficient of DCP metamaterial is $\alpha_{DCPm} = -4.4 \times 10^{-3}$/K. This value is quite large, compared to values of NTEC, available in the literature. The results presented here have been verified in a series of experiments on many different samples. We have found that the behaviour of pulullan metamaterial is the same, confirming a negative thermal expansion with NTEC of the order 10^{-3}/K.

Thermo-osmotic mechanism of negative thermal expansion

As explained above, negative and large TEC cannot be explained by usual and simple thermal effects (thermal dilatation and refractive-index variation). In this section, the peculiar behavior of DCP metamaterial is explained through thermo-osmosis,[32] a process defined as fluid or gas diffusion through a membrane due to a temperature gradient.[32,33] This phenomenon was found in many areas from biology[34] to energy harvesting.[35]

We should note that the pullulan layers are very thin (about 100 nm) and their mutual separation is of the same order of magnitude. In such a small volume, only a small number of air molecules are entrapped between the pullulan layers (the mean path length of air molecules is 67 nm under normal conditions)[36] and molecules diffuse through the layers, depending on the temperature difference between the layer and their environment. In a thermal equilibrium, a net flow of molecules between the layer and the environment is zero. If the temperature of the layer rises, more molecules escape the layer, lowering the pressure inside the layer. The resulting pressure difference compresses the layers, supported only by tiny nanopillars (Fig. 1).

Diffusion through permeable membranes is described by Fick's law,[37] which determines the diffusive flux per unit area Φ as a function of pressure p_0 and membrane thickness l:

$$\varnothing = \frac{Pp_0}{l} \quad (6)$$

where P is membrane permeability, which is an intrinsic property of the material.

Effects of temperature on gas permeability were previously analyzed.[38,39] For gases, the temperature-dependence of permeability is defined according to the Arrhenius relationship:

$$P = P_0 \exp^{\frac{-E_p}{RT}} \quad (7)$$

where P_0 is a constant (a kinetic frequency factor), R is the gas constant, and E_P is the activation energy for permeation. According to the above equation the gas permeability increases with temperature.

For simplicity of the further analysis, we will explore a single membrane separating a closed compartment from the surrounding air environment; see Fig. 4.

We suppose that the environment is a thermal reservoir with infinite capacity at constant temperature T_0 and pressure p_0. If a compartment with a membrane is at temperature T_1 and pressure p_1, we have a flux Φ_1 of molecules diffusing out of the compartment into the environment and flux Φ_0 of particles flowing from the environment into the compartment, *i.e.* by combining eqn (6) and (7):

$$\varnothing_0 = \frac{p_0}{l} P_0 \exp^{-\frac{E_p}{RT_0}} \quad (8)$$

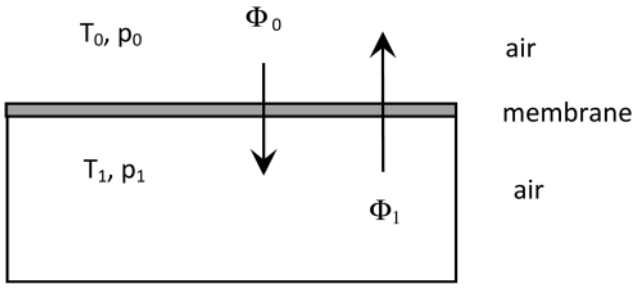

Fig. 4 Compartment with a single membrane, where T and p are temperatures and pressures, while Φ are fluxes.

$$\varnothing_1 = \frac{p_1}{l} P_0 \exp^{-\frac{E_p}{RT_1}} \quad (9)$$

Due to the temperature difference between the compartment and its external environment, ingoing and outgoing fluxes are not equal any more, and there is a net molecular flow. Suppose that the temperature inside the compartment is larger than that of the surrounding air, molecules will leak out and reduce the pressure p_1 inside the compartment. The resulting pressure difference will exert a mechanical force on the membrane and compress it until a new equilibrium is reached, *i.e.* when $\Phi_1 = \Phi_0$. From eqn (8) and (9) we can easily find that this will happen when:

$$p_1 = p_0 \exp^{-\frac{E_p}{R\left(\frac{1}{T_0} - \frac{1}{T_1}\right)}} \quad (10)$$

As stated before, this pressure difference is compensated by the mechanical resistance of nanopillars to compression.

In the case of DCP metamaterial, we have a number of pullulan membranes stacked one above the other and separated by tiny nanopillars. Air is gradually leaking from one layer to another until it goes out to the atmosphere. Air leakage is a process that takes some time, before thermo-mechanical equilibrium is reached.

Dependence of pressure p_1 on temperature was calculated from eqn (10) and is shown in Fig. 5(a). The activation energy of air permeation through the polysaccharide membrane is about 40 kJ mol^{-1}.[40] The graph shows that p_1 decreases with increasing temperature of the pullulan layers. Based on this dependence, Fig. 5(b) and (c) show the dependence of pressure p_1 on the measured time to achieve a new equilibrium state and the dependence of pressure p_1 on the air layer thickness, respectively.

Discussion and conclusions

We have shown that the proposed thermo-osmotic mechanism explains well all the experimentally recorded properties of the pullulan NTE metamaterial. However, there are other, less obvious mechanisms that could contribute to the negative thermal expansion, most notably the effect of air humidity.

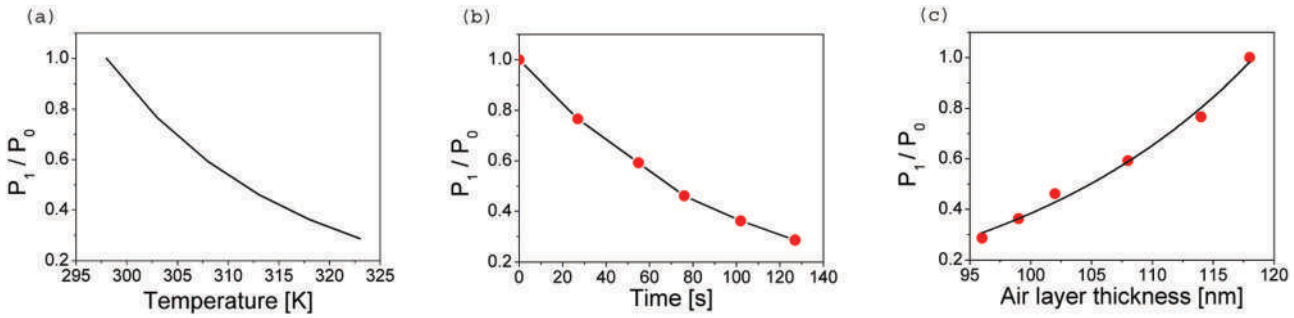

Fig. 5 Ratio of the pressure inside and outside of the compartment as a function of (a) DCP temperature, (b) time needed to reach a new equilibrium state, and (c) air layer thickness. The points on graphs (b and c) correspond to experimentally measured values.

 This journal is © The Royal Society of Chemistry 2021

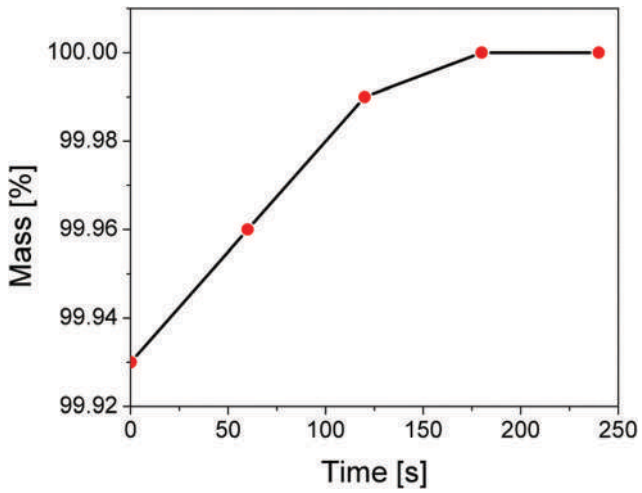

Fig. 6 The change of mass of DCP metamaterial in time due to humidity.

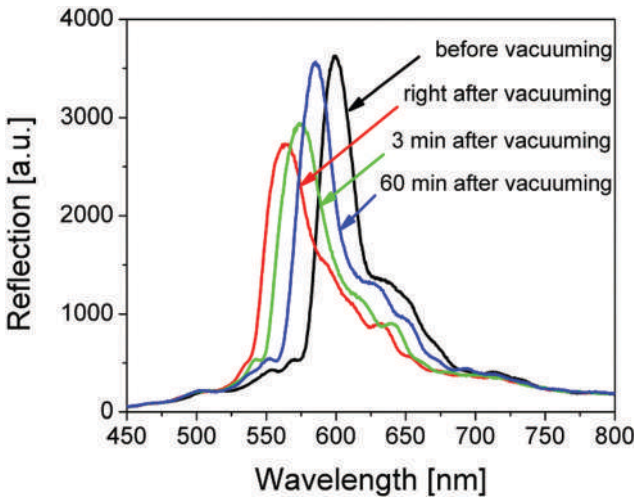

Fig. 7 Reflectance before and after vacuuming and exposing to air.

To test if pullulan absorbs water from the air we performed a simple gravimetric experiment with an analytical balance. First, the DCP metamaterial was measured under normal laboratory conditions, it was then heated to 373 K for 45 min, to eliminate moisture, and measured again. After that, the sample was kept under normal laboratory conditions and the mass was measured every hour until it reached its original value, see Fig. 6. It can be seen that the change of mass, caused by moisture, is only 0.07%. Bearing in mind that pullulan does not form the gel, and does not swell significantly, we conclude that the influence of moisture on the pullulan structure is negligible.

As a final proof of diffusion of air through pululan layers and the corresponding thermo-osmosis, as a dominant mechanism, we placed the pullulan metamaterial in a vacuum chamber, at the pressure of 4×10^{-2} Pa, for 45 minutes. During that time, entrapped air diffused out of the pullulan layers. The reflection spectra measured immediately after the sample was removed from the vacuum and placed back to the normal atmospheric conditions, were shifted towards lower wavelengths. This shift was caused by the air pressure compressing the layers due to the large pressure difference between the inside ($p \sim 0$ Pa) and outside of the metamaterial ($p_{\mathrm{atm}} \sim 100\,000$ Pa). Following the prolonged stay in the atmosphere the air diffuses into the layers, equilibrating pressures and expanding the material as evidenced by the spectral shift, see Fig. 7.

It is also important to note that when the temperature excised a certain maximum value (higher than 383 K) the DCP metamaterial loses its NTE properties. We believe that in this case there are no more air molecules entrapped within the pullulan layers, and the pressure difference is large enough to break the pullulan nanopillars, which otherwise will sustain the mechanical integrity of the whole structure. Bear in mind that all the mentioned effects (dilatation, thermo-optical, and humidity) are simultaneously present, but nevertheless our experiments show that the thermo-osmosis is a dominant one, which converts an ordinary PTE into an NTE material. Without diffusion, a pressure of entrapped air between the pullulan multilayers will follow the temperature variation–increasing upon heating, and decreasing upon cooling. This will turn the pullulan multilayer into a positive thermal expansion material, in contrast to what we observed experimentally.

Regarding the thermo-osmotic process, we emphasize the simplicity of the presented model, which very well describes the complex phenomenon responsible for NTE. First of all, the pullulan layers have a stochastic distribution of thicknesses, size and position of nanopillars, which is difficult to take into account in the model. Also, the mechanical properties of materials at the nanoscale level can be quite different, compared to those of the bulk. Additionally, for such thin layers, air cannot be treated as continuum and more complex effects come into play, such as thermophoresis and thermoconvection. In our case, the situation is further complicated by extremely small (100 nm) separation between the layers when the number of entrapped molecules is correspondingly small. This means that losing a single molecule from the layer significantly reduces the pressure. In spite of this, the proposed model is able to explain the most distinctive properties of the system: negative thermal expansion and the corresponding optical properties.

In conclusion, we have found that holographically patterned dichromated pullulan is a new mechanical metamaterial with a large NTE of $\alpha_{\mathrm{DCPm}} = -4.4 \times 10^{-3}$/K in a temperature range between 295 K and 323 K. Our investigations are in this temperature range because most of the practical interests and potential applications of organic devices are around room temperature. We show that it is simple to fabricate a stable and durable material using the holographic technique. Our explanation of the mechanism that converts an ordinary positive thermal expansion material into an NTE material is based on thermo-osmosis of the air molecules through the pullulan nanolayers. Dependence of the optical response on temperature of the pullulan metamaterials was investigated. The reflection spectra show a blue shift with increasing temperature, which originates from the contraction of air nanolayers due to the thermo-osmosis of the air molecules through the pullulan nanolayers.

The proposed mechanism can be applied to various holographic structures and materials, as well as to different gases and temperature ranges. We have performed the same measurements using holographically patterned dextran (another polysaccharide) and found NTE, too. While pullulan is linear, dextran has a branching structure but shows the same behavior as pullulan, and the reflectance peaks are blue-shifted during heating. Our multilayer design is simple and the proposed mechanism is useful for surfaces of arbitrary size. We have shown that experimental results can be explained by simple relationships, in the nanoscale, linking the structures, mechanical and optical properties, and temperature-response. The disclosed mechanism is universal and opens a range of possibilities to construct engineered materials with tailored negative thermal expansion.

Conflicts of interest

There are no conflicts to declare.

Acknowledgements

The authors acknowledge funding provided by the Institute of Physics Belgrade, through the grant by The Ministry of Education, Science, and Technological Development of the Republic of Serbia. B. Kolaric acknowledges support from the F.R.S.-FNRS.

Notes and references

1 K. Takenaka, *Front. Chem.*, 2018, **6**, 267.
2 J. P. Attfield, *Front. Chem.*, 2018, **6**, 371.
3 R. Lakes, *J. Mater. Sci. Lett.*, 1996, **15**, 475–477.
4 M. Szafránski, *J. Mater. Chem. C*, 2013, **1**, 7904–7913.
5 H. Liu, J. Chen, X. Jiang, Z. Pan, L. Zhang, Y. Rong, Z. Lin and X. Xing, *J. Mater. Chem. C*, 2017, **5**, 931–936.
6 K. Takenaka, Y. Okamoto, T. Shinoda, N. Katayam and Y. Sakai, *Nat. Commun.*, 2017, **8**, 14102.
7 L. Cabras, M. Brun and D. Misseroni, *Proc. Natl. Acad. Sci. U. S. A.*, 2019, **475**, 20190468.
8 J. Qu, M. Kadic, A. Naber and M. Wegener, *Sci. Rep.*, 2017, **7**, 40643.
9 E. Boatti, N. Vasios and K. Bertoldi, *Adv. Mater.*, 2017, **29**, 1700360.
10 J. Chen, L. Hu, J. Deng and X. Xing, *Chem. Soc. Rev.*, 2015, **44**, 3522–3567.
11 A. Versluisl, W. Douglasl and R. Sakaguchi, *Dent. Mater.*, 1996, **12**, 290–294.
12 R. Bastaits, G. Rodrigues, P. Jetteur, P. Hagedorn and A. Preumont, *Smart Mater. Struct.*, 2012, **21**, 064004.
13 O. Sigmund and S. Torquato, *J. Mech. Phys. Solids*, 1997, **45**, 1037–1067.
14 A. Sanson and J. Chen, *Front. Chem.*, 2019, **7**, 284.
15 Y. Zhou, X. Y. Chen, Y. H. Fu, G. Vienne, A. I. Kuznetsov and B. Luk'yanchuk, *Appl. Phys. Lett.*, 2013, **103**, 123116.
16 E. Almeida, O. Bitton and Y. Prior, *Nat. Commun.*, 2016, **7**, 12533.
17 M. S. Rill, C. Plet, M. Thiel, I. Staude, G. von Freymann, S. Linden and M. Wegener, *Nat. Mater.*, 2008, **7**, 543–546.
18 C. Enkrich, F. Pérez-Willard, D. Gerthsen, J. Zhou, T. Koschny, C. M. Soukoulis, M. Wegener and S. Linden, *Adv. Mater.*, 2005, **17**, 2547–2549.
19 D.-Y. Kang, W. Lee, D. Kim and J. H. Moon, *Langmuir*, 2016, **32**, 8436–8441.
20 T. K. Kormilina, E. A. Stepanidenko, S. A. Cherevkov, A. Dubavik, M. A. Baranov, A. V. Fedorov, A. V. Baranov, Y. K. Gun'ko and E. V. Ushakova, *J. Mater. Chem. C*, 2018, **6**, 5278–5285.
21 X. Zheng, W. Smith, J. Jackson, B. Moran, H. Cui, D. Chen, J. Ye, N. Fang, N. Rodriguez, T. Weisgraber and C. M. Spadaccini, *Nat. Mater.*, 2016, **15**, 1100–1107.
22 Y. Enomoto-Rogers, N. Lio, A. Takemura and T. Iwata, *Eur. Polym. J.*, 2015, **66**, 470–477.
23 D. Pantelic, S. Savic and D. Jakovljevic, *Opt. Lett.*, 1998, **15**, 807–809.
24 S. Savic-Sevic and D. Pantelic, *Appl. Opt.*, 2007, **46**, 287–291.
25 S. Savic-Sevic and D. Pantelic, *Opt. Express*, 2005, **13**, 2747–2754.
26 S. Savic-Sevic, D. Pantelic, B. Jelenkovic, B. Salatic and D. V. Stojanovic, *Soft Matter*, 2018, **14**, 5595–5603.
27 G. Strobl, *The Physics of Polymers*, Springer-Verlag, Berlin Heidelberg, 2007.
28 M. Wada and Y. Saito, *J. Polym. Sci., Part B: Polym. Phys.*, 2001, **39**, 168–174.
29 V. Ramiah and D. A. I. Goring, *J. Polym. Sci., Part C: Polym. Symp.*, 1965, **11**, 27–48.
30 B. Edlen, *Metrologia*, 1966, **2**, 71–80.
31 T. Handa, H. Tahara, T. Aharen and Y. Kanemitsu, *Sci. Adv.*, 2019, **5**, eaax0786.
32 K. G. Denbigh and G. Raumann, *Proc. R. Soc. London, Ser. A*, 1952, **210**, 377–387.
33 K. G. Denbigh, *Nature*, 1949, **163**, 60.
34 W. Groβe, *Aquat. Bot.*, 1996, **54**, 101–110.
35 A. P. Straub, N. Y. Yip, S. Lin, J. Lee and M. Elimelech, *Nat. Energy*, 2016, **1**, 1–6.
36 S. G. Jennings, *J. Aerosol Sci.*, 1988, **19**, 159–166.
37 N. Gontard, R. Thibault, B. Cuq and S. Guilbert, *J. Agric. Food Chem.*, 1996, **44**, 1064–1069.
38 C. G. Biliaderis, A. Lazaridou and I. Arvanitoyannis, *Carbohydr. Polym.*, 1999, **40**, 29–47.
39 N. Acharya, P. Yadav and Y. Vijay, *Indian J. Pure Appl. Phys.*, 2004, **42**, 179–181.
40 L. A. El-Azzami and E. A. Grulke, *J. Polym. Sci., Part B: Polym. Phys.*, 2007, **45**, 2620–2631.

 This journal is © The Royal Society of Chemistry 2021

Journal of Physics D: Applied Physics

PAPER

$YVO_4:Eu^{3+}$ nanopowders: multi-mode temperature sensing technique

To cite this article: D Sevic *et al* 2019 *J. Phys. D: Appl. Phys.* **53** 015106

View the article online for updates and enhancements.

IOP ebooks™

Bringing you innovative digital publishing with leading voices to create your essential collection of books in STEM research.

Start exploring the collection - download the first chapter of every title for free.

This content was downloaded from IP address 147.91.1.41 on 11/12/2019 at 09:35

IOP Publishing Journal of Physics D: Applied Physics
J. Phys. D: Appl. Phys. **53** (2020) 015106 (10pp) https://doi.org/10.1088/1361-6463/ab499f

$YVO_4:Eu^{3+}$ nanopowders: multi-mode temperature sensing technique

D Sevic[1,3], M S Rabasovic[1], J Krizan[2], S Savic-Sevic[1], M G Nikolic[1], B P Marinkovic[1] and M D Rabasovic[1]

[1] Institute of Physics Belgrade, University of Belgrade, Serbia
[2] Ami DOO, Ptuj, Slovenia

E-mail: sevic@ipb.ac.rs

Received 18 May 2019, revised 14 September 2019
Accepted for publication 1 October 2019
Published 15 October 2019

Abstract

In this paper we study several temperature sensing techniques using the same thermographic phosphor: luminescence intensity ratio, lifetime, rise time. Moreover, we analyze some recently presented techniques, based on host luminescence intensity ratio method and delayed gate intensity ratio technique. We have selected $YVO_4:Eu^{3+}$ nano powder as an appropriate material for this study, because it has easily detectable luminescence rise time and host luminescence. The material was prepared using simple solution combustion synthesis. The time resolved analysis of emission spectra was achieved using the streak camera system. We present a very detailed analysis of measured lifetimes and rise times of all emission lines and their temperature dependence. We propose a multi-mode temperature sensing technique based on the concept of luminescence detection part of the temperature sensor capable of switching between several measurements modes to obtain the best sensitivity in desired range of operation.

Keywords: temperature sensing, phosphors, optical properties, luminescence, time-resolved optical spectroscopy

(Some figures may appear in colour only in the online journal)

1. Introduction

Thermographic phosphors offer many advantages for temperature measurement compared to other methods [1–10]. Optical thermometry is very accurate, contactless method of remote sensing. Moreover, it is conceptually simple. There are several ways to use phosphors for thermometry purposes. Spectroscopy techniques are usually employed to remotely measure effects of temperature on phosphors photoluminescence. The most common method is based on intensity ratio of two, appropriately selected, spectral peaks of thermophosphor. The method is called fluorescence intensity ratio (FIR). The second commonly used method is based on phosphor luminescence lifetime. This technique needs to measure only one spectral peak. Some phosphors have temperature dependent luminescence rise time sufficiently long to be of practical use for thermometry. Many thermophosphors offer the possibilities for two promising modifications of the FIR method. First, using of host luminescence instead of one of the two dopant luminescence peaks for intensity ratio calculations could improve the sensitivity or overall characteristics of the FIR basic, in regard of simplicity and reliability [11–15]. Another possible improvement of the sensitivity could be achieved by proper selection of the time frame for calculating the intensity ratio [3, 15, 16].

Aim of this study is to compare the before mentioned thermometry techniques using the same nanophosphor. Our previous studies of europium, dysprozium or samarium doped hosts implied that, among the nanophosphors analyzed in [15–21], only Yttrium Vanadate (YVO_4) doped with europium ions ($YVO_4:Eu^{3+}$) offers the long enough luminescence rise time, in microsecond domain, to be of practical use for thermometry. Nano phosphors Y_2O_3 [8, 22–24], SrY_2O_4 [25] and

[3] Author to whom any correspondence should be addressed.

 © 2019 IOP Publishing Ltd Printed in the UK

BaY_2ZnO_5 [26] are also used for temperature measurements based on rise time.

It is well known fact that absorption and excitation times are typically in femtosecond domain, see [8]. The detected long rise time of some $^5D_0$ emission lines is related to the specific energy transfer mechanism of analyzed nanophosphor. A detailed time resolved luminescence analysis of optical emission presented in this paper will provide an insight into energy transfer mechanism of YVO_4:Eu^{3+}.

Studies of structural and luminescent characteristics of YVO_4:Eu^{3+} phosphors, including various methods of synthesis, are reported in [27–50] and references therein. Compared with other oxide luminescence compounds such as Y_2O_3, YVO_4 has lower formation energy and higher crystallinity, which makes it easier to form regular morphology and shows higher luminous efficiency [27].

Transitions from the $^5D_0$ state, from which most of europium luminescence comes, have a slow decay. Lifetimes of slow decay lines of europium doped YVO_4 are measured and reported in many publications. The luminescence intensity of $^5D_0$-$^7F_2$ transition is the most intensive, so it is usually used for europium luminescence lifetime measurements [42, 48, 51, 52]. However, there are not so many publications regarding any europium doped host, where measured lifetimes of europium fast decay transitions or rise times of slow decay transitions [23, 25, 26, 35, 51, 53] are provided. To the best of our knowledge, the results of measurements of the rise time of transitions from the $^5D_0$ state and lifetime of fast decay transitions from the $^5D_1$ state of YVO_4:Eu^{3+} phosphors are only presented in [19], measured only at the room temperature and [35] measured at and bellow room temperature. In this work we will focus on temperature dependency of YVO_4:Eu^{3+} luminescence, not analyzed in our previous papers.

2. Experimental procedures

Europium doped YVO_4 nanophosphor was efficiently prepared using a solution combustion synthesis (SCS) method [54]. The structure of synthesized $Y_{0.98}VO_4 : Eu^{3+}_{0.02}$ material has been confirmed and characterized in our earlier publication [19], using x-ray powder diffraction (XRD), scanning electron microscope (SEM), Raman and photoluminescence (PL) techniques. The average grain size of about 51 nm was estimated by the Scherer equation.

As an excitation source for photoluminescence measurements we used the optical parametric oscillator (Vibrant OPO), continuously tunable over a spectral range from 320 nm to 475 nm. The emission spectra and luminescence lifetimes and rise time of synthesized nanopowders were analyzed using the streak camera system. The camera is equipped with the spectrograph. The details of our experimental setup can be found in [16, 19]. The part of experimental setup for luminescence measurement as a function of temperature is described in [55].

3. Results and discussion

3.1. Optical properties

The streak images of time resolved photoluminescence spectrum of YVO_4:Eu^{3+} material are presented in figure 1. It was shown that optical spectral properties reported for YVO_4:Eu^{3+} in the literature remain the same for $GdVO_4$:Eu^{3+} as well [56]. Excitation spectra of VO_4 groups are very similar for both phosphors. This fact is explained, proved in detail and generalized for rare earth doped vanadates in [57–60]. Moreover, it was shown in [57–61] that absorption of VO_4^{3-} group shifts to longer wavelengths with increasing temperature, and that it could be used for improved temperature sensing characteristics [57–60].

In [38, 46, 49, 50, 56–60, 62] it was shown that the VO_4 excitation spectra consist of a strong absorption band between 250 and 350 nm, corresponding to the charge transfer from O_2- to the central vanadium ion V^{5+} of vanadate VO_4^{3-} groups. So, it should be pointed out that the excitation of Eu^{3+} ion is basically caused by energy transfer from vanadate groups to Eu^{3+} ion. Due to the weak intensities of *f–f* transitions of Eu^{3+} ions compared with that of VO_4^{3-} ion, these transition lines often have not been observed in measured excitation spectra, or simply neglected in many publications. In our work [16] we showed that it is possible to exploit the direct excitation of europium for temperature and pressure sensing purposes.

However, there is another interesting phenomenon regarding the direct excitation of europium. It is discovered and explained for the first time in [57]. As described there, excitation spectra with respect to the characteristic excitations of Eu^{3+} ions from $^7F_0$, $^7F_1$ and $^7F_2$ states to $^5D_2$ state are temperature dependent, so the phenomenon could be used for temperature measurements. Further, it is explained that beside temperature quenching, another factor that affects the emission intensity is the population of the initial state for the excitation. Namely, the populations between $^7F_0$, $^7F_1$ and $^7F_2$ states of Eu^{3+} ions follow Boltzmann distribution due to their appropriate energy gaps [57]. Thus, with increasing temperature, the population of the ground state $^7F_0$ as the initial state of 395 nm excitation decreases because of the thermally populating of high energy levels ($^7F_1$ and $^7F_2$), leading to the decreasing of response intensity for excitation at 395 nm [57]. Because of the relatively weak measured signal of optical response of europium excited at this wavelength in our present experimental setup, we declined of further analysis of this mode of operation for temperature sensing.

We have used the excitation at 330 nm, which is slightly on right-hand side from the excitation peak of YVO_4:Eu^{3+} on wavelength scale. As usual, the streak image is presented in pseudocolor. Note that, because of streak camera automatic lookup table (LUT) for generating pseudocolor which is nice to eye, the luminescence intensities on different streak images should not be compared visually. The Eu transitions

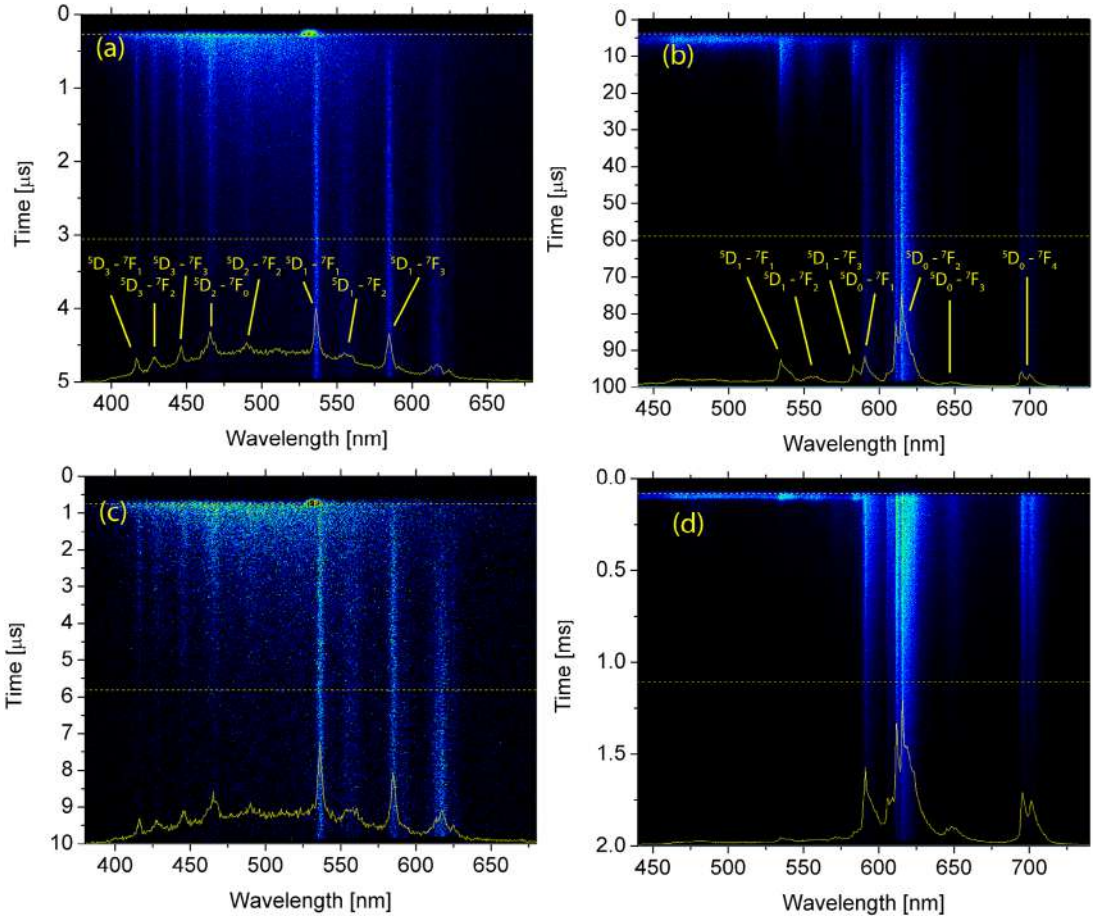

Figure 1. Streak images of photoluminescence spectrum of YVO_4:Eu^{3+} nano phosphor. Time ranges of acquired spectral streak images are (a) 5 μs, (b) 100 μs, (c) 10 μs and (d) 2 ms. Spectral line profiles (yellow curves) are integrated-in-time as marked by dashed yellow lines. OPO excitation is at 330 nm.

are denoted in figure 1 according to [51, 63]. Because we use OPO blocking filter, host optical emission is measured only above 400 nm, showing wide luminescence band up to about 550 nm. The host emission of similar spectral shape is presented and analyzed in [31, 35, 41]. It could be seen in figure 1 that the host emission, compared to europium transitions, has very fast decay. The observed host emission is also of very short duration in [35]. The slow decay transitions observable in figure 1, originating from $^5D_0$ level, are well explained in literature and their detailed description can be found in our previous work [19]. In this study, we have conducted the time resolved analysis for all transitions which are identified in figure 1.

Looking at streak image presented in figure 1(a) or (c) it could be estimated that the raising edges of optical emissions of YVO_4 host and of lines originating from transitions from $^5D_3$, $^5D_2$ and $^5D_1$ europium levels are almost instantaneous and that the lifetimes of host emission and transitions from $^5D_3$ and $^5D_2$ are very short. Figure 1(b) implies that the lifetime of transitions from $^5D_1$ level and rise time of transitions from $^5D_0$ level are in the microsecond domain. Figure 1(d)

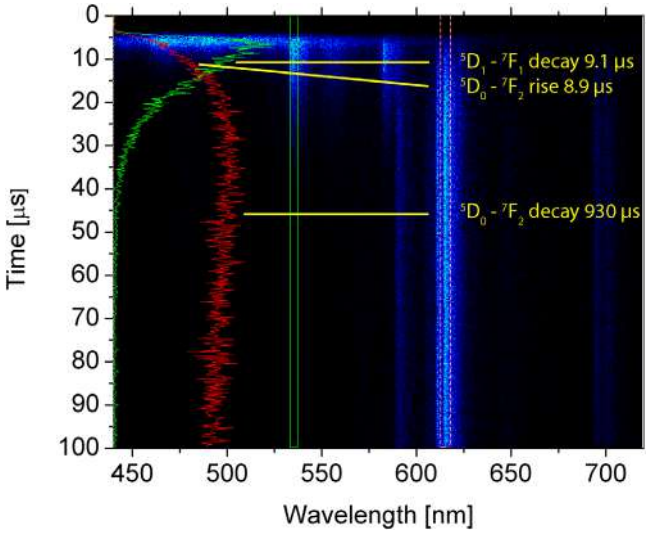

Figure 2. Temporal responses of optical emission of two europium lines in YVO_4:Eu^{3+} nano phosphor, shown as projections on time axis, integrated in spectral range marked as green for $^5D_1$-$^7F_1$ transition (green curve) and dashed red for $^5D_0$-$^7F_2$ transition (red curve).

Table 1. Values of lifetimes of detected $YVO_4:Eu^{3+}$ transitions measured at room temperature, excited at 330 nm. The rise time of $^5D_0$ transitions is 8.9 μs.

Transition	$^5D_3$-$^7F_1$	$^5D_3$-$^7F_2$	$^5D_3$-$^7F_3$	$^5D_2$-$^7F_0$	$^5D_2$-$^7F_2$	$^5D_1$-$^7F_1$	$^5D_1$-$^7F_2$	$^5D_1$-$^7F_3$	$^5D_0$-$^7F_1$	$^5D_0$-$^7F_2$	$^5D_0$-$^7F_3$	$^5D_0$-$^7F_4$	YVO_4 host
Wavelength (nm)	416	428	446	465	490	537	556	584	591	615 618	648	693 700	Up to 550 nm
Lifetime (μs)	2.2			2.7			9.1			930			2

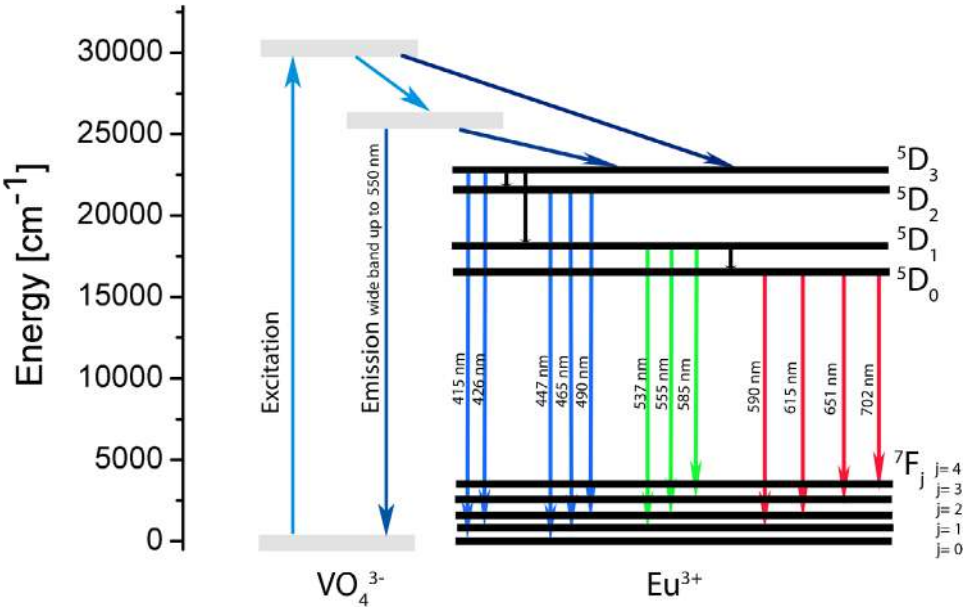

Figure 3. Schematic view of $YVO_4:Eu^{3+}$ energy transfer processes.

shows that the lifetime of transitions from $^5D_0$ level is in millisecond domain.

General shapes of temporal response of optical emissions of fast decay $^5D_1$-$^7F_1$ transition and slow decay $^5D_0$-$^7F_2$ transition of $YVO_4:Eu^{3+}$ nano phosphor are illustrated in figure 2. The rise component of $^5D_0$-$^7F_2$ transition and the decay component of $^5D_1$-$^7F_1$ transition look almost mirrored, implying that there is an energy transfer mechanism between them. The phenomenon that the rise time of europium slow decay $^5D_2$ luminescence is similar to the lifetime of fast decay $^5D_1$ emission was observed long ago [53]; and analyzed in detail, including energy transfer, in [35]. The explanation of energy transfer between the host YVO_4 and Eu^{3+} ions is also provided in [32].

To check the presumption that the rise times of fast decay transitions can be considered as instantaneous, we have used the time scales of streak camera even shorter than 5 μs.

We have concluded that, at the present time, rise times of fast decay transitions of $YVO_4:Eu^{3+}$ are not of any practical use for temperature sensing. The only measurable rise time is of $^5D_0$ transitions; it is 8.9 μs. We have calculated the rise time according to Ranson equation [23, 24].

The values of lifetimes of $YVO_4:Eu^{3+}$ transitions detected in our study, measured at room temperature, excited at 330 nm, are presented in table 1. We also made preliminary estimations of temperature dependences of lifetimes of transitions from YVO_4 host and $^5D_3$ and $^5D_2$ levels. We concluded that lifetime measurements of $^5D_3$ and $^5D_2$ transitions are not so appropriate for temperature sensing, because of small signal intensities compared to intensities of luminescence of $^5D_0$ and $^5D_1$ transitions. The host luminescence is more rapidly quenched by temperature than europium transitions, providing possibility of improved sensitivity in physiological temperature range. The integrated-in-time host luminescence signal strength is quite satisfactory for intensity ratio calculations. On the other hand, measuring the host luminescence lifetime with temperature raise, although possible, showed itself to us as unreliable at the present time. However, with some improvements in detection, the lifetime of host could be of interest for temperature sensing in physiological temperature range.

Based on our estimations of shape of temporal response and time durations of luminescence of host and of europium transitions shown in figures 1 and 2, we propose the schematic view of $YVO_4:Eu^{3+}$ energy transfer processes presented in figure 3.

3.2. Temperature sensing using luminescence intensity ratio with variable delayed gating

Luminecence intensity ratio technique is based on measuring the intensities of two emission lines in luminescence spectra of thermographic phosphors. The temperature is calculated by the emission intensity ratio of these two lines. Many problems

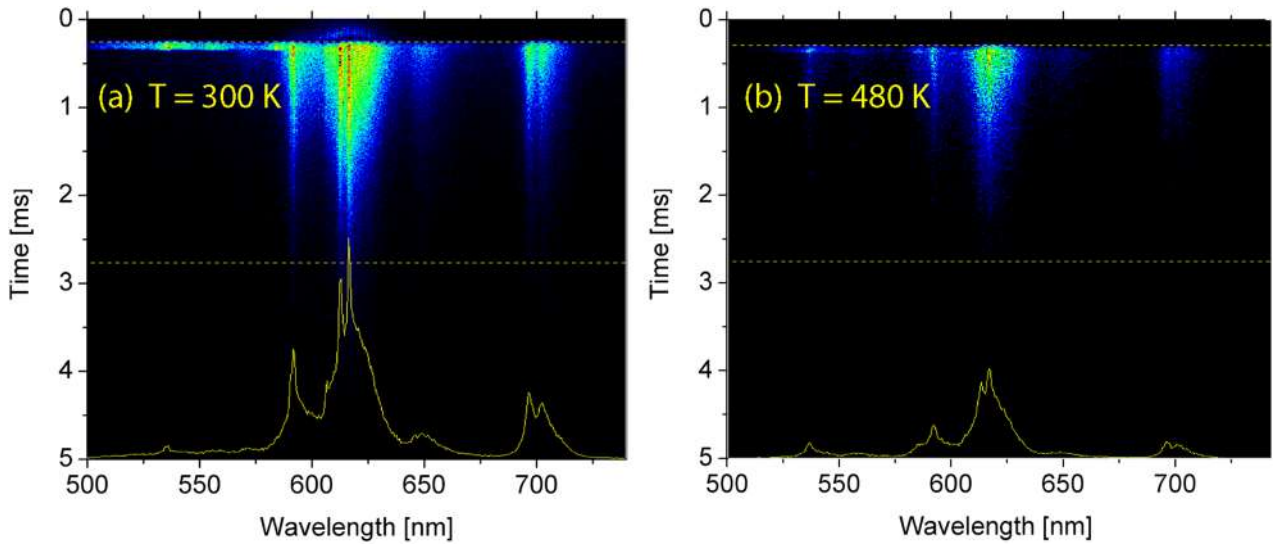

Figure 4. Streak images of photoluminescence spectra of YVO_4:Eu^{3+} and their integrated-in-time (time range marked by yellow dashed line) spectral line profiles (yellow curves): (a) $T = 300$ K, (b) $T = 480$ K, selected for illustration of FIR analysis.

regarding measuring errors, optical condition deviations and excitation power fluctuation are eliminated in this way. Two closely spaced energy levels of rare earth ion, which are thermally coupled, are usually selected for temperature sensing. Small energy gap between these two levels allows the upper level to be populated from the lower level by thermalization. The upper level becomes more populated as the temperature increases and hence the fluorescence from this level gradually increases. Relative population between two levels, $^5D_1$ level (I_1) and $^5D_0$ level (I_0), IR, follows Boltzmann type population distribution given by [1, 2]:

$$\mathrm{IR} = \frac{I_1}{I_0} = C \cdot \exp\left(-\frac{\Delta E}{kT}\right) \tag{1}$$

where k is the Boltzmann constant, $k = 0.69503476(63)$ cm^{-1} K^{-1}, C is a constant and ΔE is the energy gap between two excited levels, in case analyzed here, between $^5D_1$ and $^5D_0$ europium levels.

Instruments for measuring luminescence often detect small signals, even when there is no emission, because of detector dark currents, etc. Moreover, spectrograph stray light introduces error in measured intensity of a signal. Therefore, another constant, A, should be introduced to equation (1), to account for the finite value of IR at low temperatures [14]:

$$\mathrm{IR} = A + C \cdot \exp\left(-\frac{\Delta E}{kT}\right). \tag{2}$$

It should be noted that ΔE corresponds to energy gap between two excited states only in the case of measuring the intensity ratio in conventional way, i.e. without any gate delay in our study. However, when we introduce the delay for gating of measured signals, using ΔE from equation (2) for an estimation of energy gap of excited levels would be quite misleading, although it can be well exploited for fitting the temperature calibration curve. The same holds for calculating the intensity ratio between optical emissions of the host and the selected europium line.

The spectral line intensities from the $^5D_0$ and $^5D_1$ transitions depend on two physical processes. The first process is the thermalization of the $^5D_1$ level with rising temperature, where the energy difference to populate the $^5D_1$ level from the $^5D_0$ level is fully covered by phonons. The second process is nonradiative quenching of the $^5D_0$ and $^5D_1$ levels through the charge transfer state. Both processes can be recognized by the analysis of integrated-in-time profiles of luminescence spectra in figure 4. Namely, the intensity ratio between the lines at 537 nm and 618 nm increases with temperature. However, both lines are thermally quenched. Again, because of streak camera automatic LUT, comparison of luminescence intensities should be not done simply by looking at images.

In our study the intensity ratio method has been improved by introducing the temporal dependence in the intensity ratio measurements, as proposed in [3]. We have implemented this method in [15, 16] where we have shown that it is possible to increase the sensitivity of temperature calibration curve if appropriately selected part of luminescence temporal evolution is used in calculation.

To determine the temperature calibration curves, the luminescence spectra of YVO_4:Eu^{3+} nano phosphor were measured at various temperatures, using OPO excitation at 330 nm and the streak camera. For calculation of intensity ratio in a usual way the narrow bands (5 nm) of europium luminescence around 537 nm and around 618 nm were used integrated in time from their beginning. Then, to improve the temperature sensitivity of the FIR method, we have varied the gating times for beginning of 618 nm signal in-time-integration. In this way, because smaller portion of falling 618 nm luminescence signal was integrated, the intensity ratio was increased in favor of 537 nm signal, following the general increase of ratio of 537 nm and 618 nm signals with temperature.

Here, the thermalization and quenching through charge transfer both have significant influence on the fluorescence intensity ratio (FIR). This means that the measured results cannot be simply fitted to the Boltzmann distribution. To

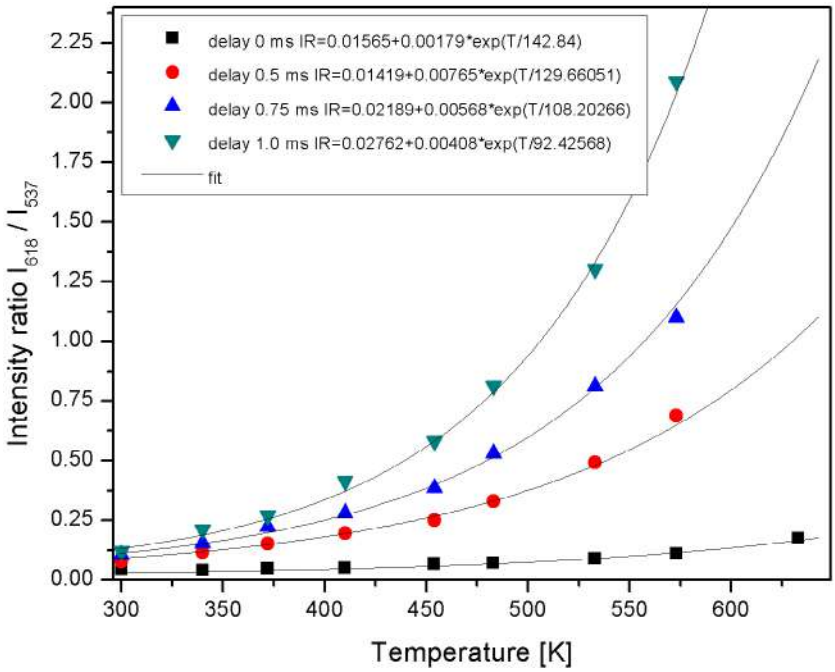

Figure 5. Temperature sensing calibration curve of $YVO_4:Eu^{3+}$ nanopowder sample.

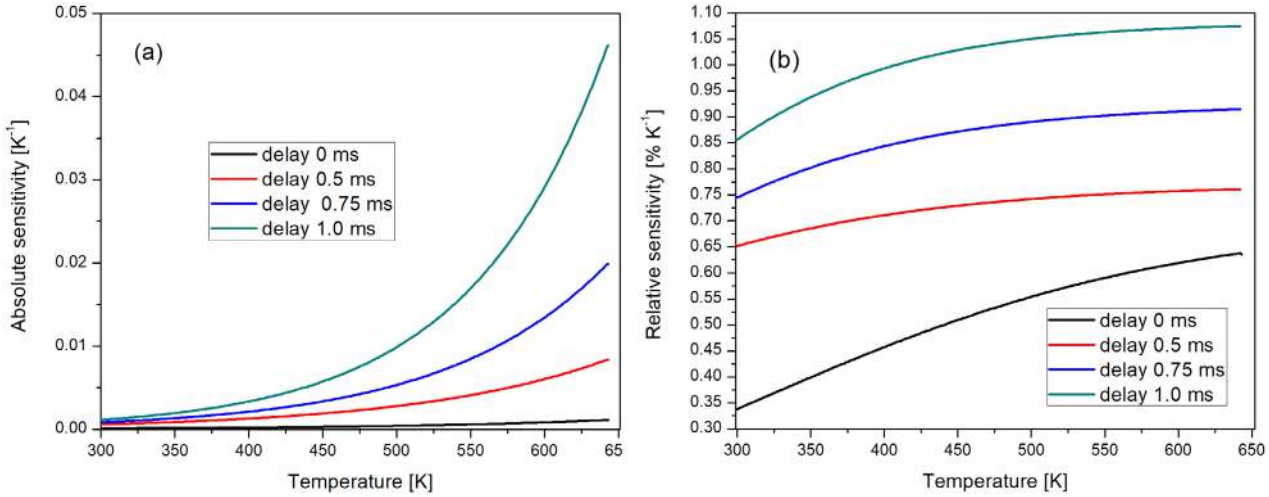

Figure 6. (a) Absolute and (b) relative sensitivities of $YVO_4:Eu^{3+}$ nanopowder as the functions of temperature shown in figure 4.

implement the fluorescence intensity ratio method in thermometry it is necessary to fit a calibration function of analyzed thermophosphor. Based on considerations in [15, 16, 55, 64] we decided to use the simple empirical equation for fitting the calculated intensity ratios of experimental data: $\mathrm{IR}(T) = A + C \cdot \mathrm{e}^{-T/\alpha}$, where T is temperature in K, and A, C and α are empirical constants obtained through fitting of measured data. In principle, for temperature sensing, it is enough to determine the temperature calibration sensing curve, no further knowledge regarding the underlying physics is necessary [65]. The results are shown in figure 5, where delay of 0 ms corresponds to the FIR, the usual way of calculating the intensity ratio.

It could be seen in figure 5 that intensity ratio increases with increasing the gate delay time of signal. However, increasing the gate delay time decreases the integrated signal intensity, so we refrained from using delays longer than 1 ms.

The absolute thermal sensitivity Sa of the intensity ratio method is defined as the rate at which IR changes with the temperature:

$$\mathrm{Sa} = \left|\frac{d\mathrm{IR}}{dT}\right|. \tag{3}$$

The relative thermal sensitivity of the intensity ratio method Sr is determined using formula:

$$\mathrm{Sr} = \left|\frac{1}{\mathrm{IR}}\frac{d\mathrm{IR}}{dT}\right|. \tag{4}$$

Absolute sensitivity is of a small or no use for comparison of different samples. We will provide its values here for comparison of the improvements of various FIR methods used with the same sample.

Absolute and relative temperature sensitivities of $YVO_4:Eu^{3+}$ nanophosphor are shown in figure 6. Best

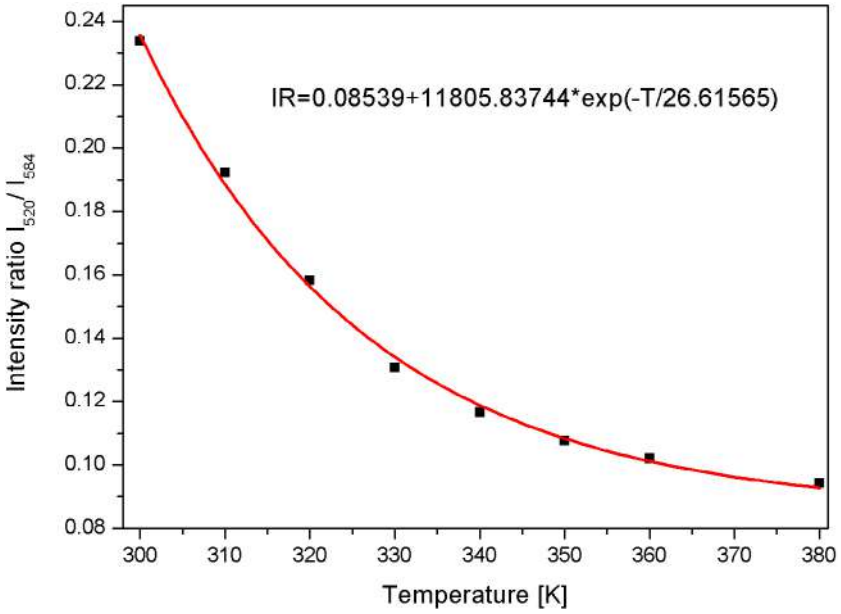

Figure 7. The temperature sensing calibration curve, calculated as intensity ratio of host luminescence and $^5D_2$-$^7F_3$ transition (584 nm).

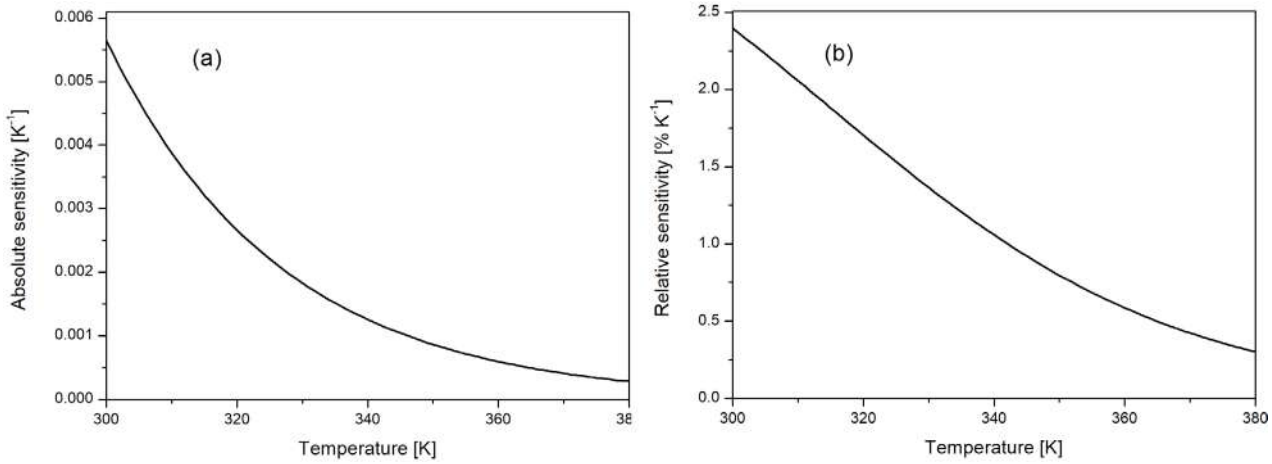

Figure 8. (a) Absolute and (b) relative sensitivities of YVO_4:Eu^{3+} nanopowder as the function of temperature shown in figure 7.

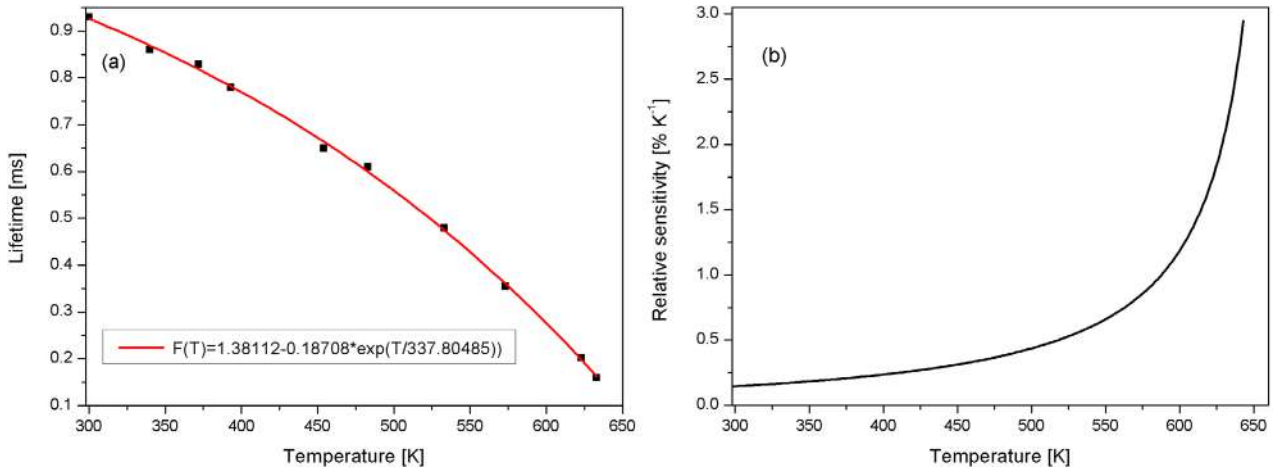

Figure 9. (a) Luminescence lifetime temperature dependence of YVO_4:Eu^{3+} nano phosphor and (b) its relative sensitivity.

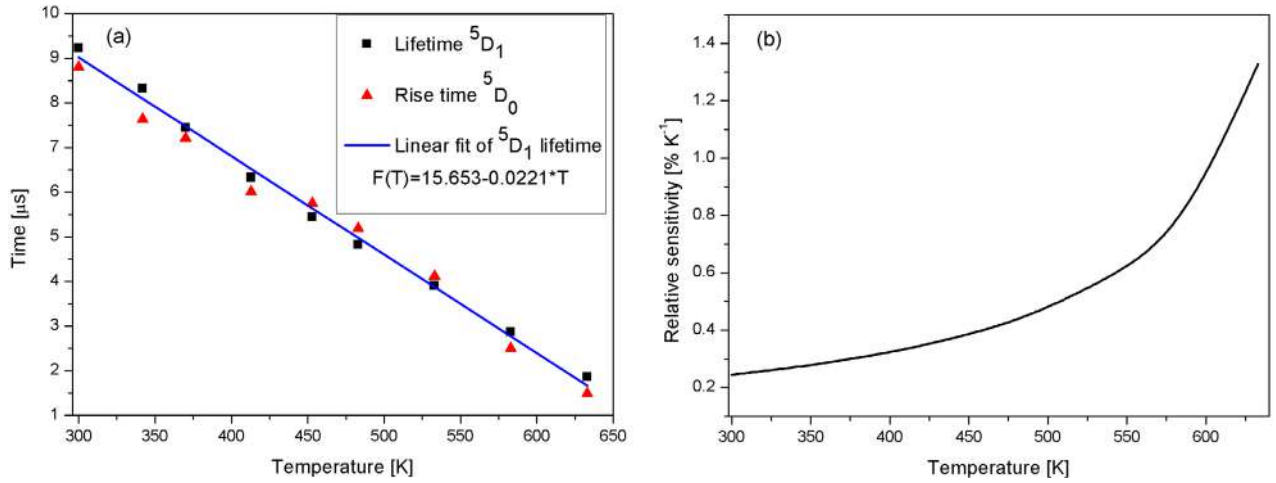

Figure 10. (a) Temperature calibration curve of luminescence lifetime of $^5D_1$ and rise time of $^5D_0$ transitions of $YVO_4:Eu^{3+}$ nano phosphor and (b) the relative sensitivity of temperature calibration curve based on fit $^5D_1$ lifetime.

sensitivity is obtained by gate time of 1 ms. We estimate that this kind of temperature sensing is useful up to about 650 K, where intensities of both measured signals become too low for reliable calculating.

3.3. Temperature sensing using luminescence intensity ratio between YVO$_4$ host and europium $^5D_1$-$^7F_2$ transition

Our measurements show that the host luminescence, although much weaker than emission from $^5D_1$ and $^5D_0$ transitions, is easily detected. Its emission is in the wide band, so its integration could be done in a wider spectral range (we used a band of 10 nm). Host luminescence is rapidly quenched with temperature. We have determined the temperature sensing calibration curve, presented in figure 7, as intensity ratio of host luminescence and $^5D_2$-$^7F_3$ transition (584 nm). The line at 584 nm is prominent and it has no overlap with the host luminescence, see figure 1. We see that the sensitivity in physiological temperature range is greatly improved; however, the sensing range is reduced to about 380 K.

Absolute and relative sensitivities of $YVO_4:Eu^{3+}$ nanopowder are shown in figure 8. Compared to sensitivities of other temperature sensing curves of this nano phosphor shown in figures 6, 9 and 10, we see that this method offers the best sensitivity in physiological range of temperatures.

3.4. Luminescence lifetime temperature dependency

All transitions from the same level have the same lifetime, so it is usual practice for estimation of decay time to use the line with highest intensity of luminescence. To determine the temperature sensing calibration curve we used the most prominent europium spectral line at 618 nm. Analysis presented in [11] confirms that it is possible to use the same form of empirical equation for fitting the lifetime experimental data as we have used for fitting the intensity ratio, namely: $F(T) = A + C \cdot e^{-T/\alpha}$, [15, 16, 55, 64], where T is temperature in K, and A, C and α are empirical constants obtained through fitting of measured data. The temperature sensing calibration curve is shown in figure 9. For our sample of $YVO_4:Eu^{3+}$ nano phosphor the method is reliable up to 650 K. The sensitivity increases by temperature raising.

Table 2. The sensing characteristics of various temperature sensing modes.

	Quality of sensing at temperature (K)		
Sensing mode	300–340	340–500	500–650
Intensity ratio	Poor	Between poor and good	Good
Intensity ratio with delayed gating	Good	Good	Good
Intensity ratio using host	Excellent	Good up to 380	No signal
Slow decay lifetime	Poor	Good	Excellent
Slow decay rise time/ fast decay lifetime	Poor	Good	Fairly excellent

3.5. Luminescence rise time temperature dependency

Temperature dependence of luminescence lifetime of $^5D_1$ and rise time of $^5D_0$ transitions of $YVO_4:Eu^{3+}$ nano phosphor and the relative sensitivity of temperature calibration curve based on fit $^5D_1$ lifetime are shown in figure 10.

In this range of temperatures, the rise time dependence is linear, similarly as observed in [22, 23, 25]. Moreover, it seems that it is the same if we use decay of 537 nm line, or rise time of 618 nm line. The choice would be dependent on which signal is overall stronger and easier to analyze for a given sample. It should be also mentioned that, instead of measuring the rise time, the measured time of achieving the signal maximum at 618 nm could be efficiently used for temperature measurements [22, 25, 66].

3.6. Multi-mode temperature sensing technique

Comparing temperature sensing characteristics of $YVO_4:Eu^{3+}$, shown in figures 5–10, we conclude that europium lines intensity ratio method, the luminescence lifetime method and rise time method offer the same sensing range. Lifetime and rise

Table 3. The sensing characteristics of various hosts doped with Eu^{3+}.

Host	Sensing range (K)	Relative sensitivity (% K^{-1})	Reference
YVO_4	300–650	0.2–2.9	This work
YVO_4	300–650	0.33–0.63	This work, FIR
YVO_4	300–650	2.4–2.9	This work, optimal sensing mode
$Gd_2Zr_2O_7$	300–650	0.4–0.92	[21]
Sr_2CeO_4	300–400	1.0–2.4	[16]
$YNbO_4$	300–720	0.3–2.6	[67, 68]
Gd_2O_3	300–800	0.25–3.25	[69]
$Lu2O_3$	300–800	0.3–0.33	[70]
$Gd2Ti_2O_7$	300–420	0.3–0.95	[14]
TiO_2	300–530	0.12–2.3	[11]
$GdAlO_3$	300–750	0.3–2.9	[71]
YBO_3	330–760	0.3–1.8	[72]

time methods have improved sensitivity on higher temperatures. Delayed gating of intensity ratio method provides improved sensitivity. The sensing characteristics of various temperature sensing modes are summarized in table 2. The luminescence detection part of the temperature sensor should be capable of switching between several measurements modes, so the best sensitivity could be obtained in desired range of operation.

Comparison of temperature sensing characteristics of various hosts doped with Eu^{3+} is presented in table 3. The values of relative sensitivity are usually used for comparison purposes between various materials because relative sensitivity is much better performance indicator than absolute sensitivity. We can see that only Gd_2O_3:Eu^{3+} has slightly better value of maximal relative sensitivity and higher sensing range. Some of hosts listed in table 3 have similar but slightly inferior performances compared to YVO_4:Eu^{3+}. Other hosts are obviously inferior. We conclude that performance of YVO_4:Eu^{3+} nano phosphor analyzed here is more than satisfactory. However, it seems that analysis of multi-mode technique applied to the Gd_2O_3:Eu^{3+} nano phosphor could be a worthy effort.

4. Conclusions

In this paper we have analyzed the several temperature sensing techniques using the YVO_4:Eu^{3+} nanopowder. The material was prepared by simple solution combustion synthesis method. We have showed that, for analyzed YVO_4:Eu^{3+} material, the temperature sensing techniques based on ratio of intensities of two lines, lifetime or rise time are useful up to 650 K. We have obtained sensitivity improvement of the intensity ratio method by simulating the delayed gating of integrating-in-time intensity of one of spectral lines. If the YVO_4 host luminescence is used in intensity ratio method, the sensitivity in physiological temperature range is greatly improved; however, the sensing range is reduced to about 380 K.

So, our analysis shows that remote temperature sensor based on of YVO_4:Eu^{3+} nano phosphor has good sensitivity not only in the physiological temperature range but also for the higher temperatures that are of interest when monitoring the thermal behavior of electronic devices and engines. The luminescence detection part of the temperature sensor should be capable of switching between several measurements modes in order to obtain the best sensitivity in desired range of operation. We have proved the proposed concept by using the streak camera. Real application should be based on less expensive equipment.

Beside luminescence kinetics of slow decay transitions we also estimated rise times and lifetimes of fast decay transitions and the host luminescence. The rise times of fast decay transitions and host luminescence is estimated as negligible for effects that are here of interest. At the present time, the lifetimes of luminescence of fast decay transitions, $^5D_3$ and $^5D_2$, and the host are also too small to be of interest. However, with some improvements in detection, the lifetime of host could be of interest for temperature sensing in physiological temperature range.

Acknowledgment

This work was financially supported by Ministry of Education, Science and Technological Development of the Republic of Serbia under Project OI171020.

ORCID iDs

D Sevic https://orcid.org/0000-0002-7206-6370
M S Rabasovic https://orcid.org/0000-0002-4882-8080
J Krizan https://orcid.org/0000-0003-4195-8322
S Savic-Sevic https://orcid.org/0000-0002-6406-0745
B P Marinkovic https://orcid.org/0000-0002-6904-6360
M D Rabasovic https://orcid.org/0000-0002-9235-4388

References

[1] Jaque D and Vetrone F 2012 *Nanoscale* **4** 4301–26
[2] Brites C D S, Lima P P, Silva N J O, Millan A, Amaral V S, Palacio F and Carlos L D 2012 *Nanoscale* **4** 4799–829
[3] Aldén M, Omrane A, Richter M and Särner G 2011 *Prog. Energy Combust. Sci.* **37** 422–61
[4] Allison S W and Gillies G T 1997 *Rev. Sci. Instrum.* **68** 2615–50
[5] Goss L P, Smith A and Post M E 1989 *Rev. Sci. Instrum.* **60** 3702–6

[6] Heyes A L 2009 *J. Lumin.* **129** 2004–9
[7] Gentleman M M and Clarke D R 2004 *Surf. Coat. Technol.* **188–9** 93–100
[8] Khalid A H and Kontis K 2008 *Sensors* **8** 5673–744
[9] Wade S A, Collins S F and Baxter G W 2003 *J. Appl. Phys.* **94** 4743–56
[10] Wade S A, Forsyth D I and Grattan K T V 2001 *Rev. Sci. Instrum.* **72** 3186–90
[11] Nikolic M G, Antic Z, Culubrk S, Nedeljkovic J M and Dramicanin M D 2014 *Sens. Actuators* B **201** 46–50
[12] Dramicanin M D, Antic Z, Culubrk S, Ahrenkiel S P and Nedeljkovic J M 2014 *Nanotechnology* **25** 485501
[13] Lojpur V, Nikolic M G, Jovanovic D, Medic M, Antic Z and Dramicanin M D 2013 *Appl. Phys. Lett.* **103** 141912
[14] Lojpur V, Culubrk S and Dramicanin M D 2016 *J. Lumin.* **169** 534–8
[15] Rabasovic M S, Krizan J, Savic-Sevic S, Mitric M, Rabasovic M D, Marinkovic B P and Sevic D 2018 *J. Spectrosc.* **2018** 3413864
[16] Vlasic A, Sevic D, Rabasovic M S, Krizan J, Savic-Sevic S, Rabasovic M D, Mitric M, Marinkovic B P and Nikolic M G 2018 *J. Lumin.* **199** 285–92
[17] Rabasovic M S, Sevic D, Krizan J, Terzic M, Mozina J, Marinkovic B P, Savic Sevic S, Mitric M, Rabasovic M D and Romcevic N 2015 *J. Alloys Compd.* **622** 292–5
[18] Rabasovic M S, Sevic D, Krizan J, Rabasovic M D, Savic-Sevic S, Mitric M, Petrovic M, Gilic M and Romcevic N 2015 *Opt. Mater.* **50** 250–5
[19] Sevic D, Rabasovic M S, Krizan J, Savic-Sevic S, Mitric M, Gilic M, Hadzic B and Romcevic N 2017 *Mater. Res. Bull.* **88** 121–6
[20] Rabasovic M S, Krizan J, Gregorcic P, Rabasovic M D, Romcevic N and Sevic D 2016 *Opt. Quantum Electron.* **48** 163
[21] Nikolic M G, Rabasovic M S, Krizan J, Savic-Sevic S, Rabasovic M D, Marinkovic B P, Vlasic A and Sevic D 2018 *Opt. Quantum Electron.* **50** 258
[22] Khalid A H and Kontis K 2009 *Meas. Sci. Technol.* **20** 025305
[23] Allison S W, Goedeke S M, Cates M R, Hollerman W A, Eldridge J I and Bencic T J 2005 *Oak Ridge National Laboratory Report* No. 123055
[24] Ranson R M, Evangelou E and Thomas C B 1998 *Appl. Phys. Lett.* **72** 2663–4
[25] Lojpur V, Antic Z and Dramicanin M D 2014 *Phys. Chem. Chem. Phys.* **16** 25636–41
[26] Li X, Wei X, Qin Y, Chen Y, Duan C and Yin M 2016 *J. Alloys Compd.* **657** 353–7
[27] Liu R, Liu L and Liang Y 2018 *Opt. Mater. Express* **8** 1686
[28] Riul A, Justino L G and Caiut J M A 2017 *Nanotechnology* **28** 235601
[29] Xie D, Peng H, Huang S, You F, Zhang X and Wang G 2015 *Mater. Lett.* **157** 307–10
[30] Huong T T, Phuong H T, Vinh L T, Khuyen H T, Anh T K and Minh L Q 2016 *J. Sci.* **1** 295–300
[31] Shirmane L, Feldmann C and Pankratov V 2017 *Physica* B **504** 80–5
[32] Ningthoujam R S, Singh L R, Sudarsan V and Singh S D 2009 *J. Alloys Compd.* **484** 782–9
[33] Huignard A, Gacoin T and Boilot J-P 2000 *Chem. Mater.* **12** 1090–4
[34] Huignard A, Buissette V, Laurent G, Gacoin T and Boilot J-P 2002 *Chem. Mater.* **14** 2264–9
[35] Riwotzki K and Haase M 2001 *J. Phys. Chem.* B **105** 12709–13
[36] Bhatkar V B 2013 *Int. J. Eng. Sci.* **2** 426–32
[37] Georgescu S, Cotoi E, Voiculescu A M and Toma O 2008 *Rom. Rep. Phys.* **60** 947–55
[38] Park W J, Jung M K, Masaki T, Im S J and Yoon D H 2008 *Mater. Sci. Eng.* **146** 95–8
[39] Sanson A, Giarola M, Rossi B, Mariotto G, Cazzanelli E and Speghini A 2012 *Phys. Rev.* B **86** 214305
[40] Thakur S and Gathania A K 2015 *J. Electron. Mater.* **44** 3444–9
[41] Grandhe B K, Bandi V R, Jang K, Ramaprabhu S, Yi S-S and Jeong J-H 2011 *Electron. Mater. Lett.* **7** 161–5
[42] Chang Y-S, Huang F-M, Tsai Y-Y and Teoh L-G 2009 *J. Lumin.* **129** 1181–5
[43] Han R, Hu R and Chen K 2009 *Opt. Mater.* **32** 329–33
[44] Yan-bo Q, Xiao-feng L, Qiang Z, Dan-ping C, Ye-wen W and Wen-bo M 2010 *Mater. Lett.* **64** 1306–8
[45] Yu M, Lin J, Wang Z, Fu J, Wang S, Zhang H J and Han Y C 2002 *Chem. Mater.* **14** 2224–31
[46] Matos M G, de Faria E H, Rocha L A, Calefi P S, Ciuffi K J, Nassar E J, Hugo V and Sarmento V 2014 *J. Lumin.* **147** 190–5
[47] Kumari P, Baitha P K and Manam J 2015 *Indian J. Phys.* **89** 1297–306
[48] Shanta Singh N, Ningthoujam R S, Niraj Luwang M, Dorendrajit Singh S and Vatsa R K 2009 *Chem. Phys. Lett.* **480** 237–42
[49] Saltarelli M, Matos M G, de Faria E H, Ciuffi K J, Rocha L A and Nassar E J 2015 *J. Sol-Gel Sci. Technol.* **73** 283–92
[50] Saltarelli M, Luz P P, Matos M G, de Faria E H, Ciuffi K J, Calefi P S, Rocha L A and Nassar E J 2012 *J. Fluoresc.* **22** 899–906
[51] Chambers M D, Rousseve P A and Clarke D R 2009 *J. Lumin.* **129** 263–9
[52] Chang Y-S, Lin H-J, Chai Y-L and Li Y-C 2008 *J. Alloys Compd.* **460** 421–5
[53] Darwent J R, Flint C D and O'Grady P J 1986 *Chem. Phys. Lett.* **127** 547–50
[54] Krizan J, Mazaj M, Kaucic V, Bajsic I and Mozina J 2014 *Acta Chim. Slov.* **61** 608–14
[55] Rabasovic M D, Muric B D, Celebonovic V, Mitric M, Jelenkovic B M and Nikolic M G 2016 *J. Phys. D: Appl. Phys.* **49** 485104
[56] Anitha M, Ramakrishnan P, Chatterjee A, Alexander G and Singh H 2002 *Appl. Phys.* A **74** 153–62
[57] Zhou S, Duan C, Yin M, Zhang S and Wang C 2019 *J. Alloys Compd.* **784** 970–4
[58] Zhou S, Duan C and Han S 2018 *Dalton Trans.* **47** 1599–603
[59] Zhou S, Duan C, Yin M, Liu X, Han S, Zhang S and Li X 2018 Optical thermometry based on cooperation of temperature-induced shift of charge transfer band edge and thermal coupling *Opt. Express* **26** 27339–45
[60] Zhou S, Duan C and Wang M 2017 *Opt. Lett.* **42** 4703–6
[61] Nikolic M G, Jovanovic D J and Dramicanin M D 2013 *Appl. Opt.* **52** 1716–24
[62] Shao B, Zhao Q, Guo N, Jia Y, Lv W, Jiao M, Lu W and You H 2013 *CrystEngComm* **15** 5776–83
[63] Binnemans K 2015 *Coord. Chem. Rev.* **295** 1–45
[64] Ananias D, Brites C D S, Carlos L D and Rocha J 2016 *Eur. J. Inorg. Chem.* **2016** 1967–71
[65] Culubrk S, Lojpur V, Ahrenkiel S P, Nedeljkovic J M and Dramicanin M D 2016 *J. Lumin.* **170** 395–400
[66] Dramicanin M D 2016 *Methods Appl. Fluoresc.* **4** 042001
[67] Đacanin L R, Dramicanin M D, Lukic-Petrovic S R, Petrovic D M and Nikolic M G 2013 *Radiat. Meas.* **56** 143–6
[68] Đacanin L R, Lukic-Petrovic S R, Petrovic D M, Nikolic M G and Dramicanin M D 2014 *J. Lumin.* **151** 82–7
[69] Nikolic M G, Al-Juboori A Z, Djordjevic V and Dramicanin M D 2013 *Phys. Scr.* **T157** 014056
[70] Lojpur V, Antic Z, Krsmanovic R, Medic M, Nikolic M G and Dramicanin M D 2012 *J. Serb. Chem. Soc.* **77** 1735–46
[71] Lojpur V, Culubrk S, Medic M and Dramicanin M D 2016 *J. Lumin.* **170** 467–71
[72] Lu Z, Zhongmin C, Xiantao W, Min Y and Yonghu C 2017 *J. Rare Earths* **35** 356–60

Dental Materials 39 (2023) 903–912

Contents lists available at ScienceDirect

Dental Materials

journal homepage: www.elsevier.com/locate/dental

Real-time multispectral transmission of hard tooth tissues and dental composites with their heating

Maja Lezaja Zebic [a,*], Branka Muric [b], Svetlana Savic-Sevic [b], Bojan Dzeletovic [a], Djordje Stratimirovic [c], Dejan Pantelic [b]

[a] Department of Restorative Odontology and Endodontics, School of Dental Medicine, University of Belgrade, Rankeova 4, Belgrade, Serbia
[b] Institute of Physics, University of Belgrade, Pregrevica 18, 11080 Belgrade, Serbia
[c] Department of Biophysics, School of Dental Medicine, University of Belgrade, Dr Subotica 1, Belgrade, Serbia

ARTICLE INFO

Keywords:
Light curing unit
Red curing light
Quadwave
Multispectral
Transmittance
Polymerization temperature
Radiation uniformity
Tooth tissue attenuation

ABSTRACT

The objective of the study was to investigate the real-time transmission of Violet, Blue, Red and Near Infra-Red (NIR) irradiation through 2 or 4 mm thick dental composites and tooth tissue samples at varying positions of Light Curing Unit (LCU) with polymerization temperature monitoring.

Methods: The composites tested were: Filtek Universal Restorative (FUR), Filtek One Bulk Fill (FBF), Tetric EvoCeram (TEC), Tetric Bulk Fill (TBF) and Tetric PowerFill (TPF). The new LCU Pinkwave (a four-wavelength source manufactured by Vista Apex, USA) was placed either centrally or eccentrically for 3 mm above the sample. A Fiber spectrometer detected irradiation and Infrared Thermal camera polymerization temperatures.

Results: All eccentric LCU positions significantly weaken transmitted spectra for all composites in both thickness, jeopardizing Blue light. The LCU position did not affect transmitted irradiation for tooth tissues. The reduction in wavelength intensity when penetrating through thicker compared to thinner composite samples was 62%, 50% and 31% for Blue, NIR and Red, respectively, and 90%, 50% and 35% for tooth tissue samples, respectively. The temperature of bulk fill composites with additional photoinitiators rises faster. Eccentric LCU positions cause a significant decrease in both speed and the maximal value of temperature rise. Red and NIR irradiations contribute to the polymerization temperature.

Significance: Tested LCU source cause considerable inhomogeneity in the emitted and transmitted spectra. Tooth tissues homogenize irradiation, but drastically attenuates it. Red light has better potential than Blue light concerning penetration and could be further investigated as the wavelength for activation of an adjusted photoinitiator.

1. Introduction

Composite polymerization has drawn attention for quite a long time, with rising demands concerning both the quality and time consumption. The dental industry every so often presents new products, either composites with enhanced polymerization and light penetration [1] or curing units with higher power output [2,3]. Adjustments of filler particles refraction indexes and organic matrix could allow deeper irradiation penetration, which is the main improvement achieved with bulk fill in regard to conventional composites [4]. Further addition to the organic matrix, such as β-allyl sulfone (Tetric PowerFill, Ivoclar,Vivadent, Liechtenstein) [5] or the additional fragmentation monomer AFM (Filtek One Bulk Fill, 3 M ESPE) [6], can improve the polymerization process [5,6].

Light emitted on the surface of dental composite is being reflected, scattered and absorbed inside the resin composite [7] depending on the many factors inside the composite (such as filler particle size, shape, distribution [8], differences in refractive index between organic compound and fillers [4,9], light absorption spectrum of photoinitiators [10], etc.) Light penetration depth describes how much light remains for potential polymerization of the deeper composite layers [11]. During the photoactivation process, the wavelength absorbed by the photoinitiator is spent within the material and that absorption reflects the dynamics of its activation, which is not the case with the rest of the spectrum. Par et al. [12] even used this change in transmittance to determine the curing time required for complete polymerization.

* Correspondence to: University of Belgrade, School of Dental Medicine, Rankeova 4, 11000 Belgrade, Serbia.
E-mail address: maja.zebic@stomf.bg.ac.rs (M.L. Zebic).

https://doi.org/10.1016/j.dental.2023.08.174
Received 23 May 2023; Accepted 16 August 2023
Available online 26 August 2023
0109-5641/© 2023 The Academy of Dental Materials. Published by Elsevier Inc. All rights reserved.

Transmission of tooth tissue could be used to polymerization composite that is sheltered from the direct curing light beam.

The maximal temperature rise in composite during setting is due to the exothermic polymerization reaction but also due to warming caused by the LCU (Light Curing Unit) [13–15] and above all it is important as a potential risk for overheating of soft tissues in and around the tooth. The speed of temperature rise is a property that indirectly shows the dynamics of the polymerization process as released heat is mainly produced in propagation phase of polymerization [16]. Changes in temperature rise may also be result of changes in light energy absorption during polymerization but it is not expected to be that much pronounced [17]. The trend of rising power output from LCU causes temperature to increase more [18,19]. On the other hand, preheating of composites may increase monomer conversion and improve composite properties [20, 21], decrease shrinkage [22], and reduce their viscosity, which provides better cavity adaptation [23]. The disadvantage is that they become cooled during transport from the composite preheating device to the tooth cavity [21]. Also, the irradiation with longer wavelengths (within the infrared region) is expected to penetrate deeper and produce heat in the material that absorbs it [24].

Previous scientific papers described poly-wave LCUs that emitted two or three wavelengths in the 405–480 nm (violet and blue light) range. Spectral differences across the curing unit tip were already demonstrated for LCUs possessing 3 or 4 LED diodes [25,26], and it was shown that inhomogeneous spectral output affects localized microhardness of resin-based composites [25,27] and may affect dentin adhesive bond strength distribution [28]. In 2021, Light Curing Unit with quad-wave technology appeared on the market for the first time, emitting radiation with a wider spectral range (in the Red and Near Infra-Red (NIR) part of the spectrum). Such a device, a Pinkwave LCU (Vista Apex, Dental Materials Inc. Racine, USA), was used in this research. The penetrability of Red and NIR wavelength through either composite materials or tooth tissues is unknown. Further, LCU comprising even 8 LED diodes provokes questions about the spectral distribution beneath samples irradiated with various regions of this wide area curing source. Nonetheless, the role of "new" wavelengths in dental composite curing temperature deserves to be investigated.

The aim of the present study was to investigate the effect of using LCU (Pinkwave) in four different positions with respect to the composite sample on the real-time transmitted spectra during polymerization of five dental composites (conventional or bulk fill with CQ (Camphorquinone) as the only photoinitiator or combined with Lucirin or Ivocerin), made in two thicknesses (2 mm and 4 mm), during 20 s of irradiation in standard mode. Further, the effect of LCU position was investigated on the real-time temperature of composites, i.e., to the speed and maximal temperature rise during polymerization. Transmitted spectra were also analyzed for tooth tissues. Traced wavelengths were Violet (406 nm), Blue (483 nm), Red (633 nm) and NIR (862 nm). Further, the properties of Red and NIR irradiation will be compared for the first time with the properties of Blue and Violet light, regarding penetration ability, i.e., attenuation with thickness of both the composites and tooth tissue samples. The null hypotheses tested were:

1) There is no difference in transmitted spectra among different composite materials and among different LCU positions for composite and tooth tissue samples;.

2) There is no difference in transmitted spectra attenuation with sample thickness among various wavelengths for both composite samples and tooth tissue samples;.

3) There is no difference in speed of temperature rise and maximal temperature rise among tested composites and among various LCU positions.

2. Material and methods

The Light Curing Unit (LCU) used in present study, Pinkwave™ (Vista Apex, Dental Materials Inc., Racine, USA), emits Red and NIR irradiation in addition to Blue and Violet light. It was used in the Standard curing mode with irradiation time of 20 s as recommended in the recent research [29]. Composite sample surface area was 0.18 cm^2. Power output was measured with Bluephase ®Meter II (Ivoclar Vivadent). This LCU contains 8 LED diodes (two Blue, two Red, two NIR, one Violet and one "day light" diode), distributed within two distances from the center of the LED panel (Fig. 1) and emits through a lens-like tip with diameter of about 11.7 mm.

Five dental composites, conventional or bulk fill, were used in the present study (Table 1). They also differed in terms of photoinitiator, with either CQ as the solephotoinitiator or Ivocerin or Lucirin as additional photoinitiators. They were investigated in two thicknesses (2 mm and 4 mm) and in four LCU positions with respect to them (Fig. 1), with 5 samples in each group. The spectra were detected using a High-Resolution fiber-optic Spectrometer (HR2000CG-UV-NIR, Ocean Optics Inc. with 400 μm fiber), positioned beneath the center of the sample and only the LCU varied the position above the sample. Temperature was detected by an Infrared Thermal Camera (FLIR A65, FLIR Systems, Inc.). Further analysis was done on a PC.

The experimental setup is presented in Fig. 2. LCU was fixed in its holder during the irradiation. The thermal camera detected temperature simultaneously with polymerization on the composite side surface, which was left free of mold (Fig. 2, insert a). Eccentric positions were achieved by moving the LCU for 3 mm in various directions and, if necessary, rotating the LCU with its holder on the mounting desk. For the thicker samples only mold holder (MH on Fig. 2, insert e and f) was replaced with thicker one, and Fiber-optic spectrometer was moved lower for 2 mm. An auxiliary metal plate with perforations indicating sample position made positioning of the LCU toward the sample easier and provided a distance of one millimetre between the curing unit's convex lens and the sample surface. This distance simulated the clinical condition in which the cusps of the tooth impede direct contact between the light source and composite. The plate was removed during measurements. Heavy silicon material (Elite HD+, Zhermack, Italy) was used to precisely ensure the position of the LCU in its holder. The repeatability of the detected spectrum was checked when putting the LCU in its holder. The detection of the spectra was conducted with an empty mold in four LCU position described, on both distances among LCU and fiber-optic spectrometer (5 and 7 mm) to detect emitted spectra without composites. Uncured composite was inserted into mold, positioned in mold holder, and simultaneously irradiated and monitored with thermal camera.

The composite sample geometry was cut out from a disk diameter 5 mm (Fig. 2, insert a), producing two opposite flat side surfaces (about 3 mm wide), so that one of them can serve for temperature tracking (Fig. 2, insert e and f). Mold used for composite samples were made of white epoxy resin, with optical properties similar to those of composites and tooth tissues. The outer diameter of this mold was 11 mm (approximating the size of a molar tooth), and thickness of 2 or 4 mm. Space between epoxy mold and the box in the mold holder (Fig. 2, insert g) was filled with the silicon (Elite HD+, Zhermack, Italy) (Fig. 2, insert g) to enable and facilitate precise fast return of molds filled with unpolymerized composite. For composite sample preparation, the Mylar strip vas used at the bottom and the top of the composite and the measurements of the transmitted spectra were done within 60 s from opening the composite tube, doing all the operations in the dark room. Spectra were detected for 20 s, which was the time of irradiation in the standard curing mode of the LCU used, and the temperature was monitored during 30 s, continuing for 10 s after the irradiation is finished. The measurements were conducted at room temperature (21 °C ± 1 °C), and for the results initial detected temperature of each sample was used as starting, counting increase from that temperature as a result.

The temperature of the TEC composite was monitored for an additional 10 samples. Five of them were irradiated by the Pinkwave LCU, in central position, but with the use of filters that stop wavelengths above

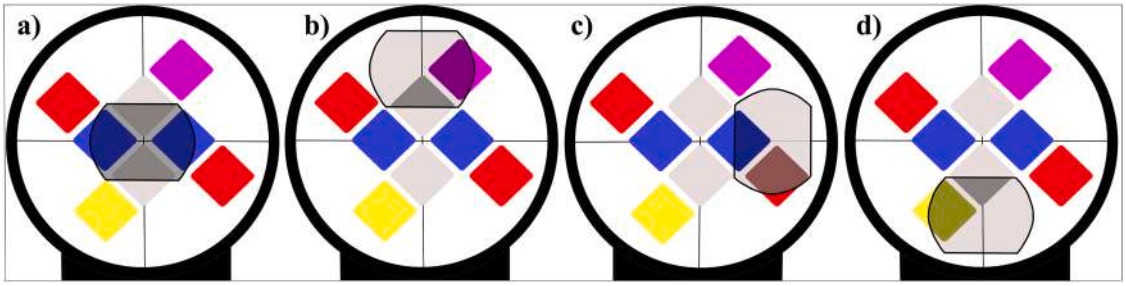

Fig. 1. The LCU with schematically presented diodes and the projection of the composite sample position – transparent grey surface. a) Central position ("c"), with the sample under NIR and Blue diodes; b) First eccentric position ("e1"), with the sample under NIR and Violet diodes; c) Second eccentric position ("e2"), with the sample under Blue and Red diodes and d) Third eccentric position ("e3"), with the sample under NIR and day light diode (yellow).

Table 1
Materials used in the study.

Dental Composite/ shade	Abbreviation/ Type	Manufacturer	Photoinitiator Batch number	Composition
Tetric **E**vo**C**eram/ A2	**TEC** Conventional composite	Ivoclar vivadent, Schaan, Leichtenstein	Camphorquinone +Lucirin LOT Z02JCN	UDMA, Bis-GMA, Bis-EMA, ytterbium trifluoride, 76 wt% filler load 40 nm-3 μm size
Tetric EvoCeram **B**ukl **F**ill/ IVA	**TBF** Bulk fill composite	Ivoclar vivadent, Schaan, Leichtenstein	Camphorquinone +Ivocerin LOT Y18018	Dimethacrylate, Ba-Al-Si glass, prepolymer filler, spherical mixed oxide, 76–77 wt% filler load
Tetric **P**owerFill/ IVA	**TPF** Bulk fill composite	Ivoclar vivadent, Schaan, Leichtenstein	Camphorquinone +Ivocerin LOT Z01PHK	Bis-GMA, ytterbium trifluoride, urethane dymethacrylate, DCP, β-allyl sulfone, 76–77 wt% filler load
Filtek Universal **R**estorative/ A2	**FUR** Conventional composite	3 M ESPE, St. Paul, MN, USA	Camphorquinone LOT NA62517	AUDMA, AFM, diurethane-DMA, and 1,12-dodecane-DMA, ytterbium trifluoride, zirconia/ slica, 76,5 wt% filler load
Filtek One **B**ulk **F**ill/ A2	**FBF** Bulk fill composite	3 M ESPE, St. Paul, MN, USA	Camphorquinone LOT NE57625	AUDMA, AFM, DDMA, UDMA,ytterbium trifluoride, zirconia/slica, 76,5 wt% filler load.

Bis-GMA: bisphenol A-glycidyl methacrylate, AUDMA: aromatic urethane dimethacrylate, AFM: addition- fragmentation monomer, DDMA: dodecyl methacrylate, UDMA: urethane dimethacrylate, TEGDMA: triethyleneglycol dimethacrylate, DCP: tricyclodecane–dimethanol dimethacrylate, DMA: dimethacrylate, DDMA: 1,12-dodecane dimethacrylate.

600 nm, thus the Red and NIR were annulled. The use of filters between the lens of the LCU and the composite sample needed an increased distance among them (15 mm), which is the reason why irradiation from the same LCU position was done without filters for an additional 5 samples. These findings provided a new control group for determining a Red and NIR contribution to composite material warming during polymerization. The same composite was irradiated using filter which stop wavelength below 600 nm (thus excluding Violet and Blue light), and it was determined that composite did not change the consistency, remained soft, completely un-polymerized.

2.1. Tooth tissue transmitted spectra

Transmitted spectra were also detected for the samples of human extracted tooth tissues in different thicknesses (2 mm and 4 mm), also with 5 samples for each thickness, just not in real-time because there are no variations during time. Approval from the Ethical Board was obtained (No. 36/32 from December 7th, 2022). Flatter tooth parts were chosen - proximal tooth surfaces (Fig. 2, insert b). Upper premolars were used, within 3 months from extraction because of orthodontic reasons. After extraction, teeth were thoroughly cleaned and stored in 0.5% chloramine at 4 °C until use. Proximal surfaces of the teeth were separated using Isomet 4000 linear precision saw (Buehler, Lake Bluff, Illinois), with tooth root fixed in resin (Ortopoli, Polident, Slovenia). The measuring segment of each tooth (with irregular outer enamel surface morphology) was immersed in white epoxy resin to fill the total sample of each individual tooth sample to the size of a disc 11 mm in outer diameter (Fig. 2, insert c and d), like the size of a mold for composite samples, while leaving the central enamel surface and beneath tooth tissue surface free of epoxy resin. Transmitted spectra were only detected beneath the central point of each sample.

The obtained data was statistically analyzed using OriginPro software. For data showing normal data distribution (Shapiro-Wilk test) and homogeny variances (Levene's test), One Way ANOVA with Tukey's means comparison was used; otherwise, Kraskal-Wallis ANOVA with Dunn's post hock analyses was performed. The level of significance was set at 0.05. Only relevant comparisons were conducted.

3. Results

40 tested composite groups (two thicknesses, four LCU positions, 5 composites), with 5 samples in each group and at the four different wavelengths were evaluated. Furthermore, because the transmitted spectra intensities differed at the beginning and end of the irradiation time (blue wavelength increasing and others decreasing), 1st second and 20th second values separately were used for statistical comparison.

Estimated Emitted Power per unit area of the LCU, for the Standard curing mode was 2180 mW/cm2. Irradiance at the distance of the composite sample was 1651 mW/cm2 and the power received at the composite sample surface thus was 297 mW.

3.1. Spectra at various LCU positions

The arrangement of LED diodes inside two rings, i.e., at two distances from the center of the LCU source, caused significant variations in the emitted spectral distribution in a different segment of these new wide curing sources, as shown in Fig. 3 (Emitted spectra). Increased distance between LCU and optic-fiber for thicker samples with empty mold cause minimal change in detected spectra (2–6%) and is provided as supplement file (FIG S1).

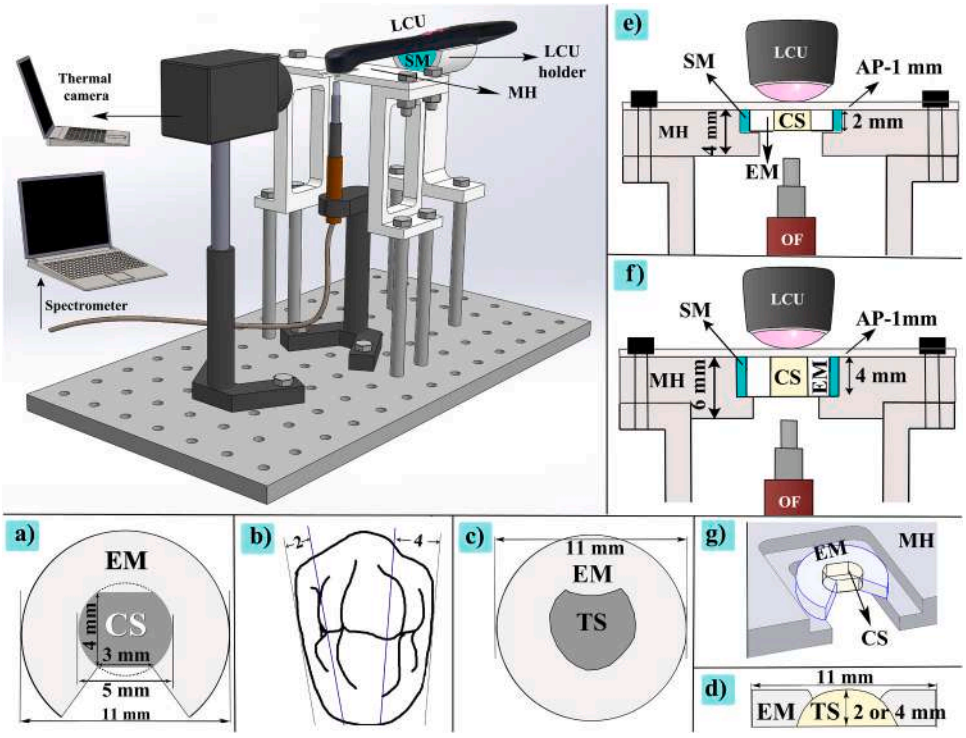

Fig. 2. The scheme of the experimental setup. All setup components were fixed to the mounting desk. Two computers were used simultaneously, one to record data obtained by the spectrometer, and the other to record data from the thermal camera. LCU is Light Curing Unit, SM is the silicon material in the LCU holder, and MH is the mold holder. a) The insert shows the scheme of an epoxy mold (EM) for the composite sample (CS) with its' dimensions and shape, as seen from the LCU tip. Note that one lateral side of an epoxy mold is missing, providing a mold-free surface for temperature monitoring during polymerization. b) The insert shows scheme of premolar tooth sectioning projections for obtaining tooth tissue samples thick 2 and 4 mm. c) The insert shows the scheme of an epoxy mold (EM) for the tooth sample (TS), the view seen from the LCU tip and d) a lateral view, demonstrating the fulfilment of an irregular tooth sample shape into disk with 11 mm diameter. An individual epoxy mold was made for each tooth tissue sample. e) Insert and f) inserts show a lateral view of the setup from the view of the thermal camera, with composite samples thick 2 and 4 mm, with free of mold surface for temperature monitoring, epoxy mold and silicon mold (SM). Auxiliary plate (AP), thick 1 mm was used only during the positioning of the LCU within its holder, providing the necessary distance, and was removed during the irradiation. The mold holder (MH) had additional thickness for composite samples thick 4 mm (f insert), so the LCU didn't need to be moved, but the Optical fiber (OF) was positioned 2 mm lower for thicker samples. It was the same for the tooth tissue samples. g) The insert shows relation of the epoxy mold with the composite sample within the mold holder (MH). Fitting was enabled with a silicon material.

Averaged values from five measurements of a real-time transmitted spectra for tested composites in different LCU positions (c, e1, e2 and e3) are also presented at Fig. 3. The trend of transmitted spectra intensities for different dental composites was in most cases in descending order: TBF > TPF > FBF > TEC > FUR. The effect of LCU position on transmitted intensities of various wavelengths in different LCU positions (c, e1, e2 and e3) for all materials in 1st and.

20th seconds, for composite thicknesses of 2 mm, was statistically analysed. Due to the large number of data points, only the results for TBF are shown as an example (see Fig. 3, Transmitted Spectra for TBF). The other materials showed a similar trend and the data is available as supplement FIG S2. The change in LCU position had a significant impact on detected values. The order of intensities for Violet wavelength was: c > e3 > e1 > e2, with significantly different values for all eccentric positions in comparison to central for every tested material and both times. The order for Blue light was c > e1 > e3 > e2, with only a marginal difference between e1 and c position values for FBF in both times and FUR and TPF in the first second, whereas e2 and e3 cause significant differences in comparison to c position for all tested materials in both times. Red wavelength values were ordered as follows: e1 > c > e3 > e2, with similar values for FUR, TBF, and TEC in the first second between e1 and c position in both times, while e2 and e3 cause significant differences in comparison to c position for all tested materials in both times. The NIR wavelength values were in the following order: c > e1 > e3 > e2, with significant differences for all tested materials at both times.

The results of the change in intensity during the irradiation time (20 s) are given in Table 2, showing that Blue light had the highest percent of change (28.16%) between the 1st and 20th second. As a result of the photoinitiator reaction, transmission increases during the irradiation time, contrary to the other three wavelengths, whose relative transmitted spectra decreases as materials polymerize.

3.2. Thickness attenuation dependence for each wavelength and material

Table 3 shows the average percent decrease in the intensity of the transmitted spectra among 2 mm and 4 mm thick samples ($\frac{2mm\ \ value-4mm\ \ value}{2mm\ \ value}$,) detected in the central position for all materials combined and each separately. The One Way ANOVA with Tukey's post hock corrections was used to compare values detected in the central position in the 1st second and showed that Blue light had a significantly greater decrease with composite thickness compared to Red light for all tested materials. The differences for the 20th second were similar, so further analyses were not necessary to confirm the previous conclusion. This comparison was done in order to investigate the potential of different wavelengths to penetrate throughout a thicker material layer. The change in Violet light was opposite from what was expected, i.e., higher intensity was detected beneath the thicker sample.

3.3. Detected temperatures for the composite samples during 30 s

The temperature detected during and shortly after irradiation (Fig. 4) did not differ for different composite thicknesses (2 mm and 4 mm), and only the data for 2 mm thick composites were analysed for further comparison. The speed of temperature rise (mean inclination of an initial linear part of the temperature/time curve) of different materials in the same LCU position was investigated, and it was discovered that TBF and TPF had significantly faster temperature rise than FUR and FBF (except for FBF in e2). The speed of temperature rises of the same material in different positions revealed the same relation for all materials, c > e1 = e2 > e3, indicating that the use of LCU in eccentric positions significantly affects (decreases) the temperature rise (within

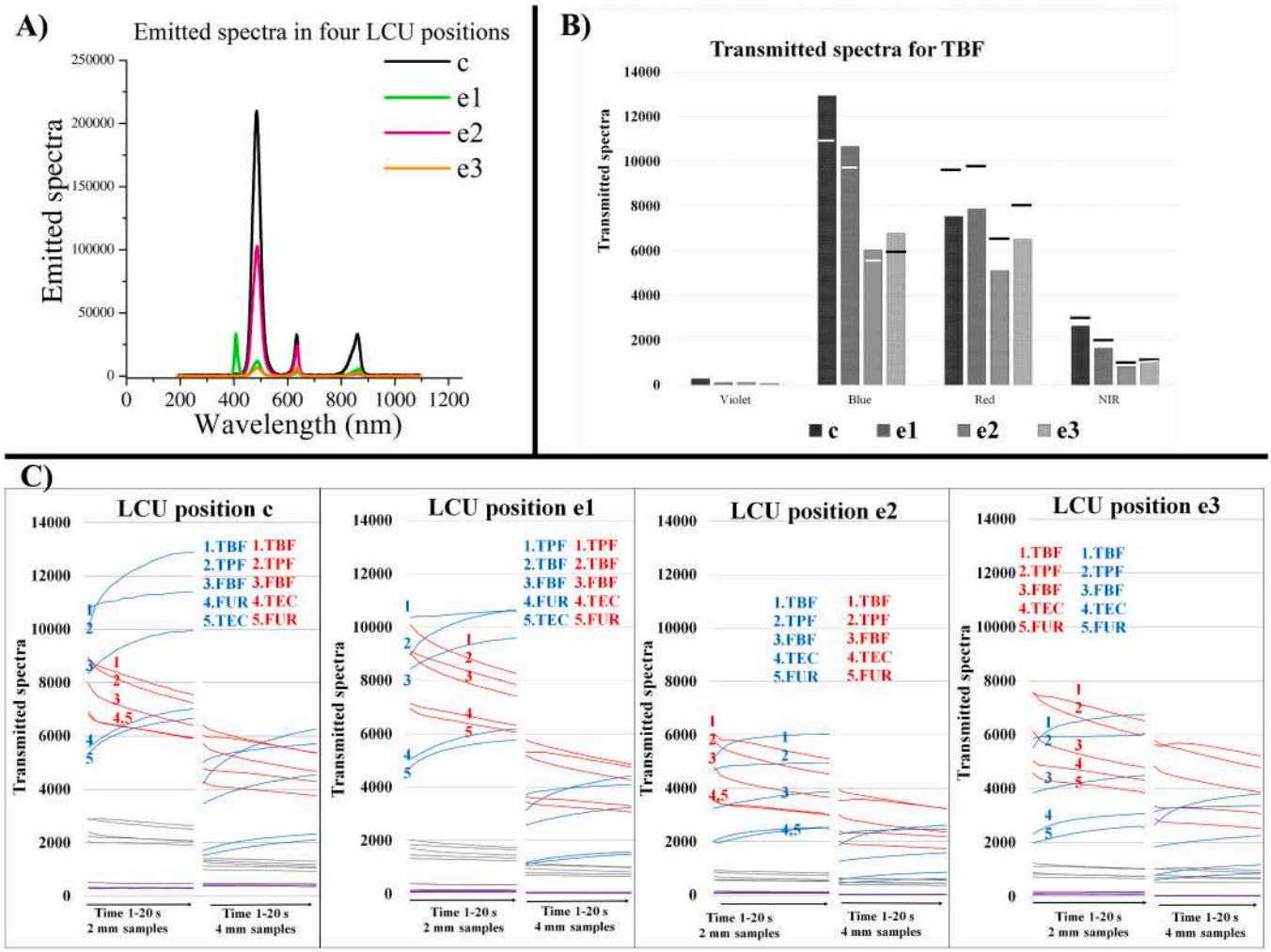

Fig. 3. Averaged spectra detected in four LCU positions, central (c) and eccentric (e1, e2 and e3). a) Represents emitted spectra, without a sample. b) Represents average values of transmitted wavelengths in the first and 20th seconds (line below or above the upper end of each rod), as an example for composite samples. The remaining materials produced similar results but were not presented due to the large number of data points. c) Represents averaged real-time transmitted intensities in four LCU positions for traced wavelengths (406 nm – Violet, 483 nm – Blue, 633 nm – Red and 862 nm – NIR – represented with grey color) for five composites (FBF, FUR, TBF, TPF and TEC), and for two composite thicknesses (2 mm and 4 mm). Results for 4 mm thick composites continue after those for 2 mm thick composites. The figure is of an informative nature for quick general visual comparison, without annotation for material belonging, with the exception of Blue and Red for 2 mm thick samples, whose order is marked.

Table 2
Average percent of change in transmitted spectra intensity during monitoring time in central LCU position, calculated using the equation: $\frac{1sts\ value - 20ths\ value}{1sts\ value}$. For better understanding increase during irradiation time will be presented as positive values, and decrease as negative values.

	Both thicknesses and all materials together (%)	Only Tetric composites	Only Filtec composites	Only 2 mm thick composites	Only 4 mm Thick composites
Violet	-5.23	-4.10	-6.92	-5.02	-5.44
Blue	+ 28.16	+ 26.96	+ 29.96	+ 21.11	+ 35.21
Red	-16.03	-15.25	-17.19	-17.63	-14.42
NIR	-10.46	-9.77	-11.51	-11.25	-9.68

Fig. 4).

The maximal temperature rise (ΔTmax) detected during monitoring time (30 s), calculated as the maximal recorded value minus the initial value, is also presented within Fig. 4. The temperature rise for all materials was significantly higher in the central position and significantly lower in the e3 position. The LCU position had a more pronounced effect than the material. Descending order for the materials (median values) in central position were: TEC > FUR > FBF > TPF > TBF with significant difference only comparing first two (TEC and FUR) with the last one (TBF).

3.4. Contribution of Red and NIR to polymerization temperature

A comparison of the polymerization temperature for TEC when irradiated with or without the additional use of specific filters that stop Red and NIR irradiation is presented in Fig. 5. Annulation of a Red and NIR cause a reduction in the detected temperature, with the maximum temperature rise decreasing by nearly 18%. The exact mechanism of the warming contribution was not further analysed.

3.5. Tooth tissue transmission

The transmitted irradiation through the tooth tissues (Fig. 6.) barely varied due to the varying positions of the LCU with respect to the tooth sample (c, e1, e2, e3). Different wavelengths had different intensities, with decreasing order being Red > Blue > NIR > Violet for 2 mm

Table 3
Average percent of change in the transmitted spectra intensity among the different composite sample thicknesses calculated using the equation: $\frac{2mm\ value - 4mm\ value}{2mm\ value} * 100$.

	Comparison of values in 1st second (%)	Comparison of values in 20th second (%)	Material	FBF	FUR	TBF	TPF	TEC
Violet	-30.16 *	-52.60 *	AVERAGE	9.18	25.34	48.92	17.72	40.57
			± STDEV	± 4.73	± 13.26	± 21.48	± 10.82	± 8.73
			Statistic	c	abc	a	bc	ab
			letter	D	AB	AB	B	B
Blue	62.43	57.44	AVERAGE	58.49	72.78	58.84	53.57	68.25
			± STDEV	± 2.85	± 1.24	± 2.15	± 2.34	± 2.84
			Statistic	c	a	c	d	b
			letter	A	A	A	A	A
Red	31.10	29.00	AVERAGE	27.89	37.69	32.45	27.96	29.29
			± STDEV	± 1.76	± 2.28	± 1.96	± 2.60	± 3.13
			Statistic	c	a	b	bc	bc
			letter	C	B	B	B	C
NIR	50.42	49.75	AVERAGE	46.32	51.24	51.50	53.52	49.17
			± STDEV	± 2.66	± 0.72	± 2.49	± 11.82	± 0.46
			Statistic	a	a	a	a	a
			letter	B	AB	AB	A	B

Statistic letter: the different small letters indicate statistically significant different values among the different materials for the same wavelength (read horizontally), and the different uppercase letter indicate statistically different values among the different wavelength for the same material (read vertically).
*Negative values for Violet light mean that through the thicker samples pass more irradiation compared to thinner samples

thickness and Red > NIR > Blue > Violet for 4 mm thickness.

The percent decrease in transmitted irradiation intensity for various wavelengths in the central position as the sample thickness increases from 2 mm to 4 mm was calculated as ($\frac{2mm\ \ value - 4mm\ \ value}{2mm\ \ value}$) and is shown as a table in Fig. 6. A.

comparison with One Way ANOVA with Tukey's post hock test showed that attenuation with thickness was statistically significantly higher for Blue and Violet in comparison to Red and NIR wavelengths.

4. Discussion

Since the behavior of the Blue and Violet wavelengths has been extensively investigated in previous studies, and considering the fact that there is no other LCU on the market that emits Red and NIR wavelengths, the use of control LCU was skipped in the present study and the Blue and Violet wavelengths from the same LCU were used for comparison.

The first null hypothesis was partially rejected since the tested composites and the LCU positions cause different transmitted intensities. The first hypothesis was accepted for tooth tissues because there was no difference when the LCU position was changed. The second null hypothesis was rejected since different wavelength attenuations with sample thickness differed among each other, for both, composites and tooth tissue samples. The third null hypothesis was also rejected since different composite materials and different LCU positions differ in the speed of temperature rise as well as in the maximal increase in temperature during the monitoring time.

The increased number of wavelengths requires an increased number of LED diodes and more space for their positioning within the LCU tip. The Pinkwave has a curing tip diameter of about 11.7 mm, but the diodes beneath the convex lens are only about 1.8 mm square and are not completely symmetrically distributed. That is the reason why the position of the LCU and the sample were varied, tracking the changes in the spectral distribution. The LCU tip's canter was moved 3 mm in three directions (e1, e2, and e3). The forth eccentric position was skipped because it would be the repetition of the LED diodes from the e2 position. The edge of the LCU lens itself was avoided. Because precise and stable LCU positioning was required during irradiation, the LCU was held within the holder during experiments (Fig. 2), allowing for reproducible positioning of the LCU between uncured composite sample insertion into the holder.

Tooth tissues for transmission measurements were used in a clinically relevant way, leaving the outer smooth enamel surface and taking the necessary tissue thickness of the inner tooth tissues to obtain samples 2 mm and 4 mm thick. This was done regardless of the variations in the samples' geometries and the inequality in the sample thickness along the whole sample in order to simulate undamaged enamel surface reflection in a clinical condition. The data obtained for the tooth tissue transmission could provide information about the potential of transmitted irradiation to polymerize materials when some part of it is obscured from direct irradiation exposure because of the cavity geometry or imperfect bundle direction. Both, the composite samples and the tooth tissue samples were surrounded with a white epoxy resin in the shape of a disc, approximating an 11 mm wide molar tooth and "occupying" almost the whole curing area. These were done in order to mimic the light transparency, reflection and absorption of the clinical surrounding.

All the eccentric LCU positions cause the detected spectra to be different, indicating that the irradiation emitted and transmitted with respect to the dental composites is inhomogeneous. Previous studies have also shown that no matter the type of tip (a lens or an optical fiber bundle light guide), the inhomogeneity of the emitted spectrum is present for the polywave kind of LCU [26] and it has a significant effect on a localized microhardness [25]. The effort should be directed toward solving this problem in order to obtain a uniform spectral distribution regardless of the number of diodes (chips) within the LCU tip. The tooth tissues, as shown in the present study, do this, but it weakens the irradiation too much.

The results from this study indicate better penetration of Red and NIR wavelengths compared to Blue. The percentage wise reduction of each wavelength irradiation through thicker samples compared to thinner samples was 62% for Blue, 50% for NIR, 31% for Red, for composites, and 90%, 35% and 50% for the tooth tissues, respectively. This property describes the potential of each wavelength to be used for the polymerization in the deeper composite layer, which is the main trend nowadays for saving chairside time. The attenuation of the red wavelength with the additional 2 mm of composite is half that of the blue wavelength, indicating that red light penetrates better. This finding should be checked in future research, as should the possibility of producing experimental composites with the photoinitiator activated with a Red wavelength. The reason more to favour Red light might be the potential harmfull effect of the blue curing light, discussed by Oliveira and Rocha [30,31].

The values of transmitted spectra intensities were higher for Violet

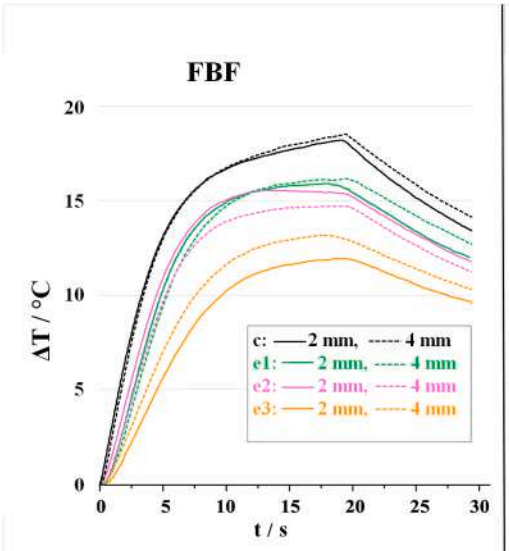

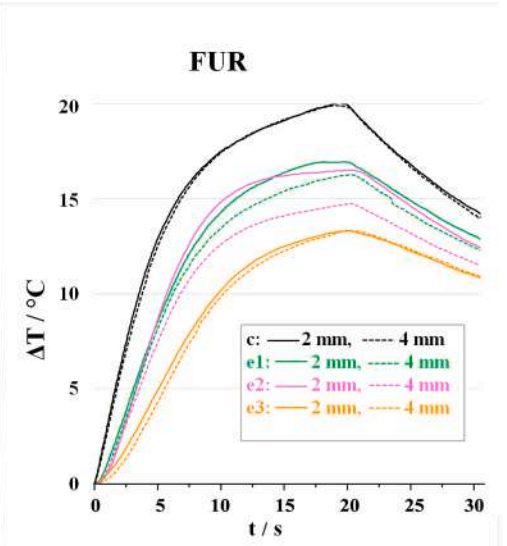

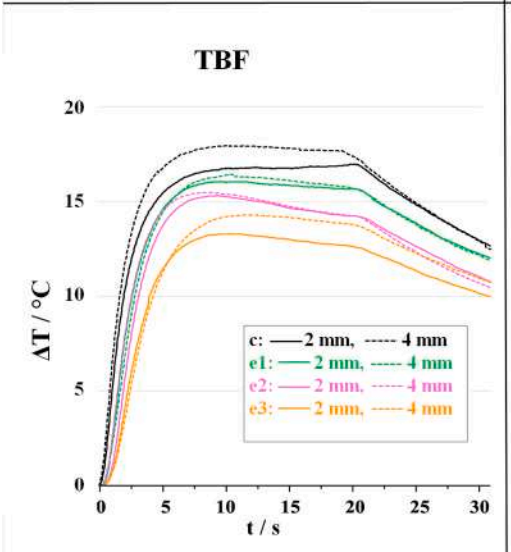

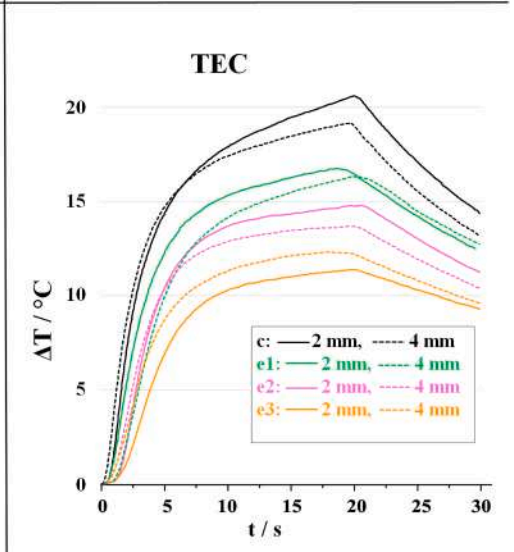

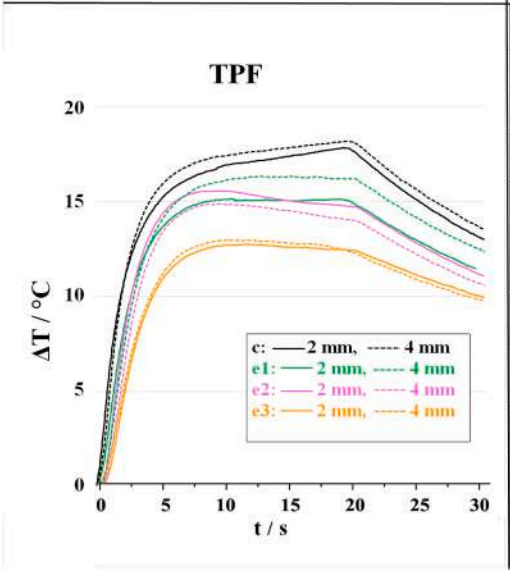

ΔT max

	FBF	FUR	TBF	TPF	TEC
c	a 18.24 AB	a 19.57 A	a 17.08 B	a 17.88 AB	a 20.66 A
e1	b 15.94 BC	b 17.20 A	b 16.13 ABC	b 15.31 C	b 16.82 AB
e2	b 15.58 B	b 16.56 A	c 15.37 B	b 15.61 B	c 14.85 B
e3	c 11.97 BC	c 13.32 A	d 13.35 A	c 12.78 AB	d 11.40 C

Slopes of initial temperature rise

	FBF	FUR	TBF	TPF	TEC
c	a 2.81 BC	a 2.70 C	ab 4.49 AB	a 4.89 A	a 3.67 ABC
e1	b 2.39 C	b 1.93 C	a 4.83 A	b 3.97 B	a 3.32 B
e2	b 2.40 BC	b 2.19 C	ab 4.39 AB	a 5.20 A	a 3.36 ABC
e3	c 1.35 B	c 1.28 B	b 3.60 A	b 3.05 AB	b 1.77 AB

Fig. 4. Averaged real-time temperature detected for each tested composite in two thicknesses and in different LCU positions. Starting temperature was the room temperature, and only temperature increase was used for analysis. Black represents the central position, Green "e1", Pink "e2" and Orange "e3" positions (like on Fig. 3a). Dash lines represent values for samples thick 4 mm. Data for 2 mm thick sample is additionally presented in tables for ΔTmax and Initial slop i.e., speed of temperature rise, with statistical denotations. For both tables, the same small letters indicate no statistically significant difference among various LCU positions for the same material, and the same uppercase letters indicate no statistically significant difference among various materials in the same LCU position.

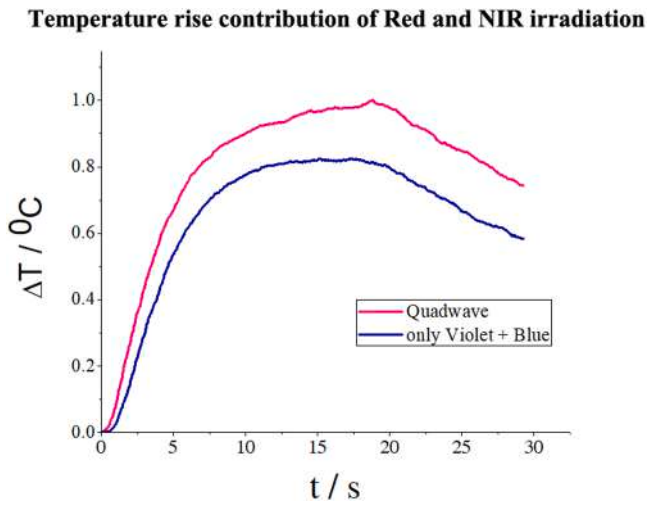

Fig. 5. Averaged temperatures detected during polymerization (TEC thickness of 2 mm) using the Pinkwave LCU alone or with inserted filters that cut off Red and NIR irradiation. The contribution of "new" wavelengths to temperature rise is obvious, despite the fact that Red and NIR do not play a role in photo-initiator activation.

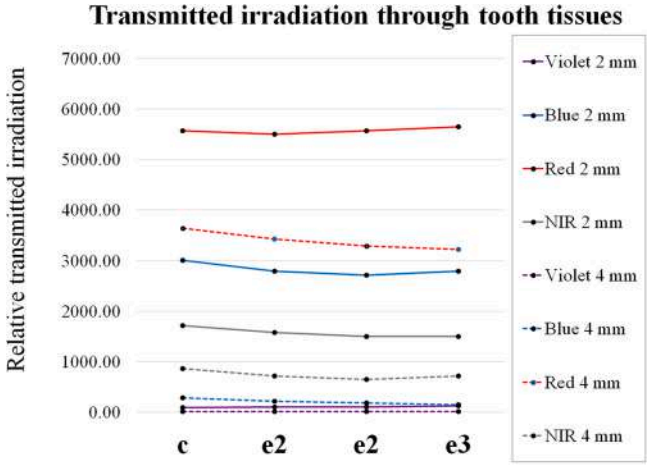

Average % of attenuation with tooth tissues thickness

	Violet	Blue	Red	NIR
(2-4)/2	89.17	90.48	34.62	50.00
Statistic	A	A	B	B
2 mm	85.80	3003.00	5577.00	1716.00
4 mm	9.30	286.00	3646.50	858.00

Fig. 6. Averaged transmitted irradiation through tooth tissues for sample thicknesses of 2 mm (full line) and 4 mm (dash line) in various LCU positions. No statistically significant difference was found among different LCU positions. Wavelength dependent attenuation with tooth tissue thickness for the central LCU position is presented as a Table, with different letters representing statistically significant differences among attenuations. The values used for the calculation of the attenuation are presented below the main result.

light for sample thick 4 mm in comparison with 2 mm thick composites in the central position. The reason for this appearance could be in the greater scattering inside a thicker composite layer, which surpasses the greater attenuation of the thicker material so that a higher amount of irradiation can reach and leave the middle of the composite sample bottom surface. Besides, the Violet light source comes from the LCU tip periphery, unsymmetrically, and has a drastically lower intensity compared to the other wavelengths, which was the reason why the data variances for Violet irradiation was the highest in all groups, together with more expressed effects of eventual flaws within the composite sample.

Previous study dealing with the light transmission of wavelengths 400 – 800 nm showed that transmittance through the polymerized composites is twofold greater than through the un-polymerized ones and that the higher the wavelength, the higher the transmittance values are [32]. The findings in our study were the opposite if we consider the first second values as transmission for an unpolymerized material and the values in the 20th second as transmission for a polymerized material.

The eventual potential of the NIR irradiation was previously investigated in the context of inducing an internal upconversion process in the dental composites with added rear earth (Y_2O_3, $NaYF_4$), which interacted with the NIR iradiation, changing it into Blue luminiscence, further activating camphorquinone, provoking polymerization [33–35], but this doesn't seem promising.

The speed of temperature rise was calculated to represent the measure of polymerization speed and needed irradiation, i.e., chairside time. The maximally reached temperature was represented as a potential risk factor for vital tooth tissues overheating but also indirectly indicated the extent of polymerization. Both of these characteristics (speed of temperature rise and ΔT max) were compromised in eccentric LCU positions, which might indicate jeopardized polymerization, but this assumption should be further investigated and checked. Limitation of present study is that the temperature tracking during polymerization started at room temperature, and not at the simulated mouth temperature, and that the irradiation was not repeated after composite cooling to determine polymerization reaction contribution to the warming, but only used to detect eventual differences among various LCU positions. The exact simulation was already analysed in previous studies testing the same LCU [18], just without determining the contribution of new wavelengths to the warming. Our study found approximately 18% of the Red and NIR wavelengths contribution to composite warming during polymerization, which is not insignificant. The mechanism of this contribution was not further analysed.

The temperature of the composites during polymerization was increased from room temperature up to 20 °C. The study by Adams et al. [36] detected a higher LCU tip temperature for the Pinkwave, and Maucoski et al. [18] found a higher temperature increase for composites during the polymerization with a Pinkwave activated for 10 s compared to the Valo Grand LCU (Ultradent), which value is in agreement with the results from our study. The concerns related to overheating of vital tooth tissues due to rising power output from the LCU are controversial. So many times, the results from Zach since a long time ago (1965 year) have been cited, claiming that the critical temperature rise is 5.5 °C [37]. On the other side, a recent study showed that the temperature increase in the pulp of 8.9–14.7 °C did not cause pulp injury, but the dentin trauma did, as the consequence of an anatomical and functional relation between these two tissues [38]. Mouhat et al. investigate the direct effect of eight brands of LED LCU directly onto the dentin surface and in the pulp chamber with 0.6 mm remaining dentin thickness in a recent study. It was found that the temperature increase of 15 °C resulted in only a 4 °C temperature increase in the pulp chamber [39], and the in-vivo study of Zarpellon showed that the polywave Bluephase 20i LCU operating during 30 s caused a peak temperature in the pulp of 37.5 [40], which is, let's say, quite a bit lower than the temperature during the febrile condition. In Class I and Class V cavities, newly published data testing Pinkwave-induced polymerization of a different composite found a temperature increase in the pulp chamber of 3.4–4.6 °C with 32 °C as a starting temperature and approximately 1 mm of remaining dentin thickness [41].

The composites' preheating was quite well investigated [42]. According to the literature, light polymerization at a moderately raised curing temperature (54.5 °C) resulted in significantly higher conversion values than light curing at room temperature [21]. Other studies dealing with the effect of the outer heat on the dental composites also found a significant effect of the temperature on the polymerization, showing

better and faster conversion and increased Knoop hardness for the pre-heated composites [43]. It was also shown that the temperature of the composites decreased rapidly during the transportation of the material from the heater to the cavity [23], thus this in situ heating with additional wavelengths (Red and NIR) during the polymerization seems quite a reasonable innovation.

The potential of the "new" two wavelengths (Red and NIR) doesn't seem to activate any photo-initiator in the commercially available dental composites for now, but their penetration through the dental tissues or the dental composites is less attenuated with thickness compared to a Blue wavelength. Further, these "new" wavelengths can contribute to the material's warming in situ instead of its pre-heating in a dedicated device.

5. Conclusion

The wide LCU source tested caused considerable inhomogeneity in the emitted and transmitted spectra. The transmitted spectra, the speed of temperature rise, and the maximal temperature increase during polymerization are decreased beneath the LCU periphery compared to the central LCU zone. The tooth tissues homogenize irradiation, but they drastically attenuate it. A Red light has better potential than a Blue light concerning penetration through both composites and tooth hard tissues, and it should be further investigated as a wavelength for the activation of an adjusted photoinitiator.

Declaration of Competing Interest

We declare NONE conflict of interest regarding the manuscript entitled "**Real-time multispectral transmission of hard tooth tissues and dental composites with their heating".**

Acknowledgements

This work was supported by the Ministry of Education, Science and Technological Development of the Republic of Serbia through the grant for Institute of Physics, University of Belgrade and for School of Dental Medicine, University of Belgrade (Contract No. 451–03-47/2023–01/200129).

Appendix A. Supporting information

Supplementary data associated with this article can be found in the online version at doi:10.1016/j.dental.2023.08.174.

References

[1] Bucuta S, Ilie N. Light transmittance and micro-mechanical properties of bulk fill vs. conventional resin based composites. Clin Oral Invest 2014;18:1991–2000.
[2] Marovic D, Par M, Crnadak A, Sekelja A, Negovetic Mandic V, Gamulin O, et al. Rapid 3 s curing: what happens in deep layers of new bulk-fill composites? Materials 2021;14:515.
[3] Watts DC, Kaiser C, O'Neill C, Price RB. Reporting of light irradiation conditions in 300 laboratory studies of resin-composites. Dent Mater 2019;35:414–21.
[4] Fujita K, Nishiyama N, Nemoto K, Okada T, Ikemi T. Effect of base monomer's refractive index on curing depth and polymerization conversion of photo-cured resin composites. Dent Mater J 2005;24:403–8.
[5] Gorsche C, Griesser M, Gescheidt G, Moszner N, Liska R. β-allyl sulfones as addition–fragmentation chain transfer reagents: A tool for adjusting thermal and mechanical properties of dimethacrylate networks. Macromolecules 2014;47:7327–36.
[6] Shah PK, Stansbury JW, Bowman CN. Application of an addition–fragmentation-chain transfer monomer in di (meth) acrylate network formation to reduce polymerization shrinkage stress. Polym Chem 2017;8:4339–51.
[7] Emami N, Sjödahl M, Söderholm KJ. How filler properties, filler fraction, sample thickness and light source affect light attenuation in particulate filled resin composites. Dent Mater 2005;21:721–30.
[8] Arikawa H, Kanie T, Fujii K, Takahashi H, Ban S. Effect of filler properties in composite resins on light transmittance characteristics and color. Dent Mater J 2007;26:38–44.
[9] Shortall A, Palin W, Burtscher P. Refractive index mismatch and monomer reactivity influence composite curing depth. J Dent Res 2008;87:84–8.
[10] Kowalska A, Sokolowski J, Bociong K. The photoinitiators used in resin based dental composite—a review and future perspectives. Polymers 2021;13:470.
[11] Miletic V. Dental composite materials for direct restorations: Springer; 2018.
[12] Par M, Repusic I, Skenderovic H, Sever EK, Marovic D, Tarle Z. Real-time Light Transmittance Monitoring for Determining Polymerization Completeness of Conventional and Bulk Fill Dental Composites. Oper Dent 2018;43. E19-e31.
[13] Novta E, Lainović T, Grujić D, Savić-Šević S, Tóth E, Cvejić Ž, et al. Internal photo-activation of a dental composite using optical fibers: a holographic, thermographic and Raman study. Opt Quantum Electron 2022;54:1–18.
[14] Uhl A, Mills RW, Jandt KD. Polymerization and light-induced heat of dental composites cured with LED and halogen technology. Biomaterials 2003;24:1809–20.
[15] Bouillaguet S, Caillot G, Forchelet J, Cattani-Lorente M, Wataha JC, Krejci I. Thermal risks from LED- and high-intensity QTH-curing units during polymerization of dental resins. J Biomed Mater Res B Appl Biomater 2005;72:260–7.
[16] Vaidyanathan l, Vaidyanathan T, Wang Y, Viswanadhan T. Thermoanalytical characterization of visible light cure dental composites. J Oral Rehabil 1992;19:49–64.
[17] Price R, Ferracane J, Shortall A. Light-curing units: a review of what we need to know. J Dent Res 2015;94:1179–86.
[18] Maucoski C, Price RB, Arrais CAG. Temperature changes and hardness of resin-based composites light-cured with laser diode or light-emitting diode curing lights. Odontology 2022:1–14.
[19] Repusic I, Skenderovic H, Milat O, Spajic J, Tarle Z. The effects of extended curing time and radiant energy on microhardness and temperature rise of conventional and bulk-fill resin composites. Clin Oral Invest 2019;23:3777–88.
[20] Price RB, Whalen J, Price TB, Felix CM, Fahey J. The effect of specimen temperature on the polymerization of a resin-composite. Dent Mater 2011;27:983–9.
[21] Trujillo M, Newman SM, Stansbury JW. Use of near-IR to monitor the influence of external heating on dental composite photopolymerization. Dent Mater 2004;20:766–77.
[22] Tauböck TT, Tarle Z, Marovic D, Attin T. Pre-heating of high-viscosity bulk-fill resin composites: effects on shrinkage force and monomer conversion. J Dent 2015;43:1358–64.
[23] Lohbauer U, Zinelis S, Rahiotis C, Petschelt A, Eliades G. The effect of resin composite pre-heating on monomer conversion and polymerization shrinkage. Dent Mater 2009;25:514–9.
[24] Bonardi AH, Bonardi F, Dumur F, Gigmes D, Fouassier JP, Lalevée J. Fillers as Heaters for Photothermal Polymerization upon NIR Light 2019;40:e1900495.
[25] Price RB, Labrie D, Rueggeberg FA, Sullivan B, Kostylev I, Fahey J. Correlation between the beam profile from a curing light and the microhardness of four resins. Dent Mater 2014;30:1345–57.
[26] De Oliveira DCRS, Rocha MG, Correr AB, Ferracane JL, Sinhoreti MAC. Effect of beam profiles from different light emission tip types of multiwave light-emitting diodes on the curing profile of resin-based composites. Oper Dent 2019;44:365–78.
[27] Ko H, Kim D, Park S-H. Homogeneity of dental curing unit beam profile and its effect on microhardness of dental composites with varying thicknesses. Dent Mater 2022;38:e231–43.
[28] Soto-Montero J, Nima G, Dias CT, Price RB, Giannini M. Influence of beam homogenization on bond strength of adhesives to dentin. Dent Mater 2021;37:e47–58.
[29] Maucoski C, Price RB, Rocha MG, Roulet J-F, Sullivan B. Ability of short exposures from laser and quad-wave curing lights to photo-cure bulk-fill resin-based composites. Dent Mater 2023;39:275–92.
[30] Oliveira D, Rocha MG. Dental light-curing—assessing the blue-light hazard. Dent Clin 2022;66:537–50.
[31] Oliveira D, Rocha M, Correr A, Silvino A, Sinhoreti M. From blue to red: New photoinitiator systems for dental materials. Dent Mater 2017;33:e88–9.
[32] Dos Santos G, Alto RM, Sampaio Filho H, Da Silva E, Fellows C. Light transmission on dental resin composites. Dent Mater 2008;24:571–6.
[33] Chuang S-F, Liao C-C, Lin J-C, Chou Y-C, Lee T-L, Lai T-W. Novel Polymerization of Dental Composites Using Near-Infrared-Induced Internal Upconversion Blue Luminescence. Polymers 2021;13:4304.
[34] Uo M, Kudo E, Okada A, Soga K, Jogo Y. Preparation and properties of dental composite resin cured under near infrared irradiation. J Photopolym Sci Technol 2009;22:551–4.
[35] Stepuk A, Mohn D, Grass RN, Zehnder M, Krämer KW, Pellé F, et al. Use of NIR light and upconversion phosphors in light-curable polymers. Dent Mater 2012;28:304–11.
[36] Adams K.R., Savett D.A., Lien W., Raimondi C., Vandewalle K.S. Evaluation of a Novel "Quad" Wavelength Light Curing Unit. 2022.
[37] Zach L. Pulp response to externally applied heat. Oral Surg Oral Med Oral Pathol 1965;19:515–30.
[38] Baldissara P, Catapano S, Scotti R. Clinical and histological evaluation of thermal injury thresholds in human teeth: a preliminary study. J Oral Rehabil 1997;24:791–801.
[39] Mouhat M, Stangvaltaite-Mouhat L, Mercer J, Nilsen BW, Örtengren U. Light-curing units used in dentistry: Effect of their characteristics on temperature development in teeth. Dent Mater J 2021. 2020-305.
[40] Zarpellon D, Runnacles P, Maucoski C, Coelho U, Rueggeberg F, Arrais C. Controlling in vivo, human pulp temperature rise caused by LED curing light exposure. Oper Dent 2019;44:235–41.
[41] Maucoski C., Price R.B., Sullivan B., Guarneri J.A.G., Gusso B., Arrais C.A.G.In-vitro pulpal temperature increases when photo-curing bulk-fill resin-based

composites using laser or light-emitting diode light curing units. Journal of esthetic and restorative dentistry: official publication of the American Academy of Esthetic Dentistry[et al.].

[42] Daronch M, Rueggeberg FA, De Goes MF, Giudici R. Polymerization kinetics of pre-heated composite. J Dent Res 2006;85:38–43.

[43] Lovelh L, Newman S, Bowman C. The effects of light intensity, temperature, and comonomer composition on the polymerization behavior of dimethacrylate dental resins. J Dent Res 1999;78:1469–76.

Book of abstracts

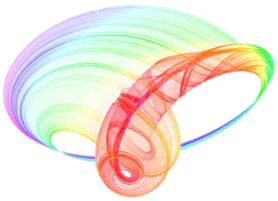

PHOTONICA2021

VIII International School and Conference on Photonics

& HEMMAGINERO workshop

23 - 27 August 2021,

Belgrade, Serbia

Editors

Mihailo Rabasović, Marina Lekić and Aleksandar Krmpot

Institute of Physics Belgrade, Serbia

Belgrade, 2021

Interplay between ordered multilayer structure and randomly distributed nanospheres and nanopillars in dichromated pullulan increases the width of the photonic bandgap

S. Savic-Sevic[1], D. Pantelic[1] and B. Jelenkovic[1]
[1]*Institute of Physics, Belgrade, Serbia*
e-mail:savic@ipb.ac.rs

Complex nanostructures with interesting properties for photonic applications received great attention. Initially, highly ordered photonic crystal structures have been manufactured and investigated [1]. Interesting physical phenomena were discovered, such as: complete band gaps, nonlinearities, slow light, negative refraction. Later, attention was drawn to disordered materials [2], random lasing and rediscovering effects like coherent backscattering, Anderson localization [3].

Usually, ordered and disordered photonic structures have been generated and analyzed separately. However, in nature, biological photonic structures are complex and inherently disordered. Here, we present structures having both ordered and disordered components, integrated into novel photonic structure. Ordered Bragg layers are mutually separated and supported by nanopillars, while internal voids are filled with randomly distributed nanospheres. This complex morphology is formed simultaneously by the holographic method and the nonsolvent induced phase separation. Depending on the film thickness, there can be as many as 50 Bragg layers. We show that the interplay between the Bragg regularity and random scattering increases the width of the photonic band-gap significantly, up to a 35% wide band gap, ($\Delta\lambda max/\lambda max = 35$ %).

Photonic structures are holographically recorded in pullulan , a linear homopolysaccharide produced by micro-organisms (Aureobasidium pullulans), doped with ammonium dichromate. Here we use the dichromated pullulan for volume (Bragg) grating generation using a simple counter- propagating beam configuration.

Our photonic material has both properties of ordered photonic crystals: band gap and high reflectivity; and disordered structures: weak localization [4].

REFERENCES

[1] J. D. Joannopoulos, S. G. Johnson, J. N. Winn, R. D. Meade, Photonic Crystals: Molding the Flow of Light, 2nd ed., Princeton University Press, Princeton, NJ (2008).
[2] D. Wiersma, Nat. Photon. 7, 188 (2013).
[3] D. Wiersma, P. Bartolini, A. Lagendijk, R. Righini, Nature 390, 671 (1997).
[4] S. Savic-Sevic, D. Pantelic, D. Grujic, B. Jelenkovic, Opt Quant Electron 48:289 (2016).

Natural waveguides on *Hoplia argentea* elytra

D. Pavlović[1], B. Salatić[1], S. Savić-Šević[1], N. Vesović[2] and D. Pantelić[1]
[1] *Institute of Physics, University of Belgrade, Pregrevica 118, 11080 Belgrade, Serbia*
[2] *University of Belgrade - Faculty of Biology, Studentski Trg 16, 11000 Belgrade, Serbia*
e-mail:danica.pavlovic@ipb.ac.rs

Light waveguides are structures with a role in receiving and channeling light and filtering certain wavelengths of the electromagnetic spectrum [1]. That's how it comes to light capturing and local reinforcement of its intensity, which can be further utilized for various purposes (e.g conducting light to pigments in the eye, forming structural coloration, etc.) [2]. Based on their geometric structure waveguides can be planar or linear (banded or fibrous) [3].

Microstructures with a waveguide role have been studied a lot in the living world [4]. Structures with a function of optical waveguides have also been discovered in insects. They can be found on antennae, in complex eyes, on wing scales and other parts of the body [5], and can work as integral part of light or IR receptors, thermoregulatory systems, or can play an important role in the formation of structural coloration [6].

Here we present cuticular structures on beetle elytra (Insecta: Coleoptera) that produce structural coloration thanks to morphology and function of light waveguides. *Hoplia argentea* from family Rutelidae was used as a model organism. We found out that individuals of this species posses linear type of waveguides on its front hardened wings, which are responsible for the production of structurally green coloration.

REFERENCES

[1] M. J. Adams, *An introduction to optical waveguides,* 14 (Wiley, New York, 1981).
[2] A. W. Snyder, R. Menzel, *Photoreceptor optics* (Springer Science & Business Media, 2012).
[3] G. T. Reed, A. P. Knights, *Silicon photonics: an introduction* (John Wiley & Sons, New Jersey, 2004).
[4] M. Bass, E. W. Van Stryland, D. R. Williams, *Handbook of optics* (McGrawHill, New York, 1995).
[5] P. S. Callahan, Appl. Opt. **7** (8), 1425-1430 (1968).
[6] N. N. Shi, C. C. Tsai, F. Camino, G. D. Bernard, N. Yu, R. Wehner, Science 349 (6245), 298-301a (2015).

Influence of light guide type on dental composite polymerization shrinkage – a holographic and thermographic study

E. Novta[1], T. Lainović[1], S. Savić-Šević[2], D. Grujić[2], D. Pantelić[2] and L. Blažić[1,3]
[1]*University of Novi Sad, Faculty of Medicine, School of Dental medicine, Novi Sad, Serbia*
[2]*University of Belgrade, Institute of Physics, Belgrade, Serbia*
[3]*Dental Clinic of Vojvodina, Novi Sad, Serbia*
e-mail: evgenije.novta@mf.uns.ac.rs

Polymerization shrinkage stress (PSS) is generated at the tooth-restoration interface, during setting of a dental resin-based composite (RBC) inside a tooth cavity. As a result, various negative clinical outcomes may arise. In addition, the polymerization reaction is followed by heat release due to its exothermic nature. The aim of this study was to investigate the influence of two different light guides on PSS, by detecting tooth model deformation using digital holographic interferometry (DHI). Simultaneously, temperature rise measurements were conducted using infrared thermography (IRT).

Standardized tooth models made of dental gypsum, with a mesial-occlusal-distal (MOD) cavity, were used for the purposes of this study. The specimens were mounted in aluminum blocks and fixed in the custom-made holographic set-up with a Nd:YVO_4 laser at 532nm wavelength and power of 400mW. The cavities were filled with a bulk-fill RBC. Two groups of specimens (n=10) were used. In the first group (G1), a light guide (ϕ 8mm) of a commercial LED light source was used in continuous 40s curing mode. In the second group (G2), three optical fibers (ϕ 1mm), connected to the same light source, were inserted into the dental filling to cure the RBC from within [1] (the first phase–3x40s). After removal of the optical fibers from the RBC, the remaining voids were filled and the specimens were additionally cured (the second phase–40s). Tooth model deformation due to PSS was detected in real-time using DHI, while simultaneously monitoring temperature rise of the RBC using IRT. Statistical analysis was performed using student's t-test for independent samples.

In group G2, the DHI images during the first phase of light curing using optical fibers, demonstrated initiation of the polymerization reaction and tooth model deformation. The final deformation value (after the first and second phase) in group G2 (M=14.3μm) was significantly lower (on average 5.2μm, $p<0.05$) compared to final deformation value in group G1 (M=9.1μm) (Figure 1.). The resulting IRT images, presented a gradual temperature increase in group G2, postponing the estimated gel-point of the polymerization reaction, which could be related to PSS relaxation (Figure 2.).

Within the limitations of this study, it was concluded that polymerization reaction initiation using optical fibers influenced lower polymerization shrinkage and gradual temperature increase during polymerization. Accordingly, optical fibers could contribute to overcoming the dental PSS problem.

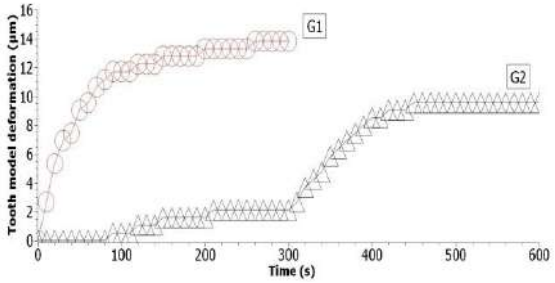

Figure 1. Ellipse-G1 group, standard curing mode; triangle-G2 group, two-phase curing with optical fibers and standard light guide

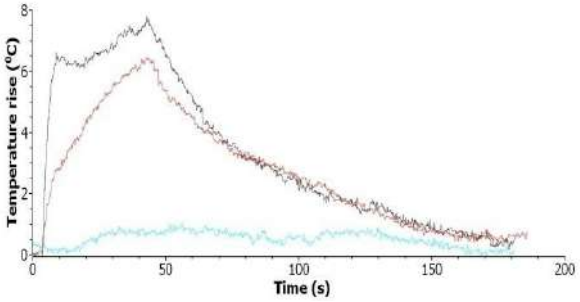

Figure 2. Black-G1 group, standard curing mode; green-G2 group, first phase curing with optical fibers; red-G2 group, second phase-standard curing mode

REFERENCES [1] F.A. Rueggeberg. Dent. Mater. 2011;27(1):39–52.
Supported by the contract NIO200114 and Mikodental, Šabac (distributers of Shofu®, Japan in Serbia)

Effects of laser heating on luminescent properties of Gd_2O_3:Er,Yb nanophosphor

D. Sevic[1], M.S. Rabasovic[1], J. Krizan[2], S. Savic-Sevic[1], M.D. Rabasovic[1], B.P. Marinkovic[1] and M.G. Nikolic[1]
[1]*Institute of Physics, Belgrade, Serbia*
[2]*AMI d.o.o., Ptuj, Slovenia*
e-mail:sevic@ipb.ac.rs

In this study we analyze effects of laser heating on luminescent properties of nanocrystalline Gd_2O_3 doped with Er^{3+} and Yb^{3+} cations. Material was synthesized by combustion method, as described in [1]. Our experimental setup is presented in detail in [2,3,4]. In this study we have used pulsed laser diode excitation at 980 nm. Variable laser pulse energy was obtained by varying the laser pulse duration. Used laser diode has both continual and pulse mode. In continual mode its power is 1 W; in pulse mode it is possible to tune pulse duration and repetition, thus obtaining different average excitation powers. Here, we have used repetition rate of 200 Hz, with varying pulse duration between 20 μs and 200 μs, so average excitation power is between 8 mW and 80 mW.

Generally, laser power heating effects are unwanted and should be avoided in luminescence thermometry experiments; external heater and thermometer are used to calibrate the temperature sensing curve. Interestingly enough, the thermometry system, based on laser heating of sample, applicable for biomedical purposes, is described in [5].

Luminescence spectra of Gd_2O_3:Er^{3+},Yb^{3+} excited at room temperature with different laser excitation powers are shown in Figure 1. It should be noted that excitation power is intentionally much higher than used in [3]. Based on temperature sensing calibration curve presented in [3] for the same sample it could be estimated that the material is locally heated to about 375 K for pulse time of 200 μs.

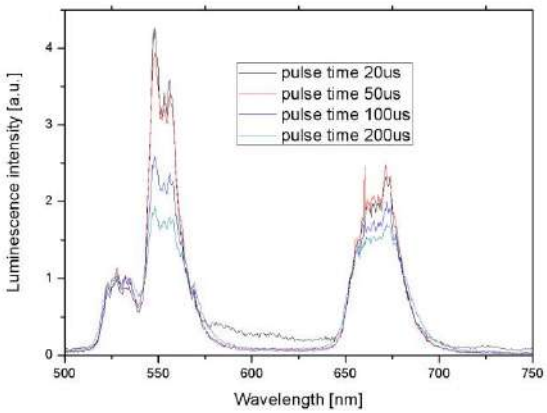

Figure 1. Luminescence spectra of Gd_2O_3:Er^{3+},Yb^{3+} excited at room temperature with different laser powers.

REFERENCES

[1] J. Krizan, M. Mazaj, V. Kaucic, I. Bajsic, J. Mozina, Acta Chim. Slov. 61, 608 (2014).
[2] A. Vlasic, D. Sevic, M.S. Rabasovic, J. Krizan, S. Savic-Sevic, M.D. Rabasovic, M. Mitric, B.P. Marinkovic, M.G. Nikolic, Journal of Luminescence, 199, 285 (2018).
[3] D. Sevic, M.S. Rabasovic, J. Krizan, S. Savic-Sevic, M.D. Rabasovic, B.P. Marinkovic, M.G. Nikolic, Optical and Quantum Electronics 52, 232 (2020).
[4] D. Sevic, M.S. Rabasovic, J. Krizan, S. Savic-Sevic, M.G. Nikolic, B.P. Marinkovic, M.D. Rabasovic, J. Phys. D: Appl. Phys. 53**,** 015106 (2020).
[5] M.F. Ferreira, K.Z.R. de Sousa, W.L. Massarotto, E.G. Ricci, E.H. de Faria, K.J. Ciuffi, D. Sevic, L.A. Rocha, E.J. Nassar, J. Braz. Chem. Soc., 32(2) 376 (2021).

Using SOLO software package for classification of temperature dependent luminescence spectra

D. Sevic[1], M.S. Rabasovic[1], J. Krizan[2], S. Savic-Sevic[1], M.D. Rabasovic[1], M.G. Nikolic[1] and B.P. Marinkovic[1]
[1]*Institute of Physics, Belgrade, Serbia*
[2]*AMI d.o.o., Ptuj, Slovenia*
e-mail:sevic@ipb.ac.rs

In this study we use SOLO software package (Version 8.8, Eigenvector Research Inc, USA) for classification of temperature dependent luminescence spectra of nanocrystalline Gd_2O_3 doped with Er and Yb. Material was synthesized by combustion method, as described in [1]. Our experimental setup is presented in detail in [2,3]. In [4,5] we have used Principal Component Analysis of luminescence spectra of thermophosphors; here, we use classification tools based on more sophisticated K-Nearest Neighbor and K-Means Nearest Group algorithms.

Classification results (shown as dendrograms) of luminescence spectra of Gd_2O_3:Er^{3+},Yb^{3+} at different temperatures using K-Nearest Neighbor and K-Means Nearest Group algorithms are shown in Figure 1. Although dendrograms are different, the groups determined by both methods are the same; moreover, the test luminescence spectra are also classified in temperature groups where they belong. So, the machine could be trained to differentiate spectral data obtained on different temperatures.

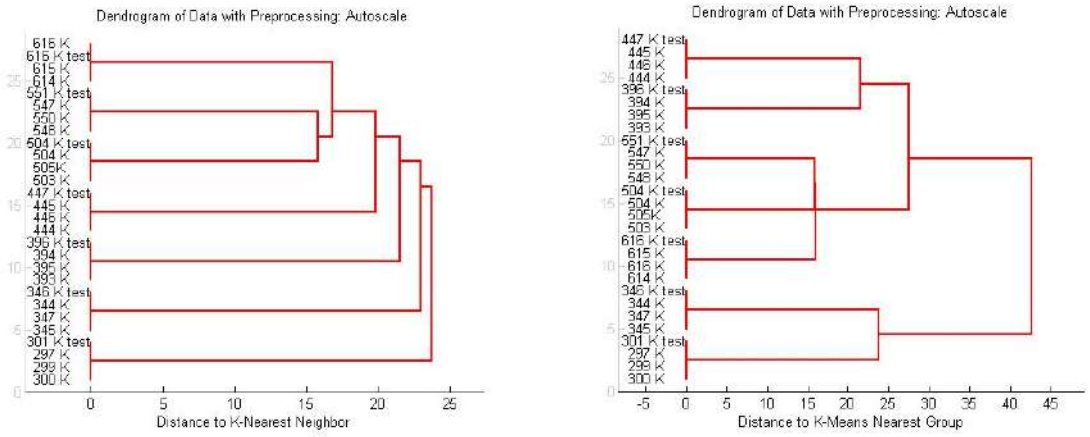

(a) (b)

Figure 1. Classification results (shown as dendrograms) of luminescence spectra of Gd_2O_3:Er^{3+},Yb^{3+} at different temperatures using (a) K-Nearest Neighbor and (b) K-Means Nearest Group algorithms.

REFERENCES

[1] J. Krizan, M. Mazaj, V. Kaucic, I. Bajsic, J. Mozina, Acta Chim. Slov. 61, 608 (2014).
[2] D. Sevic, M.S. Rabasovic, J. Krizan, S. Savic-Sevic, M.D. Rabasovic, B.P. Marinkovic, M.G. Nikolic, Optical and Quantum Electronics 52, 232 (2020).
[3] D. Sevic, M.S. Rabasovic, J. Krizan, S. Savic-Sevic, M.G. Nikolic, B.P. Marinkovic, M.D. Rabasovic, J. Phys. D: Appl. Phys. 53**,** 015106 (2020).
[4] D. Sevic, A. Vlasic, M.S. Rabasović, S. Savic-Sevic, M.D. Rabasović, M.G. Nikolić, B. D. Muric, B. P. Marinković, J. Križan, Tehnika 75(3), 279 (2020).
[5] D. Sevic, J. Krizan, M. S. Rabasovic, B.P. Marinkovic, Eur. Phys. J. D 75, 56 (2021).

Book of abstracts

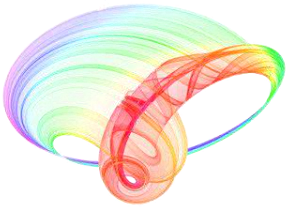

PHOTONICA2017

The Sixth International School and Conference on Photonics

& COST actions: MP1406 and MP1402

&H2020-MSCA-RISE-2015 CARDIALLY workshop

28 August – 1 September 2017

Belgrade, Serbia

Editors

Marina Lekić and Aleksandar Krmpot

Institute of Physics Belgrade, Serbia

Belgrade, 2017

Bifurcation in reflection spectra of holographic pullulan diffraction grating

S. Savić-Šević, D. Pantelić, V. Damljanović and B. Jelenković

Institute of Physics, University of Belgrade, Pregrevica 118, 11080 Zemun, Belgrade, Serbia
e-mail:savic@ipb.ac.rs

Reflection volume hologram gratings, fabricated using a single-beam method, usually have only one Bragg peak in the spectrum. Z. Wang et al. [1]noted the appearance of multiple peaks in the spectrum of volume diffraction grating recorded in dichromated gelatin, phenomenon that looks like bifurcation within the Bragg plateau. We also observed bifurcation phenomenain the spectrum of diffraction gratings recorded in dichromated pullulan (DCP), which is a polysaccharide doped with chromium. Compared to dichromated gelatin, the DCP material is simpler to prepare and process, it is insensitive to humidity, thusretaining high resolution and diffraction efficiency [2]. The typical number of appeared peaks in the spectrum is two, three, or four. It was found that a multi-peak phenomenon isaccompanied by wider band gap.

In order to understand multi-peak structure of band gaps, experimental results were compared with theoretically predicted results. The theoretical model investigates effects of several important parameters: absorption of radiation within the photosensitive layer, non-uniform thickness of the layer, refractive index modulation and non-uniform spatial period of the grating. Numerical reflection spectra of volume Bragg gratings have been calculated by the method of characteristic matrix [3]. Our model suggests that multi peak structures are produced by uneven modulation of Bragg layersinside the volume hologram. The results of calculation are in agreement with experimental results.

REFERENCES

[1] Z. Wang, D. Liu, J. Zhou, Opt. Lett.31, 3270 (2006).
[2] S. Savić-Šević, D. Pantelić, Applied optics 46, 287 (2007).
[3] M. Born, E. Wolf, *Priciples of Optics*, Pergamon (1980).

Luminescence thermometry using $Gd_2Zr_2O_7:Eu^{3+}$

M.G. Nikolic[1], M.S. Rabasovic[1], J. Krizan[2], S. Savic-Sevic[1], M.D. Rabasovic[1], B.P. Marinkovic[1], A. Vlasic[1] and D. Sevic[1]
[1] *Institute of Physics,Belgrade, Serbia*
[2] *AMI d.o.o., Ptuj, Slovenia*
e-mail:sevic@ipb.ac.rs

Thermographic phosphors are materials that are synthesized in such a way that their structural stability regarding various parameters including the temperature, pressure, magnetic field, electromagnetic radiation could be obtained. They typically consist of a ceramic host and rare-earth dopant. These materials are widely used in many applications [1-9]. The temperature dependency of their luminescence is used for temperature sensing.

In this study we investigate temperature dependence of luminescence spectra of nanopowder samples of $Gd_2Zr_2O_7:Eu^{3+}$. Europium doped $Gd_2Zr_2O_7$ nanopowders were prepared by Solution Combustion Synthesis (SCS) method [10]. The structural characteristics of obtained material were confirmed by SEM images and XRD analysis [10]. The identification and time resolved analysis of fast decayed (from $^5D_1$ state) and slow decayed (from $^5D_0$ state) europium lines in this host were performed using TR-LIF (Time resolved Laser induced Fluorescence) spectroscopy experimental setup. The setup consist of tunable OPO (Optical Parametric Oscillator) laser and streak camera, explained in more detail in [11].

The photoluminescence spectra used for analysis of $Gd_2Zr_2O_7:Eu^{3+}$ nano phosphor optical emission temperature dependence were acquired using continuous laser diode excitation at 405 nm and Ocean Optics spectrometer USB2000. We plotted the temperature sensing calibration curves based on various combinations of ratio of intensities of two europium optical emission lines. It seems that any combination of one slow decayed and one fast decayed line could be an optimal choice for temperature measurements. Finally, we concluded that the intensity ratio of spectral lines at 613 nm and 539 nm seems to be a good choice for temperature measurements. Our results show that the synthesized material can be efficiently used as thermographic phosphor up to 700 K.

REFERENCES

[1] M. Aldén, A. Omrane, M. Richter, G. Särner, 37**,** 422 (2011).
[2] S. W. Allison., G. T. Gillies, Rev. Sci. Instrum, 68, 2615 (1997).
[3] L.P. Goss, A.A. Smith, M.E. Post, Rev Sci. Instrum, 60, 370 (1989).
[4] J.P. Feist, A.L. Heyes, K.L. Choy, B. Su, Proceedings of IEEE; 6.1 (1999).
[5] A.L. Heyes, Journal of Luminescence, 129, 2004 (2009).
[6]M.M. Gentleman, D.R. Clarke, Surface & Coatings Technology, 93, 188 (2004).
[7] A. H. Khalid, K. Kontis, Sensors, 8, 5673 (2008).
[8] M R. Cates, S. W. Allison, S. L. Jaiswal, D. L. Beshears, Oak Ridge National Laboratory, Report ORNL/TM-2002/71
[9] J.I. Eldridge, T.P. Jenkins, S.W. Allison, D. E. Wolfe, E. H. Jordan, Development of YAG:Dy Thermographic Phosphor Coatings for Turbine Engine Applications, 58h International Instrumentation Symposium San Diego, CA, June 5-8, (2012).
[10] M.S. Rabasovic, D. Sevic, J. Krizan, M. Terzic, J. Mozina, B.P. Marinkovic, S. Savic-Sevic, M. Mitric, M.D. Rabasovic, N. Romcevic, Journal of Alloys and Compounds, 622, 292 (2015).
[11] M.S. Rabasovic, D. Sevic, M. Terzic, and B.P. Marinkovic, Nucl. Inst. Meth. B.279, 16(2012).

Film-coupled silver nanoparticles on flat and periodically corrugated aluminium substrates

G. Isić[1], U. Ralević[1], S. Aškrabić[1a], S. Graovac[1], S. Savić-Šević[2], A. Mikhailov[3], A. Antanovich[3], A. Prudnikau[3], M. Artemyev[3], I. Fabijanić[4], V. Janicki[4], B. Okorn[4], J. Sancho-Parramon[4] and R. Gajić[1]
[1]*Graphene Laboratory of*[1a]*Center for Solid State Physics and New Materials, Institute of Physics Belgrade, University of Belgrade, Belgrade, Serbia*
[2]*Photonics Center, Institute of Physics Belgrade, University of Belgrade, Belgrade, Serbia*
[3]*Research Institute for Physical Chemical Problems, Belarusian State University, Minsk, Belarus*
[4]*Ruđer Bošković Institute, Zagreb, Croatia*
e-mail: isicg@ipb.ac.rs

The strong scattering of light by noble metal nanoparticles has, since ancient times, been utilized in various ways, from Roman stained glass to modern day hCG pregnancy tests. At optical frequencies, both the "lightning rod effect" associated with nanometer geometric features and the excitation of collective charge oscillations known as localized surface plasmons (LSPs) contribute to the formation of strong and highly localized electric field "hotspots" at the nanoparticle surface. Understanding the "hotspot" formation mechanism and its attributes such as resonant wavelength, excitation efficiency or spatial confinement, as well as mastering the technology to efficiently produce LSP systems with desired properties, has been at the focus of plasmonics and nanooptics in the past decade and motivated by the perspective of producing a new generation of ultrasensitive spectroscopic sensors [1] or controlling the photon generation by quantum emitters [2]. A significant recent development has been realized by the use of the layer-by-layer polyelectrolite deposition technique [2,3], providing cheap means to produce dielectric layers the thickness of which can be controlled with subnanometer precision.

Here we report on a comprehensive study of optical properties of silver nanospheres or nanocubes separated from a flat or periodically corrugated aluminium substrate by a few nanometer thick layer of oxide and several polyelectrolite layers. Combining theoretical methods based on the mixed representation of the Dyadic Green function for the electric field, numerical simulations employing the finite element method, various colloidal synthesis protocols for silver nanoparticle generation, holographic generation of periodically corrugated surfaces, electron beam deposition of aluminium films, layer-by-layer polyelectrolite deposition, spectrophotometry, spectroscopic ellipsometry, Raman spectroscopy and atomic force microscopy, we investigate the properties of surface plasmon polaritons of the aluminum surface [4] and their role in the formation of LSPs highly localized in tiny gaps between the nanoparticle and aluminium substrate.

REFERENCES

[1] L. Rodriguez-Lorenzo, R. A. Alvarez-Puebla, I. Pastoriza-Santos, S. Mazzucco, O. Stephan, M. Kociak, L. M. Liz-Marzan, F. J. Garcia de Abajo, J. Am. Chem. Soc. 131, 4616 (2009).
[2] O. Kulakovich, N. Strekal, A. Yaroshevich, S. Maskevich, S. Gaponenko, I. Nabiev, U. Woggon, M. Artemyev, Nano Lett. 2, 1449 (2002).
[3] J. J. Mock, R. T. Hill, A. Degiron, S. Zauscher, A. Chilkoti, D. R. Smith, Nano Lett. 8, 2245 (2008).
[4] D. Gerard, S. K. Gray, J. Phys. D: Appl. Phys. 48, 184001 (2015).

UNIVERZITET U BEOGRADU
Institut za fiziku

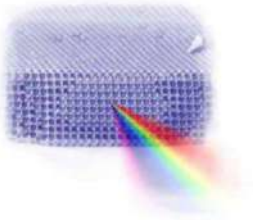

Konferencija

Jedanaesta radionica fotonike (2018)

Zbornik apstrakata

PHOTONICS CENTER

Kopaonik, 11–14.3.2018.

Effects of temperature on luminescent properties of $YVO_4:Eu^{3+}$ nanophosphor

D. Šević[1], M.S. Rabasović[1], J. Križan[2], S. Savić-Šević[1], M. G. Nikolic[1], B. P. Marinkovic[1], and M.D. Rabasović[1]

(1) *Institute of Physics, University of Belgrade, Belgrade, Serbia*

(2) *AMI d.o.o., Ptuj, Slovenia*

Contact: Dragutin Sevic (sevic@ipb.ac.rs)

Abstract. In this study we investigate time resolved luminescence spectra of nano powder samples of $YVO_4:Eu^{3+}$. Intensity ratios of spectral lines were used for determining the calibration curves for remote temperature sensing. Possibilities of using the luminescence lifetime and risetime for temperature sensing are also investigated. Our experimental setup and some results regarding this phosphor are presented in detail in [1,2]. We used OPO (Optical Parametric Oscillator) for excitation. The output of the OPO can be continuously tuned from 320 nm to 475 nm. For measurements presented here the output energy of OPO was about 5 mJ. The structure of material was observed by high resolution scanning electron microscope (SEM). The experimental setup for luminescence measurement as a function of temperature is described in [3]. Effects of temperature on luminescent properties of $YVO_4:Eu^{3+}$ nanophosphor, for two temperatures, are shown in Fig. 1.

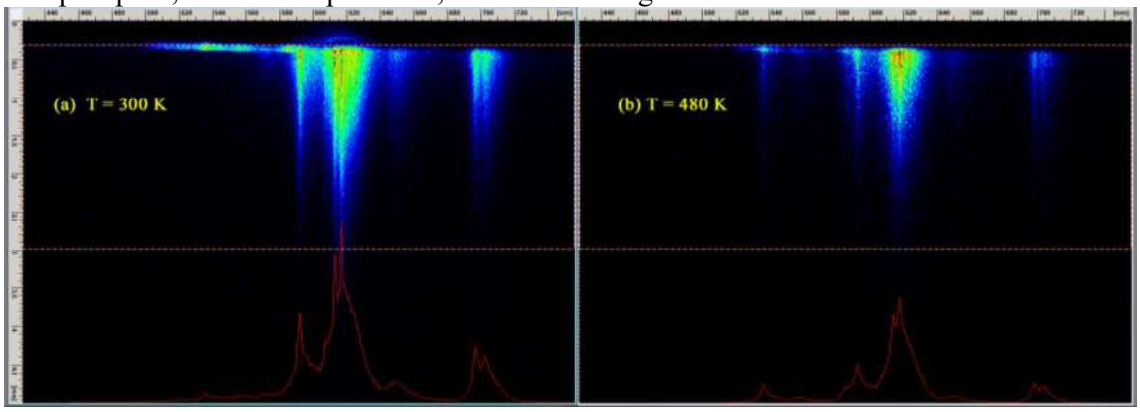

Figure 1. Streak images of Eu doped YVO_4 nanopowder, at (a) T = 300 K , (b) T = 480 K. Laser excitation is at 330 nm.

The luminescence lifetime and risetime of this phosphor were determined by streak camera (HPD-TA) software. We obtained that the lifetime of the level $^5D_1$ is about 8.7 μs and the level $^5D_0$ lifetime is about 0.93 ms [1]. We calculated the rise time according to Ranson equation [4]. We obtained that the rise time of luminescence of our sample of $YVO_4:Eu^{3+}$ for the $^5D_0 - {}^7F_2$ line is about 8.1 μs. Our results show that Eu doped YVO_4 nanopowder could be used for remote temperature sensing.

REFERENCES

[1] D. Sevic, M.S. Rabasovic, et al, *Materials Research Bulletin* **88** (2017) 121–126.
[2]M. S. Rabasovic J. Krizan, et al, *Opt. Quant. Electron.* **48** (2016) 163.
[3]M. D. Rabasovic, B. D. Muric, M. G. Nikolic, et al, *J. Phys. D: Appl. Phys.* **49** (2016) 485104-1-6.
[4]R. M. Ranson, E. Evangelou, and C. B. Thomas, *Applied Physics Letters* **72** (1998) 2663-2664.

Formation of LIPSS on Al/Ti thin metal films by scanning of low-fluence femtosecond beam during cross-directional scanning

Aleksander Kovačević[1], Suzana Petrović[2], Marina Lekić[1], Davor Peruško[1], Vladimir Lazović[1], Svetlana Savić-Šević[1], Borislav Vasić[1], Branislav Salatić[1], Radoš Gajić[1], Dejan Pantelić[1], Branislav Jelenković[1]

(1) *Institute of Physics, Pregrevica 118, 11080 Belgrade, Serbia*

(2) *Institute of Nuclear Sceinces „Vinča“, PO Box 522, 11000 Belgrade, Serbia*

Contact: M. Lekić (aleksander.kovacevic@ipb.ac.rs)

Abstract. Formation of periodic nanostructures on thin metal films by femtosecond laser beam (laser induced periodic nanostructures – LIPSS) influences the tribological properties of the surfaces. Having excellent mechanical properties, multilayer thin films, like 5x(Al/Ti)@Si, are interesting direction of investigation, because their multilayer structure enables forming of high quality LIPSS [1]. Two types of LIPSS are described, high spatial frequency LIPSS (HSFL) and low spatial frequency LIPSS (LSFL), which differ in their spatial frequency. During exposition of thin film metal systems with femtosecond beams, we changed scanning configuration [2]. We have exposed 5x(Al/Ti)@Si multilayer system with femtosecond beam from the laser system Coherent Mira 900 in NIR. Same areas have been exposed with two different scanning directions. The direction of the second scanning over the same area was orthogonal tothe first one. The polarization direction during second scanning was orthogonal to the polarization direction during first scanning. In this way, several crossed LIPSS can be seen.

Acknowledgements. The work has been supported by the Ministry of Science, Republic of Serbia, under No. III45016, OI171038 and OI171005.

REFERENCES

[1]A. G. Kovačević, S. Petrović, et al., *Appl.Surf. Sci.* **326** (2015), 91–98.
[2]A. G. Kovačević, S. Petrović, et al., *Appl.Surf. Sci.* **417** (2017), 155–159.

Formation of LIPSS on Al/Ti thin metal films by scanning of low-fluence femtosecond beam during multi-pass scanning

Marina Lekić[1], Aleksander Kovačević[1], Suzana Petrović[2], Davor Peruško[1], Vladimir Lazović[1], Svetlana Savić-Šević[1], Borislav Vasić[1], Branislav Salatić[1], Radoš Gajić[1], Dejan Pantelić[1], Branislav Jelenković[1]

(1) *Institute of Physics, Pregrevica 118, 11080 Belgrade, Serbia*

(2) *Institute of Nuclear Sceinces „Vinča“, PO Box 522, 11000 Belgrade, Serbia*

Contact: M. Lekić (lekic@ipb.ac.rs)

Abstract. During interaction of femtosecond laser beam with metal surfaces, periodic nanostructurrees can be formed – laser induced periodic nanostructures, LIPSS. Two types of LIPSS have been recorded, of low and high spatial frequency (LSFL and HSFL, respectively). Thin metal films in multilayer systems, like 5x(Al/Ti)@Si are convenient for forming high quality LIPSS due to their multilayer structure [1] and are interesting because of their excellent mechanical properties. We have exposed the multilayer thin film metal systems 5x(Al/Ti)@Si with femtosecond beams with various scanning configurations [2]. The laser system was Coherent Mira 900 in NIR. The same areas have been exposed to several scans of the beam (multi-pass scanning). In this way, it is possible to see that the LIPSS maintain their structure during consecutive scans.

Acknowledgements. The work has been supported by the Ministry of Science, Republic of Serbia, under No. III45016, OI171038 and OI171005.

REFERENCES

[1]A. G. Kovačević, S. Petrović, et al., *Appl.Surf. Sci.* **326** (2015), 91–98.
[2]A. G. Kovačević, S. Petrović, et al., *Appl.Surf. Sci.* **417** (2017), 155–159.

Institute of Physics Belgrade
University of Belgrade
Kopaonik, March 08-12, 2020

Book of Abstracts

13th Photonics Workshop

(Conference)

Machine learning for laser induced fluorescence spectroscopy

D. Šević[1], M.S. Rabasović[1], J. Križan[2], S. Savić-Šević[1], M.D. Rabasović[1], M. G. Nikolic[1] and B. P. Marinkovic[1]

(1) *Institute of Physics, University of Belgrade, Belgrade, Serbia*

(2) *AMI d.o.o., Ptuj, Slovenia*

Contact: Dragutin Sevic (sevic@ipb.ac.rs)

Abstract. Artificial Inteligence (AI) became the writing on the wall in regard the science and, evenmore, generally in human society. Machine learning (ML) algorithms build a mathematical model of analyzed data enabling the computer to make predictions or decisions. ML is considered as a subset of AI. Recently, we have started to follow this trend in scientific research by introducing application of ML for analysis of data obtained by laser induced fluorescence measurements. ML algorithms require large training sets; so we have decided to use, for our starting tests and exercises in ML, data obtained by our previous measurements of nanophosphor luminescence presented in [1-4]. Based on experiences of other authors [5] and references therein, where the beer luminescence was analyzed, we have selected to use ML implemented by the Solo software package (Version 8.8, Eigenvector Research Inc, USA).

Figure 1. shows principal component analysis of measurements of temperature dependence of Gd_2O_3:Er,Yb nano phosphor luminescence excited at 980 nm. It could be seen that measurement number 8 (luminescence at 660 K) strongly differs from measurements on other temperatures, so it should be discarded. The same conclusion was obtained from the classical analysis of the same data set, based on fitting error. However, in the case of very complex biomedical data, the classification is usually far from so simple; so the use of ML becomes crucial.

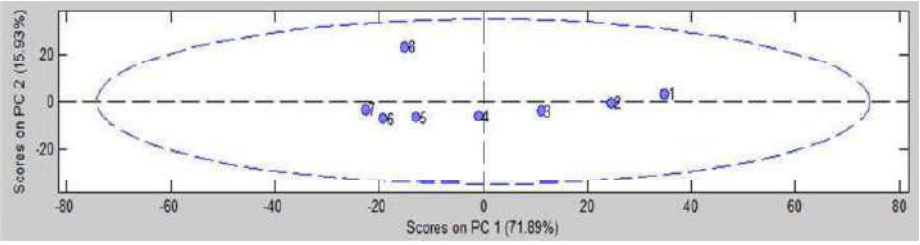

Figure 1. Scores on first two principal components of measurement data of temperature dependence of luminescence of Er and Yb doped Gd_2O_3 nanopowder.

REFERENCES

[1] D. Sevic, M.S. Rabasovic, et al, *Materials Research Bulletin* **88** (2017) 121–126.
[2] A. Vlasić, D. Šević, M.S. Rabasovic, et al, *Journal of Luminescence*, **199** (2018), 285-292.
[3] D. Sevic, M. S. Rabasovic, et al, *J. Phys. D: Appl. Phys.* **53** (2020) 015106-1-10.
[4] D. Sevic, M. S. Rabasovic, et al, submitted to *Opt. Quant. Electron.*
[5] T. Dramicanin, I. Zekovic et al, *J. Fluoresc.* **29** (2019), 1103-1111.

Negative thermal expansion in nanolayered pullulan

Svetlana Savic-Sević, Dejan Pantelić, Branka Murić, Darko Vasiljević, Branko Kolarić, Branislav Jelenković

Institute of Physics, University of Belgrade, Pregrevica 118, 11080 Zemun, Serbia.

Contact: S. Savic-Sevic (savic@ipb.ac.rs)

Abstract. The change of temperature leads to thermal expansion. Most materials expand, but, some materials contract upon heating. A small number of natural materials show negative thermal expansion effects. Such negative thermal expansion (NTE) materials have great applications because they can control the thermal expansion of materials. The linear coefficient of thermal expansion, α_L, can be expressed as: $\alpha_L = (1/L_0)\ (dL/dT)$, where L_0 is the initial length at temperature T_0, dL is length change and dT is the change in temperature [1].

Photonic structure is recorded in pullulan doped with ammonium dichromate (DCP). We fabricate a one-dimensional photonic structure, pullulan layers are mutually separated and supported by nanopillars. This complex morphology is formed simultaneously by the holographic method and the nonsolvent induced phase separation [2]. Under white light illumination the grating acts as a reflector of the light for a specific band of wavelengths.

We have observed that heating leads to a reduction in the thickness of the structure, resulting in the reflectance peak shift towards shorter wavelengths. We calculated the change of thickness, corresponding to experimentally-recorded spectral shift. We have obtained the value of the negative thermal expansion coefficient, $\alpha_L = -3.8 \times 10^{-3}\ K^{-1}$.

The reflection spectra show blue shift with increasing of temperature, which originates from the contraction thickness of the air nanolayers due to the permeability of the air molecules through the pullulan nanolayers. This results in a large negative thermal expansion coefficient.

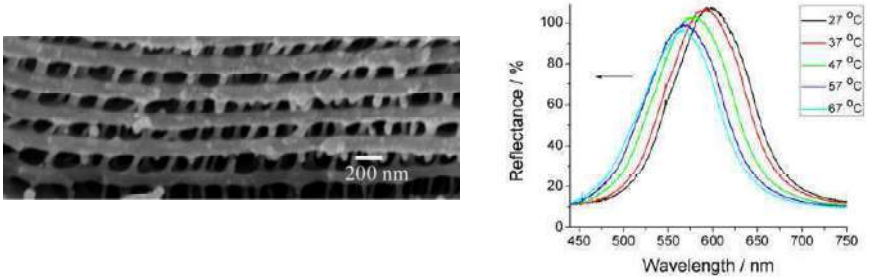

Figure 1. SEM image of a cross - section of nanolayered structure and experimentally recorded reflection spectra during heating.

REFERENCES

[1] K. Takenaka, *Frontiers in Chemistry*, **6** (2018), 267:1–13.

[2] S. Savić-Šević., D. Pantelić, Branislav Jelenković, Branislav Salatić, Dejan V. Stojanović, *Soft Matter*, **14** (2018), 5595–5603.

Book of abstracts

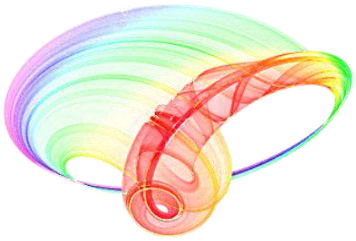

IX International School and Conference on Photonics

PHOTONICA2023

with joint events:

Understanding interaction light - biological surfaces: possibility for new electronic materials and devices

&

Biological and bioinspired structures for multispectral surveillance

&

Quantum sensing integration within microfluidic Lab-on-a Chips for biomedical applications

&

Advanced Biophysical Methods for Soil Targeted Fungi-Based Biocontrol Agents

August 28 - September 01, 2023, Belgrade, Serbia

Editors

Jelena Potočnik, Maja Popović, Dušan Božanić

Vinča Institute of Nuclear Sciences – National Institute of the Republic of Serbia, University of Belgrade

Belgrade, 2023

Real-time fabrication of microstructures on the modified chitosan

B. Murić, S. Savić-Šević, A. Kovačević, D. Pantelić and B. Jelenković
Institute of Physics, Belgrade, Serbia
e-mail: muric@ipb.ac.rs

Chitosan is a natural polymer, partially deacetylated derivative of chitin extracted from crustaceous shells, insoluble in pure water and organic solvents, but dissolves in diluted acidic solutions. Biocompatible, biodegradable and nontoxic nature of chitosan makes it a suitable polymer for various applications (biomedical, engineering, food, pharmacy, etc.) [1,2].
A simple and cheap method for preparing modified chitosan (MC) layer as ecofriendly, optically transparent, elastic, and durable material, for microstructures fabrication is presented. The anthocyanin food dye (E163) was used for MC layer sensitization makes it responsive to experimentally used blue laser light. The MC has no toxic effect, that confirmed by the biocompatibility test. The various microstructures were produced on the MC layer by direct focused laser radiation at 488 nm, with maximum output power of 100 mW, using homemade laser writing system. The fast produced concave or convex, aspheric microlenses (individual or closely packed arrays), microchannels, diffraction gratings, various complex structures etc. can be used directly, without any additional chemical processing and any waste, for a variety of applications such as: lab on a chip, medical laser, optical sensors, light-field cameras, security, biological structure, etc [3-5].

REFERENCES
[1] A. Pellis *et al.*, Gels 8, 393 (2022).
[2] B. Ozcelik *et al.*, Acta Biomater. 9, 6594 (2013).
[3] S.T. Koev *et al.*, Lab. Chip 10, 3026 (2010).
[4] R. D'Amato *et al.*, Sensors 21, 3348 (2021).
[5] Z-Y. Hu *et al.*, Nat. Commun. 13, 5634 (2022).

Optical fiber curing of a dental composite: a holographic, thermographic, and Raman study

E. Novta[1], T. Lainović[1], D. Grujić[2], S. Savić-Šević[2], E. Toth[3], Ž. Cvejić[3], L. Blažić[1,4] and D. Pantelić[2]
[1]*University of Novi Sad, Faculty of Medicine, School of Dental Medicine, Novi Sad, Serbia*
[2]*University of Belgrade, Institute of Physics, Belgrade, Serbia*
[3]*University of Novi Sad, Faculty of Sciences, Department of Physics, Novi Sad, Serbia*
[4]*Dental Clinic of Vojvodina, Novi Sad, Serbia*
e-mail: evgenije.novta@mf.uns.ac.rs

The main limitation of dental resin-based composites (RBC) is shrinkage during polymer chain formation. As a consequence, at the tooth-restoration interface polymerization shrinkage stress (PSS) is generated, impairing restoration longevity. The study aimed to introduce a novel photo-activation protocol using optical fibers inserted into the RBC, for reducing PSS and guiding light directly into deeper layers of the restoration.
Tooth models with standardized cavities were filled with the RBC (Filtek™ Bulk-fill Posterior, 3M ESPE), and the proposed experimental curing was designed as follows: in the first step, two optical fibers (ϕ 1.5 mm) connected with a commercial dental LED curing unit were inserted into the filling to cure the RBC from within; in the second step, fibers were extracted, remaining voids were filled with the RBC and final conventional curing was performed with the commercial light guide positioned above the sample. As a control, conventional curing was performed on a separate group of samples (n=15 models per curing protocol). Tooth model deformation as a secondary manifestation of PSS was measured in real-time using digital holographic interferometry. Simultaneous monitoring of RBC temperature change was conducted with an infrared thermal camera. The degree of monomer-to-polymer conversion (DC) was measured immediately after curing and after 24 h of dark storage, using Raman spectroscopy (n=5 models per curing protocol; three measurements points for each sample).

Table 1. Photo-activation parameters and results.

Curing protocol	Radiant exposure (J/cm^2)	Tooth model deformation (μm)	Temperature change (^{0}C)	Time to reach the maximum temperature (s)	Immediate DC (%)	24 h post-cure DC (%)
Conventional	20	13.4	10.7	7.5	41.4	46.3
Experimental (1st + 2nd step)	14.5	8.8	6.5	8.2	33.5	38.1

The results showed a 34 % reduction of tooth model deformation using the experimental curing compared with the control. Such a finding was related to a lower temperature change (39 %), leading to a lower thermal shrinkage during the cooling process, as suggested by Palagummi et al. [1]. Furthermore, the time to reach the maximum exothermal temperature was prolonged compared with the control, allowing polymer chains to re-arrange and accommodate the volume reduction by viscous flow. Meanwhile, significantly lower immediate DC contributed to the reduction of model deformation as well. After 24 h of dark storage, the DC increased in both groups of samples as expected, but remained significantly lower for the ones cured using the experimental protocol compared with the control.
In conclusion, the proposed photo-activation using optical fibers was presented as beneficial for PSS reduction and could be easily implemented into dental clinical practice by coupling the fibers with standardized commercial light guides. However, it should be noted that measuring the irradiance of the selected light source is necessary to adequately determine exposure time since it was presented that insufficient radiant exposure (i.e. lower than suggested by the manufacturer) compromises the DC and therefore material biocompatibility and mechanics.

REFERENCES
[1] S.V. Palagummi *et al.*, Dent. Mater. 37, 1772 (2021).

Book of abstracts

PHOTONICA 2025

X International School and Conference on Photonics

25 - 29 August 2025

Belgrade, Serbia

Editors

Mihailo Rabasović, Uroš Ralević, Marina Lekić, Aleksandar Krmpot
Institute of Physics Belgrade, Serbia

Belgrade, 2025

Temperature tunable biopolymer photonic structure

S. Savic-Sevic[1], B. Muric[1] and J. Potocnik[2]
[1]*Institute of Physics, Belgrade, Serbia*
[2]*Vinca Institute of Nuclear Sciences, Belgrade, Serbia*
e-mail: savic@ipb.ac.rs

Tunable biopolymer photonic structures responsive to temperature changes are investigated. Two types of biopolymers are employed: pullulan, characterized by a linear polysaccharide structure, and dextran, which has a branched configuration. The photonic structures are fabricated by holographic recording in dichromate-doped pullulan and dextran. Properties of pululan [1,2] and dextran [3] films as holographic material - surface gratings, its diffraction efficiency, copying and environmental stability, were previously investigated.

Photonic structures, fabricated using a simple counter-propagating beam holographic setup, consist of multilayered biopolymer configurations, separated and supported by nanopillars. This complex morphology is formed through the combined action of holographic recording and nonsolvent-induced phase separation.

The optical properties of the resulting biopolymer photonic structures were analyzed during heating and cooling cycles. A Peltier element was used to control the sample temperature, while reflection spectra from white halogen light were recorded using a fiber-optic spectrometer. During heating, the reflectance peaks shifted toward shorter wavelengths (blue-shifted), showing a negative spectral shift of 60 nm for pullulan and 27 nm for dextran with a temperature increase of +50 K. Upon cooling, the spectral peaks nearly returned to its original position.

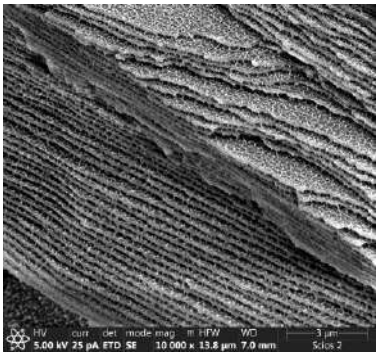

Figure 1. A cross-section of dextran structure.

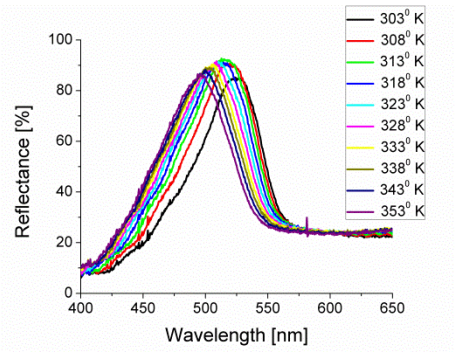

Figure 2. Reflectance spectra of dichromate-sensitized dextran photonic structure as a function of temperature

REFERENCES

[1] S. Savic-Sevic, D. Pantelic, Appl. Opt. 46, 287 (2007).
[2] S. Savic-Sevic, D. Pantelic, Optics Exp. 13, 2747 (2005).
[3] S. Savic-Sevic, D. Pantelic, Optical Mater. 30, 1205 (2008).

ORCID: S.S-S. 0000-0002-6406-0745, B.M. 0000-0003-3003-1708, J.P. 0000-0001-7206-5952

Temperature tunable biopolymer photonic structure

S. Savic-Sevic[1], B. Muric[1] and J. Potocnik[2]
[1]*Institute of Physics, Belgrade, Serbia*
[2]*Vinca Institute of Nuclear Sciences, Belgrade, Serbia*
e-mail: savic@ipb.ac.rs

Tunable biopolymer photonic structures responsive to temperature changes are investigated. Two types of biopolymers are employed: pullulan, characterized by a linear polysaccharide structure, and dextran, which has a branched configuration. The photonic structures are fabricated by holographic recording in dichromate-doped pullulan and dextran. Properties of pululan [1,2] and dextran [3] films as holographic material - surface gratings, its diffraction efficiency, copying and environmental stability, were previously investigated.

Photonic structures, fabricated using a simple counter-propagating beam holographic setup, consist of multilayered biopolymer configurations, separated and supported by nanopillars. This complex morphology is formed through the combined action of holographic recording and nonsolvent-induced phase separation.

The optical properties of the resulting biopolymer photonic structures were analyzed during heating and cooling cycles. A Peltier element was used to control the sample temperature, while reflection spectra from white halogen light were recorded using a fiber-optic spectrometer. During heating, the reflectance peaks shifted toward shorter wavelengths (blue-shifted), showing a negative spectral shift of 60 nm for pullulan and 27 nm for dextran with a temperature increase of +50 K. Upon cooling, the spectral peaks nearly returned to its original position.

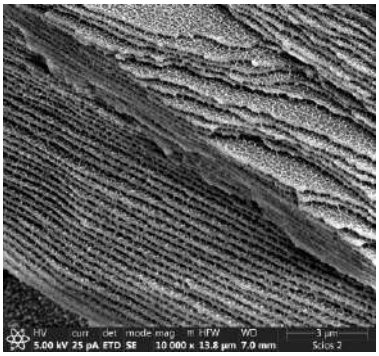

Figure 1. A cross-section of dextran structure.

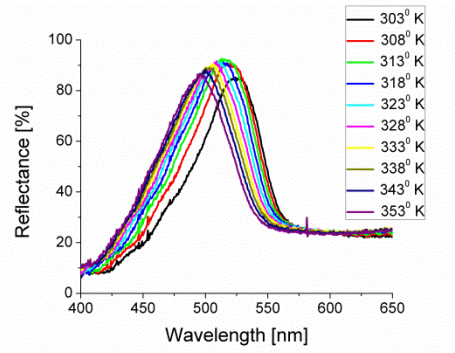

Figure 2. Reflectance spectra of dichromate-sensitized dextran photonic structure as a function of temperature

REFERENCES

[1] S. Savic-Sevic, D. Pantelic, Appl. Opt. 46, 287 (2007).
[2] S. Savic-Sevic, D. Pantelic, Optics Exp. 13, 2747 (2005).
[3] S. Savic-Sevic, D. Pantelic, Optical Mater. 30, 1205 (2008).

ORCID: S.S-S. 0000-0002-6406-0745, B.M. 0000-0003-3003-1708, J.P. 0000-0001-7206-5952

PHOTONICA2015

V International School and Conference on Photonics
& COST actions: MP1204, BM1205 and MP1205
& the Second international workshop "Control of light and matter waves propagation and localization in photonic lattices"
www.vin.bg.ac.rs/photonica 2015

Book of Abstracts

Editors
Suzana Petrović, Goran Gligorić and Milutin Stepić

Belgrade, 2015.

This work was supported by the Serbian Ministry of Education and Science through project III 45005. D.S. is grateful to the Italian Ministry of Foreign Affairs-Science and Technology Cooperation for a Travel Grant to visit CNR-IFN.

REFERENCES
[1] J. F. Galisteo-Lopez et al., Adv. Mater. 23, 30 (2011).
[2] J. Joannopoulus et al., *Molding the flow of light*, Princeton University Press (2011).
[3] P. Jiang, M. J. McFarland, J. Am. Chem. Soc. 126, 13778 (2004).
[4] P. Jiang et al., Chem. Mater. 11, 2132 (1999).
[5] A. Chiappini et al, J. Non-Cryst. Solids 355, 1167 (2009).

Localization of light in a polysaccharide-based complex nanostructure

S. Savić-Šević, D. V. Pantelić, D. Ž. Grujić and B. M. Jelenković
Institute of Physics, University of Belgrade, Pregrevica 118, 11080 Zemun, Belgrade, Serbia
e-mail: savic@ipb.ac.rs

Complex nanostructures are interesting research topic, due to remarkable properties for photonic applications [1]. Photonic structures are generated by many methods. Holographic method [2] has several advantages: it is simple and fast, capable of producing one-, two- and three- dimensional periodic nanostructures over a large area. We combine the holographic method with non-solvent induced phase separation to generate complex photonic structures.

Polysaccharide sensitized with ammonium dichromate was used as recording material. Photonic structures were fabricated as a volume Bragg reflection grating recorded with the single-frequency, diode pumped Nd-YAG laser, at 532 nm. After exposure, grating was chemically processed in a developer. The resulting Bragg layers, upon phase separation, is filled with polydisperse, almost spherical nanoparticles arranged in a random way.

We investigated optical bandgap properties in the complex nanostructure, as a measure of the photon confinement in the layer, and we have measured the backscattered light cone and determined the mean free path of light in structure. The width of backscattering cone indicates a weak localization regime.

REFERENCES
[1] W. G. Bae et al., Adv. Mater. 26, 675 (2014).
[2] M. Birnkrant et al., Nano Lett. 7, 3128 (2007).

UNO-4

4th International Workshop on Ultrafast Nanooptics

collocated with

COST Action MP1403 - Nanoscale Quantum Optics - Work Group Meeting

Nonlinearities and Ultrafast Processes in Nanostructured Media

October 18-22, 2015

Bad Dürkheim

DFG SPP 1391

cost EUROPEAN COOPERATION IN SCIENCE AND TECHNOLOGY

Poster 10:

Inducing nanoparticles and periodic nanostructures on thin metal films by low-fluence femtosecond beam

Aleksander G. Kovačević[1], Suzana Petrović[2], Peter Panjan[3], Vladimir Lazović[1], Davor Peruško[2], Svetlana Savić-Šević[1], Dejan Pantelić[1], Branislav M. Jelenković[1]

[1] *Institute of Physics, University of Belgrade, Pregrevica 118, 11080 Belgrade, Serbia*

[2] *Institute for Nuclear Sciences Vinča, University of Belgrade, PO Box 522, 11001 Belgrade, Serbia*

[3] *Institute Jožef Štefan, Jamova cesta 39, 1000 Ljubljana, Slovenia*

In many fields, like semiconductor technology, optics, chemistry, mechanics, magnetics, electricity, the applications of thin films play an important role. Various types of coatings for protection, diffusion barriers, filtering, reflection/antireflection, sensing, waveguiding, decorative and other purposes are just some to mention. Structuring of thin films can enhance their characteristics. From the other side, nanoparticles are of great interest due to their position between bulk materials and atomic/molecular structures. The interaction of femtosecond laser beam with thin films can have various outcomes, in which the generation of nanoparticles and of surface periodic structures gains more interest. We have used low-fluence femtosecond beam of various wavelengths and expositions to thin film samples: Al on Si, CrVN, multilayer Al/Ti on Si and multilayer Ni/Pd on Si. Having excellent mechanical characteristics (wearing, corrosion resistance), some samples have prospective applications in holography. The expositions yielded the generation of nanoparticles and the formation of periodic surface structures (LIPSS). The processes of liquid or solid-state dewetting could be responsible for regrouping of generated nanoparticles and nanoparticle clusters, while LIPSS is most probably induced by the occurrence of the surface plasmon polariton. The presence of the sublayer, depending on its optical characteristics, strongly influences both the shape and the quality of the LIPSS.

Acknowledgements: This work has been supported by the Ministry of Science of the Republic of Serbia with projects OI171005 and III45016, as well as by COST action MP1403.

СРПСКА АКАДЕМИЈА НАУКА И УМЕТНОСТИ

ЕКОЛОШКИ И ЕКОНОМСКИ ЗНАЧАЈ ФАУНЕ СРБИЈЕ

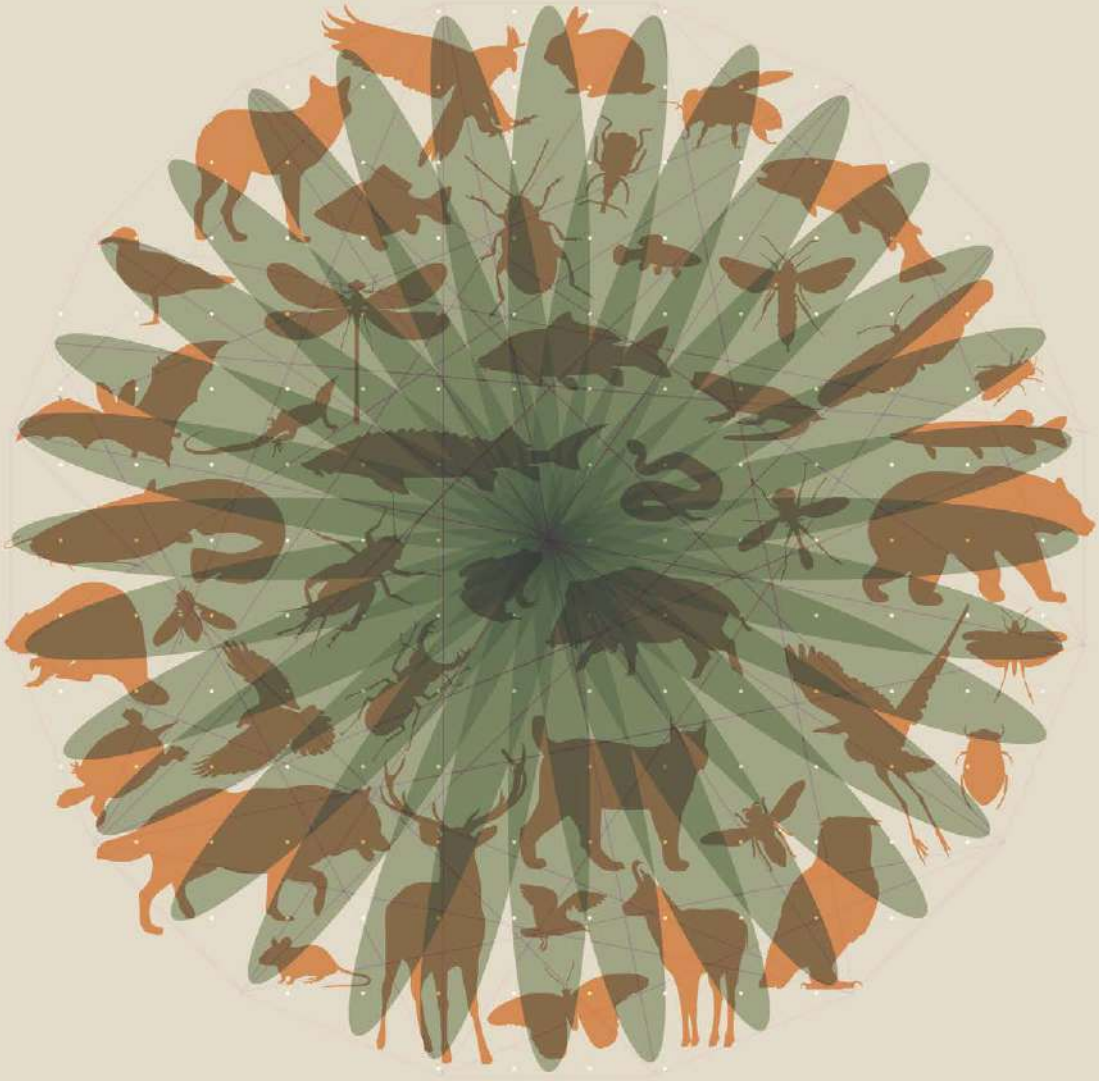

МОРФОЛОШКЕ СТРУКТУРЕ НЕКИХ ПРЕДСТАВНИКА ЕНТОМОФАУНЕ СРБИЈЕ КАО МОДЕЛИ У БИОМИМЕТИЦИ

Дејан ПАНТЕЛИЋ*, Срећко ЋУРЧИЋ**, Александар КРМПОТ*, Дејан В. СТОЈАНОВИЋ***, Михаило РАБАСОВИЋ*, Светлана САВИЋ-ШЕВИЋ*

С а ж е т а к. – Током веома дугог еволутивног развоја живи организми су развили добро адаптиране материјале и структуре који представљају напредна решења у области оптике, механике, термике или акустике, чак и са аспекта модерне науке, што је довело до интензивног развоја биомиметике као области која се бави стварањем нових технологија инспирисаних биолошким макроструктурама и микроструктурама. Код већег броја таксона лептира и тврдокрилаца, елемената фауне Србије, примећује се структурна обојеност њихових крила и покрилаца. Она настаје због присуства низа наизменичних ваздушних и хитинских слојева кутикуле (нпр. ребра, ламеле и гребени на љуспицама крила лептира), на којима се испољава таласна природа светлости кроз појаве интерференције, дифракције и расејања. При томе долази до селективне рефлексије светлосних таласа и појаве структурних боја. Овде су представљене методе генерисања биоморфних структура применом холографије, микролитографије и сродних оптичких техника. Указано је на могућности практичне примене морфолошких структура појединих врста инсеката из Србије у области сензора, заштите докумената и нових оптичких материјала.

Кључне речи: биофотоника, биомиметика, инсекти, структурне боје

---

* Институт за физику, Универзитет у Београду, pantelic@ipb.ac.rs, krmpot@ipb.ac.rs, rabasovic@ipb.ac.rs, svetlana.savic@ipb.ac.rs

** Институт за зоологију, Универзитет у Београду – Биолошки факултет, srecko@bio.bg.ac.rs

*** Институт за низијско шумарство и животну средину, Универзитет у Новом Саду, dvstojanovic@uns.ac.rs

УВОД

Природа је одувек била инспирација обичном човеку, уметнику или научнику. Сетимо се Ван Гогових пејзажа, слике са цветовима ириса или вазе са сунцокретима. Поменимо и писца научне фантастике Станислава Лема и његов роман „Непобедиви“, у коме ројеви минијатурних, летећих, инсектоликих робота, на далекој планети, нападају моћну интергалактичку крстарицу, исказујући своју колективну интелигенцију. Роман је превазишао уметност и имао је утицај на развој концепта „паметне прашине“ (енгл. smart dust) [1] као система бежично повезаних сензора.

И многе друге идеје, открића и проналасци су произашли из посматрања природе. Ото Лилијентал је објавио књигу „Лет птица као основа вештине летења“ [2] и конструисао низ летећих машина инспирисаних птицама. Протезе спринтера Оскара Писторијуса, конструисане од композита са угљеничним влакнима, акумулирају механичку енергију и имају велику сличност са ногама кенгура. Поменимо и проналазача Жоржа де Местрала и његову чичак траку, чије само име указује на извор инспирације. Многе рачунарске и алгоритамске технике, попут целуларних аутомата [3], неуронских мрежа, еволуционих и генетских алгоритама, интелигенције роја [4] „позајмљене“ су из природе.

Тешко је одредити тачан историјски тренутак када је посматрање и имитирање природе претворено у посебну научну област. Пре ће бити да је целокупни развој цивилизације у доброј мери био везан за учење од природе, да би данас овај правац истраживања добио назив биомиметика. Њен циљ је да се посматрањем организама и биолошких система открију потенцијално корисне особине или „инжењерско-технолошка“ решења, која ће се затим копирати. Као пример ћемо навести сложене очи зглавкара, које имају веома широк видни угао, за разлику од стандардних оптичких система. Иако постоје панорамски објективи и технике панорамског снимања и међусобног повезивања слика, опрема је скупа, процедура компликована, а процес снимања је дуготрајан. Насупрот томе, еволуција је код већине зглавкара проблем решила на једноставан и ефикасан начин: уместо једног компликованог система, употребила је мноштво малих и једноставних (оматидије као делови сложеног ока) [5].

Сродна биомиметици је бионика, која означава инжењерски приступ имитацији природе, где није битно само разоткрити принципе функционисања живих организама, већ на ефикасан начин конструисати и направити производ. Као пример, наведимо фабрикацију материјала са суперхидрофобним својствима (способних да их не кваси вода). Одавно се зна да кутикула инсеката и површина листа лотоса одбијају воду [6], те да кожа ајкуле значајно смањује хидродинамички отпор [7]. У оба случаја, површина тела организама је покривена микронским и субмикронским избочинама, чиме се значајно мењају хидростатичке и хидродинамичке особине. Користећи ове принципе,

развијена је једноставна техника која користи савремени композитни материјал (полимер и угљеничне нанотубе) да рационално произведе суперхидрофобну површину [8].

Биомиметика понекад произлази из физичких услова који се постављају пред сложене системе, независно од тога да ли их је „конструисала“ природа или их је конструисао човек. Погледајмо само велику сличност између архитектуре римског Колосеума и „архитектуре“ дијатоме (сл. 1(а) и 1(б)). Као што је констатовано у раду [9], механичка отпорност фрустуле дијатома је веома добра, те се предлаже директно копирање биолошке механичке конструкције у архитектонску.

Често се среће и термин биоинспирација [10, 11], са прилично магловитом разликом у односу на биомиметику. Можда би се могло рећи да је то област којој биолошки системи служе само као полазна тачка за конципирање нових материјала, машина или уређаја. Не тежи се детаљном копирању биолошких функција, већ се неке од њих задржавају, а друге изостављају, са циљем задржавања жељене функције, уз могућност техничке реализације савременим технологијама. Истраживања сложеног ока рака *Odontodactylus scyllarus* (Linnaeus, 1758) показала су супериорна поларизациона својства у односу на савремене оптичке елементе овог типа [12]. У том смислу, ово је биоинспиративни путоказ за конструкцију нових оптичких компонената, као и других вештачких материјала, наравно, модерним технологијама.

На крају, један од интересантних праваца представља и функционализација биолошких структура или структура биолошког порекла. Овде се директно користе организми или њихови делови, који се затим модификује тако да раде ствари за које нису предвиђени својом биолошком природом. Занимљив је пример раније употребе (у XIX веку) нити паукове мреже као кончанице у окуларима оптичких инструмената и нишанских справа [13]. Све до појаве микролитографије, то је био једини начин да се у оптичке инструменте угради веома фине нишанске линије, у распону дебљина од 2 до 10 μm (што је особина нити мреже паука крсташа –*Araneus diadematus* (Clerck, 1757)).

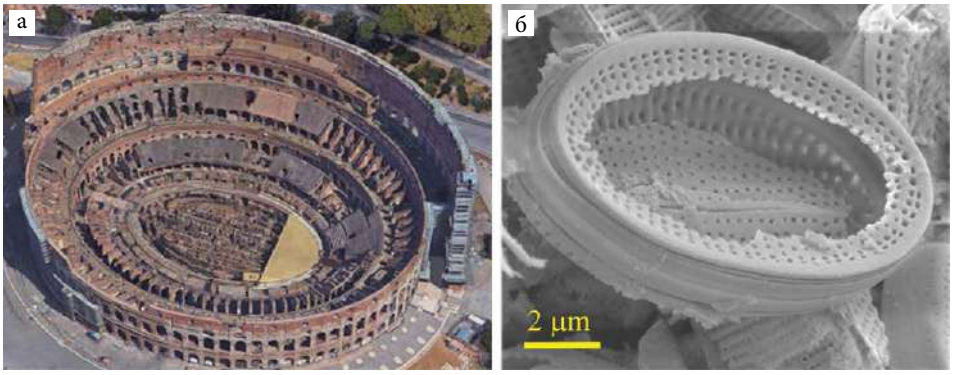

Слика 1. Сличност архитектуре (а) римског Колосеума и (б) дијатоме

Биомиметика, бионика, биоинспирација или функционализација нису термини којима се описује једна, добро дефинисана, област истраживања. У зависности који се аспект посматра, можемо бити инспирисани механиком, оптиком, термиком, трибологијом, адхезијом, акустиком, радиометријом, али и хемијом, организацијом или структуром. Истраживања су стога увек мултидисциплинарна, одређена знањем, искуством и интересовањем истраживача који их спроводе. Ми ћемо у овом раду приказати оне аспекте биомиметике који се тичу оптичких ефеката у живом свету [14] и могућности њихове практичне примене.

ИНСЕКТИ КАО ИНСПИРАЦИЈА У БИОФОТОНИЦИ И БИОМИМЕТИЦИ

Инсекти су једна од најбројнијих група живих организама. Настањују скоро све екосистеме, а током еволуције су се развили различити механизми опстанка код бројних врста. Између осталог, на телу одређених инсеката се могу наћи зупчаник (*Issus coleoptratus* (Fabricius, 1781) [15]), супер хидрофобне (*Morpho aega* (Hübner, 1822) [16]) и адхезивне структуре [17], као и сложене очи [18, 19].

Зато је поље биомиметике инсеката широко отворено за откривање нових принципа и њихово практично коришћење. Посебно је интересантна оптика, где постоји велики број студија заснованих на структурама инсеката – нпр. површински појачано Раманово расејање (енгл. surface-enhanced Raman scattering (SERS)), као метод детекције ниске концентрације аналита [20], љуспице крила лептира као сензори (*Euploea mulciber* (Cramer, 1777) [21], *Morpho sulkowskyi* (Kollar, 1850) [22]), инсектима инспирисани оптички филтери у заштити докумената (*Pierella luna* (Fabricius, 1793) [23]), радијативно хлађење (*Cataglyphis bombycina* Roger, 1850 [24]), ефикасни детектори инфрацрвеног зрачења (*Merimna atrata* (Gory & Laporte, 1837) [25], *M. sulkowskyi* [26]), итд.

Оптика кутикуле инсеката

Да би се добро разумела оптика инсеката, посветићемо ово кратко потпоглавље ефектима који постоје на њиховој кутикули. Основна намена им је да инсекту дају карактеристично обојење које му омогућава мимикрију, апосемију, дисруптивне ефекте (привидну промену контуре тела), што као последицу има ефикасније преживљавање у природном окружењу.

Са оптичке тачке гледишта, највише је заступљена апсорпција на различитим пигментима, попут меланина, птерина или каротеноида (пигментна обојеност) [27]. Дијапазон боја, који се на овај начин добија, је релативно ограничен, па је природа морала да посегне за напреднијим оптичким ме-

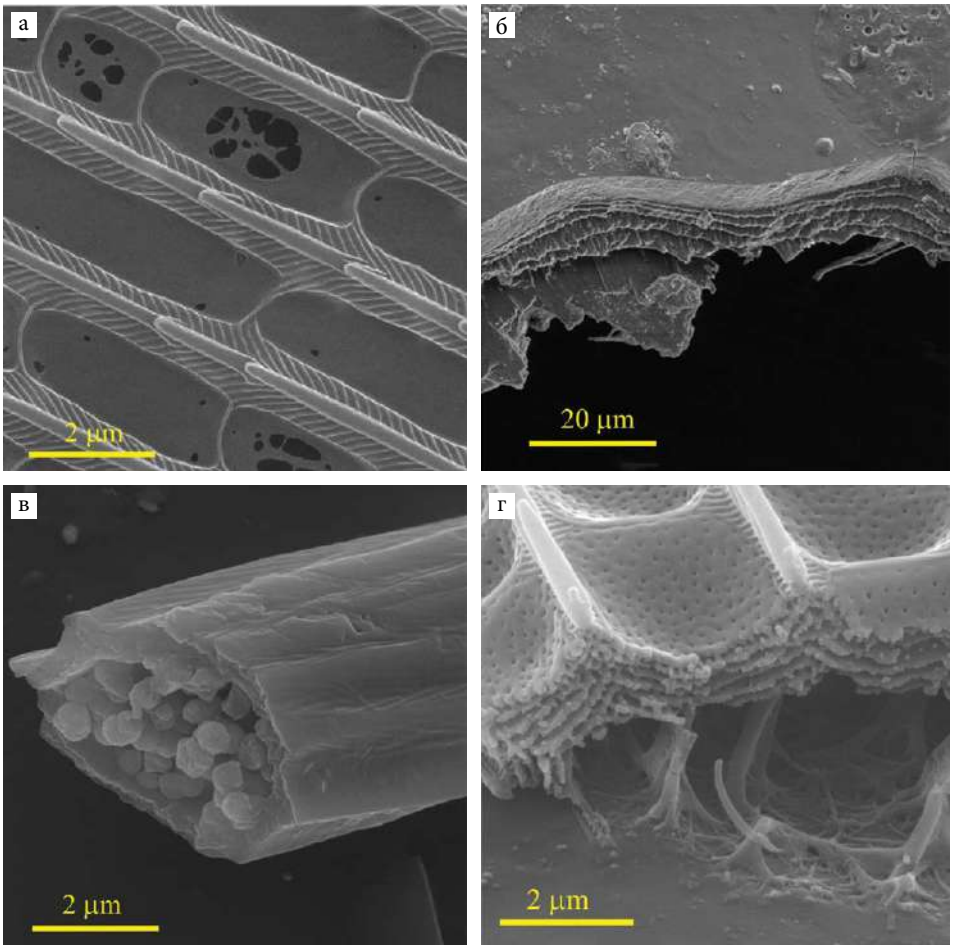

Слика 2. Примери (а) површинске (*Argynnis adippe* (Denis & Schiffermüller, 1775)) и (б) слојевите структуре кутикуле инсеката (*Calosoma sycophanta* (Linnaeus, 1758)), (в) запреминске структуре длачица (*Agapanthia violacea* (Fabricius, 1775)) и (г) мешовите површинско-запреминске структуре (*Jordanita globulariae* (Hübner, 1793))

ханизмима, као што су интерференција, расејање, поларизација, дифракција, преламање и таласоводна пропагација. Већина поменутих ефеката се ослања на таласне особине светлости, што се у крајњем исходу своди на селективну рефлексију појединих спектралних интервала, чиме се постиже неопходна обојеност. Код инсеката се на овакав начин добијају боје из плавог и зеленог дела спектра, као и златне и сребрне боје. Занимљиво је да се код многих инсеката боје мењају са углом посматрања – ова појава се назива иридесценција.

Сви ови ефекти се виде само онда када је кутикула структурирана на микронском и субмикронском нивоу. Уочавају се паралелне линије (које

функционишу као дифракционе решетке – сл. 2(а)), слојевите структуре (сл. 2(б)), правилни (сл. 2(в)), комплексни (сл. 2(г)), запремински облици (фотонски кристали), низови брадавичастих испупчења, храпаве, неправилне површине, и све то у невероватном броју међусобних комбинација. Ове структуре се могу налазити у дубини кутикуле, као што је то најчешће случај код Coleoptera, или на љуспицама и длачицама које облажу кутикулу код Lepidoptera или неких Coleoptera. Боје настале на овакав начин (нпр. код лептира са сл. 3) називамо структурним.

Понекад морфолошке структуре немају улогу у стварању обојења, већ служе као помоћна компонента у смањивању губитака у оптичком систему ока. Велики број инсеката користи правилне структуре на површини корнее оматидија, које тада функционишу као антирефлексиони слој, који обезбеђује да највећи део светлосне енергије стигне до фоторецептора (кућна мува [28]).

Слика 3. Структурна обојеност крила лептира *Apatura metis* (Freyer, 1829). На левом предњем крилу се види иридесцентна љубичаста боја, која мења своју нијансу са променом угла посматрања

Кратак преглед техника анализе оптичких структура инсеката

Биомиметика суштински има два дела. Први се бави анализом природних структура, мерењем њихових оптичких особина (спектар, усмереност, поларизација) и разоткривањем физичких принципа који стоје иза примећених ефеката. Други покушава да искористи постојеће технологије ради имитације поменутих структура и ефеката.

С обзиром на минијатурност структура које се посматрају, најважније су микроскопске методе анализе: скенирајућа (SEM) и трансми-

сиона електронска микроскопија (TEM), микроскопија атомских сила (AFM), конфокална и нелинеарна микроскопија (NLM) [29], микротомографија и нанотомографија, дигитална холографија [30, 31] и холографска микроскопија [32].

Дифрактометрија проучава распршивање светлости због дифракције на структурама чије су димензије поредиве са таласном дужином видљиве светлости. Тиме се зрачење расипа у широком просторном углу, а његово мерење омогућава да се стекне увид у природу самих структура. Ако се користе могућности холографије, могуће је добити и слику самих структура (дигитална холографска микроскопија).

Спектрална анализа је једна од важних техника, јер облик спектра одређује обојеност кутикуле [33] и служи као путоказ ка објашњењу оптичких ефеката. Анализа угаоне расподеле расејане светлости једнако је важна, јер суштински зависи од структура на кутикули [34, 35].

Полариметријом се утврђује да ли кутикуларне структуре утичу на поларизацију рефлектоване или пропуштене светлости. Ово има биолошку важност зато што су поједине врсте инсеката способне да виде и стање поларизације те да га користе као сигнал.

Разоткривање доминантних оптичких ефеката се највећим делом своди на симулирање простирања електромагнетног таласа кроз компликоване структуре кутикуле, те поређење са експерименталним мерењима. Примењују се следеће нумеричке технике: метод коначних елемената, метод преносне матрице, ригорозна анализа спрегнутих таласа и др.

Преглед техника за генерисање биомиметских оптичких структура

Анализа фотонских структура указује на доминантне оптичке ефекте, које је потребно имитирати на вештачки начин. С обзиром на микронске и субмикронске структуре и њихову тродимензионалност, оптику инсеката је могуће имитирати неком од мноштва литографских техника: двофотонском стереолитографијом [36], холографском и интерференционом литографијом [37], директним ласерским исписивањем, утискивањем (енгл. embossing, nano-imprint) [38], директним копирањем (енгл. templating, molding, soft-lithography) [39], јонском литографијом [40] или комбинацијом различитих метода [41]. Немогуће је дати детаљно објашњење поменутих техника у овом релативно кратком тексту па ћемо се концентрисати само на оне методе које су важне за даљи ток излагања.

Двофотонска стереолитографија се заснива на скенирању фотоосетљивог материјала ласерским снопом са ултракратким импулсима дужине трајања од неколико десетина фемтосекунди (један десетомилионити део милионитог дела секунде). У веома малој запремини око фокалне тачке снопа, интензитет светлости је довољно велики да изазове експозицију материјала – испред и иза фокуса материјал је неекспониран. Након

хемијске обраде, појављују се тродимензионалне структуре микронских и субмикронских димензија [42].

Холографска литографија је заснована на контролисаној интерференцији два и више снопова унутар фотоосетљивог материјала [43]. Као што је познато, интерференција формира области повећаног или смањеног интензитета, које различито експонирају материјал. Након хемијске обраде, а у зависности од броја снопова, њихове међусобне оријентације и стања поларизације, могуће је добити велики број правилних кристалних структура [44], сличних онима које се срећу код лептира (нпр. *Callophrys rubi* (Linnaeus, 1758) [45]).

Богатство фотонских морфолошких структура инсеката Србије

Ентомофауна Србије свакако није онако богата као у бразилској прашуми, али и даље пружа изворе инспирације за истраживања на граници биологије, физике, хемије, али и технике и технологије. Са гледишта оптике, визуелни показатељи присуства структура јесу иридесценција, присуство боја из плаво-зеленог дела спектра, као и сребрнкасте или златне боје. Веома често су бела или црна боја (које, стриктно физички говорећи, и нису боје) појачане и потпомогнуте присуством структура.

Посебно су интересантни лептири и мољци (Lepidoptera) и неки тврдокрилци (Coleoptera) (фамилије Buprestidae, Cerambycidae, Rutelidae, Curculionidae и Carabidae), вилини коњици (Odonata), мрежокрилци (Neuroptera) и опнокрилци (Hymenoptera). Крилне љуспице лептира и мољаца могу бити структурно обојене (са типичном структуром као на сл. 4(а) и 4(б)), а код тврдокрилаца и љуспице (сл. 4(в)) и дубински делови кутикуле (сл. 2(б)) учествују у формирању структурних боја. Чак и пигментне љуспице крила лептира имају субмикронску структуру (сл. 4(г)), али се интерференциони ефекти не виде, због тога што је апсорпција светлости доминантна. У табели 1 су приказане неке од биомиметски занимљивих врста инсеката Србије.

У наредна два потпоглавља приказаћемо примере анализе фотонских морфолошких структура инсеката из Србије, њихове миметике и практичне употребе.

Табела 1. Неки од таксона инсеката Србије занимљиви са аспекта биомиметике

Таксон	**Ред**	**Фамилија**	**Тип структуре**
Apatura ilia (Denis & Schiffermüller, 1775)	Lepidoptera	Nymphalidae	Брегова структура љуспица, сл. 4(а)
Apatura iris (Linnaeus, 1758)	Lepidoptera	Nymphalidae	Брегова структура љуспица, сл. 4(а)

Таксон	**Ред**	**Фамилија**	**Тип структуре**
Apatura metis (Freyer, 1829)	Lepidoptera	Nymphalidae	Брегова структура љуспица, сл. 4(а)
Argynnis adippe (Denis & Schiffermüller, 1775)	Lepidoptera	Nymphalidae	Слојевита структура љуспица, сл. 2(а)
Argynnis aglaja (Linnaeus, 1758)	Lepidoptera	Nymphalidae	Слојевита структура љуспица, сл. 2(а)
Argynnis paphia (Linnaeus, 1758)	Lepidoptera	Nymphalidae	Слојевита структура љуспица, сл. 2(а)
Autographa bractea (Denis & Schiffermüller, 1775)	Lepidoptera	Noctuidae	Сложена дифракциона решетка, сл. 4(б)
Autographa gamma (Linnaeus, 1758)	Lepidoptera	Noctuidae	Површинска структура љуспица
Autographa jota (Linnaeus, 1758)	Lepidoptera	Noctuidae	Површинска структура љуспица
Callophrys rubi (Linnaeus, 1758)	Lepidoptera	Lycaenidae	Фотонски кристал
Diachrysia chrysitis (Linnaeus, 1758)	Lepidoptera	Noctuidae	Расејавајући планарни слој, сл. 5(в)
Issoria lathonia (Linnaeus, 1758)	Lepidoptera	Nymphalidae	Површинска структура љуспица, сл. 2(а)
Jordanita globulariae (Hübner, 1793)	Lepidoptera	Zygaenidae	Конкавна запреминска решетка, сл. 2(г)
Pieris brassicae (Linnaeus, 1758)	Lepidoptera	Pieridae	Флуоресцентне наночестице
Pieris rapae (Linnaeus, 1758)	Lepidoptera	Pieridae	Флуоресцентне наночестице
Polyommatus bellargus (Rottemburg, 1775)	Lepidoptera	Lycaenidae	Расејавајућа запреминска решетка
Calosoma sycophanta (Linnaeus, 1758)	Coleoptera	Carabidae	Кутикуларна запреминска структура, сл. 2(б)
Hoplia argentea (Poda, 1761)	Coleoptera	Rutelidae	Рандомизована површинска решетка, сл. 4(в)
Laemostenus punctatus (Dejean, 1828)	Coleoptera	Carabidae	Кутикуларна запреминска структура
Morimus asper funereus Mulsant, 1862	Coleoptera	Cerambycidae	Апсорпционе длачице
Rosalia alpina (Linnaeus, 1758)	Coleoptera	Cerambycidae	Апсорпционе длачице

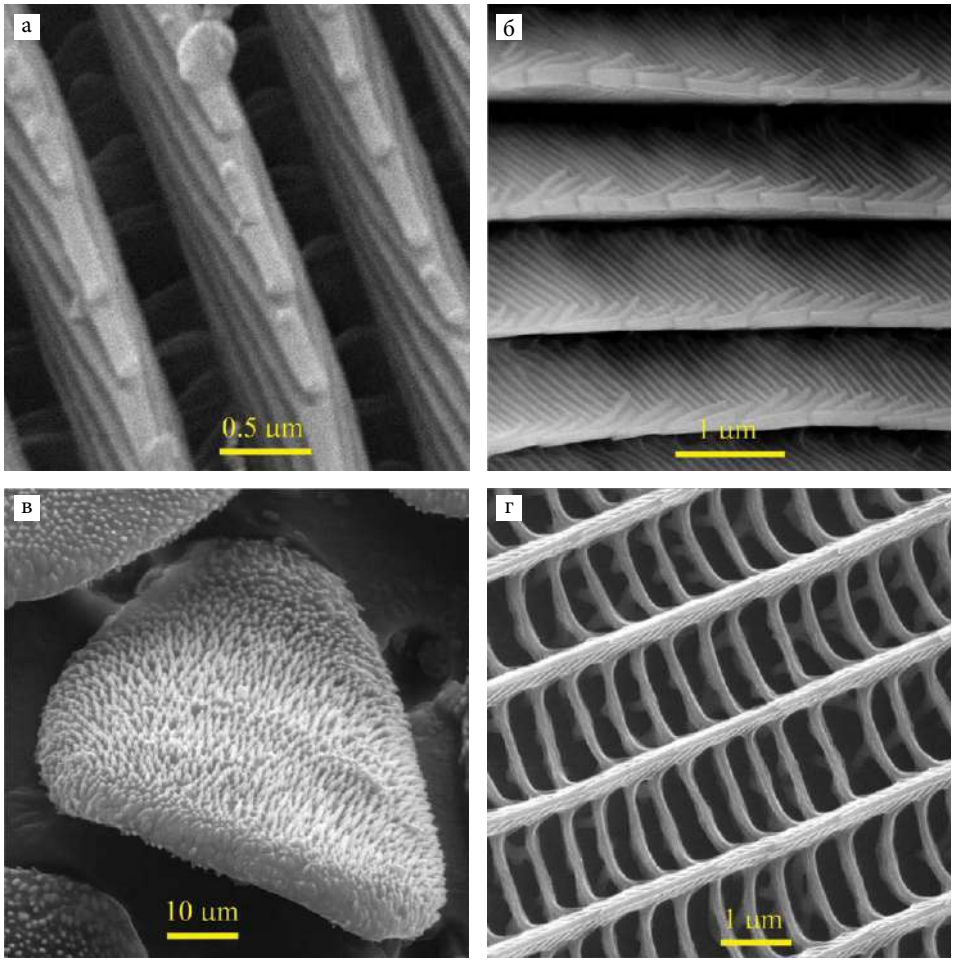

Слика 4. Изглед (а) структурно обојених љуспица лептира *Apatura iris* (Linnaeus, 1758), (б) мољца *Autographa bractea* (Denis & Schiffermüller, 1775) и (в) тврдокрилца *Hoplia argentea* (Poda, 1761) и (г) пигментне љуспице лептира *A.adippe* (Denis & Schiffermüller, 1775)

Холографска биомиметика Diachrysia chrysitis (Linnaeus, 1758)

Совица *D. chrysitis* (сл. 5(а)) поседује изражену структурну обојеност на широким зонама дорзалне стране предњих крила. Златна обојеност ових области највероватније има дисруптивну функцију, која обезбеђује разбијање контуре тела и теже препознавање од стране предатора. Занимљиво је да посматрање под оптичким трансмисионим микроскопом показује да су појединачне љуспице веома провидне (сл. 5(б)), али њихов просторни распоред у виду двоструког слоја (који чине покровне и базне љуспице) даје интензивну златну рефлексију. Скенирајућа електронска

микроскопија (сл. 5(в)) показује једноставну површинску структуру, која се састоји од широко размакнутих гребена (на међусобном растојању од око 2 μm), који су повезани густо распоређеним попречним ребрима (на растојању од око 0.15 μm), облика рибље кости. Прорачун показује да је за златну боју одговорна неравна површина унутрашњости љуспице (сл. 5(в)). Расејање на овој површини уклања плави део спектра из светлости, док веће таласне дужине рефлектује, што одговара златној боји (сл. 5(г)).

Оптичке структуре овог мољца могуће је имитирати холографски. Ми смо користили интерференцију два контра-пропагирајућа ласерска снопа (таласне дужине 532 nm). Као фотоосетљиви материјал, коришћен је танак слој пулулана (природни полисахарид), са додатком јона хрома (дихромирани пулулан). Након хемијске обраде, формиран је низ слојева између којих се налази велики број наночестица (сл. 6(а)). У рефлексији овако добијен слој има златни одсјај попут оног код *D. chrysitis* (сл. 6(а) и 6(б)).

Варијабилност, јединственост и функционализација љуспица крила лептира Issoria lathonia (Linnaeus, 1758), Argynnis aglaja (Linnaeus, 1758) и A. adippe

Посматрање љуспица крила лептира под оптичким микроскопом открива велику разноврсност њихових облика и боја (сл. 7(а)). На већим увеличањима, посматрајући скенирајућим електронским микроскопом, видимо да постоји одговарајућа варијабилност микронских и субмикронских морфолошких структура (сл. 7(б) и 7(в)). Математичка анализа распореда боја на слици снимљеној под оптичким трансмисионим микроскопом (сл. 7(а)) или међусобног положаја попречних ребара на слици добијеној помоћу скенирајућег електронског микроскопа (сл. 7(в)), показује да је вероватноћа проналажења две идентичне љуспице екстремно мала – чак 10^{-92}. У практичном смислу, можемо да тврдимо да је немогуће наћи две идентичне љуспице, тј. да је свака потпуно јединствена – онако како су јединствени отисци прста, боје дужице ока или распоред крвних судова очног дна код човека.

Јединственост указује на висок потенцијал коришћења љуспица крила Lepidoptera као елемената за заштиту докумената [46, 47]. Ако се љуспица перманентно интегрише у документ (новчаницу, личну карту, пасош), он постаје непоновљив и веома компликован за фалсификовање због тродимензионалне, субмикронске структуре љуспица. Ово је значајан напредак у односу на тренутно коришћене технике заштите [48], које се заснивају на сложености заштитних елемената (нпр. холограм), али без јединствености (сви холограми на новчаницама од 1000 динара су потпуно идентични). Тиме се приближавамо савременим настојањима да се документи персонализују [49]. Још једна од предности овог вида

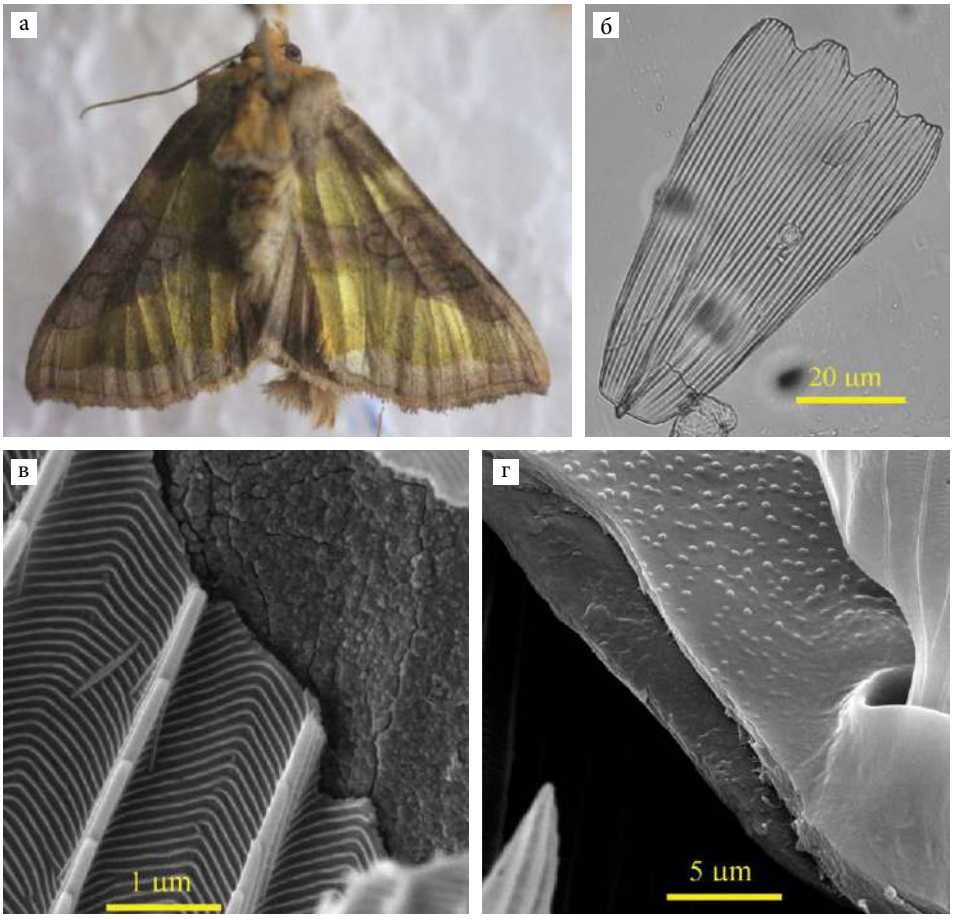

Слика 5. (а) Структурна обојеност предњих крила, (б) појединачна крилна љуспица снимљена под оптичким трансмисионим микроскопом, (в) неравна површина унутрашњости љуспице и (г) расејавајућа површина крилне мембране мољца *D. chrysitis*

заштите је и велика трајност хитинских структура, које у ентомолошким збиркама преживљавају десетине, па и стотине година без икакве промене оптичких својстава. Штавише, пронађени су фосилизовани остаци мољца старог 47 милиона година [50], чија је структурна обојеност била очувана!

Код свих елемената за оптичку заштиту важна је и могућност уписа додатних информација (попут личних података, слика или биометријских карактеристика). Показали смо да је применом ултракратких ласерских импулса могуће на контролисан начин уписивати податке на појединачне љуспице крила Lepidoptera. Модификован је раније развијен систем за ласерску микроскопију [29], тако да ласерски сноп може да исписује про-

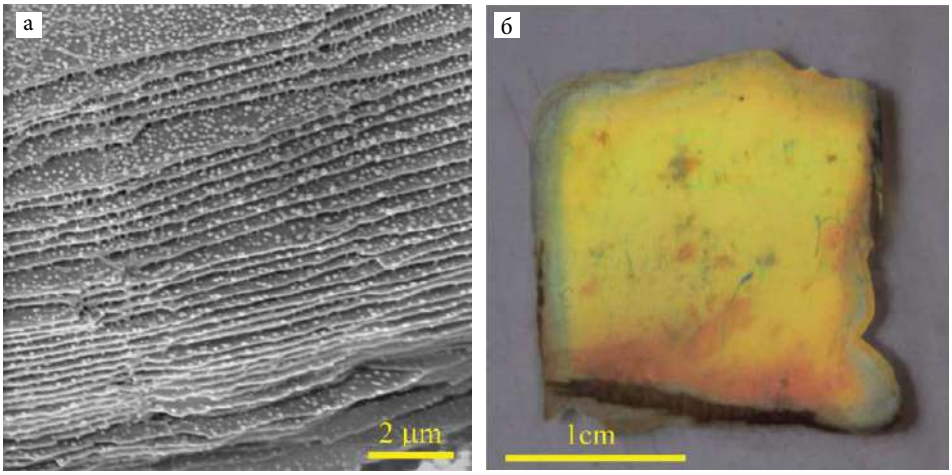

Слика 6. (а) Холографски добијени слојеви на дихромираном пулулану, као имитација унутрашње структуре љуспице *D. chrysitis***.** Снимак је добијен скенирајућим електронским микроскопом. (б) Фотографија рефлексије са холографски модификованог слоја дихромираног пулулана

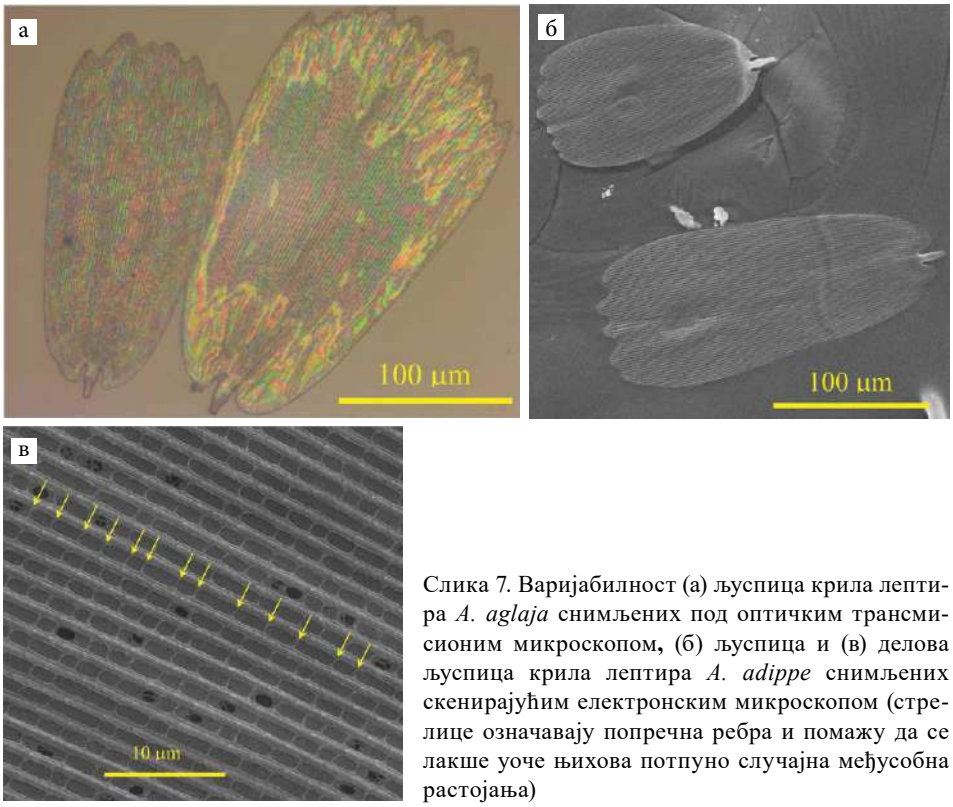

Слика 7. Варијабилност (а) љуспица крила лептира *A. aglaja* снимљених под оптичким трансмисионим микроскопом**,** (б) љуспица и (в) делова љуспица крила лептира *A. adippe* снимљених скенирајућим електронским микроскопом (стрелице означавају попречна ребра и помажу да се лакше уоче њихова потпуно случајна међусобна растојања)

извољно задату слику [51]. У зависности од интензитета ласерског снопа, исписивање је могуће реализовати променом флуоресцентних особина хитина, избељивањем (сл. 8(а)) или сечењем (сл. 8(б)).

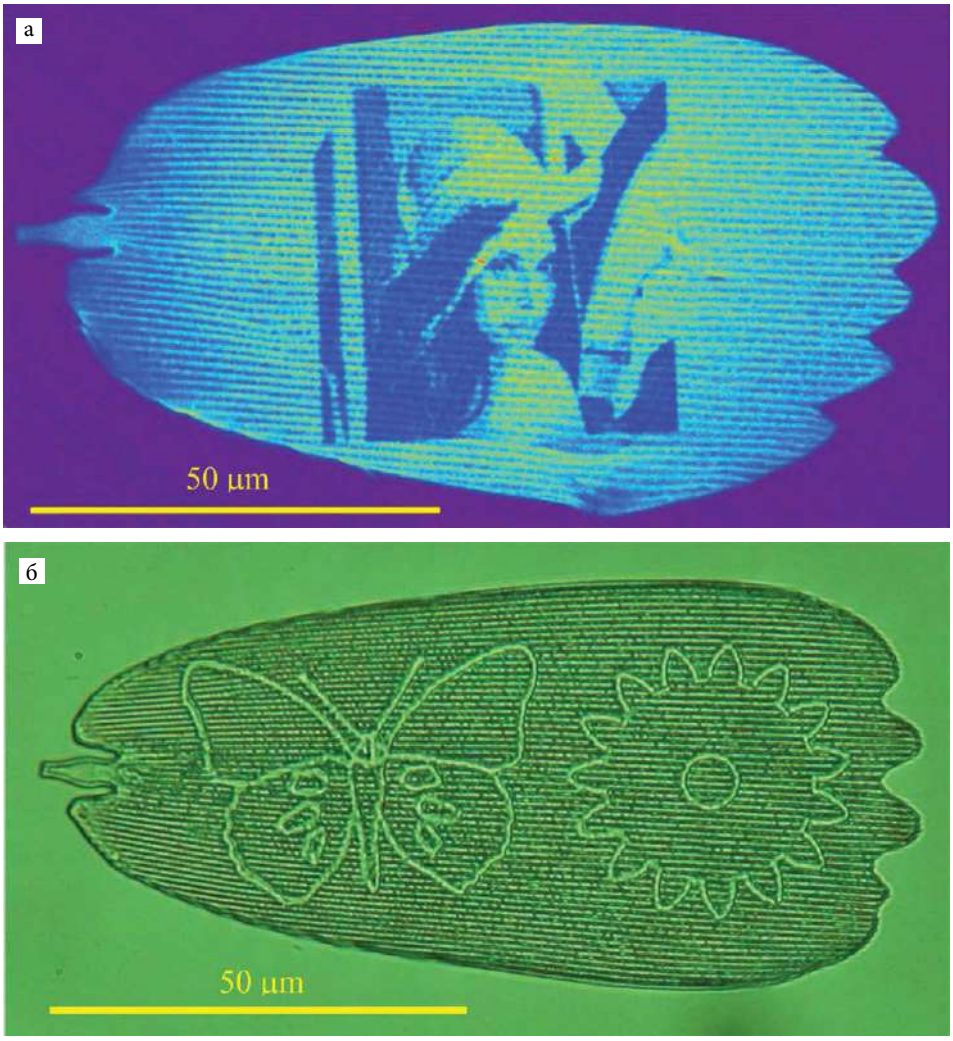

Слика 8. Слике добијене (а) ласерским избељивањем и (б) ласерским сечењем љуспице крила лептира *I. lathonia*

ЗАКЉУЧНА РАЗМАТРАЊА

Биомиметика, биоинспирација и функционализација биолошких структура су области које се веома интензивно развијају [52]. Широко су конципиране и тешко их је јасно дефинисати – можда је најисправније рећи да се више ради о погледу на свет него о јасно дефинисаном правцу истраживања [53]. Ипак, истраживања из ових области су обимна по броју објављених радова и веома значајна (мерено бројем цитата). Стога су се појавили и специјализовани часописи, попут "Bioinspiration and Biomimetics" или "Robotics and Biomimetics", а у реномираним научним часописима, као што су "Nature" и "Science", чести су радови из ових области. Сем тога, резултати су већ нашли и практичне, индустријске примене у области адхезива, дисплеја, козметике и др.

Свака техничка област истраживања лако може наћи свој пандан у живом свету: машинство – у необичној структури биолошких композита или механици покрета животиња, рачунарство – у комплексним неуронским мрежама животиња и еволуционим принципима, оптика – у интегументу или сложеним очима инсеката, хемија – у богатству биолошких супстанци, аеронаутика – у птицама и летећим инсектима а, нажалост, и војна наука има изванредног учитеља у живом свету, угледајући се на вечиту борбу за опстанак. Овом списку заиста нема краја и у томе је и велика привлачност биомиметике. У овој области, биолози и стручњаци из других области се налазе на заједничком задатку уочавања занимљивих особина живих организама и проналажењу начина да се ове особине искористе.

Инсекти су најбогатији извор инспирације због чињенице да је еволутивним развојем настало више милиона врста, а присутна је и велика разноврсност форми. И у Србији постоји велики број врста инсеката, али мало је доступних података о њиховим кутикуларним структурама од потенцијалног интереса за биомиметику. Мислимо да би било од великог практичног значаја да се направи нека врста илустрованог каталога микроструктура и нано-структура инсеката Србије, посебно за редове Lepidoptera и Coleoptera. Каталог би укључивао морфолошке карактеристике микроструктура и наноструктура кутикуле (очију, крила, антена, ногу и др.), али и њихове оптичке и механичке карактеристике. Тиме би се значајно олакшао посао будућим истраживачима у области биомиметике.

РЕФЕРЕНЦЕ

[1] Wood, R., Nagpal, R., Wei, G.-Y. (2013): Flight of the robobees. *Sci. Am.*, 308: 60–65.

[2] Lilienthal (1889): *Der Vogelflug als Grundlage der Fliegekunst. Ein Beitrag zur Systematik der Flugtechnik*, Berlin, R. Gaertners Verlagsbuchhandlung, p. 187.

[3] Gardner, M. (1970): Mathematical games: the fantastic combinations of John Conway's new solitaire game "life". *Sci. Am.*, 223: 120–123.

[4] Bonebeau, E., Dorigo, M., Theraulaz, G. (2000): Inspiration for optimization from social insect behaviour. *Nature*, 406: 39–42.

[5] Song, Y.M., Xie, Y., Malyarchuk, V., Xiao, Y., Jung, I., Choi, K.-J., Liu, Z., Park, H., Lu, C., Kim, R.-H., Li, R., Crozier, K.B., Huang, Y., Rogers, J.A. (2013): Digital cameras with designs inspired by the arthropod eye. *Nature*, 497: 95–99.

[6] Feng, L., Li, S., Li, Y., Li, H., Zhang, L., Zhai, J., Song, Y., Liu, B., Jiang, L., Zhu, D. (2002): Super-hydrophobic surfaces: from natural to artificial. *Adv. Mater.*, 14: 1857–1860.

[7] Dean, B., Bhushan, B. (2010): Shark-skin surfaces for fluid-drag reduction in turbulent flow: a review. *Phil. Trans. R. Soc. A*, 368: 4755–4806.

[8] Park, S.-H., Lee, S., Moreira, D., Bandaru, P.R., Han, I., Yun, D.-J. (2015): Bioinspired superhydrophobic surfaces, fabricated through simple and scalable roll-to-roll processing. *Sci. Rep.*, 5: 15430.

[9] Hamm, C.E., Merkel, R., Springer, O., Jurkojc, P., Maier, C., Prechtel, K., Smetacek, V. (2003): Architecture and material properties of diatom shells provide effective mechanical protection. *Nature*, 421: 841–843.

[10] Wegst, U.G.K., Bai, H., Saiz, E., Tomsia, A.P., Ritchie, R.O. (2015): Bioinspired structural materials. *Nat. Mater.*, 14: 23–36.

[11] Whitesides, G.M. (2015): Bioinspiration: something for everyone. *Interface Focus* 5: 20150031.

[12] Roberts, N.W., Chiou, T.-H., Marshall, N.J., Cronin, T.W. (2009): A biological quarter-wave retarder with excellent achromaticity in the visible wavelength region. *Nat. Photonics*, 3: 641–644.

[13] Darius, J., Thomas, P.K. (1981): Crosswires in a guiding eyepieces. *J. Phys. E: Sci. Instrum.*, 14: 761–765.

[14] Parker, A.R., Townley, H.E. (2007): Biomimetics of photonic nanostructures. *Nat. Nanotechnol.* 2: 347–353.

[15] Burrows, M., Sutton, G. (2013): Interacting gears synchronize propulsive len movements in a jumping insect. *Science*, 341: 1254–1256.

[16] Zheng, Y., Gao, X., Jiang, L. (2007): Directional adhesion of superhydrophobic butterfly wings. *Soft Matter*, 3: 178–182.

[17] Dirks, J.-H. (2016): Adhesion in insects. In: Bhushan, B. ed. *Encyclopedia of Nanotechnology*, 2nd ed., Dordrecht, Springer, pp. 1–10.

[18] Stavenga, D.G., Foletti, S., Palasantzas, G., Arikawa, K. (2006): Light on the moth-eye corneal nipple array of butterflies. *Proc. Roy. Soc. B*, 273: 661–667.
[19] Jeong, K.-H., Kim, J., Lee, L.P. (2006): Biologically inspired artificial compound eyes. *Science*, 312: 557–561.
[20] Garrett, N.L., Sekine, R., Dixon, M.W.A., Tilley, L., Bambery, K.R., Wood, B.R. (2015): Bio-sensing with butterfly wings: naturally occurring nano-structures for SERS-based malaria parasite detection. *Phys. Chem. Chem. Phys.*, 17: 21164–21168.
[21] Tan, Y., Gu, J., Xu, W., Chen, Z., Liu, D., Liu, Q., Zhang, D. (2013): Reduction of CuO butterfly wing scales generates Cu SERS substrates for DNA base detection. *ACS Appl. Mater. Interfaces*, 5: 9878–9882.
[22] Potyrailo, R.A., Ghiradella, H., Vertiatchikh, A., Dovidenko, K., Cournoyer, J.R., Olson, E. (2007): *Morpho* butterfly wing scales demonstrate highly selective vapour response. *Nat. Photonics*, 1: 123–128.
[23] England, G., Kolle, M., Kim, P., Khan, M., Muñoz, P., Mazur, E., Aizenberg, J. (2014): Bioinspired micrograting arrays mimicking the reverse color diffraction elements evolved by the butterfly *Pierella luna*. *Proc. Natl. Acad. Sci. USA*, 111: 15630–15634.
[24] Shi, N.N., Tsai, C.-C., Camino, F., Bernard, G.D., Yu, N., Wehner, R. (2015): Keeping cool: enhanced optical reflection and heat dissipation in silver ants. *Science*, 349: 298–301.
[25] Kahl, T., Bousack, H., Schneider, E.S., Schmitz, H. (2014): Infrared receptors of pyrophilous jewel beetles as model for new infrared sensors. *Sensor Rev*., 34: 123–134.
[26] Pris, A.D., Utturkar, Y., Surman, C., Morris, W.G., Vert, A., Zalyubovskiy, S., Deng, T., Ghiradella, H.T., Potyrailo, R.A. (2012): Towards high-speed imaging of infrared photons with bio-inspired nanoarchitectures. *Nat. Photonics*, 6: 195–200.
[27] Fox, D.L. (1976): *Animal Biochromes and Structural Colours: Physical, Chemical, Distributional & Physiological Features of Colored Bodies in the Animal World*, 2nd ed., Berkeley, University of California Press, p. 433.
[28] Huang, J., Wang, X., Wang, L.W. (2008): Bio-inspired fabrication of antireflection nanostructures by replicating fly eyes. *Nanotechnology*, 19: 025602.
[29] Rabasović, D.M., Pantelić, D.V., Jelenković, B.M., Ćurčić, S.B., Rabasović, M.S., Vrbica, M.D., Lazović, V.M., Ćurčić, B.P.M., Krmpot, A.J. (2015): Nonlinear microscopy of chitin and chitinous structures: a case study of two cave-dwelling insects. *J. Biomed. Opt.*, 20: 016010.
[30] Aguayo, D.D., Mendoza Santoyo, F., De la Torre-I, M.H., Salas-Araiza, M.D., Caloca-Mendez, C., Gutierrez Hernandez, D. A. (2010): Insect wing deformation measurements using high speed digital holographic interferometry. *Opt. Express*, 18: 5661–5667.

[31] Pantelić, D.V., Grujić, D.Ž., Vasiljević, D.M. (2014): Single-beam, dual-view digital holographic interferometry for biomechanical strain measurements of biological objects. *J. Biomed. Opt.*, 19: 127005.
[32] Martinez-Leon, L., Pedrini, G., Osten, W. (2005): Applications of short-coherence digital holography in microscopy. *Appl. Opt.*, 19: 3977–3984.
[33] Pantelić, D., Ćurčić, S., Savić-Šević, S., Korać, A., Kovačević, A., Ćurčić, B., Bokić, B. (2011): High angular and spectral selectivity of purple emperor (Lepidoptera: *Apatura iris* and *A. ilia*) butterfly wings. *Opt. Express*, 19: 5817–5826.
[34] Savić-Šević, S., Pantelić, D., Grujić, D., Jelenković, B., Ćurčić, S., Ćurčić, B., Stojanović, D. (2012): *Localization of light in photonic crystals of biological origin*, Conference Proceedings, 14th International Conference on Transparent Optical Networks (ICTON), Coventry, 02–05 July 2012. pp. 1–3.
[35] Pantelić, D., Savić-Šević, S., Grujić, D. (2013). Zoom system for measurement of coherent backscattering of light in micro- and nanomaterials. *Phys. Scr.*, T157: 014020.
[36] Liu, Y., Nolte, D., Pyrak-Nolte, L.J. (2010): Large-format fabrication by two-photon polymerization in SU-8. *Appl. Phys. A*, 100: 181–191.
[37] Siddique, R.H., Hünig, R., Faisal, A., Lemmer, U., Hölscher, H. (2015): Fabrication of hierarchical photonic nanostructures inspired by *Morpho* butterflies utilizing laser interference lithography. *Opt. Mater. Express*, 5: 996–1005.
[38] Savić-Šević, S., Pantelić, D. (2005): Relief hologram replication using a dental composite as an embossing tool. *Opt. Express*, 13: 2747–2754.
[39] Kang, S.-H., Tai, T.-Y., Fang, T.-H. (2010): Replication of butterfly wing microstructures using molding lithography. *Curr. Appl. Phys.*, 10: 625–630.
[40] Juodkazis, S., Rosa, L., Bauerdick, S., Peto, L., El-Ganainy, R., John, S. (2011): Sculpturing of photonic crystals by ion beam lithography: towards complete photonic bandgap at visible wavelengths. *Opt. Express*, 19: 5802–5810.
[41] Burgess, I.B., Aizenberg, J., Loncar, M. (2013): Creating bio-inspired hierarchical 3D-2D photonic stacks via planar lithography on self-assembled inverse opals. *Bioinspir. Biomim.*, 8: 045004.
[42] Gan, Z., Turner, M.D., Gu, M. (2016): Biomimetic gyroid nanostructures exceeding their natural origins. *Sci. Adv.*, 2: e1600084.
[43] Campbell, M., Sharp, D.N., Harrison, M.T., Denning, R.G., Turberfield, A.J. (2000): Fabrication of photonic crystals for the visible spectrum by holographic lithography. *Nature*, 404: 53–56.
[44] Wang, X., Gao, W., Hung, J., Tam, W.Y. (2014): Optical activities of large-area SU8 microspirals fabricated by multibeam holographic lithography. *Appl. Opt.*, 53: 2425–2430.

[45] Saranathan, V., Osuji, C.O., Mochrie, S.G., Noh, H., Narayanan, S., Sandy, A., Dufresne, E.R., Prum, R.O. (2010): Structure, function, and self-assembly of single network gyroid (I4132) photonic crystals in butterfly wing scales. *Proc. Natl. Acad. Sci. USA*, 107: 11676–11681.

[46] Pantelic, D., Rabasovic, M., Krmpot, A., Lazovic, V., Pavlovic, D. (2015): Security device individualized with biological particles. *PCT/EP2015/081398*.

[47] Pantelic, D., Rabasovic, M., Krmpot, A., Lazovic, V., Pavlovic, D. (2015): Security tag containing a pattern of biological particles. *PCT/EP2015/081400*.

[48] Van Renesse, R.L. (2005): *Optical Document Security*, 3rd ed., Boston-London, Artech House, p. 386.

[49] Nam, H., Song, K., Ha, D., Kim, T. (2016): Inkjet printing based mono-layered photonic crystal patterning for anti-counterfeiting structural colors. *Sci. Rep.*, 6: 30885.

[50] McNamara, M.E., Briggs, D.E.G., Orr, P.J., Wedmann, S., Noh, H., Cao, H. (2011): Fossilized biophotonic nanostructures reveal the original colors of 47-million-years-old moths. *PLoS Biol.*, 9: e1001200.

[51] Pantelic, D., Rabasovic, M., Krmpot, A., Lazovic, V., Pavlovic, D. (2015): Security tag with laser-cut particles of biological origin. *PCT/EP2015/081407*.

[52] Lepora, N.F., Verschure, P., Prescott, T.J. (2013): The state of the art in biomimetics. *Bioinspir. Biomim.*, 8: 013001.

[53] Vincent, J.F.V., Bogatyreva, O.A., Bogatyrev, N.R., Bowyer, A., Pahl, A.-K. (2006): Biomimetics: its practice and theory. *J. R. Soc. Interface*, 3: 471–482.

ЗАХВАЛНИЦА

Захваљујемо се Министарству просвете, науке и технолошког развоја Републике Србије за подршку кроз следеће пројекте: ОН171038, ОН173038, ИИИ45016 и ИИИ43002.

THE MORPHOLOGICAL STRUCTURES OF SOME REPRESENTATIVES OF THE ENTOMOFAUNA OF SERBIA AS MODELS IN BIOMIMETICS

Dejan PANTELIĆ, Srećko ĆURČIĆ, Aleksandar KRMPOT,
Dejan V. STOJANOVIĆ, Mihailo RABASOVIĆ, Svetlana SAVIĆ-ŠEVIĆ

S u m m a r y

Biomimetics, bioinspiration and functionalization of biological structures are disciplines of intense research. They are wide in scope but not easy to define – this is more a worldview, rather than a well defined research direction. Anyway, the research is voluminous measured by the number of scientific papers and very important by numerous citations. This is why specialized journals have appeared such as "Bioinspiration and Biomimetics" and "Robotics and Biomimetics", while renowned journals "Nature" and "Science" frequently publish papers in this area. Apart from this, the practical results have found the application in adhesives, displays, cosmetics, etc.

Each and every technical research area can find its counterpart in the living world: machine engineering in the unusual properties of biological composites or mechanics of animals, computing in the complex neural networks or evolutionary principles, optics in the integument and compound eyes of insects, chemistry in the richness of biological substances, aeronautics in birds and flying insects, and, regrettably, military science has an excellent teacher in the living world too, inspired by the eternal battlefield of survival. There is no end of this list, which is one of the main appeals of biomimetics. In this area, biologists and specialists in other disciplines have a common task of finding interesting properties of living organisms and discovering ways to use their properties.

Insects are the richest source of inspiration due to the number of several million species created during the evolutionary history, with the enormous diversity in both form and function. There is a great diversity of insect species in Serbia as well, but with a small amount of available information on the cuticular structures of interest for biomimetics. We think that it would be of practical interest to make an illustrated catalogue of the micro- and nano-structures of insects of Serbia, in particular for the orders of Lepidoptera and Coleoptera. Catalogue would include morphological characteristic of the micro- and nano-structures of (cuticle, eyes, wings, antennas, legs, etc.), but also their optical and mechanical properties. This will significantly facilitate the future research in biomimetics.

FIRST INTERNATIONAL CONFERENCE ON ELECTRON MICROSCOPY OF NANOSTRUCTURES

ELMINA 2018

ПРВА МЕЂУНАРОДНА КОНФЕРЕНЦИЈА О ЕЛЕКТРОНСКОЈ МИКРОСКОПИЈИ НАНОСТРУКТУРА

САНУ

August 27-29, 2018, Belgrade, Serbia
27–29. август 2018. Београд, Србија

Assessment of Three Microscopic Techniques in Observing Morphology of Pygidial Glands of Ground Beetles

Marija Nenadić[1], Aleksandar Krmpot[2], Nikola Vesović[1], Mihailo Rabasović[2], Srećko Ćurčić[1], Danica Pavlović[2], Vesna Lačković[3], Svetlana Savić-Šević[2] and Dejan Pantelić[2]

[1] *Institute of Zoology, University of Belgrade - Faculty of Biology, Belgrade, Serbia*
[2] *Institute of Physics, University of Belgrade, Belgrade, Serbia*
[3] *Institute of Histology and Embryology "Aleksandar Đ. Kostić", University of Belgrade - Faculty of Medicine, Belgrade, Serbia*

Pygidial glands represent an exocrine glandular system situated in abdomen of ground beetles and other representatives of the suborder Adephaga within the order Coleoptera [1]. This system plays a major role in the defense against predators [2] by discharging its products (secretions) outwards. It includes two sets of secretory lobes, collecting canals, collecting reservoirs and efferent ducts [1,3]. From a biological point of view, observing pygidial glands of ground beetles is important in taxonomy and promising due to potential medical significance of the secretions [4,5]. In order to better understand glandular functional mechanisms, it is necessary to examine the morphological aspects in detail.

Morphology of pygidial gland structures of certain ground beetle species (Insecta: Coleoptera: Carabidae) has been observed via three different microscopic techniques. Scanning electron microscopy (SEM), two-photon excitation fluorescence (TPEF) microscopy and conventional light microscopy (LM) were applied in order to identify complementarity of different methods of investigating the above-mentioned morphological structures. It is indisputable fact that the highest information content (level of details) on external morphology of biological structures is obtained by SEM. Examination of soft, fragile structures by SEM includes preparation of samples in a *series of alcohol/acetone* solutions of *increasing* concentrations up to 100% followed by a critical point drying (CPD), which is a well-established method for dehydrating biological tissues. In the case of pygidial glands of ground beetles, it has been noticed that tissue drying was excessive, resulting in the irreversible damage.

Samples somewhat changed their shape and their volume shrunk, precluding detailed analysis (Fig. 1a). This is not the case when CPD is omitted, and dehydration is applied only through a *series of ethanol* solutions of *increasing* concentrations (30, 50, 70, 90 and 100%) (Fig. 1b).

Concerning simplicity of different techniques, undeniable advantage must be given to LM (Fig. 2a), although the flaw of this technique is its insufficient informativity regarding a detailed insight into micro- and nanostructures of pygidial gland system (e.g., arrangement of reservoir myofibrils; diameter of collecting and efferent ducts; diameter, thickness and a more detailed structure of radial canals of secretory lobes). Additional three-dimensional information is obtained by TPEF (Fig. 2b). On the basis of all advantages/disadvantages of the three microscopy techniques compared, it can be concluded that the combination of SEM and TPEF enables the most detailed morphological and anatomical surveys of analyzed biological structures [6].

References:

[1] A Giglio *et al*, ZooKeys 100 (2011), 193-201.
[2] K Dettner, Annual Review of Entomology **32** (1987), 17-48.
[3] DJ Forsyth, Transactions of the Zoological Society of London **32** (1972), 249-309.
[4] M Nenadić *et al*, Bulletin of Entomological Research **106** (2016), 474-480.
[5] M Nenadić *et al*, The Science of Nature **103** (2016), 34.
[6] This study is financially supported by the Serbian Ministry of Education, Science and Technological Development (Grants Nos. ON173038, ON171038 and III45016).

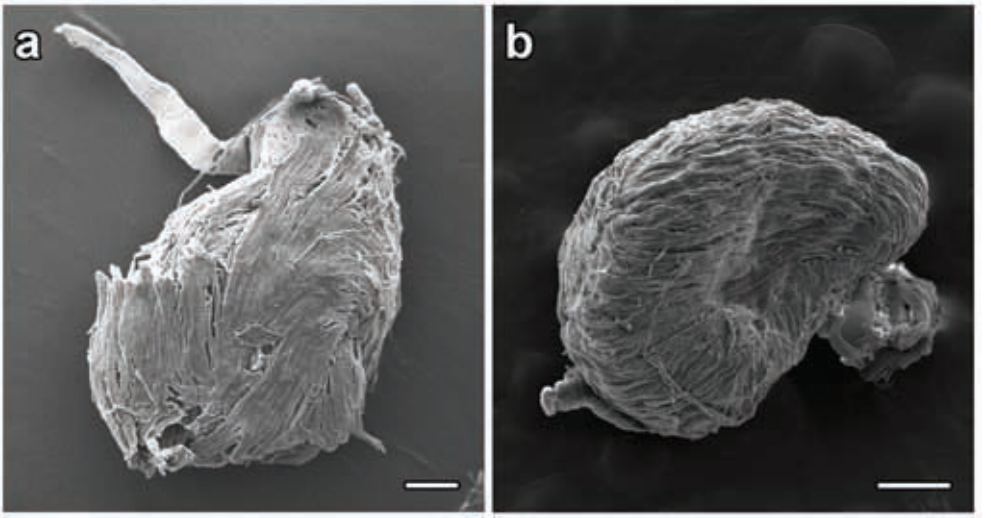

Figure 1. Morphology of a muscle-coated collecting reservoir of pygidial glands of ground beetle species *Laemostenus* (*Pristonychus*) *punctatus* (Dejean, 1828). SEM image after treating sample with CPD (a) and without this procedure (b). Scales: 200 μm.

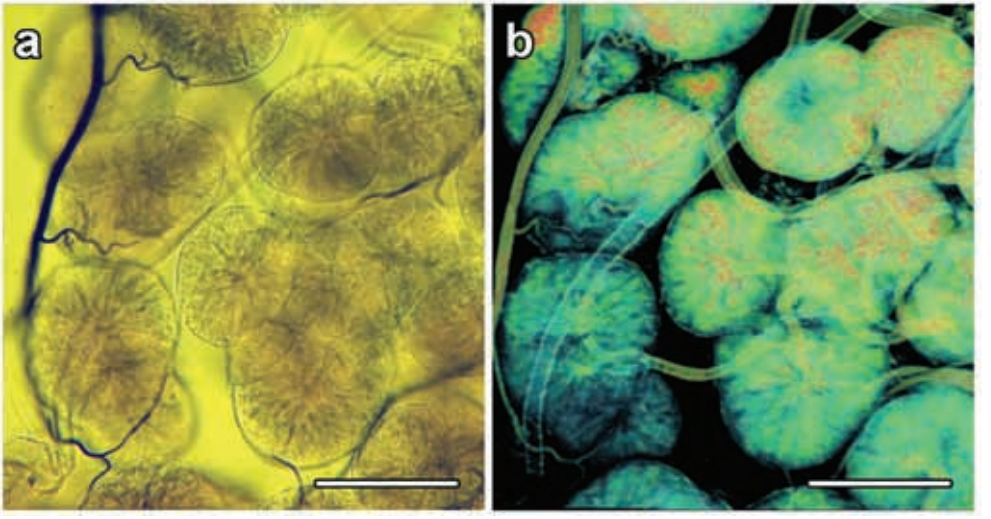

Figure 2. Pygidial gland secretory lobes associated with afferent ducts of ground beetle species *Carabus* (*Eucarabus*) *ullrichii* Germar, 1824. Comparison of images taken using LM (a) and TPEF microscopy (b). Scales: 100 μm.

UNIVERZITET U BEOGRADU
Institut za fiziku

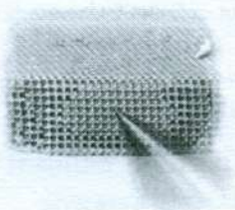

Konferencija

Sedma radionica fotonike (2014)

Zbornik apstrakata

PHOTONICS CENTER

Kopaonik, 10.-14.3.2014.

Konferencija **Sedma radionica fotonike 2014**
ZBORNIK APSTRAKATA
Kopaonik 10-14.3.2014.

Izdaje
Institut za fiziku Univerziteta u Beogradu

Za izdavača
dr Aleksandar Belić, direktor

Urednci
dr Aleksander Kovacević
dr Dragan Lukić

Tiraž
100 primeraka

ISBN 978-86-82441-39-7

Štampa
Razvojno-istraživački centar,
Tehnološko-metalurškog fakulteta u Beogradu
Karnegijeva 4, Beograd

CIP - Каталогизација у публикацији
Народна библиотека Србије, Београд

535(048)
681.7(048)
66.017/.018(048)

КОНФЕРЕЦИЈА радионица фотонике (7 ; 2014 ; Копаоник)
Zbornik apstrakata / Konferencija Sedma radionica fotonike (2014), Kopaonik, 10.-14.3.2014. ;[urednici Aleksander Kovacević, Dragan Lukić]. - Beograd : Institut za fiziku, 2014 (Beograd : Razvojno-istraživački centar grafičkog inženjerstva TMF). - XI, 52 str. :ilustr; 25 cm

Na vrhu nasl. str.: Univerzitet u Beogradu. - Apstrakti na srp. i engl. jeziku. - Tekst ćir. i lat. - Tiraž 100. - Reč urednika: str. VII. - Registar.

ISBN 978-86-82441-39-7

a) Оптика - Апстракти b) Оптоелектроника - Апстракти c) Технички материјали - Апстракти
COBISS.SR-ID 205669644

Programski i organi

dr Aleksandar Krm
Odbora)

dr Aleksander Kov
Zbornika i Sajta)

dr Dragan Lukić, vi

Akademik dr Branis

Sponzori Konferenc

Ministarstvo prosve

Optičko društvo Srb

„Senzor Infiz" d.o.o

Kompleksne fotonske strukture u biopolimeru

Svetlana Savić-Šević, Dejan Pantelić, Branislav Jelenković

Institut za fiziku, Univerzitet u Beogradu, Pregrevica 118, 11080 Zemun, Srbija

Kontakt: S. Savić-Šević (savic@ipb.ac.rs)

Apstrakt. Kompleksne fotonske strukture generisane su u biopolimeru. Kao biopolimer korišćen je polisaharid, pululan, dopiran jonima hroma. Strukture su formirane kombinacijom holografske metode i fazne separacije. Holografskom metodom formirana je zapreminska refleksiona rešetka. U eksperimentu je korišćen jednomodni Nd-YAG laser, talasne dužine 532 nm. Eksponirani slojevi su hemijski obrađeni.

Fotonske strukture su karakterisane korišćenjem visoko rezolucionog skenirajućeg elektronskog mikroskopa sa elektronskim topom Šotkijevog tipa. Formirane su linearne i sferne (onion-like) višeslojne Bregove strukture. U Bregovim ravnima zarobljene su šuplje sfere pululana koje su formirane u procesu fazne separacije u toku hemijske obrade materijala.

Sa ciljem optičke karakterizacije ovih kompleksnih struktura mereni su transmisioni spektri korišćenjem spektrometra.

UNIVERZITET U BEOGRADU
Institut za fiziku

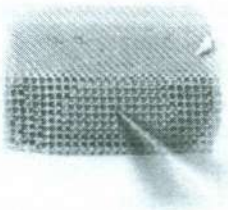

Konferencija

Osma radionica fotonike (2015)

Zbornik apstrakata

PHOTONICS
CENTER

Kopaonik, 8.-12.3.2015.

Konferencija **Osma radionica fotonike 2015**
ZBORNIK APSTRAKATA
Kopaonik 8-12.3.2015.

Izdaje
Institut za fiziku Univerziteta u Beogradu

Za izdavača
dr Aleksandar Belić, direktor

Urednik
dr Dragan Lukić

Tiraž
100 primeraka

ISBN 978-86-82441-41-0

Štampa
Razvojno-istraživački centar,
Tehnološko-metalurškog fakulteta u Beogradu
Karnegijeva 4, Beograd

CIP - Каталогизација у публикацији
Народна библиотека Србије, Београд

535(048)
681.7(048)
66.017/.018(048)

КОНФЕРЕЦИЈА Радионица фотонике (8 ; 2015 ; Копаоник)
Zbornik apstrakata / Konferencija Osma radionica fotonike (2015), Kopaonik, 8.-12. 3. 2015. ; [urednik Dragan Lukić]. - Beograd : Institut za fiziku, 2015 (Beograd : Razvojno-istraživački centar grafičkog inženjerstva TMF). - XII, 46 str. : ilustr. ; 25 cm

Na vrhu nasl. str.: Univerzitet u Beogradu. - Apstrakti na srp. i engl. jeziku. - Tiraž 100. - Reč urednika: str. VII. - Registar.

ISBN 978-86-82441-41-0 (broš.)

a) Оптика - Апстракти b) Оптоелектроника - Апстракти c) Технички материјали - Апстракти

COBISS.SR-ID 213633292

Ordered multilayer structure with randomly distributed nanospheres and nanopillars

Svetlana Savić-Šević, Dejan Pantelić, Dušan Grujić, Branislav Jelenković

Institute of Physics, University of Belgrade, Pregrevica 118, 11080 Zemun, Belgrade, Serbia

Contact: Svetlana Savić-Šević (savic@ipb.ac.rs)

Abstract. Complex nanostructures with interesting properties for photonic applications received great attention [1]. Here we present structures having both ordered and disordered components, integrated into novel photonic structure. Photonic structure consisting of ordered multilayer grating and randomly distributed nanospheres and nanopillars is fabricated through a combination of holographic method and non-solvent induced phase separation in a polysaccharide-based material. We show that the interplay between regularity and irregularity significantly increases the width of the photonic bandgap, which can be wide about two hundred nanometers. The resulting photonic material has properties of both ordered photonic crystals (band gap and high reflectivity) and disordered structures (weak localization, as a precursor to Anderson localization).

Photonic structures are recorded in Pullulan, a linear homo-polysaccharide produced by micro-organisms (*Aureobasidium pullulans*) [2], doped with ammonium dichromate - (DCP). Multilayer structures were fabricated as a volume Bragg reflection grating using a simple counter-propagating beam configuration. DCP was exposed with a single longitudinal mode, diode pumped Nd-YAG laser, at 532 nm.

The morphology of the resulting photonic structure was investigated using a high resolution scanning electron microscope equipped with a high brightness Schottky Field Emission gun (FEGSEM).

REFERENCES

[1] W. G. Bae, H. N. Kim, D. Kim, S. H. Park, H. E. Jeong, K. Y.Suh, *Adv. Mater.* **26**, (2014) 675–700.

[2] V. Prajapati, G. Jani, and S. Khanda, *Carbohyd. Polymers* **95**, (2013) 540–549.

THE UNIVERSITY OF WARWICK

14th International Conference on Transparent Optical Networks

2nd - 5th July, 2012

University of Warwick, Coventry, UK

co-located with:

- 11th European Symposium on Photonic Crystals (ESPC)
- 11th Workshop on All-Optical Routing (WAOR)
- 9th Global Optical & Wireless Networking Seminar (GOWN)
- 8th Reliability Issues in Next Generation Optical Networks Workshop (RONEXT)
- 8th Photonic Integrated Components & Applications Workshop (PICAW)
- 7th Nanophotonics for All-Optical Networking Workshop (NAON)
- 7th Special Session on Photonic Atoms & Molecules (PAM - former MPM)
- 7th Special Industrial Session
- 6th Special Session on Novel Glasses for photonic devices
- 5th Special Session on Market in Telecommunications (MARS)
- 4th ACCORDANCE Workshop on Broadband Access
- 3rd Workshop on Communication in Transportation Systems (CTS)
- 2nd Workshop on Green Optical Communications (GOC)
- 2nd Special Session on Intelligent Systems for Optical Networks Design (ISOND)
- 2nd Special Session on Microwave Photonics (MP)
- Sub-Wavelength Photonics Workshop (SWP)
- EU FP7 Project SOFI Special Session on Silicon Photonics Based Components
- EU FP7 Project NAVOLCHI Special Section on Plasmonics Based Components
- Optical Wireless Workshop (OWW)
- Tutorial on "Optical Interconnects for Future Data Center Networks"
- Tutorial on "Optical OFDM"

IEEE Catalog Number: CFP12485-USB
ISBN: 978-1-4673-2227-0

Formal publisher:
National Institute of Telecommunications
Department of Transmission and Optical Technologies
1 Szachowa Street, Warsaw, Poland.

Editors: Marek Jaworski, Marian Marciniak

Copyright and Reprint Permission: Abstracting is permitted with credit to the source. Libraries are permitted to photocopy beyond the limit of U.S. copyright law for private use of patrons those articles in this volume that carry a code at the bottom of the first page, provided the per-copy fee indicated in the code is paid through Copyright Clearance Center, 222 Rosewood Drive, Danvers, MA 01923. For other copying, reprint or republication permission, write to IEEE Copyrights Manager, IEEE Operations Center, 445 Hoes Lane, Piscataway, NJ 08854. All rights reserved. Copyright © 2012 by IEEE.

Localization of Light in Photonic Crystals of Biological Origin

Svetlana Savić-Šević[1], Dejan Pantelić[1], Dušan Grujić[1], Branislav Jelenković[1]*, Srećko Ćurčić[2], Božidar Ćurčić[2], Dejan Stojanović[3]

[1]*Institute of Physics, University of Belgrade, Pregrevica 118, 11080 Zemun, Belgrade, Serbia*

[2]*Institute of Zoology, Faculty of Biology, University of Belgrade, Studentski Trg 16, 11000 Belgrade, Serbia*

[3]*Fruška Gora National Park, Zmajev Trg 1, 21208 Sremska Kamenica, Serbia*

**Corresponding author's e-mail: branaj@ipb.ac.rs*

ABSTRACT

Structures similar to those found on butterfly wings were produced holographically on thin layers of dichromated pullulan. Light propagation and scattering is studied in these nanometre periodic structures, and in the wings of Lepidoptera (moths and butterflies). We have found that the width of photonic band-gaps in each case is influenced by light localization (either weak or strong), due to certain amount of disorder. We have also measured experimentally characteristics of backscatter signal (amplitude and angular width) on wings of *Apatura ilia* butterfly as well as on *Diachrysia chrysitis* and *Autographa bractea* noctuid moths. It was found that both spectral and scattering characteristics of the artificial material could mimic those found in butterflies and moths.

1. INTRODUCTION

Photonic structures are frequently found in living organisms, especially in insects [1]. The evolution produces intricate patterns which generate iridescent coloration by physical mechanisms like interference, diffraction or scattering. The final result is better adaptation of an organism to its environment through crypsis, aposematism or mimicry.

Photonic crystals introduce photonic band-gap, thus significantly altering spectral properties of the material. It was thought that high refractive index modulation is a necessary condition for achievement of wide band gaps. However, disorder in photonic crystals significantly widens the band gap even for materials with low refractive index. Indeed, insects are an excellent example of such behavior – the refractive index of insect chitin (the main constituent of integument) is rather low (of the order of 1.5), but the band-gap can be rather wide, as in *Morpho* butterflies [2].

Disordered photonic crystals are an interesting research topic, due to interesting possibility of weak or strong (Anderson) light localization [3]. In that respect measurement of coherent backscattering is important as it gives information on the mean free path of light [4]. This enables estimation of the fulfilment of Ioffe-Regel criterion ($k \cdot l < 1$ where k is wave-number and l is mean free path) as a border between strong and weak localization.

We have previously analyzed optics and biological significance of nanometer size structures on the wings of *Apatura ilia* (Denis & Schiffermüller, 1775) and *A. iris* (Linnaeus, 1758) butterflies [5]. In the present paper we intend to investigate the contribution of backscattering and localization to overall optical properties of *Apatura ilia* and two interesting species of moths (*Autographa bractea* (Denis & Schiffermüller, 1775) and *Diachrysia chrysitis* (Linnaeus, 1758)).

Apatura ilia butterfly is an interesting insect whose wings show, angularly and spectrally rather limited, UV-purple iridescence (Fig. 1a). On the other hand *Autographa bractea* and *Diachrysia chrysitis* are moths exhibiting patches with golden color (Figs. 2a and 3a). We have measured their wide backscattering cones which are very close to Ioffe-Regel criterion, but still in the weak localization zone.

2. EXPERIMENTAL SETUP

We have built a setup for measurement of backscattered radiation. Unpolarized HeNe laser (633 nm wavelength) was used as a light source. Laser beam was transmitted through a combination of a linear polarizer and a quarter-wave plate in order to produce circularly polarized light. The sample was irradiated and observed through non-polarizing beam-splitter. A second wave plate and linear polarizer were placed in scattered beam. Condenser was used to efficiently couple the scattered radiation into entrance pupil of a camera (Canon EOS 50D with zoom objective 17-85 mm). In this way we were able to observe backscattering cone with different magnifications and resolution.

We used milk and Teflon (PTFE) for calibration purposes as it is known that they possess a narrow backscattering peak (bellow the resolution of our camera at low magnification) and behaves as Lambert scatterer (Fig. 4a). Barium sulphate reflectance standard was also used as a material with wide backscattering cone (see Fig. 4b), due to short mean free path.

978-1-4673-2229-4/12/$31.00 ©2012 IEEE

a) b)

Figure 1: a) Apatura ilia butterfly; b) A. ilia backscattering cone.

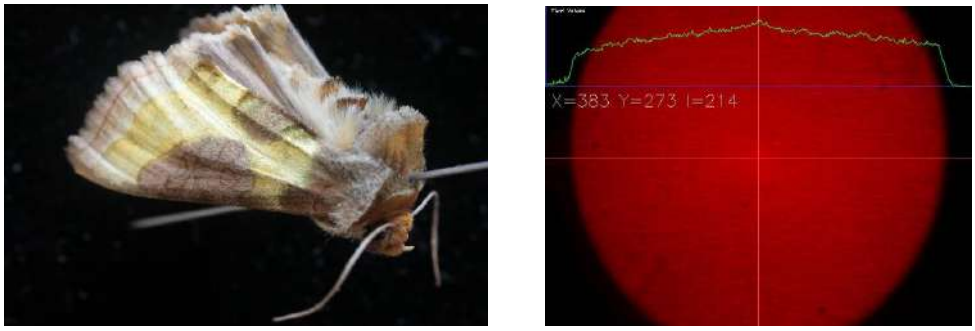

a) b)

Figure 2: a) Diachrysia chrysitis; b) D. chrysitis backscattering cone

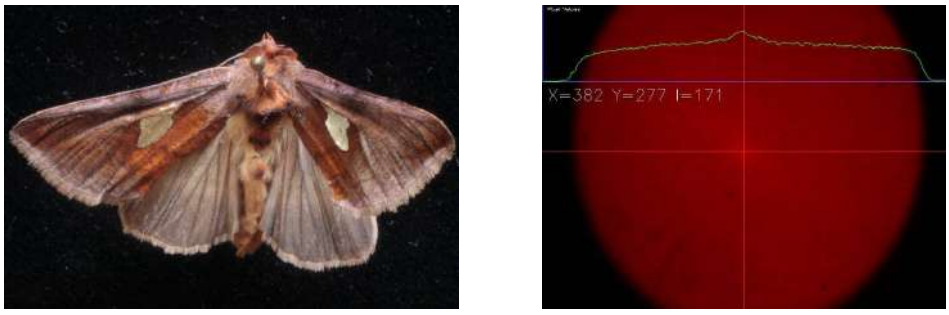

a) b)

Figure 3: a) Autographa bractea; b) A. bractea backscattering cone.

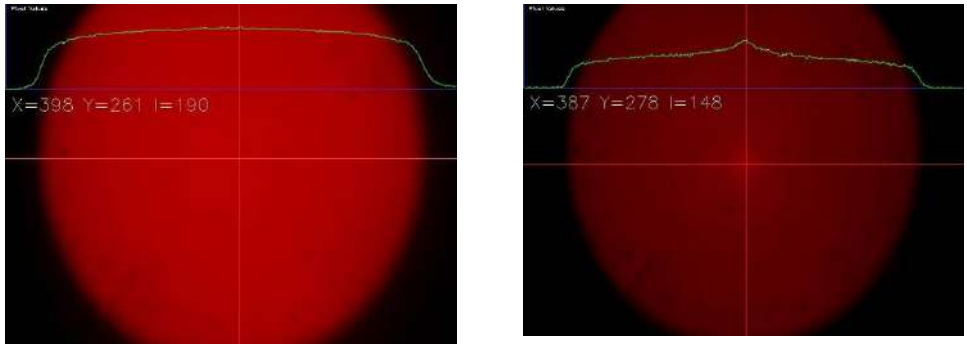

a) b)

Figure 4. Backscattering cone of: a) milk, b) barium sulphate ($BaSO_4$).

We have found that the backscattering cone of *Apatura ilia* and *Diachrysia chrysitis* (Figs. 1b and 2b) is significantly wider compared to barium-sulphate (see Fig. 5). By fitting experimental results to theory we have found that the mean free path is approximately 200 nm (In terms of Ioffe-Regel criterion $k\,l$ product is 2), in

contrast to 400 nm for barium sulphate, which is the same as in the case of *Autographa bractea* (Figs. 3b and 4b). As can be seen, for *A. ilia* and *D. chrysitis* scattering is quite close to Anderson localization.

This seems to be consistent with the anatomy of scales which cover wings of lepidopera. Photonic structures are a combination of volume Bragg and surface relief grating and examination under scanning electron microscope reveals numerous defects and disorder [6]. Judging by the width of backscattering cone and mean free path, light is "expelled" from the butterfly wings for two reasons: band-gap produced by regular structures and weak localization due to disorder.

In order to mimic structure of butterfly scales we used volume holography to generate Bragg gratings and direct laser writing to superpose surface relief grating. Dichromated pullulan was used as a photosensitive material. Depending on exposure and chemical processing we are able to manufacture photonic structures whose color ranges from purple to golden, just like in previously described insects. Scattering properties artificial material are almost the same as in insects.

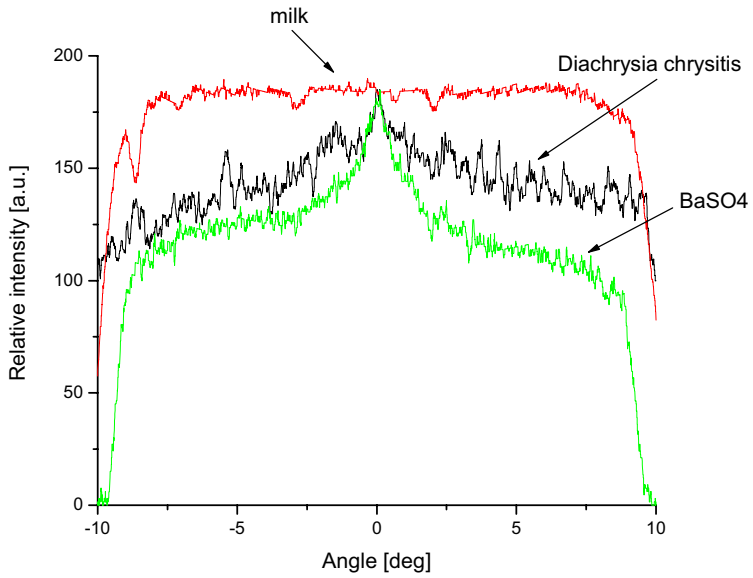

Figure 5. Comparison of backscattering cones of milk (identical to teflon), barium suplhate and Diachrysia chrysitis.

3. CONCLUSIONS

We have measured the coherent backscattering on the wings of three insects exhibiting iridescent coloration. The width of backscattering cone indicates that the mean free path of light is rather short (between 200 and 400 nm depending on the species). It looks that the interplay between band-gap and localization results in characteristic color of insects. We have succeeded in mimicking biological structures using holography.

REFERENCES

[1] S. Berthier, *Iridescences – The Physical Colors of Insects*, (2007) Springer Science + Business Media, LLC

[2] S. Yoshioka, S. Kinoshita, Wavelength-selective and anisotropic light-diffusing scale on the wing of the *Morpho* butterfly, *Proc. R. Soc. Lond. B*, 271 (2004), p. 581-587

[3] T. Schwartz, G. Bartal, S. Fishman, M. Segev, Transport and Anderson localization in disordered two-dimensional photonic lattices, *Nature*, 446 (2007), p. 52–55

[4] D. S. Wiersma, P. Bartolini, A. Lagendijk, R. Righini, Localization of light in a disordered medium, *Nature*, 390 (1997), p. 671 - 673

[5] D. Pantelić, S. Ćurčić, S. Savić-Šević, A. Korać, A. Kovačević, B. Ćurčić, B. Bokić, High angular and spectral selectivity of Purple Emperor (Lepidoptera: Apatura iris and A. ilia) butterfly wings, *Opt. Express* 19, (2011) p. 5817-5826

[6] S. B. Ćurčić, D. V. Pantelić, B. P.M. Ćurčić, S. N. Savić-Šević, S. E. Makarov, V. B. Lačković, M. M. Labudović-Borović, N. B. Ćurčić, D. V. Stojanović, Micro- and nanostructures of iridescent wing scales in purple emperor butterflies (Lepidoptera: Apatura ilia and A. iris), to be published in *Microscopy Research and Technique*, DOI: 10.1002/jemt.22021.

Application of Tot'hema Eosin Sensitized Gelatin Film for Adaptive Microlenses

BRANKA D. MURIĆ, University of Belgrade,
Institute of Physics, Belgrade
DEJAN V. PANTELIĆ, University of Belgrade,
Institute of Physics, Belgrade
DARKO M. VASILJEVIĆ, University of Belgrade,
Institute of Physics, Belgrade
SVETLANA N. SAVIĆ-ŠEVIĆ, University of Belgrade,
Institute of Physics, Belgrade
BRANISLAV M. JELENKOVIĆ, University of Belgrade,
Institute of Physics, Belgrade

Original scientific paper
UDC: 617.7-76
DOI: 10.5937/tehnika1706787M

In this paper we showed that tot'hema eosin sensitized gelatin (TESG) film can be used for adaptive microlenses fabriacation. The mechanical properties of a pure gelatin film were improved by adding tot'hema solution. We found that the elasticity of TESG film depend on the tot'hema concentration. By stretching the film, the microlenses were deformed uniaxially, and microlenses focal length can be tuned. The achieved microlenses focal lengths range from 0.05 to 0.2 mm.

Key words: *gelatin film, eosin, tot'hema, adaptive microlenses, optical properties, mechanical properties*

1. INTRODUCTION

Optical lenses are widely used in science, industry, and daily life. Microlenses are lenses with dimensions smaller than 1mm. It can be used, either individually or as microlens arrays, in a various applications such as: wavefront sensors, medicine, quantum computer research and so on [1-7].

Direct laser writing, photolithography, and thermal reflow, as well as copying techniques such as hot embossing, and injection molding are various methods of microlens fabrication [8-14].

Various materials such as polymers, photosensitive glass, composites, and many other are used in the microlens fabrication[15-20].

Development of tunable lenses with variable focal lengths is very important for different applications. It can be used in eyeglasses for vision correction, zooming devices in photocameras and integrated in many electrooptical systems. Also, adapive microlenses is significant for tunable photonic waveguides, miniature optical sensing, electronic display, and widezoom cell phone [21-24].

Today, in many cases is necessary to use adaptive microoptical devices, primarily microlenses. In most optical devices, microlenses have an important role in a focusing, imaging, detection, etc. Different variants of adaptive microlenses arrays were proposed [25, 26].

Gelatin is a biocompatible and biodegradable polymer extensively used in food, pharmaceutical, biophysics and biomedical fields. Poor mechanical properties of gelatin film can be improved by crosslinking with various chemical agents such as formaldehyde, epoxy compounds, genipin and glutaraldehyde (GTA) [27–29].

Previously, by modifying the gelatin with tot'hema solution, we improved the mechanical properties of the brittle film of pure gelatin. So we get a film based on gelatin doped with tot'hema and sensitized with eosin dye [30–33], (denoted as tot'hema-eosin sensitized gelatin, abbreviated as TESG.

The TESG film is easy to prepare, low cost nontoxic, and became stretchable by adding tot'hema

Author's address: Branka Murić, University of Belgrade, Institute of Physics, Belgrade, Pregrevica 118
e-mail: muric@ipb.ac.rs
Paper received: 01.12.2017.
Paper accepted: 08.12.2017.

solution. On the film microlenses can be formed by direct laser writing. Our main intention was to use TESG, as biocompatible, thermally stable, soft and elastic material, for tunable microlens fabrication. The microlenses with different diameter and depth were produced on a TESG layer using Nd:YAG laser light (2nd harmonic wavelength of 532 nm).

In this paper, TESG microlenses focal length tunability was obtained by applying controlled strain. The produced adaptive concave TESG microlenses (individual or microlens array) are suitable for numerous applications. Also, they can be copied onto polydimethylsiloxane (PDMS) and used as convex lenses. The shape change of TESG microlenses (and consequently the focal length) was reversibly changed as the applied strain is inside the elastic limit, that be presented in our future work.

2. EXPERIMENTAL PROCEDURE

Film preparation

All chemical components used for the film preparation are easily available, cheap and nontoxic. Tot'hema (Laboratoire Innotech International-France) - the trade name of a mixture of iron gluconate (equivalent to 50 mg iron), manganese gluconate (equivalent to 1.33 mg manganese), copper gluconate (equivalent to 0.7 mg copper) and excipients. It is a drinkable solution frequently used to treat anemia.

The 100 ml of 5% aqueous gelatin (Gelatin from bovine skin gel strength ~225 g Bloom, Type B, Sigma) solution with 20% of sodium chloride (puriss, p.a. Sigma Aldrich) by weight of dry gelatin, and 0.3 ml of 1% aqueous eosin (5wt.% in H_2O, Sigma Aldrich) solution was prepared as describred previously [31, 32]. The five TESG solutions with different tot'hema concentrations (5%, 10%, 15%, 20%, and 30% v/v) were made.

TESG film was prepared by the gravity-settling method pouring 2 ml of TESG solution onto a leveled and cleaned microscope glasses slide covered with a very clean thermoplastic foil. The net result is a film, which is highly absorptive in the green part of the spectrum, permanently soft and elastic. Dried film can be easily removed from the foil. It can be peeled from one substrate and placed on another (plane or curved). The film was dumbbell-shaped specimens cut by the brass mold made according to the standards for elastic materials (ASTM D412).

Microlens fabrication

If TESG film irradiated with laser radiation in the green part of spectrum, (direct, focused or unfocused) laser beam produces lens like-dips. We have shown that concave microlenses can be produced by direct laser writing using second harmonic Nd:YAG laser (wavelength of 532 nm). Microlens formation was followed by the creation of a diffraction picture on a diffuse screen, with millimeter scale, placed behind the film. This pattern was recorded by a CCD camera. The used experimental setup is shown in Figure 1. The laser power of 60 mW and exposure time of 20 s was used in experiment.

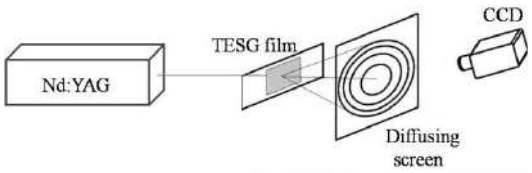

Figure 1 – Experimental setup for microlens fabrication

Film thickness

Film thickness was measured with a digital micrometer with 0.01 mm accuracy. Six thickness measurements were taken for each TESG film, and the averages were taken as the result.

Water content of TESG film

To estimate varying of water content during the film dehydration, the TESG films were weighed (m_w), dried at ambient temperature (20±2°C) for different time, and weighted (m_d) again. Water content (or moisture content) was determined as the percentage of initial TESG film weight lost during drying and reported on a wet basis i.e:

$$\%\, moisture\ content = 100(m_w - m_d)/m_w$$

Triplicate measurements of water content were done for each film, and an average was taken as the result.

Swelling of TESG film

TESG films were weighted in air-dried conditions (W_d). Afterward, they were immersed in a physiological saline solution, containing 9 g/l sodium chloride, for different time periods. Wet samples were wiped with filter paper to remove excess of liquid and reweighted (W_w). The amount of adsorbed water was calculated:

$$W(\%) = 100(W_w - W_d)/W_d$$

Stress−Strain Measurements

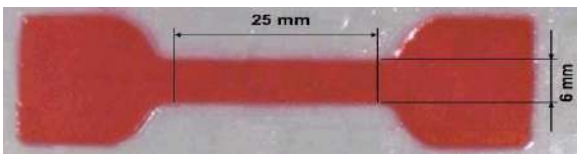

Figure 2 – TESG films used for tensile testing with dimensions according to the ASTM standards (gauge length 25 mm, width 6 mm)

Stress−strain measurements of TESG films were determined in a tensile stress testing machine. Tests were carried out at 25 °C with a strain rate of 20 mm/min, using dumbbell-shaped film (see Figure 2) mounted at a specified gauge length (25 mm) into the system.

Using the appropriate software recorded force and corresponding displacement were recalculated into stress and strain.

The average value of five measurements for every film was calculated. The video camera was used to record the tensile responses of all films.

SEM analysis of microlenses

The morphology of produced TESG microlenses were investigated using a high resolution scanning electron microscope equipped with a high brightness Schottky field emission gun (FEGSEM).

3. RESULTS AND DISCUSSIONS

Variation of water content in TESG films with different tot'hema concentration with drying time is presented in Figure 3.

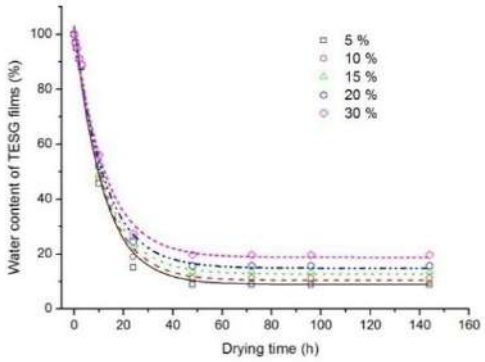

Figure 3 – Variation of water content of TESG films with drying time

It can be seen that the water content of each TESG films decreases with drying time up to 48 hour. After drying of two days, there is no additional change in the water content for all TESG films.

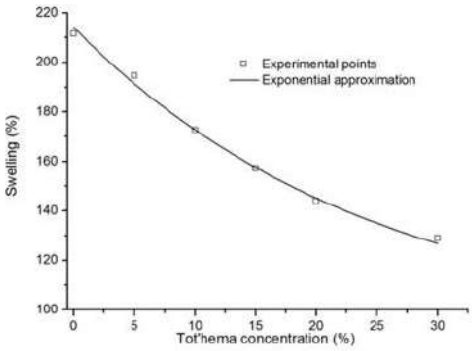

Figure 4 – Swelling of gelatin films as a function of tot'hema concentrations

The degree of swelling of pure gelatin films stored in physiological solution increases up to about 220 % after 24 h. Tot'hema induces a reduction of swelling. From Figure 4 can be seen that swelling of TESG films exponentially decreases with increasing of tot'hema concentration. We found that swelling improve the film elasticity.

During a laser irradiation, eosin bleaches, thus making TESG film colorless. In this case, as result of dye discolouration under the influence of optical radiation the transparent microlenses are formed, as can be seen in Figure 5.

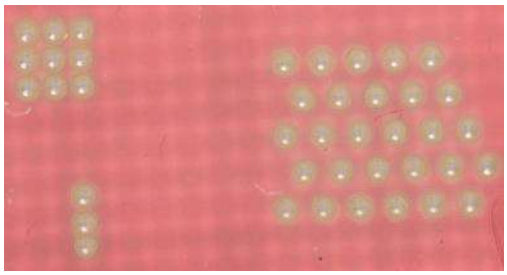

Figure 5 – Transparent 3x3 microlens array, and row of three microlenses (left) and hexagonal microlens array (right) on the TESG film

Figure 6 shows the stretching of microlens formed in the centre of a dumbbell-shaped TESG film.

Figure 6 – The TESG microlens on the dumbbell-shaped TESG film: 1) unstretched; and 2) stretched

The stretching value can be read on the ruler located parallel to film. It can be seen that TESG film stretched from the initial 25 mm to 80 mm.

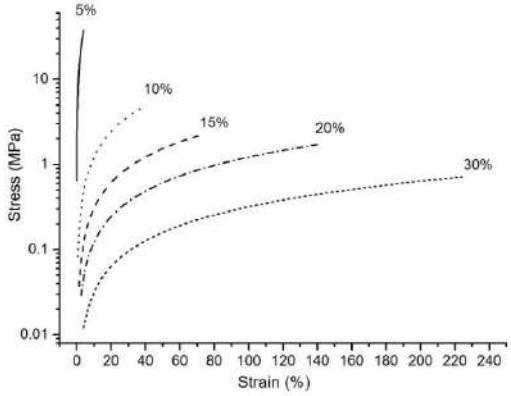

Figure 7 – Stress versus strain curves of TESG films

The results of uniaxial stress–strain measurements for all examined films are shown in Figure 7. The tensile responses of TESG films were measured up to the breaking point. As can be seen, mechanical

properties of TESG films strongly depend on the tot'hema concentrations. The extensibility of the films increases, with increasing of tot'hema concentration up to 250%..

The Young's modulus, the stress at break and the deformation at break of the films were calculated from the stress–strain curves. We found that Young's modulus and stress at break considerably decrease with increasing of tot'hema concentration.

Further we investigated the microlenses uniaxial stretching. Microlenses fabrication is followed by formation of diffraction picture on the diffuse screen. The recorded diffraction pictures extensions on a screen with a millimeter scale are shown in Figure 8.

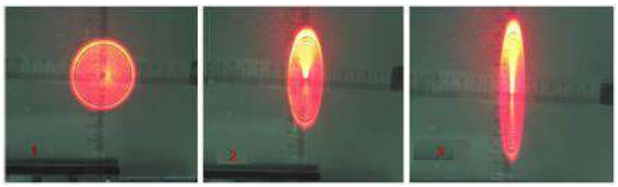

Figure 8 – Diffraction picture recorded after the TESG microlens was: 1) formed; 2) and 3) stretched in one direction. Millimeter scale is visible.

The toric microlenses were produced due to the uniaxial strain. The astigmatic microlenses have two focal lengths along orthogonal directions. For uniform extension (along x and y direction) sphericity of microlenses can be retained.

It was shown that produced TESG microlenses change their optical properties, for example focal length, in response to material elasticity.

The relation between the focal length and strain is shown in Figure 9.

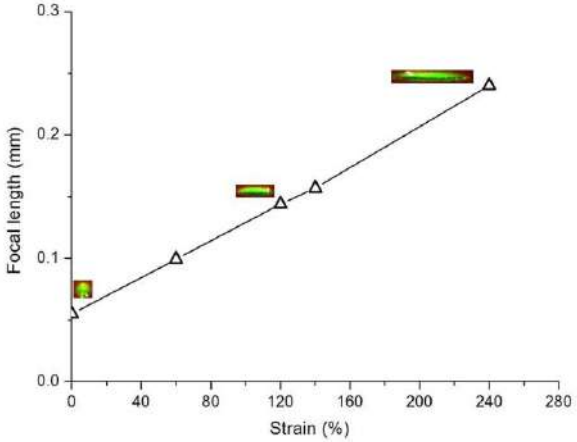

Figure 9 – TESG microlens focal length versus strain

The microlens focal length exponentially increases with increasing strain of TESG film. The focal length was reversibly changed as long as the applied strain is inside the elastic limit. It was noticed that there is a linear dependence between the microlens focal length and diffraction pattern width (see Figure 10).

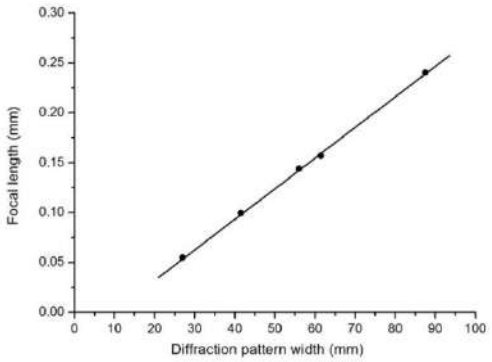

Figure 10 – TESG microlens focal length versus diffraction patern width

The strain responsive, transparent TESG microlenses offer interesting possibilities in tunable optical devices and sensors. Also, closely packed (hexagonal or square) microlenses arrays can be used to mimicking biological structure such as compound eyes. Hexagonal TESG microlenses arrays observed with an electron microscope is shown in Figure11.

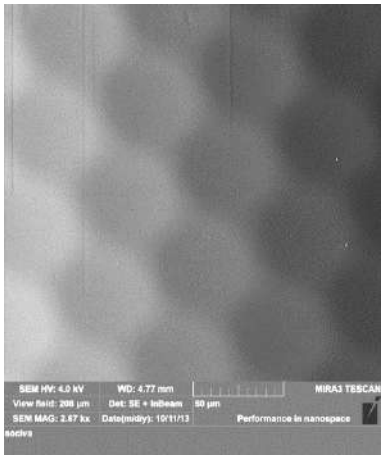

Figure 11 – Image of hexagonal TESG microlenses array is recorded using a field-emission gun scanning electron microscope (FEGSM)

Using of microlenses for visualization it is possible to obtain high-quality images. The picture of hexagonal TESG microlenses arrays with observed milimeter paper at its centre is shown in Figure 12.

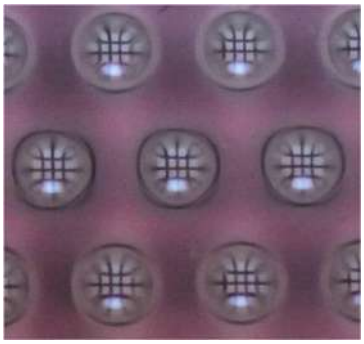

Figure 12 – Image of hexagonal TESG microlenses array recorded using an optical microscope

4. CONCLUSION

Tunable (strain responsive) microlenses were prepared on elastic TESG film. Stretching the film of about 250%, microlenses are uniaxial deformed so that the focal lengths were changed.The microlenses focal lengths from 0.05 mm to 0.2 mm were obtained. As TESG proved to be a good material for adaptive microlensess, we plan to retain sphericity of microlenses in the future and to achieve uniform stretching along both axes.

The TESG microlenses show good optical and imaging properties. The individual concave microlenses can be used. Also, the large-area square or hexagonal close-packed microlenses array can be used for various applications such as: medical laser, optical sensors, light-field cameras, biological structures. Convex microlenses can be produced by coping TESG lenses onto polydimethylsiloxane (PDMS).

5. ACKNOWLEDGEMENT

This paper was written as a part of research on the projects ON 171038 and III 45016 supported by the Ministry of Education, Science and Technological Development of the Republic of Serbia.

REFERENCES

[1] Liang W. L, Su G. D. J, Wide-angle and ultrathin camera module using a curved hexagonal microlens array and all spherical surfaces, *Appl. Opt.* Vol. 53, No 29, pp. H121-H128, 2014.

[2] Deng Z, Chen F, Yang Q, Bian H, Du G, Yong J, Shan C, Hou X, Dragonfly-eye-inspired artificial compound eyes with sophisticated imaging, *Adv. Funct. Materials* Vol 26, No 12, pp. 1995-2001, 2016.

[3] Zhang H, Li L, McCray D. L, Scheiding S, Naples N. J, Gebhardt A, Risse S, Eberhardt R, Yi A. Y, Development of a low cost high precision three-layer 3D artificial compound eye, *Opt. Express* Vol. 21, No 19, pp. 22232-22245, 2013.

[4] Zhang W, Zappe H, Seifert A, Wafer-scale fabricated thermo-pneumatically tunable microlenses, *Light: Science & Applications* Vol. 3, pp. e145, 2014.

[5] Varshney A, Gohil S, Tadavani S. K, Yethiraj A, Bhattacharya S, Ghosh S, Large scale arrays of tunable microlenses, *Lab Chip* Vol. 4, pp. 1330-1335, 2014.

[6] Lu D. X, Zhang Y. L, Han D. D, Wang H, Xia H, Chen Q. D, Ding H, Sun H. B. J, Solvent-tunable PDMS microlens fabricated by femtosecond laser direct writing, *Mater. Chem. C* Vol. 3, pp. 1751-1756, 2015.

[7] Pavia J. M, Wolf M, Charbon E, Measurement and modeling of microlenses fabricated on single-photon avalanche diode arrays for fill factor recovery, *Opt. Express* Vol. 22, No 4, pp. 4202-4213, 2014.

[8] Sadasivuni K. K, Ponnamma D, Ko H. U, Zhai L, Kim H. C, Kim J, J, Electroactive and optically adaptive bionanocomposite for reconfigurable microlens, *Phys. Chem. B* Vol. 120, No 20, pp. 4699-4705, 2016.

[9] Kim S, Kang S, Replication qualities and optical properties of UV-moulded microlens arrays, *J. Phys. D:Appl. Phys.* Vol. 36, No 20, pp. 2451–2456, 2003.

[10] Naessens K, Ottevaere H, Baets R, Van Daele P, Thienpont H, Direct writing of microlenses in polycarbonate with excimer laser ablation, *Appl. Opt.* Vol. 42, No 31, pp. 6349–6359, 2003.

[11] Wu M. H, Park C, Whitesides G. M, Fabrication of arrays of microlenses with controlled profiles using gray-scale microlens projection photolithography, *Langmuir* Vol. 18, No 18, pp. 9312–9318, 2002.

[12] Lee B. K, Kim D. S, Kwon T. H, Replication of microlens arrays by injection molding, *Microsyst. Technol.* Vol. 10, No 6-7, pp. 531–535, 2004.

[13] Ong N. S, Koh Y. H, Fu, Y. Q, Microlens array produced using hot embossing process, *Microelectron. Eng.* Vol. 60, No 3-4, pp. 365–379, 2002.

[14] PericetCamera R, Best A, Nett S. K, Gutmann J. S, Bonaccurso E, Arrays of microlenses with variable focal lengths fabricated by restructuring polymer surfaces with an ink-jet device, *Opt. Express* Vol. 15, No 15, pp. 9877–9882, 2007.

[15] Calixto S, Scholl M. S, Relief optical microelements fabricated with dichromated gelatin, *Appl. Opt.* Vol. 36, No 10, pp. 2101–2106,1997.

[16] Jones C. D, Serpe M. J, Shroeder L, Lyon L. A, Microlens formation in microgel/gold colloid composite materials via photothermal patterning, *J. Am. Chem. Soc.* Vol. 125, No 18, pp. 5292–5293, 2003.

[17] Jung H, Jeong Ki-H, Monolithic polymer microlens arrays with high numerical aperture and high packing density, *ACS Appl. Mater. Interfaces* Vol. 7, No 4, pp. 2160–2165, 2015.

[18] Wu M. H, Park C, Whitesides G. M, Fabrication of arrays of microlenses with controlled profiles using

gray-scale microlens projection photolithography, *Langmuir* Vol. 18, No 24, pp. 9312–9318, 2002.

[19]Fu Y, Bryan N. K, Semiconductor microlenses fabricated by one-step focused ion beam direct writing, *IEEE Trans.Semicond. Manuf*. Vol. 15, No 2, pp. 229–231, 2002.

[20]He M, Yuan X. C, Ngo N. Q, Bu J, Tao S. H, Single-step fabrication of a microlens array in sol–gel material by direct laser writing and its application in optical coupling, *J. Opt. A: Pure Appl. Opt*.Vol. 6, No 1, pp. 94–97, 2004.

[21]Peer A, Biswas R, Park J-M, Shinar R, Shinar Light management in perovskite solar cells and organic LEDs with microlens arrays, *Opt. Express* Vol. 25, No 9, pp. 10704–10709, 2017.

[22]Wrzesniewski E, Eom S.H, Cao W, Hammond W.T., Lee S, Douglas E.P, Xue J, Enhancing light extraction in top-emitting organic light-emitting devices using molded transparent polymer microlens arrays, *Small* Vol. 8, No 17, pp. 2647–2651, 2012.

[23]Tvingstedt K, Zilio S. Dal, Inganńs O, Tormen M, Trapping light with micro lenses in thin film organic photovoltaic cells, *Opt. Expr*ess Vol. 16, No 26, pp.21608–21615, 2008.

[24]Chen Y, Elshobaki M, Ye Z, Park J.M, Noack M.A, Ho K. M, Chaudhary S, Microlens array induced light absorption enhancement in polymer solar cells, *Phys. Chem. Chem. Phys*. Vol.15, pp. 4297–4302, 2013.

[25]Song Y. M, Xie Y, Malyarchuk V, Xiao J, Jung I, Choi K.J, Liu Z, Park H, Lu C, Kim R. H, Li R, Crozier K. B, Huang Y, Rogers J. A, Digital cameras with designs inspired by the arthropod eye, *Nature* Vol. 497, pp. 95–99, 2013.

[26]Li Z, Xiao J, Mechanics and optics of stretchable elastomeric microlens array for artificial compound eye camera, *J. Appl. Phys*. Vol. 117, pp. 014904, 2015.

[27]Bigi A, Bracci B, Cojazzi G, Panzavolta S, Roveri N., Drawn gelatin films with improved mechanical properties, *Biomaterials* Vol.19, No 24, pp. 2335–2340, 1998.

[28]Bigi A, Cojazzi G, Panzavolta S, Roveri N, Rubini K, Mechanical and thermal properties of gelatin films at different degrees of glutaraldehyde crosslinking, *Biomaterials* Vol. 22, No 8, pp. 763–768, 2001.

[29]Bigi A, Cojazzi G, Panzavolta S, Roveri N, Rubini K, Stabilization of gelatin films by crosslinking with genipin, *Biomaterials* Vol. 23, No 24, pp. 4827–4832, 2002.

[30]Muric B. D, Pantelic D. V, Vasiljevic D. M, Panic B. M. Properties of microlenses produced on a layer of tot'hema and eosin sensitized gelatin, *Appl. Opt*. Vol. 46, No 35, pp. 8527–8532, 2007.

[31]Muric B, Pantelic D, Vasiljevic D, Panic B, Microlens fabrication on tot'hema sensitized gelatin, *Opt. Mater*. Vol. 30, No 7, pp. 1217–1220, 2008.

[32]Muric B, Pantelic D, Vasiljevic D, ZarkovB, Jelenkovic B, Pantovic S, Rosic M, Sensitized gelatin as a versatile biomaterial with tailored mechanical and optical properties, *Phys. Scr*. Vol. T157, pp. 014018, 2013.

[33]Muric B, Pantelic D, Vasiljevic D, Panic B, Jelenkovic B, Thermal analysis of microlens formation on a sensitized gelatin layer, *Appl. Opt*. Vol. 48, No 19, pp. 3854–3859, 2009.

REZIME

PRIMENA FILMA ŽELATINA SENZIBILIZOVANOG TOT' HEMOM I EOZINOM ZA ADAPTIVNA MIKROSOČIVA

U ovom radu smo pokazali da se film želatina dopiran tot'hemom i senzibilizovan eozinom (TESG) može koristiti za proizvodnju adaptivnih mikrosočiva. Mehaničke osobine čistog želatinskog filma poboljšane su dodavanjem rastvora tot'heme. Utvrdili smo da elastičnost TESGfilma zavisi od vrednosti koncentracije tot'heme. Istezanjem filma, mikrosočiva su deformisana duž jedne ose, pa se žižna daljina mikrosočiva može podešavati. Postignute vrednosti žižne daljine kreću se od 0.05 do 0.2 mm.

Ključne reči: *film želatina, eozin, tot'hema, adaptivna mikrosočiva, optičke osobine, mehaničke osobine*

EUROPEAN MOLECULAR IMAGING MEETING

18th Annual Meeting of the European Society for Molecular Imaging

EMIM 2023 | 14th-17th March

Salzburg Congress, Austria

supported by:

(https://www.milabs.com/events/emim-2023/?utm_source=EMIM&utm_medium=banner&utm_campaign=2023)

(https://www.bruker.com/en/products-and-solutions/preclinical-imaging.html)

(https://mediso.com/)

(https://www.miltenyibiotec.com/DE-en/)

(https://www.mrsolutions.com/)

(https://nvision-imaging.com/)

Author Index
(/contxt_emim2023/online-program/author-index)

Keyword Index
(/contxt_emim2023/online-program/keyword-index)

Chair Index
(/contxt_emim2023/online-program/chair-index)

Full text search:

Todorovic | ✕ (/contxt_emim2023/online-program/set-search-session) | 🔍

To search for a specific ID please enter the hash sign followed by the ID number (e.g. #123).

Day overview (/contxt_emim2023/online-program/day?dt=2023-03-17)

Tissue Omics & Optical Technologies

*.ics (/contxt_emim2023/online-program/session-ics?s=PW36)

Session chair: **Dale Waterhouse** (London, UK); **Alan Race** (Unterschleißheim, Germany)

Shortcut: **PW36**

1095 # Laser nano-surgery of fungal cell wall to enable patch clamping

Tanja Pajić[1], Katarina Stevanović[1], Nataša V. Todorović[2], Steva Lević[3], Svetlana Savić Šević[4], Dejan Pantelić[4], Miroslav Živić[1], Mihailo D. Rabasović[4], Aleksandar J. Krmpot[4, 5]

[1] University of Belgrade, Faculty of Biology, Institute of Physiology and Biochemistry, Belgrade, Serbia
[2] University of Belgrade, Institute for Biological Research "Siniša Stanković", National Institute of the Republic of Serbia, Belgrade, Serbia
[3] University of Belgrade, Faculty of Agriculture, Belgrade, Serbia
[4] University of Belgrade, Institute of Physics Belgrade, National Institute of the Republic of Serbia, Belgrade, Serbia
[5] Texas A & M University at Qatar, Doha, Qatar

Introduction

Electrophysiology studies of ion channels, in live filamentous fungi by patch clamp method are not possible due to presence of rigid chitinous cell wall that prevents patch clamp pipette to access the plasma membrane. We present laser nano-surgery of the fungal cell wall that enables patch clamp electrophysiology studies. Similar approaches as one-time reports utilizing nanosecond laser pulses long time ago were not pursued further [1,2]. Here, we demonstrate reproducible method using femtosecond lasers accompanied by two-photon excitation fluorescence (TPEF) imaging of hyphae.

Methods

A wild-type strain of filamentous fungus *Phycomyces blakesleeanus* (Burgeff) [NRRL 1555(-)] were grown on glass coverslips with hand-etched grid, coated with a thin layer of 50% collagen type I as an immobilizer. Home built nonlinear laser scanning microscope [3,4] utilizing Ti:Sa tunable fs laser was used for TPEF imaging of hyphae and the cell surgery. The latter is enabled with the custom made add-on in software. Coverslip with hyphae is transferred to another microscope setup for patch clamp, consisting of micromanipulators and precise electronics for pA current measurements. The surgical incisions and released protoplasts were additionally imaged by scanning electron microscopy for which treated hyphae had to undergo critical point drying procedure.

Results/Discussion

Hyphae were stained by Calcofluor White and treated with an exocytosis inhibitor (brefeldin A) and a respiration inhibitor (sodium azide) to prevent cell wall regeneration. Since the cell wall and the plasma membrane are in the close contact [4] hyphae were kept in hyperosmotic solution to retract the cytoplasm from the cell wall. Surgical spot-wise pattern was precisely positioned at TPEF image of selected hypha at the place where the plasma membrane was retracted. The dwell time (1s) and the laser power (4-15mW) were set with fixed repetition rate (76MHz), pulse duration (160fs) and laser wavelength (730nm). Upon the surgery, hyphae were gently deplasmolysed. A protoplast with plasma membrane accessible for the patch clamp pipette was released through the surgical incision (Fig 1). The >GΩ seal resistance was achieved. Numerous ion channels are recorded in different configurations (on cell, inside-out, whole cell and out-out) (Fig 2).

Conclusions

The whole process (cell surgery + patch clamping) is rather complex and specific steps have to be strictly followed for high success rate and reproducibility. Also, chemicals concentrations, solutions osmolarity, timing and cutting parameters have to be kept in the specified narrow range. Obtained current recordings provide valuable information on fungal cell membrane ionic channels.

Acknowledgement

This work was supported by the Ministry of Education, Science and Technological Development, Republic of Serbia [contract numbers: 451-03-68/2022-14/200178, 451-03-68/2022-14/200116 and 451-03-68/2022-14/200007]; the Project HEMMAGINERO [Grant number 6066079] from Program PROMIS, Science Fund of the Republic of Serbia; and the Institute of Physics Belgrade, through the grant by the Ministry of Education, Science and Technological Development of the Republic of Serbia.
We acknowledge support from the Qatar National Research Fund (project #NPRP12S-0205-190047).

Disclosure

I or one of my co-authors have **no financial interest** or **relationship** to disclose regarding the subject matter of this presentation.

References

[1] Roberts, Stephen K., Graham K. Dixon, Stuart J. Dunbar, Dale Sanders, 'Laser Ablation of the Cell Wall and Localized Patch Clamping of the Plasma Membrane in the Filamentous Fungus Aspergillus: Characterization of an Anion-Selective Efflux Channel', The New Phytologist 137, no. 4 (1997): 579–85.

[2] Véry AA, Davies JM, 'Laser microsurgery permits fungal plasma membrane single-ion-channel resolution at the hyphal tip', Applied and Environmental Microbiology, 1998 Apr;64(4):1569-72.

[3] Mihailo D Rabasović, Dejan V Pantelić, Branislav M Jelenković, Srećko B Ćurčić, Maja S Rabasović, Maja D Vrbica, Vladimir M Lazović, Božidar PM Ćurčić, Aleksandar J Krmpot "Nonlinear microscopy of chitin and chitinous structures: a case study of two cave-dwelling insects", Journal of Biomedical Optics 20(1), 016010 (2015).

[4] Tanja Pajić, Nataša V Todorović, Miroslav Živić, Stanko N Nikolić, Mihailo D Rabasović, Andrew HA Clayton, Aleksandar J Krmpot, "Label-free third harmonic generation imaging and quantification of lipid droplets in live filamentous fungi" Scientific Reports 12, 18760 (2022)

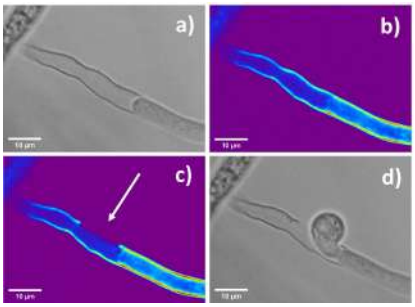

(https://www.eventclass.org/contxt_emim2023/download/media?hash=%242y%2413%24qDqAjFDeKnUd3PMbiqVjEOrllbj2vlZ10XI0kCDCF2rVW1l2BDhYq) **Fig 1. Cell nano-surgery of chitinous cell wall of filamentous fungi.**

Bright field **(a)** and TPEF **(b)** image of plasmolised hyphae *Phycomyces blakesleeanus* prior to the surgery. **c)** TPEF image of the same hyphae after the surgery. Surgical incision is pointed by the arrow. **d)** Bright filed image of the same hyphae with the protoplast released through the surgical incision.

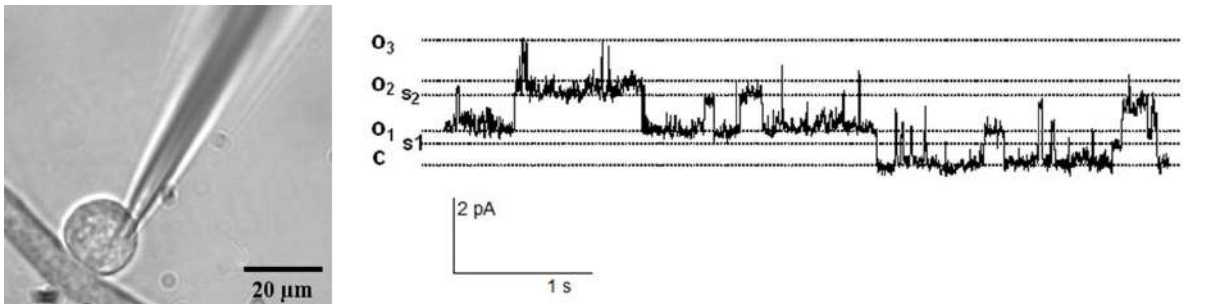

(https://www.eventclass.org/contxt_emim2023/download/media?hash=%242y%2413%24%2F6F87Dsrd8O0zVWZ49H%2F8uRh%2FW%2FLcWoMiqaaUvuA28X0yy3WyYhf.)

Fig 2. Patch clamping upon the cell nano-surgery.

Left: Bright filed image of the patch clamp pipette in contact with membrane of the protoplast released through the surgical incision. **Right:** representative single channel current recording in "outside/out" configuration at voltage -10mV. o: open channel current level; c: closed channel current level; sub-conductivity level. Calibration bar is at the bottom

Keywords: laser nanosurgery, patch clamp, electrophysiology, two-photon imaging, cell surgery

University of Belgrade
Institute of Physics Belgrade
Kopaonik, March 13-16, 2022

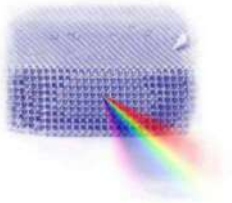

Book of Abstracts

15th Photonics Workshop

(Conference)

PHOTONICS
CENTER

Synergy of interference, scattering and pigmentation for structural coloration of *Jordanita globulariae* moth

Danica Pavlović[1], Svetlana Savić-Šević[1], Branislav Salatić[1], Dejan Pantelić[1]

(1) *Institute of Physics Belgrade, Pregrevica 118, 11080 Belgrade, Serbia*

Contact: Danica Pavlović (danica.pavlovic@ipb.ac.rs)

Abstract. Structural coloration has attracted a lot of attention due to its significance in biophotonics and biomimetics. Structural and pigment colorations are omnipresent in insects, producing a range of colors for camouflage, warning, mimicry and other strategies necessary for survival. The coupling of structural and pigment colorations has been largely unnoticed. Herein we show how pigments, scattering and interference work together in two-dimensional waveguiding structures to produce the coloration of *Jordanita globulariae* (Huebner, 1793), a moth whose forewings sparkle with slightly iridescent green scales. we reveal the structure and function of the scales of the *Jordanita globulariae* moth through morphological characterization, spectral measurement and numerical simulation. The synergistic operation of structure and pigments is analyzed. We also discuss the role of this particular coloration in the moth's lifestyle.

BASIC SCIENCES SUSTAINABLE DEVELOPMENT BELGRADE 2022

International Year of Basic Sciences for Sustainable Development

World Conference on Basic Sciences and Sustainable Development

September 19–22, 2022

Belgrade, Serbia

Natural waveguides on *Hoplia argentea* elytra

– Danica Pavlović

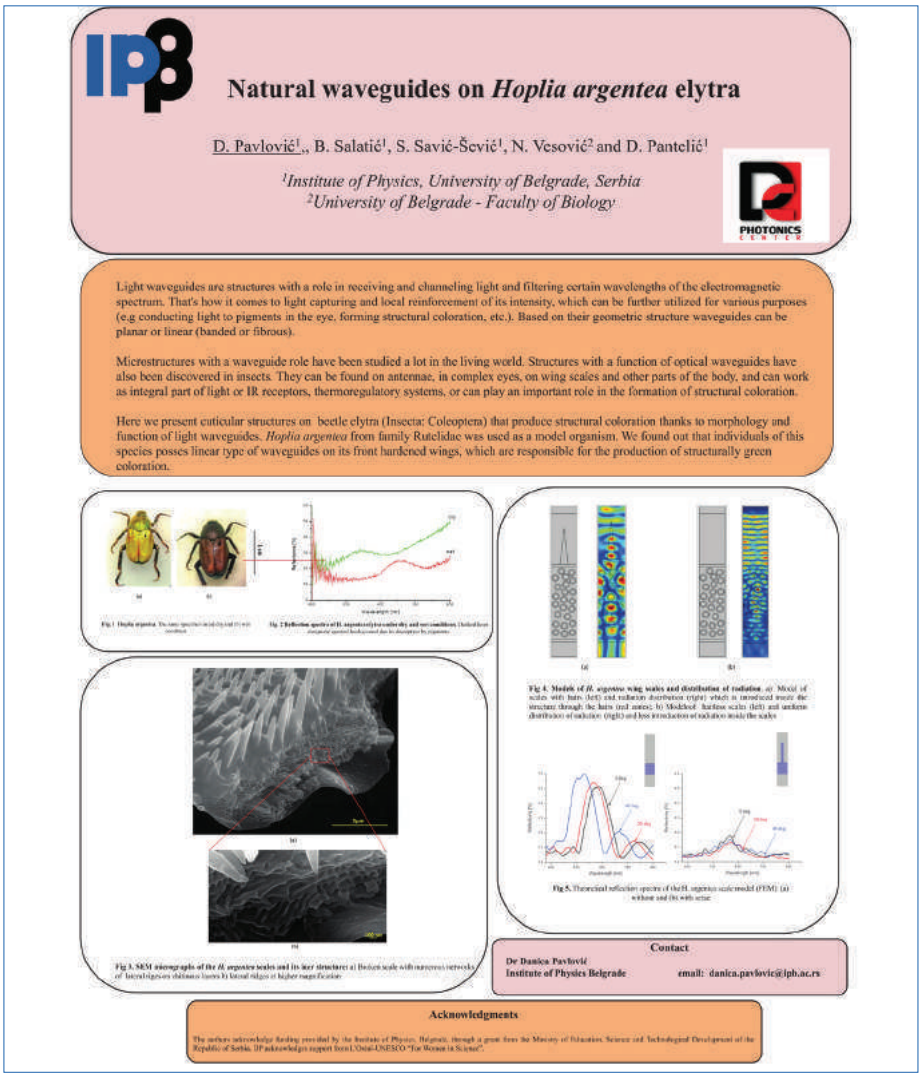

Advanced optical and photonic structures, such as microlenses, photonic crystals and diffraction gratings, have been found on many insect species, enabling their survival in a hostile environment. This study reported on *Hoplia argentea* scarab beetle, whose non-iridescent yellow-green coloration is achieved by the scales with internal Bragg reflector and the external surface covered with a dense arrangement of fiber-like protrusions.

Light, which is guided, diffracted and selectively absorbed outside the green part of the spectrum, produces a dull, yellow-green appearance, making the insect unnoticeable on the background of green foliage, its natural habitat. If exposed to water, the insect quickly turns brown-red, making him unnoticeable on the wet soil. The structures have been analyzed using electron and optical microscopy and a finite element method devised revealing that the fine fiber-like surface structures preclude the iridescence of internal Bragg grating. As a result, the insect color is constant irrespective of the illumination and observation directions. In spite of the dense surface structure, the insect is not superhydrophobic, but rather hydrophilic, enabling a fast color change in wet conditions.

This poster was co-authored by Branislav Salatić, Svetlana Savić-Šević, and Dejan Pantelić, Institute of Physics, Belgrade, Serbia, and Nikola Vesović and Srećko Ćurčić, Faculty of Biology, University of Belgrade, Serbia.

Book of abstracts

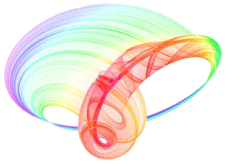

PHOTONICA2019

The Seventh International School and Conference on Photonics, 26 August – 30 August 2019, Belgrade, Serbia

& Machine Learning with Photonics Symposium (ML-Photonica 2019)

& ESUO Regional Workshop

& COST action CA16221

Editors: Milica Matijević, Marko Krstić and Petra Beličev

Belgrade, 2019

Effects of temperature on luminescent properties of $CaGdAlO_4$:Er,Yb nanophosphor

D. Sevic[1], M. S. Rabasovic[1], J. Krizan[2], S. Savic-Sevic[1], M. D. Rabasovic[1], B. P. Marinkovic[1] and M. G. Nikolic[1]
[1]*Institute of Physics, Belgrade, Serbia*
[2]*AMI d.o.o., Ptuj, Slovenia*
e-mail: sevic@ipb.ac.rs

$CaGdAlO_4$ crystal doped with Er, Yb or other rare earth is commonly used as infrared lasing material [1-4]. In this study we analyze effects of temperature on luminescent properties of nanocrystalline $CaGdAlO_4$ doped with Er^{3+} and Yb^{3+} cations. Material was synthesized by combustion method, as described in [5].

Our experimental setup is presented in detail in [6]; and its use for analysis of thermometric phosphors in [7-9]. However, in this study, because $CaGdAlO_4$:Er,Yb is upconverting material, we have used pulsed laser diode excitation at 980 nm. The structure of material was observed by high resolution scanning electron microscope (SEM). The experimental setup for luminescence measurement as a function of temperature is described in [10].

By using the results of our measurements of $CaGdAlO_4$:Er,Yb nanophosphor in temperature range from 300 K up to 680 K we have determined temperature sensing calibration curve and absolute and relative sensitivity of this material. The relative sensitivity is about 0.7 % K^{-1} on room temperature and decreases with temperature increase. Comparing this results with characteristics of other thermographic phosphors we conclude that synthesized $CaGdAlO_4$:Er,Yb nanophosphor is appropriate material for remote temperature sensing.

REFERENCES
[1] K. Hasse et al., Opt. Lett. 40, 3552 (2015).
[2] J Q. Di et al., Laser Phys. 26, 045803 (2016).
[3] P. Loiko, Opt. Mater. Express 4, 2241 (2014).
[4] Z. Zhu et al., Opt. Lett. 37, 4838 (2012).
[5] J. Krizan et al., Acta Chim. Slov. 61, 608 (2014).
[6] M. S. Rabasovic et al., Nucl. Inst. Meth. B 279, 16 (2012).
[7] A. Vlasic et al., J. Lumin. 199, 285 (2018).
[8] M. S. Rabasovic et al., J. Spectrosc. 2018, 3413864 (2018).
[9] M. G. Nikolic et al., Opt. Quant. Electron. 50, 258 (2018).
[10] M. D. Rabasovic, J. Phys. D: Appl. Phys. 49, 485104 (2016).

Negative thermal expansion of pullulan multilayers

S. Savic-Sevic[1], D. Pantelic[1], B. Muric[1], D. Vasiljevic[1], B. Kolaric[1] and B. Jelenkovic[1]
[1]*Institute of Physics, Belgrade, Serbia*
e-mail: savic@ipb.ac.rs

The change of temperature leads to thermal expansion. Most materials expand, but, some materials contract upon heating, characterized by negative thermal expansion [1]. Such negative thermal expansion material have various applications such as photoelectric devices, fillers in controlled thermal expansion composites, aerospace technology, as dental fillings [2].

We combine holography and phase separation [3] to design complex photonic structures that exhibit negative thermal expansion behavior. The structures were recorded in pullulan, (linear polysaccharide) doped with ammonium dichromate, and consist of a multilayer composed of pullulan and air.

We study optical response during heating and cooling of the synthesized pullulan nanostructures. The reflection wavelength of the hologram was used to characterize the temperature dependence of their shrinkage and swelling behavior. By heating and cooling the sample partially reversible shifts of the photonic band gap could be observed. We have observed that heating leads to a reduction in the thickness of the structure, resulting in the reflectance peak shift towards shorter wavelengths. With temperature decreasing the band gap position shifts back towards longer wavelengths. We reveal temperature sensitive responses of the structure, which are the consequence of the mechanical deformation of air nanolayers upon heating or cooling. The temperature change leads to the increased permeability of air molecules through the pullulan nanolayers, which causes mechanical changes.

REFERENCES

[1] J. Paul Attfield, Front. Chem. 6, 371 (2018).
[2] D. Tam Ho et al., Nano Lett. 17, 5113 (2017).
[3] S. Savic-Sevic et al., Soft Matter 14, 5595 (2018).

PHYSICAL CHEMISTRY 2016

13th International Conference on
Fundamental and Applied Aspects of
Physical Chemistry

Proceedings
Volume I

B E L G R A D E
September 26 - 30, 2016

TUNABLE (STRAIN RESPONSIVE) MICROLENSES

B. Murić, D. Pantelić, D. Vasiljević, S. Savić-Šević, and B. Jelenković

Institute of Physics, University of Belgrade
Pregrevica 118, Zemun 11 080, Belgrade, Serbia (muric@ipb.ac.rs)

ABSTRACT
Microlenses prepared on elastic tot'hema eosin sensitized gelatin (TESG) layer can be tuned in a focal length by controlled strain application. By varying the strain, the lenses were deformed uniaxially such that focal lengths from 0.05 mm to 0.2 mm were obtained.

INTRODUCTION
The microlenses are the small lenses ranging in diameter from several micrometers to nearly 1mm. Tunable microlenses offer attractive applications such as: tunable photonic waveguides, miniature optical sensing, displays, cell phone cameras, and artificial compound eyes [1-5]. Different methods are used for microlenses fabrication: direct laser writing, hot embossing, thermal reflow, droplet process and gray scale photolithography [6-9]. In this paper, TESG microlenses focal length tynability, obtained by applying controlled strain, was presented. The microlenses with different diameter and depth, were produced on a TESG layer using Nd:YAG laser light (532 nm). The elastic, biocompatible, thermally stable, nontoxic, cost-effective layer was prepared easily [10, 11]. The produced adaptive concave TESG microlenses (individual or microlens array) are suitable for various applications. They can be copied onto polydimethylsiloxane (PDMS) and used as convex lenses.

EXPERIMENTAL
The TESG layer was prepared on a very clean thermoplastic foil that can be easily removed. The TESG preparing procedure described in our previous papers [10, 11]. The layers were dumbbell-shaped specimens (see Fig. 1a) cut from the mold brass (ASTM D412) as shown in Fig.1b.

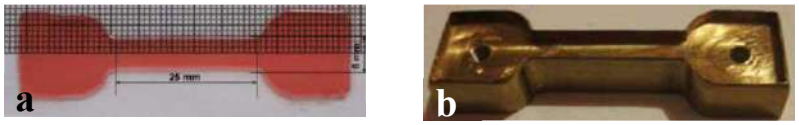

Figure 1. The photograph of: a) TESG layer; b) brass mould- (with ASTM standards dimensions -gauge length 25 mm, width 6 mm)

The microlenses were produced by direct laser writing, using 2nd harmonic Nd:YAG laser. The laser power was 60mW with an exposure time of 20 s. The mechanical properties of the TESG layers were determined in a tensile stress testing machine, as described in [12]. The morphology of TESG microlenses were investigated using a high resolution scanning electron microscope equipped with a high brightness Schottky field emission gun (FEGSEM) [13].

RESULTS AND DISCUSSION

According the TESG layer elasticity it can be removed from the substrate easily, without damage, even when microlenses are already fabricated. It can be successfully transferred to other, even curved, substrates. During laser irradiation, eosin bleaches, making TESG microlens colorless. The dumbbell-shaped TESG layer (before and after stretching) with a formed microlens is shown in Figure 2.

Figure 2. The microlens produced on the dumbbell-shaped TESG layer: a) unstretched; and b) stretched

Microlens fabrication was followed by formation of a diffraction picture on a diffuse screen, with a millimeter scale, placed behind the TESG layer. A camera was used to record this diffraction patterns shown in Figure 3.

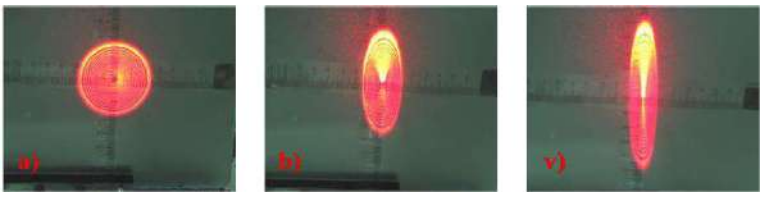

Figure 3. Diffraction picture recorded after the TESG microlens was: a) formed; b and v) stretched in one direction. Millimeter scale is visible.

As a result of material elasticity, it is shown that microlenses formed on the TESG layer change their properties in response to strain. The stretching of TESG microlenses in one direction is investigated and extension of the diffraction picture is recorded, as shown in Figure. 3. The toric microlenses were obtained, because of uniaxial strain. They are astigmatic, with two

focal lengths along orthogonal directions. For uniform extension (along x and y direction) sphericity of microlenses can be retained.
The relation between the focal length, strain, and diffraction pattern width is shown in Figure 4. As can be seen the microlens focal length exponentially increases with increasing strain of TESG layer. It was noticed that there is a linear dependence between the microlens focal length and diffraction pattern width. The microlenses focal length was reversibly changed as long as the applied strain is inside the elastic limit.

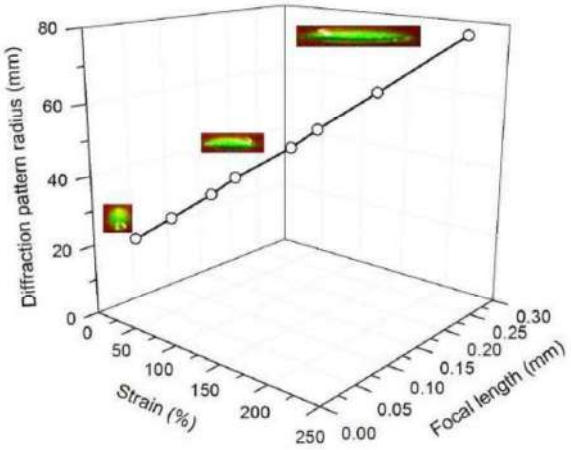

Figure 4. TESG microlens focal length variation with strain and diffraction pattern width

Strain responsive, transparent TESG microlenses offer interesting possibilities in tunable optical devices and sensors [4-9]. Also, closely packed microlenses arrays can be used to imitate biological compound eyes structure. Hexagonal and 3x3 TESG microlenses arrays are shown in Figure. 5. The microlenses are capable of producing high-quality image of the any text at its centre (see Figure 5(b)).

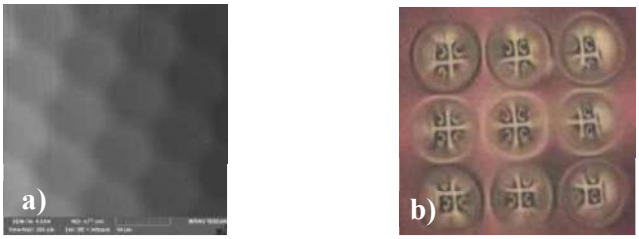

Figure 5. Image of hexagonal TESG microlenses array is recorded using a field-emission gun scanning electron microscope (a) and image of 3x3 microlenses array is recorded using an optical microscope (b)

CONCLUSION

Tunable (strain responsive) microlenses were prepared on a flexible TESG layer. By varying the strain to about 250%, the lenses were deformed uniaxially such that focal lengths were changed. The microlenses focal lengths from 0.05 mm to 0.2 mm were obtained.

The TESG microlenses show good optical and imaging properties. The individual concave microlenses can be used. Also, the large-area square or hexagonal close-packed microlens array can be used for various applications such as: medical laser, optical sensors, light-field cameras, biological structure. Convex microlenses can be produced by coping TESG lenses onto polydimethylsiloxane (PDMS).

Acknowledgement

This paper was written as a part of research on the projects ON 171038 and III 45016 supported by the Ministry of education, science and technological development of the Republic of Serbia.

REFERENCES

[1] W. L. Liang, G. D. J. Su, Appl. Opt. 2014, **53**, H121-H128.
[2] Z. Deng, F. Chen, Q. Yang, H. Bian, G. Du, J. Yong, C. Shan, X. Hou, Adv. Funct. Materials 2016, **26**, 1995-2001
[3] H. Zhang, L. Li, D. L. McCray, S. Scheiding, N. J. Naples, A. Gebhardt, S. Risse, R. Eberhardt, A. Y. Yi, Opt. Expr. 2013, **21**, 22232-22245.
[4] W. Zhang, H. Zappe, A. Seifert, Light: Science & Applications 2014 **3**, e145.
[5] A. Varshney, S. Gohil, S. K. Tadavani, A. Yethiraj, S. Bhattacharya, S. Ghosh, Lab Chip 2014,**14**, 1330-1335.
[6] D. X. Lu, Y.L. Zhang, D. D. Han, H. Wang, H. Xia, Q. D. Chen, H. Ding, H. B. Sun, J. Mater. Chem. C 2015, **3**, 1751-1756.
[7] J. M. Pavia, M. Wolf, E. Charbon Opt. Express 2014, **22**, 4202-4213.
[8] T. Nisisako, H. Suzuki, T. Hatsuzawa, Micromac. 2015, **6**, 1435-1444.
[9] K. K. Sadasivuni, D. Ponnamma, H. U. Ko, L. Zhai, H. C. Kim, J. Kim, J. Phys. Chem. B 2016, **120**, 4699-4705.
[10] B. Murić, D. Pantelić, D. Vasiljević, B. Panić, Opt. Mater. 2008, **30,** 1217-1220.
[11] A. J. Krmpot, G. J. Tserevelakis, B. D. Murić, G. Filippidis, D. V. Pantelić, J. Phys. D: Appl. Phys. 2013, **46**, 195101.
[12] B. Murić, D. Pantelić, D. Vasiljević, B. Zarkov, B. Jelenković, S. Pantović, M. Rosić, Phys. Scr. 2013, **T157**, 014018 (4pp).
[13] B. Murić, D. Pantelić, D. Vasiljević, S. Savić-Sević, B. Jelenković, Current Appl. Phys. 2016, **16**, 57-62.

PHYSICAL CHEMISTRY 2024

17th International Conference
on Fundamental and Applied Aspects of
Physical Chemistry

Proceedings
Volume I

This conference is dedicated to the 100th anniversary of the birth of Professor Slobodanka Caca Veljković

September 23-27, 2024
Belgrade, Serbia

REAL-TIME PHOTORESPONSIVE CHITOSAN FOR DIRECT LASER WRITING OF MICROSTRUCTURES

B. Murić[1], S. Savić-Šević[1], D. Pantelić[2] and B. Jelenković[1]

[1] *Institute of Physics Belgrade, University of Belgrade, Pregrevica 118,11080 Belgrade, Serbia (muric@ipb.ac.rs)*
[2] *Senzor INFIZ, Institute of Physics, University of Belgrade, Serbia*

DOI: https://doi.org/10.46793/Phys.Chem24I.337M

ABSTRACT

Photoresponsive, nontoxic, elastic chitosan was prepared for rapid, one-step fabrication of various microstructures. Concave or convex microlenses (individual or microlenses arrays), gratings, microchannels, and many other complex microstructures were produced on the chitosan layer by direct laser writing at 488 nm. Any waste material not created during the microstructures formation. The microstructures can be used directly as prepared or contact copied into PDMS without additional chemical processing, for various applications such as: lab on a chip, sensors, cameras, security, etc.

INTRODUCTION

Microoptical components such as positive and negative single microlenses, square or hexagonal microlenses arrays, gratings, microchannels, and various complex microstructures are used in different sensors, medical devices, cameras, labs on a chip, security, and numerous other applications. The microstructures were produced on various photosensitive materials (polymers, composites, photosensitive glasses, etc.) by a range of techniques such as: hot embossing, direct laser writing (DLW), photolithography, droplet process, ink yet process, etc Some of them are mostly complex and expensive techniques that partially use of toxic chemicals [1-4].

Chitosan is biodegradable and biocompatible linear polysaccharide derived by deacetylation of chitin (polysaccharide found in the exoskeleton of crustaceans and insects). Chitosan, as a natural polysaccharide, consisting of β-(1-4)-linked d-glucosamine and N-acetyl-d-glucosamine, and is available in a range of molecular weights and degrees of deacetylation. It is insoluble in water and organic solvents, but dissolves in diluted acidic aqueous solutions depending on pH and deacetylation degree. Chitosan as nontoxic, antibacterial, biocompatible and biodegradable was initially used in pharmacy and biomedicine. However, the need for new natural materials has expanded the applications range of chitosan to bioengineering, agriculture, dentistry, food industry, cosmetics, water filtration, etc [5, 6].

Chitosan, chemically modified with a nontoxic (food grade) compounds, was used for a fast, one-step production of microoptical structures, by direct laser writing (DLW) at 488 nm. Individual positive and negative microlenses or their arrays, gratings, microchannels and various complex microstructures can be produced on the chitosan layer. The microstructures, which do not produce any waste material at all, can be used as such without any additional chemical treatment. They can also be contact copied into dental composite, PDMS and other related materials [7]. Their application areas are diverse, so they can be used for sensors, security, compound eyes, lab on a chip and numerous other applications.

RESULTS AND DISCUSSION

The 2% chitosan solution was prepared by dissolving low molecular weight, 85% deacetylated chitosan supplied from Sigma-Aldrich, in 1% aq. solution of acetic acid (purchased from Sigma Aldrich). The solution was stirred at 50^{o}C for a long time, until a homogeneous solution was obtained. Chemical modification of chitosan was achieved with an aqueous solution composed of glycerol, sucrose, glucose, polysorbate 80, citric acid and sodium benzoate, which act as plasticizers, humectants and preservatives. 0.2 ml of this solution was added per 1 ml of chitosan solution, with stirring. The photosensitivity of chitosan was achieved by adding 0.1 ml of anthocyanin food coloring (E163) also per 1 ml of solution. After complete dissolution the prepared chitosan solution was centrifuged in order to remove all remained impurities. As a result of chemical modification, both mechanical and optical properties of the chitosan layer were changed.

The gravity settling method [8] was used for preparing of chitosan layer dried in the dark overnight, under ordinary environmental conditions (T=25 ^{o}C and RH=50-60%). The layer thickness of 100 μm was obtained for a volume of 2 ml modified chitosan solution. Using a digital micrometer the thickness was determined as the average of six random layer locations measurements. The thickness can be changed varying the quantity and chemical composition of chitosan solution.

The microstructures were produced on the chitosan layer using a homemade laser writing device occupied with a blue laser at 488 nm and 100 mW maximal output power. The precise xy - linear translation stage with step resolution of 25 nm and position repeatability of 2 μm, allows good layer positioning placed on it. The laser beam focused on the layer by the microscope objective (50×0.55NA). Synchronization of laser and coordinate table operation is achieved by software control using standard g-code. By controlling the laser power, exposure time and speed of laser writing the various microstructures were created. Diffraction gratings were recorded line by line using a program that determines the line parameters (number, length and width) from the corresponding image file.

Figure 1. Diffraction gratings recorded on the chitosan layer.

By writing a series of gratings the spatial resolution of 100 lp/mm was found, for the laser power of 35 mW, exposure time of 200 ms, and line width of 0.01 mm. The image of diffraction grating taken by a digital camera through the optical microscope is shown in Fig. 1.

The arrays of convex microlenses were recorded lens by lens using the program that determines the lens parameters (polygon diameter, number of polygonally positioned spots, and distance among neighbors) from the image file. The spherical surface in the polygon center arranged from 8 polygonally positioned spots acts as a good quality positive (convex) microlens. The radius of

curvature and corresponding focal length of microlenses can be controlled by the diameter of a polygon.

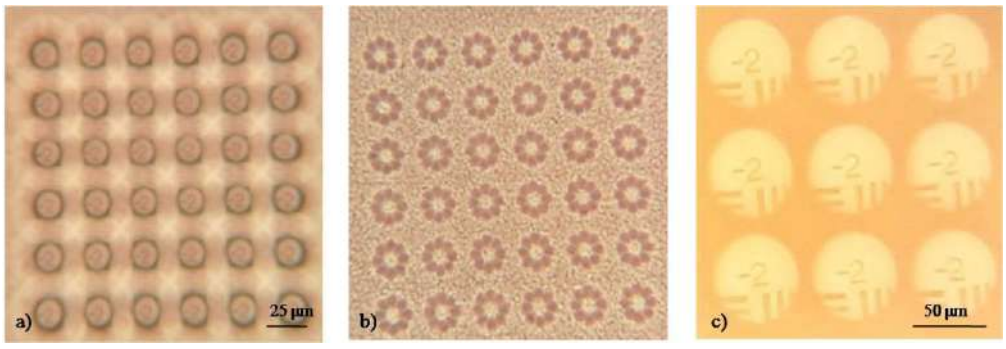

Figure 2. Transmission images of digit "-2" formed by array of 6x6 convex microlenses (a) and by array of 3x3 concave microlenses on the chitosan layer (c). Reflection image of 6 x 6 array convex microlenses on the chitosan layer (b).

The good repeatability of microlenses was obtained. An image of digit "-2" taken by a digital camera through the optical microscope and 6x6 convex microlens array is shown in Fig. 2a (the diameter of polygon was 25 µm, while microlenses were fabricated using 50 mW of laser power and 200 ms exposure time), while the reflection image of 6 x 6 array convex microlenses is shown in Fig. 2b. The concave lens was formed by controlled and local melting of the chitosan layer, following the laser beam profile. An image of digit "-2" taken by a digital camera through the optical microscope and 3x3 concave microlens array is shown in Fig. 2c (lens diameter of 50 µm with 35 mW of laser power and 200 ms exposure time).

By controlled guiding of the laser beam across the surface, microstructures of various shapes (rather complex) can be produced on the chitosan layer. Based on our previous investigations [1], we assume that by varying the laser power, exposure time, writing speed, and layer thickness, the structures with a width and depth of up to several hundred micrometers can also be obtained on the modified chitosan layers. Exposure time can be reduced by using higher laser powers. In most cases, there is no postprocessing, so the microstructures are usable immediately after fabrication. An image of a half of rather complex microchannel structure on a chitosan layer, taken by a digital camera through the optical microscope, is presented in Figure 3. With regard to the cross section of the microchannel, preliminary investigations have shown that it is approximately semicircular in shape.

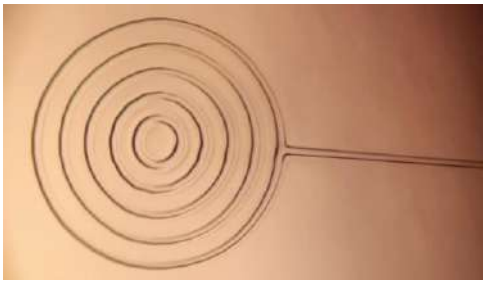

Figure 3. Microchanels (complex structure) recorded on chitosan layer.

CONCLUSION

Chitosan was chemically modified to be ecofriendly, biocompatible, elastic, nontoxic and to allow fast, one-step fabrication of different microoptical structures by direct laser writing (DLW) at 488 nm. The microstructures such as: convex, concave, aspherical microlenses, microchannels, diffraction gratings, etc. can be produced using cheap lasers. The microlenses with good optical and imaging properties were obtained. The elasticity of the chitosan layer is suitable for adaptive optics.

The microstructures can be used immediately, without additionally chemical treatment and waste. They can be used for a variety of applications such as: optical sensors, medical devices, cameras, security, biological structure, etc.

The subject of further research will be profile analysis and more detailed characterization of the obtained microstructures, as well as further improvement of the physicochemical properties of chitosan layer.

Acknowledgment

This paper was supported by the Ministry of Education, Science and Technological Development of the Republic of Serbia.

REFERENCES

[1] B. D. Murić, D. V. Pantelić, D. M. Vasiljević, B. M. Panić, Appl. Opt., 46 (2007) 8527.
[2] H. Jiang, S. Fraser, B. Kaminska, H. Porras, M. Raymond, Adv. Opt. Mater., 7 (2019) 1900237.
[3] B. D. Murić, D. V. Pantelić, D. M. Vasiljević, S. N. Savić-Šević, B. M. Jelenković, Curr. Appl. Phys., 16 (2016) 57.
[4] J. Tang, G. Qiu, X. Cao, Y. Yue, X. Zhang, J. Schmitt, J. Wang, Lab Chip, 20 (2020) 2334.
[5] R. Ye, S. Liu, W. Zhu, Y. Li, L. Huang, G. Zhang, Y. Zhang, Polymers, 15(2023) 2482.
[6] M. Monier, I. Youssef, D.A. Abdel-Latif, React. Func. Polymers, 124 (2018) 129.
[7] J. Xu, J.Ma, J. Lian, Y. Liao, L. Wang, L. Dong, H. Sun, J. Phys. D: Appl. Phys., 55 (2022) 315401
[8] B. Murić, D. Pantelić, D. Vasiljević, B. Panić, Opt. Mater., 30 (2008) 1217.

University of Belgrade
Institute of Physics Belgrade
Kopaonik, March 13-16, 2022

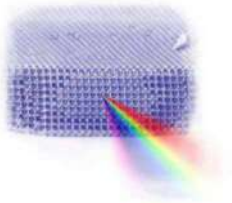

Book of Abstracts

15th Photonics Workshop

(Conference)

PHOTONICS
CENTER

Synergy of interference, scattering and pigmentation for structural coloration of *Jordanita globulariae* moth

Danica Pavlović[1], Svetlana Savić-Šević[1], Branislav Salatić[1], Dejan Pantelić[1]

(1) *Institute of Physics Belgrade, Pregrevica 118, 11080 Belgrade, Serbia*

Contact: Danica Pavlović (danica.pavlovic@ipb.ac.rs)

Abstract. Structural coloration has attracted a lot of attention due to its significance in biophotonics and biomimetics. Structural and pigment colorations are omnipresent in insects, producing a range of colors for camouflage, warning, mimicry and other strategies necessary for survival. The coupling of structural and pigment colorations has been largely unnoticed. Herein we show how pigments, scattering and interference work together in two-dimensional waveguiding structures to produce the coloration of *Jordanita globulariae* (Huebner, 1793), a moth whose forewings sparkle with slightly iridescent green scales. we reveal the structure and function of the scales of the *Jordanita globulariae* moth through morphological characterization, spectral measurement and numerical simulation. The synergistic operation of structure and pigments is analyzed. We also discuss the role of this particular coloration in the moth's lifestyle.

ЦИКЛУС ПРЕДАВАЊА

СВЕТЛОСТ У РАЗВОЈУ ДРУШТВА

СВЕТЛОСТ
У РАЗВОЈУ ДРУШТВА

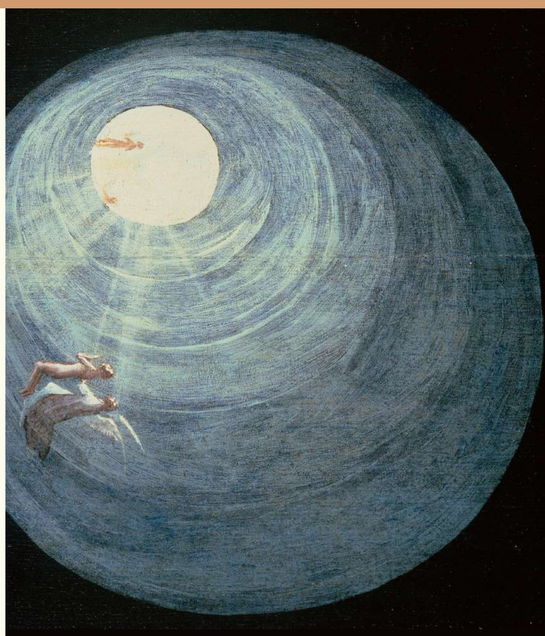

ЦИКЛУС ПРЕДАВАЊА

Српска академија наука и уметности
175 година
1841–2016

1. СВЕТЛОСТ У РАЗВОЈУ ДРУШТВА
2. ГЕНИ И ГЕНОМ

Д. ПАНТЕЛИЋ[1], А. КРМПОТ[1], Д. В. СТОЈАНОВИЋ[2,4], М. Д. РАБАСОВИЋ[1],
С. ЋУРЧИЋ[3], С. САВИЋ-ШЕВИЋ[1], В. ЛАЗОВИЋ[1], Д. ПАВЛОВИЋ[1]

СВЕТЛОСТ НА КРИЛУ ЛЕПТИРА

А п с т р а к т . – Боје у живом свету су последица како пигмената, тако и физичких ефеката на нанометарским структурама. Овде ће бити речи о низу оптичких механизама који одређују боје припадника реда инсеката Lepidoptera (лептира и мољаца): интерференцији, дифракцији, расејању и поларизацији. Као пример ћемо навести три врсте које живе у Србији: *Apatura ilia* (Denis & Schiffermüller, 1775), *Diachrysia chrysitis* (Linnaeus, 1758) и *Jordanita globulariae* (Hübner, 1793).

УВОД

Многи софистицирани механизми, за које често сматрамо да су производ савремене цивилизације, постоје већ милионима година у живом свету: ултразвучни локатор код слепих мишева и његово активно ометање код неких ноћних Lepidoptera (мољаца), жироскоп код неких врста инсеката лепезара (Strepsiptera), хемијско оружје код буба бомбардера (Carabidae: Brachininae), детекција инфрацрвеног зрачења код пирофилних инсеката, а листу би било могуће наставити у недоглед. Поменућемо још само једну од најновијих студија у којој је утврђено постојање функционалног система од два спрегнута зупчаника код ларве инсекта *Issus coleoptratus* (Fabricius, 1781) [1].

У овом тексту ћемо се детаљније задржати на оптичким феноменима у свету лептира и мољаца, који овим, изванредно прилагодљивим бићима омогућавају интра- и интерспецијску комуникацију. На телима инсеката могуће је наћи дифракционе решетке, поларизационе елементе, антирефлексионе

[1] Институт за физику, Универзитет у Београду
[2] Национални парк Фрушка гора
[3] Институт за зоологију, Универзитет у Београду – Биолошки факултет
[4] Универзитет у Новом Саду, Институт за низијско шумарство и животну средину

слојеве, фотонске кристале, селективне оптичке филтере – чуда модерне технологије, за која смо дуго сматрали да су искључиви производ човекове интелигенције [2]. За оне који се баве овом облашћу, „домишљатост“ еволуције представља инспирацију за развој нових оптичких уређаја и техника [3].

СТРУКТУРНЕ БОЈЕ У СВЕТУ ЛЕПТИРА И МОЉАЦА (LEPIDOPTERA)

Богатство боја у живом свету, а посебно код инсеката, је последица њихове потребе да се сакрију и стопе са околином, пошаљу сигнал упозорења или сигнал привлачења јединкама супротног пола. Неке од боја су последица хемијске структуре пигмената који се налазе на површини њиховог тела (интегумента). Ипак, опсег боја које су у стању да хемијски синтетишу је ограничен. Зато је током еволуције искоришћен читав низ оптичких ефеката, попут интерференције и дифракције да се генеришу боје од љубичасте преко плаве, до зелене, па и даље, према инфрацрвеном делу спектра. Боје које се на овај начин добијају називају се структурним, јер су условљене микронским и субмикронским структурама на телу живих јединки. Код неких организама структурна обојеност може бити независна од угла осветљавања и посматрања. Код других, боја се, у зависности од упадног угла светлости, мења. Ову појаву називамо иридесценцијом.

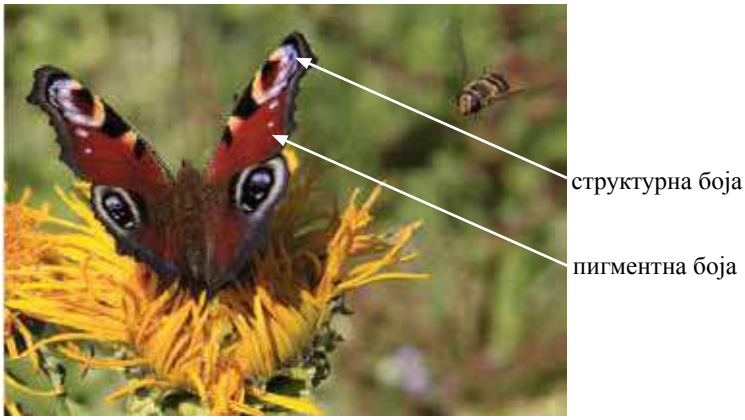

Слика 1. Црвена, жута и црна боја лептира дневног пауновца (*Aglais io*) (Linnaeus, 1758) су последица пигмената, док плава и бела боја настају због структурних ефеката

Опште је позната раскошна обојеност крила дневних лептира (нпр. пауновац – *Aglais io* (Linnaeus, 1758) – сл. 1). Занимљиво је да су често неки делови крила обојени структурно, док је боја других зона пигментна. Код дневног лептира *Apatura ilia* (Denis & Schiffermüller, 1775) (сл. 2а) лако се уочава иридесцентна природа љубичасте боје крила – дорзална страна левог крила има жуто-мрку, пигментну боју, док је дорзална страна десног крила љубичаста, због погодног угла осветљавања. У анатомском смислу, боју генеришу танке

микронске плочице (љуспице), које покривају читаву површину крила попут црепова на крову куће (сл. 2б). Само крило као основу има двоструку мембрану, у коју су љуспице усађене са обе стране у издигнуте дршке. На сл. 3 се види део крила са једном љуспицом, снимљен помоћу нелинеарне двофотонске флуоресцентне микроскопије. Ова техника даје могућност да се формира тродимензионална слика, те да се крило посматра под различитим угловима. Дата су два карактеристична погледа на којима се види сама двострука крилна мембрана, једна љуспица и неколико дршки из којих су љуспице испале.

Једино детаљно посматрање под електронским микроскопом омогућава разумевање порекла структурних боја. На малом повећању (сл. 4) види се да свака љуспица има структуру дифракционе решетке. На већем увеличању (сл. 5а), види се да дифракциона решетка поседује ламеларну структуру, где се појединачни гребени (на међусобном растојању од око 1 μm) састоје од низа слојева. Попречни пресек (добијен помоћу трансмисионог електронског микроскопа – сл. 5б) показује да се слојеви налазе на међусобном растојању од око 150 nm. На истој слици је шематски приказана делимична рефлексија светлости на сваком од слојева. Услов за конструктивну интерференцију свих рефлектованих снопова одређује да ће светлост таласне дужине од око 380 nm бити одбијена, што заиста и одговара љубичастој боји крила [4].

а) б)

Слика 2. а) Љубичаста структурна боја крила код лептира преливача (*A. ilia*). б) Увеличани део крила који показује присуство иридесцентних љубичастих љуспица, које покривају крило лептира

И неки ноћни лептири (у народу звани мољци) имају структурну обојеност крила, иако је геометрија њихових љуспица значајно другачија. Ламеларна решетка постоји, али има велики период (неколико микрона) и мали број ламела, те су дифракциони ефекти слабо изражени. Зато је доминантна попречна решетка, која има периоду мању од таласне дужине светлости у видљивом делу спектра (између 380 и 760 nm). Овакве решетке не допуштају формирање виших дифракционих редова и функционишу у режиму нултог реда [5].

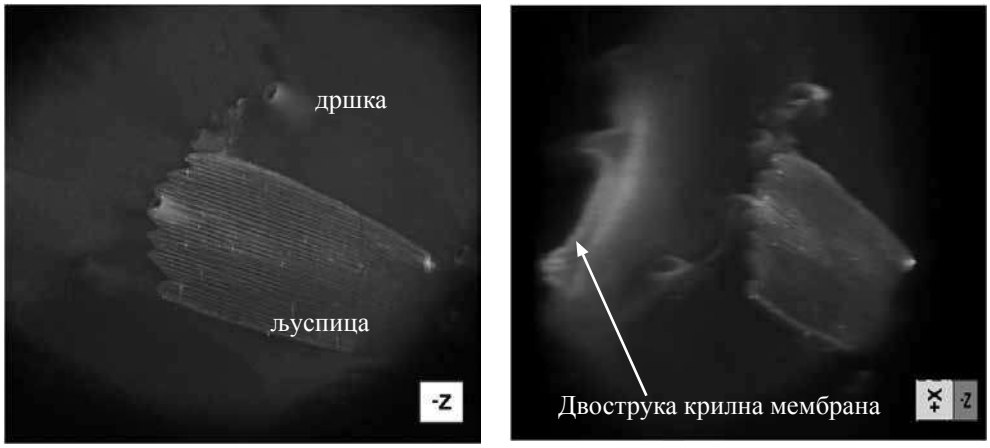

а) б)

Слика 3. Положај љуспице на двострукој крилној мембрани лептира *A. ilia*, снимљен под два различита угла (а, б). Коришћена је нелинеарна дво-фотонска флуоресцентна микроскопија развијена у Центру за фотонику, Института за физику у Београду

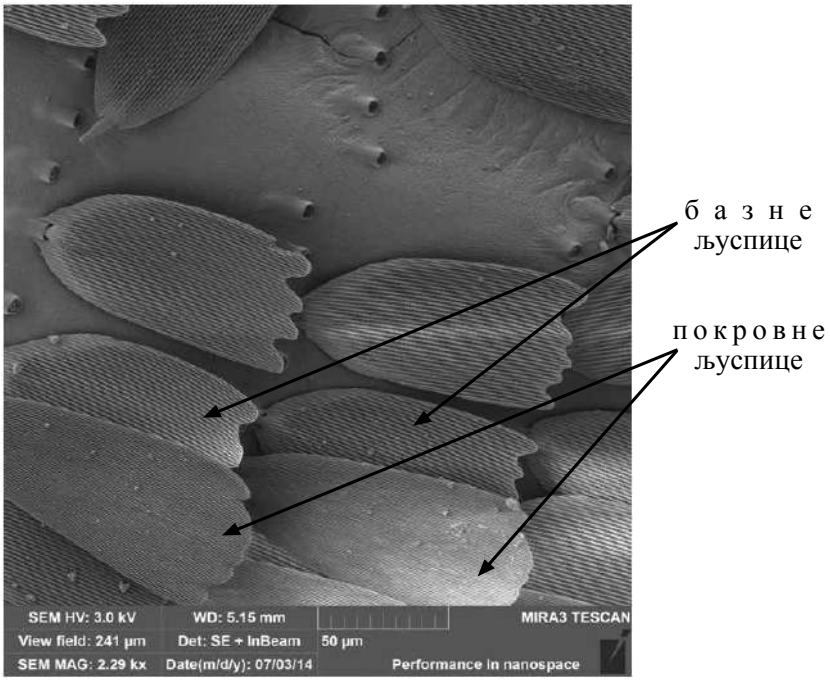

Слика 4. Два типа љуспица лептира A. Ilia (покровне и базне) имају структуру дифракционе решетке

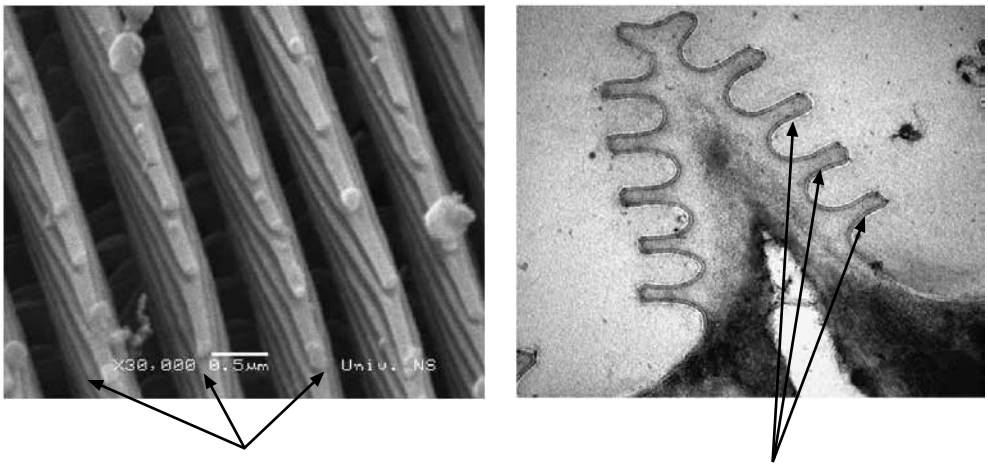

Слика 5. а) Слојевита структура љуспице дневног лептира *A. ilia*, посматрана под скенирајућим електронским микроскопом. б) Попречни пресек љуспице дневног лептира *A. ilia* посматран под трансмисионим електронским микроскопом

Слика 6. а) Мољац *Diachrysia chrysitis* (Linnaeus, 1758), чија крила имају један део површине златне боје. б) Увеличана слика златног дела крила *D. chrysitis*, снимљена оптичким рефлексионим микроскопом, на којој се виде појединачне љуспице

У том погледу, занимљив је пример ноћног лептира *Diachrysia chrysitis* (Linnaeus, 1758), који има лепу златну боју дорзалне површине предњих крила (сл. 6а и 6б). Слика 7а, снимљена под скенирајућим електронским микроскопом, приказује љуспицу крила *D. Chrysitis* која је преломљена, тако да се јасно види да постоје две мембране – вентрална, која нема значајних и добро организованих структура и дорзална, која је структурисана двема ортогоналним решеткама, једном ламеларном велике периоде (око 2.5–3 μm) и другом

веома густом (периоде 100–150 nm) профила рибље кости (сл. 7б). Запажа се да је унутрашњост и дорзалне и вентралне мембране веома неправилна (сл. 7в). Дебљина сваке од њих је око 150 nm и налазе се на међусобном растојању 150 nm, што чини читаву љуспицу изузетно танком (мање од 500 nm).

У оптичком погледу, трансверзална дифракциона решетка је толико густа да није могуће формирање других дифракционих редова осим нултог. Могуће је, међутим, да се део енергије користи за формирање еванесцентног или вођеног таласа [6], који се простире дуж мембрана љуспице (сл. 7в). Овај процес код Lepidoptera није до краја разјашњен, али спектар рефлектованог зрачења показује да се таласне дужине изнад 500 nm ефикасно рефлектују, што даје спектралну расподелу и визуелни изглед сличан злату.

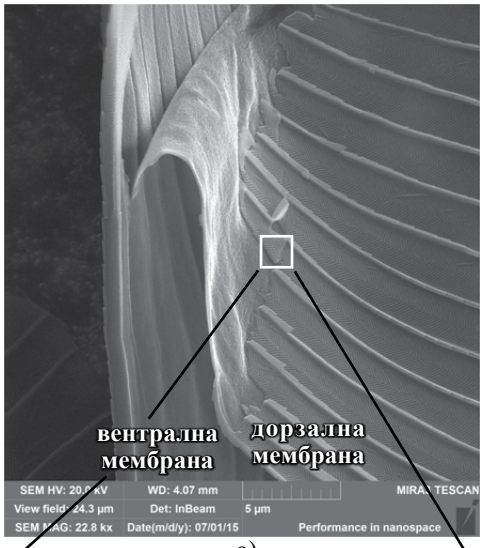

а)

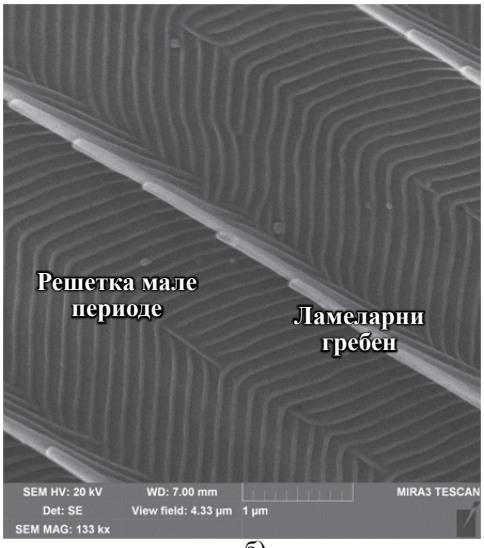

б)

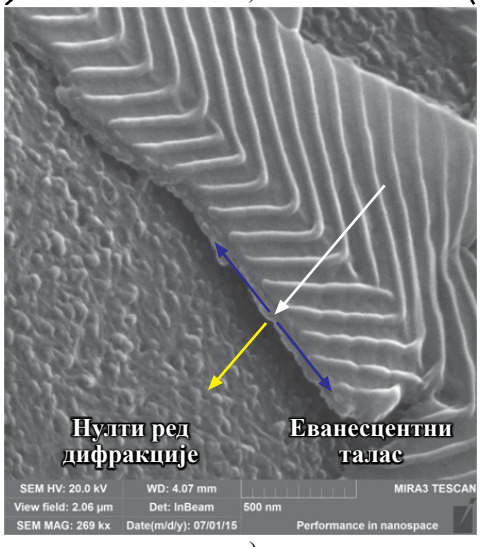

в)

Слика 7. Љуспице крила лептира *D. chrysitis* снимљене под скенирајућим електронским микроскопом. а) Љуспица чија су дорзална и вентрална мембрана насилно раздвојене. б) Увеличана површина љуспице на којој се виде ламеларни гребени, који су код ове врсте на великом међусобном растојању и веома танки. в) Увеличани део слике 7а) (бели квадрат) на коме се детаљно види спољашња и унутрашња структура љуспице, са неправилним унутрашњим површинама. Упадни светлосни талас (бела стрелица) се дели на еванесцентни део (плаве стрелице) и дифракциони сноп нултог реда (жута стрелица)

У бескрајном низу могућих структура љуспица погледајмо још једну, којом се одликује мољац *Jordanita globulariae* (Hübner, 1793) (сл. 8а). Предња крила су покривена низом зелених, иридесцентних, као и браон, пигментних, љуспица које су ретко распоређене и не прекривају се. Известан број љуспица је иридесцентан, као што се види на сл. 8б, која је снимљена под оптичким микроскопом. Уколико се слика иридесцентне љуспице додатно повећа види се да на њој постоји низ дискретних тачака зеленог и жутог обојења (сл. 8в). Да бисмо објаснили њихово постојање неопходно је да завиримо у дубљи ниво, повећавајући преломљену љуспицу скоро 100.000 пута (сл. 9). На попречном пресеку је најуочљивија вишеслојна структура која се налази испод горње мембране и прати њен конкавни облик. Она функционише као Брагова решетка, што значи да представља селективни спектрални филтер. Из спектра беле светлости ће бити рефлектована само она боја светлости (таласна дужина) која је одређена растојањем између слојева и упадним углом светлости. Са сл. 9 видимо да се, за светлост која пада на центар удубљења, упадни угао на Брагову решетку разликује од светлости која пада на ивичне делове. Последица је да се боја рефлектоване светлости у ове две зоне разликује, као што потврђује сл. 8в.

На основу свега што је речено, запажамо да је свака љуспица код Lepidoptera пљосната структура дебљине неколико микрона, ширине око 50–100 μm, а дужине од 150–300 μm. Она представља мртви остатак једне једине ћелије, састављен од хитина, пигмената и протеина. Уочавамо и општи принцип конструкције љуспице (слика 10). Она се састоји од две мембране – вентралне, која је скоро сасвим равна и дорзалне која је структурисана системом уздужних ламеларних гребена и попречних решетки. Две мембране повезују, ретко постављени, стубови између којих постоји простор, који може бити празан или испуњен додатним структурама попут гранула, запреминских решетака и фотонских кристала. Структуре могу бити веома сложене на нанометарском нивоу, а оптички ефекти који се на њима уочавају јесу комбинација интерференције, дифракције, расејања, флуоресценције и апсорпције.

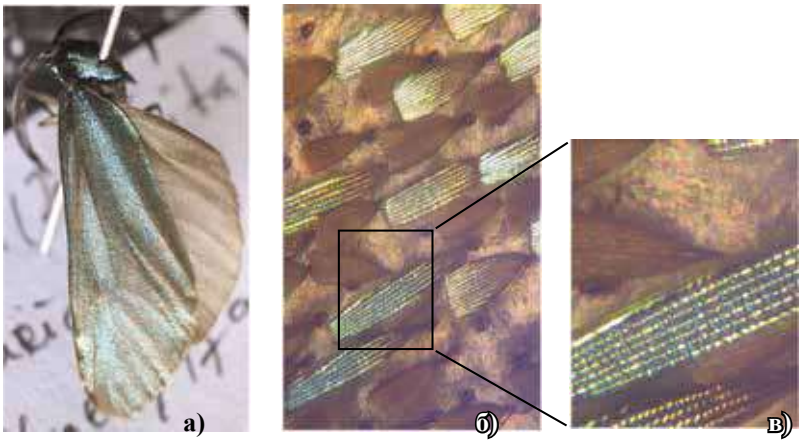

Слика 8. а) Мољац *J. globulariae*. б) Увеличана слика крила *J. globulariae* под оптичким микроскопом на којој се истовремено виде иридесцентне и неиридесцентне љуспице. в) Увеличани део слике 8б) где се види да се иридесценција састоји од дискретних тачака зелене и жуте боје

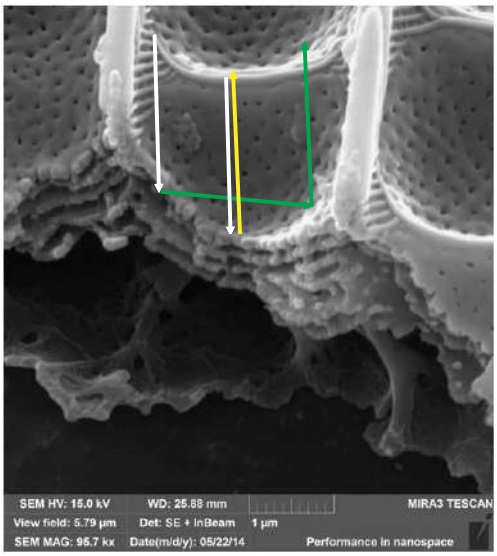

Слика 9. Попречни пресек љуспице мољца *J. globulariae*. Испод дорзалне мембране уочава се низ конкавних слојева који функционишу као Брагова решетка. Беле стрелице означавају упадни сноп светлости, који се у централној зони директно рефлектује (жута стрелица), а у бочној трпи две рефлексије (зелене стрелице)

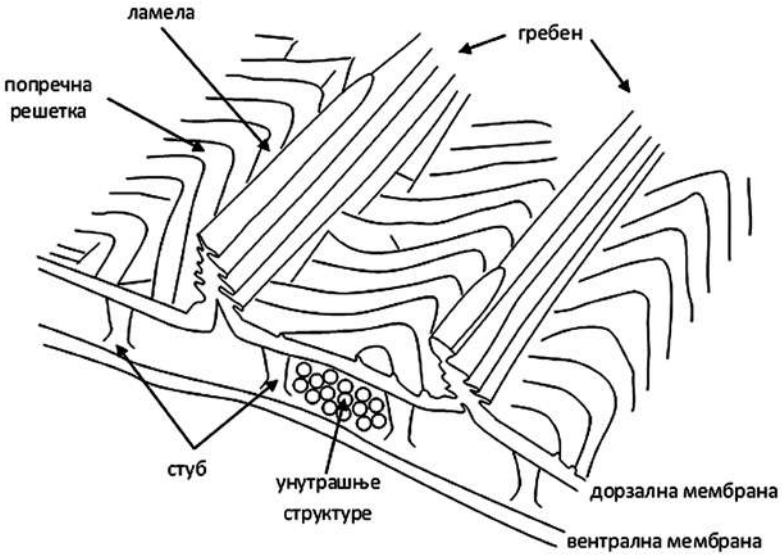

Слика 10. Општа шема структуре љуспице на крилима Lepidoptera

ЗАКЉУЧАК

Овај текст представља кратак приказ оптичких ефеката на крилима лептира и мољаца, који овим инсектима дају карактеристично обојење. Ради се о постојању структура микронских и субмикронских димензија на којима се одигравају процеси карактеристични за таласну природу светлости. Њихово проучавање даје увид у фасцинантне резултате еволутивног развоја живих бића, али и идеје како да се откривени ефекти практично искористе за нове типове козметичких препарата, иридесцентне боје, заштиту докумената али и детекцију зрачења и нове типове сензора.

ЛИТЕРАТУРА

[1] M. Burrows, G. Sutton, Interacting gears synchronize propulsive leg movements in a jumping insect, *Science* **341**,1254–1256 (2013)
[2] P. Vukusic, J. R. Sambles, Photonic structures in biology, *Nature* **424**, 852–855 (2003)
[3] F. P. Barrows, M. H. Bartl, Photonic Structures in Biology: A Possible Blueprint for Nanotechnology, *Nanomater. Nanotechnol.* **4**, 1–12 (2014)
[4] D. Pantelić, S. Ćurčić, S. Savić-Šević, A. Korać, A. Kovačević, B. Ćurčić, B. Bokić, High angular and spectral selectivity of purpleemperor (Lepidoptera: Apatura iris and A. ilia) butterfly wings, *Opt. Express* **19**, 5817–5826 (2011)
[5] D. J. Brink, J. E. Smit, M. E. Lee, A. Moeller, Optical diffraction by the microstructure of the wing of a moth, *Appl. Opt.* **34**, 6049 – 6057 (1995)
[6] D. W. Peters, S. A. Kemme, G. R. Hadley, Effect of finite grating, waveguide width, and end-facet geometry on resonant subwavelength grating reflectivity, *JOSA A* **21**, 981–987 (2004)

D. Pantelić, A. Krmpot, D. V. Stojanović, M. D. Rabasović,
S. Ćurčić, S. Savić-Šević, V. Lazović, D. Pavlović

LIGHT ON THE BUTTERFLY WING

Summary

Colors in the living world are either a consequence of pigments, or physical effects on nanometer-sized structures. Here we explain the mechanisms responsible for colors of Lepidoptera (butterflies and moths): interference, diffraction, scattering, polarization. Three species, living in Serbia, will be analyzed as an example of structural coloration: *Apatura ilia* (Denis & Schiffermüller, 1775), *Diachrysia chrysitis* (Linnaeus, 1758) and *Jordanita globulariae* (Hübner, 1793).

23rd INTERNATIONAL CONFERENCE
AND SCHOOL
ON QUANTUM ELECTRONICS

LASER PHYSICS AND APPLICATIONS

BOOK OF ABSTRACTS

23-27 September 2024,
Ravda, Bulgaria

IL.D2

NONLINEAR IMAGING AND LASER NANO-SURGERY OF FUNGAL CELLS TO ENABLE ELECTROPHYSIOLOGICAL MEASUREMENTS

Tanja Pajić[1], Katarina Stevanović[1], Nataša Todorović[2], Steva Lević[3], Svetlana Savić Šević[4], Dejan Pantelić[4], Miroslav Živić[1], Mihailo Rabasović[4] and Aleksandar Krmpot[4]

[1]*Faculty of Biology, University of Belgrade, Belgrade, Serbia*
[2]*Siniša Stanković Institute for Biological Research, University of Belgrade, Serbia*
[3]*Faculty of Agriculture, University of Belgrade, Serbia*
[4]*Institute of Physics Belgrade, University of Belgrade, Serbia*

e-mail: krmpot@ipb.ac.rs

Electrophysiology studies of ion channels in live filamentous fungi by the patch clamp method are not possible due to presence of rigid chitinous cell wall that prevents the patch clamp pipette to access the plasma membrane. We present laser nano-surgery of the fungal cell wall that enables patch clamp electrophysiology studies. Similar approaches as one-time reports utilizing nanosecond laser pulses long time ago were not pursued further [1,2]. Here, we demonstrate reproducible method using femtosecond lasers accompanied by two-photon excitation fluorescence (TPEF) imaging of hyphae.

A wild-type strain of filamentous fungus *Phycomyces blakesleeanus* (Burgeff) [NRRL 1555(-)] were grown on glass coverslips with hand-etched grid coated with a thin layer of 50% collagen type I as an immobilizer. A home-built nonlinear laser scanning microscope [3,4] utilizing a Ti:Sa tunable fs laser was used for TPEF imaging of hyphae and cell surgery. The latter was enabled with a custom-made add-on to software. A coverslip with hyphae was transferred to another microscope setup for patch clamp consisting of micromanipulators and precise electronics for pA current measurements. The surgical incisions and released protoplasts were additionally imaged by scanning electron microscopy for which the treated hyphae had to undergo a critical point drying procedure.

Hyphae were stained by Calcofluor White and treated by an exocytosis inhibitor (brefeldin A) and a respiration inhibitor (sodium azide) to prevent cell wall regeneration. Since the cell wall and the plasma membrane are in the close contact [4], the hyphae were kept in hyperosmotic solution to retract the cytoplasm from the cell wall. Surgical spot-wise pattern was precisely positioned at TPEF image of selected hypha at the place where the plasma membrane was retracted. The dwell time (1 s) and the laser power (4-15 mW) were set with a fixed repetition rate (76 MHz), pulse duration (160 fs) and laser wavelength (730 nm). Upon the surgery, hyphae were gently deplasmolysed. A protoplast with plasma membrane accessible for the patch clamp pipette was released through the surgical incision. A seal resistance >GΩ was achieved. Numerous ion channels were recorded in different configurations (on cell, inside-out, whole cell and out-out).

The whole process (cell surgery + patch clamping) is rather complex and specific steps have to be strictly followed for high success rate and reproducibility. Also, the chemicals concentrations, solutions osmolarity, timing and cutting parameters have to be kept in the specified narrow range. The current recordings obtained provide valuable information on fungal cell membrane ionic channels.

References:

[1] S.K. Roberts et al, "Laser Ablation of the Cell Wall and Localized Patch Clamping

of the Plasma Membrane in the Filamentous Fungus Aspergillus: Characterization of an Anion-Selective Efflux Channel", The New Phytologist, 137, 579-85, (1997)

[2] A.A. Véry, J.M. Davies, "Laser microsurgery permits fungal plasma membrane single-ion-channel resolution at the hyphal tip", Applied and Environmental Microbiology, 64, 1569-72, (1998)

[3] M.D. Rabasović et al, "Nonlinear microscopy of chitin and chitinous structures: a case study of two cave-dwelling insects", Journal of Biomedical Optics, 20, 016010, (2015)

[4] T Pajić et al, "Label-free third harmonic generation imaging and quantification of lipid droplets in live filamentous fungi", Scientific Reports, 12, 18760, (2022)

Acknowledgements: Project BioPhysFUN [Grant number 4545] from Program GREEN, Science Fund of the Republic of Serbia; and all institutions from the affiliations, through the grant by the Ministry of Education, Science and Technological Development of the Republic of Serbia.

IL.D3

NANOARCHAEOSOMES COUPLED GOLD NANORODS: A SYNERGISTIC APPROACH TO CHEMO-PHOTOTHERMAL CANCER THERAPY

Shaik Sameer Basha[1], Poornima Budime Santhosh[2,3], Lyubomir Stoychev[2], Julia Genova[2], Swathi Sudhakar[1]*

[1]*Department of Applied Mechanics and Biomedical Engineering, Indian Institute of Technology Madras, Chennai, India*
[2]*Institute of Solid State Physics, Bulgarian Academy of Sciences, Tsarigradsko Chaussee 72, 1784 Sofia, Bulgaria*
[3]*Central Laboratory of Solar Energy and New Energy Sources, 72 Tsarigradsko Chaussee, 1784 Sofia, Bulgaria*

e-mail: swathi.s@iitm.ac.in

Recent advances making use of near-infrared (NIR) lasers and gold nanorods (AuNRs) have paved the way to innovative cancer treatment strategies[1]. In this work, we propose a NIR laser-induced synergistic chemo-phototherapeutic approach by fabricating the nanoarchaeosomes (NA), which are novel, nano-sized liposomes synthesized from archaeal lipids, encapsulated with the PEGylated gold nanorods (PEG-AuNRs) and cisplatin (CIS), an anticancer drug. Comprehensive characterization techniques, including transmission electron microscopy (TEM), dynamic light scattering (DLS), and UV-Vis spectroscopy, confirmed the successful synthesis of the NA-PEG-AuNR-CIS complex. Under irradiation by an 808-nm wavelength laser (1 W/cm^2, 5 min), the AuNRs effectively induced localized photothermia and controlled drug release from the NA. *In vitro* studies on MCF-7 breast cancer cells demonstrated that this complex exhibits enhanced cellular uptake and a significant reduction in the cell viability. Our findings suggest that not only does our system enhance the therapeutic index of the drug, but it also minimizes systemic toxicity and paves the way to a more efficient and less invasive cancer treatment method.

Temperature Effects on Luminescent Properties of $Sr_2CeO_4:Eu^{3+}$ Nanophosphor: a Machine Learning Approach

DRAGUTIN ŠEVIĆ, University of Belgrade,
Institute of Physics Belgrade, Belgrade
ANA VLAŠIĆ, University of Belgrade,
Institute of Physics Belgrade, Belgrade
MAJA S. RABASOVIĆ, University of Belgrade,
Institute of Physics Belgrade, Belgrade
SVETLANA SAVIĆ-ŠEVIĆ, University of Belgrade,
Institute of Physics Belgrade, Belgrade
MIHAILO D. RABASOVIĆ, University of Belgrade,
Institute of Physics Belgrade, Belgrade
MARKO G. NIKOLIĆ, University of Belgrade,
Institute of Physics Belgrade, Belgrade
BRANKA D. MURIĆ, University of Belgrade,
Institute of Physics Belgrade, Belgrade
BRATISLAV P. MARINKOVIĆ, University of Belgrade,
Institute of Physics Belgrade, Belgrade
JANEZ KRIŽAN, AMI, d. o. o, Ptuj, R. Slovenia

Original scientific paper
UDC: 535.37
DOI: 10.5937/tehnika2003279S

In this paper we analyze possibilities of application of $Sr_2CeO_4:Eu^{3+}$ nanopowder for temperature sensing using machine learning. The material was prepared by simple solution combustion synthesis. Photoluminescence technique has been used to measure the optical emission temperature dependence of the prepared material. Principal Component Analysis, the basic machine learning algorithm, provided insight into temperature dependent spectral data from another point of view than usual approach.

Key words: *Photoluminescence, New materials, Thermographic phosphors*

1. INTRODUCTION

Nowadays, nano materials have more and more advantages over bulk materials. Nano science inevitably entered our world [1]. Thermographic nano phosphors are widely used in many applications [2-7]. They typically consist of a ceramic host and rare-earth dopant. The temperature dependency of their luminescence is used for remote temperature sensing. For obvious reasons, non contact measurements have many advantages. Thermographic remote monitoring of laser cleansing is described in [8].

Strontium cerium oxide (Sr_2CeO_4) nano phosphors doped with europium ions (Eu^{3+}), $Sr_2CeO_4:Eu^{3+}$ are described in many scientific papers. As shown in [9], emission color change in a wide range of temperatures proves a great potential of $Sr_2CeO_4:Eu^{3+}$ nanocrystals for industrial applications, particularly in nanothermometric technology. Moreover, additional application possibilities for this material are provided by the fact that the samples with different grain sizes are characterized by various luminescence colors [9]. The possibility of application of this nanophosphor in single-color and two-color fluorescence thermometry techniques in temperature range of 303–523 K has been proposed in [10]. In [11] it was shown that the Eu^{3+} doped Sr_2CeO_4 phosphors emitting white light (by combining blue, green and red emissions) has potential

Author's address: Dragutin Šević, University of Belgrade, Institute of Physics Belgrade, Belgrade, Pregrevica 118
e-mail: sevic@ipb.ac.rs
Paper received: 26.05.2020.
Paper accepted: 30.05.2020.

applications not only in the fields of lamps and display devices under 280 nm excitation, but also in the field of LEDs under near UV (350 nm) excitation. $Sr_2CeO_4:Eu^{3+}$ considered as a source of anti-stokes white light generated under near infrared excitation was analyzed in [12]. Various methods of synthesis and studies of structural and luminescent characteristics of nanophosphors based on $Sr_2CeO_4:Eu^{3+}$ or nondoped Sr_2CeO_4 are reported in [9-13], and references therein.

In this study, we analyze $Sr_2CeO_4:Eu^{3+}$ nanopowders, efficiently prepared using a solution combustion synthesis (SCS) method [14,15]. The main characteristics of this process are simplicity and low cost. The structure of prepared materials has been confirmed and characterized using X-ray powder diffraction (XRD), scanning electron microscope (SEM) and photoluminescence (PL) techniques [15]. The most of europium luminescence comes from transitions from the $^5D_0$ and $^5D_1$ state; and they are usually used for fluorescence intensity ratio technique for remote temperature sensing.

In our recent publication [16] we have shown that $Sr_2CeO_4:Eu^{3+}$ made by solution combustion synthesis could be used as a red phosphor. In [15] we have studied the possibility of using the synthesized $Sr_2CeO_4:Eu^{3+}$ for temperature measurements, using usual approach of calculating the calibration curves.

However, availability of more and more fast computers, capable of machine learning, gave us an idea of different approach. Here, we analyze the possibilities of training the computer to recognize optical emission spectra of $Sr_2CeO_4:Eu^{3+}$ at different temperatures. So, this paper describes extension of our work presented in [15].

2. EXPERIMENTAL PROCEDURE

The preparation of samples

Europium doped Sr_2CeO_4 nanopowders were prepared by solution combustion method, similarly as described in [14,15]. Stoichiometric quantities of starting chemicals $Sr(NO_3)_2$, CH_4N_2O, $Ce(NO_3)_3{\times}6H_2O$, and $Eu(NO_3)_3{\times}6H_2O$ with the purity of 99.99% were chosen to obtain the Eu^{3+} concentration in Sr_2CeO_4 of 2.5 at.% ($Sr_{2-0.05}Eu_{0.05}CeO_4$). The used chemicals were purchased from ABCR, and urea, $(NH_2)_2CO$, from Sigma-Aldrich.

The dry mixture of 10.32 g (48.75 mmol) of $Sr(NO_3)_2$, 15.015 g (250 mmol) of CH_4N_2O, 10.86 g (25 mmol) of $Ce(NO_3)_3{\times}6H_2O$ and 0.558 g (1.25 mmol) of $Eu(NO_3)_3{\times}6H_2O$ was combined with the mixture of 4.8 g (60 mmol) of ammonium nitrate and 3.003 g (50 mmol) of urea which were used as organic fuels.

The prepared starting reagents were combusted with the flame burner at approximately 500 °C, yielding a voluminous foamy pink powder in an intensive exotermic reaction. After the solution combustion synthesis, the nanopowder was annealed for 2 hours, in air atmosphere, at 900 °C. The annealing of the material is needed to achieve optimal optical characteristics of synthesized material.

Experimental details

As an excitation source for photoluminescence measurements we used the output of the optical parametric oscillator (Vibrant OPO), continuously tunable over a spectral range from 320 nm to 475 nm. Laser pulse duration is about 5 ns, at a repetition rate of 10 Hz. Time-resolved streak images of the luminescence response of $Sr_2CeO_4:Eu^{3+}$ nanopowder excited by the OPO system were acquired by Hamamatsu streak camera equipped with a spectrograph.

Emission spectra of $Sr_2CeO_4:Eu^{3+}$ were also acquired using Ocean Optics USB2000 and AVANTES AvaSpec 2048TEC USB2 spectrometers and continuous laser diode excitation at 405 nm. The experimental setup for luminescence measurement as a function of temperature is described in [17].

For machine learning simulation experiments we have used Solo software package (Version 8.8, Eigenvector Research Inc, USA).

3. RESULTS AND DISCUSSION

The structure of material was confirmed by XRD patterns and SEM images, see [15].

The streak image of the time resolved photoluminescence spectrum of the $Sr_2CeO_4:Eu^{3+}$ using the 330 nm excitation is presented in Figure 1. Horizontal scale of streak image corresponds to wavelength, vertical scale shows development of spectra in time. Images are presented in pseudocolor, where different colors mean different optical intensities.

The $^5D_1$-$^7F_3$ transition (583 nm), located closely between the $^5D_0$-$^7F_0$ (582 nm) and the $^5D_0$-$^7F_1$ (587 nm) transitions is easy to identify on the time resolved image. Its time integrated peak has a comparable intensity to the intensities of peaks originating from nearby $^5D_0$ levels (see the line profile denoted by a red curve in Fig. 4).

The luminescence spectra presented in publications usually do not have the time resolution, so it is hard to guess which transitions are short lived. Streak image presented in Figure 1 shows clearly that the $^5D_1$-$^7F_3$ transition (583 nm) has a much higher intensity and a much shorter lifetime than nearby transitions from $^5D_0$ state.

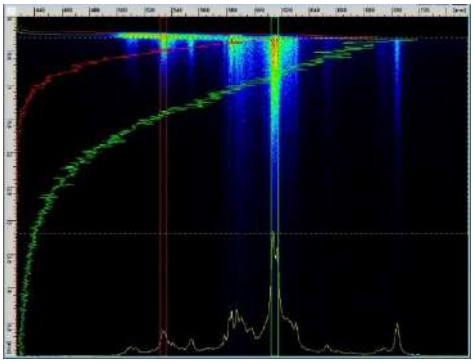

Figure 1 - Streak image of the photoluminescence spectrum of $Sr_2CeO_4:Eu^{3+}$ nanophosphor. (OPO excitation at 330 nm).

The temperature dependency of intensity ratio of spectral lines

The luminescence of samples was measured both using pulsed (OPO) and continuous excitation. The measured luminescence spectra of Eu^{3+} doped Sr_2CeO_4 at various temperatures are presented in Figure 2. The spectra were obtained by using continuous laser diode excitation at 405 nm.

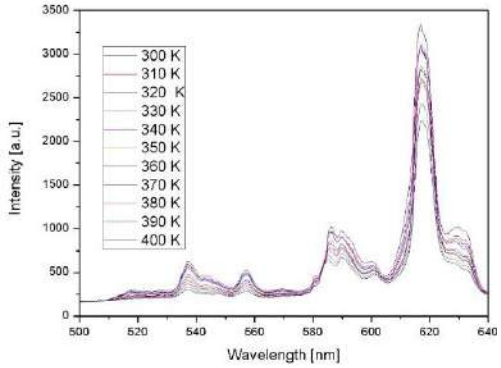

Figure 2 - Luminescence spectra of Eu^{3+} doped Sr_2CeO_4 at various temperatures. (Continuous laser diode excitation at 405 nm).

The fluorescence intensity ratio (FIR) of spectral line intensities from the $^5D_0$ and $^5D_1$ transitions depend on two physical processes: the thermalization of the $^5D_1$ level with rising temperature, where the energy difference to populate the $^5D_1$ level from the $^5D_0$ level is fully covered by phonons; and the nonradiative quenching of the $^5D_0$ and $^5D_1$ levels through the charge transfer state. Looking at Figure 2 we can see that intensity ratio between lines at 614 nm and 537 nm is temperature dependent.

The Principal Component Analysis of temperature dependent $Sr_2CeO_4:Eu^{3+}$ spectra

Principal component analysis (PCA) finds combinations of variables, or *factors*, that describe major trends in the data [18].

If X is a data matrix with *m* rows and *n* columns, each variable being a column and each sample a row, PCA decomposes X as the sum of rt_i and p_i, where *r* is the rank of the matrix X:

$$\boldsymbol{X} = \boldsymbol{t_1 p^T}_1 + \boldsymbol{t_2 p^T}_2 + ... + \boldsymbol{t_k p^T} k + ... + \boldsymbol{t r p^T} r$$

where $r \leq \min\{m,n\}$

The t_i, p_i pairs are ordered by the amount of variance captured. The t_i vectors are known as scores and contain information on how the samples relate to each other. The p_i vectors are known as loadings and contain information on how the variables relate to each other.

For analysis presented here, we use luminescence spectra of Eu^{3+} doped Sr_2CeO_4 at temperatures between 300 and 400 K, measured with the step of 5 K. About a half of the spectral data (measured at 300, 310, 320 ... K) are used to train the PCA algorithm. Another half of the spectral data (measured at 305, 315, 325 .... K) are used to test the obtained PCA model.

Scores on first two principal components of measurement data of temperature dependence of luminescence of $Sr_2CeO_4:Eu^{3+}$ nanophosphor are shown in Figure 3. It could be seen that scores on PC 1 gradually move along the x axis, while scores on PC 2 oscillate along the y axis.

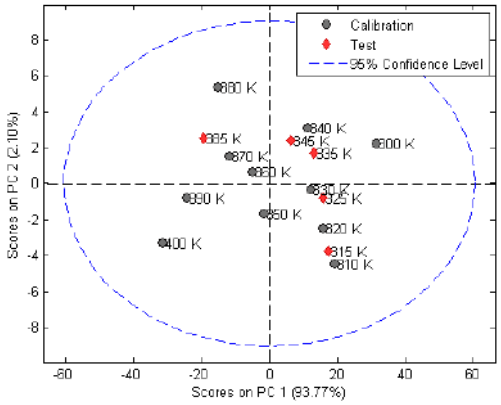

Figure 3 - Scores on first two principal components of measurement data of temperature dependence of luminescence of $Sr_2CeO_4:Eu^{3+}$ nanophosphor.

We see that the predictions for future measurements are well within the 95% confidence level. However, it should be noted that this approach is different, and not necessarily better, than usual method based on fitting the temperature sensing calibration curve. Namely, the machine is trained on restricted size of training data set. The remote temperature estimation is based on classification of newly obtained data in regard the calibrated data. The classification is implemented by comparing the scores distances between the calibrated data and the newly measured ones. So, the larger the training set, the better is resolution of the remote temperature sensing.

4. CONCLUSION

In this paper we have applied the Principal Component Analysis, the basic machine learning algorithm, on temperature dependent Sr_2CeO_4:Eu^{3+} spectral data. We have shown that the machine could be trained to differentiate spectral data obtained on different temperatures. However, the resolution of this remote temperature sensing technique depends on the size of spectral data training set. For relatively small training set, the predicted data are well within the confidence level of 95 %.

5. ACKNOWLEDGEMENT

This work was financially supported by funding provided by the Institute of Physics Belgrade, through the grant by the Ministry of Education, Science, and Technological Development of the Republic of Serbia.

REFERENCES

[1] Uskokovic V, Nanoscience: Whence it entered our World, *Tehnika*, Vol. 22, pp 795-803, 2013.

[2] Jaque D, Vetrone F, Luminescence nanothermometry, *Nanoscale*, Vol. 4, pp 4301-4326, 2012.

[3] Brites C. D. S, Lima P. P, Silva N. J. O, Millan A, Amaral V. S, Palacio F, Carlos L. D, Thermometry at the nanoscale, *Nanoscale*, Vol. 4, pp. 4799-4829, 2012.

[4] Aldén M, Omrane A, Richter M, Särner G, Thermographic phosphors for thermometry: A survey of combustion applications, *Progress in Energy and Combustion Science*, Vol. 37, pp. 422-461, 2011.

[5] Allison S. W, Gillies G. T, Remote thermometry with thermographic phosphors: Instrumentation and applications, *Rev. Sci. Instrum*, Vol. 68, pp 2615-2650, 1997.

[6] Goss L. P, Smith A. A, Post M. E, Surface thermometry by laser-induced fluorescence, *Rev Sci. Instrum*, Vol. 60, pp 3702-3706, 1989.

[7] Heyes A. L, On the design of phosphors for high-temperature thermometry, *Journal of Luminescence*, Vol. 129, pp 2004-2009, 2009.

[8] Ristic S, Polic S, Knjezevic D, Radojkovic B, Linic S, Jegdic B, Termografija u kontroli efikasnosti i bezbednosti laserskog čišćenja, *Tehnika*, Vol. 28, pp 623-629, 2019.

[9] Stefanski M, Marciniak L, Hreniak D, Strek W, Size and temperature dependence of optical properties of Eu^{3+}:Sr_2CeO_4 nanocrystals for their application in luminescence thermometry, *Mat. Res. Bull.*, Vol. 76, pp 133–139, 2016.

[10] Shi L, Zhang H, Li C, Su Q., Eu^{3+} doped Sr_2CeO_4 phosphors for thermometry: single-color or two-color fluorescence based temperature characterization, *RSC Advances*, Vol. 1, pp. 298–304, 2011.

[11] Suresh K, Poornachandra Rao N. V, Murthy K. V. R, Photoluminescent properties of Sr_2CeO_4:Eu^{3+} and Sr_2CeO_4: Eu^{2+}phosphors suitable for near ultraviolet excitation, *Bull. Mater. Sci.*, Vol. 37, pp 1191–1195, 2014.

[12] Stefanski M, Lukaszewicz M, Hreniak D, Strek W, Laser induced white emission generated by infrared excitation from Eu^{3+}: Sr_2CeO_4 nanocrystals, *Jour. Chem. Phys.*, Vol. 146, pp 104705-1-7, 2017.

[13] Stefanski M, Marciniak L, Hreniak D, Strek W, Influence of grain size on optical properties of Sr_2CeO_4 nanocrystals, *Jour. Chem. Phys.*, Vol. 142, pp 184701-1-7, 2015.

[14] Rabasovic M. S, Sevic D, Krizan J, Terzic M, Mozina J, Marinkovic B. P, Savic Sevic S, Mitric M, Rabasovic M. D, Romcevic N, Characterization and luminescent properties of Eu^{3+} doped $Gd_2Zr_2O_7$ nanopowders, *J. Alloys and Compounds* Vol. 622, pp 292-295, 2015.

[15] Vlasic A, Sevic D, Rabasovic M. S, Krizan J, Savic-Sevic S, Rabasovic M. D, Mitric M, Marinkovic B. P, Nikolic M. G, Effects of temperature and pressure on luminescent properties of Sr_2CeO_4: Eu^{3+} nanophosphor, *Journal of Luminescence*, Vol. 199 pp 285–292, 2018.

[16] Rabasovic M. S, Krizan J, Gregorcic P, Rabasovic M. D, Romcevic N, Sevic D, Time-resolved luminescence spectra of Eu^{3+} doped YVO_4, Sr_2CeO_4 and $Gd_2Zr_2O_7$ nanopowders, *Optical and Quantum Electronics*, Vol. 48, pp163-1-4, 2016.

[17] Rabasovic M. D, Muric B. D, Celebonovic V, Mitric M, Jelenkovic B. M, Nikolic M. G, Luminescence thermometry via the two-dopant intensity ratio of Y_2O_3:Er^{3+}, Eu^{3+}, J. *Phys. D: Appl. Phys*., Vol. 49, pp 485104-1-6, 2016.

[1] Hoteling H, Analysis of a Complex of Statistical Variables into Principal Components. *Journal of Educational Psychology*, Vol. 24, 417-441, 1933.

REZIME

TEMPERATURNA ZAVISNOST LUMINESCENTNIH OSOBINA SR_2CEO_4:EU^{3+} NANOFOSFORA: PRISTUP MAŠINSKIM UČENJEM

U ovom radu analizirali smo mogućnosti primene Sr_2CeO_4:Eu^{3+}nanopraha za merenje temperaruture primenom mašinskog učenja. Materijal je pripremljen jednostavnom metodom sinteze sagorevanja rastvora. Fotoluminescentna tehnika je korišćena za merenje temperaturne zavisnosti optičke emisije pripremljenog materijala. Analiza ključnih faktora omogućila nam je uvid u temperaturnu zavisnost spektralnih podataka sa drugačije tačke gledišta nego što je uobičajeni pristup.

Ključne reči: *fotoluminescencija, novi materijali, termografski fosfori*